FEDERAL UNIVERSITY OF SANTA CATARINA
DEPARTMENT OF MECHANICAL ENGINEERING
GRADUATE PROGRAM IN MECHANICAL ENGINEERING

Rafael Franklin Lázaro de Cerqueira

Experimental and Numerical Investigation of Gas-liquid Flows in the Presence of Taylor and Dispersed Bubbles

Florianópolis-SC, Brasil
2020

Rafael Franklin Lázaro de Cerqueira

Experimental and Numerical Investigation of Gas-liquid Flows in the Presence of Taylor and Dispersed Bubbles

Thesis submitted to the Graduate Program in Mechanical Engineering at the Federal University of Santa Catarina for the degree of Doctor in Mechanical Engineering.
Orientador: Prof. Emilio Ernesto Paladino, Dr.

Florianópolis-SC, Brasil

2020

Ficha de identificação da obra elaborada pelo autor,
através do Programa de Geração Automática da Biblioteca Universitária da UFSC.

Lázaro de Cerqueira, Rafael Franklin
Experimental and Numerical Investigation of Gas-liquid Flows in the Presence of Taylor and Dispersed Bubbles / Rafael Franklin Lázaro de Cerqueira ; orientador, Emilio Ernesto Paladino, 2020.
422 p.

Tese (doutorado) - Universidade Federal de Santa Catarina, Centro Tecnológico, Programa de Pós-Graduação em Engenharia Mecânica, Florianópolis, 2020.

Inclui referências.

1. Engenharia Mecânica. 2. Slug flow. 3. Bubbly flow. 4. CFD. 5. PIV. I. Paladino, Emilio Ernesto . II. Universidade Federal de Santa Catarina. Programa de Pós Graduação em Engenharia Mecânica. III. Título.

Rafael Franklin Lázaro de Cerqueira

Experimental and Numerical Investigation of Gas-liquid Flows in the Presence of Taylor and Dispersed Bubbles

O presente trabalho em nível de Doutorado foi avaliado e aprovado por banca examinadora composta pelos seguintes membros:

Prof. Oscar M. H. Rodriguez, Dr. Eng.
Escola de Engenharia de São Carlos da Universidade de São Paulo

Prof. Jader Riso Barbosa Jr., Ph.D.
Universidade Federal de Santa Catarina

Prof. Julio Cesar Passos, Dr.
Universidade Federal de Santa Catarina

Prof. César José Deschamps, Ph.D.
Universidade Federal de Santa Catarina

Certificamos que esta é a **versão original e final** do trabalho de conclusão que foi julgado adequado para obtenção do título de Doutor em Engenharia Mecânica.

Documento assinado digitalmente
Paulo de Tarso Rocha de Mendonca
Data: 14/10/2020 17:32:36-0300
CPF: 149.822.691-49

Prof. Paulo de Tarso R. de Mendonça, Dr.
Coordenador do Programa

Documento assinado digitalmente
Emilio Ernesto Paladino
Data: 13/10/2020 14:15:28-0300
CPF: 006.446.479-22

Prof. Emilio Ernesto Paladino, Dr.
Orientador

Florianópolis-SC, Brasil, 2020.

Este trabalho é dedicado a todos aqueles que acreditam
em uma sociedade mais justa.

Acknowledgements

First, I would like to thank my supervisor Dr. Emilio Paladino for his support and guidance throughout this work and also throughout my academic trajectory.

I would like to thank my love Lilian, who always encouraged me to pursue a doctoral degree and supported all my decisions.

I would also like to thank my friends Celso, Dani, Pedro, Pietro, Camila and Gabi, who I shared great moments (and a couple of beers) every Friday at Bar do Alex, later Juliano (the best "pastel de queijo com carne" from Córrego Grande) and occasionally Silvinho (place of the famous "pão com bolinho") during the last years.

I would also to thank my colleagues at SINMEC lab, with whom I had fruitful conversations and nice laughs during the last years.

Additionally, I would like to thank Prof. Clovis R. Maliska and Tatiane Schveitzer for welcoming me back in 2003 when I joined SINMEC lab.

I would also like to thank Prof. Berend van Wachem, Dr. Fabian Denner and Dr. Fabien Ervrad for the sharing the MultiFlow code, for the support during my stay at Otto-von-Guericke Universität in Magdeburg and for providing computational infrastructure.

Também gostaria de agradecer aos meus pais, Tereza e Mineiro, e minha irmã Maria Luísa e toda família Lázaro/Cerqueira pelo suporte durante todo o trabalho.

Agradeço também aos meus sogros, Inês e Haroldo, por todo auxílio dado a mim e a Lilian nos últimos anos.

Agradeço também por todo o investimento em ciência e tecnologia realizado durante as administrações dos governos Lula e Dilma, que forneceu grande parte da infraestrutura necessária para realização da presente tese de doutorado.

To PETROBRAS for the doctoral scholarship through the Human Resources Formation Program – PFRH 009 and by CAPES – Coordination for the Improvement of

Higher Education Personnel, through the call: Doctorate PDSE - Call No. 47/2017.

To the National Laboratory for Scientific Computing (LNCC/MCTI, Brazil) for providing HPC resources of the SDumont supercomputer, which have contributed in part of the results reported within this paper.

RESUMO

Escoamentos multifásicos desempenham um papel importante em processos industriais, especialmente na indústria química e de petróleo. Escoamentos desse tipo podem ocorrer em linhas horizontais, verticais e inclinadas, abrangendo inúmeras áreas e processos de engenharia, como por exemplo o projeto de equipamentos para transporte de fluidos, sistemas de medição em linhas, produção de petróleo e gás, sistemas de arrefecimento, etc. Em geral, escoamentos bifásicos líquido-gás podem apresentar diferentes padrões, afetando de modo complexo a sua hidrodinâmica e também a transferência de calor e de massa. Devido à complexidade dos diferentes padrões de escoamento presentes em situações reais, um grande esforço é dedicado a melhor compreensão de escoamentos bifásicos líquido-gás, em especial aqueles com diferentes escalas de interface. Nos últimos anos, a fluidodinâmica computacional (*Computational Fluid Dynamics*, CFD em inglês) tornou-se uma ferramenta importante, permitindo uma análise detalhada dos mecanismos físicos que regem o fenômeno. O objetivo do presente trabalho consiste em um estudo numérico e experimental em escoamentos gás-líquido com diferentes escalas de interface. O estudo será realizado a partir da análise de um escoamento bifásico do tipo pistonado (*slug*, em inglês) manufaturado, produzido a partir da injeção independente de bolhas de Taylor e bolhas dispersas em uma corrente de líquido. Desse modo, em um mesmo domínio é possível produzir, de forma controlada, um escoamento bifásico com diferentes escalas de interface. Para o estudo experimental foram desenvolvidas técnicas experimentais e de processamento de imagem para caracterização experimental do escoamento através das técnicas de PIV (Particle Image Velocimetry) e de filmagem por câmera rápida, permitindo uma análise detalhada dos fenômenos de interação entre as diferentes escalas de interface. Além disso, foi realizada a implementação de um modelo de CFD multi-escala baseado no acoplamento entre o método *Volume-of-Fluid* (VOF) e *Discrete Bubble Method* (DBM), sendo o primeiro utilizado para modelagem da interface de grande escala e o último para as bolhas dispersas. O modelo VOF-DBM desenvolvido foi utilizado para a realização de um estudo numérico em escoamentos bifásico com diferentes escalas de interface.

Palavras-chave: Escoamento pistonado, Escoamento borbulhado, CFD, PIV.

RESUMO EXPANDIDO

Introdução

Escoamentos multifásicos são escoamentos com a presença de mais de uma fase, presentes em quase todas áreas da engenharia, em especial na indústria petrolífera e no setor energético. O foco do presente trabalho são sistemas gás-líquido, precisamente escoamentos bifásicos líquido-gás. Escoamentos desse tipo podem ocorrer em linhas horizontais, verticais e inclinadas, abrangendo inúmeras áreas e processos de engenharia, como por exemplo o projeto de equipamentos para transporte de fluidos, sistemas de medição em linhas, produção de petróleo e gás, sistemas de arrefecimento, etc. Devido à complexidade dos diferentes padrões de escoamento presentes em situações reais, um grande esforço é dedicado a melhor compreensão de escoamentos bifásicos líquido-gás. A fluidodinâmica computacional (*Computational Fluid Dynamics*, CFD em inglês) é uma ferramenta que permite uma análise detalhada dos mecanismos físicos que regem o fenômeno. Para aplicações industriais, em sistemas que incluem interfaces de pequena escala, modelos baseados em médias devem ser utilizados, uma vez que é inviável do ponto de vista do custo computacional desenvolver simulações "diretas" da dinâmica das interfaces, isto é, capturando a posição instantânea das interfaces. Por outro lado é comum a aplicação de modelos de captura de interfaces, como *Volume-of-Fluid* (VOF) e *Level-set*, para casos em que as interface são de grande escala e, assim, estas podem ser capturadas com um custo computacional razoável. De forma geral, estes estudos consideram escoamentos multifásicos simples, considerando escoamentos com morfologias de interface simples, como escoamentos estratificados e bolhas, de tamanho comparável com as escalas do domínio (como bolhas de Taylor, por exemplo). Entretanto, em muitas aplicações interfaces com diferentes escalas de comprimento estão presentes no domínio de cálculo. Dentro desse contexto, analisando o fenômeno a partir de uma abordagem numérica, as diferentes escalas de comprimento de uma interface podem ser caracterizadas a partir de um comprimento de referência da malha computacional, utilizada para discretizar o domínio físico. Assim, costuma-se caracterizar uma interface como sendo de grande escala quando o modelo numérico consegue capturar a interface a partir uma malha computacional praticável, como por exemplo no escoamento de uma bolha de gás ascendendo em um meio contínuo. Entretanto, quando a interface não pode ser capturada através de uma malha computacional praticável, diz-se que a escala possui pequena escala, como em um escoamento do tipo bolha dispersas (ou *bubbly flow*). Em virtude dos motivos citados nas seções anteriores, em muitas situações

de aplicação de CFD em escala industrial, é necessário a utilização de modelos numéricos mais sofisticados e capazes de lidar com essa diferença de escala da interface.

Objetivos

O objetivo geral deste trabalho é o estudo experimental e numérico de um escoamento bifásico com diferentes escalas de interface. Para tal, foi estudado o padrão de escoamento manufaturado pistonado "quasi-real" (*"quasi-real" slug flow*), produzido a partir da injeção independente de bolhas de Taylor e bolhas dispersas em uma corrente de líquido. Em virtude do caráter numérico e experimental do trabalho, os objetivos podem ser divididos em duas categorias, uma relacionada ao estudo experimental e outra ao desenvolvimento, validação e aplicação de um modelo numérico CFD multi-escala. Para a caracterização experimental de escoamentos bifásicos com diferentes interfaces escalas de comprimento, os objetivos específicos são: i) análise da modificação na estrutura do escoamento devido à adição de bolhas dispersas em escoamentos verticais em regime laminar e turbulento; ii) realização de um estudo detalhado da interação entre os diferentes comprimentos de interface escalas em escoamentos gás-líquido na presença de Taylor e bolhas dispersas e iii) geração de dados experimentais para validação de modelos numéricos multi-escala CFD multidimensionais. No âmbito numérico, os objetivos específicos são: i) desenvolvimento de um modelo CFD para modelagem de escoamentos bifásicos com diferentes escalas de comprimento de interface baseadas no acoplamento dos métodos DBM (*Discrete Bubble Model*) e VOF e ii) análise da capacidade do modelo CFD multidimensional e multi-escala na reprodução dos resultados experimentais.

Metodologia

Devido à complexidade das diferentes morfologias de escoamento encontradas em escoamentos bifásicos reais, grande esforço é dedicado para melhor compreensão dos escoamentos bifásicos gás-líquido, com morfologias de fase e escalas de comprimento interfacial diferentes no mesmo domínio de escoamento. Estas podem vir através de investigações experimentais, que buscam caracterização detalhada do escoamento por meio de diferentes métodos e técnicas, e também, por meio de estudos numéricos multidimensionais detalhados. Seguindo essas duas abordagens, o presente trabalho realizou um estudo experimental e numérico de escoamentos gás-líquido com diferentes escalas de comprimento de interface, visando à caracterização e melhor compreensão das interações entre as diferentes

escalas de comprimento de interface. Desse modo, a tese focou no estudo de um padrão de escoamento manufaturado, produzido a partir da injeção independente de bolhas de Taylor e bolhas dispersas em uma corrente de líquido. A partir dessa abordagem, foi possível estudar um escoamento semelhante ao padrão pistonado (*slug flow*) real, onde coexistem interfaces gás-líquido com diferentes escalas de comprimento, em condições controladas. A utilização de um padrão de escoamento manufaturado permitiu o controle das velocidades superficiais do gás e do líquido, o comprimento das bolhas de Taylor e a quantidade de bolhas dispersas presentes no escoamento. A caracterização experimental de escoamentos bifásicos gás-líquido é uma tarefa desafiadora, uma vez que a presença das interfaces interfere no processo de medição e um esforço adicional é necessário para contornar esses problemas. Em particular, a aplicação da técnica de Velocimetria por Imagem de Partículas (*Particle Image Velocimetry*, PIV em inglês), a principal técnica experimental utilizada na presente tese, para caracterização de escoamentos gás-líquido exige medidas adicionais para a aquisição de campos de velocidade consistentes. Assim, o presente trabalho apresenta um novo método de discriminação das fases gás-líquido em imagens PIV, permitindo a utilização da técnica em escoamentos borbulhados (*bubbly flows*) com elevadas frações de vazio. Em conjunto, o presente trabalho apresenta uma técnica de Velocimetria por Rastreamento de Partículas (*Particle Tracking Velocimetry*, PTV em inglês) que permite a caracterização experimental da fase gás a partir do rastreio individual das bolhas dispersas em filmagens obtidas com uma câmera de alta velocidade. Na implementação da técnica PTV utilizada no presente trabalho, a detecção das bolhas dispersas e a posterior reconstrução do seus formatos é realizada através de um método baseado em Redes Neurais Convolucionais (CNN). Para a caracterização do escoamento ao redor das bolhas de Taylor, técnicas de processamento de imagem também são aplicadas em conjunto com o PIV para obtenção de campos de velocidade média. Um sistema de sincronização foi desenvolvido para permitir a caracterização detalhada do escoamento ao redor da cauda e do nariz das bolhas de Taylor. Além disso, técnicas adicionais de processamento de imagem, baseados nas filmagens em câmera rápida, permitiram a obtenção da velocidade terminal das bolhas de Taylor e a reconstrução do perfil do nariz das bolhas. No âmbito numérico, um modelo CFD tridimensional multiescala foi implementado no código de CFD *MultiFlow* para a simulação de escoamento bifásico gás-líquido com diferentes escalas de comprimento de interface. O modelo numérico foi desenvolvido a partir do acoplamento entre o método VOF e o DBM, incorporando uma abordagem física consistente para modelagem das interações entre bolhas dispersas e as interfaces de grande escala. Além da implementação do modelo VOF-DBM multiescala, os métodos VOF e DBM foram verificados de forma independente por meio da comparação dos resultados

numéricos com dados experimentais.

Resultados e discussões

O primeiro estudo da análise da modificação na estrutura do escoamento devido à adição de bolhas dispersas em escoamentos verticais em regime laminar e turbulento mostram que a presença de bolhas altera o perfil de velocidade média e flutuações turbulentas em escoamentos verticais em regime laminar e turbulento. No regime laminar, observa-se que as bolhas dispersas modificam o perfil de velocidades parabólico monofásico para um perfil mais "achatado" e induzem flutuações nas estatísticas turbulentas. Para escoamentos em regime turbulento, as bolhas dispersas induzem um perfil de velocidade mais próximo do parabólico e provocam um aumento da intensidade turbulenta. O estudo experimental buscando analisar o efeito das bolhas dispersas na estrutura do escoamento ao redor de bolhas de Taylor indicou que as pequenas escalas de interface modificam o escoamento ao redor da cauda e do nariz das bolhas de Taylor. Em especial, a velocidade terminal das bolhas de Taylor é afetada pela fração de vazio relativa as bolhas dispersas. Observou-se também uma relação entre o movimento oscilatório e deformação do nariz da bolha de Taylor e o aumento da velocidade terminal. O estudo numérico de um escoamento simplificado na presença de bolhas de Taylor e dispersas a partir do modelo multiescala tridimensional VOF-DBM implementado mostram que a fração de vazio influencia na velocidade terminal e no escoamento ao redor das bolhas de Taylor. Uma verificação experimental foi realizada a partir resultados experimentais produzidos neste trabalho. Para escoamentos borbulhados e também ao redor de bolhas de Taylor (sem a presença de bolhas dispersas) o modelo CFD resultou em uma boa concordância entre os resultados experimentais e numéricos. A comparação entre os resultados do modelo VOF-DBM implementado os resultados experimentais do escoamento pistonado manufaturado mostraram que o modelo numérico é capaz de reproduzir o efeito da fração de vazio das bolhas dispersas na velocidade terminal e o movimento oscilatório do nariz. Entretanto, os resultados numéricos não foram capazes de reproduzir o escoamento na região posterior das bolhas de Taylor.

Conclusões

O presente trabalho realizou um estudo experimental e numérico em escoamentos bifásicos gás-líquido com diferentes escalas de interface. Para tal, foi realizada a análise deum

padrão de escoamento manufaturado pistonado "quasi-real" (*"quasi-real" slug flow*), produzido a partir da injeção independente de bolhas de Taylor e bolhas dispersas em uma corrente de líquido. Em função das dificuldades associadas a caracterização experimental do escoamento manufaturado, em especial relacionadas a quantificação da interação entre as diferentes escalas de interface, foi necessário o desenvolvimento de novas técnicas e aparatos experimentais, destacando-se um método quer permite a utilização da técnica PIV em escoamentos borbulhados e na presença de bolhas de Taylor e uma técnica de PTV baseado em ferramentas de aprendizado profundo de máquina. O estudo experimental revelou que a presença de bolhas dispersas altera a estrutura do escoamento ao redor das bolhas de Taylor, em especial na região da cauda da bolha de Taylor, resultando em modificações no campo de velocidade médio e nas estatísticas turbulentas. Foi também implementado um modelo numérico multidimensional multiescala a partir do acoplamento dos métodos VOF e DBM. De acordo com os resultados numéricos obtidos, o modelo VOF-DBM é capaz de reproduzir parte das modificações introduzidas pela presença das bolhas dispersas observadas experimentalmente.

Palavras-chave: Escoamento pistonado, Escoamento borbulhado, CFD, PIV.

ABSTRACT

Multiphase flows play an important role in natural and industrial processes, especially in the chemical and oil industry. This sort of flow can occur in horizontal, vertical and inclined pipelines and equipment as separators, heat exchangers, pumps, valves, etc., covering numerous areas and engineering processes. In general, two-phase liquid-gas flows can present different geometric arrangements or morphologies. Due to the complexity of the different flow patterns present in real situations, great effort is devoted to a better understanding of liquid-gas two-phase flows, especially those with different interface scales. In recent years, Computational Fluid Dynamics (CFD) has become an important tool, allowing a detailed analysis of the physical mechanisms that govern multiphase flows. The objective of the present work consists of a numerical and experimental study on gas-liquid flows with different interface scales. Thus, the manufactured "quasi-real" slug flow regime, similar to the slug flow is studied, through the independent injection of Taylor bubbles in a bubbly flow stream. Through this manufactured flow regime, it is possible to reproduce, in a controlled way, a two-phase flow with different interface scales. For the experimental study, novel image processing techniques and apparatus were developed for the flow characterization through the Particle Image Velocimetry (PIV) and high-speed camera techniques, allowing a detailed analysis of the interaction phenomena between the different interface scales. In addition, a multi-scale CFD model was implemented based on the coupling between the Volume-of-Fluid (VOF) and Discrete Bubble Method (DBM), with the first being used for modelling the large-scale interface and the last for the small dispersed bubbles. The developed VOF-DBM model was used to perform a numerical study on two-phase flows with different interface scales.

Keywords: Slug flow, Bubbly flow, CFD, PIV.

RELATED PUBLICATIONS

The following publications resulted from this thesis:

Articles in indexed journals

1. **CERQUEIRA, R. F. L**. et al. Image processing techniques for the measurement of two-phase bubbly pipe flows using particle image and tracking velocimetry (PIV/PTV). *Chemical Engineering Science*, v. 189, p. 1-23, 2018.
2. **CERQUEIRA, R. F.L.** et al. Experimental apparatus and flow instrumentation for the investigation of a quasi-real slug flows in vertical ducts. *Experimental Thermal and Fluid Science*, v. 102, p. 421-451, 2019.
3. **CERQUEIRA, R. F.L.** and PALADINO, E. E., Experimental study of the flow structure around Taylor bubbles in the presence of dispersed bubbles. *International Journal of Multiphase Flow*, v. 133, p. 103450, 2020.
4. **CERQUEIRA, R. F. L.** and PALADINO, E.E. Development of a Deep Learning-based Image Processing Technique for Bubble Pattern Recognition and Shape Reconstruction in Bubbly Flows. *Chemical Engineering Science,* v. 230, p. 116163, 2021.

Articles in preparation for indexed journals

1. **CERQUEIRA R. F.L.**, PALADINO E. E., EVRARD D., DENNER F. and VAN WACHEM, B.G.M, Multiscale modeling and validation of slug flow with small dispersed bubbles. In preparation for *International Journal of Multiphase Flows*, 2021.
2. **CERQUEIRA R. F.L.**, PALADINO E. E., EVRARD D., DENNER F. and VAN WACHEM, B.G.M, Numerical modeling of quasi-real slug flows in air-water systems. In preparation, 2020.

Prizes and Awards

1. **BEST POSTER AWARD – R. F. L. CERQUEIRA**, E. E. PALADINO, and C. R. MALISKA. Development of high-speed image processing techniques for the study of gas-liquid flows with different interfacial length scales in vertical ducts. In:

16th Multiphase Flow Conference and Short Course: Simulation, Experiment and Application, Dresden-Germany, 2018.

Full papers and abstracts in conference proceedings

1. **R. F. L. CERQUEIRA**, F. EVRARD, F. DENNER, B. G. M. VAN WACHEM, and E. E. PALADINO. Implementation and validation of a CFD model for two-phase gas-liquid flows with different interface length scales. In: *Proceedings of the 10th International Conference on Multiphase Flow*, Rio de Janeiro-RJ-Brazil, 2019.
2. E. E. PALADINO, **R. F. L. CERQUEIRA**, and C. R. MALISKA. Experimental investigation of the flow structure around taylor bubbles in the presence of dispersed bubbles in vertical ducts. In *16th Multiphase Flow Conference and Short Course: Simulation, Experiment and Application*, Dresden-Germany, 2018.
3. Y. A. S. FERNANDES, **R. F. L. CERQUEIRA**, E. E. PALADINO, and C. R. MALISKA. Deep learning techniques applied to the measurement of two-phase bubbly pipe flows using particle image velocimetry. In: *16th Multiphase Flow Conference and Short Course: Simulation, Experiment and Application*, Dresden-Germany, 2018.
4. E. E. PALADINO, **R. F. L. CERQUEIRA**, and C. R. MALISKA. Development of a particle tracking velocity measurement technique for the study of gas-liquid flows with different interfacial length scales in vertical pipes. In: *17th Brazilian Congress of Thermal Sciences and Engineering - ENCIT 2018*, Aguas de Lindoia-SP-Brazil, 2018.
5. **R. F. L. CERQUEIRA**, E. E. PALADINO, B. K. YNUMARU, and C. R. MALISKA. Development of a dynamic masking procedure for the taylor bubble identification in the piv/lif tecnhique application for slug flow. In: *17th Brazilian Congress of Thermal Sciences and Engineering - ENCIT 2018*, Aguas de Lindoia-SP-Brazil, 2018.
6. **R. F. L. CERQUEIRA**, E. E. PALADINO, and B. K. YNUMARU. A novel robust technique for the measurement of liquid phase velocity in two-phase bubbly flows using particle image velocimetry. In: *V Journeys in Multiphase Flows (JEM 2017)*, Sao Paulo-Brazil, 2017.
7. **R. F. L. CERQUEIRA**, E. E. PALADINO, R. BRITO, and C. R. MALISKA. Development of an experimental apparatus and measurement techniques for the study of quasi-real slug-flow in vertical ducts. In: *Proceedings of the 9th International Conference on Multiphase Flow*, Firenze-Italy, 2016.

8. E. E. PALADINO, **R. F. L. CERQUEIRA**, R. BRITO, C. R. MALISKA, and C. MENEGHINI. Experimental investigation of the flow structure around taylor bubbles in vertical ducts in the presence of dispersed bubbles. In: *Proceedings of the 9th International Conference on Multiphase Flow*, Firenze-Italy, 2016.

List of Figures

List of Tables

List of Abbreviations and Acronyms

BSD	Bubble Size Distribution
CCD	Charge-Coupled Device
CNN	Convolutional Neural Network
DBM	Discrete Bubble Model
DEM	Discrete Element Model
DPM	Discrete Particle Model
FFT	Fast Fourier Transform
FPS	Frames per Second
FRF	Fixed Frame of Reference
FTT	Flow Through Time
HFA	Hot Film Anemometry
LDP	Laser-Diode Photocell
LDR	Light Dependent Resistor
LDV	Laser Doppler Velocimetry
LDA	Laser Doppler Anemometer
LE	Lagrangian-Eulerian
LED	Light-Emitting Diode
LES	Large Eddy Simulation
LIF	Laser-Induced Fluorescence

MFR	Moving Frame of Reference
MUSIG	MUltiple-SIze-Group
PDE	Partial Differential Equation
PDF	Probability Density Function
PFBI	Planar Fluorescence for Bubble Imaging
PIV	Particle Image Velocimetry
PID	Proportional-Integral-Derivative
PTV	Particle Tracking Velocimetry
PST	Pulsed Shadowgraphy Technique
RANS	Reynolds-Averaged Navier-Stokes
ReLU	Rectified Linear Units
SNR	Signal-to-Noise Ratio
SIT	Shear-Induced Turbulence
SGS	Subgrid-scale
TFM	Two-Fluid Model
TTL	Transistor-Transistor Logic
VFD	Variable Frequency Drive
VOF	Volume-of-Fluid

List of Symbols

A_{duct}	Transverse area of the duct, m^2
$a_{b,i}$	Minor of an i-th dispersed bubble in the DBM, m
A_{ij}	Sub-grid scale model variable
$b_{b,i}$	Major of an i-th dispersed bubble in the DBM, m
B_{β}	Sub-grid scale model variable
C_f	Courant number
C_{VM}	Virtual mass coefficient
C_L	Lift coefficient
C_D	Drag coefficient
C_{wl}	Wall lubrication coefficient
C_{LSI}	Large-Small scale collision force sensitivity in the VOF-DBM coupled framework
C_{SIT}	Sub-grid scale model constant
D	Internal pipe diameter, m
d_b	Dispersed bubble diameter, m
$d_{b,i}$	Dispersed bubble diameter of an i-th dispersed bubble in the DBM, m
$d_{\perp b,i}$	Major axis diameter of an i-th dispersed bubble in the DBM, m
Eo	Eötvös number
$Eo_{\perp}$	Eötvös number based on the major axis buble diameter in the DBM

$\boldsymbol{f}_{\sigma}$	Surface tension force, Nm^{-3}
$\boldsymbol{f}_{b,i}^{b}$	Buyonacy forces acting in a i-th dispersed bubble in the DBM, N
$\boldsymbol{f}_{b,i}^{h}$	Continuous fluid-bubble interaction forces acting in a i-th dispersed bubble in the DBM, N
$\boldsymbol{f}_{b,ij}^{c}$	Collisional forces acting in a i-th dispersed bubble in the DBM, N
$\boldsymbol{f}_{b,i}^{wl}$	Wall lubrication force in the DBM, N
$\boldsymbol{f}_{DBM}$	DBM-liquid phase momentum coupling term, $Nm^{-}3$
$\boldsymbol{f}_{col,LSI}$	Large-Small scale interface collision force in the VOF-DBM coupled framework, N
Fr	Froude number
I	Number of PIV interrogation window in a given direction
$I_{\text{def.}}^{\text{nose}}$	Nose deformation index calculated from the high-speed camera images
I_{diff}	Approximate ratio of the total bubble occupied area of the reconstructed bubbles in relation to the "ground truth" reference in a bubbly flow image.
g	Gravitational acceleration, ms^{-2}
H_0	Initial height of a bubble column, m
H_f	Increased bubble column height due to the injected gas flow, m
j_l	Superficial liquid velocity, ms^{-1}
j_g	Superficial gas velocity, ms^{-1}
k_1	Taylor bubble terminal velocity constant rising in a stagnant column
k	Turbulent kinetic energy, m^2s^{-2}
K_i	Collisional stiffness of an i-th dispersed bubble in the DBM, Nm^{-1}
$\boldsymbol{l}_{1,2}$	Ellipses major (1) and minor (2) axes, m
L	Domain length, m
L_{LDP}	Distance between two LDP sensors, m
L_{tb}	Taylor bubble length, m

$\mathrm{Mat_{PIV}}$	Probability occurrence matrix of the Taylor bubble nose interface from the PIV results
$\mathrm{Mat_{HSC}}$	Probability occurrence matrix of the Taylor bubble nose interface from the HSC results
$\mathrm{Mask_{manual}}$	"Ground truth" of a bubbly flow image.
$\mathrm{Mask_{CNN}}$	"Mask-like" bubbly flow image from the CNN reconstruction method.
$\mathrm{Mask_{diff}}$	Absolute difference between the $\mathrm{Mask_{CNN}}$ and $\mathrm{Mask_{manual}}$ masks.
$\boldsymbol{M}_{kj}$	Closure terms for modeling interfacial transfers in the TFM, Nm^{-3}
Mo	Morton number
N_f	Inverse viscosity number
$N_{\boldsymbol{l}_{1,2}}$	Number of local minimum points in the single bubble image detection
$N_{bubbles}$	Total number of bubbles in a given image frame
$A_{proj.}$	Projected area of a bubble in a given image, m^2
$N_{bubbles}^{total}$	Total number of captured bubbles in a given image frame
N_{frames}	Total number of frames
N_{PIV}	Number of PIV frames in a given experimental acquisition
n_{ij}	Normal interface vector that points from phase i to phase j
$\boldsymbol{n}$	Interface normal vector in the VOF method
$\boldsymbol{n}_{LSI}$	Unit vector normal to the large scale interface
m_{12}^{σ}	Surface tension force term in the jump condition, Nm^{-2}
$m_{b,i}$	Dispersed bubble mass in the DBM, kg
$P_{thresh.}$	PIV/LIF discriminator threshold value
$P_{ellipsoid}$	Ratio between the non-zero elements and the number of elements in a single bubble image candidate
p_i	Internal pressure of the interface in the Young-Laplace equation, Nm^{-2}
p_o	Externa pressure of the interface in the Young-Laplace equation, Nm^{-2}

Q_g	Volumetric gas flow rate, $m^3 s^{-1}$
Q_l	Volumetric liquid flow rate, $m^3 s^{-1}$
R	Internal pipe radius, m
Re	Reynolds number
$r_{b,i}$	Radius of an i-th dispersed bubble in the DBM, m
S_t	Bubble surface area during a collision , m^2
$S_{t-\Delta t}$	Bubble surface before a collision, m^2
S_{sphere}	Surface area of a sphere, m^2
S_{oblate}	Surface area of an oblate spheroid, m^2
t	Time, s
t_{open}	Taylor bubble injection valves opening instant, s
t_{close}	Taylor bubble injection valves closing instant, s
t_{wait}	Taylor bubble injection cycle period, s
$t_{stab.}$	Taylor bubble injection stabilization period, s
$t_{m,n}$	Taylor bubble nose (n=1) and bottom(n=2) detection instant in the m-th LDR probe, s
$\boldsymbol{T}_k$	Stress tensor of a phase k, Nm^{-3}
$\overline{\overline{\boldsymbol{T}}}_k$	Constitutive relations for the stress tensors in the TFM, Nm^{-3}
y_{nose}	Taylor bubble nose radial position, m
$U_{tb,N}$	Taylor bubble nose rising velocity, ms^{-1}
$U_{tb,B}$	Taylor bubble bottom rising velocity, ms^{-1}
$\boldsymbol{u}_m$	Mixture velocity, ms^{-1}
u_{unc}	Expanded uncertainty associated with $U_{tb,N}$, ms^{-1}
$\boldsymbol{u}_k$	Velocity of a given phase k, ms^{-1}
$\boldsymbol{u}$	Shared velocity in the VOF method, ms^{-1}
$v'_{l,rms}$	R.m.s. values of the radial velocity component fluctuations, ms^{-1}
$\overline{v'w'}$	Reynolds turbulent stress, $m^2 s^{-2}$
$\boldsymbol{u}_c$	Interfacial compressive velocity in the VOF method, ms^{-1}

v_g	Radial gas velocity, ms^{-1}
v_l	Radial liquid velocity, ms^{-1}
v_{l,rms^+}	Wall friction dimensionless liquid radial velocity
$v^j_{l,rms}$	Root mean square (r.m.s) of the axial(j=1) and (j=2) velocity fluctuations, ms^{-1}
$V_{b,i}$	Dispersed bubble volume in the DBM, m^3
$V_{r,n}$	Relative volume of the particle mesh cell occupied by underlying fluid mesh cell n
V_{PC}	Particle mesh cell volume from the background mesh in the DBM, m^3
V_i	Volume of fluid mesh cell i, m^3
$\mathrm{V_{P,i}}(j)$	Volume of a bubble i lying in a particle mesh cell j, m^3
$V(t)$	Instantaneous signal acquired by the light detector in a time instant t, V
$V^{'}(t)$	Voltage signal fluctuation acquired by the light detector in a time instant t, V
W_i	Weighting coefficients background mesh interpolation of the DBM
w_l	Axial liquid velocity, ms^{-1}
w_g	Axial gas velocity, ms^{-1}
$w_l^{norm.}$	Normalized liquid axial velocity
w_{l,rms^+}	Wall friction dimensionless liquid axial velocity
$w_{l,\tau}$	Wall friction velocity, ms^{-1}
w_{g-l}	Gas-liquid interface velocity, ms^{-1}
$w'_{l,rms}$	R.m.s. values of the axial velocity component fluctuations, ms^{-1}
$w_b(t)$	Instantaneous bubble velocity , m/s
$\boldsymbol{x}_{PCC}$	Particle cell corner position of the background mesh in the DBM, m
$\boldsymbol{x}_j$	Dispersed bubble position of bubble i in the DBM, m
$z_b(t)$	Instantaneous bubble position , m

Greek letters

α_l	Liquid volume fraction
α_g	Gas volume fraction
α_n	Phase indicator scalar from the different interface length scales, where n represents (1) liquid phase, (2) Taylor and (3) dispersed bubbles.
β	Gas to total superficial velocities ratio
γ_k	Phase indicator scalar of a given phase k
γ	Phase indicator scalar in the VOF method
γ_D	VOF phase indicator scalar value at the *donor* cell
γ_A	VOF phase indicator scalar value at the *acceptor* cell
γ_U	VOF phase indicator scalar value at the *upwind* cell
γ_f	VOF phase indicator scalar value in the cell face
$\tilde{\gamma}$	Normalized VOF phase in the NVF
γ_{par}	VOF phase indicator scalar threshold value in the VOF-DBM coupling scheme
Γ	Sum of r.m.s. of the deviation between the axial velocity profile in a position z and away from the Taylor bubble (nose or bottom), ms^{-1}
δij	Overlap between two bubbles i and j in the DBM, m
δ_{LSI}	Thin-liquid film between the small bubble and the large-scale interface, m
Δt_{delay}	Interval between the bubble passage and the PIV or HSC acquisition, s
ΔW_σ	Interfacial deformation energy, Nm
Δ_i	SGS filter width, m
Δt_N	Time interval from the LDR signal used in the Taylor bubble nose calculation, s
Δt_B	Time interval from the LDR signal used in the Taylor bubble bottom calculation, s

$\Delta t_{b,crit}$	DBM critical time step, s
ϵ_k	Dispersed phase void fraction of a given phase k in the TFM
θ_f	Angle between the interface and cell face value in the CICSAM scheme
κ	Interface curvature, m^{-1}
λ	Light source wavelength, m
μ_m	Mixture dynamic viscosity, $m^2 s$
μ_l	Liquid dynamic viscosity, $m^2 s$
μ_g	Gas dynamic viscosity, $m^2 s$
$\mu_{l,L}$	Molecular liquid dynamic viscosity, $m^2 s$
$\mu_{l,SIT}$	Shear-induced turbulent liquid dynamic viscosity, $m^2 s$
$\mu_{l,SIT}$	Bubble-induced turbulent liquid dynamic viscosity, $m^2 s$
ρ_l	Liquid density, kgm^{-3}
ρ_g	Gas density, kgm^{-3}
ρ_m	Mixture density, kgm^{-3}
$\sigma_{\mathrm{PDF}}^{\mathrm{nose}}$	Standard deviation of the nose position PDFs
σ_f	Blending scheme value in the CICSAM scheme
σ	Surface tension coefficient
ϕ_{PCC}	Particle cell corner value of the background mesh in the DBM
ϕ_{PC}	Particle cell center value of the background mesh in the DBM
ϕ	Cell center value in of fluid mesh in the DBM
$\phi_{\mathrm{B},i}$	Lagrangian value of a ϕ variable at bubble i
Φ	Flux or force value in of fluid mesh in the DBM
Φ_{PC}	Flux or force value in a particle cell center of the background mesh in the DBM
χ	Phase indicator function

Operators

$\overline{\bullet}$	Spatial average operator

$\langle \bullet \rangle$ Time or ensemble average operator

Contents

Chapter 1

Introduction

Multiphase flows are flows with the presence of more than one phase, present in almost all areas of engineering, especially in the oil industry and in the energy sector. A phase is defined as a region in space delimited by an interface with an infinitesimal thickness that encloses a material with homogeneous chemical composition, transport properties, and definable state (ROSA, 2012). Within the broad area of multiphase flows, the term "phase" refers to easily identifiable regions, which physical scales are much larger than molecular dimensions. From the phase definition, multiphase flows can be classified according to the phases involved, being: i) liquid-gas systems; ii) gas-solid systems; iii) liquid-solid systems; iv) liquid-liquid systems and v) multiphase systems. The focus of the present work is on liquid-gas systems, more specifically, liquid-gas two-phase flows.

Liquid-gas two-phase flows play an important role in natural and industrial processes, especially in the chemical and oil industries. This sort of flow can occur in horizontal, vertical and inclined pipelines and equipment as separators, heat exchangers, pumps, valves, etc., covering numerous areas and engineering processes, such as the design of equipment for fluid transportation, line measurement systems, oil and gas production, cooling systems, among others. In general, liquid-gas two-phase flows can present different geometric arrangements or morphologies. When flowing in pipelines, due to confinement, the phases arrange in different flow patterns, which may involve different phase morphologies in different regions of the domain, affecting in a complex manner its hydrodynamics and also the heat and mass transfer processes. In unconfined environments, such as vessels or separators, phases may arrange in a continuous-disperse way, as droplets entrained in

the gas phase or bubbles in the liquid phase, while in other regions different morphologies may arise, such as film formation in gas-droplet flows or entrained bubbles and droplets in stratified flows. Therefore, the study and modeling of flows with different morphologies are of fundamental importance in different areas of engineering and industry.

1.1 TWO-PHASE FLOW PATTERNS IN VERTICAL DUCTS

In liquid-gas two-phase flows in ducts, the phases can be spatially distributed with different morphologies, which constitutes different phase arrangements occurring at specific flow conditions called "flow patterns". These distributions depend on the channel geometry, flow inclination angle, the flow rates of the two phases, and also its physical properties. Figure 1.1 present an schematic picture of these different flow patterns.

Figure 1.1 – Different two-phase flow patterns in vertical ducts: a) bubbly flow; b) spherical-cap flow; c) slug flow; d) churn flow and e) annular flow.

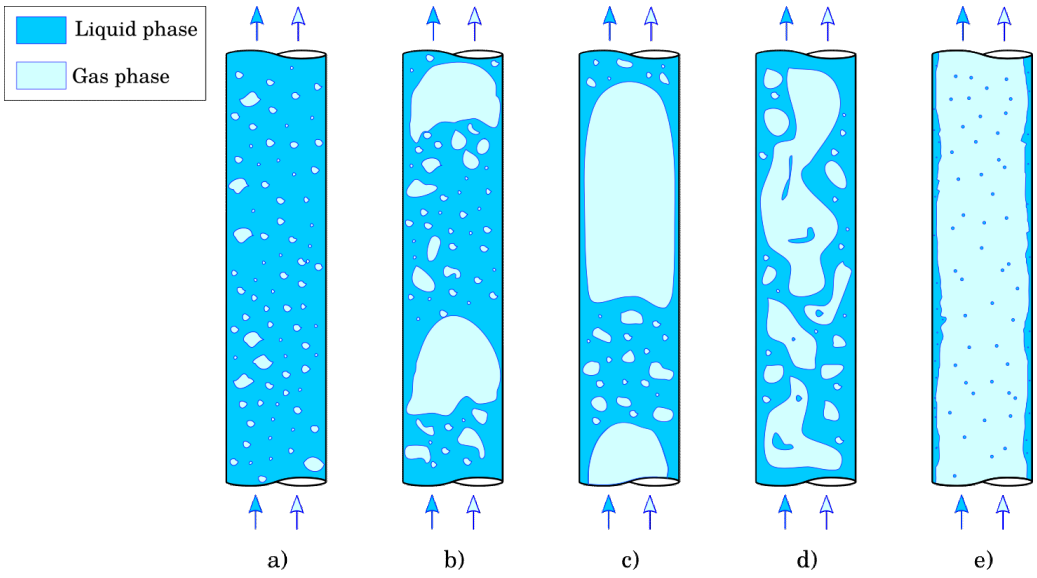

Source - Adapted from Faghri and Zhang (2006).

The usual practice of distinguishing the different phases is to classify them based on their morphologies. The nomenclature helps to distinguish between the different arrangements. However, not all authors use the same names and patterns, often differentiating the patterns in sub-patterns (ROSA, 2012; ISHII; HIBIKI, 2011; FAGHRI; ZHANG, 2006; WALLIS, 1969). In this work the different patterns are classified in a similar way to that presented in Rosa (2012), being defined as: bubbly flow, spherical-cap flow, slug flow, churn flow and annular flow. The characteristics of each pattern are described in the following paragraphs.

In the bubbly flow pattern, Fig. 1.1a), the gas phase is spatially distributed as dispersed bubbles present in a liquid phase. These bubbles have a spherical or distorted shape and may rise in a straight or "zig-zag" paths. During its rising motion, these bubbles may interact with each other and this interaction, as well as shape, rising velocity, and spatial distribution along the duct, depend on numerous factors, such as the duct diameter, the phases flow rate and its transport properties.

By maintaining the liquid phase flow rate constant and increasing the flow rate of the gas phase, the dispersed bubbles begin to coalesce, forming larger bubbles with a spherical cap shape, which occupy a considerable portion of the duct cross-section. At this point, the flow can be classified within the spherical-cap flow pattern, which is schematically depicted in Fig. 1.1b).

Increasing the flow rate of the gas phase beyond the spherical-cap flow regime, bubbles with a spherical cap shape coalesce and form elongated bubbles that, as before, occupy almost the entire duct cross-section, such bubbles are called Taylor bubbles, and are longer than those classified as spherical-caps. The space between the Taylor bubbles is filled by liquid pistons that may or may not contain dispersed bubbles, depending on the diameter of the duct, its inclination angle, the fluid properties. This flow pattern, shown in Fig. 1.1c) is classified as the slug flow pattern.

A further increase of the gas flow rate results in the "churn" flow, in which the previous elongated bubbles become distorted, losing the characteristic Taylor bubble shape, due to flow turbulence. This flow pattern, represented by Figure 1.1d) does not have a well-defined phase morphology. However, it can be said that the liquid pistons have a reduced length when compared to the distorted elongated bubbles. In the region of the liquid piston, there is a considerable amount of dispersed bubbles that tend to meet the larger bubbles, breaking them up in a "chaotic" manner.

Finally, again, increasing the flow of the gas phase, the annular flow pattern is reached (Fig. 1.1 e)), in which the break-up and coalescence results in a flow characterized by a gas-phase flow in the core region and the formation of a thin liquid-phase wavy film between close to the duct wall. Due to the difference of the relative velocity between the two phases, small liquid-phase drops may get entrained into the gas region, and, on the contrary, small dispersed bubbles may be present in the thin liquid film.

The classification described in the paragraphs above is based on the differentiation of easily distinguishable characteristics in flow regimes since the patterns have unique characteristics. However, in the transition from one regime to another, there is the appearance of one or more transitional regimes. The description of such regimes is not simple, explaining, in part, the existence of different classifications and sub-classifications in the

literature (ROSA, 2012; ISHII; HIBIKI, 2011; FAGHRI; ZHANG, 2006; WALLIS, 1969).

Due to the occurrence of multiphase flows in different fields of engineering with very different phase morphologies, which can be combined in the same flow domain, a tool is needed for the flow prediction in the different flow patterns, since each has different hydrodynamic characteristics. Different approaches were adopted to predict these flows, such as analytical equations and experimental studies. Analytical relations are, in most cases, obtained from mass, momentum, and energy balances in simplified one-dimensional flows. For the prediction through experimental results, studies are carried out from the alteration of operational conditions parameters, seeking to characterize and classify the flow patterns. Within these parameters, the phases flow rate, their transport properties, the flow inclination, the internal diameter of the duct, and the type of flow (co-current, stagnant, or counter-current) stand out. It is common in the literature (TAITEL et al., 1980; BARNEA et al., 1983), to use the two approaches together, thus obtaining semi-empirical correlations that can predict the flow pattern for a given operational condition. Aiming a simple and fast alternative to obtain this information, that is, to predict a certain flow pattern for a certain operational condition, the flow regime relations are represented by diagrams called flow maps. Figure 1.2 presents the flow patterns map for vertical ducts in co-current air-water flow obtained by Taitel et al. (1980).

In the flow pattern map shown in Figure 1.2, it is possible to identify and obtain the flow pattern from the superficial velocities of each phase (j_l and j_g). This definition, based on superficial velocities, is commonly found in other flow maps due to its experimental ease, which requires only knowledge of the flow rates of the phases, since,

$$j_k = \frac{Q_k}{A_{duct}} \tag{1.1}$$

where, k represents a given phase, Q_k its flow rate and A_{duct} the cross-sectional area of the pipe.

It is important to note that flow maps are developed from a specific configuration of working fluids and duct geometry. Thus, the level of prediction of the flow pattern maps also depends on the degree of similarity between the experimental conditions and the operating conditions of the required application.

In situations with a higher degree of complexity, with transient systems or in more complex geometries, those simple flow maps are not able to predict the flow pattern. The same occurs in transition regions, close to the lines that define the different patterns in Fig. 1.2. For these situations, advanced prediction tools are needed, such as multi-dimension, or multiscale numerical models.

Figure 1.2 – Two-phase air-water co-current flow pattern map for vertical ducts.

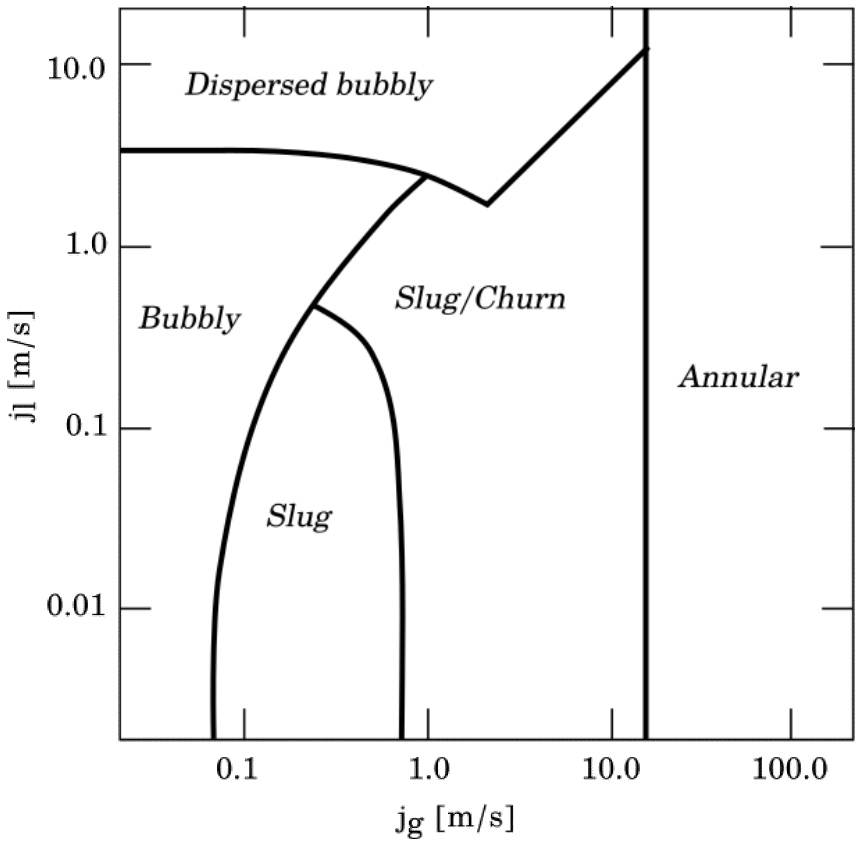

Source - Adapted from Taitel et al. (1980).

1.2 LARGE AND SMALL SCALE INTERFACES

Due to the complexity of the different flow morphologies encountered in real situations, a great effort is devoted for better understanding of liquid-gas two-phase flows. This understanding can come through experimental investigations, using methods and techniques that allow detailed measurements in certain situations, or through detailed multi-dimensional numerical investigations. In the later, Computational Fluid Dynamics (CFD) is a tool that allows a detailed analysis of the physical mechanisms that govern multiphase flows. However, despite being a powerful tool, most of the CFD models used in practical engineering applications require additional closure models for inter-phase exchanges which are usually developed for specific morphology or with a unique interface length scale.

In the present work, phase morphologies that constitute the different flow patterns are classified by their interface length scales. The reason behind this classification choice lies in the fact that most computational methods and models are usually developed for specific two-phase morphologies, which commonly posses unique interface length scales.

The interface length scale is understood as the ratio between the physical length scale of an interface and the physical domain length scale. Figure 1.3 schematically depicts the different interface length scales that can be found in a multiphase flow.

Figure 1.3 – Schematic representation showing the slug two-phase flow regime and the different interface length scales.

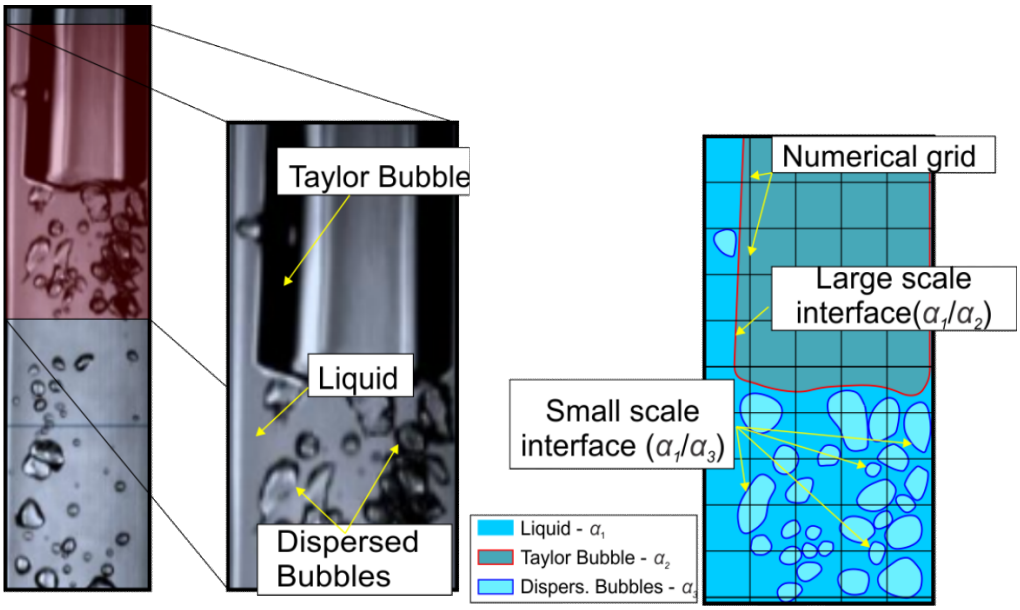

Source - Developed by the author.

In this manner, this work has a fundamental character and may find application in several multiphase flow systems, like those found in the energy as processes industry, such as measuring systems, heat and mass transfer processes, high-efficiency energy systems and so forth. This sort of application requires precise and detailed three-dimensional simulation models, particularly in design projects of pumps, phase separators, and other multiphase flow equipment.

For industrial applications, in which two-phase flows with small scale interfaces are commonly encountered, averaged based or reduced models (WALLIS, 1969; ISHII; HIBIKI, 2011) are used due to the computational requirements associated with detailed simulation of those applications. In these simulations, in order to capture the smallest time and length scales of the flow, and also the smallest interfacial length, the computational cost of such numerical grid turns the problem to extremely expensive and impossible with today's available computational power. Those averaged based or reduced based models require interfacial transport coefficients to include phase interaction mechanisms, which in turn, determinates the success or failure of the model to predict real flow characteristics. In those averaged based or reduced based models, in order to feed information to these models,

fundamental studies are conducted to characterize the phase interaction mechanisms and translate them as interfacial transport coefficients.

On the other hand, it is typical the use of interface capturing or tracking models when large scale interface lengths are present in the flow, such as the Volume-of-Fluid (VOF) (HIRT; NICHOLS, 1981), Level-Set (OSHER; SETHIAN, 1988) and other methods (e.g.,Scardovelli and Zaleski (1999) and Lakehal et al. (2002)) for fundamental studies that seek to understand the flow near the interfacial region. This type of approach is important, once it is possible to obtain interfacial transport coefficients, required in average based models (CERQUEIRA et al., 2015). In general, these studies consider simple multiphase flows (LIOVIC; LAKEHAL, 2007; HAELSSIG et al., 2010; PANDELAERS et al., 2011) with simple interface morphologies, like stratified flow patterns, bubbles, and droplets. However, as discussed in the paragraphs below and depicted by Fig. 1.1 that is not always the case, since a major part of the flow pattern regimes combines interfaces of different length scales.

In this context, analyzing the two-phase flow from a numerical approach, as already stated, the different interface length scales can be characterized based on the ratio of the physical interface length and the computational grid size reference. Therefore, an interface is said to have a large scale when the model can capture its shape and position with a practical computational mesh size[1], such as a Taylor bubble rising in a vertical duct. For a practical mesh size When that is not the case, the interface is said to have a small scale, for instance, in a bubbly flow regime.

In CFD industrial applications, interface capture models are typically applied to study problems with large scale interfaces, such as stratified flows. On the other hand, in cases where dispersed morphologies are dominant, such as droplet or bubble patterns, average based models are used. However, in several applications, multiscale models, i.e., models capable of simulating flow with interfaces with different scales, such as the presence of continuous and dispersed morphologies in the same domain, are necessary.

1.3 MOTIVATION

As discussed in the previous sections, for real liquid-gas flow regimes, it is necessary to employ sophisticated numerical models, which are capable of modeling the different interface length scales, also including the interaction among the gas, the small and large scale interfaces, and liquid phases.

[1] A practical mesh size can be seen as a high-resolution mesh that can be used to perform simulations with the currently available computational power.

The first attempt to couple a small and large scale interfaces in a CFD model was performed by Cerne et al. (2001). In the model developed in that work, each control volume of the domain was marked to be solved by the VOF (large scale interface) or the Two-Fluid-Model (small scale interface) model by a switching algorithm. The criterion used to switch between the models was based on the gradient of the VOF phase indicator function and the geometrically reconstructed interface (UBBINK, 1997) of the neighborhood cells stencil. In this work, a study was performed to carefully set the switching threshold through some benchmark cases. From these studies, the authors solve a Rayleigh-Taylor instability flow using the coupled model, obtaining good results. However, little is discussed about the interfacial momentum transfer coefficients from the TFM and the surface tension force from the VOF, important when modeling multiscale interface length scales flows.

In the work of Štrubelj and Tiselj (2011), the authors proposed a model based on the coupling of the Two-Fluid-Model (TFM) and the Level-Set method (LS). The work extracts some ideas and concepts from Cerne et al. (2001), including the switching criterion. However, in this model, the Level-Set method is used not to track the interface, as commonly seen in literature (SETHIAN; SMEREKA, 2003), but to introduce an artificial compression force that acts in the TFM void fraction field, keeping the large scale interfaces sharp. It is important to state that the replacement of the geometrically reconstructed interface from the VOF to the Level-Set method in the switching criteria is straight forward since the LS information about the interface characteristic is readily available (YEOH; TU, 2009).

Wardle and Weller (2013) developed a model with an artificial compression force similar to the one described in Štrubelj and Tiselj (2011). This hybrid model couples the Two-Fluid-Model and the VOF and, again, use the switching criteria from Cerne et al. (2001) to flag each control volume to be solved by the VOF or TFM. The model is implemented inside the OpenFOAM framework (JASAK et al., 2007) to simulate liquid-liquid extraction device flows, including three-phase, liquid-liquid-air simulations in which a sharp interface is maintained between each liquid and air, but dispersed phase modeling is used for the liquid-liquid interactions.

Yan and Che (2010) proposed a hybrid model coupling the VOF and the TFM model. In this hybrid liquid-gas model, the gas phase is divided into two phases, one with a small scale interface and a second a large scale interface. Therefore, the model has three phases: i) a liquid phase; ii) a dispersed gas phase (small scale interface), and iii) a large bubble gas phase (large scale interface). In this work, on the contrary of the other works found in literature, the coupled model modifies the interfacial transfer terms from the TFM model, adding large and small scale interfaces interaction, such as the gas phase

coalescence. Using the developed model, the authors study the hydrodynamics of a large bubble ascending inside a duct, which contains a liquid phase with small dispersed bubbles. According to the results, the large bubble shape (large scale interface) and hydrodynamics are affected by the dispersed bubbles (small scale interface). The same authors, in Yan and Che (2011) apply the previously developed model to study an upward liquid-gas slug flow regime configuration, adding a more advanced gas-phase coalescence model. The results indicates that the small-large scale interface affects the flow structure flow around the Taylor bubble. The two works (YAN; CHE, 2010, 2011) do not validate the obtained results with experimental results, leaving the experimental validation an open topic. In addition, the model uses an empirical threshold to switch between the TFM (small scale) to the VOF (large scale) methods, do not addressing the criterion used for the switching procedure, which may have a major impact on the simulations results.

In Hänsch et al. (2012), a multiscale numerical model is developed without the coupling of an averaged based model and one based in a one-fluid (e.g., Level-Set method, VOF method, etc.) model. The model relies only on modifications of the Two-Fluid Model that enables the "standard" model to distinguish the different interface length scales. The implementation is based in the non-homogeneous *MUltiple-SIze-Group* (MUSIG) (KREPPER et al., 2008) used in polydispersed flow modelling. According to the authors, the new multiscale implementation is an extension of the MUSIG model. For the large length scale interfaces, a numerical counter-diffusion term acts to maintain a sharp interface, dismissing the use of an interface capture method. The results of the developed model are qualitatively compared against two reference cases, the impingement of a liquid jet on a free surface with associated entrainment of dispersed bubbles.

In the work of Hua (2015), the author proposes a numerical framework for the simulation of multiple scales interfaces based on the coupling of the VOF and the Lagrangian particle tracking methods. The work aims to analyze the interaction between the different interfacial scales. Thus, the model was applied to simulate a large bubble flowing in a 2D channel with many suspended small bubbles. The results show that the small bubbles modify the flow around the large bubbles, affecting its rising behavior. A major drawback of the numerical model adopted by the authors, based on a Lagrangian particle method, is the limitation that the dispersed bubble diameter must be smaller than the grid size. Since the coupling between the VOF and the Lagrangian framework is based on a point-mass Lagrangian particle, if not properly accounted in the coupling scheme, problems arise when the size of the particle is larger or similar than the mesh size.

Recently, in Peng et al. (2020), the authors proposed a CFD numerical model based on the coupling strategy adopted by Hua (2015), using the VOF method to model

the large scale interface and a Lagrangian model to track the small scale interfaces. The model was developed to numerically investigate the distribution characteristics of solid particles within slurry Taylor flows. However, contrary to the work of Hua (2015), the Lagrangian model used by those authors account for collisions on the small scale interface scales and use a technique to circumvent the cell size limitations from the Lagrangian particle diameter.

According to the multiscale models found in the literature, it is observed that several aspects of the currently available models can be revisited and improved. Additionally, despite the recent attempts in the development in multi-dimensional numerical multiscale CFD models, currently, there is no experimental data to fully comprehend the interactions between the different interface length scales and verify the models found in the literature. Thus, one of the main contributions of this work will be the experimental study of two-phase flows with different interface length scales, which will generate experimental data for those models.

1.4 OBJECTIVES

The aim of this thesis is the experimental and numerical study of two-phase flows with different interface length scales. Thus, the manufactured "quasi-real" slug flow regime, similar to the slug flow will be studied, through the independent injection of Taylor bubbles in a bubbly flow stream.

As both, experimental and numerical approaches will be considered for the proposed study, the specific objectives can be divided into two main categories, related to the experimental studies performed and to the development and validation of a multiscale numerical CFD model.

For the experimental characterization of two-phase flows with different interface length scales, the specific objectives are:

- Analyze the flow modifications due to addition of dispersed bubbles in vertical laminar and turbulent flows;

- Perform a detailed study on the interaction between the different interface length scales in gas-liquid flows in the presence of Taylor and dispersed bubbles;

- Gather experimental data to validate multi-dimensional and multiscale CFD models.

On the numerical part, the specific objectives are:

- Development of a CFD model for the modeling of two-phase flows with different interface length scales based on the coupling of the DBM and VOF methods;
- Analyze the capability of the developed multi-dimensional and multiscale CFD model in reproducing air-water system experimental results.

1.5 THESIS OVERVIEW

The thesis is organized as a collection of scientific papers, which present the details of methods and results, with a general introduction in the first chapter, presenting a theoretical background and a literature review in the second chapter and a general conclusion in the last chapter. Therefore, each chapter can be comprehended independently once they have their own literature review and theoretical background on their specific subjects, results, discussions and conclusions. Chapter 2 presents the theoretical background and literature review on numerical methods and experimental methods for the simulation/characterization of two-phase flows with different interface length scales. Chapter 3 presents a novel method for the phase discrimination in PIV images, which allows the use of the technique in liquid-gas bubbly flows, and the development of a PTV technique for tracking the motion of the dispersed bubbles. Then, in Chapter 4, the previously presented PTV technique is improved to identify and reconstruct bubble shapes in dense bubbly flows through the use of Convolution Neural Networks (CNN). Chapter 5 presents the development of an experimental apparatus for the manufacturing of the "quasi-real" slug flow, including the detailed description of the three-field generator system, the measurement techniques, and image processing methods necessary for the acquisition of reliable and consistent ensemble-averaged results. In Chapter 6, the developed experimental apparatus is used to characterize the flow structure around a Taylor bubble in the presence of the dispersed bubbles, exploring the interaction between the different interfacial scales. Chapter 7 presents the numerical development of a CFD model capable of handling two-phase flows with different interface length scales. In Chapter 8, the developed multiscale CFD model is modified through the incorporation of liquid and bubble-induced turbulence models and a validation study is presented from the experimental results using the techniques developed in the present work. Finally, conclusions and recommendations for future work are presented in Chapter 9.

Figure 1.4 an overview of the thesis structure, linking the different subjects covered to Chapters 3 to 8. On the top of the diagram, the investigation of gas-liquid flows in the presence of Taylor and dispersed bubbles is represented by the manufactured "quasi-real" slug flow. The study is divided into different chapters distributed into an

experimental and numerical part. On the experimental part, Chapters 3 and 4 focus on the experimental characterization on bubbly flows, also presenting novel image processing techniques. Chapter 5 focus on the development of experimental techniques and apparatus focused on 'quasi-real" slug flows. The methods and apparatus developed in Chapters 3 to 5 are used to study gas-liquid flows in the presence of Taylor and dispersed bubbles in Chapter 6. On the numerical part, Chapter 7 focus on the numerical development of a multiscale CFD model, while Chapter 8 compares the CFD results with the experimental data gathered throughout Chapters 3 to 6.

Figure 1.4 – Schematic diagram of the thesis structure.

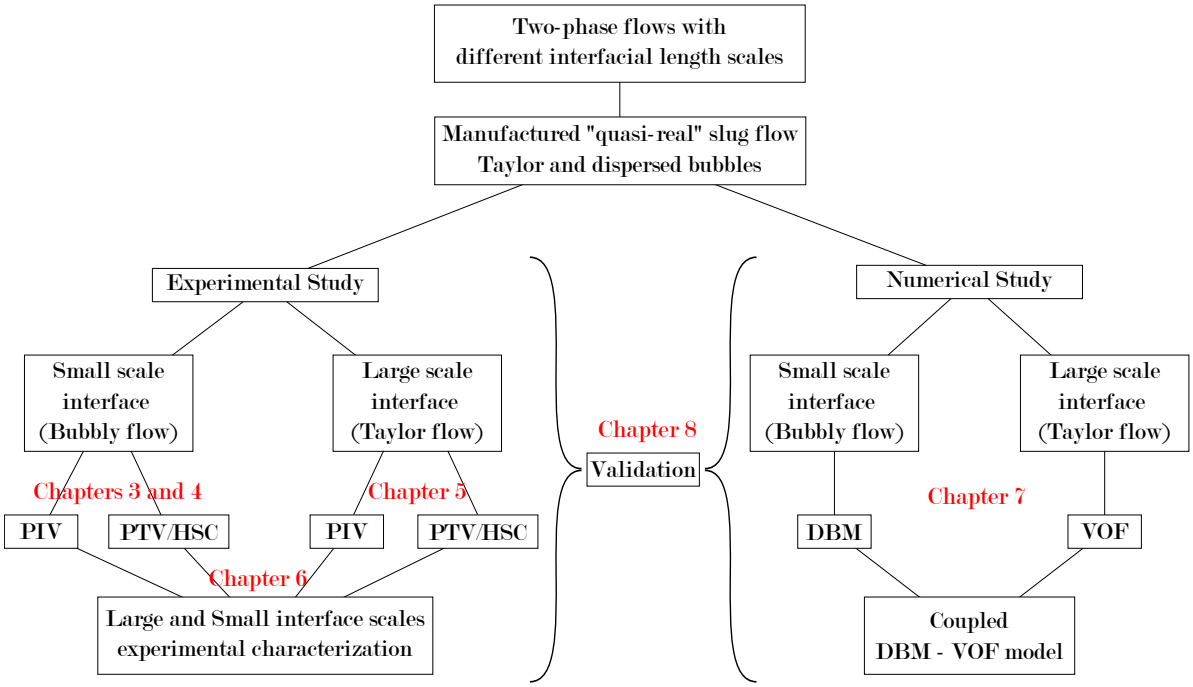

Source - Developed by the author.

Chapter 2

Literature Review and Theoretical Background

Given the general objectives of this work, which aims the development of numerical models and experimental studies of two-phase flows with different interface scales, this chapter is divided into two main sections. The first one presents a theoretical review of the numerical methodologies used to model two-phase flows with large interface length scales and models for flows with dispersed phases. The second section presents the fundamentals and experimental methodology used to characterize two-phase flow patterns with small and large interface length scales. At the end of each section, a review of the recent literature on the subject of this work is presented. In the case of numerical simulation of liquid-gas flows with different interface scales, some approaches have been presented in the literature, which are revised here. On the other side, no systematic experimental studies, i.e., with flow parameters of the phases with different length scales independently controlled, as proposed in this work, have been encountered in literature. Therefore, the review of recent experimental works is limited to studies of bubbly flows and Taylor bubbles.

2.1 NUMERICAL MODELLING

The modeling of two-phase flows requires additional treatments from the point of view of computational fluid dynamics, once the introduction of new phases results in regions of the fluid domain with very different fluid properties and in the appearance of fluid-fluid interfaces which positions over time depends on fluids motion. Due to their

existence, some sort of interfacial balance must be used to deal with the singularities at the interface region.

Figure 2.1 summarizes the multiphase flow modeling from the governing equations in a local instantaneous formulation. The set of conservation laws shown in Fig. 2.1, with boundary conditions located at the interface, are not solved in a straight-forward fashion, since in most numerical multiphase flow methods the exact location of the interface is not known (UBBINK, 1997; YEOH; TU, 2009).

Figure 2.1 – Diagram presenting the governing equation of the local instantaneous formulation of a two-phase flow.

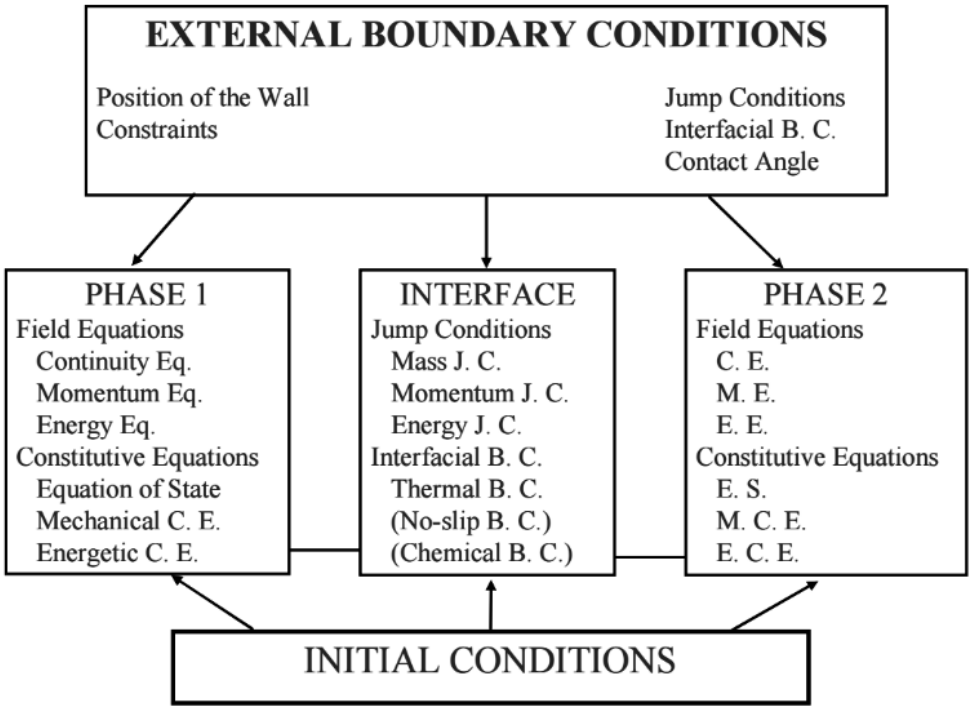

Source - Ishii and Hibiki (2011).

Thus, it becomes necessary to work with a set of more appropriate equations, which are capable of dealing with the different multiphase flow patterns and its different interface length scales. This requirement can be fulfilled by performing consistent averages of the local and instantaneous equations, resulting in a set of averaged governing equations. The works of Faghri and Zhang (2006), Ishii and Hibiki (2011) and Rosa (2012) present different averaging procedures that can be used to obtain a set of suitable equations. However, during the averaging procedure, information about the interface's position, morphology, and jump conditions are lost. For this reason, it is necessary to reintroduce this lost information back to the set of new averaged equations. This can be done by the use of constitutive equations (which are also needed in single phase flows) and by the

incorporation of closure relations that adequately model the interfacial transfer of mass momentum and energy.

For the modeling of multiphase flows by the use of the averaged field equations, the two-fluid, homogeneous and Lagrangian models are generally used. The choice of each of these models is associated with the type of structure presented by the flow. In dispersed flows, the small scale of the interface makes it impossible to capture the interface in practicable computational meshes. Hence, the two-fluid model, or in some cases, a Lagrangian-Eulerian (LE) model, are typically used to model dispersed flows, mainly in industrial applications. For free-surface flows or flows with large interface length scales, interface capturing (or tracking) methods are the most adequate since the interface can be captured/tracked in practicable computational meshes.

In the following sections, the fundamentals of each approach will be discussed, with focus on models that will be used in the modeling proposed in this work.

2.1.1 Interface Capturing/Tracking based Models

In certain applications where the interface is sharply defined and with relatively large length scale in relation to the calculation domain, it can be assumed that the phases share the same velocity field, where velocities at each point correspond to the phase present at that region. From the numerical point of view, this implies that the interface length scales must be, at least, larger than computational mesh cells. From this "one-fluid formulation" (DENNER, 2013), interface capturing or tracking based models can be used. Thus, a single velocity field (or temperatures, concentrations, etc.) shared between the phases is solved, and the presence of a given phase is a function of time and space.

The mass and momentum conservation equations, are described through the homogeneous model as,

$$\frac{\partial \rho_m}{\partial t} + \boldsymbol{\nabla} \cdot \rho_m \boldsymbol{u}_m = 0 \tag{2.1}$$

$$\frac{\partial}{\partial t}(\rho_m \boldsymbol{u}_m) + \boldsymbol{\nabla} \cdot (\rho_m \boldsymbol{u}_m \boldsymbol{u}_m) = -\boldsymbol{\nabla} P + \boldsymbol{\nabla} \cdot (\mu_m \nabla \boldsymbol{u}_m) + \rho \boldsymbol{g} + \boldsymbol{f}_\sigma \tag{2.2}$$

where $\boldsymbol{u}_m$ is the phase shared velocity field, $\boldsymbol{f}_\sigma$ represents the surface tension force, which acts only in the interfacial region.

In Eqs. (2.1) and (2.2), the subscript m indicates constitutive relations for the fluid's density ρ and dynamic viscosity μ, defined, for a two-phase flow condition, as,

$$\rho_m = \chi \rho_1 + (1 - \chi)\rho_2 \tag{2.3}$$

$$\mu_m = \chi \mu_1 + (1 - \chi)\mu_2 \tag{2.4}$$

where the subscripts 1 and 2 indicate the different phases. The phase indicator function χ is defined as,

$$\chi(\boldsymbol{x},t) = \begin{cases} 1, & \text{for a point } (\boldsymbol{x},t) \text{ inside fluid 1} \\ 0, & \text{for a point } (\boldsymbol{x},t) \text{ inside fluid 2} \end{cases} \tag{2.5}$$

According to the definition given above, values between $0 < \chi < 1$ indicate the presence of an interface.

For these specific applications, since the different phases have a single velocity field, there is no need of closure relations for the interfacial transfer modeling. However, for the correct definition of material properties and distinction of the phases, the interface needs to be resolved and captured with adequate precision. Thus, a capturing or tracking interface method must be used, and its equations must be solved together with the governing equations.

According to Ferziger and Perić (1996) and Ubbink (1997), the different capturing and tracking interface methods can be divided into two groups: i) surface based methods and ii) volume based methods. Figure 2.2 illustrates example of methods from the two groups.

Figure 2.2 – Different capturing and tracking interface methods: a) Markers particles; b) Interface fitted mesh; c) Phase indicator function.

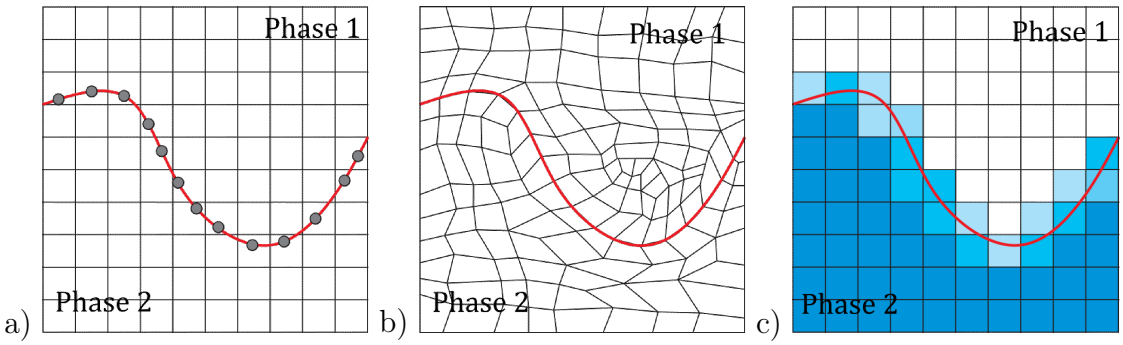

Source - Adapted from Ubbink (1997).

In Fig. 2.2a), the interface is defined by markers, whose individual monitoring of each marker indicates the position of the interface. Now, in Figure 2.2b) the computational mesh is forced to move with the interface. These two schemes fall into the category of surface-based methods, also known in the literature as interface tracking methods. As can be seen, in the interface tracking methods, the interface is defined explicitly, and its exact location is extracted from the connection of markers that move "over" a fixed mesh or through the interface. The advantage of using surface based methods is the exact knowledge of interface position. Thus, the interfacial jump conditions can be readily

applied, and the interface curvature required for modeling the surface tension force is readily available. However, those methods are not capable of simulating phenomena such as break-up and coalescence, since the markers that define the interface tend to move in an unrealistic way or in situations where the interface presents high curvature values. Due to the latter, which is commonly found on Taylor bubbles, the method is not going be described in detail, but a detailed description can be found in Cerqueira (2016).

In volume based methods, also known as interface capturing methods, the interface is defined by the adjacent volumes that define the phase by means of markers or indicator functions, as seen in Fig. 2.2c). As noted in Fig. 2.2c), in interface capturing methods, there is no clear distinction of the interface position, since the phases are characterized by the presence of markers or indicator functions. Thus, in these methods, information regarding the exact location of the interface needs to be extracted from the phase indicator function implicitly. The fact that the interface is obtained implicitly does not affect the precision of terms dependent on the interface normal vector and its curvature, such as those required when modeling surface tension forces. This is solved by using methods that reconstruct the interface and those variables from its surrounding cell neighbours (UBBINK, 1997; YEOH; TU, 2009).

2.1.1.1 Volume-of-Fluid (VOF) Method

The Volume-of-Fluid (VOF) method falls within the category of interface capture methods. The VOF method was first proposed by (HIRT; NICHOLS, 1981) and the conservation equations are valid for the entire computational domain. The phases are defined trough the phase indicator scalar γ_k, which represents a certain phase k. Below, the foundation of the VOF method presented in Gopala and van Wachem (2008) is given.

As previously described, from the definition of γ_k, admitting a two-phase flow, three situations are possible:

- Case 1: $\gamma = 1 \rightarrow$ control volume filled with phase 1
- Case 2: $\gamma = 0 \rightarrow$ control volume filled with phase 2
- Case 3: $0 < \gamma < 1 \rightarrow$ control volume has an interface segment

The conservation equations are obtained from an average procedure in a control volume smaller than the scale of the secondary phase interface in the flow, as shown in Fig. 2.3, e.g. bubbles or drops in a liquid-gas two-phase flow. In addition, the hypothesis of incompressible, isothermal flow without mass transfer between the phases is going to be adopted.

Figure 2.3 – Averaging volume compared with the secondary phase interface scale.

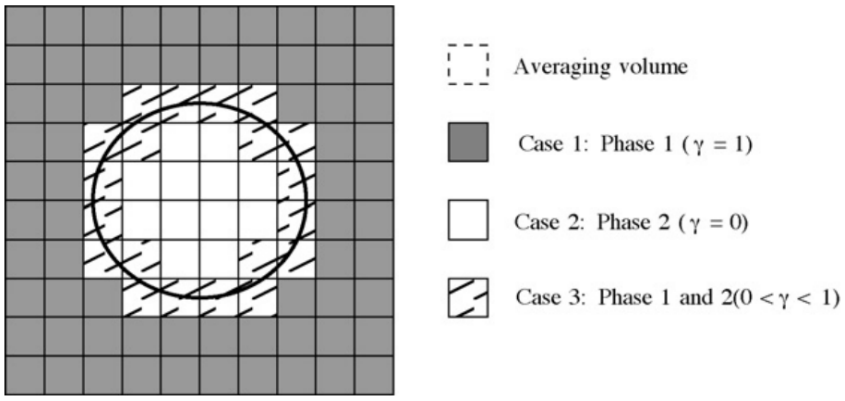

Source - Gopala and van Wachem (2008).

Following the scheme given in Fig. 2.3, the conservation equations are:

- **Case 1**: The control volume is filled with phase 1

  Continuity equation

$$\frac{\partial}{\partial t}\langle\rho_1\rangle + \boldsymbol{\nabla}\cdot\langle\rho_1\boldsymbol{u_1}\rangle = 0 \tag{2.6}$$

  Momentum conservation equation

$$\frac{\partial}{\partial t}\langle\rho_1\boldsymbol{u_1}\rangle + \boldsymbol{\nabla}\cdot\langle\rho_1\boldsymbol{u_1}\boldsymbol{u_1}\rangle = \nabla\cdot\langle\mathbf{T_1}\rangle + \langle\rho_1\boldsymbol{g}\rangle \tag{2.7}$$

- **Case 2**: The control volume is filled with phase 2

  Continuity equation

$$\frac{\partial}{\partial t}\langle\rho_2\rangle + \boldsymbol{\nabla}\cdot\langle\rho_2\boldsymbol{u_2}\rangle = 0 \tag{2.8}$$

  Momentum conservation equation

$$\frac{\partial}{\partial t}\langle\rho_2\boldsymbol{u_2}\rangle + \boldsymbol{\nabla}\cdot\langle\rho_2\boldsymbol{u_2}\boldsymbol{u_2}\rangle = \nabla\cdot\langle\mathbf{T_2}\rangle + \langle\rho_2\boldsymbol{g}\rangle \tag{2.9}$$

- **Case 3**: The control volume has an interface segment

  Continuity equation

$$\frac{\partial}{\partial t}\langle\gamma\rho_1\rangle + \boldsymbol{\nabla}\cdot\langle\gamma\rho_1\boldsymbol{u_1}\rangle = 0 \tag{2.10}$$

$$\frac{\partial}{\partial t}\langle(1-\gamma)\rho_2\rangle + \boldsymbol{\nabla}\cdot\langle(1-\gamma)\rho_2\boldsymbol{u_2}\rangle = 0 \tag{2.11}$$

Momentum conservation equation

$$\begin{aligned}&\frac{\partial}{\partial t}\langle\gamma\rho_1\boldsymbol{u_1}\rangle + \boldsymbol{\nabla}\cdot\langle\gamma\rho_1\boldsymbol{u_1}\boldsymbol{u_1}\rangle = \\ &\nabla\cdot\langle\gamma\mathbf{T_1}\rangle + \langle\gamma\rho_1\boldsymbol{g}\rangle + \frac{1}{V}\int_{A_I}\mathbf{T_1}\cdot\boldsymbol{n_{12}}\,\mathrm{d}A\end{aligned} \tag{2.12}$$

$$\begin{aligned}&\frac{\partial}{\partial t}\langle(1-\gamma)\rho_2\boldsymbol{u_2}\rangle + \boldsymbol{\nabla}\cdot\langle(1-\gamma)\rho_2\boldsymbol{u_2}\boldsymbol{u_2}\rangle = \\ &\nabla\cdot\langle(1-\gamma)\mathbf{T_2}\rangle + \langle(1-\gamma)\rho_2\boldsymbol{g}\rangle + \frac{1}{V}\int_{A_I}\mathbf{T_2}\cdot\boldsymbol{n_{21}}\,\mathrm{d}A\end{aligned} \tag{2.13}$$

Interfacial jump condition

$$\frac{1}{V}\int_{A_I}\left[-\mathbf{T_1}\cdot\boldsymbol{n_{12}} - \mathbf{T_2}\cdot\boldsymbol{n_{21}}\right]\mathrm{d}A = \frac{1}{V}\int_{A_I} m_{12}^{\sigma}\,\mathrm{d}A \tag{2.14}$$

In the equations above, the terms denoted by $\langle\bullet\rangle$ represents a volumetric average procedure, $\boldsymbol{T}_k$ is the phase k stress tensor, A_I is the interfacial surface area, n_{ij} the normal interface vector that points from phase i to phase j and m_{12}^{σ} is the surface tension force related term.

Aiming a single set of conservation equations, the following average quantities are defined,

$$\rho = \langle\gamma\rho_1 + (1-\gamma)\rho_2\rangle \tag{2.15}$$

$$\boldsymbol{T} = \langle\gamma\boldsymbol{T_1} + (1-\gamma)\boldsymbol{T_2}\rangle \tag{2.16}$$

From these new averaged quantities, admitting no phase change and assuming that the phase velocity field is shared ($\boldsymbol{u}_1 = \boldsymbol{u}_2 = \boldsymbol{u}$) and continuous along the interface, the conservation equations can be written as,

$$\frac{\partial\rho}{\partial t} + \boldsymbol{\nabla}\cdot\rho\boldsymbol{u} = 0 \tag{2.17}$$

$$\frac{\partial(\rho\boldsymbol{u})}{\partial t} + \boldsymbol{\nabla}\cdot(\rho\boldsymbol{u}\boldsymbol{u}) = -\boldsymbol{\nabla}P + \boldsymbol{\nabla}\cdot\boldsymbol{T} + \rho\boldsymbol{g} + \boldsymbol{f}_{\sigma} \tag{2.18}$$

where $\boldsymbol{f}_{\sigma}$ is the surface tension force, acting only in the interfacial region.

In summary, the set of conservation equations employed by the Volume-of-Fluid method are the following:

$$\frac{\partial\rho}{\partial t} + \boldsymbol{\nabla}\cdot\rho\boldsymbol{u} = 0 \tag{2.19}$$

$$\frac{\partial(\rho\boldsymbol{u})}{\partial t} + \boldsymbol{\nabla}\cdot(\rho\boldsymbol{u}\boldsymbol{u}) = -\boldsymbol{\nabla}P + \boldsymbol{\nabla}\cdot\boldsymbol{T} + \rho\boldsymbol{g} + \boldsymbol{f}_{\sigma} \tag{2.20}$$

$$\frac{\partial \gamma}{\partial t} + \nabla \cdot (\boldsymbol{u}\,\gamma) = 0 \tag{2.21}$$

Despite the conservative nature of the method (Eq. (2.21)), additional methods and techniques are required in order to capture the accurate interface position, since at the end of each advection step, the γ scalar field has a spatial distribution similar to the one observed in 2.4.

Figure 2.4 – Spatial distribution of the phase indicator scalar (γ_1) after an advection step. (UBBINK, 1997)

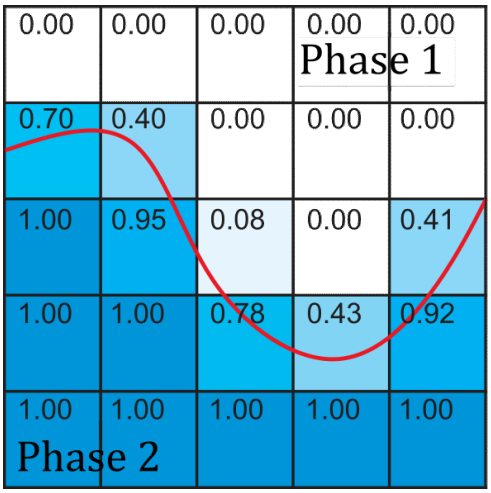

Source - Adapted from Ubbink (1997).

The methods capable of recovering information regarding the interface position and shape can be divided in: i) interface geometrical reconstruction methods, which reconstruct the geometry between the different phases from geometric elements and ii) compressive methods, which make use of high-order interpolation schemes in the γ advection equation, seeking to keep the region that defines the interface compressed (control volumes with values between $0 < \gamma < 1$).

Figure 2.5 schematically illustrates the two methods. In Fig. 2.5b) the information regarding the position of the interface is recovered through a compressive method, which aims to restrict the interface (volumes with $0 < \gamma < 1$) to a "banded" region delimited by a single control volume. Now, in Fig. 2.5c), the interface is geometrically reconstructed from the values of the neighboring control volumes, represented by the line passing through cells with $0 < \gamma < 1$.

The interface geometrical reconstruction methods approximate the interface in each control volume through geometrical segments, for two-dimensional cases this entity is a line, while in three-dimensional cases, the interface is approximated through a surface

Figure 2.5 – Schematic representation of interface reconstruction and capturing methods using an circular interface case as example: a) analytical results; b) spatial distribution of γ calculated using a compressive method; c) spatial distribution of γ calculated using a interface geometric reconstruction method.

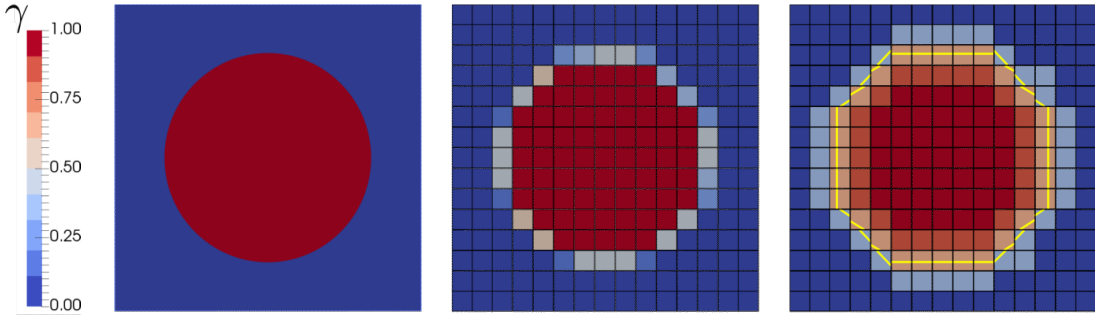

Source - Developed by the author.

plane. Among the interface geometrical reconstruction methods, highlight the Simple Line Interface Calculation (SLIC) proposed by Noh and Woodward (1976), which approximates the interface in each control volume as a line parallel to one of the coordinated axes of the system and the Piecewise Linear Interface Calculation (PLIC) proposed by Youngs (1982), which approximates the segments of the interface through lines in the two-dimensional situation and planes in the three-dimensional situation.

Despite its success in reconstructing the interface, the numerical implementation of those methods is not simple and computational costly, avoiding its use when unstructured three-dimensional meshes are involved. Furthermore, it is important to emphasize that the interface reconstruction is only used for the calculation of advective flows, not being used for the calculation of other properties of the interface, such as the interface curvature or normal vector. Thus, although interface reconstruction methods result in a sharp interface, it has several limitations from a practical point of view, especially when it is desired to model two-phase flows with different interface length scales. Thus, the method will not be described in detail in the present work, but a detailed description can be found in Yeoh and Tu (2009) and Cerqueira (2016).

2.1.1.2 Interface Compressive Methods

The basic idea of the interface compressive methods, also called algebraic methods, is the application of interpolation functions that combine high and low order approximations, necessary when advecting the phase indicator scalar. The purpose of using high-order interpolation functions is to minimize numerical diffusion while keeping the interface sharp.

However, as discussed in Maliska (2017), high-order interpolation functions imply the appearance of numerical oscillations, which can result in inconsistent values when advecting γ. Thus, the high-order interpolation functions are "blended" with low-order interpolation schemes, resulting in adequate interpolation functions capable of advecting the phase indicator scalar. By using this "blended" approach, unrealistic values, values less than 0 (negative density) and greater than 1, are avoided, while the interface region remains contained in the region delimited by only a few control volumes.

Among the interface compression methods, the Donor-Acceptor metho, proposed in Hirt and Nichols (1981), is considered by many (YEOH; TU, 2009; RUDMAN, 1997; RIDER; KOTHE, 1998) as the original proposal of Volume-of-Fluid. Despite the original work of Hirt and Nichols (1981) proposes a geometrical reconstruction of the interface (SLIC), it is, in essence, a compressive method, since the geometrical interface approximation performed by the SLIC method is only a decision parameter for choosing the interpolation function. Although the Donor-Acceptor method is considered a method with several limitations, it provides the basis for the development of more complex methods and basic definitions, such as the availability criteria and the use of the downstream volume fraction information (also called downwind cell or acceptor cell) when calculating the volumetric flow at a given face.

From the Donor-Acceptor method, Leonard (1988) presents the Normalized Variable Formulation (NVF), a tool for description and analysis for High-Resolution Schemes. The NVF is introduced in Leonard (1988) and gained popularity through the simplifications introduced by Gaskell and Lau (1988). The graphical visualization of NVF, the NVD (Normalized Variable Diagram), is an important tool in the analysis of high-order schemes (MOUKALLED et al., 2016).

The NVF is based on the normalization of the face values γ_f from the *donor* γ_D, *acceptor* γ_A e *upwind* γ_U cell values. The normalization is defined as,

$$\tilde{\gamma} = \frac{\gamma - \gamma_U}{\gamma_A - \gamma_U} \tag{2.22}$$

From this normalized variable, the relation $\gamma_f = f(\gamma_U, \gamma_D, \gamma_A)$ turns into a function of $\tilde{\gamma} = f(\tilde{\gamma}_D)$, since,

$$\tilde{\gamma}_U = 0 \ e \ \tilde{\gamma}_A = 1 \tag{2.23}$$

From this relation, values $\tilde{\gamma}_D$ between 0 and 1 indicate a monotonic profile, while $\tilde{\gamma}_D < 0$ and $\tilde{\gamma}_D > 1$ indicate min/max γ values in D. Additionally, $\tilde{\gamma}_D \approx 0$ and $\tilde{\gamma}_D \approx 1$ values indicates steep γ gradients.

Therefore, the NVF transforms classical interpolation schemes, such as those presented in Maliska (2017), in linear relations of $\tilde{\gamma}_f$ and $\tilde{\gamma}_D$. Figure 2.6 presents different

interpolation schemes plotted in the NVD.

Figure 2.6 – NVD for classical interpolation schemes.

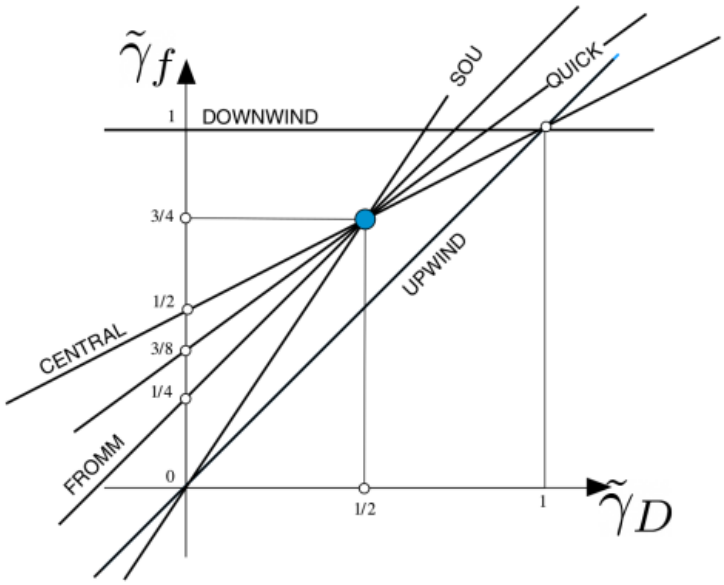

Source - Adapted from Moukalled et al. (2016).

In the diagram shown in Fig. 2.6, as the interpolation function NVD gets closer to the downwind scheme, greater is its compressiveness, and as the NVD gets closer to the upwind scheme, greater is its diffusivity. Therefore, when choosing or implementing a numerical interpolation scheme, the NVD provides valuable information.

According to Versteeg and Malalasekera (2007), an interpolation function must meet three main requirements: i) conservativeness; ii) boundedness and iii) transportiveness. As convective transport always occurs from volume D to volume A, it is interesting that an interpolation function has characteristics as close as possible to that of the upwind interpolation scheme. This can be enforced by assuring monotonicity along the control volumes D, A and U. This can be assured, when the following conditions are respected,

$$\min(\gamma_D, \gamma_A) \leq \gamma_f \leq \max(\gamma_D, \gamma_A) \tag{2.24}$$

or, by using the NVF,

$$\min(\tilde{\gamma}_D, 1) \leq \gamma_f \leq \max(\tilde{\gamma}_D, 1) \tag{2.25}$$

The conditions showed in Eqs. (2.24) and (2.25) represents the Convection Boundness Criteria (CBC) introduced by Gaskell and Lau (1988) and guarantees the conservativeness, boundedness and transportiveness for a given interpolation scheme. In the NVD, the CBC is represented by shadowed area in Fig. 2.7.

Figure 2.7 – CBC region in the NVD.

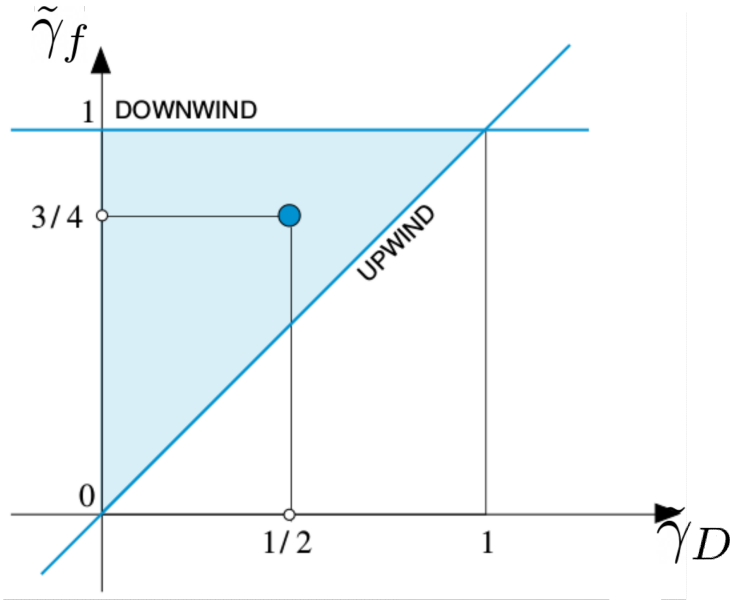

Source - Adapted from Gaskell and Lau (1988).

For discretization using an explicit formulation in time, Leonard (1991) modifies the CBC so that,

$$\begin{aligned} &\tilde{\gamma}_f = \tilde{\gamma}_D && \text{se } \tilde{\gamma}_D < 0 \text{ ou } \tilde{\gamma}_D > 0 \\ &\tilde{\gamma}_D \leq \tilde{\gamma}_f \leq \min\left(1, \frac{\tilde{\gamma}_D}{C_f}\right) && \text{se } 0 \leq \tilde{\gamma}_D \leq 1 \end{aligned} \tag{2.26}$$

where C_f is the face Courant number $C_f = |u_f \Delta t|/\Delta x$. Figure 2.8 shows this region in the NVD. According to the diagram, as the Courant number C_f increases, greater are the chances of an interpolation scheme resulting in numerical oscillations. Besides, for $C_f > 1$, any interpolation scheme presents numerical oscillations and, as commented in the paragraphs above, can lead to unphysical results.

Among the different compression methods based on CBC for two-phase flows with large scale interface lengths, highlight the Compressive Interface Capturing Scheme for Arbitrary Meshes (CICSAM) method developed by Ubbink (1997). The development of the CICSAM interpolation scheme was motivated by the need for a method that could be used to solve two-phase flows using unstructured meshes, since, until that moment, most of the proposed methods were focused on applications that used structured cartesian meshes. The method is based on the fundamentals of NVF and CBC developed in Leonard (1991), with modifications that allow its use in unstructured meshes. In short words, the method is based on the blending scheme of two High-Resolution schemes, the Hyper-C and ULTIMATE-QUICKEST interpolation functions developed and detailed in Leonard

Figure 2.8 – CBC region as a function of the Courant number C_f in the NVD.

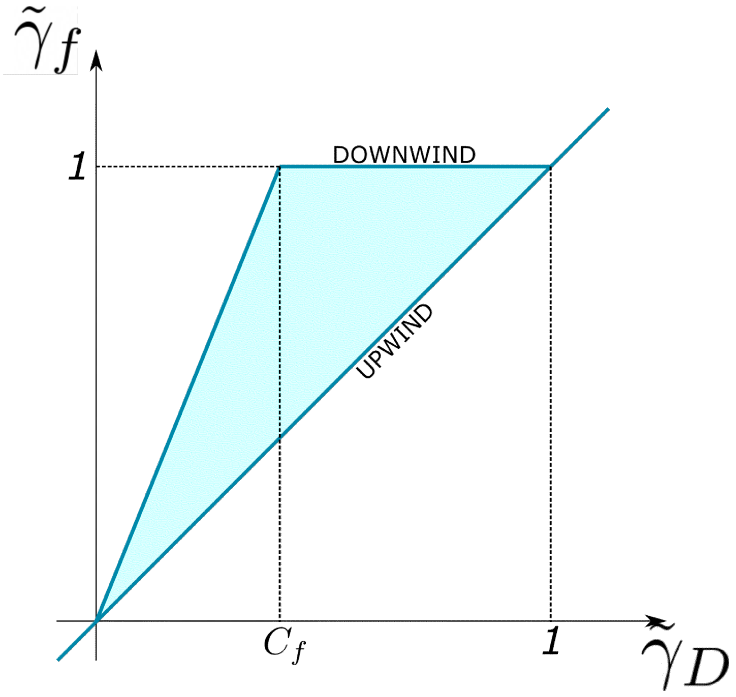

Source - Adapted from Leonard (1991).

(1991).

The Hyper-C interpolation function follows the upper limit of the NVD shown in Fig. 2.9, making it extremely compressive. Thus, the Hyper-C scheme is not advisable for the modeling of two-phase flows, since it does not correctly capture the interface and any gradient in the γ field ends up being transformed into a step-type profile, regardless of interface orientation. Therefore, in the CICSAM scheme, the blending (or weighting) is performed by the ULTIMATE-QUICKEST scheme, which follows the lower bound of the NVD, as shown in Fig. 2.9. The two interpolation schemes are blended as,

$$\tilde{\gamma}_f = \sigma_f \, \tilde{\gamma}_{f,CBC} f + (1 - \sigma_f) \, \tilde{\gamma}_{f,UQ} \tag{2.27}$$

where σ_f $(0 \leq \sigma_f \leq 1)$ is a blending variable, which its calculation depends on the angle between the interface normal vector $(\nabla\gamma_f)$ and the control volume's face normal vector $(\boldsymbol{d}_f)$,

$$\theta_f = \arccos \left| \frac{\nabla\gamma_f)_D \cdot \boldsymbol{d}_f}{|(\nabla\gamma_f)_D| \, |\boldsymbol{d}_f|} \right| \tag{2.28}$$

$$\sigma_f = \min \left\{ \frac{\cos(2\theta_f) + 1}{2}, 1 \right\} \tag{2.29}$$

Thus, when the orientation of the interface is normal to the orientation of the face of the control volume, $\sigma_f = 1$, and when those vectors are parallel, $\sigma_f = 0$.

Figure 2.9 – Interpolations schemes used by the CICSAM method plotted in the NVD .

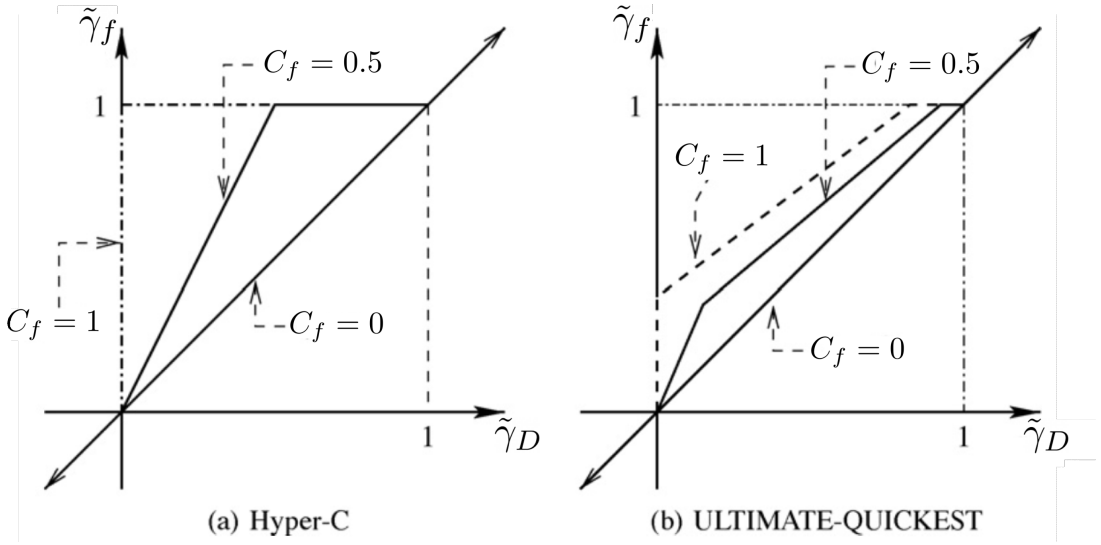

Source - Adapted from Gopala and van Wachem (2008).

Despite following the CBC, due to computational errors, at the end of each advection step, especially when using unstructured meshes, it is necessary to perform a boundness check, i.e., cycle over the mesh control volume to check for values $\gamma > 1$ and $\gamma < 0$. If there are unbounded unrealistic values, those values are renormalized conservatively. Details regarding this additional iterative cycle are described in detail in (UBBINK, 1997).

Another approach commonly found in the literature (JASAK et al., 2007) and used by Rusche (2002) for the simulation of two-phase flows, is the introduction of an artificial compressive term into the VOF equation (Eq. (2.21)) to obtain sharp interfaces. The VOF equation with the additional compressive term reads,

$$\frac{\partial \gamma}{\partial t} + \nabla \cdot (\boldsymbol{u}\,\gamma) + \nabla \cdot ([\boldsymbol{u}_c\,\gamma\,(1-\gamma)] = 0 \tag{2.30}$$

where the term $\gamma\,(1-\gamma)$ ensures that the interfacial compressive term only acts in the interfacial region. The compressive velocity, $\boldsymbol{u}_c$, is proportional to the unit normal vector $\boldsymbol{n}$, $\boldsymbol{u}_c = C_\gamma \left|\boldsymbol{u}_f\right| \boldsymbol{n}$ where $\boldsymbol{u}_f$ is the velocity in the control volume's face and C_γ is a constant that controls the strength of the artificial compressive force. Details regarding this approach can be found in Rusche (2002), Gopala and van Wachem (2008) and Cerqueira (2016).

As seen in Eq. (2.30), this artificial compressive approach is not a high-order interpolation scheme, but an additional term in the phase indicator scalar transport equation. Therefore, the method can be used in conjunction with classical interpolation function (MALISKA, 2017), NVD/CBC schemes such as the CICSAM, or with Total Variation Diminishing (TVD) schemes (VERSTEEG; MALALASEKERA, 2007; MOUKALLED

et al., 2016).

2.1.1.3 Surface Tension Force Calculation

From the thermodynamical point of view, surface tension is the work required to increase a certain amount of interfacial area. The interface, characterized by the presence of two fluids, is characterized by a surface tension coefficient σ, which represents the energy per unit area needed to increase the interfacial area. Disregarding external forces, such as gravity, surface tension can be defined using the Young-Laplace equation (FAGHRI; ZHANG, 2006),

$$\Delta p = p_i - p_o = \sigma \left(\frac{1}{r_1} + \frac{1}{r_2} \right) = \sigma \kappa \tag{2.31}$$

where κ represents the average curvature of the interface, r_1 e r_2 the main radii of curvature of a three-dimensional interface and p_i e p_o, the internal and external pressures of the interface.

In Brackbill et al. (1992), the authors propose the Continuum Surface Force (CSF) model for the numerical modeling of the surface tension force. The CSF model transforms a surface tension force, which in the momentum conservation equation represents a surface source term, into a volumetric source term, distributing the interface strength over a small finite transition region in space. The model is built under the Young-Laplace equation (Eq. (2.31)). Thus, the surface tension force acting on an interface, taking a two-phase flow situation as an example, is modeled as,

$$\boldsymbol{f}_\sigma = \sigma \kappa \frac{\nabla \gamma}{|\nabla \gamma|} \tag{2.32}$$

where κ it is defined as,

$$\kappa = \nabla \cdot \boldsymbol{n} \tag{2.33}$$

and the interface vector normal can be calculated as,

$$\boldsymbol{n} = \frac{\nabla \gamma}{|\nabla \gamma|} \tag{2.34}$$

One disadvantage of the CSF method is the occurrence of unrealistic velocity fields close to the interface, denoted as spurious, or parasitic, currents. In general, its appearance arises from the discretization of a surface tension force at the molecular level on a macroscopic scale (DENNER, 2013). These spurious fields have their origin in the imbalance between pressure gradients and surface tension forces close to the interface, due to the inadequate numerical implementation of these last two terms and also to the imprecise estimate of the curvature of the interface, as shown in Francois et al. (2006) and Denner and Wachem (2014).

When modeling multiphase flows, particularly when using the VOF method, the implementation of normal vectors and the curvature of the interface is of crucial importance, as they influence the term responsible for modeling the surface tension force.

In order to determine these two quantities, the phase indicator scalar field must have a continuous and double differentiable field. Due to the use of interfacial compressive or geometric reconstruction methods, the γ field has a continuous character. However, its variation can be abrupt in space, resulting in problems in the evaluation of its gradients. Therefore, it is necessary to apply smoothing techniques in the fields of the volumetric fraction and more refined methods for calculating their gradients. Details regarding the different numerical alternatives in obtaining those gradients, such as the interface normal and curvature can be addressed in the works of Francois et al. (2006), Denner (2013), Glitz et al. (2012) and Cerqueira (2016).

2.1.2 Average based Models

2.1.2.1 Two-Fluid Model (TFM)

From the local instantaneous formulation, through the consistent application of the averaging process, one can derive the Two-Fluid Model (TFM) (ISHII; HIBIKI, 2011, 2011; FAGHRI; ZHANG, 2006). For an incompressible, with k phase, isothermal and viscous system, the conservation equations for the two-fluid model are the following,

$$\frac{\partial}{\partial t}(\epsilon_k \rho_k) + \nabla \cdot (\epsilon_k \rho_k \boldsymbol{u}_k) = 0 \tag{2.35}$$

$$\frac{\partial}{\partial t}(\epsilon_k \rho_k \boldsymbol{u}_k) + \nabla \cdot (\epsilon_k \rho_k \boldsymbol{u}_k \boldsymbol{u}_k) = -\epsilon_k \nabla p + \boldsymbol{\nabla} \cdot \left(\epsilon_k \mu_k \overline{\overline{\boldsymbol{T}}}_k\right) + \boldsymbol{M}_{kj} + \epsilon_k \rho \boldsymbol{g} \tag{2.36}$$

where ϵ_k is the dispersed phase void fraction of a given phase k. In this model, the phases share the pressure field. However, opposed to the VOF method, the phases have different velocity fields.

As can be seen from Eqs. (2.35) and (2.36), for a two-phase, incompressible and isothermal flow, there are two mass conservation equations (continuity),one for each fase, two equations for momentum conservation equations in each direction, constitutive relations for the stress tensors ($\overline{\overline{\boldsymbol{T}}}_k$) and closure terms for modeling interfacial transfers ($\boldsymbol{M}_{kj}$).

Due to the averaging process, information about interactions between phases is lost and needs to be reintroduced into the model. This information is reintroduced through closure relations, derived from numerical and experimental results. For the momentum

conservation equation (Eq. (2.36)), the interfacial transfer is reincorporated through the source term $\boldsymbol{M}_{kj}$, which models the the interfacial transport between one phase k to another phase j. The usual procedure (ISHII; HIBIKI, 2011) is modeling the term $\boldsymbol{M}_{kj}$ through the linear combination of known interfacial forces, such as,

$$\boldsymbol{M}_{kj} = \boldsymbol{M}_{kj}^{D} + \boldsymbol{M}_{kj}^{V} + \boldsymbol{M}_{kj}^{B} + \boldsymbol{M}_{kj}^{L} + \boldsymbol{M}_{kj}^{W} \tag{2.37}$$

where $\boldsymbol{M}_{kj}^{D}$, $\boldsymbol{M}_{kj}^{V}$, $\boldsymbol{M}_{kj}^{B}$, $\boldsymbol{M}_{kj}^{L}$ and $\boldsymbol{M}_{kj}^{W}$ represents, respectively, contributions due to drag, virtual mass force, Basset force, lift force and wall lubrication force. The terms present in Eq. (2.37) are modeled through correlations found in the literature (ISHII; HIBIKI, 2011; CLIFT et al., 2005a). It is important to state that those closure relations and correlations are the major sources of uncertainty in the Two-Fluid Model. Nevertheless, the model is widely accepted in engineering applications, and the success of its application depends on the appropriate choice for the transfer relations between the phases and constitutive equations.

2.1.3 Lagrangian based Models

Lagrangian based models can be seen in a middle option between Interface Capturing and Averaged Based Models. This approach, also referred to as the Lagrangian-Eulerian (LE) formulation, requires less computational power than Interface Capturing Methods, but need fewer assumptions as Averaged Based Models. In the LE formulation, Lagrangian particles, or bubbles in the case of this thesis, are tracked independently through the solution of Newtown's second law. Thus, several bubble trajectories can be computed, including bubble-bubble and bubble-wall collisions (PEÑA-MONFERRER et al., 2018), bubble coalescence, and breakup (JAIN et al., 2014). Though the motion of different bubbles, the LE formulation can capture complex physical phenomena, multiscale interactions and nonequilibrium effects in multiphase flows (SUBRAMANIAM, 2013).

Within the Lagrangian-Eulerian formulation, the Discrete Bubble Model (DBM), first proposed by Darmana et al. (2005), is used to model bubbly flows, including bubble-bubble and bubble-wall collision models and employing a two-way coupling interaction between the continuous liquid phase and the dispersed bubbles. The Discrete Bubble Model is detailed in the section below.

2.1.3.1 Discrete Bubble Model

In the Discrete Bubble Model motion for each individual bubble is computed from Newton's second law. The liquid phase contributions are taken into account via the net

force experienced by each individual bubble. For an incompressible bubble, the equations can be written as

$$m_{b,i}\frac{d\boldsymbol{u}_{b,i}}{dt} = \boldsymbol{f}^{b}_{b,i} + \boldsymbol{f}^{h}_{b,i} + \sum_{j=1} \boldsymbol{f}^{c}_{b,ij} \tag{2.38}$$

where the subscript i represents the i-th dispersed bubble in the domain and $\boldsymbol{u}_{b,i}$ is its instantaneous velocity. In Eq. (2.38), the right hand side of the equation represents the external forces acting on the dispersed bubble. Those can be divided into the contributions due to buoyancy ($\boldsymbol{f}^{b}_{b,i}$), from the continuous fluid-bubble interaction ($\boldsymbol{f}^{h}_{b,i}$) and the collision with the surrounding j-th particles ($\boldsymbol{f}^{c}_{b,ij}$) or walls.

The buoyancy force term is defined as:

$$\boldsymbol{f}^{b}_{b,i} = V_{b,i}\,\boldsymbol{g}\,(\rho_b - \rho_l) \tag{2.39}$$

where $V_{b,i}$ ($= \pi {d_{b,i}}^3/6$) is the volume of the dispersed bubble with a diameter $d_{b,i}$.

In the present work, the hydrodynamic forces from the continuous fluid-bubble interaction considers the force due to drag, virtual mass effect, transverse lift, pressure gradient and lubrication force, as following:

$$\begin{aligned}
\boldsymbol{f}^{h}_{b,i} =& \frac{3}{4} V_{b,i}\,\rho_l C_{D,i}\left(\boldsymbol{u} - \boldsymbol{u}_{b,i}\right)\left|\boldsymbol{u} - \boldsymbol{u}_{b,i}\right| \\
&+ V_{b,i}\,\rho_l C_{VM,i}\left(\frac{D\boldsymbol{u}}{Dt} - \frac{d\boldsymbol{u}_{b,i}}{dt}\right) \\
&+ V_{b,i}\,\rho_l C_{L,i}\left[\left(\boldsymbol{u} - \boldsymbol{u}_{b,i}\right) \times \left(\nabla \times \boldsymbol{u}\right)\right] \\
&+ V_{b,i}\,\rho_l \frac{D\boldsymbol{u}}{Dt} \\
&+ \boldsymbol{f}^{wl}_{b,i}
\end{aligned} \tag{2.40}$$

where $\boldsymbol{u}$ represents the undisturbed continuous fluid velocity in the vicinity of the dispersed bubble position. The coefficients C_D, C_{VM} and C_L correspond, respectively, for the drag, virtual mass and lift force coefficients. The force $\boldsymbol{f}^{wl}_{b,i}$ represents the wall lubrication force, which represents the drainage liquid film when a bubble is moving near a wall. Different correlations for the aforementioned coefficients can be found in the literature (TOMIYAMA et al., 1998, 2002; WELLEK et al., 1966; AUTON, 1984; TOMIYAMA, 1998). The bubble-bubble and bubble-wall collisions ($\boldsymbol{f}^{c}_{b,ij}$) can be modeled through the soft-sphere model, as detailed in Peña-Monferrer et al. (2018).

The liquid phase hydrodynamics is represented by a set of continuity and momentum equations, where the presence of bubbles is reflected by the liquid-phase volume fraction α_l and additional term for the DBM contribution in the momentum equation.

Following the main objectives of the thesis, the liquid phase equations are presented as modified version of the VOF method equations (Eqs. (2.19) and (2.20)),

$$\frac{\partial(\alpha_l \rho)}{\partial t} + \boldsymbol{\nabla} \cdot \alpha_l \rho \boldsymbol{u} = 0 \tag{2.41}$$

$$\frac{\partial(\alpha_l \rho \boldsymbol{u})}{\partial t} + \boldsymbol{\nabla} \cdot (\alpha_l \rho \boldsymbol{u}\boldsymbol{u}) = -\alpha_l \boldsymbol{\nabla} P + \boldsymbol{\nabla} \cdot \alpha_l \boldsymbol{T} + \rho \alpha_l \boldsymbol{g} + \boldsymbol{f}_\sigma + \boldsymbol{f}_{DBM,i} \tag{2.42}$$

where the fluid properties and stress tensors are still modeled through the "standard" VOF method and the $\boldsymbol{f}_{DBM,i}$ address the momentum coupling between the liquid phase and the dispersed bubbles. For the phase indicator transport equations γ, the α_l corrected flux, using the continuity constraint imposed by Eq. (2.41), is used to transport the γ scalar.

The liquid-phase volume fraction α_l shown in the equations above should represent the volume occupied by the bubbles in a given control volume. However, in some cases, bubbles may be larger than the computational cell and numerical problems may arise. To circumvent those problems, recent works found in the literature circumvent those issues by using a "background" particle mesh. Details addressing this approach are found in Mallouppas and Wachem (2013), Sun and Xiao (2015), Jing et al. (2016) and Pozzetti and Peters (2018).

Regarding the DBM use in engineering applications, recently, Jain et al. (2014) and Peña-Monferrer et al. (2018) used the DBM model to simulate bubble columns in different geometries. In both works, the authors compared the model results with experiments, finding a good agreement between the numerical and experimental results for the liquid and gas phases.

2.1.4 Review of recent literature on numerical models for liquid-gas flows with different interface length sales[1]

In recent years, some authors (ŠTRUBELJ; TISELJ, 2011; CERNE et al., 2001; WARDLE; WELLER, 2013; YAN; CHE, 2010, 2011; HÄNSCH et al., 2012; HUA, 2015; POZZETTI; PETERS, 2018; PENG et al., 2020) proposed numerical models for modeling the different interface scales found in areal multiphase flow patterns. This section aims to conduct a detailed review of these works.

[1] Due to the different notations used in the reviewed works found the literature, this section does not follow the list of symbols.

Cerne et al. (2001)

In the work of Cerne et al. (2001), the authors seek to couple the VOF method and the TFM, aiming to use the VOF to model interfaces interface scales and the TFM for small length scale interface. Figure 2.10 shows an example in which a flow region, where certain control volumes are modeled by TFM (lighter regions) and others by the VOF (darker regions).

Figure 2.10 – Two-Fluid Model (TFM) and Volume-of-Fluid (VOF) coupling.

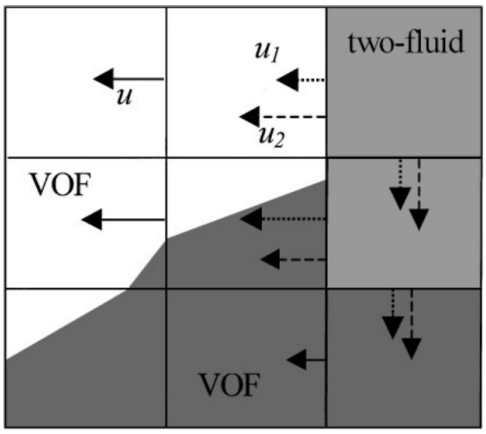

Source - Cerne et al. (2001).

Since the VOF method has only a single velocity field shared between the phases and the TFM has two velocity fields, one for each phase, a transition model is necessary to convert the velocity fields of the different formulations. This is done through the following relation, when transitioning from the VOF to the TFM,

$$\boldsymbol{u}_1^{TFM} = \boldsymbol{u}_2^{TFM} = \boldsymbol{u}^{VOF} \tag{2.43}$$

when transitioning through the TFM to the VOF,

$$\boldsymbol{u}^{VOF} = \gamma_1^{VOF}\boldsymbol{u}_1^{TFM} + (1-\gamma_1^{VOF})\boldsymbol{u}_2^{TFM} \tag{2.44}$$

It is important notice that when transitioning between the models, the velocities are redefined to conserve the volumetric flux in each face of the control volumes.

The choice between the VOF and TFM methods is based on a switching criterion. This criterion is based on the estimate of the local dispersion of the reconstructed interface in the control volume. Figure 2.11 schematically represents the variables used to define the switching criterion. The switching criterion is defined from a 3x3 control volume stencil, defined as the ratio between the value of each stencil control volume and the area under the reconstructed interface line in the control volume.

Figure 2.11 – Schematic representation of the variables used to define the switching criteria.

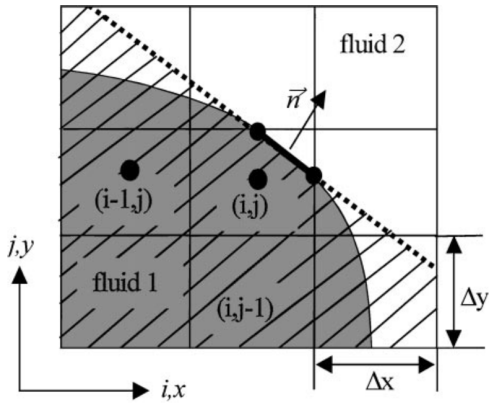

Source - Cerne et al. (2001).

In Fig. 2.11, the local dispersion of the interface is defined as the ratio of the gray area ($\gamma^{VOF}_{(i,j)}$) and the hatched area. Numerically, the calculation of the transition criterion is defined as,

$$\varphi_{i,j}(\boldsymbol{n}) = \sum_{l=-1}^{1}\sum_{k=-1}^{1}\left(\gamma^{VOF}_{(i+k,j+k)} - \gamma^{\boldsymbol{n}}_{(i+k,j+k)}\right)^2 \tag{2.45}$$

where $\gamma^{\boldsymbol{n}}_{(i+k,j+k)}$ is the value filled by a phase from the geometrically reconstructed interface (normal vector $\boldsymbol{n}$).

After calculating the value of $\varphi_{i,j}$, the interface of a control volume is marked as large scale (VOF method) if $\varphi_{i,j} < \varphi_0$ and small scale (TFM method) if $\varphi_{i,j} > \varphi_0$. According to the authors, after performing some numerical tests, the value of $\varphi_0 = 0.4$ is considered adequate for flows with different interface scales.

In order to test the developed method, the authors propose the simulation of Rayleigh-Taylor instability, since this two-phase flow present multiple interface scales and evolves from a stratified to a dispersed flow over the simulation time. Figures 2.12 and 2.13 present the Rayleigh-Taylor instability for the VOF and proposed method (VOF and TFM coupled model), respectively, at a given time for different mesh resolutions. As seen in Figs. 2.12 and 2.13, as the mesh resolution increases, at the tip of the mushroom cloud the VOF method results in thin structures. In the VOF-TFM coupled method, Fig. 2.13, the switching criterion classify the nearby control volumes as a small interface length scale region, resulting in diffuse distribution of the phase indicator function.

As the flow evolves, since surface tension is neglected in the Rayleigh-Taylor instability, the thin thickness region requires finer meshes, demonstrating that the VOF an inappropriate model for this type of small interfacial structure/scale modeling, as seen in

Figure 2.12 – Rayleigh-Taylor instability simulated through the VOF method in different mesh resolutions at t=2.0 s.

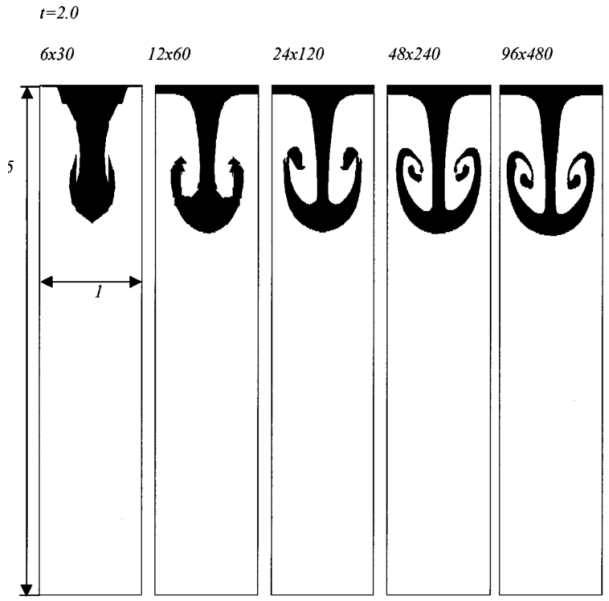

Source - Cerne et al. (2001).

Fig. 2.14. However, in Fig. 2.15, which shows the Rayleigh-Taylor instability simulated using the coupled method for several time periods, the results show a more realistic behavior than that shown in Fig. 2.14. In the first instants of the simulation shown in Fig. 2.15, the VOF method is used to capture the large-scale interfaces. After a few instants,

Figure 2.13 – Rayleigh-Taylor instability simulated through the VOF-TFM coupled method in different mesh resolutions t=2.0 s.

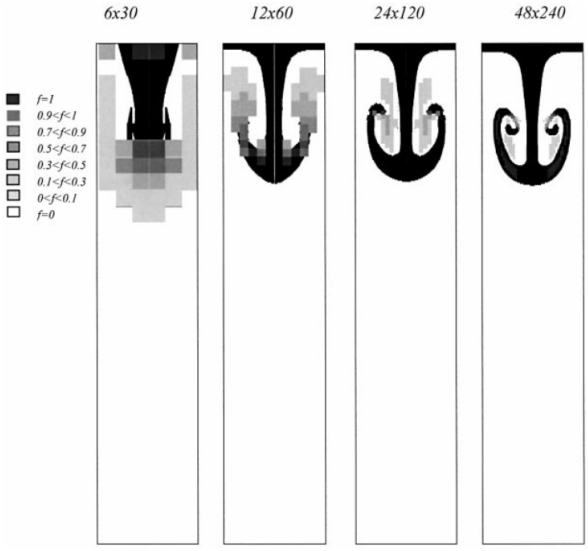

Source - Cerne et al. (2001).

the VOF method is deactivated in a large part of the domain, and the TFM is activated. In the end, the phase mixing process is interrupted and a stratification process is initiated, activating the VOF method again in a large part of the domain.

Figure 2.14 – Rayleigh-Taylor instability simulated through the VOF method in different mesh resolutions at t=8.0 s.

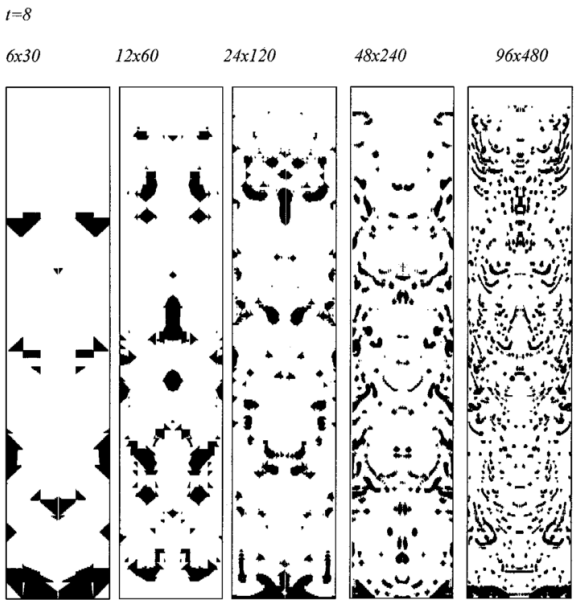

Source - Cerne et al. (2001).

Figure 2.15 – Rayleigh-Taylor instability simulated through the VOF-TFM coupled method in different time instants.

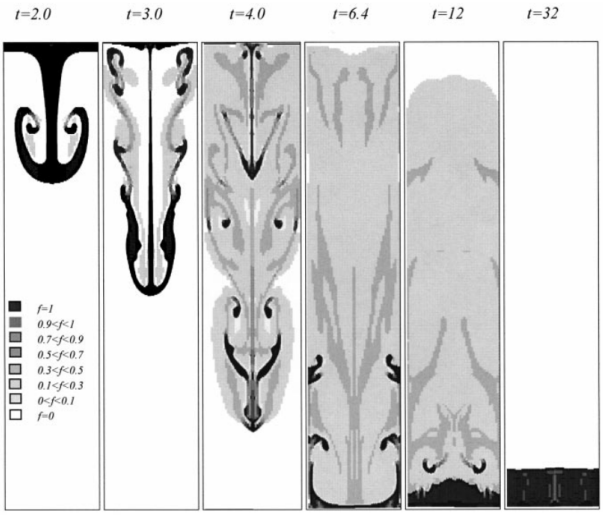

Source - Cerne et al. (2001).

From the results presented in Cerne et al. (2001), it is observed that the coupling between the VOF and TFM methods are capable of modeling flows with multiple interfaces.

However, the proposed model is not used for modeling realistic flow conditions, nor validated with experimental results. In addition, there is no discussion about the surface tension forces modeling in the coupled VOF-TFM model ($\boldsymbol{f}_\sigma$ term in Eq. (2.20)) and the TFM interfacial transfer terms ($\boldsymbol{M}_{kj}$ term in Eq. (2.36)).

Štrubelj and Tiselj (2011)

In the work of Štrubelj and Tiselj (2011), the authors propose a model based on the Two-Fluid Model and the use of an interface sharpening algorithm based on the Level-Set (LS) method. Unlike the work presented in Cerne et al. (2001), there is no coupling between models suitable for modeling for large-scale interfaces and those developed for modeling dispersed phases. In this work, the entire domain is solved by the Two-Fluid Model, with the existence of two phases, each one with its velocity field. In control volumes marked as large-scale interfaces, the method proposed by the authors seeks to modify the term $\boldsymbol{M}_{kj}$ of Eq. (2.36), so that the relative speed between the phases is zero ($\boldsymbol{u}_2^{TFM} - \boldsymbol{u}_1^{TFM} = 0$). The modification ensures that, in the interface, the velocity of the different phases must be the same. This is done through the relation,

$$\boldsymbol{M}_{12} = -\boldsymbol{M}_{21} = -\varepsilon_1^{TFM}\varepsilon_2^{TFM}\left(\boldsymbol{u}_2^{TFM} - \boldsymbol{u}_1^{TFM}\right)\rho_m \tag{2.46}$$

where,

$$\rho_m = \varepsilon_1^{TFM}\rho_1^{TFM} + (1-\varepsilon_1^{TFM})\rho_2^{TFM} \tag{2.47}$$

The detection of large and small scale interfaces is performed using the same method described in Cerne et al. (2001). In control volumes marked with a large-scale interface, an artificial compression force is introduced, seeking to keep the large-scale interface sharp. The compression force is introduced by an Level-Set (OLSSON; KREISS, 2005) evolutionary equation type defined as

$$\frac{\partial \varepsilon}{\partial \tau} + \nabla \cdot (\varepsilon\,(1-\varepsilon)\,\boldsymbol{n}) = \lambda \Delta \varepsilon \tag{2.48}$$

where τ represents a step in the iterative procedure and λ is an artificial viscosity necessary for numerical stabilization. According to the authors, only a single iteration of Eq. (2.48) at each time step is necessary to define the large-scale interface.

Likewise Cerne et al. (2001), the proposed method is tested based on the simulation of Rayleigh-Taylor instability. Figures 2.16 – 2.18 show the Rayleigh-Taylor instability flow evolution over different time instants. The results of Fig. 2.16 , modeled by the Two-Fluid Model with no modification for detecting large-scale interfaces, shows that the interface becomes diffuse throughout the Rayleigh-Taylor instability evolution. In Fig.

2.17 , in which the interfacial compression force is acting throughout the entire domain, the large-scale interface is captured satisfactorily in the initial time steps $t < 0.48$), but the solution advances, no small scale interfaces are present and the formations of thin ligaments are observed, which are divided into smaller and well-defined regions.

Figure 2.16 – Rayleigh-Taylor instability simulated through the TFM without additional modifications.

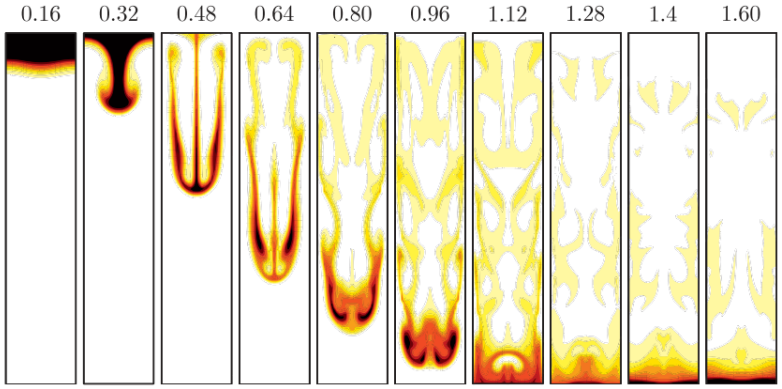

Source - Štrubelj and Tiselj (2011).

Figure 2.17 – Rayleigh-Taylor instability simulated through the TFM, solving Eq. (2.48) in the entire computational domain.

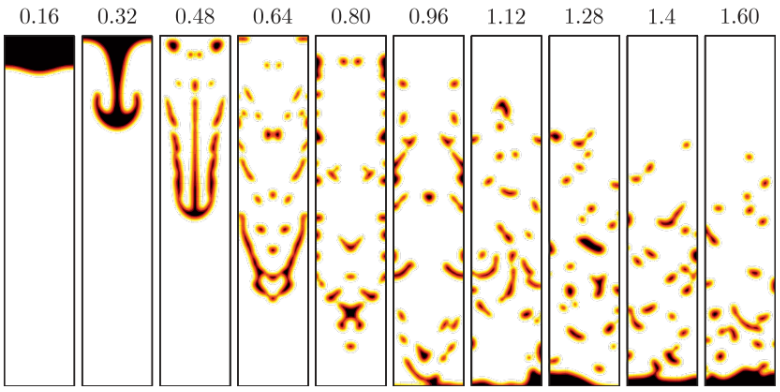

Source - Štrubelj and Tiselj (2011).

The multiscale model (Fig. 2.18), in which the large-scale interface compression force acts only in the regions detected as large-scale interfaces, results in more realistic flow evolution. In the initial time steps, the large-scale interface is detected and remains sharp until $t < 0.48$. After this instant, thin ligaments are observed, forming mixture regions, where small scale interfaces are present. As the solution evolves, those ligaments start to break-up, forming regions where the small scale interface lengths are dominant. In the end, the switching criterion starts to mark part of the control volumes as large-scale interfaces and stratification begins.

Figure 2.18 – Rayleigh-Taylor instability simulated through the TFM, solving Eq. (2.48) only in the control volumes marked as large-scale interface interfaces.

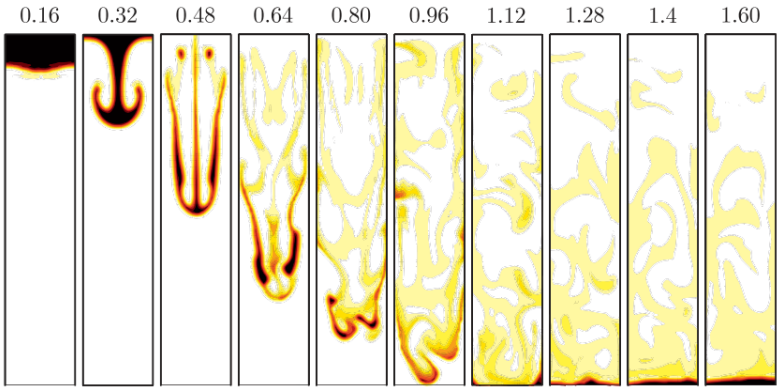

Source - Štrubelj and Tiselj (2011).

According to the results shown in Štrubelj and Tiselj (2011), it is possible to model a multiphase flow with multiple interface scales only by modifying the Two-Fluid Model. However, as in Cerne et al. (2001), there is no discussion regarding the surface tension force modeling and the TFM interfacial transfer terms, and no experimental comparison is shown.

Wardle and Weller (2013)

In the multiscale interfacial flow modeling proposed by Wardle and Weller (2013), such as the model described in Štrubelj and Tiselj (2011), there is no coupling between a model suitable for flows with large scale interfaces and small scale interfaces. The approach described by Wardle and Weller (2013) uses the artificial interface compression term, as detailed in the discussion regarding Eq. 2.30, which is rewritten here under the Two-Fluid model,

$$\frac{\partial \varepsilon}{\partial t} + \nabla \cdot (\boldsymbol{u}\, \varepsilon) + \nabla \cdot ([\boldsymbol{u}_c\, \varepsilon\, (1-\varepsilon)] = 0 \tag{2.49}$$

where the compressive velocity $\boldsymbol{u}_c$ is defined as,

$$\boldsymbol{u}_c = C_\varepsilon \left|\boldsymbol{u}_f\right| \boldsymbol{n} \tag{2.50}$$

The term C_ε of Eq. 2.50 is defined as non-zero value $C_\varepsilon > 0.0$ when the control volume is defined as a large-scale interface scale and is set to zero $C_\varepsilon = 0.0$ when its defined as small scale interface. The criterion used to define if a given control volume contains a small or large scale interface follows the method proposed by Cerne et al. (2001).

In Wardle and Weller (2013), the proposed model is used to simulate a few benchmark cases and engineering applications, such as a horizontal settler and an annular mixer,

presenting results without any sort of experimental validation. In Shonibare and Wardle (2015), the same multiscale model is used to simulate a vertical plunging jet. Here, an experimental comparison is conducted to asses the model ability in simulating flows with different interface length scales. The comparison is performed by visual inspection of the numerical and experimental results, as shown in Fig. 2.19, presenting a good agreement between the two results.

Figure 2.19 – Side-by-side comparison of the numerical and experimental results for a vertical plunging jet.

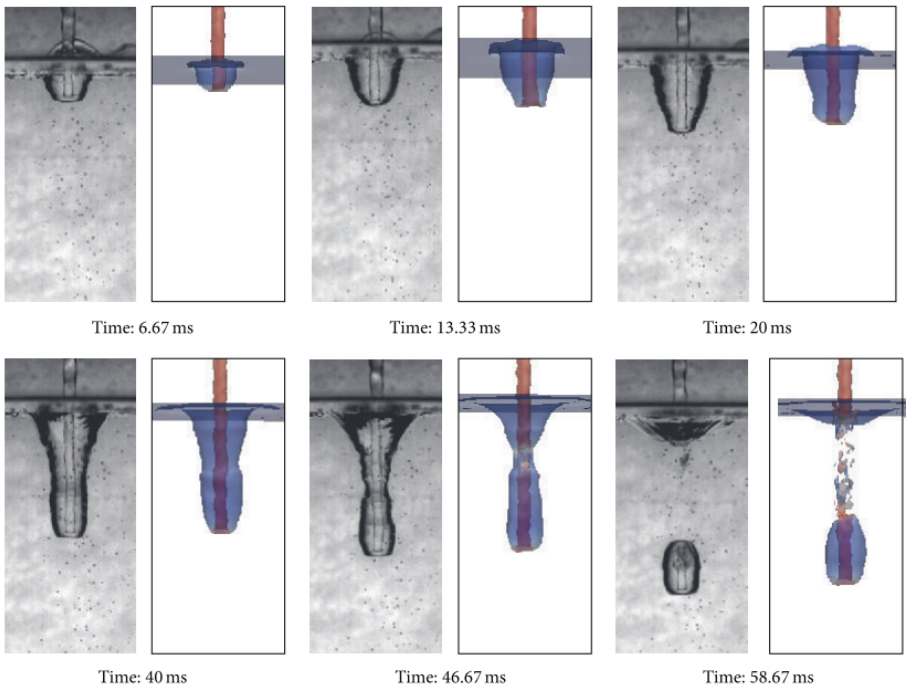

Source - Shonibare and Wardle (2015).

Thus, according to the results from Wardle and Weller (2013) and Shonibare and Wardle (2015), it can be concluded that the interfacial compression force is capable of resolving flows with multiple interface scales when using the Two-Fluid Model.

Yan and Che (2010)

In Yan and Che (2010), a hybrid model based on the coupling of the Two-Fluid Model and the Volume-of-Fluid method is presented from the division of the gas phase into two phases: i) dispersed gas phase (small scale interface) and ii) large scale gas interface.

The model proposed in Yan and Che (2010) is used in Yan and Che (2011) for the simulation of a "quasi-real" slug flow pattern, in which the gas phase is divided in i) dispersed bubbles (small scale interface) and ii) Taylor bubble gas phase (large interface scale). Figure 2.20 shows a schematic illustration of the three distinct phases.

Figure 2.20 – Schematic map of three phases proposed model in the model of Yan and Che (2010).

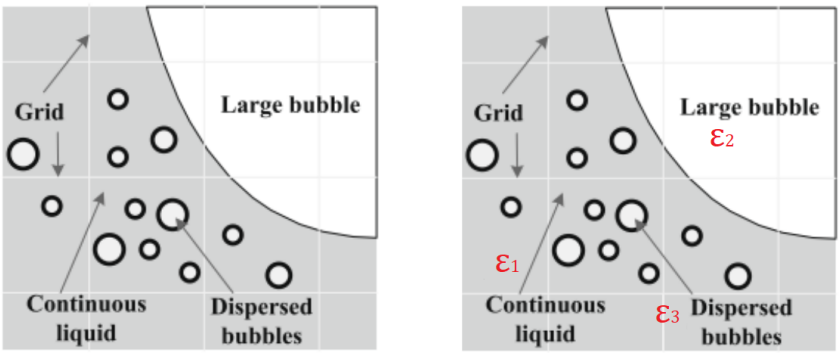

Source - Adapted from Yan and Che (2010).

In this work, the authors discuss the equivalence between the governing equations of the Two-Fluid Model (Eqs. (2.35) and (2.36)) and the VOF method (Eqs. (2.21) e (2.20)), demonstrating that the VOF can be seen with a particularization of the Two-Fluid Model in which only one velocity field is present ($\boldsymbol{u} = \boldsymbol{u}_1 = \boldsymbol{u}_2$), requiring the incorporation of a surface tension model and a mixture law to calculate the transport properties. The equations used in the work of Yan and Che (2010) are showed below, with the phase indicator scalar being defined by the ε variable,

$$\frac{\partial}{\partial t}(\varepsilon_k \rho_k) + \nabla \cdot (\varepsilon_k \rho_k \boldsymbol{u}_k) = 0 \tag{2.51}$$

$$\frac{\partial}{\partial t}(\varepsilon_k \rho_k \boldsymbol{u}_k) + \nabla \cdot (\varepsilon_k \rho_k \boldsymbol{u}_k \boldsymbol{u}_k) = -\varepsilon_k \nabla p + \boldsymbol{\nabla} \cdot \left(\varepsilon_k \mu_k \overline{\overline{\boldsymbol{D}}}_k\right) + \boldsymbol{M}_{kj} + \varepsilon_k \rho \boldsymbol{g} \tag{2.52}$$

For control volumes with a large scale interface (presence of phase 1 and phase 2, according to Fig. 2.20), the VOF method is used for advecting the phases. In the presence of phase 1 and phase 3, a Two-Fluid Model advection scheme is used. In control volumes where the three phases are present (ε_1 – liquid, ε_2 – bubbles with small scale interface and ε_3 – bubble with large scale interface), additional steps are required to transport the different phases. Thus, when the three phases are present, a void fraction redistribution is proposed, in which the ε_k field of each phase k is transformed into a new redistributed ε'_k distribution.

The void fraction, or phase redistribution, is necessary for the calculation of interfacial terms, i.e., $\boldsymbol{M}_{kj}$ term of Eq. (2.52). In the proposed model, the $\boldsymbol{M}_{kj}$ term is separated into two terms: i) the surface tension force between phase 1 to phase 2, $\boldsymbol{M}^L_{kj}$ and ii) the interfacial momentum transfer between phase 1 and phase 3, $\boldsymbol{M}^S_{kj}$. For the surface tension

force ($\boldsymbol{M}_{kj}^{L}$), in situations in which phase 3 is present, the phases are redistributed so that the void fraction of phase 2 is kept constant and phases 1 and 3 give rise to a phase ε_1',

$$\varepsilon_1' = \varepsilon_1 + \varepsilon_3 \tag{2.53}$$

Then, the surface tension force $\boldsymbol{M\prime}_{kj}^{L}$ is calculated from this arrangement of phases. After its calculation, $\boldsymbol{M\prime}_{kj}^{L}$ is converted to $\boldsymbol{M}_{kj}^{L}$ through,

$$\boldsymbol{M}_{kj}^{L} = (1 - \varepsilon_3)\boldsymbol{M\prime}_{kj}^{L} \tag{2.54}$$

The $\boldsymbol{M}_{kj}^{L}$ calculation procedure detailed in the paragraph above is schematically depicted in Fig. 2.21.

Figure 2.21 – Schematic representation of the calculation procedure of $\boldsymbol{M}_{kj}^{L}$ when the tree different phases coexist in same control volume.

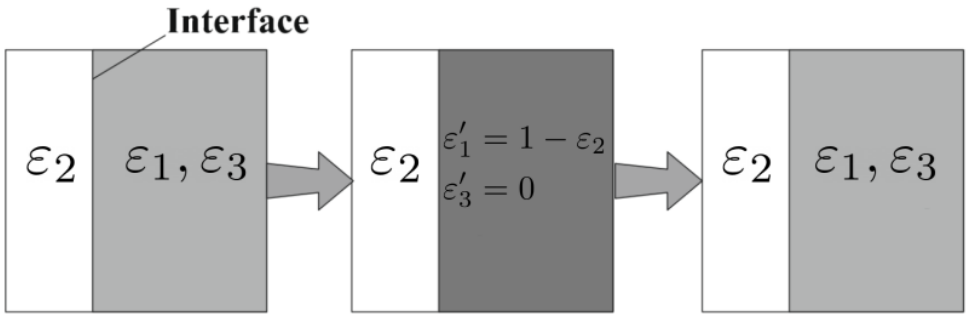

Source - Adapted from Yan and Che (2010).

For the interfacial momentum transfer term ($\boldsymbol{M}_{kj}^{S}$) between phase 1 and phase 3, in situations where phase 2 is also present, the following phase redistribution is proposed,

$$\varepsilon_1 + \varepsilon_2 + \varepsilon_3 = 1 \tag{2.55}$$

$$\varepsilon_1 + \varepsilon_3 = 1 - \varepsilon_2 \tag{2.56}$$

$$\frac{\varepsilon_1}{(1 - \varepsilon_2)} + \frac{\varepsilon_3}{(1 - \varepsilon_2)} = 1 \tag{2.57}$$

$$\varepsilon_1' + \varepsilon_3' = 1 \tag{2.58}$$

where $\varepsilon_1' = \varepsilon_1/(1 - \varepsilon_2)$ and $\varepsilon_3' = \varepsilon_3/(1 - \varepsilon_2)$. After the phase redistribution, the term $\boldsymbol{M\prime}_{kj}^{S}$, which is related to the momentum transfer between phases ε_1' e ε_3', is calculated. Finally, $\boldsymbol{M\prime}_{kj}^{S}$ is weighted by $(1 - \varepsilon_2)$, resulting in,

$$\boldsymbol{M}_{kj}^{S} = (1 - \varepsilon_2)\boldsymbol{M\prime}_{kj}^{S} \tag{2.59}$$

Figure 2.22 schematically illustrates the phase redistribution procedure used to calculate $\boldsymbol{M}_{kj}^{S}$.

Figure 2.22 – Schematic representation of the calculation procedure of $\boldsymbol{M}_{kj}^{S}$ when the tree different phases coexist in same control volume.

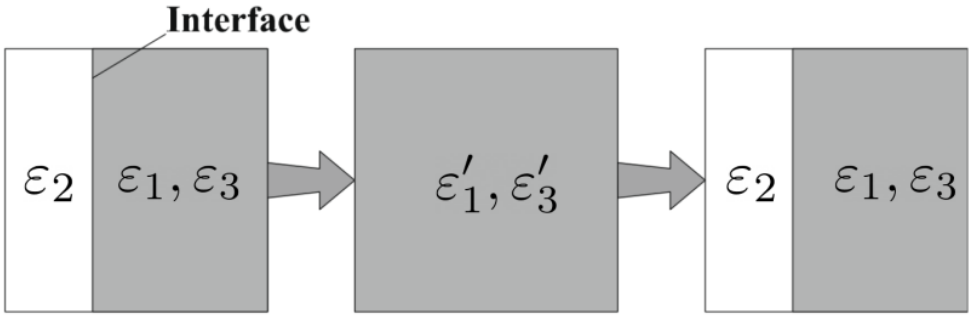

Source - Adapted from Yan and Che (2010).

In contrast to all the described works so far (ŠTRUBELJ; TISELJ, 2011; CERNE et al., 2001; WARDLE; WELLER, 2013), no switching criterion is used or proposed to alter between the TFM and the VOF method in interfacial control volumes ($0 < \varepsilon_k < 1$), seeking a classification based on the interface length scale. Here, in Yan and Che (2010), the authors adopt an empirical constant, based on the values of ε_2 to switch between the TFM and the VOF method.

The model proposed by the authors in Yan and Che (2010) is used for the modeling and simulation of a liquid-gas two-phase flow in which a Taylor bubble is injected into a stream with liquid and gas phase dispersed in Yan and Che (2011). Here, it is important to state that this numerical experiment motivated the experimental investigation conducted in the present thesis. Figure 2.23 shows the effect of different j_g and j_l bubbly flow configuration in the Taylor bubble tail shape.

As can be seen in Fig. 2.23, the tail shape of the Taylor bubble is affected by the concentration of the dispersed phase, and, according to the authors, the proposed model is capable of simulating flows with different interface scales. However, the work does not present any form of experimental validation, and the model is not verified with a benchmark case.

Hänsch et al. (2012)

In Hänsch et al. (2012), the authors propose a numerical model suitable for modeling multiphase flows with interfaces of different scales, denominated GENeralized TwO-Phase flow concept (GENTOP). The model is based on modifications of the non-homogeneous MUltiple-SIze-Group (MUSIG) model used in polydispersed flow modelling, but it can be interpreted as a modification of the Two-Fluid Model.

In GENTOP, three distinct phases are defined: i) continuous gas phase (ε_{cg}) with

Figure 2.23 – Effect of different j_g and j_l on the Taylor bubble tail shape flowing in a bubbly flow stream.

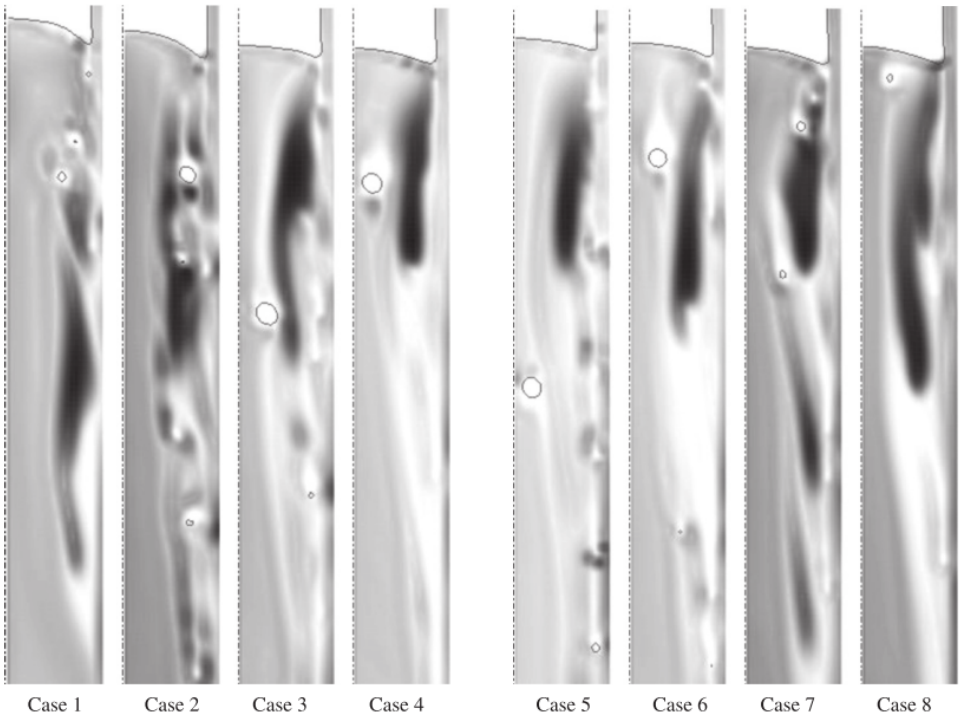

Source - Yan and Che (2011).

a large scale interface; ii) dispersed gas phase (ε_{dg}) with a small scale interface and iii) ε_l, liquid phase with a large scale interface. It is interesting to note that the definition of three phases, with the sub-division of the gas phase, follows the same procedure described in Yan and Che (2010) e Yan and Che (2011).

In order to model flows with a large scale interface, GENTOP introduces two additional procedures to the "standard" Two-Fluid Model. The first procedure aims in detecting possible large-scale interfaces by analysing the scalar fields of ε_{cg}. In the second procedure, when a large-scale interface is detected, an additional artificial compression term is added on the RHS of Eq. (2.35) of the Two-Fluid model, similar to the models detailed in the paragraphs above, resulting in sharp large-scale interface.

The large-scale interface is detected through localization function φ_{fs}, defined as,

$$\varphi_{fs} = 0.5 \tanh \left[a_{fs} \Delta x (|\nabla \varepsilon_{cg}| - |\nabla \varepsilon_{cg}|_{crit}) \right] + 0.5 \tag{2.60}$$

where a_{fs} is an empirical coefficient of the method, Δx is a characteristic dimension of the numerical mesh and $|\nabla \varepsilon_{cg}|_{crit}$ is a critical value of $|\nabla \varepsilon_{cg}|$ that defines the presence of an interface. The choice of $|\nabla \varepsilon_{cg}|$ and φ_{fs} distribution of along the interface can be seen in Fig. 2.24.

Figure 2.24 – Left: ε_{cg} and $|\nabla\varepsilon_{cg}|$ distribution in a region close to the interface position. Right: φ_{fs} distribution of along the interface.

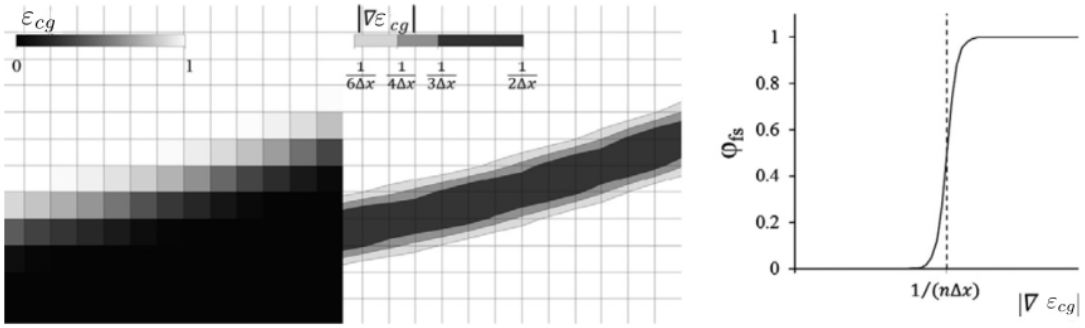

Source - Adapted from Hänsch et al. (2012).

After calculating φ_{fs} in the entire domain, the compression force M_{cg}^{clust} can be calculated. The interfacial compression force M_{cg}^{clust} acts in the ε_{cg} field, clustering dispersed phase regions originated from the numerical diffusion of the advective/interpolation schemes used in the Two-Fluid Model. The term is defined as,

$$M_{l}^{clust} = -M_{cg}^{clust} = -c_{clust}(1-\varphi_{fs})\varphi_{clust}\rho_{l}\nabla\varepsilon_{l} \tag{2.61}$$

where φ_{clust} is a coefficient that defines the intensity of the clustering force and φ_{clust} is a function that restricts the application of that force to only control volumes close to the interface, defined as

$$\varphi_{clust} = (0.5\tanh[a_B(\varepsilon_{cg}-\varepsilon_{clust,min})+0.5)](0.5\tanh[a_B(\varepsilon_{clust,max}-\varepsilon_{cg})+0.5)] \tag{2.62}$$

In Eq. (2.62) a_B is a model coefficient and $\varepsilon_{clust,min}$ and $\varepsilon_{clust,max}$ define the intervals in which the interfacial compression force is applied.

The inclusion of the clustering force (M_{cg}^{clust}) into the Two-Fluid Model is done by the adding M_{cg}^{clust} into the the term $\boldsymbol{M}_{kj}$ of Eq. (2.36). Note that the aforementioned term only acts in control volumes where the phases are ε_{cg} e ε_{l} present.

Figure 2.25 shows the effect of the interfacial compression force ($M_{l}^{clust} = -M_{cg}^{clust}$) on the ε_{cg} distribution of and the φ_{clust} function that limits its application only in regions close to the interface.

For the remainders terms of interfacial momentum transfer, the authors use the same formulation of the non-homogeneous MUltiple-SIze-Group (MUSIG) model (KREPPER et al., 2008). The effects of the surface tension force are not incorporated into GENTOP, because, according to the authors, although the interfacial compression force creates sharp interfaces, the model cannot accurately calculate the interface curvature and, consequently, model the surface tension force.

Figure 2.25 – Left: Effect of the interfacial compression term in the ε_{cg} distribution. Right: φ_{clust} distribution.

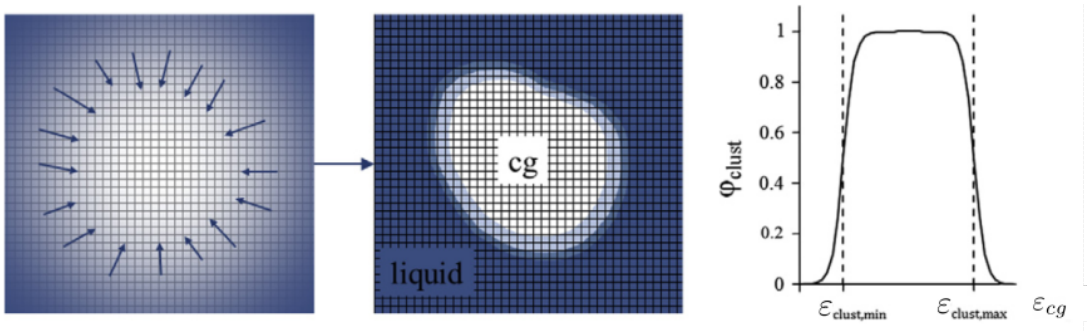

Source - Adapted from Hänsch et al. (2012).

In order to verify GENTOP's ability to simulate flows with multiple interface scales, the model is used for the simulation of a vertical plunging jet and later compared with experimental results. The numerical and experimental results are shown in Fig. 2.26. According to the results of Fig. 2.26, the developed model by Hänsch et al. (2012) can capture the some of the features of the vertical plunging jet, such as the entrainment of the gas-phase into small air bubbles below the free-surface interface.

Hua (2015)

In Hua (2015), a CFD model for multiscale flows is proposed through the coupling of a VOF and the Discrete Particle Model (DPM), where the first models the large scale interfaces, while the latter the small scales interface. Figure 2.27 illustrates the multiscale modeling proposed by the authors.

As opposed to the Discrete Bubble Model described in Section 2.1.3.1, the DPM does not include bubble-bubble and bubble-wall collisions. Additionally, the CFD cell size, used for modeling the liquid phase, is restricted to the dispersed bubble's largest diameter in the domain.

Despite the DPM limitations, the authors applied the VOF-DPM model to simulate the interaction between a large bubble and many suspended small bubbles in 2D vertical channels under different bubble shape regimes. According to the simulations results, the small dispersed bubbles may impose important effects on the rising behavior of the large bubble. For instance, in Fig. 2.28 due to the dispersed bubbles, the larger bubble deform and its bottom present an unstable motion. Compared to the case where no dispersed bubbles are not present to the flow, the terminal rising velocity of the bubble increases

According to the authors, both hindrance and acceleration effects have been revealed by the simulations. The hindrance effect occurs in the near-spherical bubble shape regime,

Figure 2.26 – Comparison between the numerical and experimental results of a vertical plunging jet at different time instants Δt (Δt_E experimental and Δt_S numerical), calculated from the moment the liquid jet hits the free-surface.

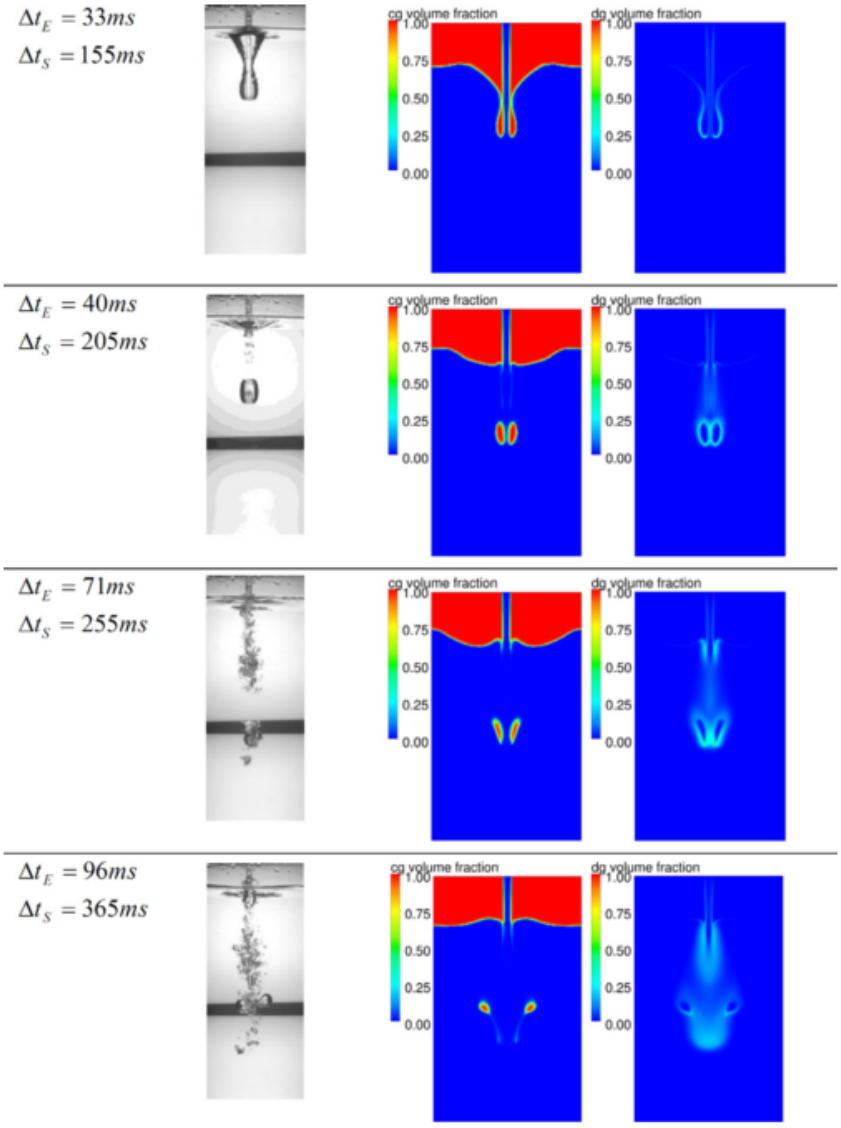

Source - Hänsch et al. (2012).

where the liquid phase can be classified as a highly viscous phase. In this case, the rise speed of the large bubble decreases as the volume fraction of small dispersed bubbles increases. The acceleration effect occurs in the other bubble shape regimes, e.g., oblate ellipsoidal and spherical cap, where the liquid viscosity is lower, with significant deformation of the large bubble nose due to the presence of small dispersed bubbles and a fairly large bubble wake zone is formed behind the large bubble. Due to the acceleration effect, the large bubble rising velocity increases when the volume fraction of small dispersed bubbles increases.

Figure 2.27 – Schematic diagram of the modeling concept for multiphase flow with multi-length–scale interface structures.

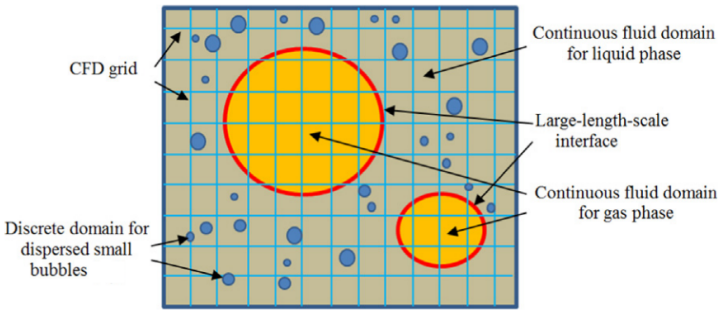

Source - Hua (2015).

Figure 2.28 – Snapshots of predicted large bubble shape and trajectories of small bubbles.

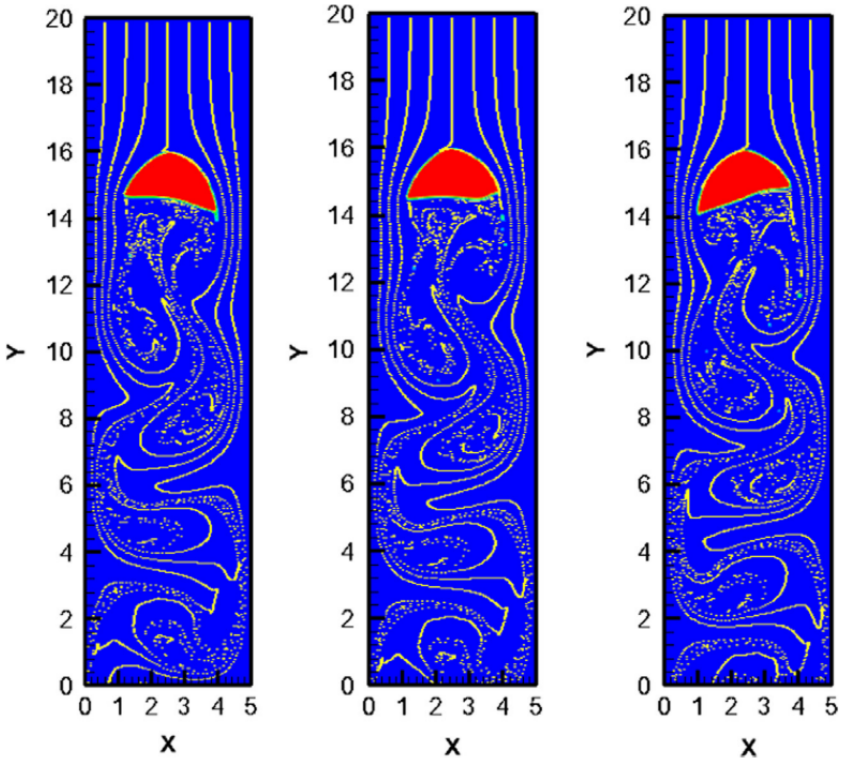

Source - Hua (2015).

Peng et al. (2020)

Recently, Peng et al. (2020) proposed a multiscale model coupling the VOF method with the Discrete Element Method (DEM) to study slurry Taylor flows, where the interfaces of multiple scales coexist. The DEM is a model similar to the Discrete Bubble Model, described in Section 2.1.3.1, but focused on modeling solid particles instead of gas bubbles. For the solid-liquid phase coupling, the authors adopt a diffusion-based averaging method (SUN; XIAO, 2015) to circumvent the cell-size limitation in the CFD solver due to the

dispersed bubble size. In their study, the Taylor bubble represents the large scale interface, while the small scale interface is represented by solid particles. Figure 2.29 illustrates a numerical result obtained from the proposed model, where is possible to visualize the different interface length scales.

Figure 2.29 – Evolution of the gas-liquid-solid three-phase flow.

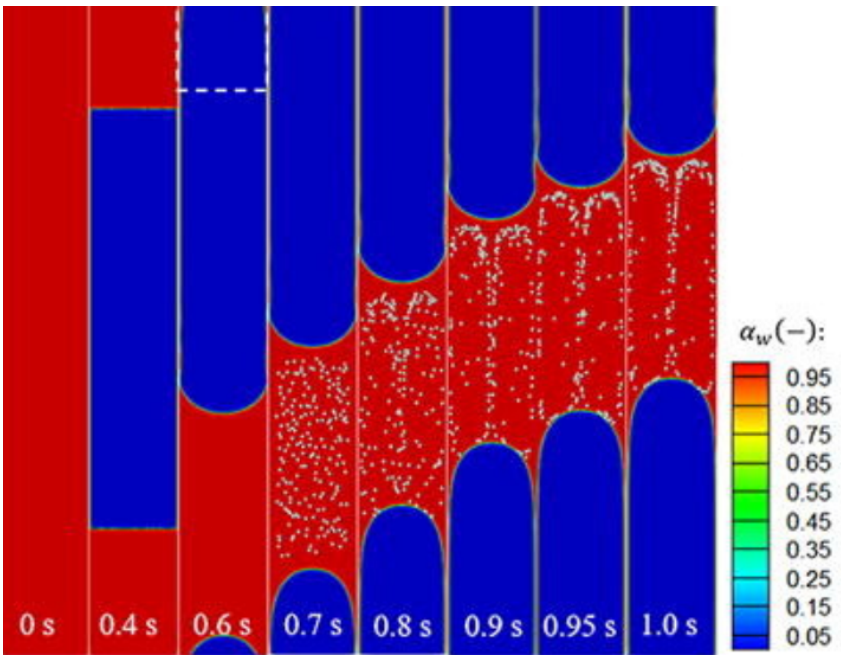

Source - Peng et al. (2020).

According ot the study, the particle distribution was found strongly dependent on the liquid flow field and particle physical properties.

Summary of the recent literature review

From the literature review presented in this section, it is possible to list characteristics of the reviewed models for modeling two-phase flows with the presence of different interface scales. A summary of the reviewed works, listing the characteristics of the proposed models, is shown in Tab. 2.1.

According to the works found in the literature, the implementation of multiscale interfacial models based on the coupling of the Two-Fluid Model and Volume-of-Fluid method (CERNE et al., 2001; YAN; CHE, 2010, 2011) is not straight-forward and its solution requires an elevated computational cost, since it is necessary to solve two sets of equations, one for each phase. Additionally, when combining using a coupled VOF-TFM formulation, a transition criterion is required, which at the moment is based on empirical relations, since its definition is a challenging task. The modeling using the Two-

Table 2.1 – Summary of literature review for modeling two-phase flows with the presence of different interface scales.

Author	**Multiscale modeling approach**	**Interfacial length scale criterion**	**Surf. tension force modeling**	**Verification/ Validation**
Cerne et al. (2001)	TFM-VOF coupling	Yes	No	No
Štrubelj and Tiselj (2011)	TFM and interface compressive force	Cerne et al. (2001)	No	No
Wardle and Weller (2013) and Shonibare and Wardle (2015)	TFM and interface compressive force	Cerne et al. (2001)	Yes	Yes, qualitative comparison
Yan and Che (2010) and Yan and Che (2011)	TFM-VOF coupling	No	Yes	Yes, qualitative comparison
Hänsch et al. (2012)	TFM and interface compressive force	No	No	Yes, qualitative comparison
Hua (2015)	Lagrangian model and VOF coupling	–	Yes	No
Peng et al. (2020)	DEM-VOF coupling	–	Yes	No

Source - Developed by the author.

Fluid Model with an interface clustering (HÄNSCH et al., 2012) or an artificial interface compressive force (ŠTRUBELJ; TISELJ, 2011; WARDLE; WELLER, 2013), despite its relative simplicity, just like the VOF-TFM formulation, requires the use of empirical relations to define where the artificial force must act. From the proposed strategies to model multiphase flows with different interfacial scales, the use of the Volume-of-Fluid method to model the large-scale interfaces and a Lagrangian model for the small-scale interfaces, as proposed by Hua (2015) and Peng et al. (2020), seems an adequate option due to its simplicity and reduced support on empirical relations. In the case of the present thesis, the VOF-DBM model only requires the use of closure relations for modeling the forces acting on the dispersed bubbles, eliminating the need for a large/small scale interface switching criterion in a given control volume.

In addition, as observed in Table 2.1, no quantitative experimental verification was conducted so far, for any of the proposed approaches. Therefore, the experimental investigation proposed in this thesis is of fundamental importance for the development and validation of CFD models for liquid-gas flows with different interface length scales.

2.2 EXPERIMENTAL STUDIES

This section presents a general overview of the experimental techniques used during the experimental work conducted in this thesis, presenting its basic concepts and appli-

cation for the study of gas-liquid flows. Then, a review of recent investigations applying these techniques for the study of bubbly and Teylor bubbles flows is presented.

2.2.1 Particle Image Velocimetry Technique

Particle Image Velocimetry (PIV) is an optical measurement technique, which consists in the addition of tracer particles in the flow. Those particles, after being illuminated by a planar light sheet, are recorded using an image acquisition method and post-processed to obtain a velocity field. The PIV measurement technique is widely used in the field of fluid mechanics (RAFFEL et al., 2018), especially in the validation of numerical results obtained by CFD, since the technique is capable of providing multi-dimensional velocity fields. The following paragraphs are going to present a brief description of the measurement technique.

The PIV technique, being an optical technique, is also a non-intrusive technique, which does not require the immersion of probe or sensors into the flow. Furthermore, through the PIV technique, it is possible to obtain multi-dimensional velocity fields without requiring the use of an external positional system, unlike other conventional methods used to characterize flows, e.g., hot-wire anemometry, Laser Doppler Velocimetry (LDV), etc. However, since the technique demands image acquisitions, it is necessary that both the working fluid and the enclosing walls, in the case of internal flows, to be transparent in the wavelength emitted by the light source.

In order to perform a PIV acquisition, tracer particles are added to the flow, reflecting and absorbing the light emitted by the light source. Thus, due to this light emission and reflection, the tracer particles can be acquired by the photographic system. Since the particles must reflect the flow velocity field, they must act as tracer particles, following the fluid velocities uniformly. Thus, the selection of tracer particles is crucial for obtaining consistent velocity fields. It is important that the particles, when subjected to an acceleration of the flow, continue to follow the fluid uniformly. Therefore, in most relevant applications, tracer particles with density close of that of flow and with a small diameter are chosen, reducing the velocity slip between the fluid and tracer particles. Besides, the particles' diameter must be adequate to allow it capture by the image acquisition system. Commercially, one can find polymeric particles with different densities, and with a diameter ranging from 5 a 200 μm. Detailed information regarding the application of the tracer particles can be found in the work of Raffel et al. (2018).

In the PIV technique the flow is illuminated by a high-intensity light sheet, generally produced by a coherent light source with uniform thickness and intensity. In most

PIV applications (RAFFEL et al., 2018), a pulsed or continuous laser source is used in conjunction with a series of lenses, producing a luminous plane of constant thickness. The set of lenses needed for generating the planar light sheet, as well as details regarding the different available light sources and its different applications, can be found in the work of Raffel et al. (2018).

The light scattered by the tracer particles, illuminated by the planar light sheet in the region of interest, is captured by a high-resolution camera. Through the acquisition of two images (or frames), formed by two pulses of the luminous plane in sequence, it is possible to obtain the particle displacement between two acquisitions through correlation methods. From the "average" particles' displacement and the information of the period between the two pulses of illumination, it is possible to calculate the velocity field in a given region of the image. Figure 2.30 illustrates summarizes the flow velocity field acquisition when using the PIV technique.

Figure 2.30 – Schematic illustration of the PIV technique.

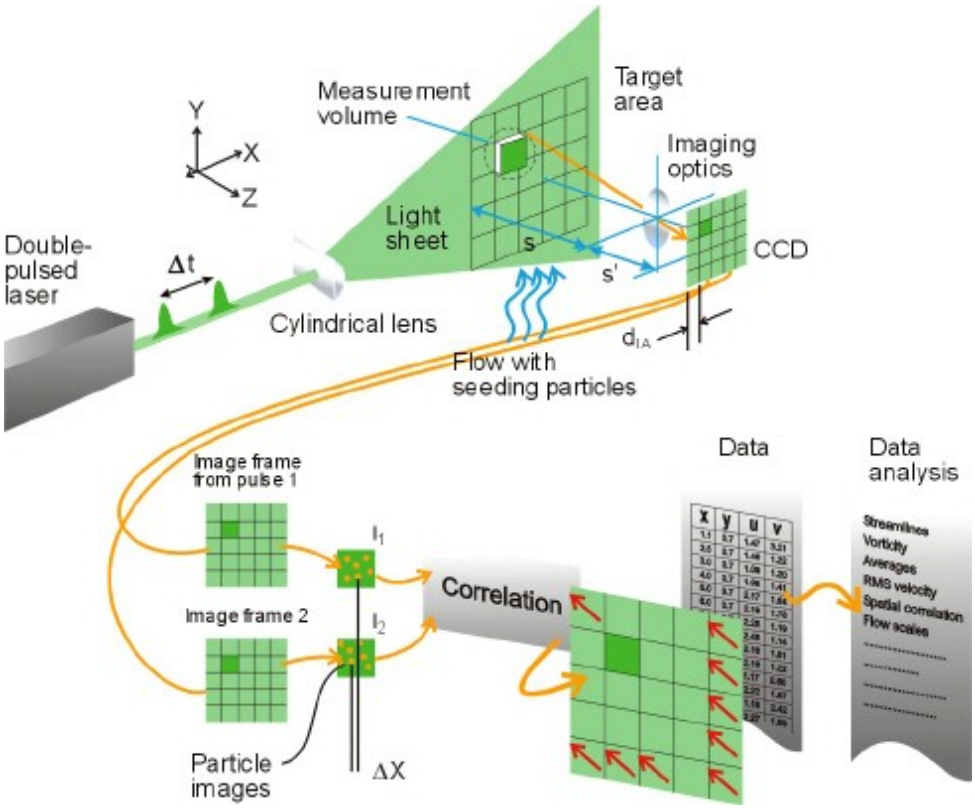

Source - Dantec Dynamics (2020 (accessed June 3, 2020)).

After capturing the two time-spaced frames through a photographic system, processing algorithms are used to transform the information contained in the two images into a flow velocity field. First, the images are divided into small regions, denominated as interrogation windows. The pixel intensity information in these small regions originated

from the tracer particles, are used to calculate the velocity fields. In order to calculate the velocity in a given interrogation window, cross-correlation techniques are used to compute the relative displacement between two sequential frames. This computation assumes that the particles contained therein move homogeneously, disregarding any perpendicular movement across the light sheet plane, also ignoring shear stresses. As long as the interval between the laser pulses is short, those assumptions are valid. In general (RAFFEL et al., 2018), the time interval must respect a value that does not allow the particles to travel a distance greater than 25 % of the characteristic length of the interrogation window. Otherwise, it is possible to obtain spurious or low correlation velocity vectors. It is important to remember that small time intervals can also result in correlation failures since the particles may not displace enough to result in a consistent displacement. Thus, it can be concluded that the interval of two sequential frames plays a major role in the accuracy and reliability of PIV results.

As defining the interval between two consecutive acquisitions is important, the size of the interrogation window also influences the correlation algorithm. According to Keane and Adrian (1992), the recommended dimension of the interrogation windows must comprise at least 10 tracer particles, thus reducing the probability of off-plane motions and tracer particles moving outside the interrogation windows in the second frame.

Figure 2.31 shows a PIV frame acquired by a high-resolution camera, presenting the image being divided into small interrogation windows, showing the pixel intensity distribution of in two sequential time instants.

Figure 2.31 – PIV frame acquired by a high-resolution camera, highlighting the pixel distribution of four interrogation windows in two time instants.

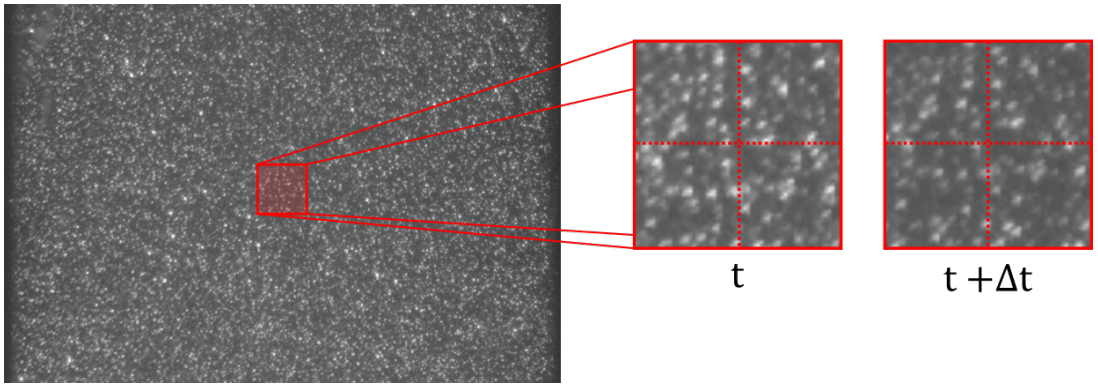

Source - Developed by the author.

The frame illustrated in Fig. 2.31 shows the pixel intensity distribution from tracer particles flowing inside an acrylic duct where only a single liquid phase is present. However,

in liquid-gas two-phase flows, due to the presence of interfaces, additional techniques are necessary to characterize those flows.

2.2.2 PIV/LIF Technique

In PIV applications to liquid-gas two-phase flows, the presence of the interfaces with much larger scales than the seeding particles, scatters the light of the laser with much more intensity than these particles, impeding the CCD camera to capture the seeding particles. Therefore, it is recommended to use the PIV technique in conjunction with the Laser-Induced Fluorescence (LIF) technique (LI; HISHIDA, 2009). The PIV/LIF technique consists of using fluorescent tracer particles that receive light at a specific wavelength (light source) and fluoresce at another wavelength, in which the camera captures only the less intense "fluorescent" light through the use of optical filters. From this arrangement, the light scattered by the interfaces from the laser source is not captured by the camera, which only records the fluoresced light coming from the seeding particles. Thus, part of the problems when using the PIV technique in liquid-gas flows are mitigated. Figure 2.32 shows a schematic illustration of the PIV/LIF technique.

Figure 2.32 – Schematic illustration of the PIV/LIF technique.

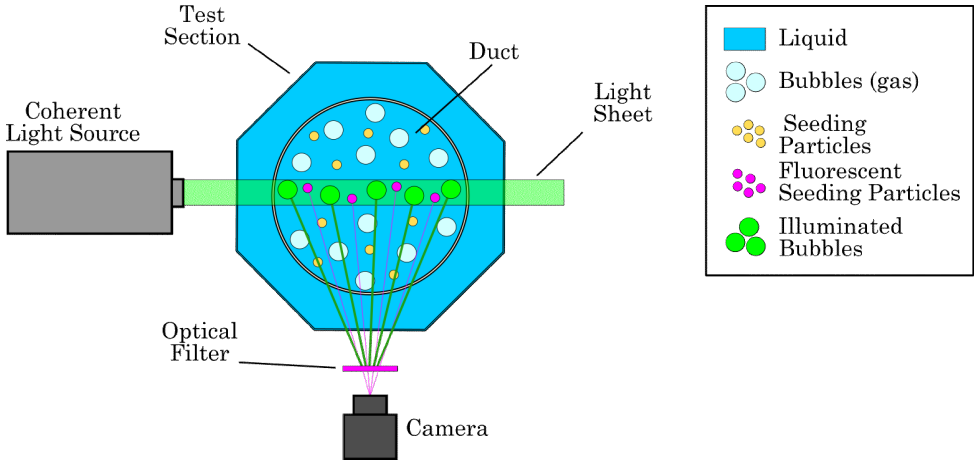

Source - Developed by the author.

In Fig. 2.32, the schematic illustration shows a longitudinal cut of a vertical duct test section. The test section is filled with liquid to minimize optical distortions due to the different refractive indexes of the liquid and duct wall material. In this arrangement, the test section walls and the vertical duct are made of a transparent material in the wavelength of the coherent light source. According to Fig. 2.32, the light source has an approximate wavelength of $\lambda = 532nm$ (closer to the green colour), while the tracer particles fluoresce $\lambda = 590nm$ (closer to the pink colour). Thus, through the placement of

a filter that allows the passage of light with wavelengths greater than $\lambda = 590nm$, only the tracer particles will be acquired by the camera.

Although the LIF technique allows the use of the PIV measurement technique in multiphase flows, it does not solve all the interface related problems. Figure 2.33 shows an typical PIV/LIF image from a air-water bubbly flow.

Figure 2.33 – Example of atypical PIV/LIF image from a air-water bubbly flow.

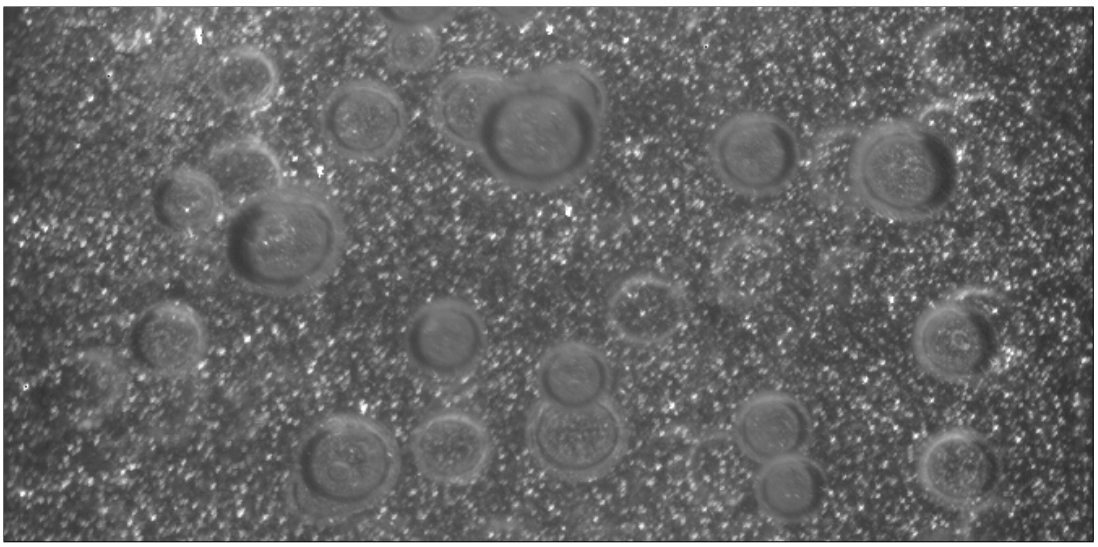

Source - Developed by the author.

As seen in Fig. 2.33, even using the LIF technique, it is possible to visualize the unrealistic "ghost" particles located in the gas phase, which appear due to the reflection of fluoresced light on interfaces and off-plane particles illuminated by scattered light. The inclusion of these unrealistic velocity vectors in the time-averaging procedure overestimates the liquid velocity averaged fields (in the case of co-current upward flows) due to the higher velocity of the bubbles.

2.2.3 Review of recent literature on experimental studies of Taylor an bubbly flows

In liquid-gas two-phase flows, the velocity fields of the liquid and its fluctuations are fundamental for understanding the physical phenomena of the flow. Thus, it is important to obtain experimental results that provide local information in certain flow regions, such as the interaction between the gas and liquid phases, that can be used as closure correlations in multiphase models. Moreover, results from an experimental investigation can be used to validate multiphase CFD models. Due to those reasons, several researchers began developing experimental techniques for the detailed characterization of two-phase flows.

This section is going to present a literature review of works which are related to the manufactured "quasi-real" slug flow investigated in this thesis, produced from the independent injection of Taylor bubbles and dispersed bubbles into a liquid stream. Thus, this section is dedicated to reviewing previous works found in the literature focused on experimental techniques employed to characterize: i) the flow structure around Taylor bubbles and ii) flows where dispersed bubbles are present (bubbly flows).

Experimental Techniques for the Flow Structure Characterization around Taylor Bubbles

In Campos and Carvalho (1988), the authors conducted a photographic study of the wakes of Taylor bubble rising in vertical ducts with different diameters. Experiments were performed using air as the gas phase and water, glycerol and a mixture of the two as the liquid phase. According to the obtained results, three flow regimes were found in the wakes region of Taylor bubbles: i) laminar regime; ii) transition regime and iii) turbulent regime. The criterion for defining each regime was defined based on the dimensionless number of inverse viscosity $N_f = \sqrt{\rho_l^3\, g\, D^2/\mu_l^2}$, where ρ_l is the liquid density, μ_l is the liquid viscosity ,g is the acceleration of gravity and D is the duct diameters.

In Polonsky et al. (1999a), the velocity field ahead of the Taylor bubble nose is studied and characterized through the PIV technique. In this work, Taylor bubbles (air) were inject in a 25 *mm* internal diameter vertical duct in following configurations: i) stagnant water column, ii) co-current and iii) counter-current flow. According to the experimental results, the Taylor bubble rising velocity is related to the maximum velocity ahead of the Taylor bubble nose in the three studied cases.

In Polonsky et al. (1999b), an image processing technique was developed to track the motion of a Taylor bubble rising on a vertical duct, capturing its shape and length, correlating the bottom frequency oscillation with the liquid flow conditions.

Van Hout et al. (2002c) used the PIV technique to study the induced flow by the passage of Taylor bubbles in stagnant water, in a 25 mm ID duct (N_f = 12300), reporting the use of about 100 instantaneous fields for the calculation of the averaged fields. In this work, despite the results presented of the averaged velocity field around the Taylor bubbles nose and tail region, there is no discussion about the masking procedure used to remove the Taylor bubbles from the PIV images.

Nogueira et al. (2003) and Nogueira et al. (2006b), using the PIV technique, presented results of the flow field around Taylor bubbles in stagnant and co-current liquid flow for N_f ranging from 17 to about 18,000. They reported the use of 7 to 20 instantaneous fields for the calculation of averaged fields. Nevertheless, even for relatively low values of

$N_f \approx 800$, visual observation of the vector fields and streamlines show the presence of several fluctuations, indicating that those fields are far from being representative of the averaged ones. To remove the Taylor bubbles from the PIV velocity fields, the authors use the Pulsed Shadowgraphy Technique (PST), which produces "binary masks" from the perpendicular projection of the Taylor bubbles into the camera plane. However, for high values of N_f, the interface fluctuations are highly three-dimensional, and the bubble projection using back-light illumination, could not be representative of the interface position at the measurement plane.

In Mayor et al. (2007) and Mayor et al. (2008) the authors developed an image processing technique, capable of tracking the motion of the Taylor bubbles in different slug flow pattern conditions, extracting from a series of video frames information about the Taylor bubbles dimension, velocity, and distance. However, the tracking algorithm described on Mayor et al. (2007) does not track the motion of the small interface length scale gas phase, neglecting the dispersed bubbles individual motion on the region between the nose of one Taylor bubble and the bottom of a subsequent one.

Shemer et al. (2007) performed PIV measurements of the liquid velocity field in the wake elongated air Taylor bubbles, performing experiments for different pipe diameters and various Reynolds Re numbers. From those experiments, ensemble-average velocity fields are calculated.

From the literature review presented in this section, it is possible to list a few characteristics of the reviewed experimental studies focused on the analysis of the flow structure around Taylor bubbles. This summary is presented on Tab. 2.2. According to the summary, it is possible to characterize the flow around the Taylor bubble through the PIV and HSC technique. However, in the experiments proposed in this thesis, due to the presence of small dispersed bubbles around the Taylor bubbles, additional techniques are necessary to acquire consistent and reliable average results. Due to small dispersed bubbles, strong flow fluctuations are expected, perturbing the Taylor bubble rising motion and deforming its nose and bottom shape. Those perturbations affect the triggering mechanisms necessary for the PIV measurements and, since small dispersed bubbles are present, the Pulsed Shadowgraphy Technique cannot be used to "mask-out" the Taylor bubble in the PIV images. When using the high-speed camera to track the motion of the Taylor bubbles, similar problems are also expected due to the same aforementioned reasons.

Table 2.2 – Summary of the main experimental studies of the flow structure around Taylor bubbles.

Author	Technique	Fluids and conditions	D	N_f	Results
Campos and Carvalho (1988)	Photography analysis	Air bubbles in stagnant water and water-glycerol solutions	19 - 52 mm	8199 - 37120	Photographic study of the wake of Taylor bubbles
Polonsky et al. (1999a)	PIV	Air bubbles in stagnant, upward and downward water flow	25 mm	12380	Investigates the effect of the liquid velocity field on the Taylor bubbles motion
Polonsky et al. (1999b)	HSC	Air bubbles in stagnant and upward water flow	25 mm	12380	Correlates the bottom frequency oscillation with the liquid flow conditions
Van Hout et al. (2002c)	PIV	Air bubbles in stagnant water	25 mm	12380	Axial and radial velocity profiles at the nose, film and wake
Nogueira et al. (2003)	PIV and PST	Air bubbles in stagnant aqueous solution	32 mm	200	Axial and radial velocity profiles at the nose, film and wake
Nogueira et al. (2006b)	PIV and PST	Air bubbles in stagnant water and water-glycerol solutions	32 mm	15-17929	Axial and radial velocity profiles at wake
Shemer et al. (2007)	PIV	Air bubbles in upward water flow	25 mm	12380	Axial and radial velocity profiles at the nose, film and wake
Mayor et al. (2007) and Mayor et al. (2008)	HSC	Air bubbles in upward water flow	32 and 52 mm	12380 and 37000	Distributions of Taylor bubble velocity, bubble length and liquid slug length

Source - Developed by the author.

Experimental Techniques applied to the Characterization of Bubbly Flows

In the work of Bröder and Sommerfeld (2002), the authors develop a PIV method based on an experimental setup, which includes two synchronized cameras, each with different optical filters. One optical arrangement is used to capture only the tracer in the liquid phase and the other to acquire only the dispersed bubbly phase. This setup was used in a bubble column with a gas hold-up varying between 0.5 and 19%. However, the method can only be used when the diameter of the bubbles is small compared to the measurement domain, such as the case of a bubble column.

An experimental procedure for phase discrimination is presented by Lindken and Merzkirch (2002), which consists in the use of PIV in combination with laser-induced fluorescence (LIF) and pulsed shadowgraphy. In this work, the LIF technique helps to visualize the liquid tracer particles by the use of fluorescent particles and narrowband optical filters. The phase discrimination is done by the pulsed shadowgraphy technique, which can also be used to calculate the bubble shape and size, creating a "binary mask" for the gas phase, that can be subtracted from the originally captured image, before applying the PIV cross-correlation procedure. The same experimental procedure is used by Fujiwara et al. (2004) to study the vertical upward driven bubbly pipe flow with void fractions of 0.5 % to 1.0 % and by Kim et al. (2016) to characterize the bubble-induced

turbulence in laminar upward flows with void fractions ranging from 0.05 % to 0.64 %. This technique is restricted to bubbly flows with low gas fractions since the fact that the phase discrimination is done volumetrically (using backlight illumination) and, as void fraction increases, the superposition of bubble shadows, turns the measurement virtually impossible.

Bröder and Sommerfeld (2007) circumvents the low gas fraction limitation by using macro optics in the CCD camera, thereby achieving a small depth of field and making possible, by a method based in the gradient of gray values, the discrimination among bubbles inside and outside the camera's focal plane. Using these additional procedures, the authors can study liquid-gas bubbly flows inside a bubble column with a range between 0.5 and 5.0% of gas volume fraction. However, the applicability of the method depends on the relationship of the bubbles to pipe diameters, as it is complicated to get such a tight focal depth, to discriminate out-of-plane bubbles.

In Akhmetbekov et al. (2010) the authors developed a phase discrimination method based on the planar fluorescence for bubble imaging (PFBI), which is based on the LIF technique. The algorithm identifies the bubbles' positions and sizes, tracking their positions in images with non-uniform intensity distribution, such as the images from the PIV/LIF technique. From the identified bubbles, its shape and location are used to mask the dispersed bubble gas phase from the PIV images. Then, the PFBI technique is employed to analyze a bubbly free jet with gas fractions ranging up to 5.2%. In this case, the method has some limitations regarding the bubble shape and overlapping on the image.

In the method described in Zhou et al. (2013) the phase discrimination is done through the image processing of the raw PIV/LIF images and can be used for liquid-gas pipe flow with void fractions up to 18.0%. A significant advantage of the proposed method is the fact that all calculations are done in a "planar" fashion since it uses the raw PIV images acquired with the light sheet illumination. However, the method creates a binary image from the raw PIV image, in which the discrimination of the tracer particles and the dispersed bubbles is done through a geometric criterion from a processed binary image. This criterion is chosen manually and can introduce errors in the cross-correlation PIV procedure used for the liquid velocity calculation.

The reviewed works so far focus on non-intrusive experimental techniques for the characterization of the liquid phase in bubbly flows. However, it is of fundamental importance the measurement of parameters such as the bubble size and velocity distributions, interfacial area concentration and void fraction, to asses the accuracy and guide the development of those models. For characterization of bubbly flows, usually image processing techniques are used together with high-speed cameras, which results in measurements with

high spatial and temporal resolutions. When using image processing techniques, usually, a light source is positioned in the back of the test section, parallel to the camera lens. This light and lens arrangement is known in the literature as shadowgraphy technique (BRÖDER; SOMMERFELD, 2007). Through the shadowgraphy technique, the bubbles are clearly visible on the captured images, where the illuminated background has a homogeneous grey intensity. In contrast, the bubbles appear as elliptical-like structures with a brighter intensity in the center and darker edges on the gas-liquid interface.

However, the bubble identification and tracking techniques, also denominate Particle Tracking Velocimetry methods, were limited to bubbly flows in dilute configurations, with small values of void fraction (up to 1.0 %) due to bubble overlapping. Thus, depending on the operating conditions and geometry, bubble overlapping may occur when using the shadowgraphy technique, especially in moderate to high void fractions, since the method is based on the projection of the recorded bubbles into an image plane.

In the past years, some authors (HONKANEN et al., 2005; ZHANG et al., 2012; FU; LIU, 2016a) developed methods capable of recognizing entities on overlapping-like structures. Those methods are all based on the image processing methods where clustered-like geometrical structures are segmented and grouped, aiming the identification of overlapping bubbles.

In Honkanen et al. (2005) and Zhang et al. (2012), the segmentation is performed by analyzing the curvature of the geometrical structures, where if its value exceeds a certain threshold, a breakpoint was introduced, segmenting the outline. Then, from the segmented portions of the outline, the bubble shape was reconstructed through an ellipse fitting method.

In Fu and Liu (2016a), the bubble is not reconstructed by an ellipse fitting method, but through the outline of obtained from binary images resulting from a watershed segmentation, bubble skeleton and adaptive threshold operations. Those three binary images are analyzed in a sophisticated algorithm, and then the bubble outline is reconstructed. As presented by the authors, the segmentation algorithm described in Fu and Liu (2016a) is capable of identifying highly deformed and overlapped bubbles.

Recently, some authors experimented with the use of Convolutional Neural Networks (CNN), a deep-learning technique, for bubble identification on gas-liquid bubbly flows, presenting similar or better results when compared to the "classical" analytical image processing based methods.

Poletaev et al. (2020) characterized bubbly flows with the PFBI method (AKHMETBEKOV et al., 2010), which uses a thin laser light-sheet and fluorescent tracer particles to capture images of bubbles in a specified plane. In their work, the authors used

a sliding window approach with three separate CNNs to classify the probability of the presence of a bubble in a portion of the image, filter the image through an autoencoder and find probable bubble centers. The authors present a comparison between the CNN-based methods and the analytical method from (AKHMETBEKOV et al., 2010), with the first obtaining superior accuracy. Despite the success of the method developed by Poletaev et al. (2020), it cannot be used on images obtained from the shadowgraphy technique.

In Haas et al. (2020), the authors develop and demonstrate the applicability of a CNN-based method for the identification of bubbles in images obtained with the shadowgraphy technique. The proposed method uses a region-based convolution neural network (R-CNN) for the identification of possible bubble locations, where each bubble is identified, labeled, and surrounded by a rectangular box. The image contained in this box, where a bubble is present, is then submitted to a shape regression CNN, where a regular CNN is used to find the best ellipsoid that correctly fits the bubble represented by the image snippet. According to the presented results, the combination of the R-CNN and a shape regression CNN produces excellent results. However, as commented by the authors, as the void fraction increases, i.e., more bubbles are present on the flow, the precision decreases due to the increased probability of bubble overlapping.

As presented in the sections before, Tab. 2.3 summarizes the work reviewed in this section, listing some characteristics of the discussed experimental techniques focused on bubbly flows. It is important to notice that in Tab. 2.3, there is a division between experimental techniques focused on the characterization of the liquid phase and techniques developed to track the motion of the dispersed bubbles.

In terms of PIV applied to bubbly flow measurements, according to the reviewed works found in the literature, only the work of Zhou et al. (2013) fits in the description of the proposed measurements in this thesis. However, those authors conduct experiments in large diameter ducts (D = 50 mm), which is approximately double the diameter of the acrylic test section of the experimental setup used in this thesis. Due to the reduced dimensions, working in similar or small void fraction as those in Zhou et al. (2013), due to the aforementioned light scattering due to the dispersed bubbles, higher are the chances of capturing “out-of-plane” bubbles in the raw PIV images. Therefore a novel image processing technique must be developed to remove the contribution of the dispersed bubbles in the PIV images. For tracking the motion of the dispersed bubbles in moderate and dense bubbly flows, the reviewed methods found in the literature cannot be used in expected experimental conditions conducted in this thesis. Thus, the development of a PTV technique capable of tracking the motion of bubbles where overlapping/clustering is frequent is also necessary.

Table 2.3 – Summary of the reviewed works focused on the development of experimental techniques applied to the characterization of bubbly flows.

Author	**Experiment**	**Experimental Technique**	**Void Fraction**
Bröder and Sommerfeld (2002)	Bubble Column	PIV/LIF e High-Speed Camera (2 cameras)	0.5 - 19 %
Lindken and Merzkirch (2002)	Bubbles injected into a reservoir	PIV/LIF e PST	2.5 %
Bröder and Sommerfeld (2007)	Bubble Column	PIV/LIF and macro lenses	5 %
Akhmetbekov et al. (2010)	Turbulent bubbly jet	PFBI	0 - 4.2 %
Zhou et al. (2013)	Vertical Duct bubbly flow (D = 50 mm)	PIV/LIF	18 %
Honkanen et al. (2005)	Stagnant bubbles in a gel	HSC and Image Processing Techniques	2 %
Zhang et al. (2012)	Computer generated images	Image Processing Techniques	-
Fu and Liu (2016a)	"Pseudo-2D" Bubble Column	HSC and Image Processing Techniques	2.4 - 9.1 %
Poletaev et al. (2020)	Turbulent bubbly jet	PFBI and CNN-based Image Processing Techniques	2.5 %
Haas et al. (2020)	Computer generated images	CNN-based Image Processing Techniques	15 %

Source - Developed by the author.

Finally, as already mentioned, no experimental works were encountered presenting systematic studies of gas-liquid flows with different interface length scales, as a combination of large bubbles and small dispersed bubbles. In this thesis, specific experimental techniques will be developed for the study of such type of flows.

Chapter 3

Image Processing Techniques for the Measurement of Two-Phase Bubbly Pipe Flows using Particle Image and Tracking Velocimetry (PIV/PTV)

This part has been published as:
CERQUEIRA, R. F. L. et al. Image processing techniques for the measurement of two-phase bubbly pipe flows using particle image and tracking velocimetry (PIV/PTV). Chemical Engineering Science, v. 189, p. 1-23, 2018.

ABSTRACT

Particle Image Velocimetry (PIV) measurement in gas-liquid bubbly flows is a challenging task, mainly due to the dispersion of the laser light caused by the gas-liquid interfaces. Therefore, the camera captures only the light fluoresced by the seeding particles, filtering the laser light dispersed by the gas-liquid interfaces and measuring a velocity field which corresponds to the liquid phase, seeded with the particles. However, even for relatively low gas fractions, the fluoresced light reflected by the interfaces distorts the measurements, as it illuminates particles out from the laser plane. In addition, the fluoresced light also reflects at the interfaces, distorting the measurements and trending to overshoot the measured liquid velocities. In this chapter, PIV measurements of air-water bubbly flows in a small

diameter pipe (D=26.2 mm) are performed with fluorescent tracer particles (PIV/LIF). A new method for the phase discrimination in PIV was developed to overcome the problems caused by the presence of bubbles in the flow, which uses the pixels intensity information of each interrogation window, to identify if that window corresponds to liquid or bubble region. To validate the PIV procedure, a Particle Tracking Velocimetry (PTV) algorithm was also developed to measure the bubbles velocities, based on similar implementations found in literature, but some corrections were also proposed to overcome the bubble overlap phenomena which arises in bubbly pipe flows, when backward illumination is used. The PIV and the PTV methods were tested and validated by a series of distinct gas volume fraction and bubble diameter experimental cases, confirming the accuracy and reliability of both methods. The proposed method was used to analyze a set of upward laminar and turbulent bubbly flows, showing that the averaged axial velocity and the dispersed gas bubbles modify the turbulence intensity profiles.

3.1 INTRODUCTION

In gas-liquid bubbly flows, information about the liquid phase velocity field is of fundamental importance to characterize the flow behavior. Therefore, it is important to gather experimental data that can give insight to local flow patterns, such as wakes and recirculation regions induced by the gas-liquid interactions, and also provide averaged values that can be used in closure relations. Another use of these experimental studies is to provide reliable data that can be used for the development of closure relations and validation of CFD two-phase flow models.

First studies in gas-liquid bubbly flows used intrusive techniques to measure gas and liquid parameters to describe the two-phase interactions. Most techniques are based on electrical resistivity probes (SERIZAWA et al., 1975a, 1975b) and hot-film anemometry (HFA) (WANG et al., 1987; LIU; BANKOFF, 1993). Kashinsky et al. (1993) used an electromechanical method (NAKORYAKOV et al., 1981) to study bubble induced turbulence in upward bubbly pipe flow, measuring liquid velocity and void fraction profiles. Hibiki et al. (1998) used the HFA and the double electrical resistivity probe to measure local flow characteristics in bubbly flows, to obtain the interfacial area concentration.

Due to the errors associated with the flow disturbance caused by the probes, non-intrusive measuring techniques are preferred over intrusive methods. In the last two decades, non-intrusive techniques, in particular, Particle Image Velocimetry (PIV), has gained attention as a measurement technique for two-phase flows. Experimental techniques for bubbly flows based on Laser Doppler Velocimetry (LDV) can also be found in the

literature (HOSOKAWA; TOMIYAMA, 2013; SUN et al., 2004).

However, in order to use the PIV method in two-phase flows, especially in bubbly flows, additional effort is needed due to the presence of the liquid-gas interfaces, turning this kind of measurement significantly more complicated when compared to single-phase flows. Experimental studies in bubbly flows using PIV are focused on the measurement of the liquid velocity fields, and since the images acquired by the camera include both phases, some additional steps are needed to distinguish the liquid and the dispersed gas phase.

In the work of Bröder and Sommerfeld (2002), the authors develop a method based on an experimental setup, which includes two synchronized cameras, each with different optical filters. One optical arrangement is used to capture only the tracer in the liquid phase and the other to acquire only the dispersed bubbly phase. This setup was used in a bubble column with a gas hold-up varying between 0.5 and 19.0 %. However, the method can only be used when the diameter of the bubbles is small compared to the measurement domain, such as the case of a bubble column.

An experimental procedure for phase discrimination is presented by Lindken and Merzkirch (2002), which consists in the use of PIV in combination with laser-induced fluorescence (LIF) and pulsed shadowgraphy. In this work, the LIF technique helps to visualize the liquid tracer particles by the use of fluorescent particles and narrow band optical filters. The phase discrimination is done by the Pulsed Shadowgraphy Technique (PST), which is used to calculate the bubble shape and size, creating a ”binary mask” for the gas phase. This mask can then can be subtracted from the originally captured image before applying the PIV cross-correlation procedure, removing the bubbles. The same experimental procedure is used by Fujiwara et al. (2004) to study the vertical upward driven bubbly pipe flow with void fractions of 0.5 % to 1.0 % and by Kim et al. (2016) to characterize the bubble-induced turbulence in laminar upward flows with void fractions ranging from 0.05 % to 0.64 %. This technique is restricted to bubbly flows with low gas fractions since the fact that the phase discrimination is done volumetrically (using backlight illumination). Thus, as the void fraction increases, the superposition of bubble shadows turns the measurement virtually impossible.

Bröder and Sommerfeld (2007) circumvents the low gas fraction limitation by using macro optics in the CCD camera, thereby achieving a small depth of field and making possible, by a method based in the gradient of gray values, the discrimination among bubbles inside and outside the camera’s focal plane. Using these additional procedures, the authors can study gas-liquid bubbly flows inside a bubble column with a range between 0.5 and 5.0 % of gas volume fraction. However, the applicability of the method depends

on the relationship of the bubbles to pipe diameters, as it is complicated to get such a tight focal depth, to discriminate out-of-plane bubbles.

In Akhmetbekov et al. (2010) the authors developed a phase discrimination method based on the planar fluorescence for bubble imaging (PFBI), which is based on the LIF technique. The algorithm identifies the bubbles' positions and sizes, tracking their positions in images with non-uniform intensity distribution, such as the images from the PIV/LIF technique. From the identified bubbles, its shape and location are used to mask the dispersed bubble gas phase from the PIV images. Then, the PFBI technique is employed to analyze a bubbly free jet with gas fractions ranging up to 5.2 %. In these higher gas fraction cases, the method has some limitations in reconstructing the bubble shape due to frequent overlapping.

In the method described in Zhou et al. (2013) the phase discrimination is done through the image processing of the raw PIV/LIF images and can be used for liquid-gas pipe flow with void fractions up to 18.0%. A significant advantage of the proposed method is the fact that all calculations are done in a "planar" fashion since it uses the raw PIV images acquired with the light sheet illumination. However, the method creates a binary image from the raw PIV image, in which the discrimination of the tracer particles and the dispersed bubbles is done through a geometric criterion from a processed binary image. This criterion is chosen manually and can introduce errors in the cross-correlation PIV procedure used for the liquid velocity calculation.

Delnoij et al. (2000) presents a method that uses only one camera and does not rely on image processing or masking techniques but employs the PIV ensemble correlation to detect gas and liquid phases. The method is based on the fact that there is a noticeable slip velocity between the gas and liquid phases, which produces two correlation peaks, one for the gas phase and a second for the liquid phase. However, since the method is based on a considerable phase velocity difference, it may not be applicable in cases where there is no large slip between the phases. Besides, the method was only applied to pseudo-2D flows (narrow channels).

In the present work, a new method for the measurement of the liquid phase velocity fields in two-phase pipe bubbly flows using the PIV/LIF technique is described, which is capable of extracting reliable experimental data, and was tested for void fractions up to 11 %. The procedure is based on the pixel intensity information of each PIV interrogation window, excluding from the averaging process the velocities from those interrogation windows, which are considered to be occupied by the gas phase.

To validate the phase discrimination procedure proposed in this work for the PIV measurements in bubbly flows, a PTV (Particle Tracking Velocimetry) method, based on

backlight illumination, was implemented to track the motion of the dispersed gas phase. The bubbles velocities were used to compare the gas volume fraction calculated from the PIV and the PTV techniques. This comparison was performed using the superficial gas and liquid velocities, directly acquired from the rotameters of the flow loop. The liquid volume fraction, α_l (which is equal to $1.0 - \alpha_g$) is calculated from the measured superficial gas velocity and the liquid average velocity, obtained from PIV. Then, this value of α_g is compared with the one obtained from the gas superficial velocity and the average gas velocity, obtained with PTV.

The PTV algorithm proposed in this work is based on similar implementations found in literature (HONKANEN et al., 2005; ACUÑA; FINCH, 2010; XUE et al., 2012; LAU et al., 2013; FU; LIU, 2016a), but some corrections on the image analysis method are proposed in order to deal with bubble shadows superposition when the images are acquired with backlight illumination. Most of the PTV implementations are focused on analyzing the flow inside narrow channels and/or reduced void fraction values (less than 1.0 %). In these cases, bubble shadows overlap is not a critical problem. In the case of the present work, the technique is applied on a small diameter (D =26.2 mm) pipe with void fractions up to 11.4 %.

This chapter is organized as follows: after the introduction of the experimental setup, the PIV/LIF technique is described, and the problems arising from the measurement of the two-phase flow are discussed. Then the proposed phase discrimination method and the PTV implementation are presented, followed by the technique validation. Finally, the bubble induced turbulence in upward bubbly flows is investigated by analyzing two particular sets of experiments (LIU; BANKOFF, 1993; HOSOKAWA; TOMIYAMA, 2013; KIM et al., 2016), where bubbles are introduced in a laminar and turbulent liquid single-phase laminar flow, respectively.

3.2 EXPERIMENTAL SETUP

This section describes the experimental setup used in this work. This system allows for the generation of a single-phase liquid stream or bubbly flow in a straight vertical duct, where the water and air flow rates, and thus, the superficial velocities, can be independently controlled.

The experimental apparatus is schematically depicted in Fig. 3.1. The test section consists of a transparent pipe with D=26.2 mm internal diameter and L=2.0 m length. At the PIV measurement section, a box constructed with transparent acrylic, made with 8 plane faces, filled with the water is included to minimize optical distortion. A two-phase

stream is generated at the bottom of the test section by combining a liquid stream (tap water), driven by a centrifugal pump, and air from the compressed air line from the building. To eliminate oil and solid particles, the air is treated and pressure is maintained constant at the injection point through a pressure regulating valve, making it independent of the line demand. The dispersed bubbles are injected at the bottom of the tube, and the gas flow rate is measured by two OMEGA FL-3802ST/FL-3861SA flow meters with ranges of 81.4-814.0 standard mL/min and 26.3-263.0 standard mL/min, both with $\pm 2.0\,\%$ full-scale accuracy. The flow rate is controlled by a needle valve downstream. In order to correct the gas superficial velocity due to gas expansion, pressure and temperature sensors were installed downstream the needle valves. As the return to the reservoir consists of a relatively short ($\sim$ 0.5 m), and 50.0 mm internal diameter duct, and the reservoir is opened to the atmosphere, it was assumed that the pressure at the test section was close to the atmospheric pressure. In order to control the sizes of the dispersed bubbles, a porous gas diffuser was installed at the bottom of the tube. The water flow rate is measured by an OMEGA FL46303 flow meter with a range of 1.00-7.50 l/min with $\pm 5.0\,\%$ full-scale accuracy. The liquid flow rate is controlled by a variable frequency drive (VFD) connected to the electric water pump motor.

For the bubble tracking algorithm, a bright white LED array is added at the back of the test section shown in Fig. 3.1. A CCD digital high-speed camera (Redlake MotionPro X3) with 52 mm lens was used to acquire the flow images using the LED illumination array, and the images were recorded in 256 grey scale levels with image size of 1024 x 1024 pixels with a frame rate of 400 fps.

Figure 3.1 – Schematic of the experimental setup.

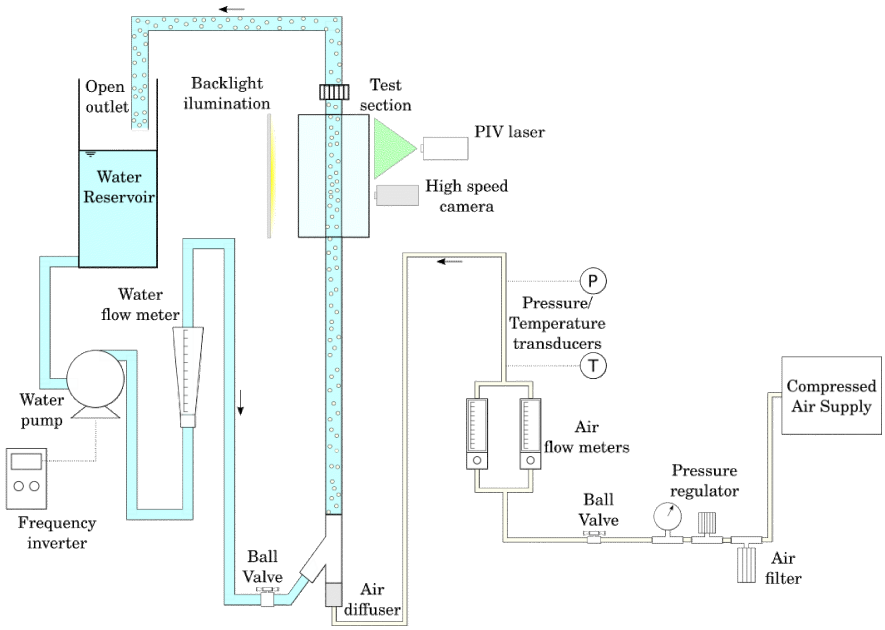

Source - Developed by the author.

3.3 PIV/LIF PHASE DISCRIMINATION

The standard PIV technique is largely described in the literature (e.g., (RAFFEL et al., 2007)). Therefore, only the specific modifications of the technique, to apply it to bubbly flows, are described here. The PIV system available at SINMEC Lab consists of a TSI 2048x2048 pixels (4 MPx) resolution CCD camera, a pulsed Nd:YAG laser with a wavelength of 532 nm and a synchronizer to match the emission of laser pulses and image capturing, which can be externally triggered. The PIV images of the duct test section occupy an area of 1568 x 640 pixels. For all the experiments done in this work, the time difference between the two consecutive frames for velocity measurement, Δt, was defined following the guidelines discussed in Raffel et al. (2007). For the PIV image data, the interrogation size was maintained constant at 32 x 32 pixels throughout the experiments, and these were overlapped by 50 %. From the acquired consecutive frames, the Fast Fourier Transform (FFT) cross-correlation of the TSI Insight 4G software was used to generate the vector fields and to remove spurious velocity vectors. The signal-to-noise ratio (SNR) was set to 2.0, in order to remove those spurious vectors.

In applications to liquid-gas two-phase flows, the presence of the interfaces with much larger scales than the seeding particles, scatters the light of the laser with much more intensity than these particles, impeding the CCD camera to capture the seeding particles. Therefore, as usually recommended for the application of the PIV technique in liquid-gas

flows, the LIF technique was employed, using fluorescent seeding particles along with an optical filter in front of the CCD camera lens. Particles of Rhodamine B with diameters ranging from 1 – 20 μm were used, capable of receiving light in a wavelength of 532 nm and emit (fluorescence) at 590 nm (peak). A high band-pass filter for the wavelengths above 545 nm is used at the camera lens, filtering all the light at the laser wavelength (the same scattered by the interfaces) and capturing the light fluoresced by the seeding particles.

Due to the characteristics of the PIV method, the cross-correlation algorithms, even when using the LIF technique, are capable of producing acceptable vectors in some interrogation windows occupied by bubbles, as can be seen in Fig. 3.2. This type of error can introduce some bias in the velocity fields, since some of the seeded particles, which are only present in the liquid phase, appear to be in the gas phase due to the reflection of fluoresced light on interfaces and off-plane particles illuminated by scattered light. The inclusion of these unrealistic velocity vectors in the time-averaging procedure overestimates the liquid velocity averaged fields (in the case of co-current upward flows) due to the higher velocity of the bubbles. From Fig. 3.2 it is noticed that in the interrogation windows occupied by the gas phase and its surroundings, there is no distinguishable difference between the velocity vectors from the spurious and the liquid velocity vectors, i.e., there is no considerable slip velocity. Thus in the present work, probably, the method developed by Delnoij et al. (2000) would not be applicable to this case. However, as will be seen in the results section, the inclusion of these spurious vectors in the averaged fields results in an overestimation of the liquid velocity fields.

In order to remove these unrealistic velocity vectors, a phase discrimination method, based on the processing of PIV raw images, was developed in this work, which can be used in bubbly flows with low to moderate void fractions.

The main goal of the proposed image processing technique is to identify the regions occupied by the gas phase in the original PIV images and remove these interrogation windows. Then, the unrealistic velocity vectors which arise from off-plane illuminated particles or "ghost" particles, are considered in the averaged velocity fields. From the works found in the literature, it has been observed that most image processing methods rely on image filtering and transformations techniques (LINDKEN; MERZKIRCH, 2002; BRÖDER; SOMMERFELD, 2002; AKHMETBEKOV et al., 2010; ZHOU et al., 2013; KIM et al., 2016). These operations are performed to “mask out” the gas phase, creating new processed frames, which are then introduced in a cross-correlation PIV algorithm, resulting in the desired liquid velocity field. In addition, since this work aims to measure the liquid velocity in bubbly flows with low to moderate void fractions, the shadowgraphy

Figure 3.2 – a) Raw image from the PIV/LIF system; b) Obtained velocity field from the non-treated image. c) Velocity vectors with gas-phase contributions, calculated from the gas-phase occupied interrogation windows.

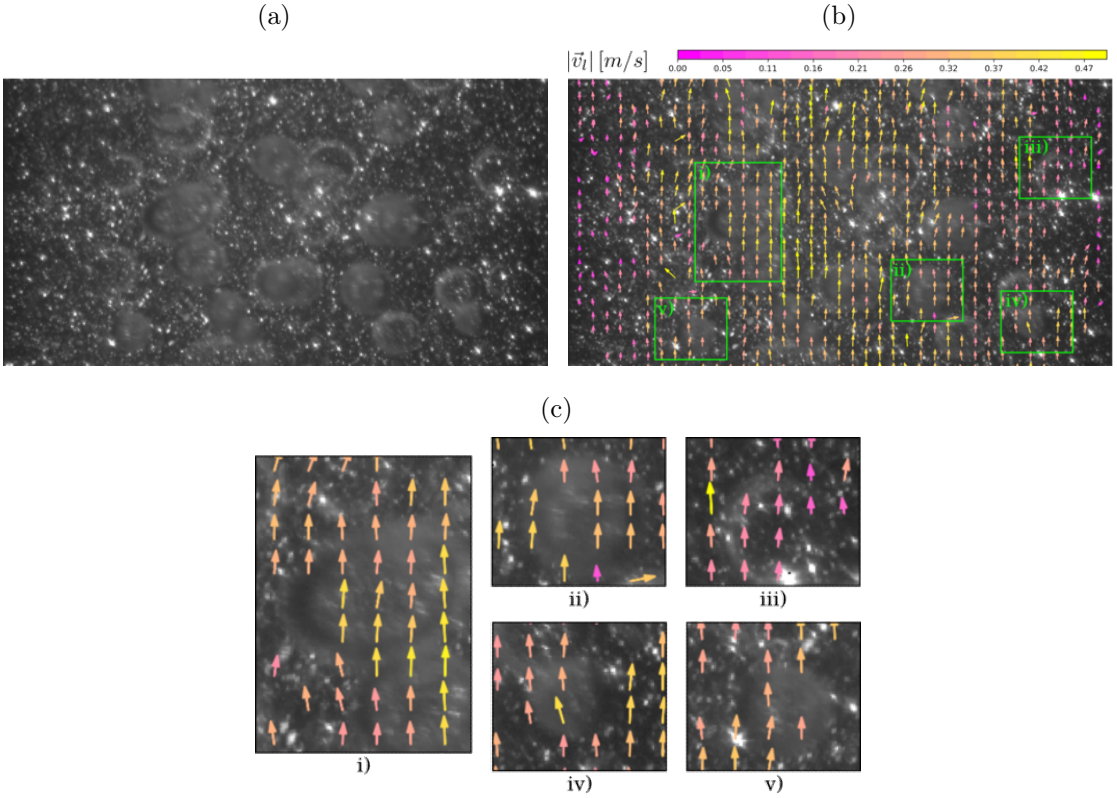

Source - Developed by the author.

technique, using back-light illumination is not suitable, since the technique is based on the perpendicular projection of the bubbles into the camera plane. Then, the superposition of bubbles shadows projections makes the images unfeasible for PIV, in cases with moderate void fractions. Most works found in the literature using this approach ((SATHE et al., 2010; PANG; WEI, 2013; ZIEGENHEIN; LUCAS, 2016; ZIEGENHEIN et al., 2016)), studies gas-liquid bubbly flows in pseudo 2D (narrow) channels, avoiding bubble shadow superposition.

An advantage of the present method is that the phase discrimination does not rely on a masking procedure, but analyzes each velocity vector from the PIV cross-correlation algorithm and verifies the presence of the gas phase. The existence of a gas or liquid phase in each interrogation window is done by a series of processing steps in their pixel intensity values and will be described in the following paragraphs.

From the PIV recordings, the velocity field and the signal-to-noise ratio (SNR) are obtained by the cross-correlation algorithm from the TSI Insight 4G software. The velocity and the signal-to-noise field, together with the raw PIV images from the camera,

are exported as an input to an in-house developed image processing algorithm based on the OpenCV (BRADSKI, 2000b) library. The first task from the developed algorithm is to divide the raw 1568 x 640 image in a collection of 32 x 32 interrogation windows (the same division used in PIV algorithm) and then link the velocity and SNR fields with its corresponding window. Also, from the SNR value, each interrogation window is classified as a valid or invalid vector, valid vector if SNR > 2.0 and invalid vector if the criterion is not fulfilled.

After the SNR classification, each interrogation window from the PIV frame is ready to be analyzed in order to check if the dispersed gas phase is present in the interrogation domain. It is important to state that the interrogation window analysis is performed on the two (frames A and B) PIV images used in the velocity field computation. Even when an interrogation window is classified as being located in a gas phase region in only one of the two PIV frames, the interrogation window is classified as a "gas-phase" and the respective velocity vector excluded from the averaging.

In the first step of the raw image processing, a Gaussian filter (3 x 3 size) is applied to remove part of the noise caused by the light reflections due to the presence of the dispersed bubbles and background, as shown in Fig. 3.3 by the operation A.

Figure 3.3 – a) Original image from the PIV recording and the grid formed by the interrogation windows, highlighting sub-windows i.), ii), iii), iv) and v). b)Image processing steps being performed in the interrogation windows highlighted in a), where operation A is the application of a Gaussian filter, operation B represents the Otsu's method and operation C is an erosion filter.

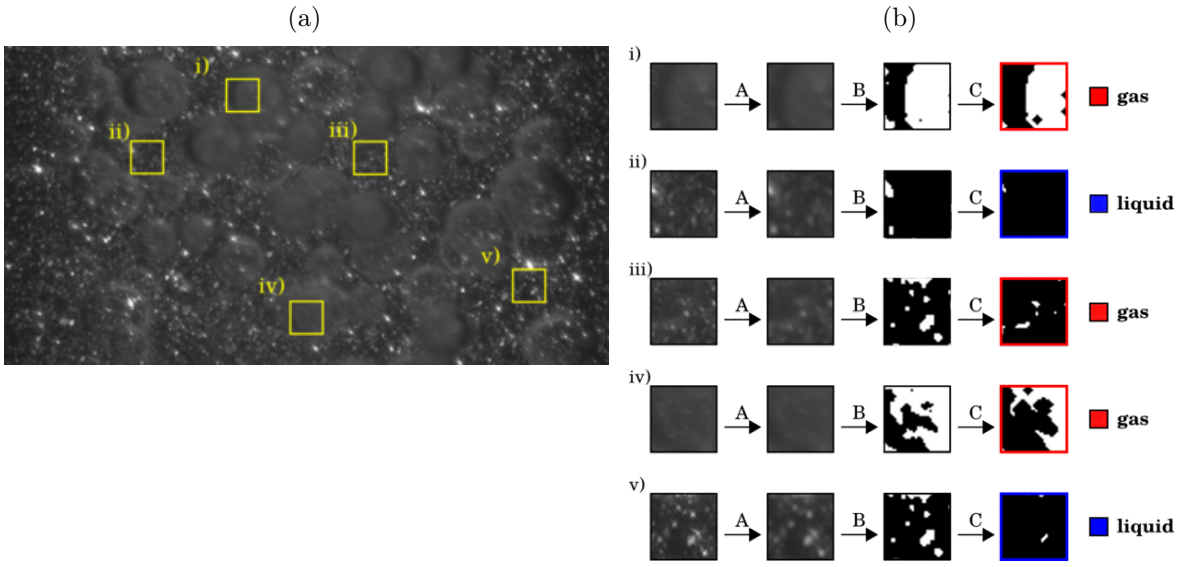

Source - Developed by the author.

From the pixel intensity distribution (after operation A), the Otsu's method (OTSU,

1979) is used to create a binary image (operation B), since the method determines an optimal pixel intensity value to define the threshold that classifies the image in two groups. In this case, the pixel intensity distribution is divided into black (pixel intensity value equal to 0) and white (pixel intensity value equal to 255). In the last image processing step (operation C), which produces the final processed interrogation window images used for the phase discrimination, an erosion filter with a 3 x 3 cross-shaped kernel (2 passes) is applied to eliminate part of the noise produced by the interaction of the fluorescent seed particles and the gas phase.

By simply using this erosion filter, it is not possible to fully discriminate a dispersed bubble from the background and the seed particles. However, the image produced by this final step can be used as a parameter to define if an interrogation window contains information of the dispersed gas phase. It can be noted from Fig. 3.3 that operation C (erosion step) the number of non-zero elements in the pixel matrix can be used, with the help of a user-defined threshold value, to define if a certain interrogation window contains information about the dispersed phase. The threshold value $P_{thresh.}$ is used for this task and it is defined as the number of non-zero intensity pixels of matrix elements in the 32 x 32 interrogation window matrix. An interrogation window is identified as being located in a gas phase region when the parameter $P_{thresh.}$ is above some certain threshold. This parameter will define if the measured velocity at that interrogation window is included in the average calculation. Therefore a more rigorous value will promote better phase discrimination but, at the same time, will produce more "false negatives", resulting in need of more acquisitions to get consistently averaged fields. Then, the optimal threshold value differs from case to case and depends on the number of dispersed bubbles in the flow and also the laser sheet's illumination power. The effect of $P_{thresh.}$ on the phase discrimination process and the averaged results will be discussed in Sec. 3.5.

In order to illustrate the phase discrimination process and the reason behind the application of the method for each interrogation window, instead of to the whole PIV image (ZHOU et al., 2013), Fig. 3.4 shows the obtained phase classification by using two different methodologies.

In the first methodology, shown in the first column in Figs. 3.4b)-g), the image processing steps are performed globally, using the pixel intensity information from the whole raw image (Fig. 3.4a)). In this methodology, when applying the binarization technique, the Otsu's method does not produce a suitable image for the next step and the subsequent phase discrimination process based on the $P_{thresh.}$ value. By the end of the phase discrimination procedure, the gas presence is overestimated, since most of the interrogation windows are classified as “gas phase” regions, as illustrated by the red filled

regions in Fig. 3.4f), when, actually, most of the interrogation windows correspond to the liquid phase with its tracer particles, as visually observed from Fig. 3.4a).

The second column of Figs. 3.4 shows the image processing steps using the methodology described in the above paragraphs, using the pixel intensity information from the interrogation windows and performing the processing steps locally. From this local procedure, the Otsu's method application and the following erosion process produces suitable images for the phase discrimination, as seen in Fig 3.4g), where a much smaller fraction of the interrogation windows are classified as the gas phase.

The difference between the final phase discrimination using the two methodologies lies on the binarization step, due to the Otsu's method application. As illustrated by the probability density function (PDF) of the pixel intensity distribution of a typical PIV/LIF bubbly image, Fig. 3.5, most of the pixel intensity information is concentrated in a small range of the image intensity histogram, where only the end of this range is attributed to the fluorescent tracer particles. For this reason, it is difficult to define an optimal intensity threshold for the whole image (ZHOU et al., 2013), as seen in Fig. 3.5, where the dotted vertical line represents the global binarization threshold.

On the other hand, when the Otsu's method is employed locally to binarize only the image portion correspondent with the interrogation window, the pixel intensity distribution has a bi-modal shape, as can be seen in Fig. 3.6. Therefore, due to the local application of the binning process in the region delimited by the interrogation windows, each portion of the image has its different threshold value calculated by the Otsu's method, resulting in more precise phase discrimination.

Figure 3.7 illustrates the output of the PIV processing, using the phase discrimination procedure for the flow configurations, which result in different bubble concentrations and shapes: a)stagnant liquid ($j_l = 0.0$ m/s), b) upward co-current bubbly flow, with low liquid superficial velocity ($j_l = 3.1 \cdot 10^{-2}$ m/s) and c) upward co-current bubbly flow, with higher liquid superficial velocity ($j_l = 21.64 \cdot 10^{-2}$ m/s). In this example, the phase discrimination process considered a conservative value of $P_{thresh.}$=8, but the effect of this parameter will be analyzed in the results section. In Fig. 3.7 caption, the estimated values of gas volume fraction, $\overline{\langle \alpha_g \rangle}$, and average bubble diameter $\overline{\langle d_b \rangle}$ were evaluated through the PTV algorithm. Details regarding its calculation are described in the following sections.

From the results presented in Fig. 3.7, the proposed method removes the majority of the gas-phase velocity vectors located in the gas regions in the three flow conditions, even though the discrimination process fails in some interrogation windows, keeping some spurious velocity vectors. In Fig. 3.7a), this small amount of spurious vectors are located inside the large gas bubbles, as the interfacial area is large and some of the reflected

Figure 3.4 – Effect of the successive image processing steps of a portion of a PIV/LIF image; a) PIV/LIF image; b) to g) application of operations A, B and C; left column: applied to the whole image; right column: applied on an interrogation window basis.

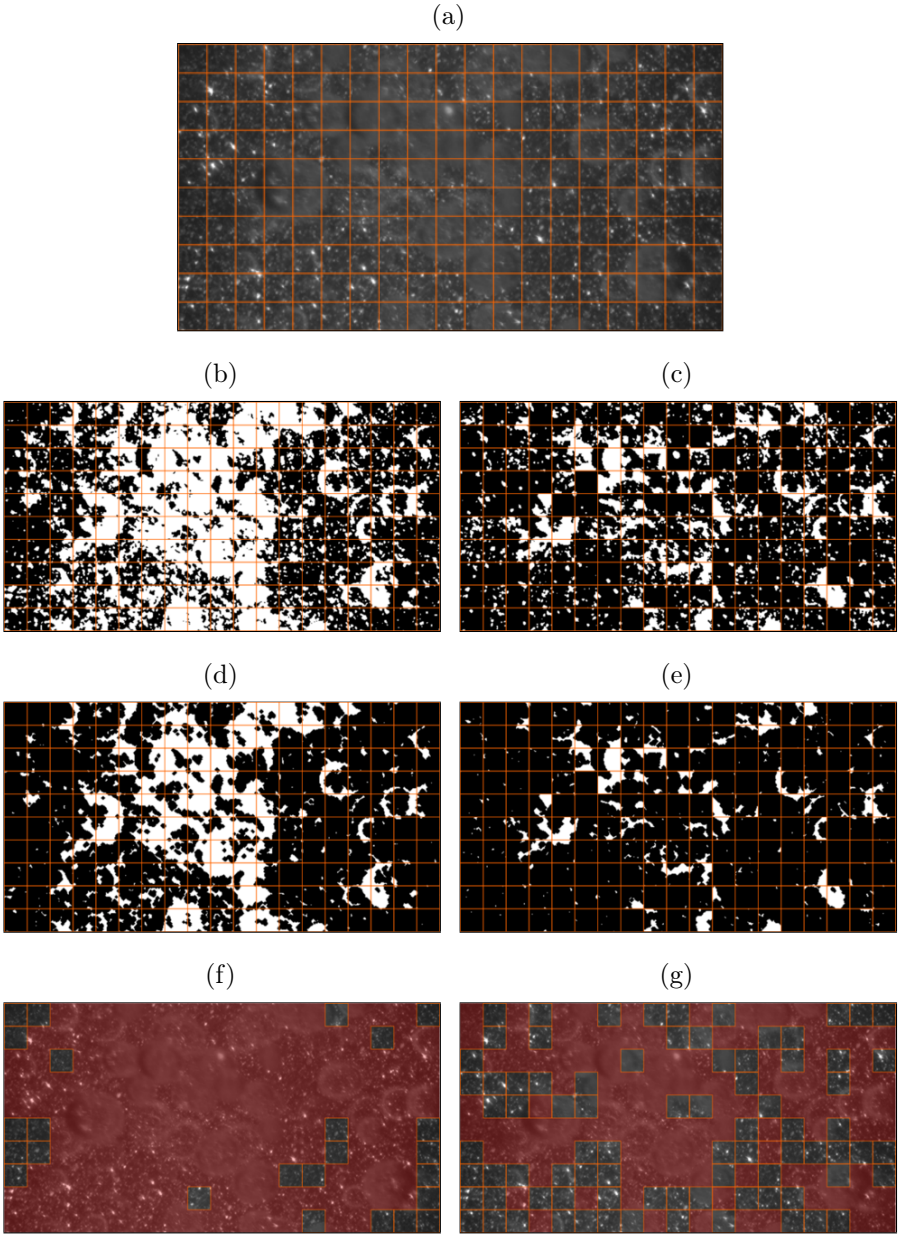

Source - Developed by the author.

tracer particles are classified as being part of the liquid phase. In Figs. 3.7 b) and c), some velocity vectors are encountered near unevenly illuminated bubble rings.

Despite the problems arising in these particular cases, which represent bubbly flows with a considerable gas fraction, these misclassified interrogation windows do not affect the effectiveness of the method. In addition, by using a stricter threshold, P_{thresh} it is possible to reduce the quantity of incorrect classified spurious velocity vectors but, as commented

Figure 3.5 – Probability density function (PDF) from a typical PIV/LIF bubbly flow image.

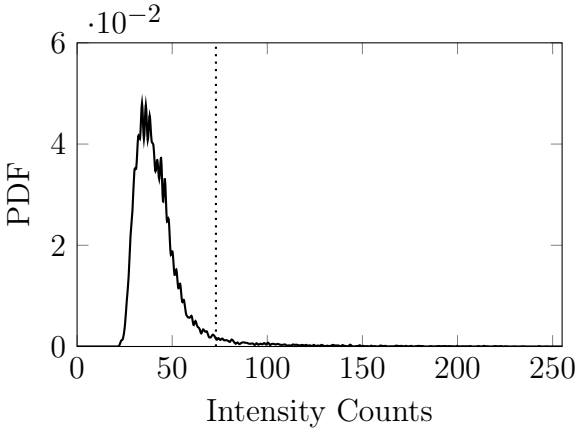

Source - Developed by the author.

before, a stricter $P_{thresh.}$ results in a larger number of PIV acquisitions required to get consistent averaged liquid velocity fields.

Figure 3.6 – Probability density function (PDF) from the interrogation windows of a typical PIV/LIF bubbly image where the pixel intensity distribution has a bi-modal distribution.

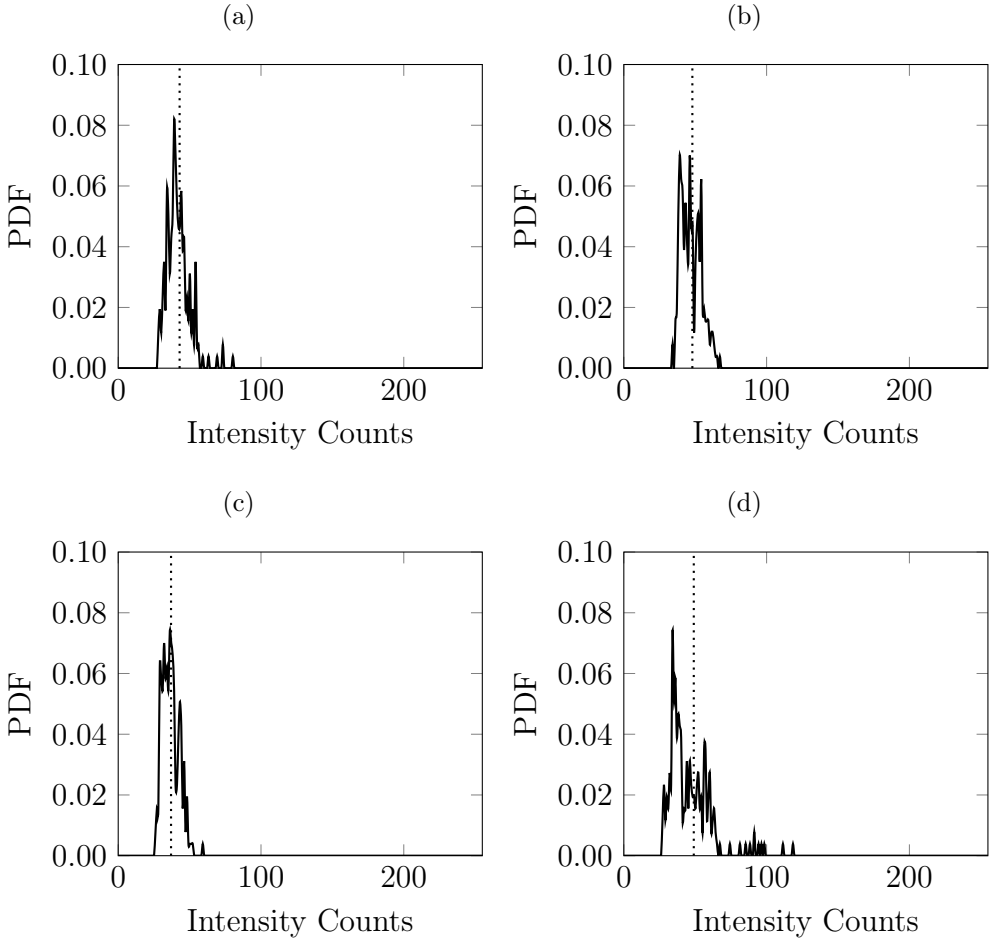

Source - Developed by the author.

Figure 3.7 – Instantaneous velocity field after the phase velocity discrimination for different flow configurations.

(a) $j_l = 0.0$ m/s, $j_g = 19.83 \cdot 10^{-2}$ m/s, $\overline{\langle \alpha_g \rangle} = 0.114$ and $\overline{\langle d_b \rangle} = 4.05$ mm

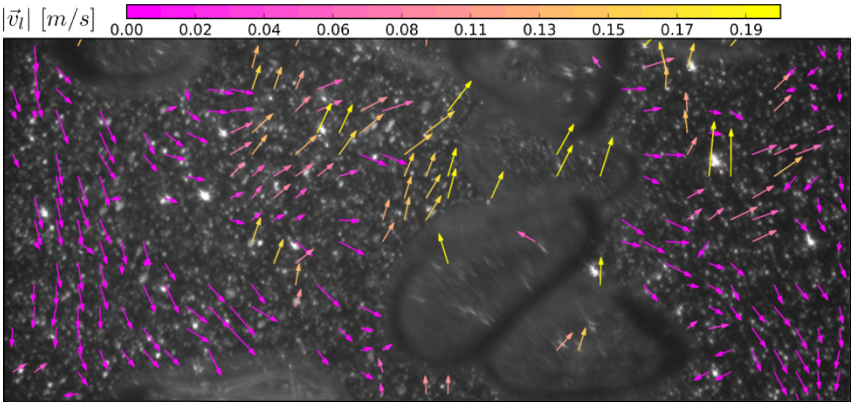

(b) $j_l = 3.09 \cdot 10^{-2}$ m/s, $j_g = 15.34 \cdot 10^{-2}$ m/s, $\overline{\langle \alpha_g \rangle} = 0.084$ and $\overline{\langle d_b \rangle} = 1.60$ mm

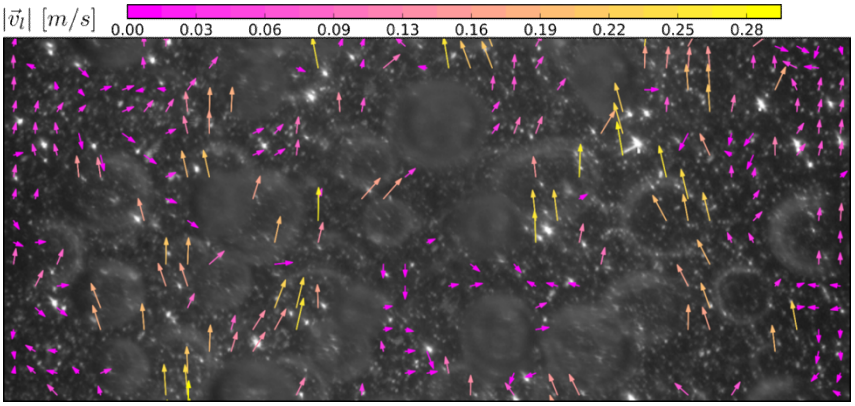

(c) $j_l = 21.64 \cdot 10^{-2}$ m/s, $j_g = 19.83 \cdot 10^{-2}$ m/s, $\overline{\langle \alpha_g \rangle} = 0.049$ and $\overline{\langle d_b \rangle} = 2.41$ mm

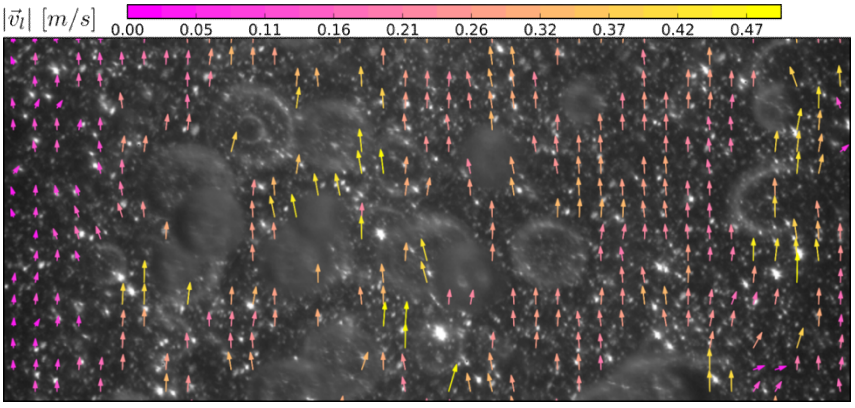

Source - Developed by the author.

3.4 PTV FOR BUBBLE TRACKING

In bubbly flow, it is important to gather information about the gas phase in order to understand the liquid-bubble interactions. Among the main advantages of the PTV in bubbly flow applications is that it is non-intrusive and can be used to measure the bubble rising velocity, bubble size and shape and, in some situations, the gas volume fraction. In the present work, this information was used for the validation of the PIV phase discrimination algorithm. Although this PTV algorithm is based on previous approaches presented in the literature, it is described here, as some modifications were incorporated in the algorithm, mainly to deal with the superposition of bubble shadows, in moderate gas fraction pipe flows.

The bubble tracking method can be implemented by using the images from a high-speed camera and back-light illumination (HONKANEN et al., 2005; XUE et al., 2012; LAU et al., 2013; FU; LIU, 2016a; ACUÑA; FINCH, 2010) or from the PIV/LIF images (AKHMETBEKOV et al., 2010). In the present work, the bubble tracking method using the first approach is used to extract information about the gas phase and to verify the liquid velocity fields obtained from the PIV/LIF method. The verification is performed by comparing the gas volume fraction obtained, for different flow conditions, using the average velocity measurement of both phases.

The backlight illumination produces images with high contrast between the liquid and gas phases. Figure 3.8 (a-f) shows some typical high-speed camera images obtained with the backlight illumination arrangement for different gas and liquid superficial velocities, where the contrast difference enables the visual discrimination of the two phases.

The first step in the bubble tracking method is the correct identification of the gas bubbles in each frame, to later find its matching pair in the subsequent frames and then calculate its velocity and trajectory. These techniques will be briefly described in the following sections, detailing the specific procedures to deal with bubbles' shadows superposition.

As can be seen in Fig. 3.8, it is observed that, in general, bubbles do not always have an ellipsoid/circular shape and, in several cases, bubble shadows overlapping occurs. The disturbances in bubbles shape are originated from the bubble-bubble interaction and the liquid phase turbulence, and for larger bubbles due to inertial effects. These disturbances also affect the bubbles' motion, causing some bubble clustering and subsequent overlapping in the projected image plane. However, in some cases, the bubble "clustering" appearing in the recorded images is not a physical feature of the flow, but a consequence of the projection of the recorded bubbles in the image plane, in virtue of the use of back-light

illumination in pipe flows. In fact, the observed clustering and overlapping also happen with bubbles that are distant from each other in the direction of the projection axis, which also causes ambiguities in the bubbles' motion in the radial direction.

Figure 3.8 – Typical high speed cameras obtained with the backlight illumination arrangement for different flow configurations: a) $j_l = 0.0$ m/s and $j_g = 2.38 \cdot 10^{-2}$ m/s; b) $j_l = 0.0$ m/s and $j_g = 19.83 \cdot 10^{-2}$ m/s; c) $j_l = 3.09 \cdot 10^{-2}$ m/s and $j_g = 2.38 \cdot 10^{-2}$ m/s; d) $j_l = 3.09 \cdot 10^{-2}$ m/s and $j_g = 15.34 \cdot 10^{-2}$ m/s; e) $j_l = 21.64 \cdot 10^{-2}$ m/s and $j_g = 2.38 \cdot 10^{-2}$m/s; f) $j_l = 21.64 \cdot 10^{-2}$ m/s and $j_g = 19.83 \cdot 10^{-2}$ m/s.

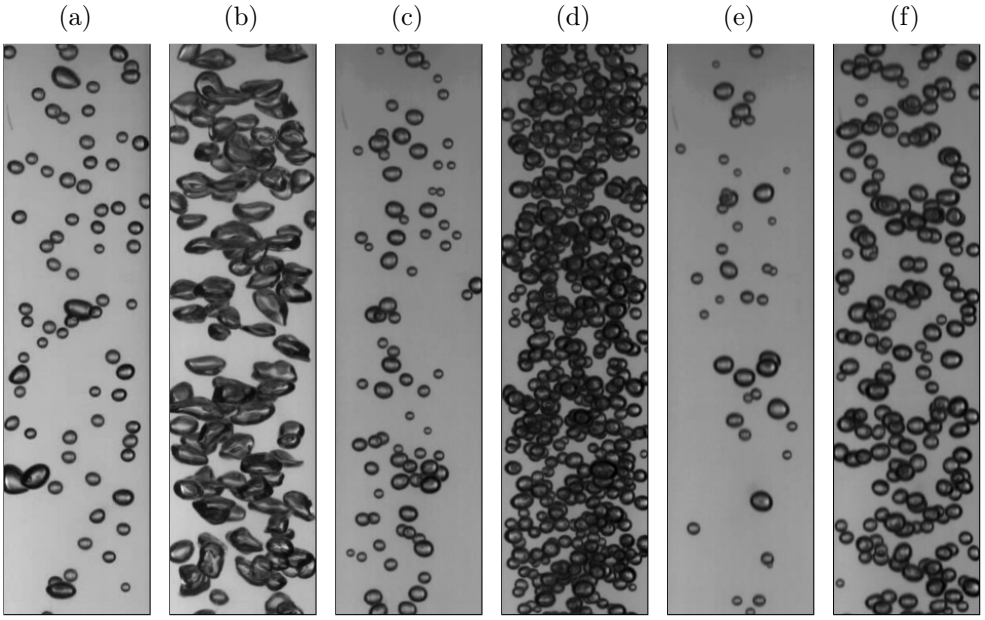

Source - Developed by the author.

Due to the difficulties associated with the bubble identification in these cases, in the present work, two different processing techniques are proposed and incorporated into the particle tracking velocimetry method. In the first case, the "classic" method, which captures the bubble outlines, is modified to deal better with bubble clustering (or shadows projections overlapping). From this method, both velocity and bubble diameter can be determined. However, for moderate void fractions, the technique is not capable of capturing many single bubbles. Then, the method is used simultaneously, with a second technique that captures the internal contours of the bubbles and, although not capable of capturing bubble shapes and sizes, their velocities can be measured.

3.4.1 Bubble Outline Tracking

In this procedure, firstly, a series of image processing methods are used to identify bubbles contours in the high-speed camera images. Then these contours are classified as

single or overlapped/clustered bubbles, as shown in Fig. 3.9. These methods are described below.

First, the raw image acquired from the high-speed camera is binned using Otsu's method (Image 1 of Fig. 3.9). Then, the contours and possible bubble outlines are detected from the binned image, as seen in Image 2 of Fig. 3.9. After the contour classification, the inner boundaries are "filled", i.e., the values inside the boundaries are set to non-zero values, as shown in Image 3 of Fig. 3.9. In this step, the contours that touch the image border are discarded to avoid errors in the shape definition. From this new binned image, contours are detected (Image 4a and 4b of Fig. 3.9) and bounded by a rectangle (Image 5a and 5b of Fig. 3.9). The pixel intensity and distribution from those bounding rectangles are then used as input in the contour classification algorithm, which decides if a given contour corresponds to the projected image of a single bubble or overlapped/clustered bubbles.

Figure 3.9 – Image processing steps in the bubble identification procedure.

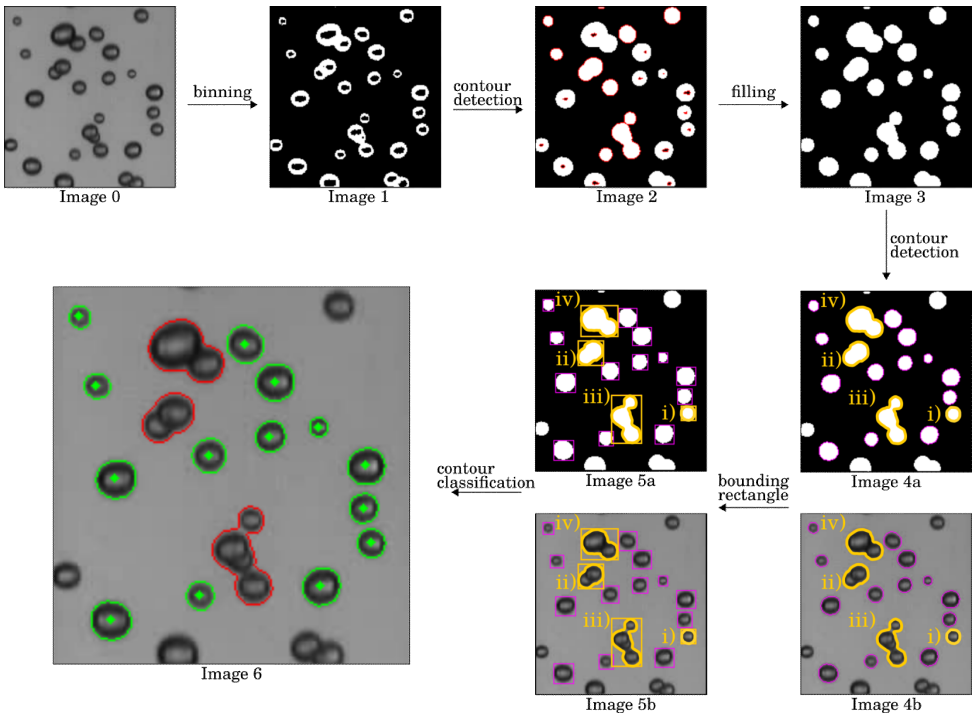

Source - Developed by the author.

The contour classification algorithm consists of a two-step process and verifies if the contour is a "valid" (single) bubble. This verification is done with the information extracted from the bounded rectangle shown in Image 5a of Fig. 3.9. In the first step, which is based on geometrical features, an ellipse is fitted through a least-squares minimization technique inside the extracted contour, as seen in Image B of Fig 3.10. Then, a mask is created using

this fitted ellipse, shown in Image C of Fig. 3.10, where the values inside the ellipse are defined as non-zero. This generated mask (Image C) is then subtracted with the original extracted contour (Image A) to generate Image D, pictured in Fig. 3.10. Image D is then used as a parameter to measure the contour shape deviation from an ellipsoid, through the $P_{ellipsoid}$ parameter, defined as the ratio between the non-zero elements and the number of elements of Image D. As $P_{ellipsoid}$ approximates to 0.0, the analyzed contour is more likely to represent a single bubble, and the opposite as the value approximates to 1.0. Figure 3.10 shows the image processing steps used in the $P_{ellipsoid}$ calculation, and its value, for the four highlighted contours of Fig. 3.9. As shown in this figure, the $P_{ellipsoid}$ value is significantly lower in contour i) than in contour iii), but this difference is not as significant in the cases with ellipsoidal and/or overlapped bubbles, as cases ii) and iv).

Figure 3.10 – Examples of the first of the two-step process contour verification, in which $P_{ellipsoid}$ is calculated for the contours i, ii), iii) and iv) of Fig. 3.9.

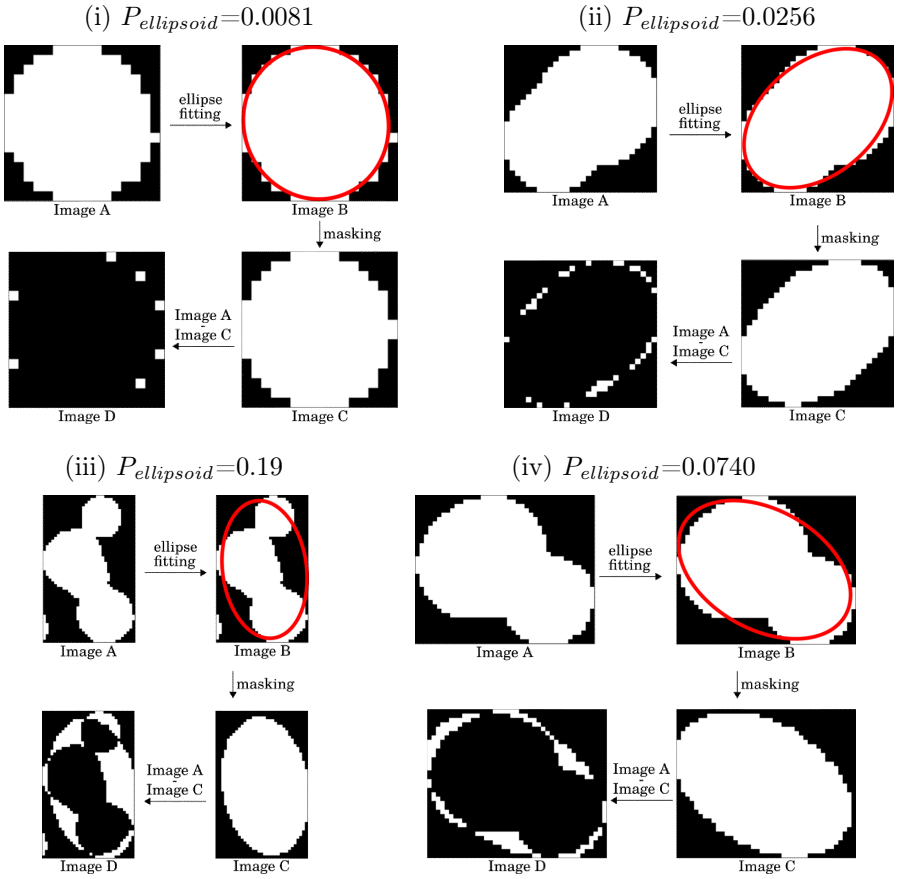

Source - Developed by the author.

In order to overcome this problem, a second verification step is proposed. The algorithm used for bubble verification is based on the analysis of the pixel intensity profiles across the two main ellipsoid axes (see Fig. 3.9). The intensity profiles across the

axes ($\boldsymbol{l}_1$ and $\boldsymbol{l}_2$) can be seen in Fig. 3.11, where the main axes and the fitted ellipsoid are drawn over the raw image extracted from the bounded rectangle seen in Fig. 3.9. As seen in Fig. 3.11a), ellipsoid bubbles have distinct intensity profiles, with two local minimum points corresponding to the bubble boundaries and higher values corresponding to the background and the inner portion of the bubble. In this second step, an algorithm is developed to found local minimum points in the $\boldsymbol{l}_1$ and $\boldsymbol{l}_2$ intensity profiles, and if the number of local minimum points ($N_{\boldsymbol{l}_1}$ and $N_{\boldsymbol{l}_2}$) is greater than 2, then the contour does not correspond a valid single bubble. From the intensity profiles presented in Fig. 3.11, it is clear that the analysis must be performed in two different directions, since if the intensity profiles were only analyzed across the centerline direction or in a single direction, clustered and overlapped bubbles would be wrongly classified as valid single bubbles. Figure 3.11 c) shows that the local minimum points can only be found below a certain pixel intensity value (direction $\boldsymbol{l}_2$), since a threshold condition is implemented on the algorithm to avoid the detection of local minima, related to background noise.

After the two-step contour classification, the contours are classified as a single bubble outline or an overlapped/clustered bubbles. Image 6 of Fig. 3.9 shows the final contour classification, where the bubbles with green outlines are classified as "valid" (single) bubbles for PTV and the ones with red outlines are detected as overlapped/clustered bubbles.

Figures 3.12 and 3.13 show the application of the previously described procedure by highlighting the bubble shape and showing the bubble velocity vectors in different flow configurations. For the two situations ($j_l = 0.0$ m/s and $j_l = 3.09 \cdot 10^{-2}$ m/s), as the gas superficial velocity increases, fewer bubbles are encountered, as a result of the clustering and overlapping effects. It is important to state that in the $j_l = 0.0$ m/s experiments (Fig. 3.12), in situations which the gas flow rate was moderate to high, the bubble diameter is larger and, due to inertial forces (higher Weber numbers), their shape was highly distorted. In these particular cases, only the geometrical method based on the ellipses fitting was employed, and the intensity profile-based method was not used due to bubble distortion. For the remaining case, $j_l = 3.09 \cdot 10^{-2}$ m/s (Fig. 3.13), only a small quantity of the total bubbles were identified due to clustering and overlap. Therefore, in these cases, an extremely high number of image samples would be needed to get consistent averaged values of the bubble velocities. Video 1 of the supplementary material given in Appendix B presents identified bubbles from the bubble outline tracking method in three different bubbly flow configurations.

Figure 3.11 – Examples of the second of the two-step contour verification, illustrating the pixel intensity profiles across the main axes of the fitted ellipses and the number of local minima in both directions.

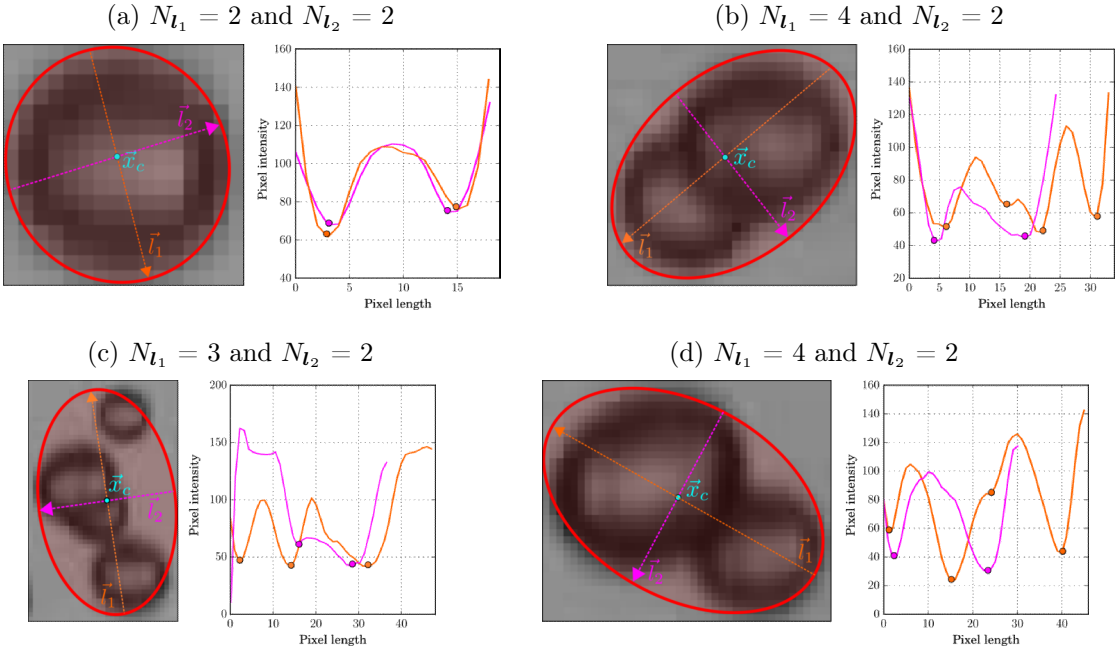

Source - Developed by the author.

Figure 3.12 – Examples of the first technique to find single valid bubbles for j_l=0.0 m/s for different gas superficial velocities: a) j_g=2.83 $\cdot 10^{-2}$ m/s; b) j_g=5.89 $\cdot 10^{-2}$ m/s; c) j_g=9.66 $\cdot 10^{-2}$ m/s; d) j_g=15.33 $\cdot 10^{-2}$ m/s and e) j_g=19.83 $\cdot 10^{-2}$ m/s

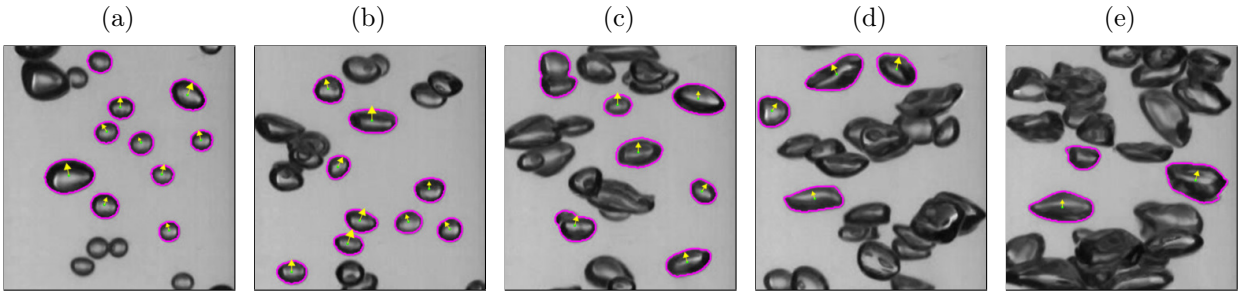

Source - Developed by the author.

3.4.2 Internal Contour Tracking

In order to reduce the number of samples in each experiment and to extract more information form each captured image, a second method was developed to calculate only the bubble velocity, ignoring its shape. The method is based on the tracking of the internal contours of the binned images from the first step of Fig. 3.9. As commented by other authors (ACUÑA; FINCH, 2010; KARN et al., 2015; FU; LIU, 2016b) and demonstrated

Figure 3.13 – Examples of the first technique to find single valid bubbles for j_l=3.09 · 10^{-2} m/s for different gas superficial velocities: a) j_g=2.83 · 10^{-2} m/s; b) j_g=5.89 · 10^{-2} m/s; c) j_g=9.66 · 10^{-2} m/s; d) j_g=15.33 · 10^{-2} m/s and e) j_g=19.83 · 10^{-2} m/s.

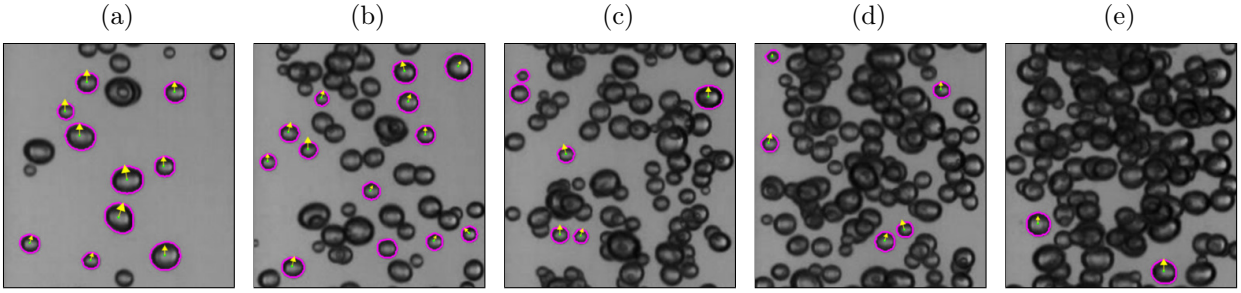

Source - Developed by the author.

in Figs. 3.9 and 3.14, the binnarization of a bubble image results with an inner and an outer boundary. The second method presented in the paragraphs below tracks the bubble motion from this inner boundary position. The application is straightforward from images were the clustering effects are not predominant, but, for the other cases, additional steps are required to verify the origin of these inner boundaries.

Figure 3.9 illustrates the overall process of the method, showing the binning steps and the contour detection and its subsequent classification stage. The classification step is necessary, once as can be seen, gaps formed between bubbles within a cluster also originates "internal" boundaries (Image 3a in Fig. 3.9) and need to be discerned from the ones originated from single bubbles. This is done by a series of threshold parameters, which uses the contour area and its average pixel intensity. For the contour area classification, a rectangle is bounded around the binary contour similarly, as presented in Fig. 3.9 and its width and height are also used as a classification parameter. The second analysis is done by thresholding the average pixel intensity inside the contour. This is done by using a binary contour as a mask in the raw image (Image 0 of Fig. 3.14) and calculating its average pixel intensity, which is usually greater inside the gaps since the gaps represent portions of the lighter background illumination.

Figures 3.15 and 3.16 illustrate both techniques. The one based on the bubble outline detection, which allows the measurement of velocity and diameter, and the other focused only on the bubble velocity measurement through the inner contours detection. By comparing the two methods in Figs. 3.15 and 3.16, it is clear that the latter is capable of tracking the motion of a superior number of bubbles. From these examples, by selecting adequate threshold values, the bubble velocity based technique extracts much more velocity vectors than the shape based one, since the clustering/overlapping effect becomes dominant

Figure 3.14 – Image processing steps for the bubble velocity calculation based on the inner contour boundaries.

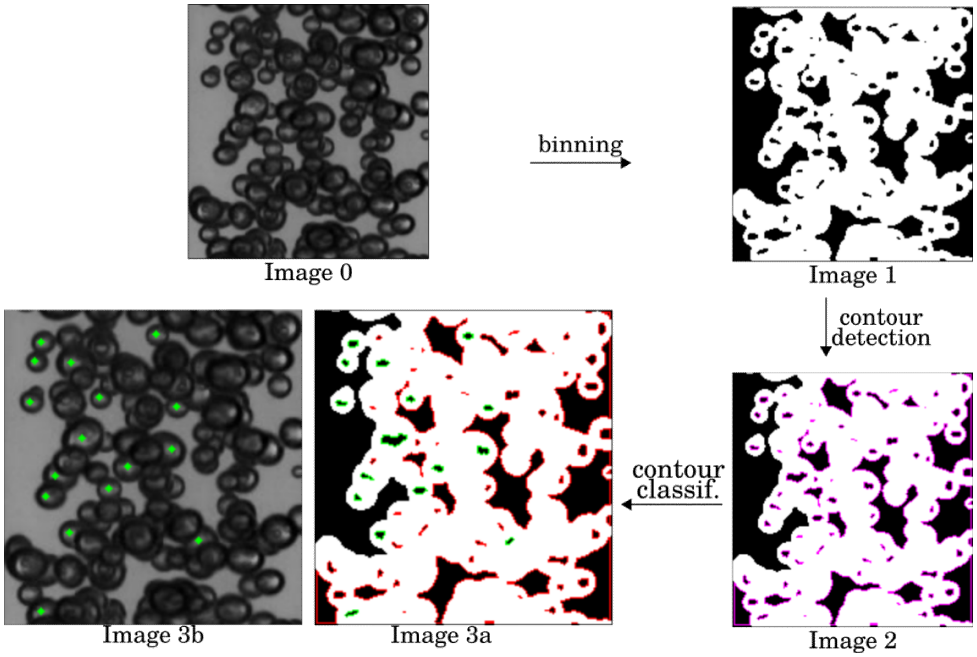

Source - Developed by the author.

as the gas volume fraction increases. Additionally, as a default procedure, the contours identified as valid single bubbles are removed from the processing steps shown in Fig. 3.14 to avoid duplicate velocity vectors, hence it is possible to obtain results as demonstrated in Figs, 3.15a) and 3.16b), which contains a greater number of velocity vectors from the shape outline technique. As a visual reference, Video 1 of the supplementary material given in Appendix B presents identified bubbles from the internal contour tracking method in two different bubbly flow configurations.

Figure 3.15 – Examples of the PTV method described in this work for j_l=0.0 m/s for different gas superficial velocities: a) j_g=$2.83 \cdot 10^{-2}$ m/s; b) j_g=$5.89 \cdot 10^{-2}$ m/s; c) j_g=$9.66 \cdot 10^{-2}$ m/s; d) j_g=$15.33 \cdot 10^{-2}$ m/s and e) j_g=$19.83 \cdot 10^{-2}$ m/s.

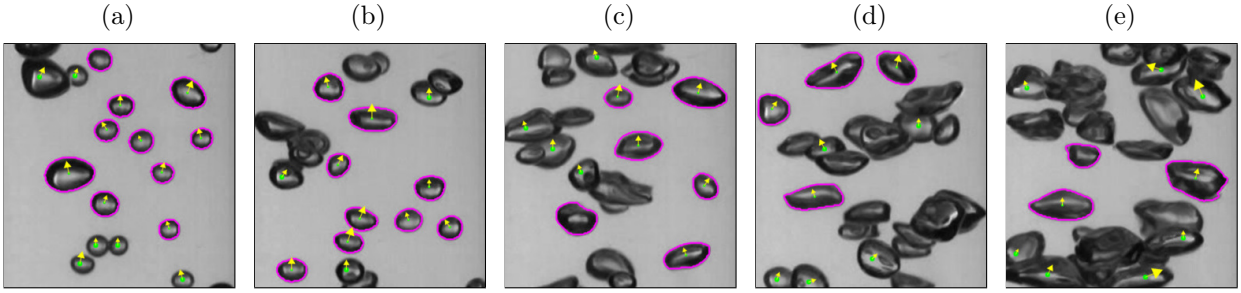

Source - Developed by the author.

Figure 3.16 – Examples of the PTV method described in this work for j_l=3.09 · 10^{-2} m/s for different gas superficial velocities: a) j_g=2.83·10^{-2} m/s; b) j_g=5.89·10^{-2} m/s; c) j_g=9.66 · 10^{-2} m/s; d) j_g=15.33 · 10^{-2} m/s and e) j_g=19.83 · 10^{-2} m/s.

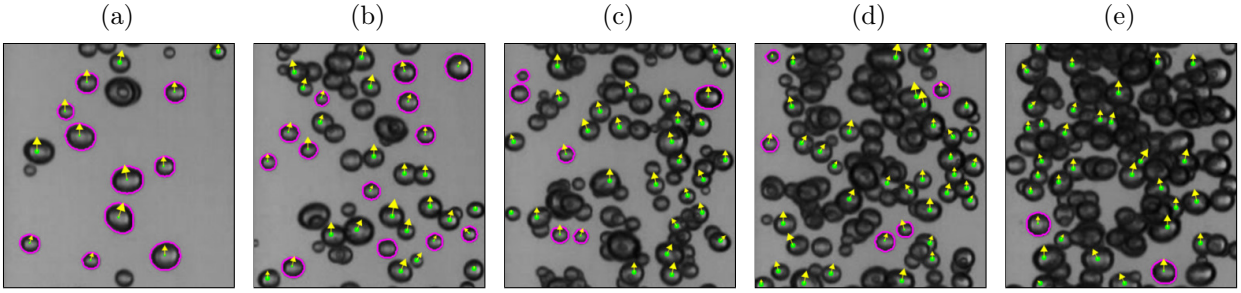

Source - Developed by the author.

3.4.3 PTV Averaging

From the bubble velocities obtained by the PTV method described in previous sections, it is possible to compute the area average gas velocity $\overline{\langle \boldsymbol{v}_g \rangle} = (\overline{\langle v_g \rangle}, \overline{\langle w_g \rangle})$ as,

$$\overline{\langle \boldsymbol{v}_g \rangle} = \frac{\sum_{n=1}^{N_{frames}} \sum_{m=1}^{N_{bubbles}} \boldsymbol{v}_g}{\sum_{n=1}^{N_{frames}} \cdot \sum_{m=1}^{N_{bubbles}}} \tag{3.1}$$

where $N_{bubbles}$ is the total number of bubbles and N_{frames} is the total number of frames in a single high-speed video acquisition. The velocity in Eq. (3.1), represents the ensemble averaged velocity, also averaged along the pipe cross section. Since the first technique for bubble identification acquires its shape and velocity and the second only acquires its velocity, the total number of $N_{bubbles}$ can be defined as,

$$N_{bubbles} = N^{I}_{bubbles} + N^{II}_{bubbles} \tag{3.2}$$

where $N^{I}_{bubbles}$ is the total number of bubbles acquired with the single bubble tracking and $N^{II}_{bubbles}$ with the internal contour tracking technique.

Additionally, by using the bubble outline information, it was possible to calculate the mean equivalent spherical bubble diameter $\overline{\langle d_b \rangle}$,

$$\overline{\langle d_b \rangle} = \frac{\sum_{n=1}^{N_{frames}} \sum_{m=1}^{N^I_b} d_b}{\sum_{n=1}^{N_{frames}} \cdot \sum_{m=1}^{N^I_b}} \tag{3.3}$$

The equivalent spherical bubble diameter d_b is calculated by,

$$d_b = \sqrt{\frac{4.0\, A_{proj.}}{\pi}} \tag{3.4}$$

where $A_{proj.}$ is the projected bubble area, i.e., the area within the contour that defines the bubble outline.

In Eqs. 3.1 and 3.3, the number of frames N_{frames} were chosen to obtain statistically representative averaged values $\overline{\langle \boldsymbol{v}_g \rangle}$ and $\overline{\langle d_b \rangle}$, i.e., the high-speed camera footage were acquired for a sufficient period to ensure that the averaged values represented the mean characteristics of the flow. According to preliminary studies, samples with 8.0 s resulted in statistically representative averages. Then, by using a frame-rate of 400 fps (frames per second), 3200 frames ($N_{frames} = 3200$) were used to calculate the averaged values from the PTV method described in this section and used in the results shown in the next section.

3.5 RESULTS AND DISCUSSION

This section presents the validation of the experimental techniques previously described. Some results for bubbly flows, including the analysis of the bubble effect on turbulence structure in pipe flow, are also presented.

First, some results for single-phase liquid flow are going to be presented to validate the experimental flow loop and the calibration of the PIV system. Then a validation of the PTV technique is going to be presented by comparing the gas volume fraction obtained with this technique and the one obtained for a stagnant liquid column ($j_l = 0$), using a technique similar to the one described in Nicklin (1962).

Subsequently, results from PTV are going to be used to validate the PIV technique, including the phase discrimination algorithm, used to measure the liquid velocity fields, through the gas volume fraction obtained with PTV, now considering a liquid phase net velocity ($j_l > 0$).

In order to validate the PTV and PIV/phase discrimination techniques, some averages of locally measured variables must be related to global variables, specifically, to gas and liquid volume flow rates.

The global gas superficial velocity j_g, given by the product of the area-averaged gas velocity and gas volume fraction, is related to the gas volume flow rate as,

$$\frac{Q_g}{A_{duct}} = j_g = \overline{\langle w_g \rangle} \cdot \overline{\langle \alpha_g \rangle} \tag{3.5}$$

where Q_g is the volumetric gas flow rate and A_{duct} is the transverse area of the duct.

The vertical component of the area averaged gas velocity ($\overline{\langle w_g \rangle}$), obtained form PTV (Eq. (3.1))is related to the gas volume fraction (or void fraction) as,

$$\overline{\langle \alpha_g \rangle} = \frac{Q_g}{A_{duct} \cdot \overline{\langle w_g \rangle}} \tag{3.6}$$

where Q_g and A_{duct} are known.

The averaged PIV velocity fields were calculated as the ensemble average of the PIV measurements as,

$$\langle \boldsymbol{v}_l(r,z)\rangle = \frac{1}{N_{PIV}} \sum_{k=1}^{N_{PIV}} \boldsymbol{v}_{l,k}(r,z). \tag{3.7}$$

where N_{PIV} is the number of samples and a PIV liquid velocity vector field corresponds to the two-dimensional vector field, $\boldsymbol{v}_{l,k}(r,z) = [v_l(r,z), w_l(r,z)]$). The validation of the PIV/phase discrimination technique will be performed using the PTV results at an axial position $z = 70D \approx 1.83$ m) away from the gas phase inlet (see Fig. 3.1). Then, in the following, the liquid velocity profiles correspond to the velocities taken at this position,

$$\langle \boldsymbol{w_l}(r)\rangle = \langle \boldsymbol{w_l}(r, z = 70D)\rangle = \frac{1}{N_{PIV}} \sum_{k=1}^{N_{PIV}} \boldsymbol{v}_{l,k}(r, z = 70D), \tag{3.8}$$

where the z dimension is dropped. At this position, it is assumed that the flow is fully developed.

The analysis of the the liquid phase turbulence fields was performed through the root mean square (r.m.s) of the velocity fluctuations $v^j_{l,rms}(r)$ defined as,

$$v^j_{l,rms}(r) = \sqrt{\frac{1}{N_{PIV}} \sum_{k=1}^{N_{PIV}} \left[v^j_{l,k}(r) - \left\langle v^j_l(r)\right\rangle\right]^2} \tag{3.9}$$

where $j = 1, 2$ corresponds to radial $v_{l,rms}$ and axial $w_{l,rms}$ velocity components, respectively.

The area averaged liquid velocity, obtained from PIV, is calculated as,

$$\overline{\langle w_l\rangle} = \frac{Q_l}{\alpha_l A_{duct}} = \frac{2}{R}\int_0^R \langle w_l(r)\rangle\, r dr = \frac{2}{R}\sum_{i=1}^{I} \left[\left\langle w_{l,i}(r_i)\right\rangle\, r_i\right]. \tag{3.10}$$

where the radial direction is divided by I interrogation windows, denoted by the index i. The liquid phase flow rate, obtained from PIV measurements in single-phase flow cases, can be calculated for $\alpha_l = 1$ in Eq. (3.10), $Q_l^{PIV} = \overline{\langle w_l\rangle} A_{duct}$, and was used to validate the PIV technique in single-phase flow cases, by comparing it with the rotameter flow rate.

3.5.1 Experimental Matrix

In this work, two single-phase flow conditions and 14 two-phase flow conditions have been tested. The experimental matrix is shown in Table 3.1, where the liquid j_l and gas j_g superficial velocities were calculated based on the gas and liquid flow rate

measurements. The parameter β corresponds to the gas to total superficial velocities relationship, $\beta = j_g/(j_g + j_l)$. The gas volume fraction $\overline{\langle \alpha_g \rangle}$ and the mean equivalent spherical bubble diameter $\overline{\langle d_b \rangle}$ (CLIFT et al., 2005b) are calculated using the bubble tracking method (PTV) described in Sec. 3.4.

Table 3.1 – Test Matrix of the experiments performed in this work.

Experiment No.	j_l $[m/s]$	j_g $[m/s]$	β $[-]$	$\overline{\langle \alpha_g \rangle}$ $[-]$	$\overline{\langle d_b \rangle}$ $[mm]$
1	0.0	$2.38 \cdot 10^{-3}$	–	0.015	2.68
2		$5.89 \cdot 10^{-3}$	–	0.029	3.31
3		$9.66 \cdot 10^{-3}$	–	0.049	3.70
4		$15.34 \cdot 10^{-3}$	–	0.083	3.95
5		$19.83 \cdot 10^{-3}$	–	0.114	4.05
6	$3.09 \cdot 10^{-2}$	0.0	–	–	–
7		$2.38 \cdot 10^{-3}$	0.084	0.013	1.78
8		$5.89 \cdot 10^{-3}$	0.160	0.029	1.81
9		$9.66 \cdot 10^{-3}$	0.238	0.052	1.51
10		$15.34 \cdot 10^{-3}$	0.331	0.084	1.60
11	$21.64 \cdot 10^{-2}$	0.0	–	–	–
12		$2.38 \cdot 10^{-3}$	0.013	0.007	1.79
13		$5.89 \cdot 10^{-3}$	0.026	0.015	1.67
14		$9.66 \cdot 10^{-3}$	0.043	0.025	1.64
15		$15.34 \cdot 10^{-3}$	0.066	0.039	1.93
16		$19.83 \cdot 10^{-3}$	0.084	0.049	2.41

Source - Developed by the author.

3.5.2 PTV Technique Validation

In order to verify the accuracy of the bubble tracking method, it was first necessary to check if the developed method resulted in reliable results. This was made by comparing the $\overline{\langle \alpha_g \rangle}$ values, by comparing them with the direct void fraction measurement from a bubbly column, as discussed in Nicklin (1962). In the work of Nicklin (1962), the authors describe a gas volume fraction measurement based on the height of a stagnant bubbly column in two instants. First, the column is filled with water, and the gas inlet is closed. In this first moment, the initial H_0 is measured. Then the gas valve is opened, and gas flows in the column. Since there is a net quantity of gas, the column height is increased, and as the process reaches a steady-state behavior, it is possible to measure the total column height H_f. Through a simple net balance, it can be stated that,

$$\overline{\langle \alpha_g \rangle} = \frac{H_f - H_0}{H_f} = \frac{H_g}{H_f} \tag{3.11}$$

where H_g is the increased column height due to the gas flow entering the column.

For this validation procedure, the illumination arrangement was slightly modified, with the removal of the LED background array to facilitate the measurement of the gas-liquid interface in the acrylic test section. Below the region captured by the camera, the remaining pipe/column section was measured with a metric tape. Through this arrangement, it was possible to calculate the velocity at which the gas-liquid interface falls, which can be interpreted as equal to the superficial gas velocity j_g, as demonstrated by Nicklin (1962). Figure 3.17a) illustrates the H_g column height and the H_o and H_f gas-liquid interfaces captured by the high speed camera in different t_i instants. The transient measurement of this H_g position, from the camera y coordinate reference, is plotted in Fig. 3.17b). As illustrated, the velocity at which the gas-liquid interface falls was calculated using the slope of a linear regression from the acquired data.

From the superficial gas velocity j_g values calculated with the velocity at which the gas-liquid interface falls, it was possible to compare the results with the values computed from Eq. (3.5), using the volumetric gas flow rate $Q_g^{rot.}$ from the gas rotameters. Figure 3.18 shows that the methods agree with each other, resulting in a maximum deviation of 6.1%, using the gas rotameter value as a reference. This validation step demonstrates that the rotameters and its temperature and pressure corrections are resulting in reliable gas flow values.

Figure 3.19 shows the comparison of the gas volume fraction values using the method described by Nicklin (1962) (Eq. (3.11)) and by measuring the $\overline{\langle w_g \rangle}$ bubble rising velocity using the PTV technique developed in this work, using Eq. (3.6). The results from both methods present excellent agreement, showing that the PTV technique used in this work is reliable and can be used for the gas phase analysis.

3.5.3 Single phase PIV validation

In order to verify the PIV accuracy and the spatial calibration including eventual optical distortions, results from two single phase flow velocity profiles are compared with theoretical results and results presented in literature. In addition, the liquid flow rate calculated from the PIV values Q_l^{PIV} (Eq. (3.10)) is compared with the liquid rotameter flow rate $Q_l^{Rot.}$ values. Two single phase flow liquid inlet configurations (Experiments 6 and 9 from Tab. 3.1) were analyzed for this purpose, with the first in the laminar flow regime ($Re_l = \rho_l \overline{\langle w_l \rangle} D/\mu_l = 812$) and the second in the turbulent flow regime (Re_l=5684).

Table 3.2 presents the comparison of the liquid flow rate measured by the liquid rotameter ($Q_l^{Rot.}$) and the numerically integrated (Q_l^{PIV}) value from the PIV liquid

Figure 3.17 – a) Sequential images of the gas-liquid interface falling after the gas flow is interrupted in the stagnant liquid configuration and its characteristics dimensions; b) Evolution of the gas-liquid interface height (marked as a dashed line in b)) and the linear regression used to calculate the gas-liquid interface velocity w_{g-l} from its slope.

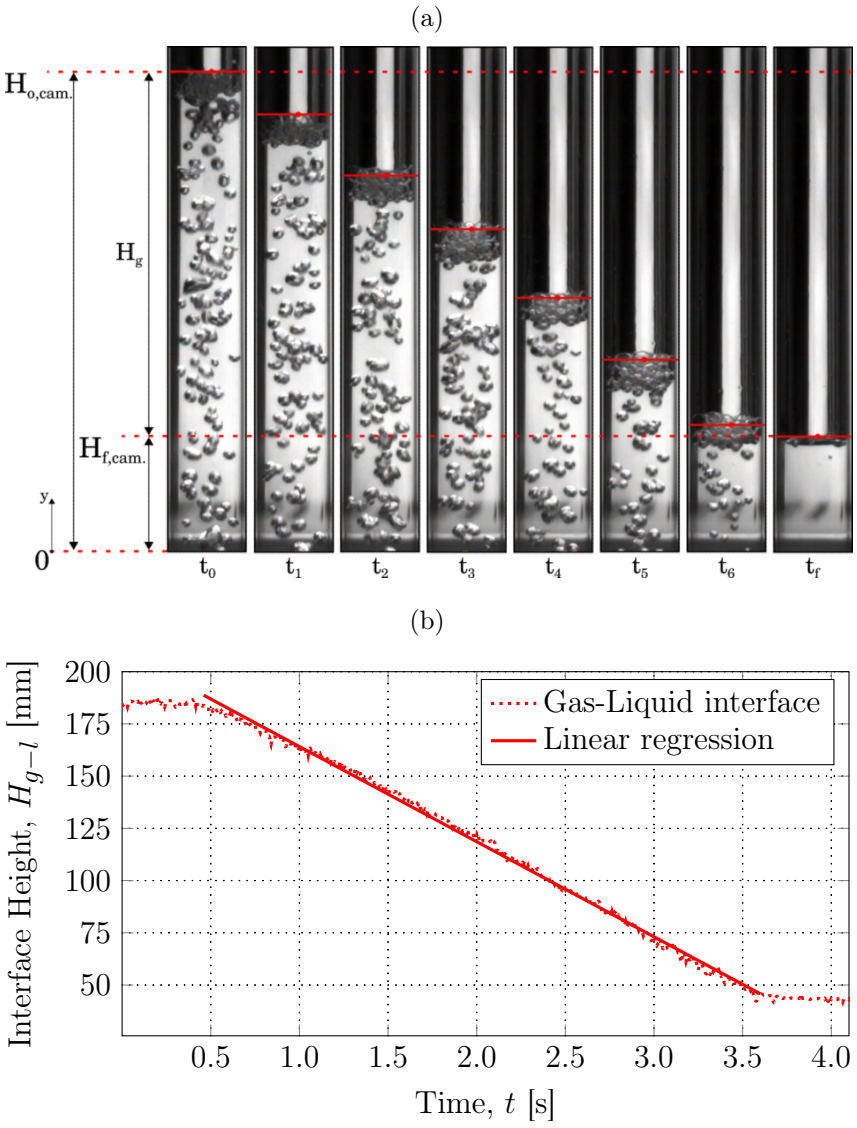

Source - Developed by the author.

velocity profiles. The results show that the deviation between the two values is within the range of the liquid rotameter accuracy (±5.0% full scale).

Figure 3.20 shows the liquid velocity profiles $\langle w_l(r) \rangle$ for the two single-phase flow configuration of Tab. 3.2. For the laminar case (Fig. 3.20a)), the PIV velocity profile is compared with the theoretical laminar parabolic profile, showing that the PIV results agree with the theoretical values.

The liquid velocity profile for the turbulent flow configuration is shown in Fig.

Figure 3.18 – Comparison withe the superficial gas velocity j_g calculated (i) using the velocity at which the gas-liquid interface falls inside the column after the gas inlet is closed (j_g, high-speed cam) and (ii) from the pressure and temperature corrected rotameter values (j_g, rotameter [m/s]).

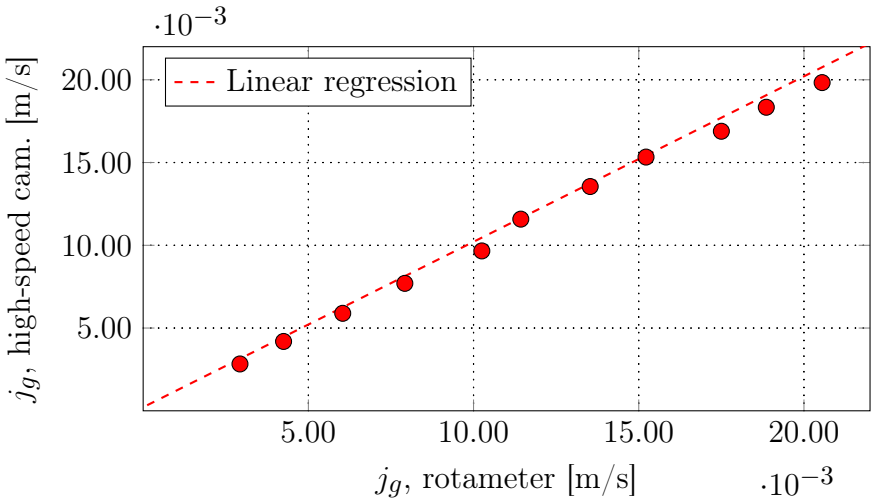

Source - Developed by the author.

Figure 3.19 – Comparison of the gas volume fractions calculated from the column height of the pipe before and after the gas flow is interrupted (Eq. (3.11)) and from the average bubble rising velocity from the PTV (Eq.(3.6)).

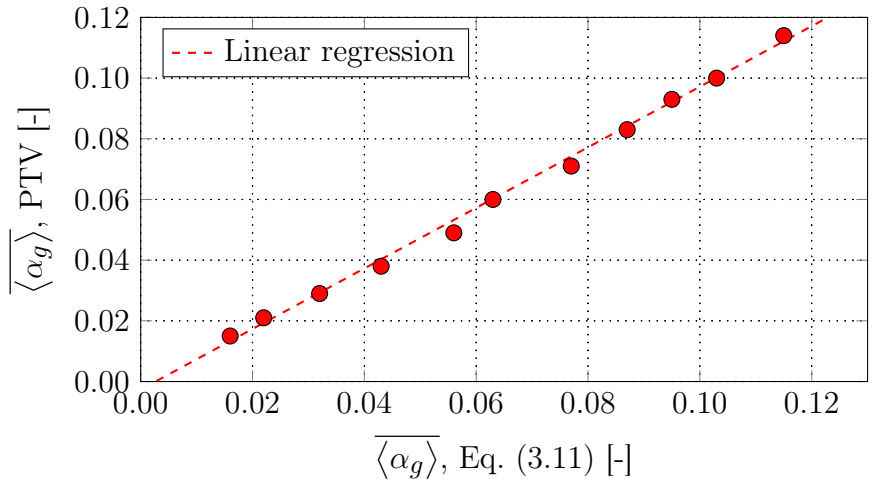

Source - Developed by the author.

3.20b). Figure 3.21 shows the PIV results from the present work and the PIV and DNS data from Eggels et al. (1994) by comparing the normalized velocity profiles $w_l^{norm.}(r)$ and the root-mean-square(r.m.s.) liquid velocities normalized by the wall friction velocity $\boldsymbol{v}_{l,rms}^{+}(r)$. The normalized velocity profile $w_l^{norm.}(r)$, defined as,

$$w_l^{norm.}(r) = \frac{\langle w_l(r) \rangle}{\langle w_l(r=0) \rangle} \tag{3.12}$$

Table 3.2 – Comparison of the liquid flow rate measured by the liquid rotameter ($Q_l^{Rot.}$) and the numerically integrated (Q_l^{PIV}) value from the PIV liquid velocity profiles.

Re_l	$Q_l^{Rot.}$ [m^3/s]	Q_l^{PIV} [m^3/s]	Relative Difference [%]
812	$1.67 \cdot 10^{-5}$	$1.75 \cdot 10^{-5}$	4.79
5684	$11.69 \cdot 10^{-5}$	$11.46 \cdot 10^{-5}$	1.96

Source - Developed by the author.

Figure 3.20 – Average liquid velocity profiles for the PIV validation for: a) laminar and b) turbulent flow regime.

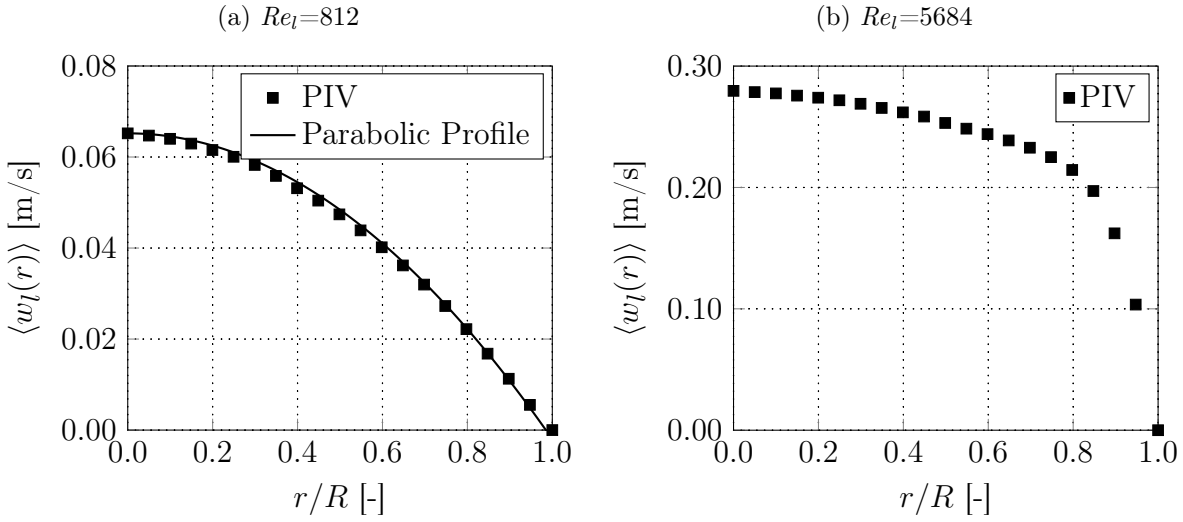

Source - Developed by the author.

and the root-mean-square(r.m.s.) liquid velocities normalized by the wall friction velocity $w_{l,\tau}$,

$$v_{l,rms}^{+}(r) = \frac{v_{l,rms}(r)}{w_{l,\tau}} \tag{3.13}$$

$$w_{l,rms}^{+}(r) = \frac{w_{l,rms}(r)}{w_{l,\tau}} \tag{3.14}$$

The wall friction velocity $w_{l,\tau}$ is given by,

$$w_{l,\tau} = \overline{\langle w_l \rangle} \sqrt{\frac{0.0791 Re_l^{-1/4}}{2}} \tag{3.15}$$

where $\overline{\langle w_l \rangle}$ is the mean liquid velocity profile, calculated from the PIV results as,

$$\overline{\langle w_l \rangle} = \frac{\int_0^{\pi} \int_0^{R} \langle w_l(r) \rangle \, r dr d\theta}{\int_0^{\pi} \int_0^{R} r dr d\theta} = \frac{\sum_{i=1}^{I} \left[\langle w_{l,i}(r_i) \rangle \, r_i \right]}{\sum_{i=1}^{I} r_i} \tag{3.16}$$

Figure 3.21 – Comparison between the (a) normalized velocity profile $w_l^{norm.}(r)$ and (b) the root-mean-square(r.m.s.) liquid velocity profiles normalized by the wall friction velocity $v^+_{l,rms}(r)$ and $w^+_{l,rms}(r)$ from the PIV results from this work and from Eggels et al. (1994) (PIV and DNS).

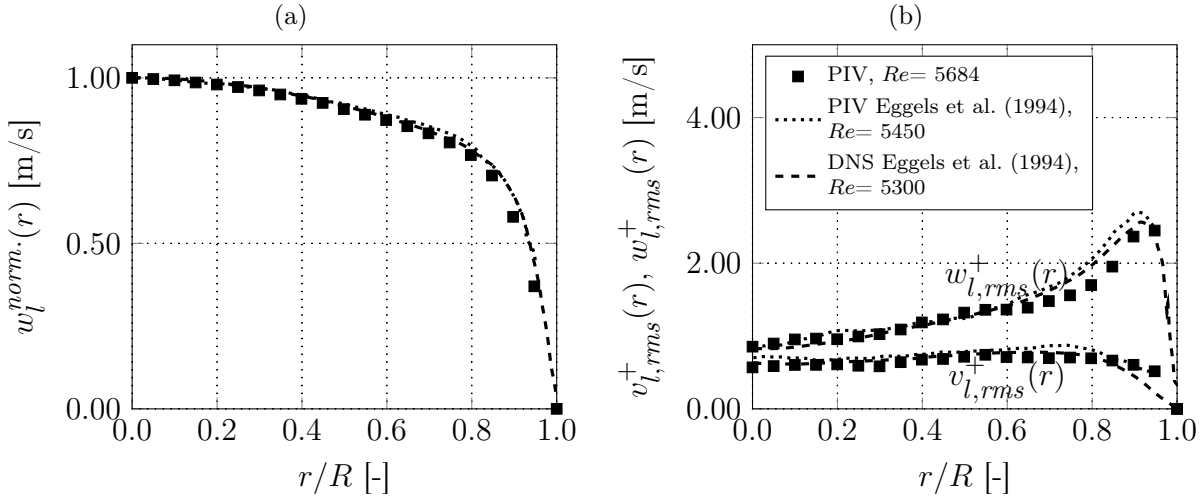

Source - Developed by the author.

where the index i denotes the total number of I interrogation windows.

As can be observed, results for single phase flow present good agreement, including near wall regions (it must be clarified that, in all cases, the values of velocities and their r.m.s of fluctuations, were set to zero at walls). Therefore, the PIV set-up, and experimental test section can be considered reliable for PIV measurements.

3.5.4 Validation of PIV for liquid phase and phase discrimination technique

To validate the phase discrimination based on the image processing steps described in Sec. 3.3 the results were first analyzed through test cases used in Sec. 3.5.2, i.e, for $j_l = 0$. This does not mean that liquid velocity is zero, but the net liquid flow rate must be zero. The validation test cases are represented by Experiments 1 – 5 in Tab. 3.1 and were used to validate the method since: i) there is no net flow of liquid across the duct section and ii) the gas volume fraction $\overline{\langle \alpha_g \rangle}$ is readily available. Additionally, the effect of the $P_{thresh.}$ threshold value, used for the gas phase discrimination in the PIV liquid velocity measurements, and the effect of the number of PIV acquisitions N_{PIV} on the averaged liquid velocity profiles are analyzed.

Figure 3.22 shows different averaged liquid axial velocity profiles $\langle w_l(r) \rangle$ for Experiments 1, 3 and 5, which result in relatively low and high global gas volume factions ($\overline{\langle \alpha_g \rangle}$=11.0 %, can be considered "high" for bubbly flow pattern) and with distinct av-

eraged bubble diameters (and, therefore, different rising velocities). From Fig. 3.22, the treated results (right) resulted in lower upward axial velocities when compared to the non-treated PIV results (left). The decrease of the upward liquid velocities is an effect of the velocity bias produced by the dispersed phase in the PIV recordings, which are removed in the phase discrimination process. Due to the aforementioned reason, the difference in both averaged liquid axial velocity profiles of Fig. 3.22 is higher near the pipe centerline, since this upward movement is produced by the dispersed bubbles, that are concentrated along the duct centerline.

Figure 3.22 – Average liquid axial velocity profiles used in the phase discrimination validation (Experiments 1,3 and 5 in Tab. 3.1). The velocity profiles on the left represent the non-treated PIV results and the liquid velocity profiles on the right are obtained after the proposed phase discrimination procedure. The PIV averaged results were obtained with 2400 frames (N_{PIV}=2400) and the phase discrimination processed using a threshold value of $P_{thresh.}$=8.

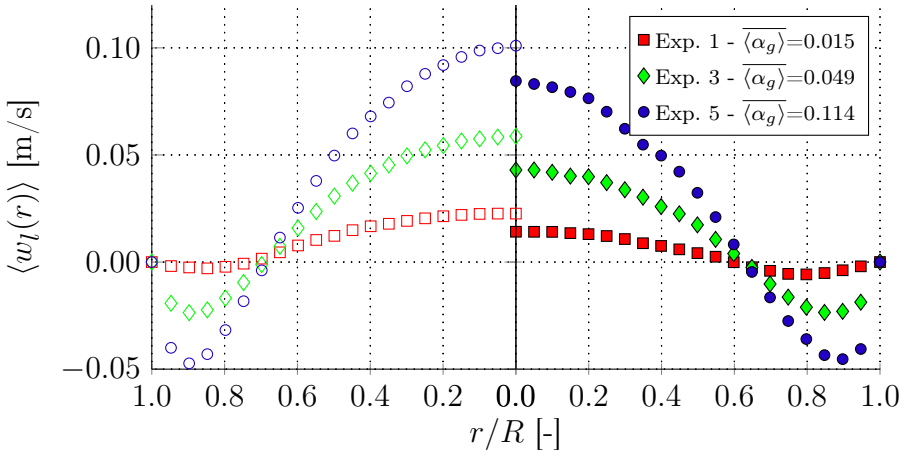

Source - Developed by the author.

Figure 3.23 shows the effect of the threshold parameter value $P_{thresh.}$ on the average liquid axial velocity profile $\langle w_l(r)\rangle$ in three distinct liquid-gas phase configurations. From the $\langle w_l(r)\rangle$ profiles of Fig. 3.23, the $P_{thresh.}$ value does not significantly affect the gas phase contribution, since the major differences in the liquid velocity profiles is observed when the results are treated or not($P_{thresh.} > 0$, independently of its value) and, for these flow conditions, the actual value of $P_{thresh.}$ parameter does not seem to have significant influence. Here, it must be recalled that lower values of $P_{thresh.}$ are more conservative. Again, there are almost no liquid velocity differences between the treated and the non-treated cases near the pipe wall, where dispersed gas bubbles are not present in the flow. The effect of the number of PIV acquisitions N_{PIV} on the average liquid axial velocity profile is shown in Fig. 3.24. The results show that N_{PIV}=1200 is sufficient to calculate

Figure 3.23 – Effect of the threshold parameter value $P_{thresh.}$ on the average liquid axial velocity profile in three liquid-gas phase configurations: a) Exp. 1, $\overline{\langle \alpha_g \rangle}$=0.015 and $\overline{\langle d_b \rangle}$=2.68 mm; b) Exp. 3, $\overline{\langle \alpha_g \rangle}$=0.049 and $\overline{\langle d_b \rangle}$=3.70 mm; c) Exp. 5, $\overline{\langle \alpha_g \rangle}$=0.114 and $\overline{\langle d_b \rangle}$=4.05 mm. The PIV averaged results were obtained with 2400 frames (N_{PIV}=2400).

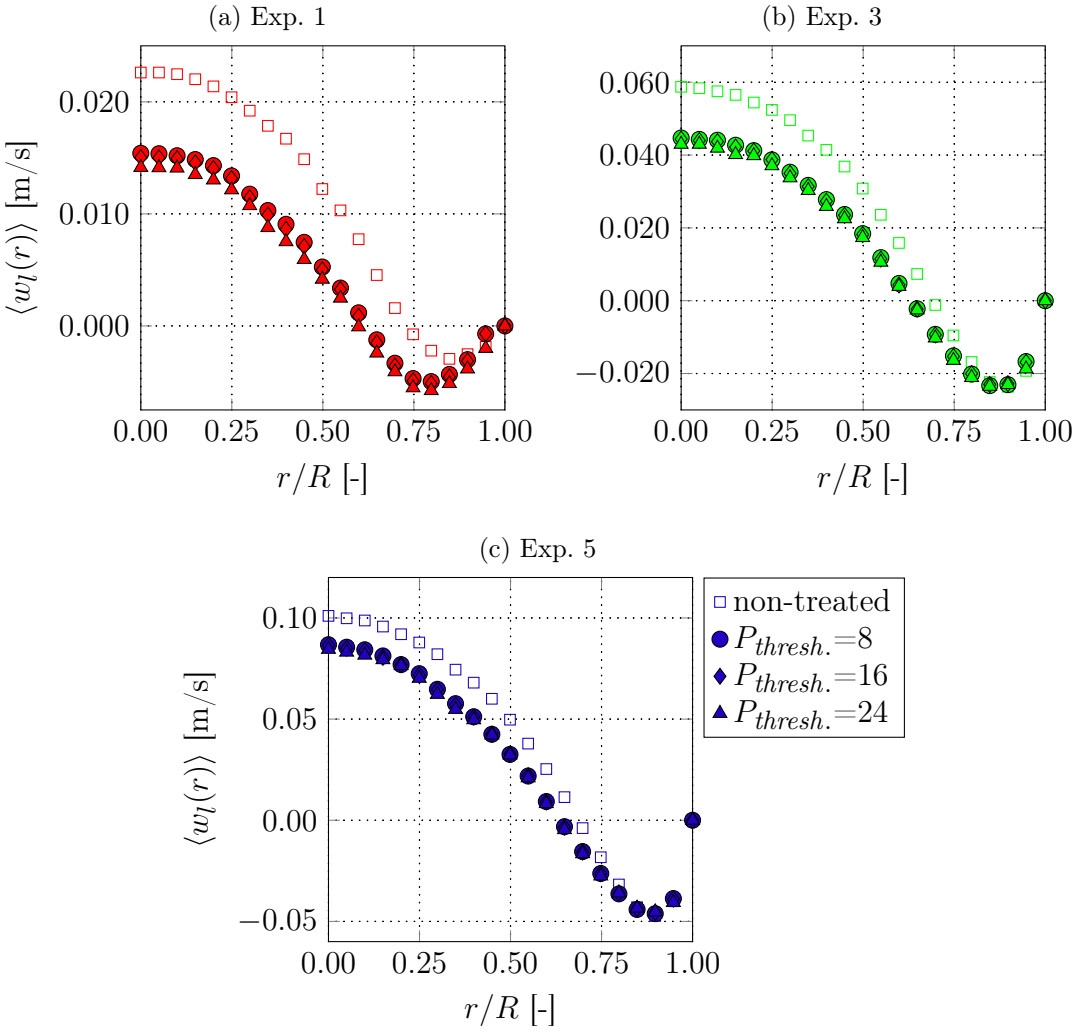

Source - Developed by the author.

consistently averaged velocity fields since the velocity profiles collapse to a single line in the three experiments shown in Fig. 3.24. Then, for the remaining cases, the value of N_{PIV}=1200 was used, since this number of acquisitions results in reliable results with a moderate experimental and processing effort.

As mentioned before, for the test cases presented in this section (Experiments 1,3 and 5 of Tab. 3.1), the liquid inlet is closed, with the duct acting as a stagnant column. As gas is injected into the duct, the flow can be seen as a bubble column case. In this sort of flow, the liquid motion is caused by the motion of the dispersed bubbles, but the

net flow of liquid at any section must be zero Nicklin (1962). Then, it is expected that calculating the liquid flow rate from the PIV results returns a Q_l^{PIV} value close to zero, indicating zero net liquid flow.

Figure 3.25 illustrates the effect of the phase discrimination procedure on the Q_l^{PIV} liquid flow rate. The results show that by treating the PIV liquid velocity fields with the phase discrimination procedure($P_{thresh.}$ >0), the Q_l^{PIV} values decrease to a value which is closer to zero than the non-treated results.

The difference between the treated and the non-treated Q_l^{PIV} values can reach up to 87% in the validation experiments of Tab. 3.1, indicating that the phase discrimination procedure is capable of removing most of the dispersed gas phase contribution on the PIV liquid velocity fields. In addition, Fig. 3.25 shows that the Q_l^{PIV} values are not sensible to the value of $P_{thresh.}$, as was observed with the liquid axial velocity profiles.

The fact that the Q_l^{PIV} does not result in null values can be attributed to the lack of PIV resolution near the pipe wall, which has a strong impact on the velocity integration, when calculating the flow rate, due to the cylindrical coordinate system. In the test validation experiments, due to the dispersed gas bubbles rising movement, the liquid is pulled upwards near the pipe center, and since the liquid net balance is zero, downward liquid motion is found near the pipe walls. Since there is no enough spatial resolution in this region, the downward liquid velocity profile is not fully captured by the PIV, resulting in positive values of Q_l^{PIV} which, nonetheless, are close to zero. Even though the non-treated velocity fields result in much higher values for the flow rate.

The effect of the PIV phase discrimination algorithm on velocity profiles the two-phase bubbly flows with $j_l > 0.0$ m/s is shown in Figs. 3.26 and 3.27, where only the results considering $P_{thresh.}$=8 are shown. As observed for the liquid stagnant cases, as the velocity fields are treated, lower axial velocities are observed. Comparing the cases shown in Figs. 3.26 and 3.27 with the ones plotted in Fig. 3.22, the effect of the treatment procedure, becomes less important as j_l increases. It is clear that, as the liquid velocity increases with relation to the relative velocity (slip factor is decreased), the effect of velocity bias in PIV measurements due to the bubbles becomes less significant.

The PTV results for gas phase can be used to validate the PIV results for liquid velocity fields, through the gas volume fraction, estimated from the measured j_g and the average bubble velocity, form PTV (Eq. (3.6)). The area averaged liquid velocity $\overline{\langle w_l \rangle}$, obtained from PIV and the gas volume fraction, $\overline{\langle \alpha_g \rangle}$ values obtained from the PTV and

Figure 3.24 – Effect of the number of instantaneous acquisitions N_{PIV} on the average liquid axial velocity profile in three liquid-gas phase configurations: a) Exp. 1, $\overline{\langle \alpha_g \rangle}$=0.015 and $\overline{\langle d_b \rangle}$=2.68 mm; b) Exp. 3, $\overline{\langle \alpha_g \rangle}$=0.049 and $\overline{\langle d_b \rangle}$=3.70 mm; c) Exp. 5, $\overline{\langle \alpha_g \rangle}$=0.114 and $\overline{\langle d_b \rangle}$=4.05 mm. The PIV averaged results were obtained with the threshold parameter value $P_{thresh.}$=8.

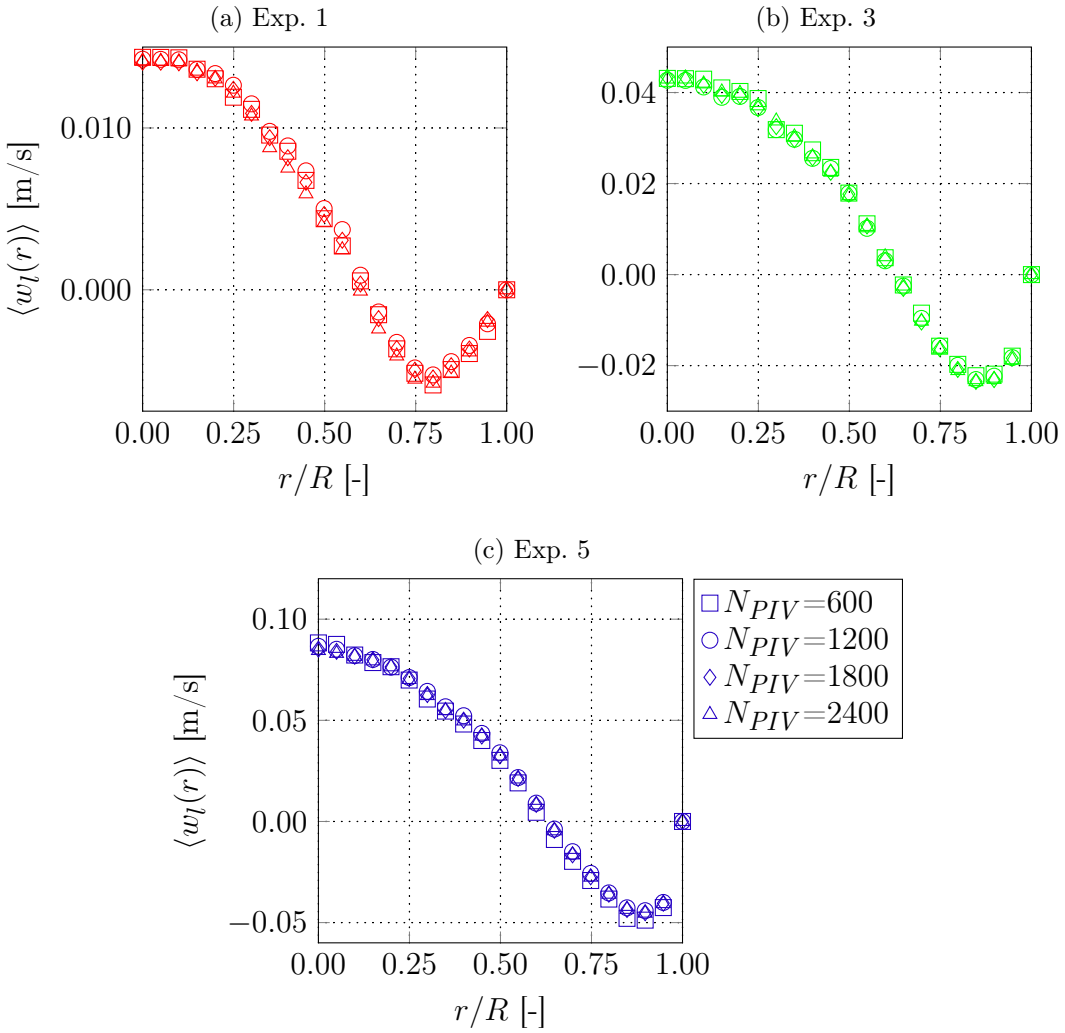

Source - Developed by the author.

j_g can be related as,

$$\overline{\langle w_l \rangle} = \frac{j_l}{(1.0 - \overline{\langle \alpha_g \rangle})} \tag{3.17}$$

where j_l obtained from the liquid flow rate from rotameters. The $\overline{\langle w_l \rangle}$ values from the PIV results are calculated by Eq. (3.10).

Figure 3.28 presents the comparison of the $\overline{\langle w_l \rangle}$ values from Eq. (3.17) (using PTV results for the calculation of $\overline{\langle \alpha_g \rangle}$) and the PIV results, showing the non-treated and treated results, for the calculation of the area averaged liquid velocity. It can be observed

Figure 3.25 – Effect of the threshold parameter value $P_{thresh.}$ on the numerically integrated liquid flow rate Q_l^{PIV} from the PIV liquid velocities.

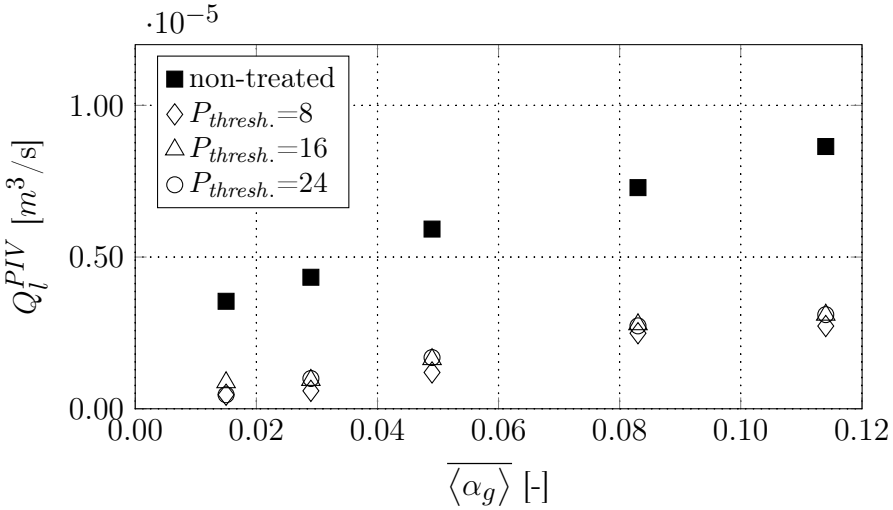

Source - Developed by the author.

Figure 3.26 – Average liquid axial velocity profiles for Experiments 7, 8 and 9 of Tab. 3.1 with $j_l = 3.09 \cdot 10^{-2}$ m/s. The velocity profiles on the left represent the non-treated PIV results and the liquid velocity profiles on the right are obtained after the proposed phase discrimination procedure. The PIV averaged results were obtained with 1200 frames (N_{PIV}=1200) and a threshold value of $P_{thresh.}$=8 was used in the treatment procedure.

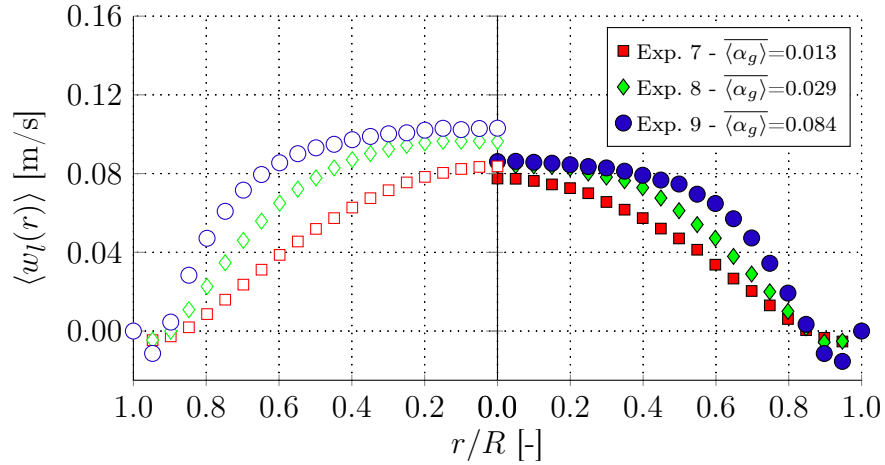

Source - Developed by the author.

that by the application of the phase discrimination method to the PIV liquid velocity measurements, its $\overline{\langle w_l \rangle}$ values become much closer from the ones calculated from Eq. (3.17) for the two j_l situations. Again, as observed in the liquid axial velocity profiles, the impact of the phase discrimination method is larger for the $j_l = 3.09 \cdot 10^{-2}$ m/s experiments, once the dispersed bubbles contribution on the liquid velocity profiles is greater than in

the cases with $j_l = 21.64 \cdot 10^{-2}$ m/s.

Figure 3.27 – Average liquid axial velocity profiles for Experiments 12, 14 and 16 of Tab. 3.1 with $j_l = 21.64 \cdot 10^{-2}$ m/s. The velocity profiles on the left represent the non-treated PIV results and the liquid velocity profiles on the right are obtained after the proposed phase discrimination procedure. The PIV averaged results were obtained with 1200 frames (N_{PIV}=1200) and the phase discrimination processed used a threshold value of $P_{thresh.}$=8.

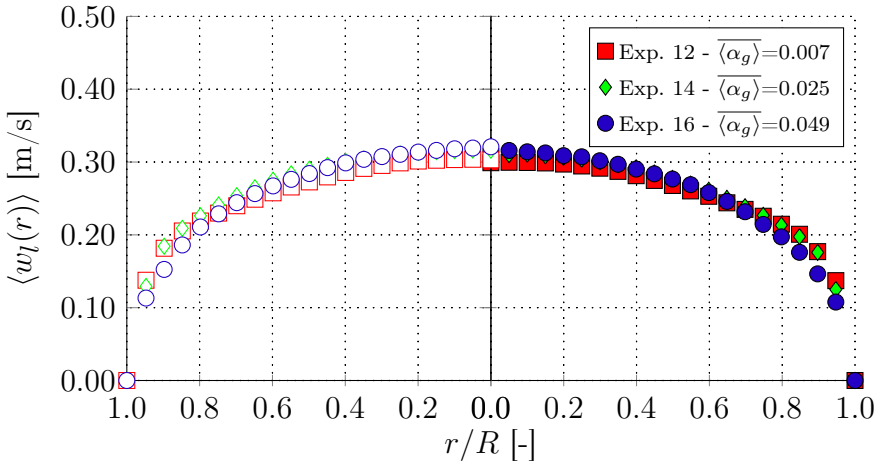

Source - Developed by the author.

In the following results, the radial distributions of axial velocity and velocity fluctuations for the experiments shown in Table 3.1 are presented. Figures 3.29 and 3.30 show the average liquid velocity in the axial direction ($\langle w_l(r) \rangle$) and its associated fluctuation r.m.s. profiles in the radial ($v_{l,rms}(r)$) and axial ($w_{l,rms}(r)$) directions. The presence of the bubbles in the flow affects the liquid velocity profiles and velocity fluctuations significantly. For the liquid "laminar" cases (Experiments 6 – 10 of Table 3.1), the rising movement of the dispersed bubbles generates a bubble induced turbulence (BIT) with velocity fluctuations even higher than the cases with liquid turbulent flow. The same trend is observed in some results presented in literature (KIM et al., 2016; HOSOKAWA; TOMIYAMA, 2013; LIU; BANKOFF, 1993), where the dispersed bubbles induce modifications on the velocity fluctuation profiles, with a plateau in the core region which decreases towards the wall. In addition, the induced turbulence get stronger as $\overline{\langle \alpha_g \rangle}$ increases in both cases, as observed in results from Hosokawa and Tomiyama (2013) and Liu and Bankoff (1993).

For the cases shown in Fig. 3.29, the turbulence induced by the gas phase increases the liquid velocity in the core region, becoming flatter as $\overline{\langle \alpha_g \rangle}$ is increased, due to the associated bubble induced turbulence.

The flat profile near the core decays rapidly as moving towards the wall for the $j_l = 3.09 \cdot 10^{-2}$ m/s case indicating the presence of a downward liquid film induced by

Figure 3.28 – Comparison of the $\overline{\langle w_l \rangle}$ values calculated with the PTV and the PIV method with and without the proposed phase discrimination procedure.

(a) $j_l = 3.09 \cdot 10^{-2}$ m/s

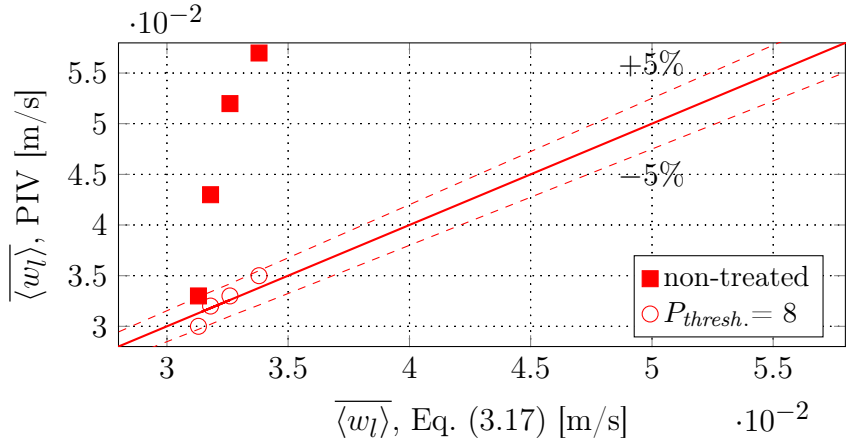

(b) $j_l = 21.64 \cdot 10^{-2}$ m/s

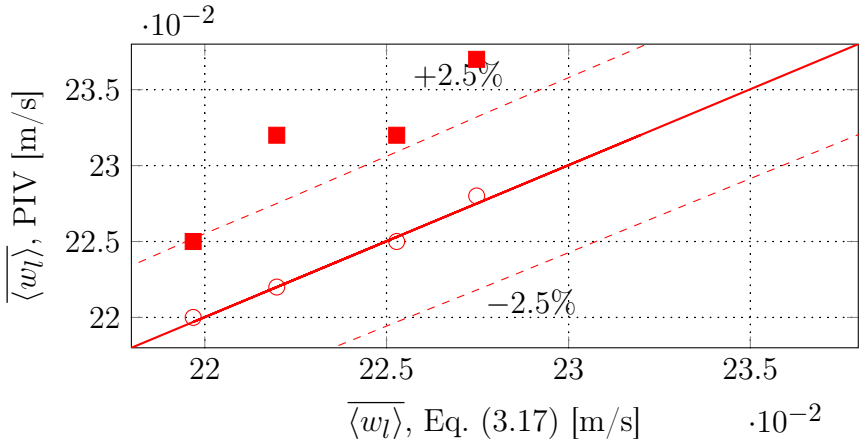

Source - Developed by the author.

liquid pulled by the gas bubbles in the core region. This downward liquid film is not observed in the axial velocity profiles of Kim et al. (2016) and Hosokawa and Tomiyama (2013) for similar superficial liquid velocities, where bubble induced turbulence is studied in upward laminar bubbly flows. The appearance of this downward film can be associated to the higher void fractions considered in this work, where for the upward laminar bubbly flows (Experiments 6 – 10 of Tab. 3.1) the void fractions ranged from $\overline{\langle \alpha_g \rangle} = 1.3\%$ to $\overline{\langle \alpha_g \rangle} = 8.4\%$, much higher than the maximum value of $\overline{\langle \alpha_g \rangle} = 0.64\%$ considered in Kim et al. (2016) and the $\overline{\langle \alpha_g \rangle} = 1.56\%$ max value in Hosokawa and Tomiyama (2013). Additionally, the $\overline{\langle d_b \rangle}$ considered in this work, differs from the other works. In this work, the average bubble diameter ranges from 1.51 mm to 1.81 mm, while in Kim et al. (2016) experiments ranges from 2.2 mm to 3.7 mm and in Hosokawa and Tomiyama (2013) from 2.62 mm to 3.48 mm, in virtue of the larger pipe diameters used in those works.

For the liquid turbulent cases (Experiments 11 – 16 of Tab. 3.1), shown Fig. 3.30, the mean axial velocity liquid profiles follow the same trend found in Liu and Bankoff (1993), where the velocity profile changes from flat in the single-phase case to convex as the $\overline{\langle \alpha_g \rangle}$ is increased, with the following increase of the liquid velocity in the core region. From the velocity fluctuation profiles, the presence of the dispersed bubbles promotes a relative uniform turbulence distribution, as seen in Fig. 3.30c), indicating that the gas bubbles promotes a stronger radial momentum transfer (LIU; BANKOFF, 1993).

Figure 3.29 – Average liquid velocity profile and velocity fluctuations for the upward laminar bubbly flows (Experiments 6 – 10 of Tab. 3.1) The PIV averaged results were obtained with 1200 frames (N_{PIV}=1200) and the phase discrimination processed used a threshold value of $P_{thresh.}$=8.

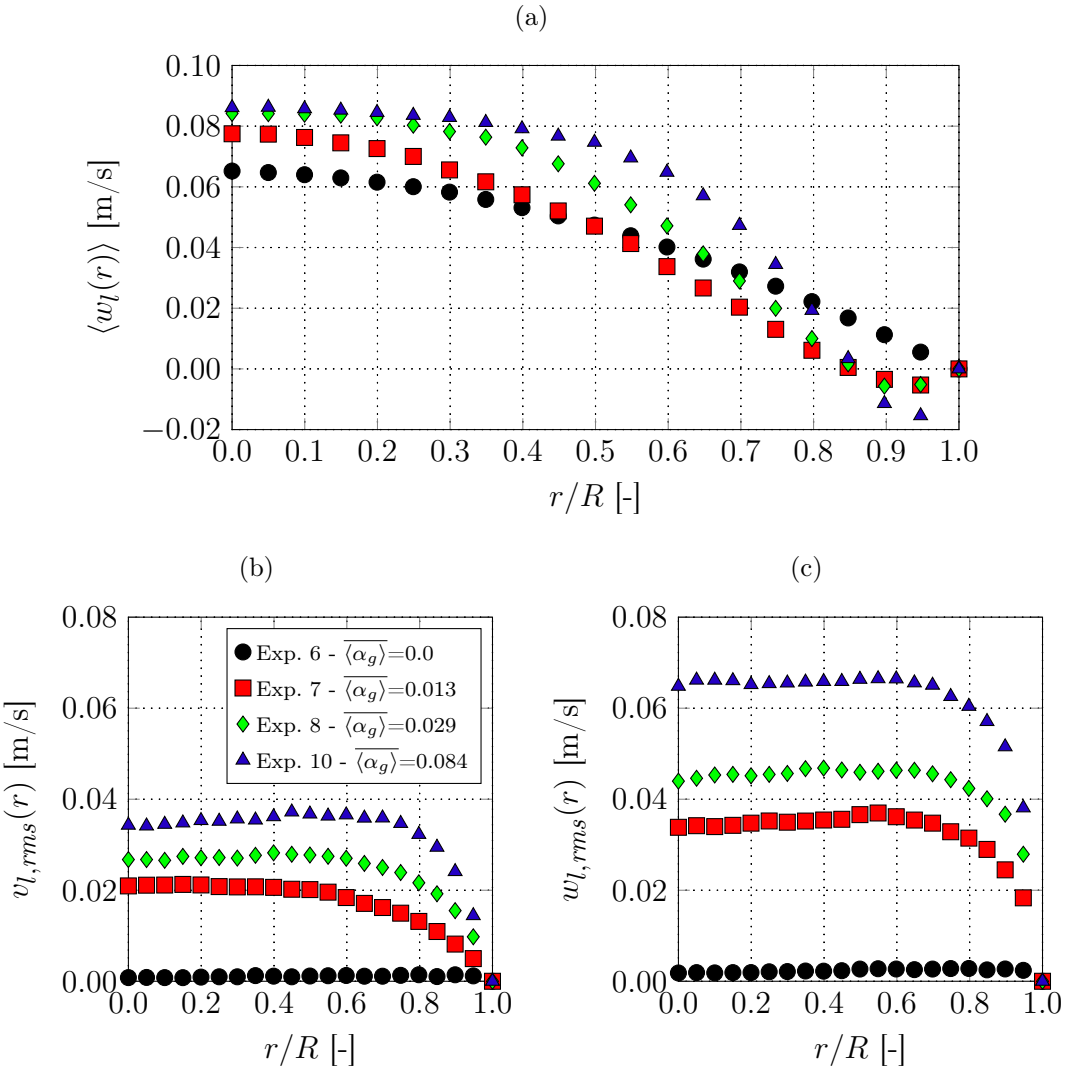

Source - Developed by the author.

Figure 3.30 – Average liquid velocity profile and velocity fluctuations for the upward turbulent bubbly flows (Experiments 11 – 16 of Tab. 3.1) The PIV averaged results were obtained with 1200 frames (N_{PIV}=1200) and the phase discrimination processed used a threshold value of $P_{thresh.}$=8.

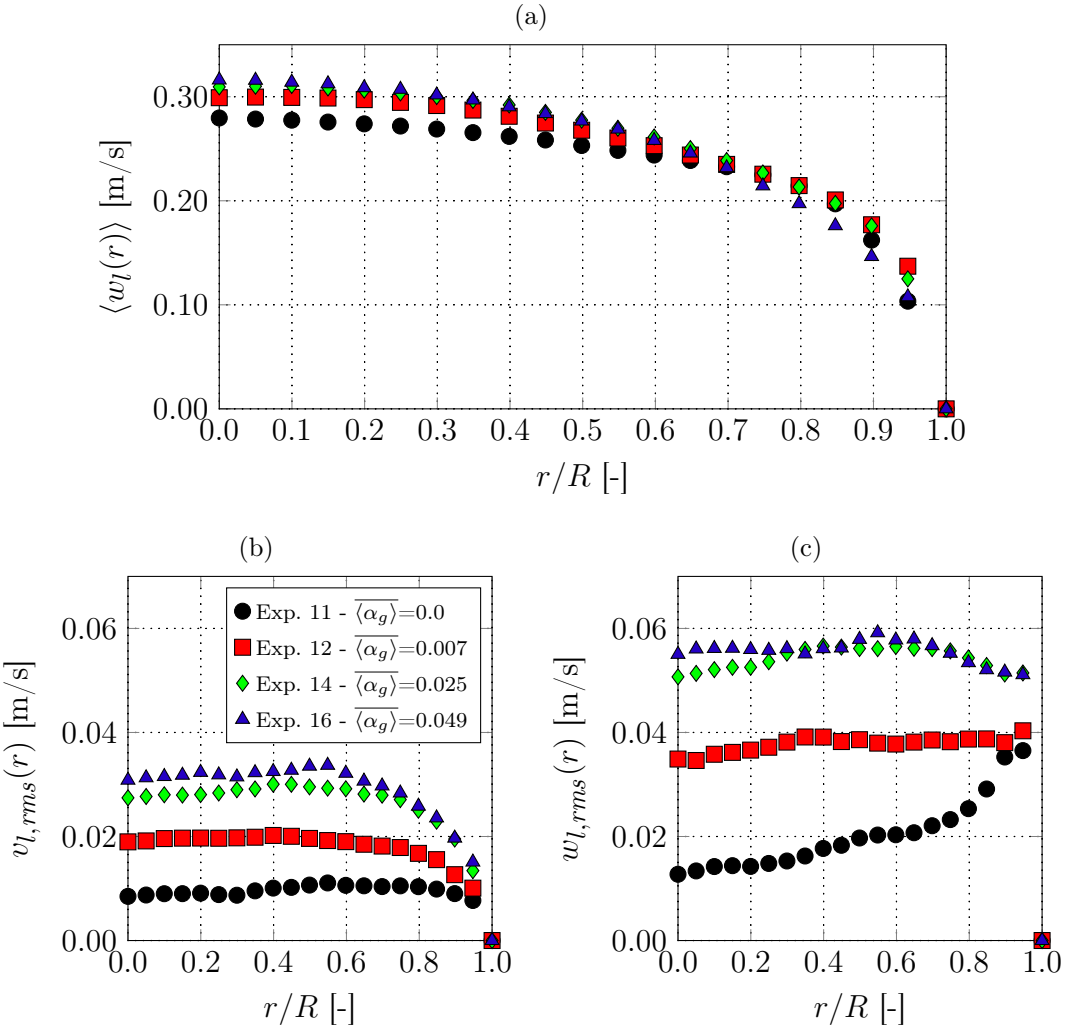

Source - Developed by the author.

3.6 CONCLUSIONS

The PIV/LIF technique is a commonly used technique for velocity measurement in bubbly air-water flows. However, for moderate to high gas fractions, the technique cannot be used without a phase discrimination method, as the light scattered by the gas bubbles can generate spurious vector velocities in the PIV cross-correlation step.

In this work, a new method for the measurement of the liquid phase velocity in two-phase pipe bubbly flows using the PIV/LIF technique was presented. According to the results of the present work, the method is capable of extracting reliable data in vertical air-water two-phase flows, overcoming the problems associated with the dispersed gas

phase. The method is based on a phase discrimination procedure that classifies the PIV obtained vector velocities by its interrogation window pixel information.

In order to validate the phase discrimination procedure proposed in this work, a PTV (Particle Tracking Velocimetry) was developed to track the motion of the dispersed gas bubble phase. The PTV implementation developed in this work was based on similar implementations found in the literature. However, some improvements were incorporated to extract and analyze information on two-phase bubbly flow inside a small diameter pipe with moderate to high void fractions since bubble shadow overlap is a critical problem in these cases.

Stagnant liquid flow cases, where volume fraction can be measured through the increment in column height (NICKLIN, 1962), were used to asses the capability of the developed PTV technique. The deviation between the PTV calculated and the know void fraction values was minor, proving the efficiency of the method implementation and the improvements proposed, even in cases where strong bubble shadows overlap is observed. The indirect calculation of the gas volume fraction from the PTV results resulted in reliable and consistent values, even in cases with high void fraction ($\overline{\langle \alpha_g \rangle} = 11.4\%$) and distinct bubble diameters ($\overline{\langle d_b \rangle}$ from 2.68 mm to 4.05 mm).

From the stagnant liquid flow cases, it was shown that the phase discrimination procedure is capable of removing the gas phase contributions from the ensemble-averaged PIV/LIF liquid velocity fields.

In order to analyze the reliability of PTV and the PIV phase discrimination implementations, the results obtained from both methods were compared for a set of particular cases, resulting in similar values in bubbly flows with gas volume fraction ranging from $\overline{\langle \alpha_g \rangle} = 0.7\%$ to $\overline{\langle \alpha_g \rangle} = 8.4\%$ and distinct bubble diameters ($\overline{\langle d_b \rangle}$) from 1.51 mm to 2.41 mm.

The effect of introducing dispersed gas bubbles on upward flows was discussed by analyzing a set of upward laminar and turbulent (liquid phase) bubbly flows. For the upward laminar bubbly flows, the increase of the gas fraction led to a change in the axial liquid velocity profile, from the typical convex in the single-phase flow case to a flat profile in the core. This transformation can be explained from the velocity fluctuation profiles, where the results showed that the dispersed gas bubbles generated strong fluctuations in the core region, which decayed towards the pipe wall. As opposed to the results found in the literature, a downward liquid film appeared in the upward laminar bubbly flow cases, whose appearance is attributed to the high void fractions considered in the present experiments, higher than those usually considered in similar works in the literature.

In the case of turbulent bubbly flows, the increase of the gas volume fraction changed

the liquid velocity profiles from the flat velocity distribution of a typical turbulent single-phase to a central peaked profile, due to the change of the turbulence structure in the central pipe region.

Chapter 4

Development of a Deep Learning-based Image Processing Technique for Bubble Pattern Recognition and Shape Reconstruction in Bubbly Flows

This part has been published as:
CERQUEIRA, R. F. L. and PALADINO, E.E. Development of a Deep Learning-based Image Processing Technique for Bubble Pattern Recognition and Shape Reconstruction in Bubbly Flows. Chemical Engineering Science, v. 230, p. 116163, 2021.

ABSTRACT

This chapter presents a Convolution Neural Network (CNN) based method for the bubble identification and shape reconstruction of bubbles in bubbly flows using high-speed camera images. In order to gain a better comprehension of the CNN-based method, experiments were conducted in two gas-liquid systems, air-water and air-aqueous glycerol solution. The bubble identification and further shape reconstruction adopted a methodology based on a set of anchor points and boxes, where a single anchor point contained the information of different anchor boxes with different sizes. For a given anchor point, different ellipsoidal shapes were suggested as bubble shape candidates and were correctly chosen by a trained CNN. The CNN training used only labeled images from the air-water system data set and

a hyperparameter analysis was performed to find the best CNN architecture configuration. From this optimal CNN architecture candidate, the different bubbly flow high-speed camera acquisitions were analyzed by the CNN-based bubble shape reconstruction method. The results showed that the deep learning method used in this work is able to detect most of the bubbles present in the high-speed camera images, even in dense bubbly flow configurations. The method developed in this work can be used to further analyze bubbly flows and generate experimental data for the implementation and validation of multidimensional CFD models.

4.1 INTRODUCTION

This chapter presents a Convolution Neural Network (CNN) based method for the bubble identification and shape reconstruction of bubbles in bubbly flows using high-speed camera images. In order to gain a better comprehension of the CNN-based method, experiments were conducted in two gas-liquid systems, air-water and air-aqueous glycerol solution.

Experimental techniques focused on the characterization of bubble parameters can be divided into two main groups, intrusive and non-intrusive methods. Example of intrusive methods are experimental tecnhiques base on conductivity probes Kim et al. (2000), impedance probes Zenit et al. (2001), fiber optic probes Garnier et al. (2002) and Simonnet et al. (2007) and wire mesh sensors Da Silva . et al. (2010). Typical non-intrusive methods are Laser Doppler Anemometry Kulkarni et al. (2001) and image processing tecnhiques Acuña and Finch (2010), Lau et al. (2013), Karn et al. (2015) and Cerqueira et al. (2018a). Intrusive methods required direct contact between the probe and the dispersed bubbles, perturbing the flow in its vicinity and increasing the associated uncertainty of the experimental measurements. In addition, since the data acquisition is based on a physical probe, the spatial resolution is limited by its dimension. Besides, since the probe needs to be immersed in the test section, requiring auxiliary and sometimes complex positioning systems. Most of the aforementioned drawbacks of the intrusive based methods are avoided when using non-intrusive methods, since they do not require direct contact with the flow stream. Hence, the flow is not perturbed while the measurement takes place, resulting in lower associated experimental uncertainties. Due to the absence of a physical probe, non-intrusive methods usually present higher spatial resolutions. For characterization of bubbly flows, usually image processing techniques are used together with high-speed cameras, which results in measurements with high spatial and temporal resolutions.

When using image processing techniques, usually, a light source is positioned in the back of the test section, parallel to the camera lens. This light and lens arrangement is known in the literature as shadowgraphy technique Bröder and Sommerfeld (2007). Through the shadowgraphy technique, the bubbles are clearly visible on the captured images, where the illuminated background has a homogeneous grey intensity. In contrast, the bubbles appear as elliptical-like structures with a brighter intensity in the center and darker edges on the gas-liquid interface.

From those high-speed cameras obtained with the shadowgraphy technique, an image processing method must be applied to identify the different bubbles present on the flow, track its motion, and compute all the related parameters, e.g., bubble size and velocity distributions. The image processing methods identify the bubbles in the image through a series of filtering and manipulation steps, such as the application of different kernel-based filters, i.e., Gaussian and Laplacian filters, image subtraction, erosion, dilatation and usually, in the final step, a binning operator. After the application of those image processing steps, the raw image captured by the high-speed camera is transformed into a new image, where geometrical features, like ellipsoidal-like outlines of filled contours, are visible in the image. From this final image, the different geometrical features need to be analyzed by a discriminator algorithm, which compares a series of parameters against fine-tune predefined values and then outputs if a specific geometrical feature of the image represents a dispersed bubble or not. Examples of the application of different image processing steps and discriminators are found in the literature, for instance, on the works of Acuña and Finch (2010), Lau et al. (2013), Karn et al. (2015), Cerqueira et al. (2018a) and Cerqueira et al. (2019a).

Depending on the operating conditions and geometry, bubble overlapping may occur when using the shadowgraphy technique, especially in moderate to high gas volume fractions, since the method is based on the projection of the recorded bubbles into an image plane. Therefore, the high bubble overlapping in captured images is a result of the geometry (eg. pipe flow, bubble columns) and high gas volume fraction. In the past years, some authors Shen et al. (2000), Honkanen et al. (2005), Zhang et al. (2012) and Fu and Liu (2016a) developed methods capable of recognizing entities on overlapping-like structures. Those methods are all based on the image processing methods and discriminator mentioned in the paragraph above, with an additional step, where clustered-like geometrical structures are segmented and grouped, aiming the identification of overlapping bubbles. In Shen et al. (2000), Honkanen et al. (2005) and Zhang et al. (2012), the segmentation is performed by analyzing the curvature of the geometrical structures, where if its value exceeds a certain threshold, a breakpoint was introduced, segmenting the outline. Then, from the

segmented portions of the outline, the bubble shape was reconstructed through an ellipse fitting method. In Fu and Liu (2016a), the bubble is not reconstructed by an ellipse fitting method, but through the outline obtained from binary images resulting from a watershed segmentation, bubble skeleton and adaptive threshold operations. Those three binary images are analyzed in a sophisticated algorithm, and then the bubble outline is reconstructed. As presented by the authors, the segmentation algorithm described in Fu and Liu (2016a) is capable of identifying highly deformed and overlapped bubbles.

Despite the success of the methods found in the literature on identifying bubbles bubbly flows, the image processing steps, discriminators, and outline segmentation algorithms heavily depend on user-dependent parameters, which needs to be fine-tuned for each operational conditional and geometry. In recent years, deep learning approaches become widespread in image classification, detection, and segmentation Dhillon and Verma (2019). Among those deep learning approaches, Convolutional Neural Networks (CNNs) is the most popular method due to its robustness and versatility. Additionally, multiple frameworks Jia et al. (2014), Martín Abadi et al. (2015) and Paszke et al. (2017) are available for the public, making it easier for the development of different CNN architectures.

Recently, some authors experimented with the use of CNNs for bubble identification on gas-liquid bubbly flows, presenting similar or better results when compared to the "classical" analytical image processing based methods.

Poletaev et al. (2020) characterized bubbly flows with the planar fluorescence for bubble imaging (PFBI) method Akhmetbekov et al. (2010), which uses a thin laser light-sheet and fluorescent tracer particles to capture images of bubbles in a specified plane. In their work, the authors used a sliding window approach with three separate CNNs to classify the probability of the presence of a bubble in a portion of the image, filter the image through an autoencoder and find probable bubble centers. The authors present a comparison between the CNN-based methods and the analytical method from Akhmetbekov et al. (2010), with the first obtaining superior accuracy. Despite the success of the method developed by Poletaev et al. (2020), it was only tested with images obtained from PIV, i.e., in a laser illuminated plane, and not from the shadowgraphy technique, which is the most commonly used in bubbly flow studies and, typically, more overlapping bubbles appear in the images. Additionally, the authors only test their method in bubbly flows with low void fraction values (below 2.5 %) and only nearly constant sized spherical bubbles are present, which is not the case in typical situations where bubbly flows occur (BESAGNI; INZOLI, 2016).

In Haas et al. (2020), the authors develop and demonstrate the applicability of a CNN-based method for the identification of bubbles in images obtained with the shad-

owgraphy technique. The proposed method uses a region-based Convolutional Neural Networks (R-CNN) for the identification of possible bubble locations, where each bubble is identified, labeled, and surrounded by a rectangular box. The image contained in this box, where a bubble is present, is then submitted to a shape regression CNN, where a regular CNN is used to find the best ellipsoid that correctly fits the bubble represented by the image snippet. According to the presented results, the combination of the R-CNN and a shape regression CNN produces acceptable results for the experimental flow conditions with a reduced number of bubbles. However, as commented by the authors, as the gas volume fraction increases, i.e., more bubbles are present on the flow, the precision decreases due to the increased probability of bubble overlapping.

In Chapter 3, a particle tracking velocimetry (PTV) was developed to measure bubble velocities and size and shape distributions. The bubble identification was based on an analytical image processing method capable of differentiating isolated bubbles of clustered bubbles. In the first case, when an isolated bubble was identified, its position and shape were computed. In contrast, on the second, only its approximate position was computed, based on the capture of the bright points at the bubble centers. With this approach, the instantaneous bubble velocities in highly overlapped conditions were accurately computed. However, the method was not able to correctly estimate the bubble size and shape distributions in bubbly flows with a large number of dispersed bubbles due to the high number of overlapped bubbles.

In the present work, inspired by the recent works using CNNs for bubble identification and shape estimation, a novel CNN-based image processing method is developed for the bubble pattern recognition in dense bubbly flows through the use of the shadowgraphy technique. In the recent works of Haas et al. (2020) and Poletaev et al. (2020), although authors claim the highly overlapped bubble images can be identified, test cases presented in the papers considered gas volume fractions only up to about 2.5%. The method presented in this work can be used to identify and reconstruct the bubble shape in highly overlapping, dense bubbly flows with high void fraction values (up to 9.0 %), and using the shadowgraphy technique, which results in even higher bubble overlapping in the images, due to planar projection of bubbles in different planes. The method is implemented in the same framework developed in Chapter 3 and allows the use of the previously developed PTV technique measuring the bubble velocities. However, the incorporation of the CNN based algorithm allows for the bubble shape reconstruction in dense bubbly regions. Similarly to previous works proposing bubble patterns reconstruction using CNNs, a region proposal step, where bubbles can be potentially identified, is required. In this work, this step is based on square boxes expansion from given anchor points. The bubbles internal

features, used in Chapter 3 to directly compute bubble velocities in highly clustered regions, which are more easily identifiable in those regions, are used as anchor points. Then a bubble shape estimation algorithm is applied in these bounding boxes, and a CNN based classification algorithm is used for the final shape reconstruction. In this way, bubble shapes can be reconstructed in bubbly flow images with such high void fractions, not reported so far in the literature. In order to test the accuracy of the proposed method, the results of the CNN-based algorithm is tested against manually labelled data presenting excellent results in different void fraction flow conditions.

4.2 EXPERIMENTAL SETUP

The experimental setup used in this investigation is the same presented in the previous chapter and is shown again in Fig. 4.1 for convenience. In this case, only the high-speed camera acquisitions were considered.

Due to the reduced inner diameter of the pipe, it is common to observe large bubbles clusters on the acquired images, due to high-probability of overlapping of bubble image projections.

In order to have a CNN model capable of properly identify and reconstruct bubbles with different shapes, high-speed video images were acquired for different bubbly flow configurations. In addition, in order to test the capabilities of the CNN-based method for flow configurations different from those used in the CNN training, image acquisitions for Air/Aqueous glycerol solution system were included in these experiments.

The experiments were conducted in two liquid-gas systems:

- System A: Air/Water, $\rho_l = 997.0$ kg/m^3, $\rho_g = 1.225$ kg/m^3, $\mu_l = 8.9 \times 10^{-4}$ Pa·s and $\mu_g = 18.6 \times 10^{-6}$ Pa·s

- System B: Air/Aqueous glycerol solution (glycerol weight fraction, $w_{glyc.} = 68.0\%$) / Air, $\rho_l = 1196.3$ kg/m^3, $\rho_g = 1.225$ kg/m^3, $\mu_l = 22.3 \times 10^{-3}$ Pa·s and $\mu_g = 18.6 \times 10^{-6}$ Pa·s

Table 4.1 summarize the experimental conditions, which shows experiments with different gas j_g and liquid j_l superficial velocities. The two air-aqueous glycerol solution experiments were filmed to asses how an air-water bubbly flow trained CNN would perform in a different flow configuration. However, as shown in Tab. 4.1, those experiments were not used for the CNN training/testing. The values of the average gas volume fraction $\overline{\langle \alpha_g \rangle}$ are determined from the gas superficial velocity, obtained from the rotameter and

Figure 4.1 – Schematic of the experimental setup.

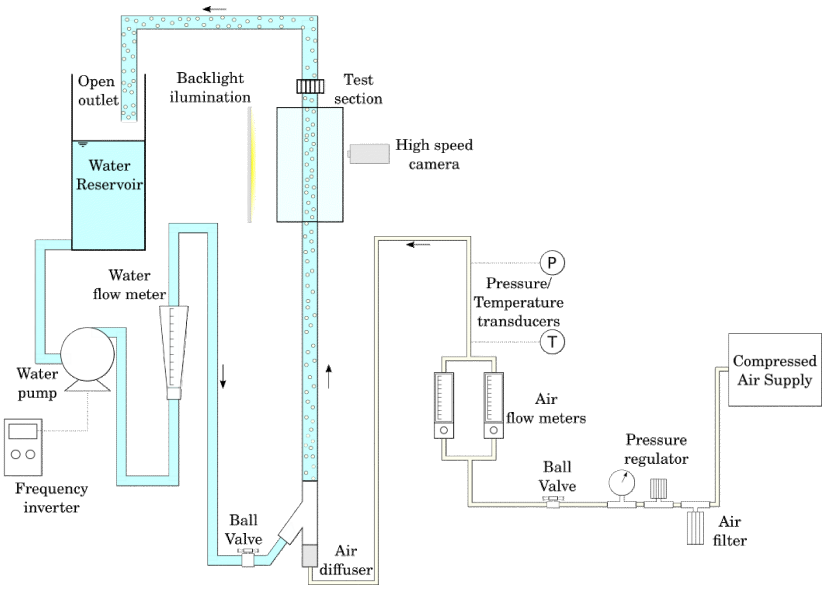

Source - Developed by the author.

the average bubble velocity, measured by the CNN-based method hereby proposed, as $\overline{\langle \alpha_g \rangle} = j_g / \overline{\langle v_g \rangle}$.

Table 4.1 – Summary of the experimental conditions.

Experiment	System	j_l [m/s]	j_g [m/s]	$\overline{\langle \alpha_g \rangle}$ [%]	CNN train/test
1	System A	$3.09 \cdot 10^{-2}$	$5.89 \cdot 10^{-3}$	2.86	Yes
2	System A		$13.55 \cdot 10^{-3}$	6.96	Yes
3	System A		$16.89 \cdot 10^{-3}$	9.03	Yes
4	System A	$21.64 \cdot 10^{-2}$	$5.90 \cdot 10^{-3}$	1.41	Yes
5	System A		$13.45 \cdot 10^{-3}$	3.23	Yes
6	System A		$16.65 \cdot 10^{-3}$	4.08	Yes
7	System B	$17.32 \cdot 10^{-2}$	$9.35 \cdot 10^{-3}$	3.85	No
8	System B		$19.83 \cdot 10^{-3}$	7.63	No

Source - Developed by the author.

Figure 4.2 show typical images obtained by the high-speed camera from the background illuminated bubbly flow, demonstrating the number of bubbles and bubble overlapping in each experimental condition. Additionally, it is possible to verify that during the high-speed camera acquisitions of the System B condition, the images are brighter due to modifications in the illumination setup (experiments in System B wee performed latter, with a more intense LED illumination system). As observed in Fig. 4.2, the porous gas diffuser used, in conjunction with the co-current liquid flow (i.e., the liquid is not stagnant), resulted in ellipsoidal bubbles with a relatively narrow size distribution.

Figure 4.2 – Example of the different bubbly flow configurations and background illumination setups

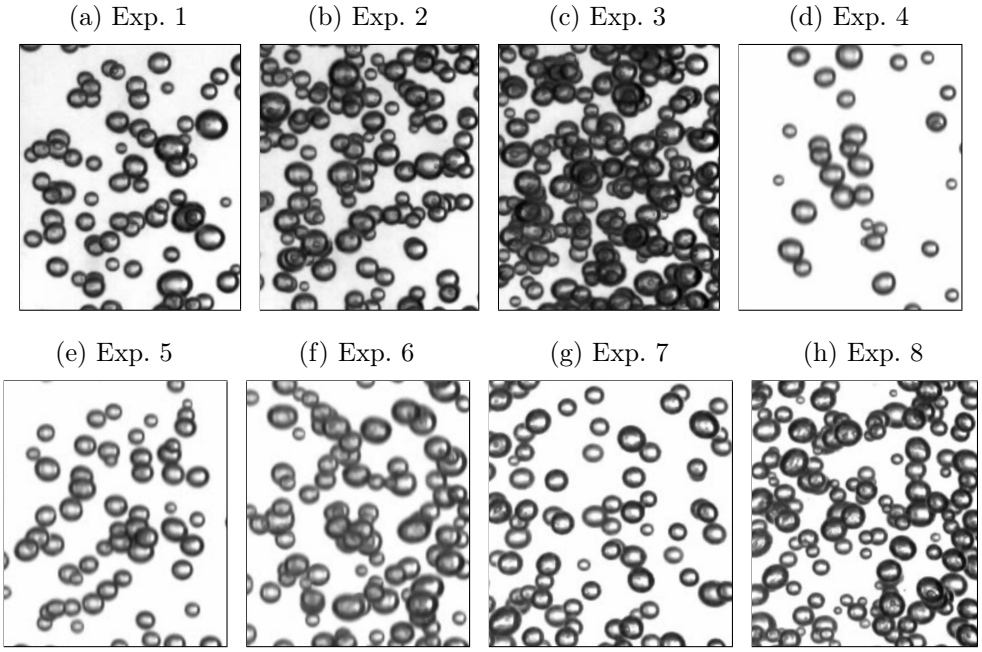

Source - Developed by the author.

4.3 CONVOLUTIONAL NEURAL NETWORKS FOR IMAGE ANALYSIS - A BRIEF OVERVIEW

Convolutional Neural Networks (CNN) are a class of deep neural networks, which can be divided into an input layer, multiple hidden layers, and an output layer.

When applied to image analysis, the input layer is an image which is represented by a matrix of pixel intensities. This matrix have two dimensions in the case of a gray-scale image, or three dimensions for RGB (red, green and blue) for color images (the third dimension varies from 1 to 3 representing the R, G and B channels). The hidden layer is typically formed by a convolutional layer, a pooling layer and a fully connected layer (FCL). Figure 4.3 presents a schematic of a typical CNN architecture, where it is possible to visualize the different layers.

The input layer represents the image, which is a two-dimensional matrix for the case of a grayscale image and a three-dimensional matrix, if the input is a color image. For an 8-bit image, the pixel intensity ranges from 0 to 255 in each channel. Usually, before proceeding to the next layer, the pixel distribution is normalized from 0.0 to 1.0 to avoid biasing due to illumination conditions and enforce generalization to the network. In the input layer, the image must have a fixed height and width. Thus, in typical image classification cases, the input image is transformed to fit into the pre-defined height and width of the input layer of the CNN. The resizing can be done through a padding/cropping

Figure 4.3 – Example of a CNN architecture presenting the input, output and hidden layers.

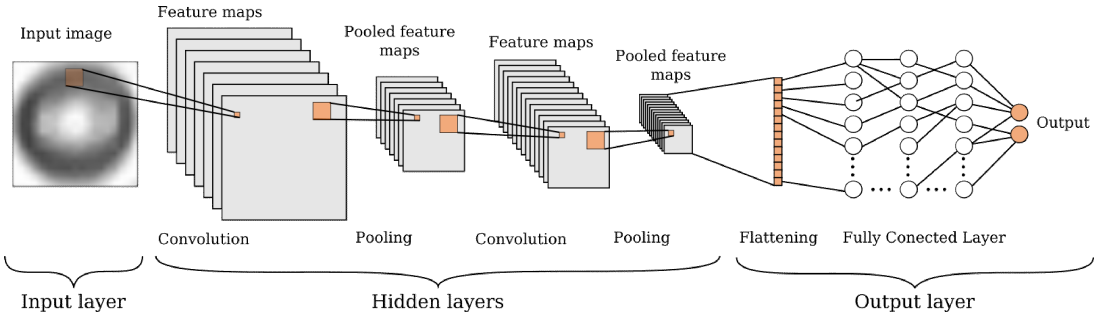

Source - Developed by the author.

transformation or using an interpolation method.

Next, the input image pass through different hidden layers, where the convolutional filters are applied, resulting in intermediate feature maps. In the convolutional step, the input matrix is convolved by a kernel with k_{ij} weights and fixed width, returning a feature map that is propagated through the remaining layers. After the convolution operation, a pooling layer is used to reduce the dimension of the network and minimize possible overfitting. The most commonly used pooling layer in the literature is the maximum pooling layer (DHILLON; VERMA, 2019), where the feature map is divided into small subregions of fixed width, and only the maxima are filtered out to next layer. This process of convolution/pooling is repeated throughout the hidden layer. It is important to note that after the first hidden layer, the input matrix changes from the input matrix to the convolved/pooled feature map. In some cases, an activation layer is added between the convolution/pooling layers, introducing non-linearity to the network, which may be beneficial in certain cases. Rectified linear units (ReLU) are usually employed in the activation layer (DHILLON; VERMA, 2019).

In the output layer, the final feature maps are reduced to a one-dimensional stride through a flattening operator. After its flattening all the aggregate information from the previous layers, the one-dimensional vector is connected to a standard deep neural network with multiple layers, with weights w_{ij} and biases b_{ij} in each neuron. Here, an activation layer may again be present to introduce non-linearity to the network. In the end, the fully connected layer output is used as input in a final classification layer, which returns the probability for each class, based on the activation of the previous layers.

After the CNN architecture is defined, the network needs to be trained to be used as a classifying tool. This is done through the iterative adjustment of the multiple bias and weights of the CNN by a forward-backward propagation. In order to perform this

iterative process, a training data set is required. This data set consists of a collection of labeled input images, which are created through careful manual labeling of images.

In the first iteration, the weights from the multiple convolution filters in the hidden layers, and the weights and biases from the fully connected layers, are initialized with random values. Then, images from the training data set are introduced to the CNN, and a loss function is used to compute the error, i.e., deviation from the predicted label from its true value. The error is then used to update the CNN weights and biases through a gradient descent approach, minimizing the total error. This training process is repeated multiple times, using all the images of the data set. The complete cycling over all the full training data set is called an epoch. The training spans through multiple epochs, where the weights and biases are updated.

Before beginning the iterative process, a sample of the data set is removed from the training to be used as a validation data set. At the end of each epoch, the CNN accuracy is computed from the validation data set. This ensures that the CNN learning process is not biased from the same samples. Typically, the CNN is trained until a certain number of epochs, until small changes of the model accuracy are observed.

4.4 BUBBLE PATTERN RECOGNITION AND SHAPE RECONSTRUCTION

As already commented, a image processing method to identify the bubble position in dense bubbly flows was developed in Chapter 3. Despite its success in tracking the bubble motion, the developed algorithm could not accurately identify the bubble contour or reconstruct its shape. The bubble velocity determination in regions of the images with high bubble overlapping was possible due to bubble representation in the images acquired through the shadowgraphy technique, where its edges have lower pixel intensities, while its center is brighter, presenting higher pixel intensity values. Thus, as carefully described in Chapter 3, the tracking algorithm was based on the identification of the inner bubble features on each consecutive high-speed camera frame and applying the PTV algorithm considering the identification of those features. In this way, the velocities of the bubbles could be determined without the need of identifying their contours.

In the present work, the idea of using these internal features as a first step of bubble identification, which detects the position of "possible bubbles" on the image, is incorporated into a novel CNN-based bubble shape pattern recognition algorithm. The method was developed in Python programming language, where the image processing routines were implemented using the OpenCV library (BRADSKI, 2000a). For the CNN development, the Keras (CHOLLET et al., 2015) framework with a Tensorflow (MARTÍN ABADI et al.,

2015) backend was employed. The description of the bubble pattern recognition and shape reconstruction is detailed in the next subsections

4.4.1 CNN Region Proposal

Despite that CNN algorithms perform well the task of image classification, the method alone is not capable to recognize patterns in a given image. In order to perform the task of image detection through the aid of CNNs, additional steps are required to search such patterns over the image. The task of finding probable rectangular samples where a classification may be successful is done by a region proposal algorithm. For instance, in Poletaev et al. (2020), the authors use a sliding window operator to subdivide the raw PIV image into small rectangle segments. Then those small segments are used as an input to a CNN, which detects if a bubble segment is present and, if positive, returns its center position and radius. In Haas et al. (2020), the authors use the *Faster* R-CNN image detection method developed in Ren et al. (2015). Through this method, the identification is based on rectangular regions returned by region proposed network (RPN), which returns rectangular regions where a bubbles are likely to appear. The identification of those rectangular regions is based on the training of the network from labeled data sets. After identification, the bubble shape is reconstructed from a second shape regression CNN, also trained from known examples.

In the present work, the features used to track the motion of the bubbles in Chapter 3 are used as an anchor point of the bounding rectangles. In this way, highly "clustered" regions can be analyzed, recalling that the bubble overlaps are not only due to the actual clustering of bubbles, but due to contour projections into the camera plane. The image processing steps described for the definition of anchor points is depicted in Fig. 4.4. These internal features are found in a manner similar to the one described in Chapter 3. Through this methodology, the internal point were used to track bubbles and compute velocities in highly overlapped regions of the images. In order to better capture the inner features of the bubbles, the image is subdivided into small regions. Then, Otsu's method Otsu (1979) is applied on each sub-region to generate a binned image. Then, the sub-images are merged to form a binned image of the entire frame, where the internal contours of each bubble are easily detectable. From this final binned image, the centroid of each internal contour is used as an anchor point for the region proposal rectangles. In order to avoid the detection of duplicate points, a simple neighbor-distance algorithm is applied to remove points close to each other. As observed in Fig. 4.4, most of the bubbles have at least one point inside its outline, even those located within bubble clusters with a high degree of

overlapping.

Figure 4.4 – Image processing steps for the anchor points definition, used in the region proposal algorithm.

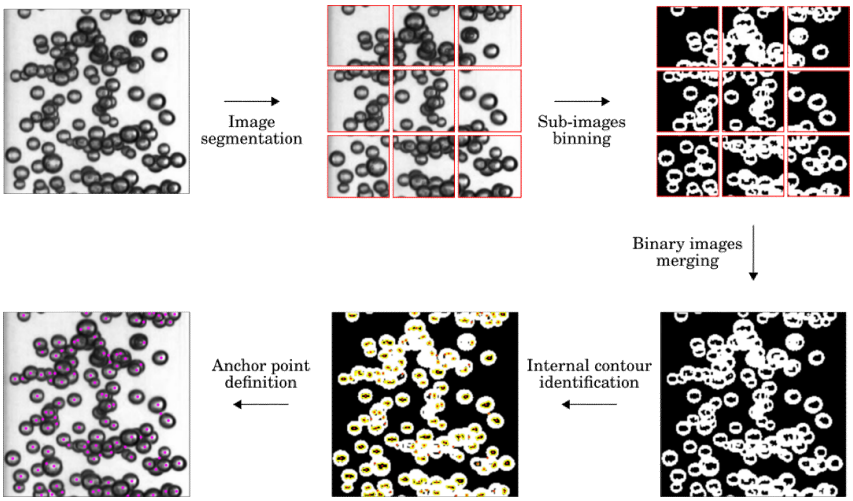

Source - Developed by the author.

After the anchor points are defined, multiple squared bounding boxes centered on those points are generated. The bubble shape identification and reconstruction method based on CNN, presented in the next subsection, uses image segments extracted from those boxes. Figure 4.5 presents the different bounding boxes from to anchor points taken as example. The acquisition of image segments with different lengths from a single anchor point is necessary to accurately capture bubbles width different sizes. From the bubbly flows analyzed in the present work, the minimum and maximum length of the bounding boxes were defined based on maximum and minimum bubbles sizes observed in images. In order to better reconstruct the bubble shape, the minimum and maximum length values were divided into ten intervals, resulting in 10 possible bounding boxes for each anchor point.

4.4.2 Bubble shape estimation

After applying the region proposal algorithm in the image to be analyzed, each anchor point has multiple bounding boxes. Now, the information contained in those sub-images is used to identify possible bubbles and reconstruct its shape.

As already noted in Chapter 3, images of ellipsoidal bubbles have distinct intensity profiles, with two local minimum points corresponding to the bubble boundaries and higher values corresponding to the background and the inner portion of the bubble. Thus, based on this typical pixel intensity distribution, the first step of the bubble shape reconstruction

Figure 4.5 – Example of bounding boxes extracted from the region proposal method used in the present work. Three squared bounding boxes of different dimensions are shown on the right, and its anchor points are highlighted on the image of the left.

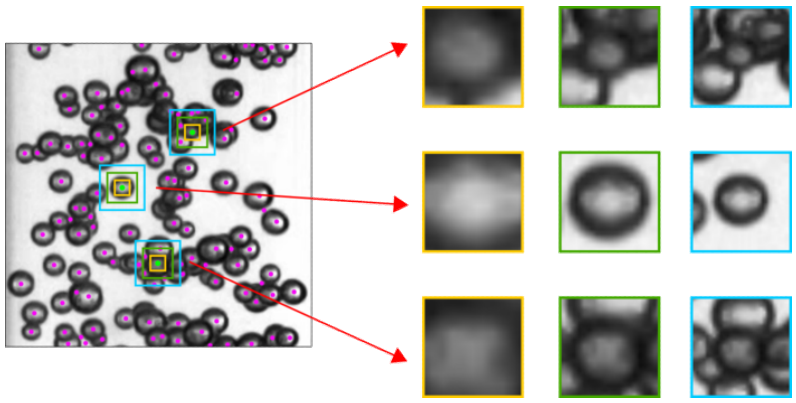

Source - Developed by the author.

algorithm consists of radially scanning the image contained by a giving bounding box. At each line scan, which is centered on the anchor point, a minimum global search is applied, and its returning values are stored for the next steps. Figure 4.6 presents the line scanning operation in two different bubbles with the same bounding box size, showing the pixel intensity distribution and its corresponding minimum point coordinates. As illustrated by the two examples of Fig. 4.6, if the bounding box size is correctly specified, it is possible to reconstruct the bubble shape outline through an ellipse-fitting method. In the example shown in Fig. 4.6, a total of 10 line scans were used to obtain the approximate bubble outline. In the application algorithm a total of 50 lines, equally spaced angularly, were scanned at each bounding box size.

This approximate bubble outline shape is performed several times for each bounding box, resulting in a different number of possible ellipses. Figure 4.7 shows the minimum point coordinates from the radial line scanning process, from the complete set of bounding boxes, and the resulting point-fitted ellipses. According to Fig. 4.7, for a given anchor point, one or more fitted ellipses is a good candidate for estimating the bubble shape outline.

4.4.2.1 CNN Training for bubble shape detection

As observed in Fig. 4.7, for a given anchor point, one or more bounding boxes resulted in correct ellipse-fitted bubble shape approximations. Thus, in the present work, a CNN is used to assess the quality of a given bubble outline shape reconstruction based on the steps presented in the previous sections. If the CNN returns high probability score

Figure 4.6 – Example of two typical bubbles and squared bounding boxes. The colored arrows indicate the line scanning direction, and the plots refer to its pixel intensity distribution. The final image shows the corresponding minimum point coordinates obtained in the radial line scanning step, illustrating how the bubble shape can be reconstructed from those points. In order to better illustrate the steps, only five, of a total of ten, pixel intensity distributions are shown.

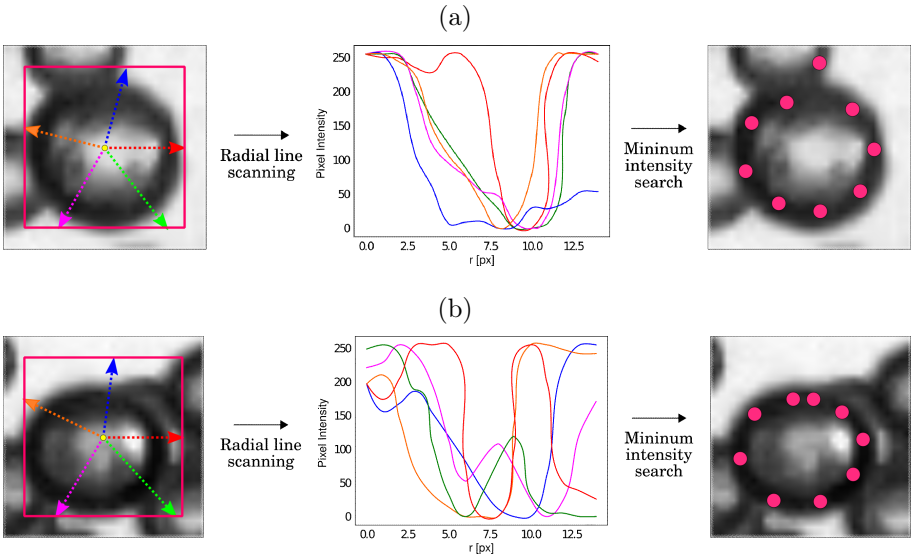

Source - Developed by the author.

for a given bubble shape reconstruction, this particular ellipse is then classified as a bubble and added to the bubbly flow characterization statistics. In the next paragraphs, the CNN training and architecture is discussed in details.

In order to train the CNN, sample images of a given flow configuration, i.e., set of superficial gas j_g and liquid j_l velocity, were used as an input to a first image processing algorithm, following the steps described in Sections 4.4.1 and 4.4.2. In this first computational routine, multiple anchor points and different bounding boxes were identified in the image. For each sub-image, the minimum pixel intensity points were located, and from those points, ellipses were fitted, following the steps presented in Sec. 4.4.2. After calculating the ellipse parameters that best fitted on those points, the original greyscale sub-images were converted to RGB color images, by copying the original pixel intensity distributions into the three RGB channels. Then, the calculated ellipse was added on top of the RGB converted sub-image, i.e., the pixels that laid on the ellipse reconstructed interface had their values altered to [255,0,0]. Those images, are schematically illustrated in Fig. 4.8, were saved on the hard-drive, to later be classified as "valid" and "invalid" bubble shapes. Since the main objective of this step was the creation of a diverse data

Figure 4.7 – Example of the bubble shape estimation: a) Resulting points from the radial line scanning process for different bounding boxes and b) resulting fitted-ellipses from those points. Ellipses obtained from bounding boxes of different sizes are represented by different colors in order to identify each one in a further classification step.

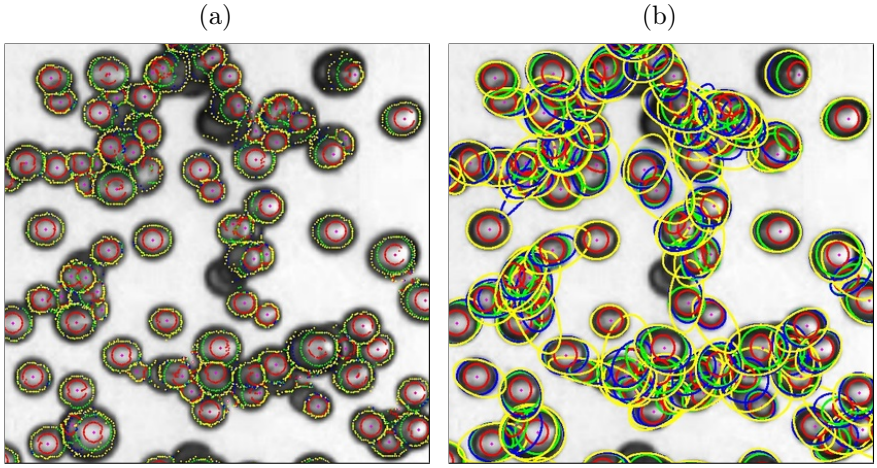

Source - Developed by the author.

set for the CNN training, bounding boxes of only a part of the anchor points were saved to the hard-drive. The anchor points were selected randomly, using approximately 10 % of the total points, thus certifying that the data set was not biased towards an specific region of the high-speed camera image

After the images were saved on the hard-drive, it was necessary to label the different files as "valid" and "invalid". This classification step, which generates the information for the CNN training, is a necessary step in this type of application, but consists in a manual and repetitive task. In order to facilitate this task a simple GUI (Graphical User Interface) software was developed for this sole purpose. Through this application, the different sub-images of bounding boxes obtained from the same anchor point are shown in a single screen, and the user manually classifies the images as "valid" and "invalid". Around 100 "valid" and 100 "invalid" images, like the ones shown on the right of Fig. 4.8, were manually labeled for each of bubbly flow configurations used in the CNN training, marked in Tab. 4.1, resulting in 600 original samples. However, the total dataset resulted in 2400 images, since each original sample returned three more images through data augmentation. The data set was augmented from the generation of new images through mirroring and random gamma correction operations, where the last was used to increase/decrease the contrast of the images.

Since the CNN uses as input images with a fixed size, when feeding the neural

Figure 4.8 – Example of bounding boxes and the resulting ellipses used for the data set generation. Left: Location of the anchor points in the original image. Right: Data set images from different bounding boxes sizes from the same anchor point. The images on the left are not in scale for better visualization.

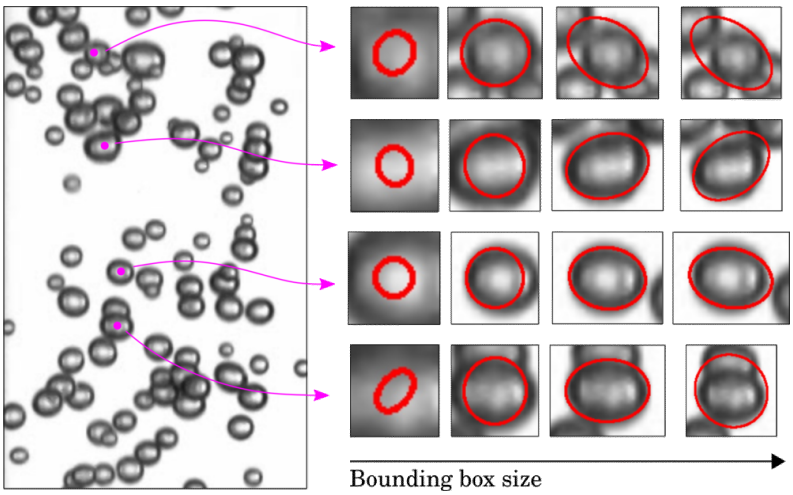

Source - Developed by the author.

networks, all the manually labeled images were re-dimensioned to a fixed size of 64 x 64 px x 3 channels by a bilinear interpolation scheme, with the "R" (red) channel containing the information about the bubble outline from the ellipse-fitting method.

4.4.2.2 CNN Architecture

As already commented, a typical CNN is divided into an input layer, multiple hidden layers, and a final output layer. Several settings can be configured in a CNN, such as the number of convolution filters, the size of its kernels, and the number of hidden layers. These settings are called hyperparameters, and different sets of them result in different CNN architectures. Thus, a hyperparameter analysis was conducted with the objective of finding an optimal CNN architecture, which correctly reconstructed the shape of the largest number of bubbles on the images with a good level of confidence.

As illustrated in Fig.4.9 the CNN was divided into multiple layers, subdivided by:

- an image input layer with size (64, 64, 3);
- a convolution layer composed by a: i) N_{conv} convolution filters of size K_{conv}; ii) a max pooling layer of size K_{pool} = (2,2) and iii) a ReLU activation layer;
- an output layer composed by: a i) a flattening operator, ii) a fully connect layer of 32 neurons N_{neuron} and iii) a Sigmoid activation layer for the final classification.

Additionally, to prevent overtraining, batch normalization (IOFFE; SZEGEDY, 2015) is applied at each convolution layer and a dropout (SRIVASTAVA et al., 2014) with 30 % rate at the fully connected layer.

Figure 4.9 – Schematic illustration of the tested CNN architectures in the hyperparameter analysis, presenting the three different base layers.

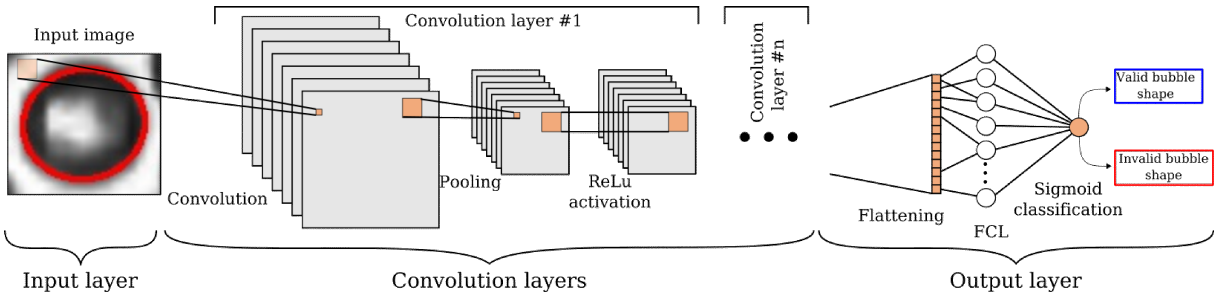

Source - Developed by the author.

For the analysis of the hyperparameters, different combination of N_{layers}=[1,3,5] and number of convolution filters N_{conv}=[8,16,32] were tested. Thus, for each N_{layers} a total of $3^{N_{layers}}$ CNN architectures were tested, where the base (3) is the length of the tested N_{conv} convolution filters. The N_{neuron} number of neurons on the final output, the kernel convolution size K_{conv} and the max pooling layer size $K_{pooling}$ were not varied, since preliminary results pointed a small effect of these hyperparameters on the CNN accuracy.

The different CNN architectures were trained with the 3/4 of the 2400 images data set, while the remaining 1/4 was not used in the training process and kept apart for the accuracy calculation, defined as,

$$\text{Accuracy} = \frac{\text{TP} + \text{TN}}{\text{TP} + \text{TN} + \text{FP} + \text{FN}} = \frac{\text{Number of correct predictions}}{\text{Total Number of predictions}} \tag{4.1}$$

where TP stands for True Positives, TN for True Negatives, FP for False Positives, and FN for False Negatives.

The CNN architectures were trained by batch stochastic gradient descent, with a batch size of 16 and by 100 training epochs. The Adam (KINGMA; BA, 2014) optimization algorithm was used for the loss minimization, which used a binary cross-entropy function. For a given CNN architecture, the resulting model weights were defined as the ones that resulted in the best validation accuracy during its training epoch.

Figure 4.10 shows the resulting accuracy from all the 274 tested CNN architectures. The 273 CNN architectures were tested through an automated script on a Google Compute Engine (GCE) Virtual Machine (VM) with 2 vCPUs and a Tesla K80 GPU, with an average

run time of about 90.0s. The worst CNN architecture resulted in an accuracy of 89.46 % and the best in a value of 94.55 %. The best CNN model comprised of 5 convolutional layers with filters sizes of [8,32, 32, 32, 32], while the worst also had 5 convolutional layers with filter sizes of [32, 32, 8, 8, 8]. The CNN architectures with a single convolutional layer presented accuracy values of [93.34 %, 92.09 %, 92.44 %.]. The architectures with 3 convolutional layers ranged from 91.33 % to 93.84 %., while the one with 5 convolutional layers resulted in accuracy values between 89.46 % and 94.55 %.

Figure 4.10 – Accuracy from all the 274 tested CNN architectures. The worst CNN architecture (CNN number 246) resulted in an accuracy of 89.46 % and the best (CNN number 110) in a value of of 94.55 %.

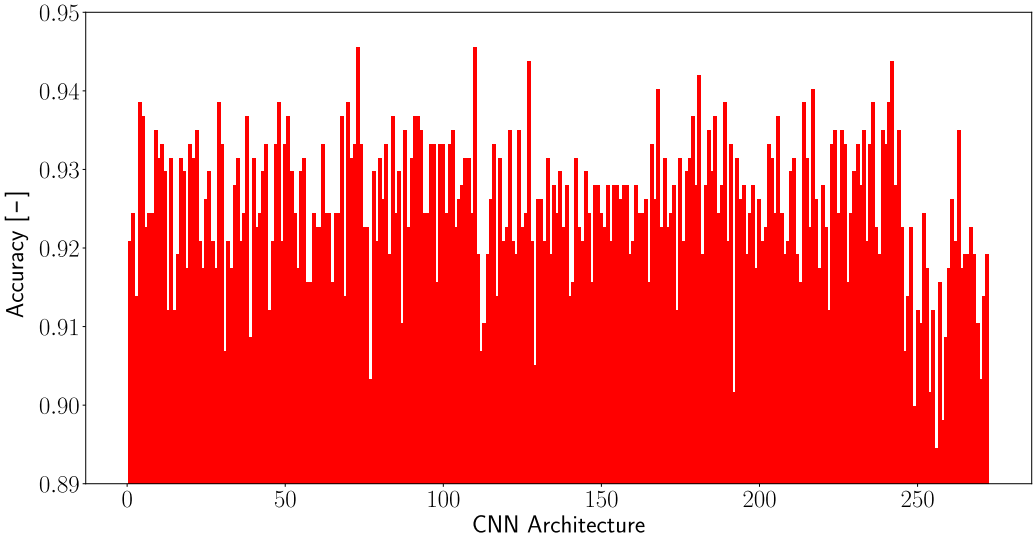

Source - Developed by the author.

Despite the small differences in the accuracy, when using a probability threshold of 0.5 for dividing the reconstructed shapes into valid and invalid, both CNN architectures (i.e., the ones which presented the minimum and maximum accuracy values) present different results. This is shown in Fig. 4.11 that present the valid reconstructed bubble interfaces with the best and worst from all the tested CNN architectures.

According to Fig. 4.11, by looking at the Exp. 2 results, it is evident the difference between the number of identified bubbles by the two CNN architectures, despite of the similar accuracy values, 89.46% vs. 94.55%, presented by both architectures. At a first glance, this may indicate that the accuracy metric given by Eq. (4.1) is not suitable for comparing the different CNN architectures. However, those differences are linked to the lack of uniformity of the images used in the present work, which spanned over different experimental bubbly flow conditions with gas void fractions ranging from $1.41\% < \langle \alpha_b \rangle < 9.03\%$. Thus, those discrepancies may arise when calculating the accuracy values during

Figure 4.11 – Example of the valid reconstructed bubble interfaces with the worst (left) and best (right) tested CNNs from two snapshots of Exps. 2 and 5.

(a) Exp. 2 (b) Exp. 5

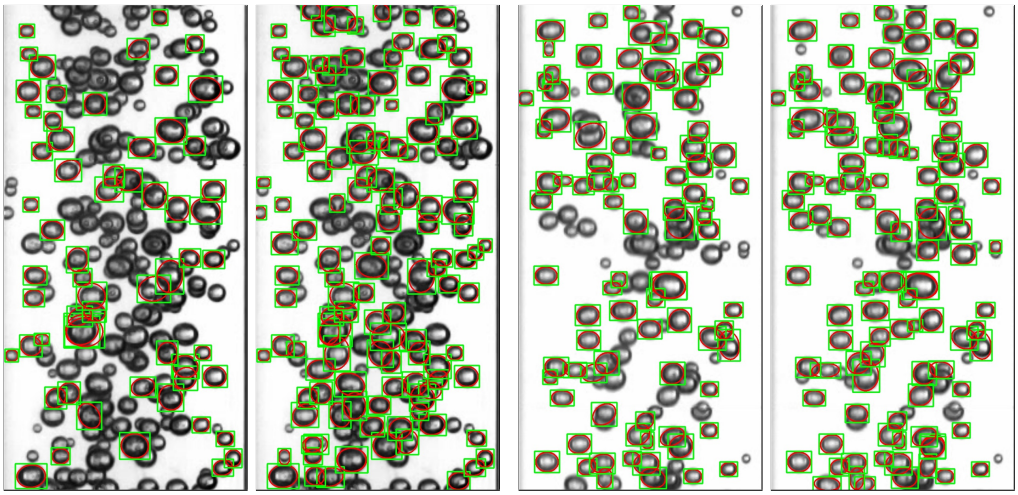

Source - Developed by the author.

the CNN training, which uses samples from the all different bubbly flow conditions. Additionally, this may be a result from the high number of TN (True Negatives) in Eq. (4.1), which could lead to anomalies on the results of Fig. 4.10.

Those results indicate that a better methodology shoud be used to analyze the CNN accuracy, accounting for the image heterogeneity in each bubbly flow condition. Therefore, in order to better visualize the CNN accuracy in the different experimental conditions evaluated, the procedure reported in Haas et al. (2020), based on the Recall and Precision parameters is used. These parameters, given by Eqs. (4.2) and (4.3), are compared as a function of the gas volume fraction $\langle \alpha_b \rangle$. The Recall parameter,

$$\text{Recall} = \frac{\text{TP}}{\text{TP} + \text{FN}} \tag{4.2}$$

measures the number o real positives found, while the Precision parameter,

$$\text{Precision} = \frac{\text{TP}}{\text{TP} + \text{FP}} \tag{4.3}$$

measures the ratio of the correctly predicted positive observations of the total predicted positive observations,

Figure 4.12 presents the Recall and Precision values calculated by the best and worst CNN architectures, CNN numbers 110 and 256 respectively, with 1/4 of the total number of samples from each different dataset. Hence, Fig. 4.12 presents a quantified parameter of the method capabilities as a function of the gas volume fraction.

The results from Fig. 4.12 show that as the gas volume fraction increases, the CNN-based method accuracy in identifying and reconstructing the dispersed bubbles is

Figure 4.12 – Precision and recall as a function of the gas void fraction for the best and worst CNN architecture from Fig. 4.10, CNN number 110 and 256, respectively. The results are grouped by its j_l configuration with a) representing Exps. 1–3 and b) Exps. 4 – 6.

(a) System A - $j_l = 3.09 \cdot 10^{-2}$ m/s

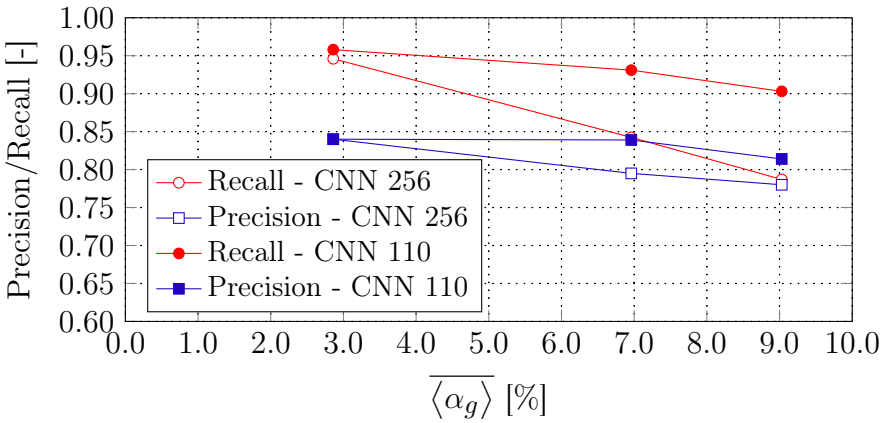

(b) System A - $j_l = 21.64 \cdot 10^{-2}$ m/s

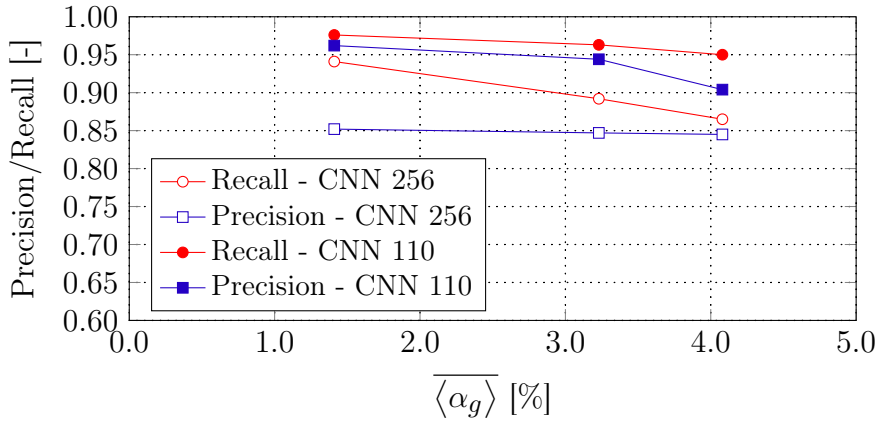

Source - Developed by the author.

reduced. This reduction on the overall accuracy arises from the clustering effect that, as pointed out earlier, decreases the bubble outline contrast, reducing the chance of the bubble identification and correct classification.

To better comprehend the effect of the CNN architecture in identifying and reconstructing the bubble shape in the recorded images, the results from the CNN-based method presented in this work were compared with manually extracted data. Images from the high-speed cameras were analyzed in the ImageJ software (RASBAND et al., 1997), where all the bubbles present in the images were identified and its shape approximated by manually fitted ellipses. This manual classification was performed in images from Exps. 1, 3, 4 and 8 of Tab. 4.1, where for each experimental condition a total of 4 frames were

used in this task.

The manually identified bubbles from the labeled images, which are the reference values in this comparison, are compared against the CNN-based results. As an example, Fig. 4.13 show the manual reconstructed bubbles in a region of a given high-speed camera frame and the results from the best and worst tested CNN architectures in different experimental points. Then, from those results, the bubble size distribution from the two different architectures shown in Fig. 4.11 are compared against the reference values. The bubble size distributions are presented as Probability Density Function (PDF) of the equivalent spherical diameter d_b.

Figure 4.13 – Example of created dataset for testing the CNN architecture in different experimental conditions. Left column: Manually identified and reconstructed bubbles; Middle column: Reconstructed bubble interfaces with the worst tested CNN architecture; Right column: Reconstructed bubble interfaces with the best tested CNN architecture.

(a) Exp. 1 - $\overline{\langle \alpha_g \rangle} = 2.86$ %

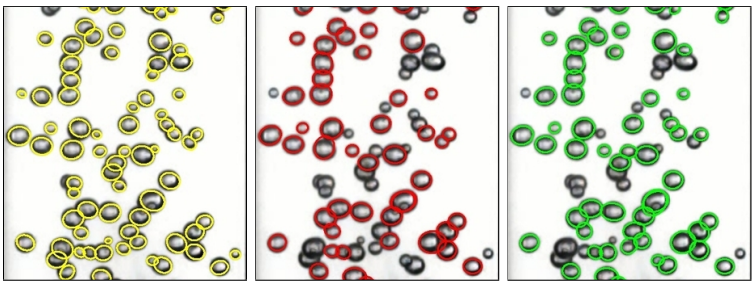

(b) Exp. 8 - $\overline{\langle \alpha_g \rangle} = 7.63$ %

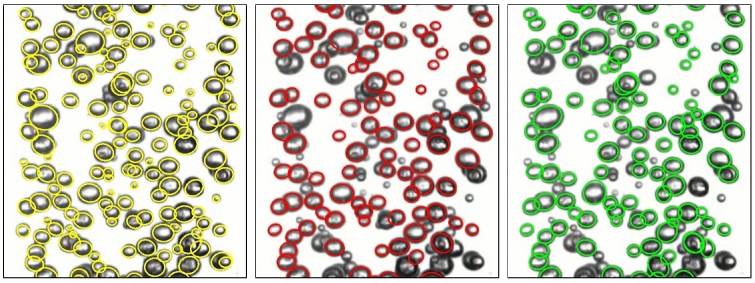

Source - Developed by the author.

As a first CNN evaluation study using the labeled data, the manually reconstructed bubble outlines were used to create "ground truth" images. This step generated "mask-like" images where the position and shape of the bubbles are represented by the white filled regions that were used to verify the CNN accuracy in more realistic scenarios. Example of one of these generated masks are shown in Fig. 4.14. As with the manual labeled bubbles, "mask-like" images were produced by the bubbles identified and reconstructed by the best (94.55% accuracy) and worst (89.46% accuracy) CNN architectures. Then, the I_{diff}

parameter was calculated from the two generated mask images as,

$$I_{\text{diff}} = \frac{\sum_{px} \text{Mask}_{\text{CNN}}}{\sum_{px} \text{Mask}_{\text{manual}}} \tag{4.4}$$

where the summation is performed over the entire pixels of the generated image, $\text{Mask}_{\text{manual}}$ represents the "ground truth" image and Mask_{CNN} the "mask-like" image from the CNN reconstruction. As shown in Eq. (4.4), the I_{diff} parameter returns an approximate ratio of the total bubble occupied area of the reconstructed bubbles in relation to the "ground truth" reference. It is important to state that this parameter may suffer from differences due to the user labeled major and minor ellipse diameters and small deviations of the CNN-based method. Figure 4.14 shows those small deviations by presenting the difference between the two masks by $\text{Mask}_{\text{diff}} = |\text{Mask}_{\text{manual}} - \text{Mask}_{\text{CNN}}|$.

Figure 4.14 – Example of the "ground truth" $\text{Mask}_{\text{manual}}$ image, the Mask_{CNN} "mask-like" image from the CNN reconstruction method and the absolute difference of the two masks ($\text{Mask}_{\text{diff}} = |\text{Mask}_{\text{manual}} - \text{Mask}_{\text{CNN}}|$). Those masks were generated from an frame in the Exp. 8 bubbly flow condition.

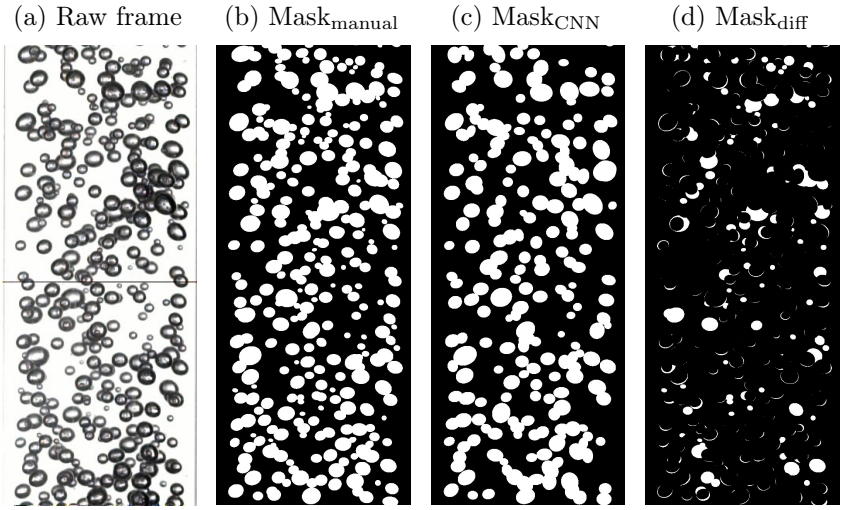

Source - Developed by the author.

Table 4.2 presents the minimum I_{diff} values from the 4 manually labeled frames of Exps. 1, 3, 4 and 8 by CNNs architecture numbers 110 and 256. As observed, in all the presented cases, the CNN number 110 resulted in higher I_{diff} values, following the results from Fig. 4.10 and 4.12. The single outlier from Tab. 4.2 is the results from Exp. 3, which resulted in lower I_{diff} values, demonstrating that the method is failing on reconstructing the bubble shape due to the difficulties associated to the frequent bubble overlapping and clustering. However, according to the results for Exp. 8 in Tab. 4.2, those issues can be overcome by modifying the illumination setup for the image acquisition, since the Exp. 3

resulted in a high I_{diff} value, operating in a flow condition with bubble overlapping and clustering similar to Exp. 8.

Table 4.2 – Minimum I_{diff} values from the 4 manually labeled frames of Exps. 1, 3, 4 and 8 by CNNs architecture numbers 110 and 256.

Exp.	System	$\langle\alpha_b\rangle$ [%]	I_{diff} [-]	
			CNN 110	CNN 256
1	A	2.86	0.9360	0.9123
3	A	9.03	0.5279	0.5150
4	A	1.41	0.9720	0.9490
8	B	7.63	0.8751	0.8499

Source - Developed by the author.

As a second verification from the manually labeled images, focus was shifted to the analysis the capability of the present method to characterize the dispersed bubbles shape through the information recorded in the high-speed camera videos. From this approach, which is closer to a more realistic experimental characterization of the dispersed bubbles, it is not necessary to identify and reconstruct the entire bubble population in a single image, but capture most of the bubbles throughout a number of frames accurately to perform time-averaged statistics. Therefore, the bubble size distribution from the two different architectures shown in Fig. 4.11 are compared against the reference values taken from the manually labeled data. The bubble size distributions are presented as Probability Density Function (PDF) of the equivalent spherical diameter d_b.

Figure 4.15 shows the BSD from the manually extracted data and from the CNN-based results. As observed in Fig. 4.15, the results with the best tested CNN architecture, with a 93.84 % accuracy value, are similar to the reference values in the four compared experimental points, even in dense bubbly flow conditions, as Exps. 3 and 6. The results of the worst tested CNN architecture, which resulted in an accuracy value of 89.46 %, shows that this configuration was able to estimate the distribution shape with small deviations from the reference dataset. From the bubble size distributions presented in Fig. 4.15 it is clear that, when using the correct architecture, the CNN-based method presented in this work is capable of identifying and reconstruct the bubble shape outline correctly even in dense bubbly flow configurations. Since the CNN with the highest accuracy was capable of capturing a large number of bubbles in the images (see Fig. 4.11) and the resultant bubble size distributions agreed well, in the next sections, only the results acquired with the best CNN model will be presented.

Figure 4.15 – Comparison of the bubble size distributions obtained from manual identification (reference result) and those estimated from the best and worst tested CNN architectures.

(a) Exp. 1 - $\overline{\langle \alpha_g \rangle}$ = 2.86 %

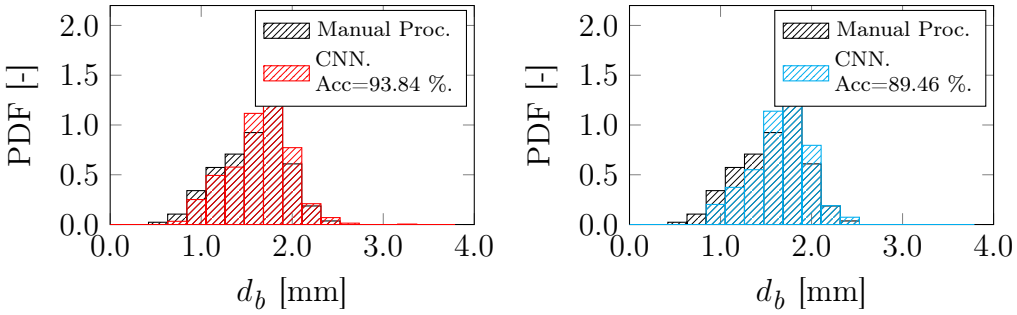

(b) Exp. 3 - $\overline{\langle \alpha_g \rangle}$ = 9.03 %

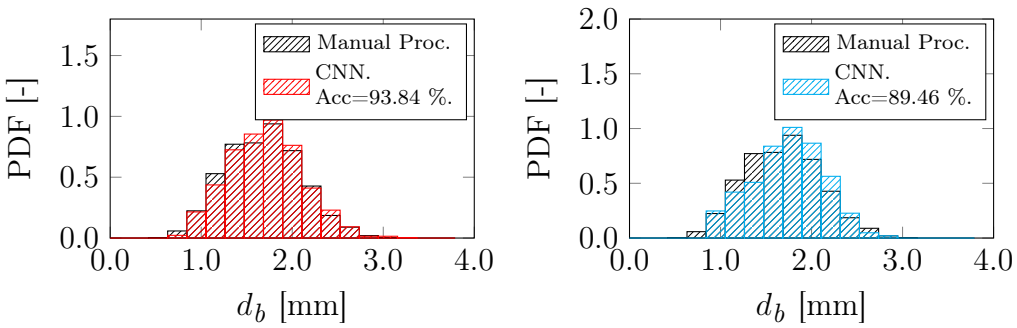

(c) Exp. 4 - $\overline{\langle \alpha_g \rangle}$ = 1.41 %

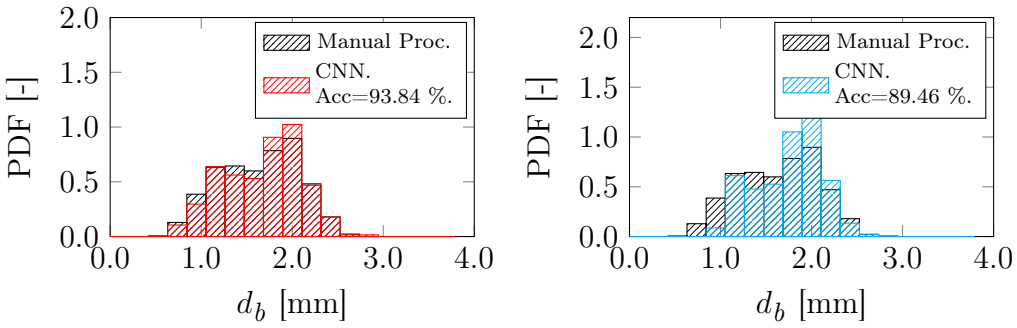

(d) Exp. 8 - $\overline{\langle \alpha_g \rangle}$ = 7.63 %

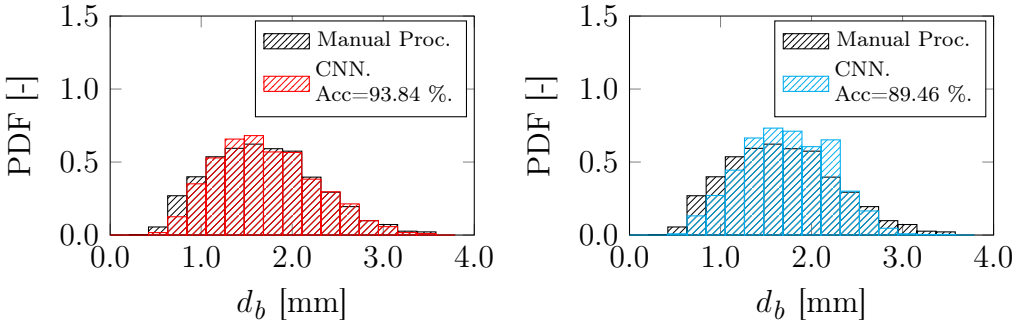

Source - Developed by the author.

4.5 RESULTS AND DISCUSSION

The current section is focused on the applicability of the CNN-based bubble shape reconstruction from the different experimental conditions given in Tab. 4.1. In order to access the robustness of the present method, the obtained results from the CNN-based method described earlier are compared with the ones from the analytical method presented in Chapter 3.

4.5.1 Bubble shape reconstruction

In order to analyze the applicability of the CNN-based method described in the present work, bubbly flows with experimental conditions as given in Tab. 4.1 were filmed for 8.0s, and its images were then processed. Due to the CNN region proposal discussed in Sec. 4.4.1, the total processing time, depends on the number of bubbles present in the image. For the cases with small amount of bubbles (i.e., low gas volume fraction), as Exp. 4 of Tab. 4.1, the developed software took around 1.5s to process each image, while the case where more bubbles were present, Exp. 3 of Tab. 4.1, the total run time took approximately 6.5s. The image bubble identification software run in an desktop computer with an Intel(R) Core(TM) i7-4770 CPU @ 3.40GHz processor, without the use of a GPU acceleration.

Figure 4.16 presents the bubble-shape identification and shape reconstruction for the experimental conditions given in Tab. 4.1. In the high-speed camera videos, a vertical length of 70 mm of the test section ($\approx$ 2.6 tube diameters) was filmed , but to better illustrate the quality of the bubble shape reconstruction, the results in Fig. 4.16 show a vertical length of only 26.2 mm (one diameter) of the test section. A processed video of 2.0s of each bubbly flow condition, with the bubble shape reconstruction and identification on the whole test section, can be visualized in Video 3 of the supplementary material given in Appendix B.

The results of Fig. 4.16 demonstrate that the region proposal and the CNN trained model identifies most of the bubbles in the presented images. Due to the high-speed camera larger distance from the test section, the low resolution from the smaller bubbles in Exps. 1 – 6 presented difficulties for their identification. Those problems were mitigated in Exps. 7 and 8, where the camera was positioned closer from the acrylic duct, and the smaller bubbles outline could be reconstructed. In Exps. 2 and 3, shown in in Figs 4.16 b) and c), some of the bubbles were not identified. By comparing the images of Exps. 2 and 3, one can visualize that the background of those experiments is not as bright as other images, which in turn may have affected the bubble shape reconstruction. Nevertheless,

Figure 4.16 – Example of the CNN-based bubble identification and shape reconstruction for the different bubbly flow conditions given in Tab. 4.1. The reconstructed bubble interfaces are given by the red ellipses and its bounding rectangles are shown in green. The bounding rectangles in the images shown here are used to better visualize the results and are not related to the bounding boxes described in Section 4.4.1.

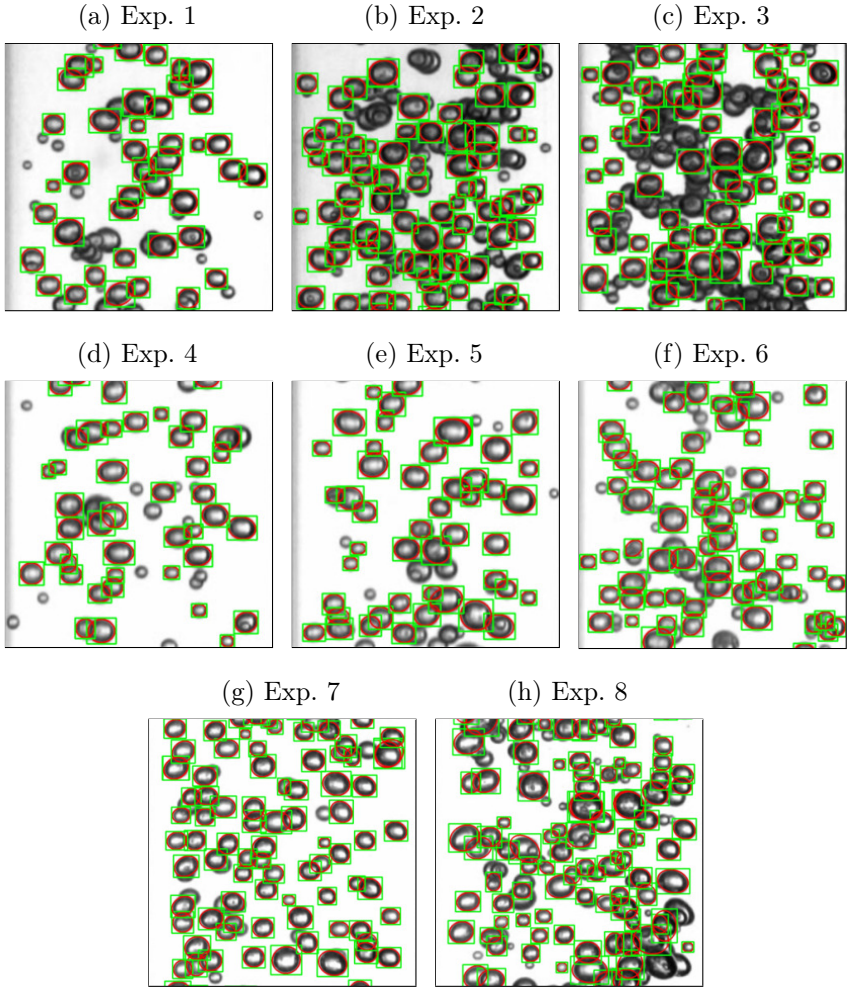

Source - Developed by the author.

the results from Figs. 4.16b) and c) still represents a superior enhancement of the bubble identification method first proposed in Chapter 3, where the shape of a few bubbles could be identified and only the center of certain bubbles could be captured in this level of overlapping. It is important to state that the current method could be applied to large distorted bubbles ($d_b > 3.5mm$), such as those shown in Lau et al. (2013). However, the CNN-based method would approximate the distorted bubbles shape through ellipses, which could result in significant deviations on the Bubble Size Distribution (BSD) and inaccuracies in shape reconstruction, in the bubbly flow characterization. Therefore, no further efforts were done to apply the method to cases with large deformed bubbles in the

present work. Even though, the bubble identification method presented here represents an important enhancement over other methods, even those based on CNN, presented in the literature operating in a dense bubbly flow condition. As discussed in Chapter 3, most previous methods for bubble identification for PTV, were restricted to very low gas volume fractions with low bubble clustering in images. Through the method described earlier the velocity computation of bubbles in clustered region was possible due to the proposal of capturing bright points in the bubbles centers, but no information about bubbles size/shape could be captured in these clustered regions. Now, even in those "worst" cases much information about bubble size distribution can be obtained, even in clustered regions.

In the remaining images from System A, air/water flow configuration, the trained CNN could even correctly reconstruct the shape of bubbles captured located in a chain-like cluster, which usually represents a challenge for identification algorithms, identifying bubbles with an accuracy level similar to those observed in Fu and Liu (2016a). Examples of those long bubble chains and its shape reconstruction can be visualized on top-left region of Fig. 4.16d), he middle-right region of Fig. 4.16e) and the top-left region of Fig. 4.16f). When analyzing those results in contrast with the ones from Fu and Liu (2016a), it is important to state that the bubble identifying strategy used in the present work does not involve the setting and manual tuning of different parameters. In addition, our experimental setup is a duct with an inner diameter of 26.2 mm, which is a more challenging geometry as the one used by the authors in Fu and Liu (2016a), a "pseudo-2D" rectangular channel with 10.0mm width, where clustering on images is much less intense as there is no superposition of bubble image from different planes. In the experimental conditions presented here, bubble overlapping is frequent even in small gas quantities, since an increased dimension in the plane perpendicular to the camera lens, also increases the probability of bubbles clusters to appear in the camera plane.

As stated in Tab. 4.1, Exps. 7 and 8, were not used in CNN model training step described in Sec. 4.4.2.1. Nevertheless, the sample results of those two experiments, Figs. 4.16g) and 4.16h) show that the CNN-based procedure was able to reconstruct the shape of most of the bubbles, even images being different from the rest of the experiments in terms of brightness intensity, contrast and bubble edge definition (in air-water system, the interfaces are more "blurred"). In order to further assess the CNN-based method robustness, bubbly flow images from Chapter 3, which were acquired with a different lighting condition (darker backlight), were processed with the best-accuracy CNN architecture. Those results are given in Fig. 4.17 and show that, despite the different illumination setup, most of the dispersed bubbles were identified in those images. Additionally, Fig. 4.17 shown the

processed results from an image taken from Lobanov et al. (2019), also providing excellent results despite of the fact that the photograph was taken in a different flow facility.

Figure 4.17 – Example of the CNN-based identification method in images with a different illumination setup. Bubbly flow images from: a)–c) our previous experiments (from Chapter 3 using the same experimental setup, but different illumination conditions, for different values of j_g, and d) from an image taken from the work of Lobanov et al. (2019).

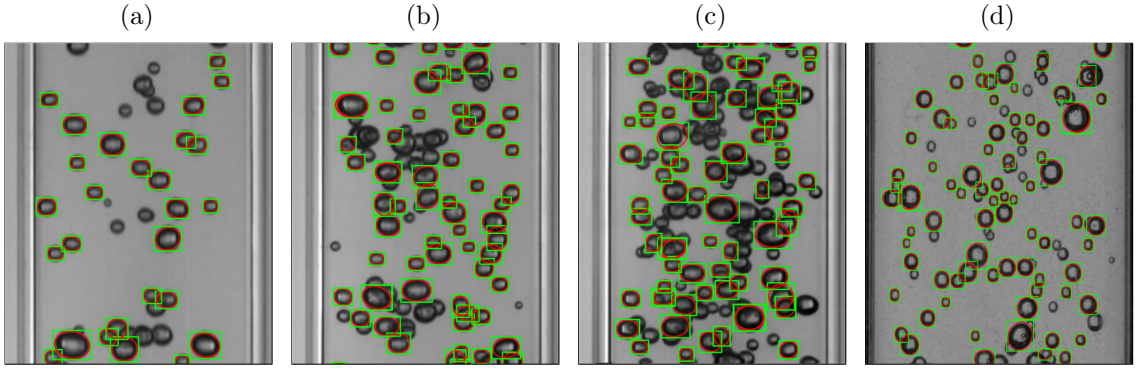

Source - Developed by the author and adpated from Lobanov et al. (2019).

From the results shown in this section, it can be concluded that the CNN model is capable of correctly reconstruct the shape of bubbles in images even with some deviations on their background illumination intensity and changes on the camera exposure.

4.5.2 Bubble size characterization and comparison with previous algorithm

According to the results presented in the previous section, the CNN-based bubble shape reconstruction is capable of analyzing bubbly flows where bubble clustering is frequent. The analytical bubble detection method developed in Chapter 3, is not capable of capturing the bubble outline in "dense bubbly" regions. In those situations where bubble clustering is frequent, the analytical method can only detect the bubble centrist and, therefore, track its velocity. In Table 4.3 the global average values from selected experiments from Tab. 4.1 (low and high "clustering") are presented, comparing the values obtained by the two methods.

The results given in Tab. 4.3 show that the average axial gas velocity, i.e., the average terminal bubble velocity, $\overline{\langle w_g \rangle}$ calculated by the two methods are similar, despite of the less precise bubble tracking option proposed in Chapter 3. As a visual example of the bubble tracking technique, Video 3 of the supplementary material given in Appendix B presents the tracking algorithm developed in Chapter 3 modified to use the bubble identification CNN-based method presented here. However, when analyzing the average

Table 4.3 – Summary of the calculated bubbly flow parameters with the CNN-based method developed in the present work and the analytical method described in Chapter 3.

Exp.	System	j_l [m/s]	j_g [m/s]	$\overline{\langle d_b \rangle}$ [mm]		$\overline{\langle w_g \rangle}$ [m/s]		$N^{total}_{bubbles}$ [-]	
				Anal.	CNN	Anal.	CNN	Anal.	CNN
1	A	$3.09 \cdot 10^{-2}$	$5.89 \cdot 10^{-3}$	1.68	1.70	0.199	0.206	60,754	277,458
3	A		$16.89 \cdot 10^{-3}$	1.47	1.80	0.184	0.187	1,232	283,36
4	A	$21.64 \cdot 10^{-2}$	$5.90 \cdot 10^{-3}$	1.57	1.58	0.402	0.417	16,420	194,785
6	A		$16.65 \cdot 10^{-3}$	1.53	1.71	0.398	0.405	12,459	310,991
7	B	$17.32 \cdot 10^{-2}$	$9.35 \cdot 10^{-3}$	1.60	1.47	0.241	0.243	74,060	215,141
8	B		$19.83 \cdot 10^{-3}$	1.18	1.59	0.258	0.260	42,447	232,257

Source - Developed by the author.

bubble diameter, the deviation between the two methods is significant, and is increased with the j_g, i.e., as bubbles are more clustered in images. The differences of the $\overline{\langle d_b \rangle}$ values between the two methods can arise from three main reasons; i) misidentification of clustered bubbles as single bubbles in the analytical method; ii) insufficient number of bubbles to perform the statistical average and iii) identification of bubbles only in specific locations of the duct (not clustered), introducing a biasing in the calculation of average bubble sizes distribution.

Regarding the first reason, misclassification of the bubbles, the different parameters used to identify single bubbles in the present work, just like in Chapter 3, were corrected defined to avoid this identification of bubble clusters or pairs. In addition, the classification of clustered bubbles as single ones, should trend to increase the average bubble size, which is not observed in the results.

On the other side, according to the results presented Tab. 4.3, there seems to be an insufficient number of bubbles identified by the analytical method, since the CNN-based method capture up to 200.0 times more bubbles, depending on the level of bubble clustering, as for instance in Exp. 3, where bubble overlapping is frequent. In order to better illustrate this difference, Fig. 4.18 show the bubble size distributions, presented as Probability Density Function (PDF) of the equivalent spherical diameter $\overline{\langle d_b \rangle}$, computed by both methods. The BSDs from Fig. 4.18 reveal distinct shape profiles from the two different methods, which, as observed in Tab. 4.3, can be due to an insufficient number of bubbles used in the computation. However, besides the small number of identified bubbles, the identification of bubbles in localized regions of the duct can also explain the difference in the calculated average bubble diameters and the BSD curves. As shown in Fig. 4.16 and also in Video 3 of the supplementary material given in Appendix B due to the

pipe geometry, it is common to find "solitary" bubbles near the lateral extremities of the images, since the cross-sectional area (parallel to the camera lens) of the duct is reduced in this region. Thus, one may expect that the analytical method captures most of the single bubbles near the image extremities, i.e., closer to the duct wall. To investigate this effect, Fig. 4.19 shows a normalized contour plot representing the location where bubbles are identified in an Eulerian frame of reference by the two identification methods. Those contour plots are assembled from the bubble shape projection into a background grid for each filmed frame. After assembling the "count" spatial field for all the processed frames, all the instantaneous fields are summed to a single matrix, which is then normalized by its maximum value to result in fields similar to the ones shown in Fig. 4.19. Therefore, these contours do not represent the actual number of captured bubbles but the regions with high/low provability of capturing bubbles, by each method.

From the comparison of the contour plots of the two different identification methods, it is clear that the analytical identify most of the bubbles at thee side region of the images (near wall regions). Therefore, it is possible to affirm that the CNN-based method used in the present work identifies bubbles in no preferred direction, identifying bubbles in highly-overlapped centre region of the images.

Finally, in order to show the potential of the method in the sense that it is able to adequately capture both velocity and size distributions, even in high concentration of bubbles in captured images, result for bubble velocity vs. diameter are presented in Fig. 4.20. Results for both flow systems, Air/Water and Air/Aqueous glycerol solution, are presented in order to show the potential of the method, recalling that images from system B (Air/Aqueous glycerol solution) were not used for CNN training. It can be observed that, as expected, the quantity of bubbles present affect their rising velocity, for the same liquid superficial velocity. However, a interesting aspect, is that for the case of glycerol solution, rising velocity is only affected by bubble concentration for a certain range of bubbles sizes (1.2 mm $< d_b <$ 2.0 mm). In addition, a change of rising regime is observed in this size range. This aspect is provably related to the internal motion induction of the air within bubbles, due to the higher viscosity of liquid phase, making the bubbles trajectories straighter and suppressing lateral oscillatory motion, as can be observed in Videos 2 and 3 of the supplementary material given in Appendix B.

Figure 4.18 – Bubble size distributions, based on the equivalent spherical diameter d_b, for the experiments listed in Tab. 4.3, from the bubbles identified by the CNN-based method described in the present work and the analytical method described in Chapter 3.

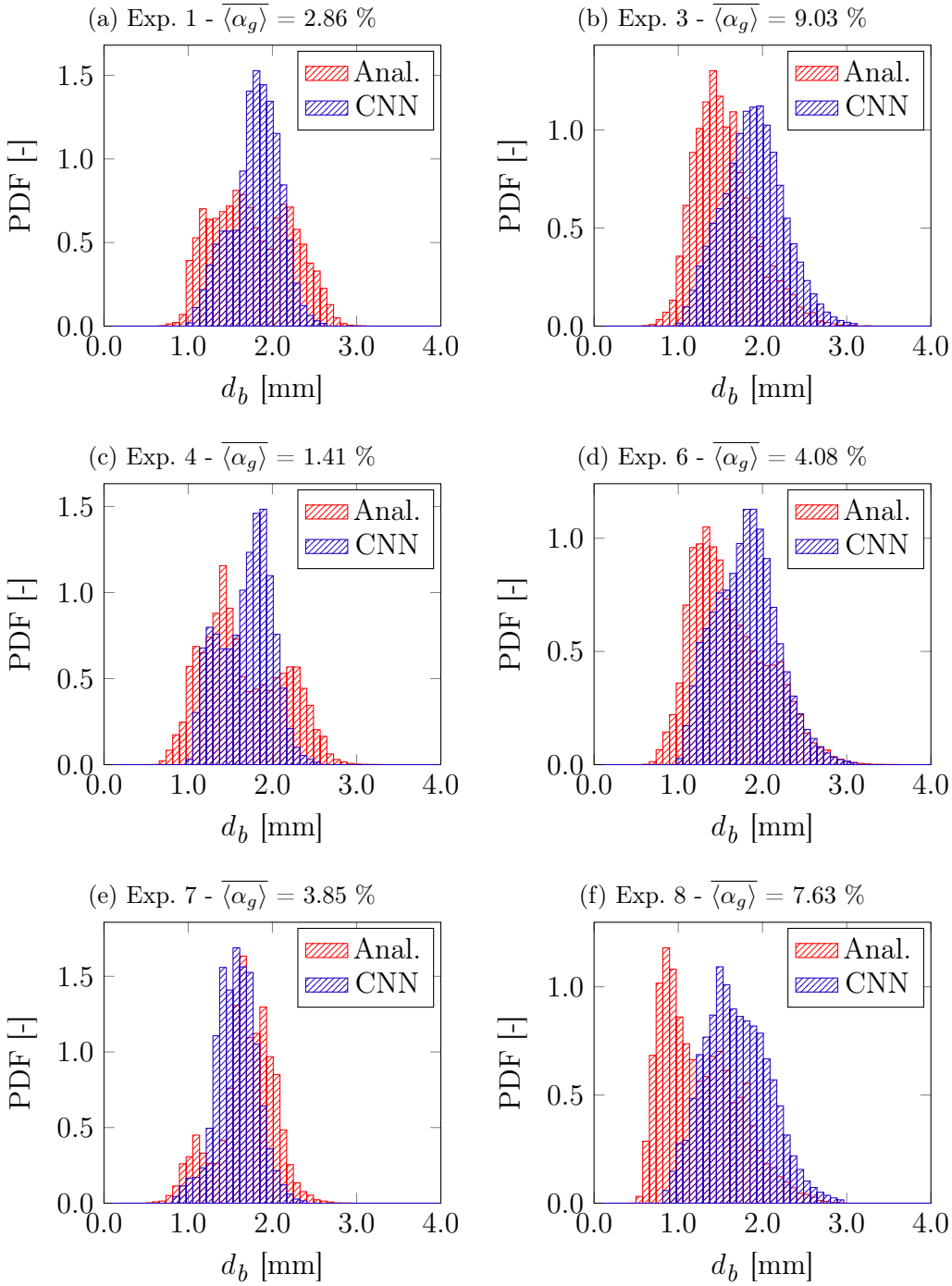

Source - Developed by the author.

Figure 4.19 – Normalized contour plot representing the location where bubbles are identified by the analytical – from Chapter 3 – (left) and the CNN-based (right) identification method. The values were normalized by the maximum count of capture bubbles by each method. Values closer to 0.0 represent a small probability of bubble identification in the region and 1.0 the opposite.

(a) Exp. 3 - $\overline{\langle \alpha_g \rangle} = 9.03$ %

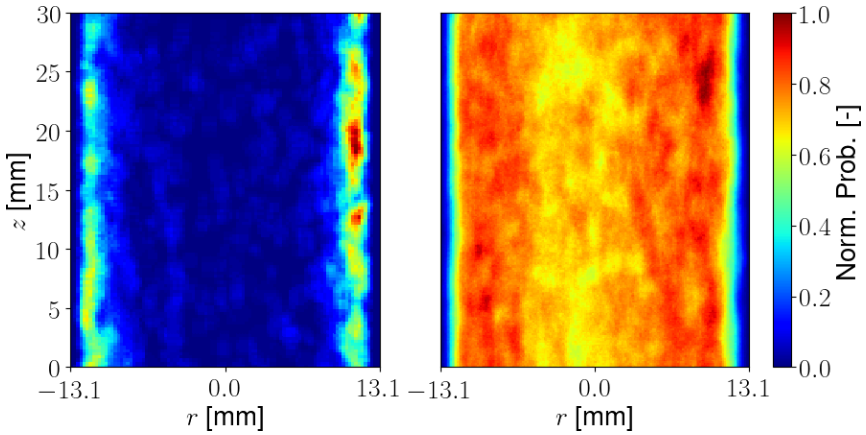

(b) Exp. 6 - $\overline{\langle \alpha_g \rangle} = 4.08$ %

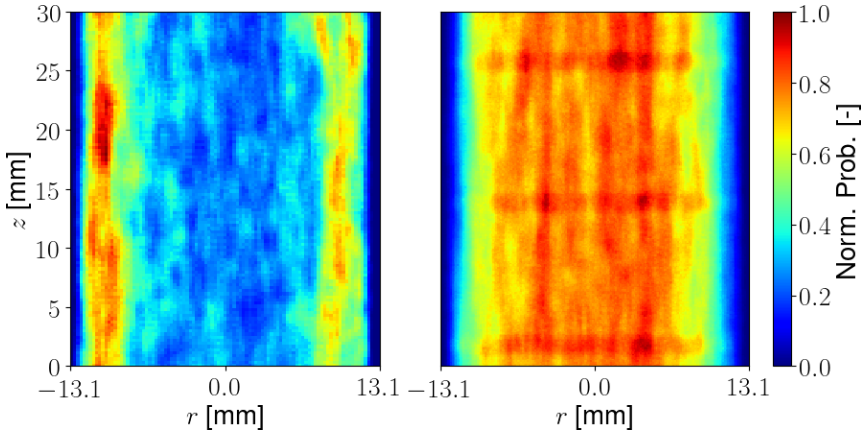

(c) Exp. 8 - $\overline{\langle \alpha_g \rangle} = 7.63$ %

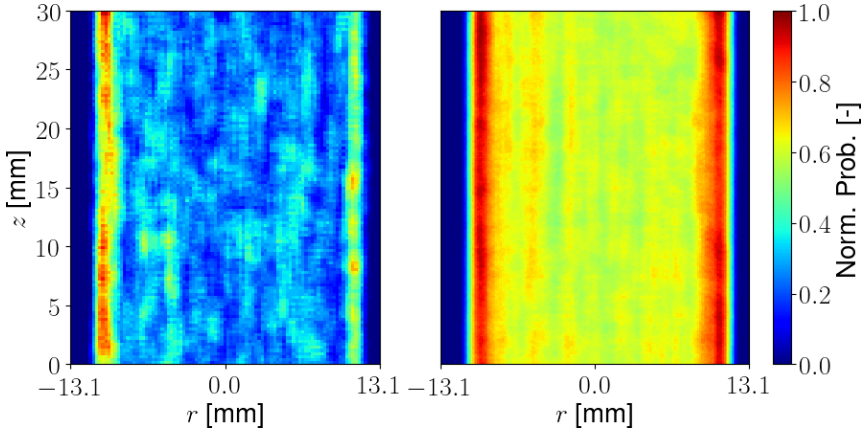

Source - Developed by the author.

Figure 4.20 – Bubble velocity vs. bubble size for different experiments of Tab. 4.1.

(a) System A - $j_l = 3.09 \cdot 10^{-2}$ m/s

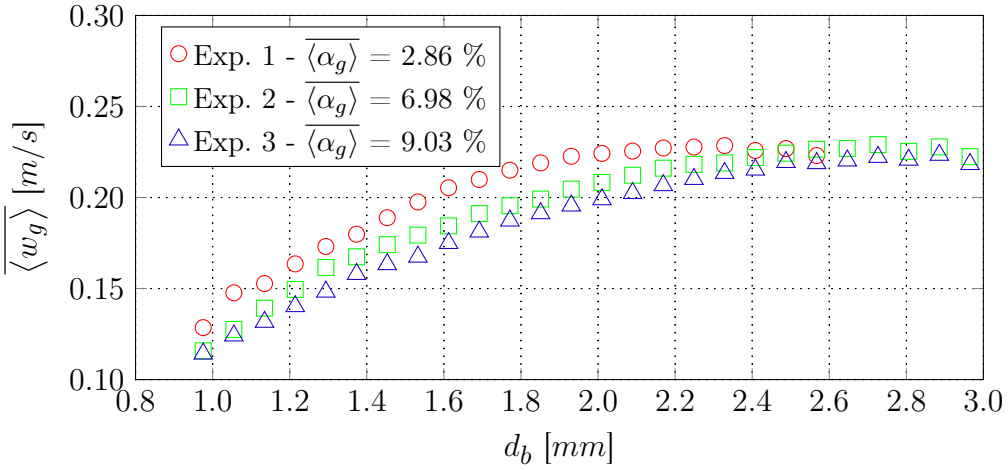

(b) System B - $j_l = 17.32 \cdot 10^{-2}$ m/s

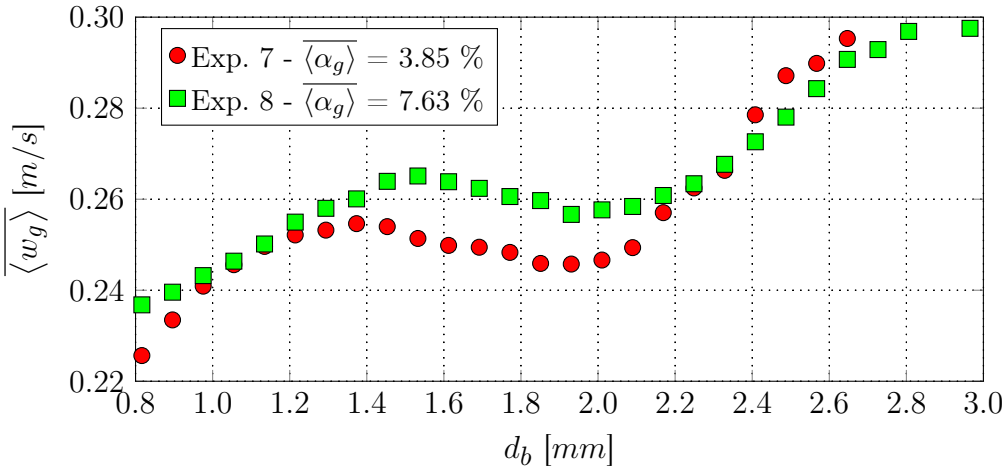

Source - Developed by the author.

4.6 CONCLUSIONS

In this chapter, motivated by the recent advances in the field of Deep Learning applied to image identification, a CNN-based algorithm was developed to identify and reconstruct the shape of bubbles in dense bubbly vertical pipe flows through high-speed camera imaging. The developed method was implemented as an extension of the PTV method presented in Chapter 3, described in the previous chapter, aiming the bubble shape reconstruction in highly bubble overlapping images of bubbly flows. Experiments were conducted with two gas/liquid systems, with the first being an air-water configuration, while the second an aqueous air-aqueous glycerol configuration. The second system was not used for CNN training/testing but the method was perfectly capable of capturing bubbles in this different system, showing its good performance.

In order to identify the bubble images and further reconstruct its shape, a methodology based in anchor points and boxes was adopted, where a single anchor point contained the information of different anchor boxes with different sizes. The bubble shape was approximated by an ellipsoid, and its definition was based on the pixel intensity distribution of the image constrained by the different anchor boxes. For a given anchor point, different ellipsoidal shapes were suggested as bubble shape estimators and were correctly chosen by a trained CNN. The data sets used for the CNN training and validation steps used only air-water configuration, while the aqueous glycerol experiments were used to asses the accuracy and generalization of the proposed CNNs.

An analysis of the hyperparameters was conducted to find the optimal CNN architecture, which correctly reconstructed the shape of the largest number of bubbles on the images with a good level of confidence. From this analysis, the set of options which resulted in the best accuracy among all the trained options was chosen as the optimal CNN architecture. This CNN was tested in the different bubbly flow experimental conditions, varying the superficial velocities and gas/liquid system configurations. Those tests revealed that the CNN could identify and capture most of the filmed bubbles, even in dense bubbly flow configurations, where the gas volume fraction was up to 9.0 % and long chain of overlapped bubbles were present in the high-speed camera images. The results from the CNN-based bubble shape estimator were verified with manually extracted data through the comparison of the bubble size distributions, resulting a good agreement between the two distributions. Additionally, the CNN also presented excellent results in the air-aqueous glycerol configuration, which was not used during the CNN training steps.

The CNN-based method was used to compute typical bubbly flow characteristic parameters, and its results were compared to the ones obtained from the PTV method

presented in Chapter 3. According to the results, the bubble velocities from both methods presented similar results, even for highly overlapped bubbly flow configurations. This first result was expected since the method proposed in Chapter 3 used the internal contours of the bubbles for tracking its motion and was not highly affected by frequent bubble overlapping.

However, the bubble size distribution resulted in distinct values from the two methodologies. The analytical method from Chapter 3, described in previous chapter, does not capture a sufficient number of bubbles to result in statistically consistent values. The bubble size distributions from both methods were also compared, with both methodologies resulting in different distributions, with the CNN-based presenting distribution profiles closer to what is observed in the high-speed camera footages. Moreover, it was suggested that the analytical bubble identification method identified bubbles in preferred regions of the acquired regions, due to bubble overlapping. According to results, the CNN-based method, developed in the present work, did not identify bubbles in preferable regions and resulted in spatial distributions similar to those found in the literature for gas-liquid vertical bubbly flows.

From the results and discussions in this chapter, the CNN-based method developed present superior results to the methods for bubble identification and shape estimators found in the literature. Thus, deep learning methods can be seen as a powerful tool in image analysis, and its applications must be further explored. Moreover, the CNN-based bubble shape estimator developed in the present work can be used to characterize bubbly flows in details, whose analysis can be employed on a better comprehension of flow details and can be used for the development of closure models for CFD application and their validation.

Chapter 5

Experimental Apparatus and Flow Instrumentation for the Investigation of Quasi-Real Slug Flows in Vertical Ducts

This part has been published as:
CERQUEIRA, Rafael F. L. et al. Experimental apparatus and flow instrumentation for the investigation of a quasi-real slug flows in vertical ducts. Experimental Thermal and Fluid Science, v. 102, p. 421-451, 2019.

ABSTRACT

This chapter presents the description of the experimental apparatus, instrumentation, and processing techniques developed for the study of quasi-real slug flow using Particle Image Velocimetry, High-Speed Camera and Laser Diode Photocell techniques. Most experimental studies of the flow fields around Taylor bubbles, aiming a deeper insight into slug flow pattern, analyze the situation of isolated Taylor bubbles rising in stagnant or co-current liquid flow. Furthermore, most of these studies, consider highly viscous fluids (or, in general, low values of the inverse viscosity number, $N_f = \sqrt{\rho^2 g D^3/\mu^2}$), to get "well behaved" Taylor bubbles, where flow fields are more easily measured. However, in most industrial situations slug flows are characterized by the presence of small dispersed bubbles in the liquid stream flowing together with large Taylor bubbles, and high values of the inverse viscosity number. On the other hand, the chaotic nature of a real slug flow would

not allow an adequate characterization of the flow around single Taylor bubbles, mainly, due to the lack of the repeatability of the flow field measurement, making difficult the calculation of the averaged fields. Thus, in this work, a specific experimental apparatus and instrumentation were developed, which allows the study of the flow around Taylor bubbles with and without dispersed small bubbles in the liquid stream under controlled conditions. This allows the PIV measurements, around Taylor bubbles in flows with high N_f numbers, be done under repeatable conditions and thus, the determination of the averaged flow fields. The laser diode photocell technique is used to synchronize the PIV system with the passage of Taylor bubbles at the test section as well as to measure the terminal velocity and length of Taylor bubbles. A dynamic masking procedure was developed to mask out the Taylor bubbles noses and tails in the PIV images, since, for high values of the inverse viscosity number ($N_f \approx 13275$) the interface fluctuations are strong and, therefore, no fixed masking can be used.

5.1 INTRODUCTION

The measurement of flow variables in two-phase gas-liquid flows has been a challenging task for scientists and engineers over decades. The highly transient behavior and strong spatial variations of these flows lead to the need of some kind of averaging in order to get consistent values of the measured variables, which can be used for models closure and/or validation. In general, averaged fields from instantaneous measurements can give a more meaningful representation of the flow behaviour in two-phase flows, and averaged data is more suitable for the development of closure relations.

Among the flow patterns encountered for gas-liquid flows in ducts, the slug pattern has drawn special attention of researchers mainly because of its intermittent characteristic which, in oil production systems, can be associated to difficulties in control system operations due to the strong pressure and velocity fluctuations and system damage in the case of sever slug conditions. Additionally, this intermittent characteristic brings additional difficulties in measuring flow variables for this flow pattern.

As depicted schematically in Fig. 5.1, the slug flow in vertical ducts consists of long bullet shaped bubbles, called Taylor bubbles, followed by liquid slugs, typically, containing dispersed small bubbles. The region between the nose of one Taylor bubble and the nose of the subsequent one is called slug unit, and the whole flow can be outlined as a sequence of several slug units. As Taylor bubbles travel faster than the liquid phase, the liquid is displaced and flows back through a thin film around the Taylor bubble. This film expands at the bubble rear, generating a recirculation pattern. The length and

intensity of these recirculations can be associated with global flow parameters, as Taylor bubble velocity and heat and mass and transfer coefficients in the liquid slug region. In addition, the transfer coefficients at the Taylor bubble nose and film, are also associated with the velocity profiles at those regions. Thus, in order to get a deeper insight of this flow pattern, several researchers presented experimental studies and techniques aiming the detailed measurement of the flow fields around Taylor bubbles, most of them using Particle Image Velocimetry techniques - PIV (BUGG; SAAD, 2002; VAN HOUT et al., 2002c; NOGUEIRA et al., 2003; SOUSA et al., 2005; NOGUEIRA et al., 2006b; SOUSA et al., 2006b, 2006a; SANTOS; COELHO PINHEIRO, 2014).

However, these works consider a very simplified figure of the flow around Taylor bubbles, particularly, when compared with the flow of these bubbles in real slug flow. The main aspect which, to the knowledge of the authors, has not been taken into account in previous experimental research works, is the presence of small dispersed bubbles in the liquid stream. In real slug flows, a significant fraction of these small bubbles remains as a dispersed phase flowing in the liquid slug and around Taylor bubbles. This is substantially different from the flow of Taylor bubbles in liquid without small dispersed bubbles in the flow, which is also called Taylor flow. In real applications, Taylor flow is usually encountered in mini and microchannels, or in cases of very low superficial liquid velocities, which promotes the coalescence of small bubbles. In addition, most of these previous studies usually consider very low values of the inverse viscosity number which is defined as, $\mathrm{N}_f = \sqrt{\rho^2 g D^3/\mu^2}$, where ρ and μ are the liquid density and viscosity, respectively, D is the pipe diameter and g is the gravity acceleration, and represents a relation between gravitational and viscous forces. Recalling that gravity is the driving force for the Taylor bubbles displacement, relative to the liquid stream, this number can be also related to the bubble Reynolds number ($Re = \rho_L U_{tb} D/\mu_L$), based on its velocity (in fact, $\mathrm{N}_f = \rho_L U_{tb} D/\mu_L \times \sqrt{gD}/U_{tb} = Re/Fr$) and thus, it is related to the fluctuating behaviour of the liquid phase flow. When N_f is set to low values, flow is stable (and, thus interfaces) and instantaneous velocity fields or averages of a low number of instantaneous fields can give a consistent representation of the flow structure around Taylor bubbles. On the other hand, large values of the inverse viscosity number, which are common in real slug flows, lead to strongly fluctuating flow, mainly in the tail region of the Taylor bubbles. According to Campos and Carvalho (1988), for values of $\mathrm{N}_f > 1500$ the viscous forces are no longer sufficient to stabilize the liquid jet expanding from the film, creating a turbulent wake behind the Taylor bubble tail. This wake induces fluctuations in the tail region, generating very unstable Taylor bubble shapes, also leading to eventual break-up of Taylor bubbles (MORGADO et al., 2016). The presence of dispersed bubbles in the liquid stream

increases further these fluctuations. In these cases, a large number of instantaneous fields is necessary to get a consistently averaged flow field around Taylor bubbles.

Figure 5.1 – Schematic representation of a slug unit.

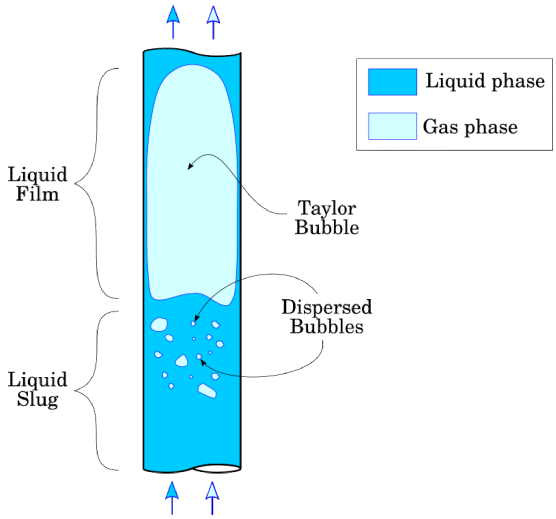

Source - Developed by the author.

Van Hout et al. (2002c) used the PIV technique to study the induced flow by the passage of Taylor bubbles in stagnant water, in a 25 mm ID duct ($N_f = 12300$), reporting the use of about 100 instantaneous fields for the calculation of the averaged fields. In this work, despite the results presented of the averaged velocity field around the Taylor bubbles nose and tail region, there is no discussion about the masking procedure used to remove the Taylor bubbles from the PIV images.

Nogueira et al. (2003, 2006b), using the PIV technique, presented results of the flow fields around Taylor bubbles in stagnant and co-current liquid flow for N_f ranging from 17 to about 18,000. They reported the use of 7 to 20 instantaneous fields for the calculation of averaged fields. Nevertheless, even for relatively low values of $N_f \approx 800$, visual observation of the vector fields and streamlines show the presence of several fluctuations, indicating that those fields are far from being representative of the averaged ones. To remove the Taylor bubbles from the PIV velocity fields, the authors use the Pulsed Shadowgraphy Technique (PST), which produces "binary masks" from the perpendicular projection of the Taylor bubbles into the camera plane. However, for high values of N_f, the interface fluctuations are highly three-dimensional, and the bubble projection using back-light illumination, could not be representative of the interface position at the measurement plane.

Mayor et al. (2007, 2008) used a technique based on image analysis for the calculation of flow parameters of real slug flow, as Taylor bubbles velocities, sizes and frequencies.

In a more recent work, Santos and Coelho Pinheiro (2014) investigated the effect of gas expansion into the flow structure around Taylor bubbles, using PIV and shadowgraphy (backlight illumination) for masking.

In this chapter, the experimental apparatus used to generate and analyze a "quasi-real" slug flow pattern is described. Through this experiment, the flow structure around single Taylor bubbles flowing into a co-current air-water bubbly flow stream, is studied. This approach allows the study of a flow type with gas phase structures similar to those found in real slug flow, where gas-liquid interfaces of different length scales co-exist, but with controlled conditions, which include constant Taylor bubbles length and fraction of dispersed in the slug region. In order to analyze the flow around single Taylor bubbles under repeatable conditions in flows with high inverse viscosity numbers ($N_f \approx 13275$) and the presence of dispersed bubbles, instrumentation and processing techniques were specifically developed to assure the calculation of consistently averaged fields in several flow conditions. The laser-photocell diode (LDP) technique was used for the synchronization of the PIV system and the passage of Taylor bubbles in the measurement section. This technique was also used for measuring Taylor bubbles length and velocity. In order to verify the accuracy of the LDP measurements, the results were compared with ones obtained with a high-speed camera.

A dynamic masking procedure was developed to remove the Taylor bubbles from the PIV images, since the PST technique described in (NOGUEIRA et al., 2003, 2006b) is not suitable in the presence of dispersed bubbles due to the superposition of Taylor and dispersed bubbles shadows on the camera plane. This masking technique was combined with a technique for the discrimination of the dispersed bubbles, described in Chapter 3, allowing for the measurement of the liquid phase velocity. The proposed experimental set-up, where a flow of large and small bubbles under controlled conditions can be generated, and the dynamic masking procedure, which made possible the PIV measurements in these flow conditions, are considered the main contributions of this chapter. In addition, the treatment of LDP signal was performed in a different way from previous works. In order to deal with the presence of dispersed bubbles, an analysis based on high-speed camera images was also incorporated, to validate the presented techniques. Due to the complexity associated with the implementation of these experimental techniques, a large part of this chapter is dedicated to the description and validation of these techniques.

In the next sections, the experimental apparatus, the image processing techniques and the instrumentation used for this research are reported.

5.2 EXPERIMENTAL APPARATUS

This section describes the experimental apparatus used in this research. This system is based on the modification of the flow circuit described in Chapter 3, and allows for the generation of a single phase liquid stream or bubbly flow in a straight vertical duct where Taylor bubbles, with controlled size, are injected. In Chapter 3 the flow system and PIV and PTV (Particle Tracking Velocimetry) measurement techniques, which will be used together with additional techniques presented in this chapter, were carefully verified and validated for bubbly flows. In this configuration, the superficial velocities of liquid and dispersed bubbles phase can be independently controlled, as well as the size and frequency of the Taylor bubbles, which are independently injected into the stream.

These controlled conditions are necessary since, maintaining the sizes, the velocity fields around the different bubbles are expected to be similar except for fluctuations. In real slug flow, although it would be theoretically possible the calculation of averaged velocity fields even if a large number of Taylor bubbles is considered, those averaged fields would be meaningless in terms of mean behaviour of the flow. Therefore, these results would not be useful for CFD model validation and development of closure correlations. Since the instantaneous liquid velocity fields would be averaged over a set of Taylor bubbles with different sizes and velocities, it would not be possible acquire consistent information of the flow structure around Taylor bubbles, in the presence of dispersed bubbles.

Figure 5.2 shows the experimental setup used in this investigation. The transparent pipe of the experimental setup is made of a transparent acrylic, with a internal diameter $D = 26.2$ mm and and $L = 2.0$ m length.

In order to minimize optical distortions, a box constructed with transparent acrylic, made with 8 plane faces, filled with the water is included at the PIV measurement section. The dispersed bubbles are injected at the bottom of the tube, and the gas superficial velocity is measured by two OMEGA FL-3802ST/FL-3861SA flow meters with ranges of 81.4-814.0 standard mL/min and 26.3-263.0 standard mL/min, both with $\pm 2.0\,\%$ full scale accuracy. A needle valve downstream controls the gas flow rate. Pressure and temperature sensors were installed downstream of the gas rotameters to correct the gas superficial velocity due to gas expansion. A porous gas diffuser was installed in the bottom of the tube, in order to control the dispersed bubbles diameters. The reservoir is opened to the atmosphere through a relatively short (≈ 0.5 m) and 50.0 mm internal diameter duct. Thus, it was assumed that the pressure at the test section was close to the atmospheric pressure.

A frequency inverter connected to the electric water pump motor controls the liquid

flow rate. The water flow rate is measured by an OMEGA FL46303 flow meter with a range of 1.00-7.50 l/min with ±5.0 % full-scale accuracy.

Figure 5.2 – Schematic representation of the experimental setup.

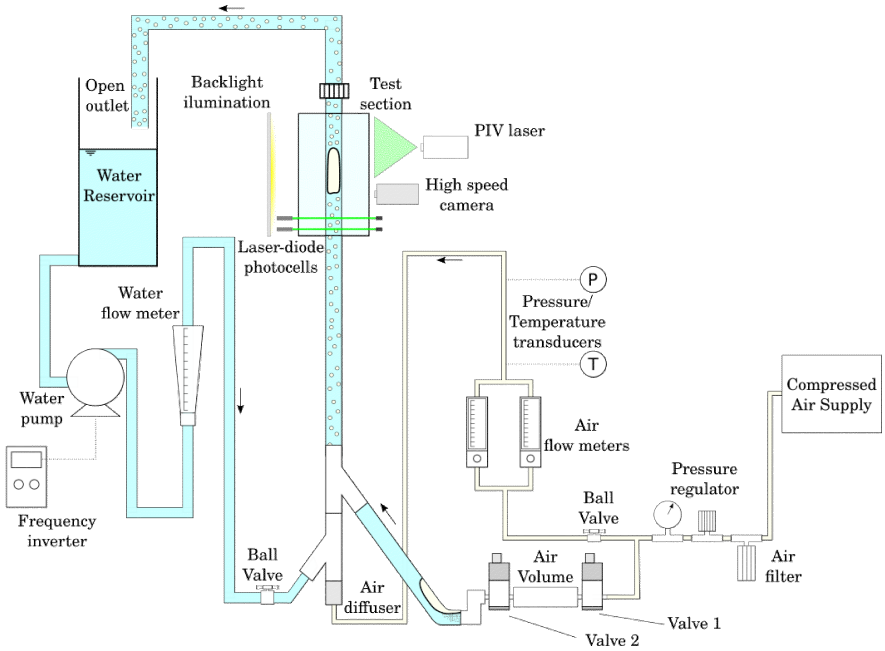

Source - Developed by the author.

The Taylor bubbles are injected through a lateral connection "Y" at the bottom of the column. The injection system is formed by a reservoir with a known volume, which has at its two ends an electronically actuated solenoid valves. From the pressure of the compressed air line, it is possible to control the volume of the Taylor bubble to be injected, since the reservoir has a constant volume. An electronic system controls the injection cycles of the Taylor bubbles, from the valve opening and closing command. The experimental acquisitions are performed during the passage of a single Taylor bubble, where the injection periods are carefully adjusted to avoid flow disturbances caused by the passage of a previous Taylor bubble. This control is necessary, since the present investigation is focused on the flow analysis around a single Taylor bubble. The air-water Taylor flow configuration in 26.2 mm diameter pipe, results in a inverse viscosity number of $N_f = 13275$, which results on the formation of a turbulent wake behind the tail.

Initially, the Valve 1 opens, filling the reservoir with known volume with compressed air at a given pressure. After a specific time, the Valve 1 is closed for equalization of the system pressure and the initially closed Valve 2 is actuated, releasing the volume of air that is led by a hose to the liquid filled duct. In order to improve the injection cycles, the valves opening and closing instants (t_{open} and t_{close}), as well as the time necessary to stabilize the process in the air reservoir ($t_{stab.}$) and the waiting time between

the different generation cycles (t_{wait}), were electronically controlled. The Taylor bubble injection system is controlled by an Arduino UNO R3 Atmega328P, which communicates through an USB interface with a dedicated PC application developed in NI LabView software. By controlling the Taylor bubble injection periods, systematic experimental acquisitions could be performed and its results could be averaged under a large quantity of single Taylor bubbles. Hence, by carefully adjusting the period between the Taylor bubble injections, it was possible to compute consistent ensemble averaged results.

For the high-speed camera acquisitions, a bright white LED array is positioned at the back of the test section, shown in Fig. 5.2, A CCD digital high-speed camera (Redlake MotionPro X3) with 52mm lens was used to acquire the flow images using the LED illumination array, the images were recorded in 256 grey scale levels with image size of 1024 x 1024 pixels with a frame rate of 400 fps. The backlight illumination produces images with high contrast between the liquid and gas phases, which can be used to conduct qualitative and quantitative analysis, such as the Taylor bubble rising velocity, motion and shape.

5.3 INSTRUMENTATION

The main measurement technique used in the investigation developed was the Particle Image Velocimetry - PIV. A high-speed camera was also used to compare the measurements performed with the laser diode technique and to visualize the interactions between large-scale (Taylor) bubbles and dispersed bubbles. One of the main issues in obtaining consistent averaged fields is to capture the velocity fields with the Taylor bubbles all in the same position at the test section. Although it is expected that the time from the bubble release at the injection section to the passage at the test section would be near the same for all Taylor bubbles, as their size is controlled, slight variations of the flow conditions around them induce fluctuations on their terminal velocity, and thus on their position at the test section. Even for stagnant liquid, differences in the position where bubbles were captured are observed. In cases with presence of dispersed bubbles, this effect is even stronger.

However, by definition, the ensemble average must be taken over a set of measurements with the same flow conditions at the same time and position. In this case, this means that the Taylor bubble must be at the same position for all measurements. Therefore, a signal from a laser diode, which was positioned immediately below the measurement section, was used as triggering system to synchronize the passage of the Taylor bubbles at the test section where PIV images are acquired.

Through this approach, it was possible to capture hundreds of PIV images with Taylor bubbles at the same position, as can be observed in Fig. 5.3, allowing for the consistent calculation of averaged velocity fields. The PIV images shown in Fig. 5.3 correspond to a flow situation without dispersed bubbles flows in the liquid stream. For these cases, the synchronization technique has shown efficient for this purpose. A similar approach was used in Van Hout et al. (2002c).

Figure 5.3 – Sequence of PIV images obtained by synchronization with laser diode in the (a) nose region and (b) tail region of Taylor bubbles.

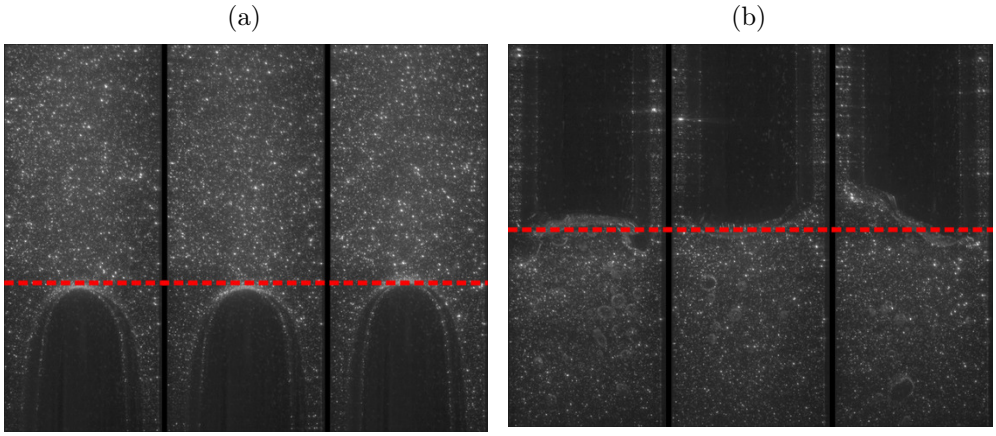

Source - Developed by the author.

As discussed in the Introduction section, for the flow conditions considered in this investigation, the bottom part of the Taylor bubble oscillates, as shown in the PIV images examples in Fig. 5.3b). For these cases, the PIV images are acquired in the same position, but in order to acquire consistent velocity vectors in this region, a dynamic masking is necessary to remove the interrogation windows associated to the inner region of the Taylor bubbles.

In addition, when dispersed bubbles are injected into the flow, due to the stronger velocity fluctuations, the laser diode synchronization cannot ensure the PIV acquisitions with Taylor bubbles at the same position, as shown in Figure 5.4.

Additionally, for the situations shown in Fig. 5.4, the velocity fluctuations generated by the bubble induced turbulence distorts the Taylor bubble noses. In the examples of Fig. 5.3, the Taylor bubbles tips were located near the duct centerline and its shape was constant on all the acquired frames. However, for the cases shown in Fig. 5.4, the strong velocity fluctuations caused by the presence of the dispersed bubbles, gives rise to a “zig-zag” motion and distort the Taylor bubbles noses. For these cases, even a more advanced and precise PIV synchronization method would fail, since the shape of the Taylor

Figure 5.4 – Sequence of PIV images obtained by synchronization with laser diode in the (a) nose region and (b) tail region of Taylor bubbles, where the nose and tail are acquired, but the position differs from frame to frame.

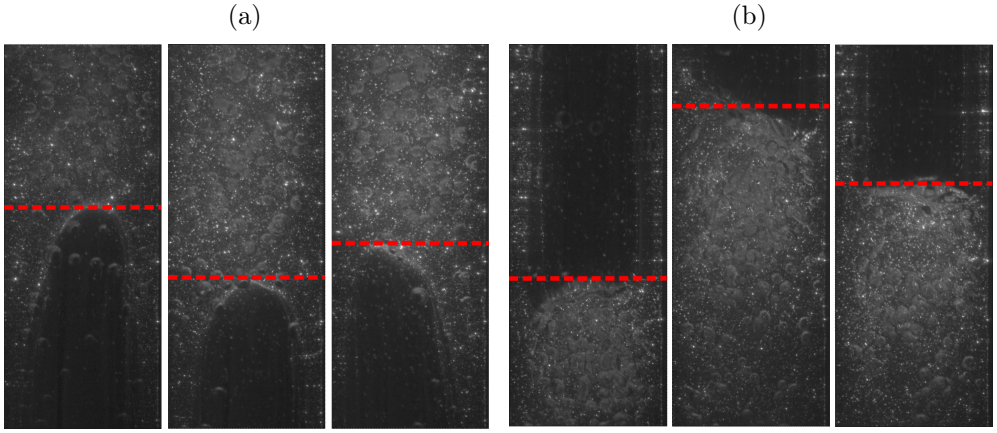

Source - Developed by the author.

bubbles changes dynamically due to the flow conditions considered and the presence of the dispersed bubbles on the stream.

Then, a dynamic masking procedure was implemented to remove the Taylor bubbles from the PIV images, and its details are discussed in Sec. 5.4. In these cases, the dynamic masking procedure is of fundamental importance, not only for the Taylor bubble tail region but also for its nose region.

The laser diode system was also used to measure the velocity and, in some cases, the length of Taylor bubbles. Also, as will be shown in the results section, the laser diode system measurements were validated by comparing the results with the ones obtained from the high-speed camera.

5.3.1 PIV in gas-liquid flows

The PIV technique is largely described in the literature (see, for instance, (RAFFEL et al., 2007)) and will not be detailed here. The PIV system available at SINMEC Lab consists of a 2048x2048 pixels (4 MPx) resolution CCD camera, a pulsed Nd:YAG laser with a wavelength of 532 nm and a synchronizer to match the emission of laser pulses and image capturing, which can be externally triggered.

In applications to gas-liquid flows, the presence of the interfaces, with much larger scales than the seeding particles, scatters the light of the laser with much more intensity than these particles, obfuscating the light scattered by them and preventing the capture by the CCD camera. Eventually, this intense reflection can damage the CCD sensor. As usually

recommended for the application of the PIV technique in gas-liquid flows, fluorescent seeding particles were used. Particles of Rhodamine B with 10 μm mean diameter were used, capable of receiving light in a wavelength of 532 nm and emit (fluorescence) at 590 nm (peak). A high bandpass filter for the wavelengths above 545 nm is used at the camera lens, filtering all the light at the laser wavelength (the same scattered by the interfaces) and capturing the light fluoresced by the seeding particles.

Despite the use of the fluorescence technique, in the case of the presence of small dispersed bubbles, some interrogation windows occupied by bubbles produce acceptable vectors due to the cross-correlations algorithms used in the PIV technique. This sort of error can introduce errors in the velocity field, generating inconsistent averaged results. In order to overcome this problem, the technique developed in Chapter 3 is used to remove the bias introduced by the dispersed gas phase, from the PIV results.

The PIV system is triggered when a Taylor bubble passes at the test section, where the CCD camera is pointed to, through the synchronization with the laser diode. In order to have a better resolution, the nose and film regions were studied separately from the tail region. The synchronization system is adjusted to trigger the PIV with different relative positions of the Taylor bubbles, depending on the region to be investigated, as can be seen in Figures 5.3 and 5.4.

5.3.2 The laser diode photocell technique

As mentioned in previous sections, laser-diode photocells (LDP) were used to trigger the PIV system synchronizing with the passage of the Taylor bubbles at the test section and to measure the Taylor bubbles lengths and velocities.

Two laser diodes were disposed perpendicularly to the duct, at a known distance L_{LDP}, as shown schematically in Fig. 5.5. Each one consists of a low power continuous laser, which emitted a beam with approximated 50.0 mm, and a photodetector (a Light Dependent Resistor, LDR). In this work, instead of using a TTL based optical probe (e.g., an Optpschmitt sensor), an LDR is used to detect the bubble passage. This approach generates an analog continuous and differentiable signal, which makes it possible to distinguish the passage of the large scale Taylor bubbles and the small scale dispersed bubbles which are injected in the flow stream.

The electronic scheme of the data acquisition system is shown in Figure 5.6.

It consists of an Arduino UNO R3 Atmega328P with 10-bit analog ports, A0 to A5, and digital ports. The maximum reached acquisition rate of the analog ports was 120Hz. Thus a simple and inexpensive card could be used. The card is connected to the

Figure 5.5 – Schematic representation of the laser diode positioning in the test section, illustrating three distinct moments: a) moment before its detection of the laser-diode photocell sets; b) detection of the Taylor bubble by the photodetector 1 (LDR1) and c) detection of the Taylor bubble by the photodetector 2 (LDR2).

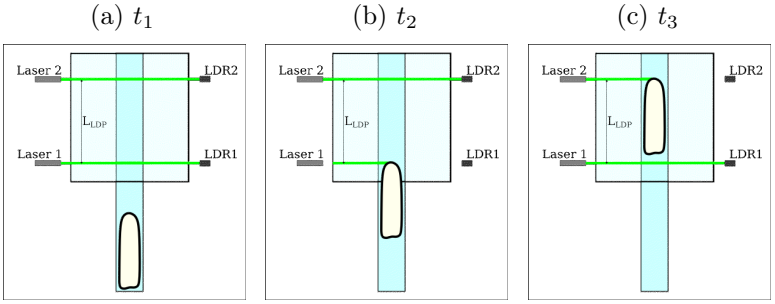

Source - Developed by the author.

Figure 5.6 – Electronic scheme of the data acquisition system.

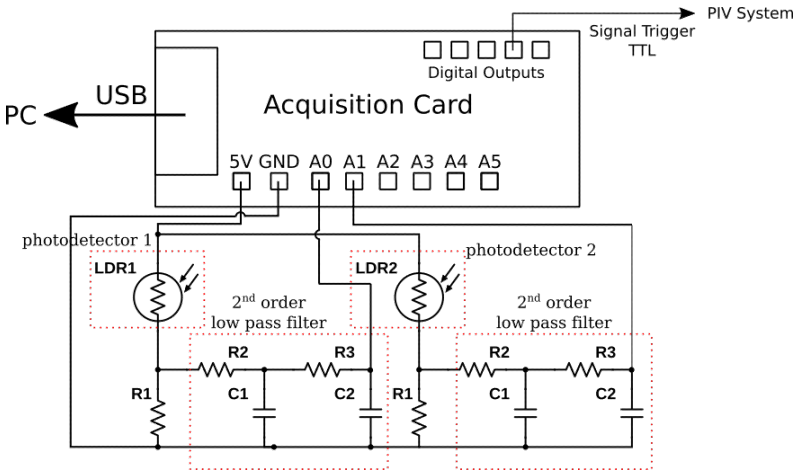

Source - Developed by the author.

PC via a USB interface, communicating with a dedicated application, developed in NI LabView software, to gather, analyze and store data, as well as to report results in an organized way. The two photodetectors (LDR1 and LDR2) and the signal filtering circuit are highlighted in Figure 5.6. The LDR1 and the resistor R1 build together a voltage splitter. When the light of the laser illuminates the LDR1, its resistance stands still at a relatively low value. When the light is deviated by the bubble, the resistance of the LDR1 increases and so the voltage level on R1 decreases, and after a specified delay so does the voltage held by the capacitor C1. The circuit composed by R2, R3, C1, and C2 is a second-order low pass filter. The gathered signal is the voltage held by the capacitor C2, and this is done through the analog input A0. The voltage value of the photodetector second circuit, which is exactly the same as the first, is acquired by the analog input A1.

The trigger signal is sent to the PIV system through one of the digital ports of the card, as shown in Figure 5.6, at the time that the Taylor bubble reaches the Laser 2 (schematically depicted in Fig. 5.5c) and instant $t_{2,2}$ in Fig. 5.5). When a bubble is detected by the second detector (LDR2), the software running in the acquisition card stands for a time delay and then sends the TTL signal. The parameter Δt_{delay} can be adjusted from the developed NI LabView software and controls the interval between the bubble passage and the PIV acquisition. So, the position of the bubbles on the image can be adjusted (to focus the analysis on the nose or tail regions, for instance). Once adjusted, for most of the cases, all bubbles will be captured at the same position. Both detectors can rule the triggering, but due to the strong bubble rising velocity fluctuations, the photodetector closer to the visualization section (LDR2) was used to minimize the errors in the bubbles axial positions.

The LDR signals are affected by the presence of dispersed bubbles. The typical signal provided by both LDR detectors and the high-speed camera footage of the associated flow condition can be observed in Fig. 5.7.

The black dotted lines indicate the signal from the lower detector (LDR1) and the continuous red lines indicate the signal from the upper detector (LDR2). The characteristic behavior of the signal taken from the laser diode photocell can be described by taking the first light detector as an example. When the bubble reaches the diode laser ray 1, the voltage on the capacitor C2 starts to drop (instant $t_{1,1}$). After the bubble leaves the laser ray way free, the capacitor voltage rises again, and (instant $t_{1,2}$).

In order to illustrate the effect of the dispersed gas bubbles on the photodetector signals, Fig. 5.7a) shows the typical signal from an experiment without dispersed bubbles, while Figs. 5.7b) and 5.7c) experiments with different amounts of the dispersed gas phase. From these figures, it is clear that the addition of dispersed bubbles affects the signal to noise ratio from the LDR measurements. This attenuation effect is not observed in previous works since these used optical probes (VAN HOUT et al., 2002a, 2002b) or the same laser-photodetector pair (SANTOS et al., 2008) with a TTL based sensor, which instead of generating lower voltage values, produces high frequency "HIGH/LOW" (square wave) values. However, this technique, probably, could not deal with the presence of dispersed bubbles.

As can be observed in Fig. 5.7a), the signal to noise ratio before the passage of the Taylor bubbles is very high, once the present noise is essentially the thermal noise from the circuit and possibly some environment radiation, which is well treated by the analog and digital filters. Additionally, the desired signal amplitude was correctly designed to provide a suitable signal to noise ratio. On the other hand when dispersed bubbles are present in

Figure 5.7 – Typical signal detected by the two laser-diode system for different flow stream configurations and high-speed camera footage of the flow configuration: a) without the presence of dispersed bubbles; b) with dispersed bubbles injected into the flow stream ($\overline{\langle \alpha_g \rangle} = 1.30\%$); c) with dispersed bubbles injected into the flow stream ($\overline{\langle \alpha_g \rangle} = 4.90\%$).

(a) j_l=0.0 m/s and j_g=0.0 m/s

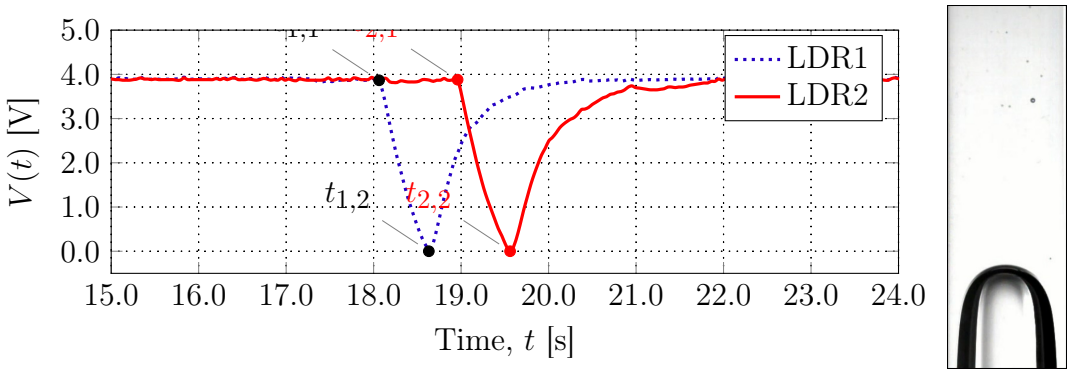

(b) $j_l = 21.64 \cdot 10^{-2}$ m/s, $j_g = 2.38 \cdot 10^{-3}$ m/s and $\overline{\langle \alpha_g \rangle} = 1.30\%$

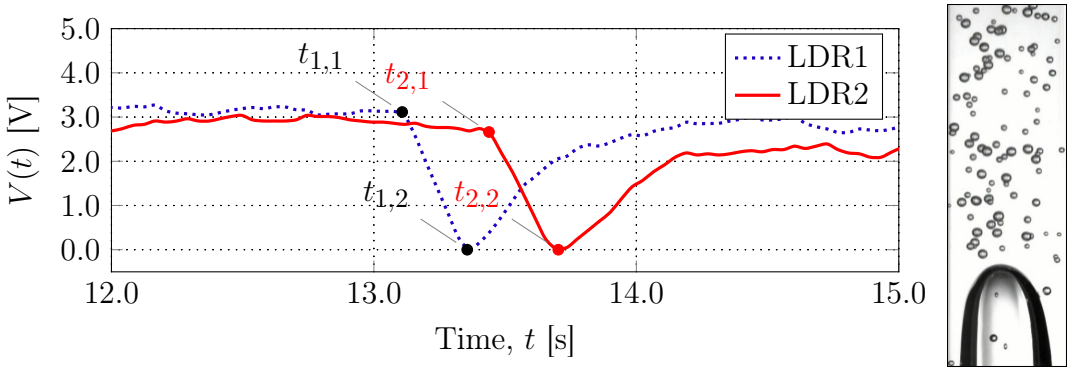

(c) $j_l = 21.64 \cdot 10^{-2}$ m/s, $j_g = 19.83 \cdot 10^{-3}$ m/s and $\overline{\langle \alpha_g \rangle} = 4.90\%$

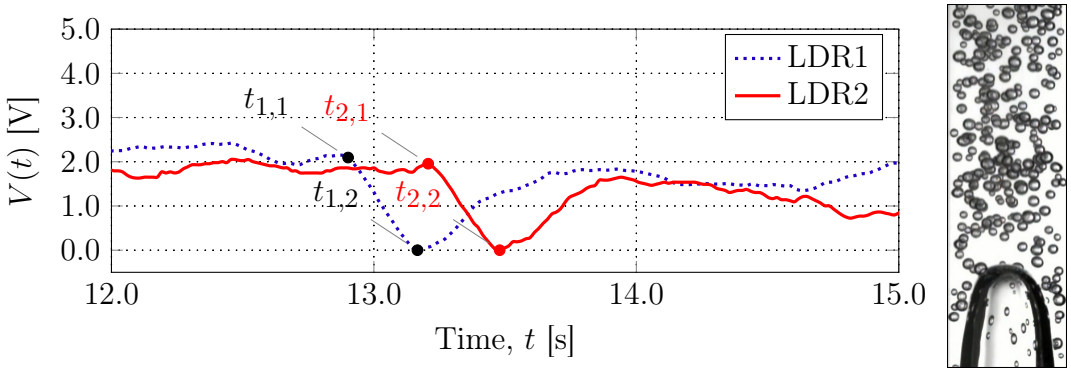

Source - Developed by the author.

the liquid stream, signal to noise ratio is much lower, once small bubbles are also able to deviate the diode laser light and then disturb the gathered signal from each detector. In fact, this is not a "noise" but a physical deviation of the laser light by dispersed bubbles. The net effect of the small bubbles over the signal is to decrease the mean voltage level that exists before the passage of a Taylor bubble.

In order to find the time instants $t_{1,1}$, $t_{1,2}$, $t_{2,1}$ and $t_{2,2}$, the average mean voltage $\overline{V}$ is calculated before the Taylor bubble passage, sampled over a time interval Δt_{avg}. This average mean voltage is sampled 10.0s before the instant $t_{1,1}$ in all cases and can be controlled through the NI LabView software. From the average mean value, the fluctuation $V^{'}(t)$ from the light detectors can be calculated as,

$$V^{'}(t) = \left[V(t) - \overline{V}\right]^2 \tag{5.1}$$

where $V(t)$ is the instantaneous signal acquired by the light detector in a time instant t. Figure 5.8 shows the signal voltage $V(t)$ and its fluctuation $V^{'}(t)$ for the lower photodetector in the case shown in Fig. 5.7c).

Figure 5.8 – The signal voltage $V(t)$ and its fluctuation $V^{'}(t)$ for the lower photodetector in the case where $j_l = 21.64{\cdot}10^{-2}$ m/s, $j_g = 19.83{\cdot}10^{-3}$ m/s and $\overline{\langle \alpha_g \rangle} = 4.90\%$.

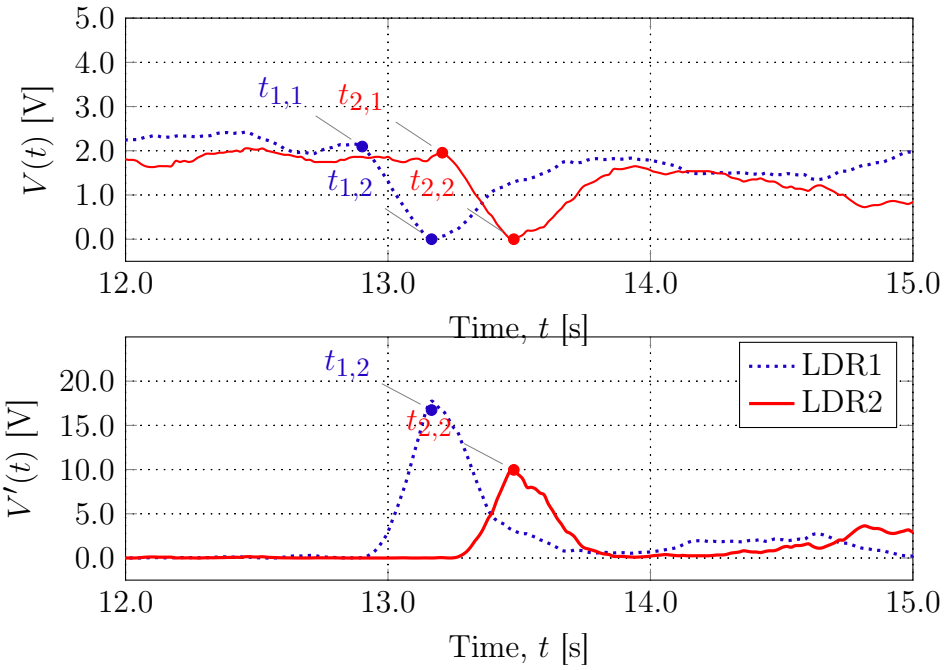

Source - Developed by the author.

From Fig. 5.8 it is possible to conclude that the maximum value of $V^{'}(t)$ coincides with the instant where the laser ray is directly aligned with the LDRs, indicating the passage of the Taylor bubble bottom.

By finding the time instants $t_{1,2}$ and $t_{2,2}$, the nose passage instants $t_{1,1}$ and $t_{2,1}$ are found by marching backward from these points, locating its local maximum value. Once all the bubble passage time instants are found in the light detectors signal, the Taylor bubble nose $U_{tb,N}$ and tail $U_{tb,B}$ rising velocity is calculated. Therefore, this technique can also be used for the calculation of bubble expansion.

The bubble nose and tail velocities can be computed by dividing the distance L_{LDP} between the two detectors, by the time delay between the detection times of a bubble on each detector.

$$U_{tb,N} = \frac{L_{LDP}}{t_{2,1} - t_{1,1}} \tag{5.2}$$

and

$$U_{tb,B} = \frac{L_{LDP}}{t_{2,2} - t_{1,2}} \tag{5.3}$$

By knowing the Taylor bubble velocity, it is possible to calculate its length L_{tb} based on the photodetector analog signal.

$$L_{tb} = U_{tb} \cdot \left(t_{2,2} - t_{2,1}\right) \tag{5.4}$$

Since the expansion effect is small, the L_{tb} based on the nose $U_{tb,N}$ and bottom $U_{tb,B}$ rising velocities is approximately the same. However, as will be discussed on Sec. 5.5, due to the strong fluctuations on the Taylor bubble tail during the upward movement along the duct and the signal attenuation associated with the dispersed bubbles, it is not always possible to calculate the bubble length by the laser diode photocell technique.

In order to compare the laser diode photocell and the high-speed camera results, the results for each experimental condition were calculated by ensemble average, and the evaluation of the uncertainty in measurement followed the guidelines shown in ISO and OIML (1995). The uncertainty analysis for the laser diode photocell technique is presented in **Appendix A**.

Due to its straightforward calculation, the fluctuation $V^{'}(t)$ signal is calculated real-time on the Arduino UNO R3 Atmega328P and send to the NI LabView software, where it is possible to define a $V^{'}$ threshold value that triggers the PIV system. As previously mentioned, the $V^{'}(t)$ fluctuation signal of the photodetector closer to the PIV camera field of view section (LDR2) was used to minimize the errors in the bubble axial positions.

Despite the effort to acquire the bubble passage in a systematic manner, as the fraction of dispersed bubbles is increased, some deviations on the position where the Taylor bubbles are captured in PIV images were observed. These deviations are associated with the large inverse viscosity N_f numbers and the interactions between the Taylor and dispersed bubbles, such as break-up/coalescence phenomena and turbulent fluctuations

induced by the dispersed bubbles. In these cases, a dynamic masking procedure was developed to identify the Taylor bubbles on the PIV images and then mask out the interrogation windows associated with them. The dynamic masking procedure is detailed in the next section.

5.3.3 High-Speed Camera Image Analysis

In order to validate the Laser Photocell Technique (LDP) and the PIV dynamic masking results, a high-speed camera image analysis was used to measure bubbles rising velocities, and lengths. The high-speed camera image analysis is detailed in Cerqueira et al. (2018b) and will be briefly described in this section. The methods described in Cerqueira et al. (2018b) incorporates the Taylor bubble tracking methods described in Mayor et al. (2007), which can be used to precisely estimate the Taylor bubble length and nose velocity. Additionally, the method developed in Cerqueira et al. (2018b) can also estimate the Taylor bubble bottom velocity and its nose shape.

A CCD digital high-speed camera (Redlake MotionPro X3) with 52mm lens was used to acquire the flow images using the LED illumination array. The images were recorded in 256 grey scale levels with an image size of 1024 x 1024 pixels and a frame rate of 800 fps. A bright white LED array is added at the back of the test section shown in Fig. 5.2, resulting in images similar to the ones shown in Fig. 5.9, where the contrast difference enables the discrimination of the two phases.

In order to identify the Taylor bubble on the acquired high-speed images, the procedure described by Mayor et al. (2007) and illustrated in Fig. 5.10 is applied. As seen in Fig. 5.10, the image processing algorithm allows the exact identification of the Taylor bubble nose and bottom position and the nose shape coordinates in a specified frame.

Due to the presence of the dispersed bubbles in the Taylor bubble tail region, the procedure fails in some cases. Examples of this problem in the binarization step are shown in Fig. 5.11, where the filling/inversion operation fails to acquire a closed contour inside the Taylor bubble.

In Mayor et al. (2007) the authors apply an additional erosion filter to "filter out" the dispersed bubble in the region and hence define the Taylor bubble bottom position. However, since the additional erosion filter was not capable of removing these spurious contributions from the Taylor bubble images, an alternative method was used to define the bottom position. The method is based on the pixel intensity profile along the bounding rectangle's center which encloses the largest contour of the filled image, as seen in Figs. 5.11 and 5.12. Figure 5.12 illustrates the method, which shows the average pixel distribution

Figure 5.9 – Typical high speed cameras obtained with the backlight illumination arrangement for different flow configurations: a) $j_l = 21.64 \times 10^{-2}$ m/s and $j_g = 0.0$ m/s; b) $j_l = 21.64 \times 10^{-2}$ m/s, $j_g = 2.38 \times 10^{-3}$ m/s and $\overline{\langle \alpha_g \rangle} = 0.7$ %; c) $j_l = 21.64 \times 10^{-2}$ m/s, $j_g = 19.83 \times 10^{-3}$ m/s and $\overline{\langle \alpha_g \rangle} = 4.9$ %.

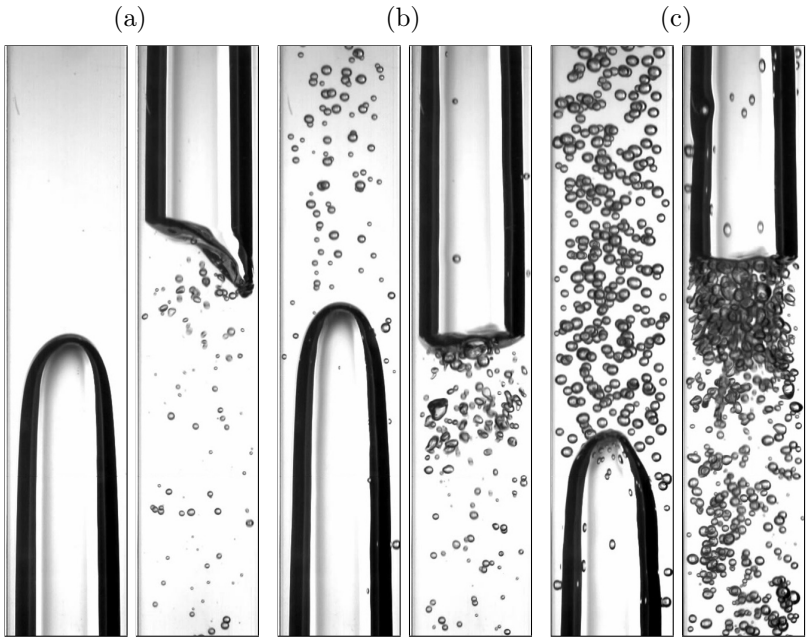

Source - Developed by the author.

on the highlighted area and the corresponding nose and bottom position project on the raw high-speed camera images.

For the bubble nose shape extraction, the external contour outline of the filled image is used. To avoid problems associated with the dispersed bubbles in the liquid film, only the contour outline below a certain distance of the nose is extracted, while the remaining is discarded. Additionally, since dispersed bubbles penetrate the liquid film, it is necessary to perform a curvature analysis in the extracted Taylor bubble nose shape coordinates, since its presence affects the binarization step in this region. In Fig. 5.11 this is shown by the red and green nose shape outlines, where the green is classified as a "valid" Taylor bubble (Fig. 5.11a)) outline and red is discarded (Fig. 5.11b)).

Figure 5.13 shows the Taylor bubble nose shape outline, the bottom and nose position in different times instants for a case with dispersed bubbles in liquid stream, with a void fraction of dispersed bubbles of $\overline{\langle \alpha_g \rangle} = 4.9$ % ($j_l = 21.64 \times 10^{-2}$ m/s and $j_g = 19.83 \times 10^{-3}$ m/s).

From the bottom and nose position at different times, it was possible to compute the Taylor bubble nose and tail velocities in a single experiment and also define its length. A visual demonstration of this procedure can be seen in Fig. 5.14, where the linear slope

Figure 5.10 – Schematic representation of the image filtering/processing steps used to identify a Taylor bubble from the high speed camera acquisitions.

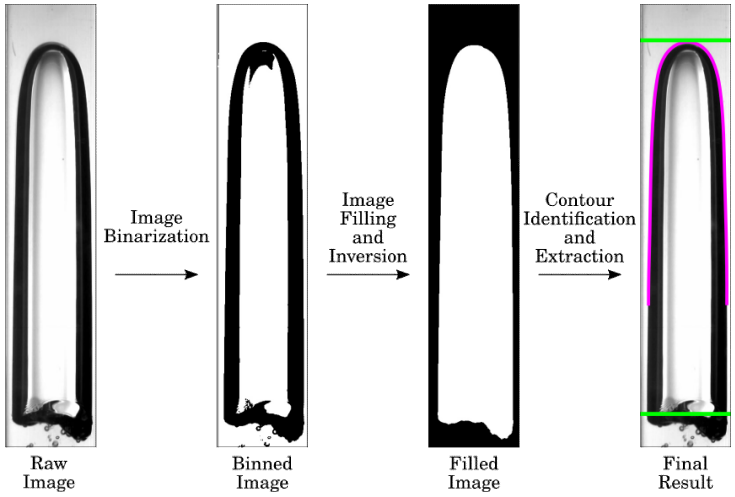

Source - Developed by the author.

approximation results in the Taylor bubble rising velocities. It is important to state that for the cases with dispersed bubbles, such as the one shown in Fig. 5.14, that it is not possible to acquire the nose and bottom position all the analyzed frames. Thus, the points in Fig. 5.14 are not continuous samples.

The method described in this section is coupled with the PTV techniques described in the previous chapters. In order to visualize the coupling between the Taylor bubble tracking and the bubbly flow PTV, Video 4 of the supplementary material given in Appendix B presents the results from the coupled tracking techniques.

Figure 5.11 – Binarization and filtering problem caused by the presence of the dispersed bubbles in the tail region for different flow configurations: a) $j_l = 21.64 \times 10^{-2}$ m/s, $j_g = 2.38 \times 10^{-3}$ m/s and $\overline{\langle \alpha_g \rangle} = 0.7$ %; b) $j_l = 21.64 \times 10^{-2}$ m/s, $j_g = 19.83 \times 10^{-3}$ m/s and $\overline{\langle \alpha_g \rangle} = 4.9$ %. The images also show the extracted nose shape, highlighting the presence of a dispersed bubble in the liquid film region in b).

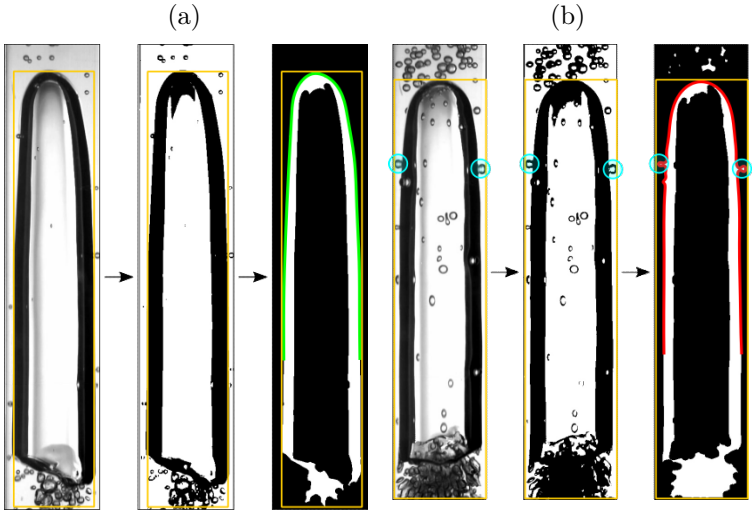

Source - Developed by the author.

Figure 5.12 – Schematic representation of the image filtering/processing steps used to identify a Taylor bubble from the high speed camera acquisitions.

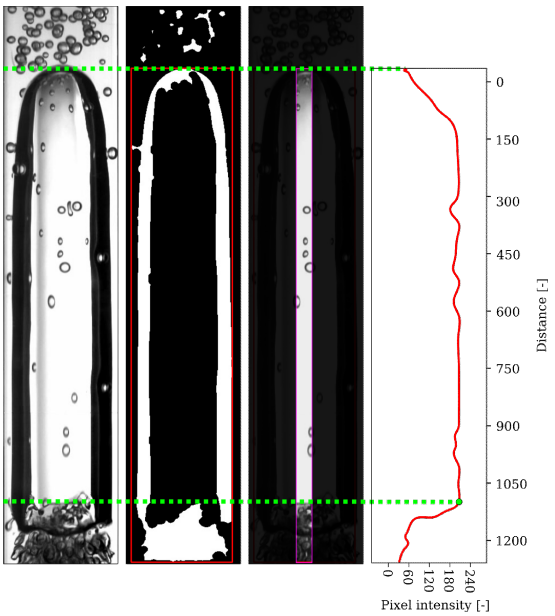

Source - Developed by the author.

Figure 5.13 – Taylor bubble rising motion in the "quasi-real" slug flow regime with a void fraction of $\overline{\langle \alpha_g \rangle} = 4.9$ % ($j_l = 21.64 \times 10^{-2}$ m/s and $j_g = 19.83 \times 10^{-3}$ m/s)

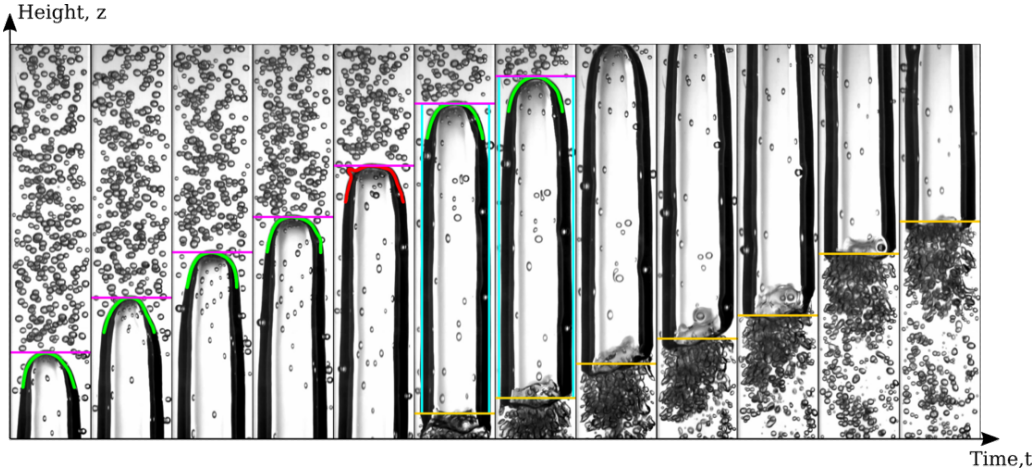

Source - Developed by the author.

Figure 5.14 – Taylor bubble nose and bottom position from the high-speed camera images in different time instants for the $j_l = 21.64 \times 10^{-2}$ m/s, $j_g = 19.83 \times 10^{-3}$ m/s and $\overline{\langle \alpha_g \rangle} = 4.9$ % flow condition. The filled points represents the data obtained from the developed algorithm and the dotted lines its linear fit regression.

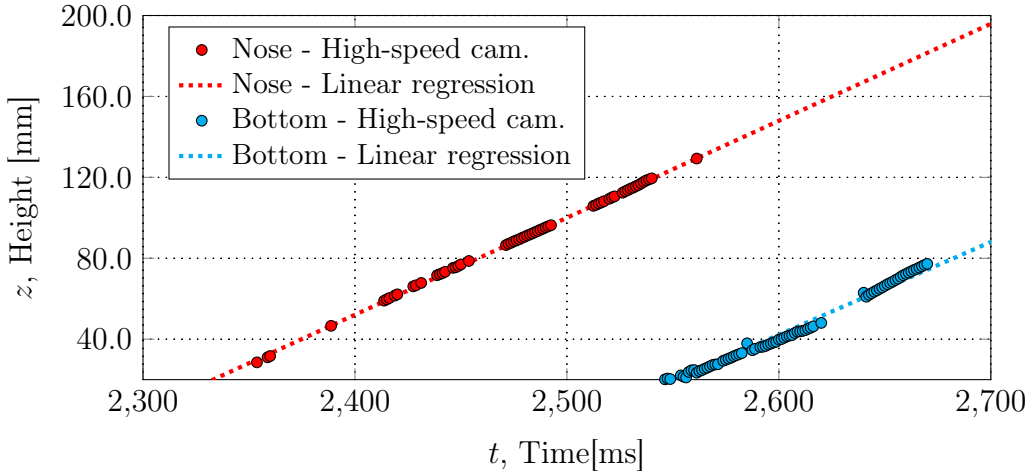

Source - Developed by the author.

5.4 DYNAMIC MASKING PROCEDURE FOR THE TAYLOR BUBBLE IDENTIFICATION IN THE PIV/LIF TECHNIQUE

As discussed on the previous paragraphs, due to the high inverse viscosity number N_f and the presence of the dispersed bubbles on the flow stream, the laser diode photocell based synchronization system alone is not sufficient to acquire ensemble averaged velocity fields around the Taylor bubbles. Thus, a dynamic masking procedure is necessary to remove the Taylor bubbles from the PIV images.

Only two works were encountered in literature (Nogueira et al. (2003) and Nogueira et al. (2006b)) which describe a method for generating the masks around the Taylor bubbles. However, these methods are based on the Pulsed Shadow Technique (PST) and cannot be used in the presence of dispersed bubbles, due to the shadow projection of the bubble's shadows in the camera plane. Van Hout et al. (2002c), analyses the flow around Taylor bubbles rising in stagnant water columns through velocity averaged fields. However, there is no discussion about the methodology used to mask the Taylor bubbles out of each instantaneous frame and therefore computed the ensemble averaged velocity fields.

In this section the dynamic masking procedure used in this work to remove the Taylor bubbles nose and bottoms from the original PIV images is described, detailing the image processing steps for these two regions. The nose/bottom frame of reference change for each PIV frame, necessary for the correct ensemble averaging process, is also described. The dynamic masking procedure algorithms were implemented using the OpenCV (BRADSKI, 2000b) library.

As shown in Fig. 5.4a), in the experiments with the presence of dispersed bubbles, the PIV synchronization only ensures that the frame will focus on a selected region (nose or tail), but the bubble position cannot be matched for all PIV acquisitions. Fig. 5.15 shows the PDF of the axial nose position from the acquired PIV frames in different flow stream conditions. In Fig. 5.15, the z/D=0 value represents the average axial position of the nose tip of Taylor bubbles. Clearly, the increase in j_l and the presence of dispersed bubbles in the flow stream, introduces large oscillations in the position of Taylor bubbles in the frames, and the use of fixed masking would not lead to reliable ensemble averages of PIV the results. A dynamic masking procedure is then needed to get consistent averages.

5.4.1 Taylor bubble nose masking

Figures 5.16 and 5.17 shows the image and signal processing steps to create the dynamic masks at bubble noses.

First, the original raw image passes through a median filter. Since the nose shape

Figure 5.15 – Nose position distribution ($|z/D|$) from the PIV frames by using the LDR synchronization trigger for different flow stream conditions: b) $j_l = 0.0$ $\times 10^{-2}$ m/s, $j_g = 0.0$ m/s; b) $j_l = 21.64$ $\times 10^{-2}$ m/s, $j_g = 0.0$ m/s; c) $j_l = 21.64$ $\times 10^{-2}$ m/s, $j_g = 2.38$ $\times 10^{-3}$ m/s and $\overline{\langle \alpha_g \rangle} = 0.7$ %; d) $j_l = 21.64$ $\times 10^{-2}$ m/s, $j_g = 19.83$ $\times 10^{-3}$ m/s and $\overline{\langle \alpha_g \rangle} = 4.9$ %.

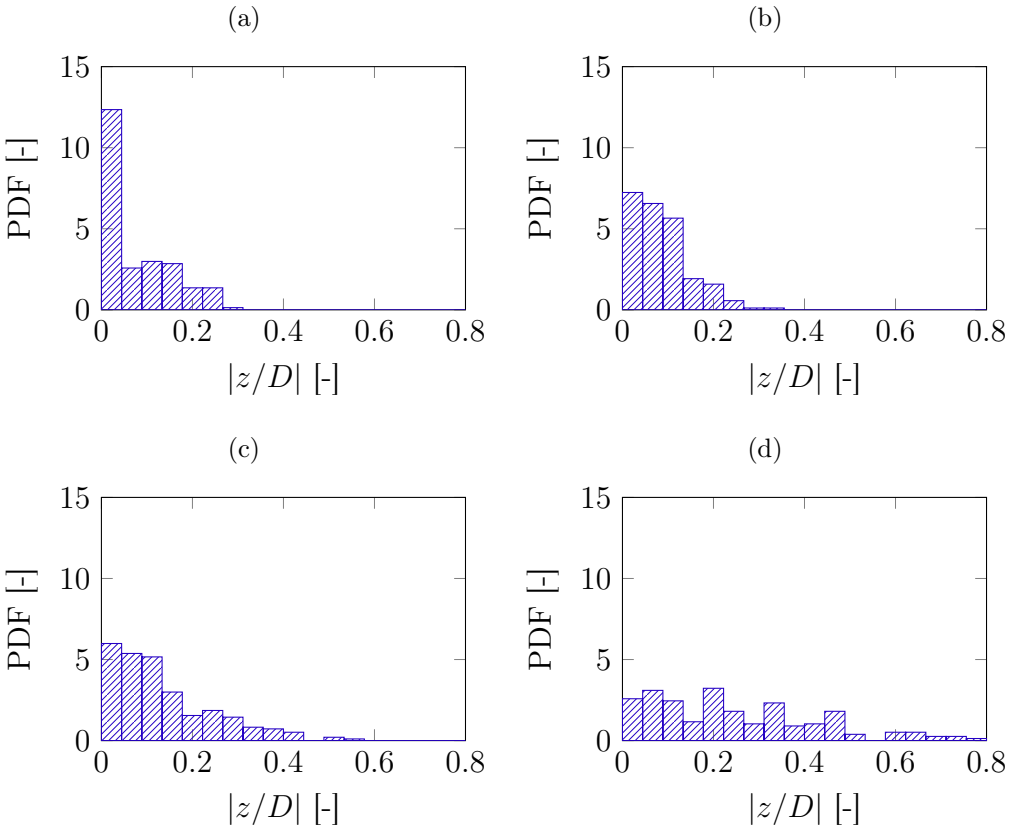

Source - Developed by the author.

varies from frame to frame, especially on the case with dispersed bubbles, it is necessary to find a "seed point" from which the nose shape can be reconstructed. In symmetrical cases, this point would represent the nose tip. In all the acquired PIV frames at the nose region, a very distinct pattern emerges from the median filtered image. This pattern is characterized by an area with brighter pixel intensity compared to the rest of the image, located near the Taylor bubble tip. This arises from the reflection of fluoresced light of seeding particles at the interface. Then, the first operation is to find the "seed point" from this distinct bright pattern, by analyzing the pixel intensity in the duct centreline. The pixel intensity is shown in Fig. 5.16 and it can be seen that the first local intensity maximum value represents the gas-liquid interface at this position. In order to find this point, the 8-bit unsigned integer values of the pixel intensity are transformed to float type, so a 1D moving average operation is used to smooth out this signal. In Fig. 5.16, the

smoothed signal is indicated by the red dotted line.

Figure 5.16 – Image filtering operations and the pixel intensity sampling at the duct centerline used to find the Taylor bubble nose "seed point" used for the complete gas-liquid interface procedure.

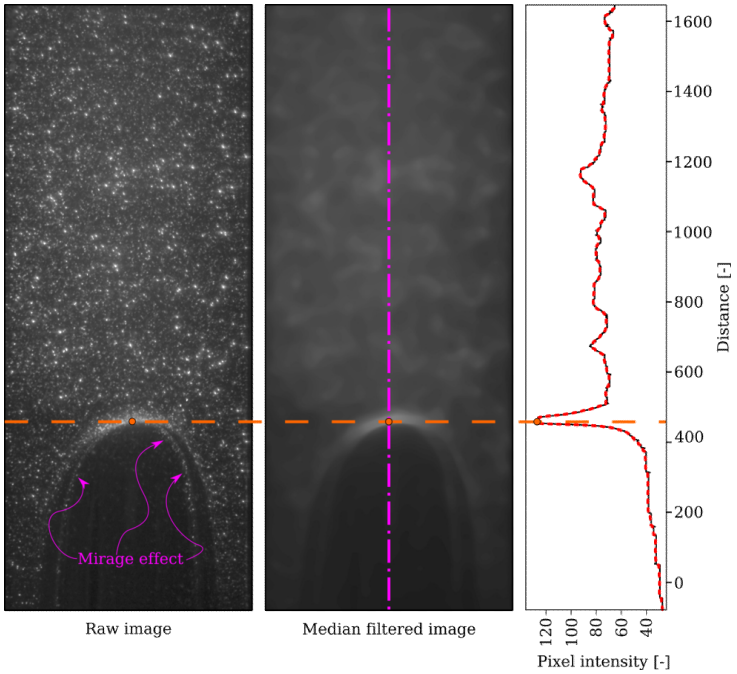

Source - Developed by the author.

After this "seed point" is found, a gas-liquid interface search is performed radially, through the same pixel analysis sampling and moving average operation, mentioned above. A "base point" is defined, positioned at a predefined distance from the seed point, from where the radial pixel intensity profiles are going to be extracted. The local maximum search operation is carried by these radially extracted intensity profiles. Figure 5.17 shows this operation, where the sampling is performed from a θ interval of $[0.0, \pi/2]$. This interval can be modified according to the image intensity of the raw PIV acquisition. In the determination of the local maximum, care is taken to position the gas-liquid interface point on the outside part of Taylor bubble. This is done by checking the existence of a smoothed out pixel region near the interface, seen by the plateaus near the points in Fig. 5.17.

After the seed point is found, an additional verification is performed to avoid spurious gas-liquid interface points. This additional procedure compares the distance between the possible gas-liquid interface position between two successive θ marching steps. Then, since the mirage effect is not present at the centreline region, by beginning the angular swept from this point, the maximum intensity captured in the next angular point

Figure 5.17 – Example of the pixel intensity profiles radially sampled from the median filtered image, which shows the Taylor bubble "seed point" and the base point used to sample the image in a radial fashion.

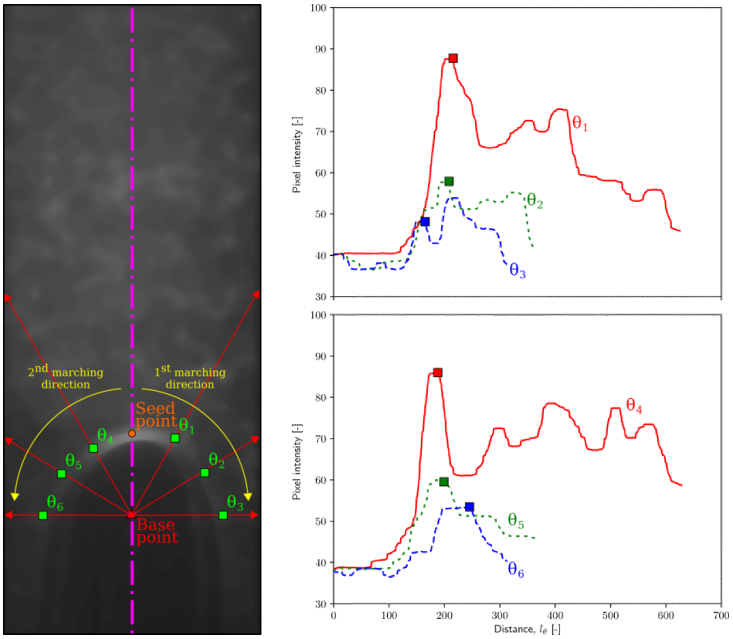

Source - Developed by the author.

is more likely to be actual gas-liquid interface position (and not the maximum intensity point resulting from the mirage effect).

It is important to state that the median filter operation, shown in Fig .5.16, removes most part these false gas-liquid interface positions through its filtering. Therefore the median filter averaged image is used on the procedures described above.

After the two marching operations (left and right), the complete gas-liquid interface can be reconstructed, as illustrated in Fig. 5.18, where the points represent the output from the procedure described.

Figure 5.18 shows the gas-liquid interface points for three distinct flow conditions, in Fig.5.18a) there are no dispersed bubbles on the flow stream, while in Figs. 5.18b) and c) the dispersed bubbles are injected into the stream. As can be observed, the procedure can be applied for cases with strong oscillations of Taylor bubbles noses (which can also occur, for instance, in counter-current flow).

For the case shown in Fig. 5.18c), the volume fraction of dispersed gas is approximated 4.9 % and the interaction between the Taylor bubble and the dispersed bubbles is strong. For these cases, the points obtained from the gas-liquid interface procedure could not precisely define the correct position of Taylor bubble nose. To overcome this problem, these points were introduced to a moving average filter, which in turn produced accept-

Figure 5.18 – Example of reconstructed gas-liquid Taylor bubble interfaces in the PIV frames acquired in the nose region for three flow stream configurations: a) without the presence of dispersed bubbles; b) with dispersed bubbles injected into the flow stream ($\overline{\langle \alpha_g \rangle} = 1.30\%$); c) with dispersed bubbles injected into the flow stream ($\overline{\langle \alpha_g \rangle} = 4.90\%$).

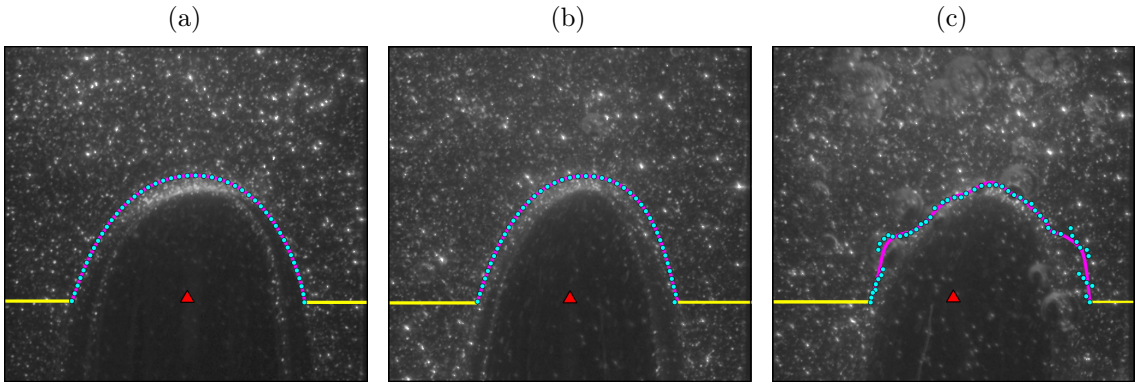

Source - Developed by the author.

able gas-liquid reconstructed interfaces. Despite the "noise" introduced by the presence dispersed bubbles, the reconstructed interface masks out adequately the Taylor bubble nose region from the PIV frames.

From these gas-liquid reconstructed interfaces, two additional curves were created to define the mask boundaries, at the axial position of the "base point" previously defined. This point was positioned at the center line at a distance $0.5D$ below the nose tip.

Figure 5.19 shows the mask obtained for three flow configurations, where the red filled PIV interrogation windows are removed from the PIV analysis. In the region out from the mask, the interrogation windows lying on the dispersed bubbles are removed as described in Chapter 3.

The square located at the nose tip in Fig. 5.19 shows a filled interrogation window, which defines the gas-liquid interface extreme point and is used as the reference position in the averaging process (i.e., the nose tip height is defined as the average height of these points).

Figure 5.20 shows schematically how the change of reference position is performed to calculate the ensemble averaged velocities. As the reference position is changed, it is necessary to create "dummy" PIV interrogation windows which are not accounted in the averaging process, as seen in Fig. 5.20b) (blank regions above and below).

After the dynamic masking application and the change of reference, the method described in Chapter 3 is used to remove the dispersed gas phase contribution from the PIV liquid velocity vector. Figure 5.21 shows the instantaneous liquid velocity vector field

Figure 5.19 – Masking procedure applied in the PIV frames, where the red filled region represents the discarded velocity vectors. The final mask is shown for three flow stream configurations: a) without the presence of dispersed bubbles; b) with dispersed bubbles injected into the flow stream ($\overline{\langle \alpha_g \rangle} = 1.30\%$); c) with dispersed bubbles injected into the flow stream ($\overline{\langle \alpha_g \rangle} = 4.90\%$).

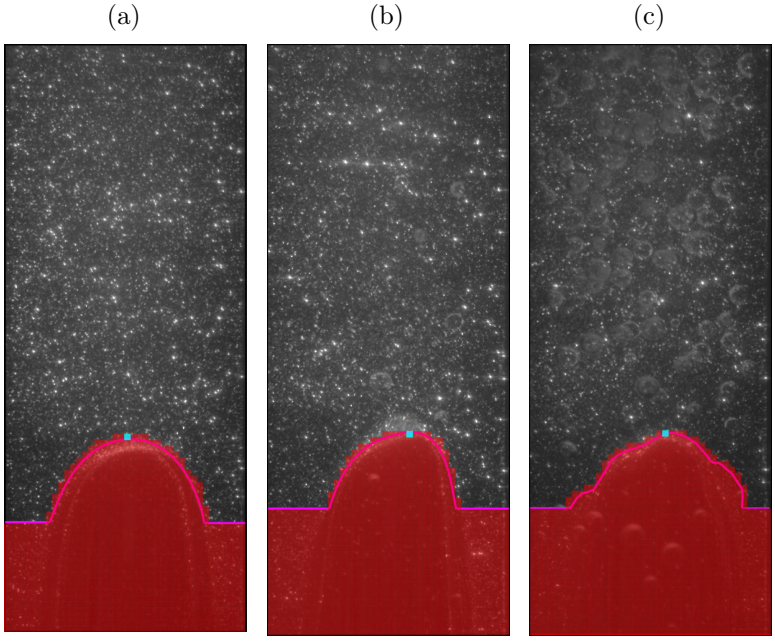

Source - Developed by the author.

around Taylor bubble noses, with different concentration of dispersed bubbles in the flow.

It is important to state that the method described in this section for the generation of the dynamic masks does not have a 100 % of success. According to the PIV frames analyzed in this work, the success rate of the dynamic masking procedure is approximate 95 % for the cases without dispersed bubbles and ranges between 80 - 90 % for the cases where dispersed bubbles are injected in the flow stream. The success rate was estimated by a simple visual analysis of the obtained dynamic masking at the end of each batch from a single flow condition procedure. If the dynamic produced mask of a PIV frame had some erroneous feature, this frame was manually removed from the ensemble averaging process.

5.4.2 Taylor bubble bottom

As previously discussed, due to the high N_f number, the Taylor bubble tail region, strongly oscillates from one PIV acquisition to another. In addition, the angular sweep used in the case of the nose region is not adequate for the tail morphology. Hence, the

Figure 5.20 – Example of the change of reference procedure for the ensemble averaging process: a) Dynamically masked PIV frames and the Taylor bubble nose tip position, represented by the cyan dashed line; b) Change of reference position of the same PIV frames, which now are aligned with bubbles nose tip position. The white interrogation windows are filled with "dummy" values that are not accounted on the averaging process.

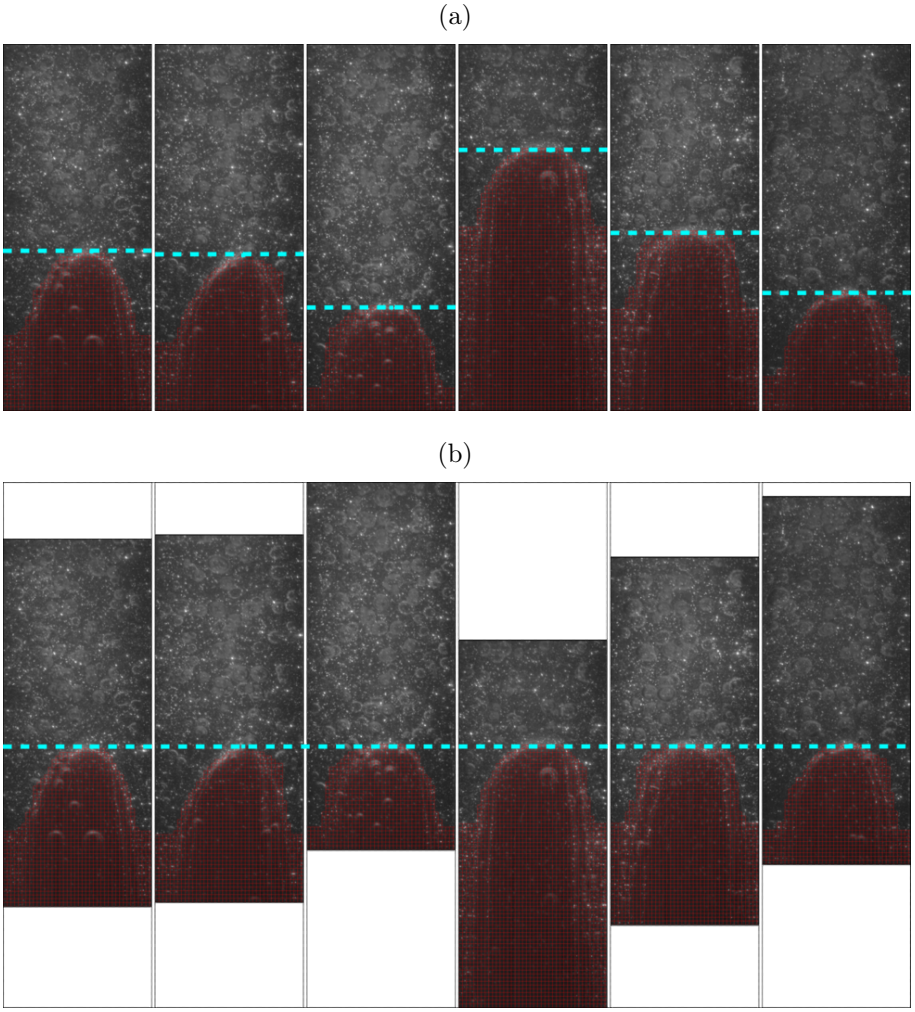

Source - Developed by the author.

procedure described in the previous subsection is modified to mask the Taylor bubble tails out of the PIV frames.

The first step is the identification of an initial "seed point" that can be used as a reference, at the duct centreline. Figure 5.22 schematically illustrates this image analysis step. Again, the raw PIV image frame is passed through a median filter, which returns a "blurred" image with brighter (strong pixel intensity) in the duct centerline. Thus, the local maxima position of these pixel intensity values encountered in the duct centerline is used as a "seed point" for the gas-liquid interface reconstruction.

Figure 5.21 – Example of the instantaneous liquid velocity vector field around two different Taylor bubble noses, where the dispersed bubbles are present on the flow. The interrogations windows where the dispersed bubbles are removed by the phase-discrimination method described in Chapter 3.

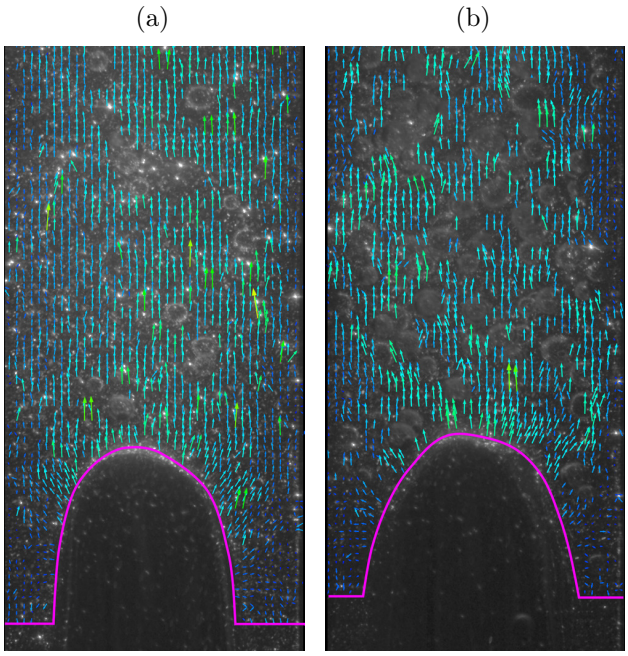

Source - Developed by the author.

After the seed point is found, it is necessary to perform a local analysis operation to find the gas-liquid interface points. As seen in Fig. 5.22, the application of a median filter alleviates the mirage effect near the gas-liquid interface. Due to the Taylor bubble bottom shape, there is no need to perform a radial search procedure, as done for the nose region. In this case, a simpler line search along vertical lines is performed, as schematically illustrated in Fig. 5.23. However, the line search analysis is carried out in a marching way, using the nearest-point to the neighbor detected in the previous step, departing from the "seed point".

Following the same steps in the Taylor bubble nose dynamic masking procedure, the points acquired during the line search operation, including the ones representing the liquid film region, are smoothed by a moving average filter, resulting in the final gas-liquid interface. The schematic illustration in Fig. 5.24 shows this step, where the cyan colored points represent some of the located gas-liquid interface positions, while the magenta colored lines represent the gas-liquid interface.

In Fig. 5.23, the liquid film region between the Taylor bubble interface and the pipe wall is removed from the line search operation. Since the liquid film thickness at the bubble rear region is almost constant for all PIV acquisitions, this operation does not

Figure 5.22 – Image filtering operations and the pixel intensity sampling at the duct centerline used to find the Taylor bubble bottom "seed point" used for the gas-liquid interface reconstruction procedure.

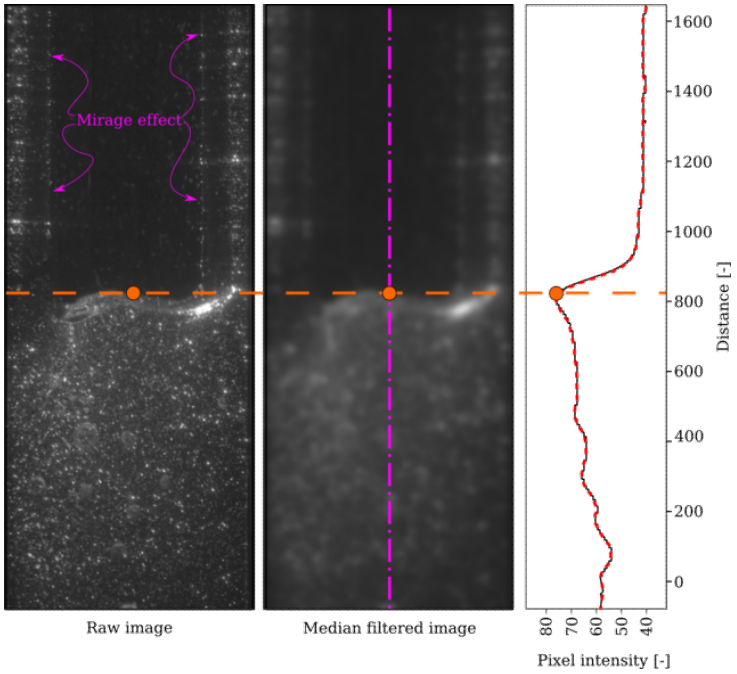

Source - Developed by the author.

compromise the accuracy of the reconstructed gas-liquid interface.

After the smoothing process, the reconstructed gas-liquid interface position is used for the masking procedure. Figure 5.25 illustrates the mask used to remove the Taylor bubble bottom region for three different flow configurations. As done for the nose region, the obtained mask is not used to erase the pixel information of the original PIV frame, but to discard the information of the interrogations windows that lie inside this region. This means that the dynamic masking procedure is performed after the computation of the velocity fields by the PIV cross-correlation procedure.

After the removal of the velocity vectors located inside the Taylor bubble bottom region, the acquired PIV frames need to be aligned to a common reference position to perform the ensemble averages, in a similar way as done for the nose region. For the tail region, the seed point, i.e., the gas-liquid interface positioned at the duct centreline (see Fig. 5.22), is used as a reference position.

For the flow experiments with the presence of dispersed bubbles, the velocities within these bubbles are removed through the application of the method described in Chapter 3. Figure 5.26 shows the liquid velocity fields acquired through the PIV method in the Taylor bubble tail region for the "quasi-real" slug flow pattern.

Source - Developed by the author.

Figure 5.23 – Pixel intensity profiles sampled in different line positions, illustrating the local maxima points and its corresponding location in the median filtered image. The nearest-point neighbour condition was used to find the gas-liquid interface position in the l_3 local analysis. The highlighted region represents the removed area from the line search operation, where the liquid film region could be present.

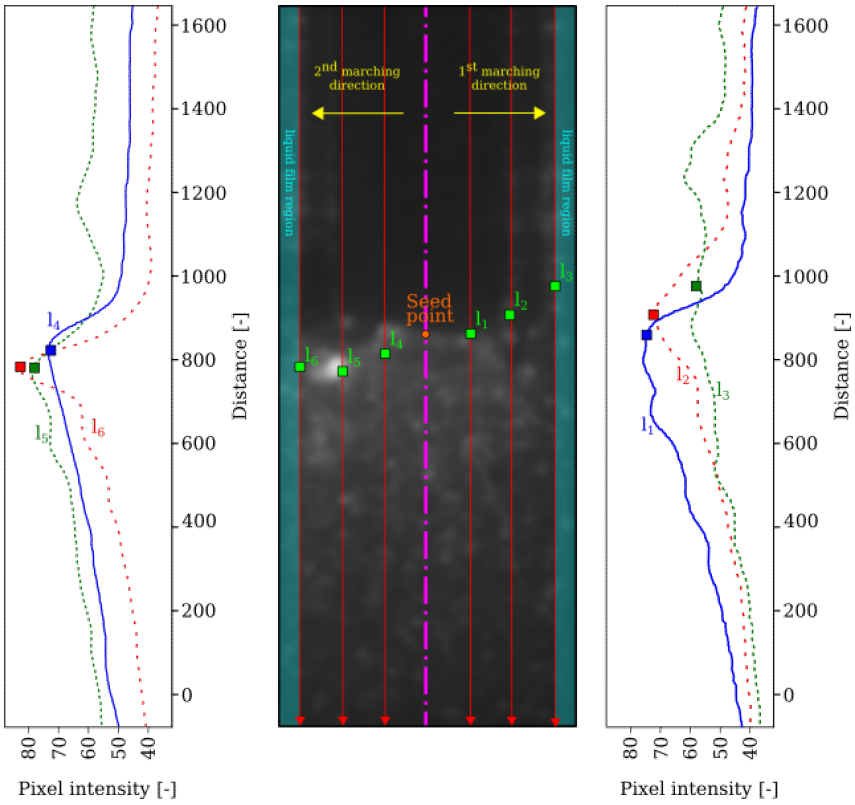

As in the dynamic nose masking procedure, the steps described in this section does have a 100 % success rate. For the cases analyzed in this study, the success rate of the dynamic masking procedure ranges between 80 - 85 % and is independent of the presence of dispersed bubbles in the flow stream. Hence, before starting the ensemble averaging procedure, some erroneous PIV frames must be removed from the ensemble group.

5.4.3 PIV ensemble averaged fields

After removing all interrogation windows, from the Taylor and dispersed bubbles, the ensemble average of the PIV measurements is calculated as,

$$\langle \boldsymbol{v}_l(r,z) \rangle = \frac{1}{N_{PIV}} \sum_{k=1}^{N_{PIV}} \boldsymbol{v}_{l,k}(r,z). \tag{5.5}$$

where N_{PIV} is the number of samples and a PIV liquid velocity vector field corresponds to the two-dimensional vector field, $\boldsymbol{v}_{l,k}(r,z) = [v_l(r,z), w_l(r,z)]$). This average is performed

Figure 5.24 – Example of reconstructed gas-liquid Taylor bubble interfaces in the PIV frames acquired in the tail region for three flow stream configurations: a) without the presence of dispersed bubbles; b) with dispersed bubbles injected into the flow stream ($\overline{\langle \alpha_g \rangle} = 1.30\%$); c) with dispersed bubbles injected into the flow stream ($\overline{\langle \alpha_g \rangle} = 4.90\%$).

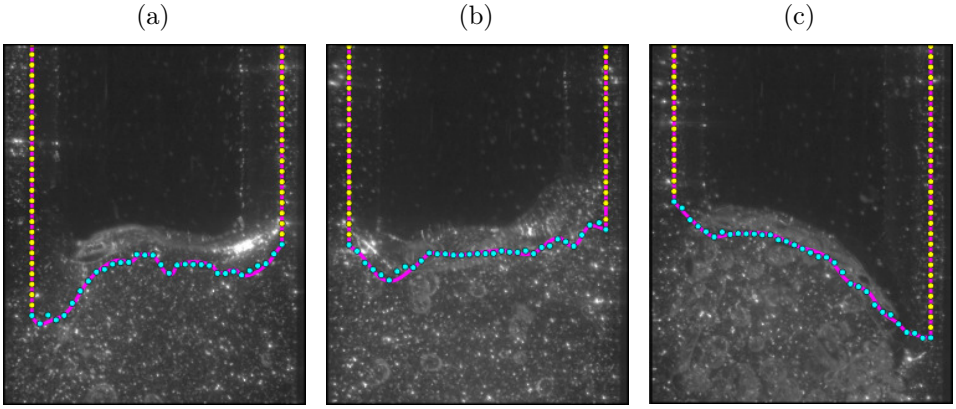

Source - Developed by the author.

for each (r, z), considering the only "valid" interrogation windows in each PIV acquisition.

The analysis of the liquid phase turbulence intensity was performed through the root mean square of the velocity fluctuations $v^j_{l,rms}(r)$ defined as,

$$v^j_{l,rms}(r,z) = \sqrt{\frac{1}{N_{PIV}} \sum_{k=1}^{N_{PIV}} \left[v^j_{l,k}(r,z) - \left\langle v^j_l(r,z) \right\rangle \right]^2} \tag{5.6}$$

where $j = 1, 2$ corresponds to radial and axial velocity components, respectively.

Figure 5.25 – Masking procedure applied in the PIV frames, where the red filled region represents the discarded velocity vectors. The final mask is shown for three flow stream configurations: a) without the presence of dispersed bubbles; b) with dispersed bubbles injected into the flow stream ($\overline{\langle \alpha_g \rangle} = 1.30\%$); c) with dispersed bubbles injected into the flow stream ($\overline{\langle \alpha_g \rangle} = 4.90\%$).

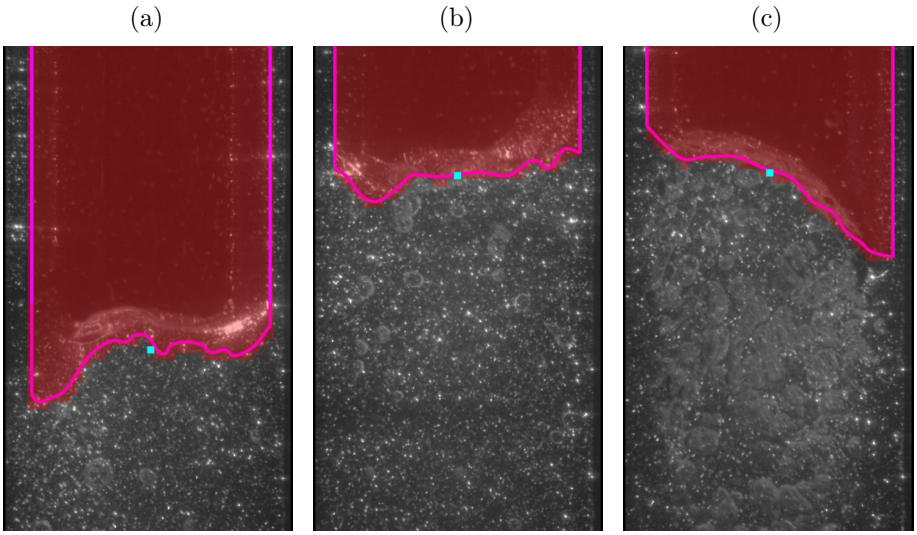

Source - Developed by the author.

Figure 5.26 – Example of the instantaneous liquid velocity vector field in the Taylor bubble tail region, for cases where dispersed bubbles are present on the flow. The interrogations windows where the dispersed bubbles are removed by the phase-discrimination method described in Chapter 3.

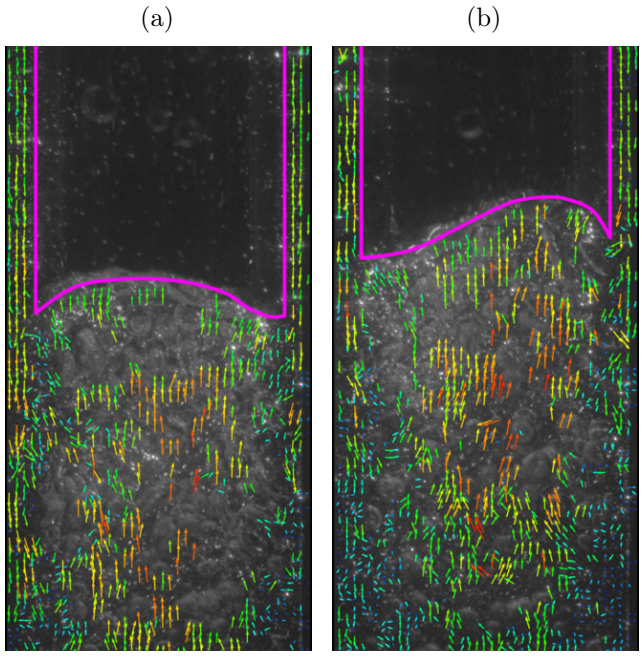

Source - Developed by the author.

5.5 RESULTS AND DISCUSSION

The main objective of the results presented in this section is the validation of the experimental techniques described in the previous sections. First, the LDP measurement of velocity and length of Taylor bubbles rising in different flow conditions (which include the presence of dispersed bubbles) will be compared with the results obtained from High-Speed Camera (HSC) analysis.

Then the masking technique for PIV measurement is analysed and its results are compared with HSC results. The effect of the number of PIV acquisitions on the averaged fields is also examined. Finally, some preliminary result are presented and discussed.

In all the following results, the controlled variables were the gas (dispersed bubbles) and liquid flowrates (i.e., j_g and j_l). The values of the volume fraction of dispersed bubbles, shown in the figures and tables, was estimated from the superficial gas velocity (dispersed bubbles) and the average gas velocity, calculated as described in Chapter 3.

5.5.1 Taylor bubbles velocity and length

The laser diode technique, described in Sec. 5.3.2 was used as the PIV synchronization system and for measurement of Taylor bubble velocities U_{tb} and lenghts L_{tb}.

The values obtained from the LDP (Laser Diode Photocell) technique are compared with the results obtained from the PIV velocity measurements and from the analysis of high-speed camera images. Therefore, a cross-validation of the three techniques is presented in this section.

An image analysis technique based on the work of Mayor et al. (2007) and described in more details in Section 5.3.3 is used to acquire the U_{tb} and L_{tb} values from the high-speed camera images. Additionally, the terminal velocity of Taylor bubbles rising in stagnant water, U_{tb} will be compared with correlations from the literature (DUMITRESCU, 1943; DAVIES; TAYLOR, 1950; WHITE; BEARDMORE, 1962), which correlates the Taylor bubble nose rising velocity as,

$$U_{tb} = k_1 \rho_l^{-1/2} \left[g\, D \left(\rho_l - \rho_g \right) \right]^{1/2} \tag{5.7}$$

where different authors propose different values of k_1, as shown in Table 5.1.

In the case of PIV, it is assumed that the bubble velocity corresponds to the liquid velocity measured at the duct centreline, at the nose tip height. However, this assumption does not hold adequate for flow conditions where strong oscillations are observed in the nose tip.

The ensemble average results from the PIV were obtained from 300 bubbles and 40 bubbles are considered for the high-speed camera, while the LDP technique results were averaged from a total of 240 samples.

Since the analog LDR signal from the LDP technique is affected by the presence of the dispersed bubbles, the validation (and application) of the LDP technique is divided into three major flow conditions: i) Taylor bubbles rising in stagnant liquid; ii) Taylor bubbles rising in co-current single-phase flow and iii) Taylor bubbles rising in co-current bubbly flows.

Figure 5.27 presents three typical high-speed camera images for Taylor bubble tail region, for these three flow conditions, and the correspondent PIV image.

Figure 5.27 – PIV frames and high-speed camera sequential images of the Taylor bubble tail region for different flow stream conditions: a) Taylor bubbles rising in stagnant liquid; b) Taylor bubbles rising in co-current single-phase flow ($j_l = 21.64 \times 10^{-2}$ m/s and $Re = 5684$); c) Taylor bubbles rising in co-current bubbly flows ($j_l = 21.64 \times 10^{-2}$ m/s, $j_g = 19.83 \cdot 10^{-3}$ and $\overline{\langle \alpha_g \rangle} = 4.9\%$).

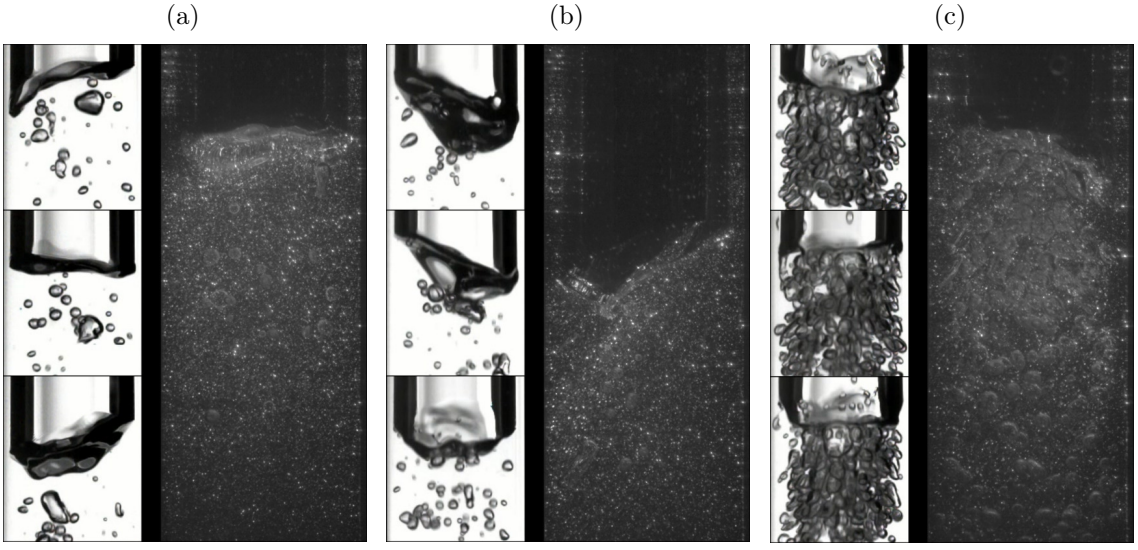

Source - Developed by the author.

5.5.1.1 Taylor bubbles rising in stagnant liquid

Table 5.1 presents the Taylor bubble terminal velocity measured in this study with the LDP technique, PIV and from the high-speed camera images. For the LDP method, the uncertainty analysis is given in Appendix A. In addition, Tab. 5.1 presents a comparison with results from correlations in the literature.

From the values of Table 5.1, it can be concluded that the three methods are capable of capturing the rising velocity of Taylor bubbles adequately. Results for the rising

Table 5.1 – Validation of the Taylor bubble terminal velocity ($\langle U_{tb,N} \rangle$ and $\langle U_{tb,B} \rangle$) rising in stagnant water.

Method/Correlation	$\langle U_{tb,N} \rangle$ [m/s]	$\langle U_{tb,B} \rangle$ [m/s]
Laser diode photocell	0.177 ± 0.001	0.176 ± 0.001
PIV	0.176	-
High-speed camera	0.175	0.173
Dumitrescu (1943) ($k_1 = 0.351$)	0.177	-
Davies and Taylor (1950) ($k_1 = 0.328$)	0.166	-
White and Beardmore (1962) ($k_1 = 0.345$)	0.175	-

Source - Developed by the author.

velocity at the tail region, $\langle U_{tb,B} \rangle$, are also presented, measured with laser diode photocell and the high-speed camera, showing good agreement. The slightly lower values can be attributed to the gas expansion effect.

The $\langle L_{tb} \rangle$ value from the laser diode photocell technique is compared with the result of the image analysis technique of the high-speed camera footages in Table 5.2. Results from different combinations of measured times and diodes used (see Fig. 5.7) are compared. It is important to recall that the Taylor bubble lengths can be obtained from the LDR1 or LDR2 signals and the $\langle U_{tb,B} \rangle$ and $\langle U_{tb,N} \rangle$ velocity. However, since the acquisition period is short, the different combinations should result in similar values of Taylor bubble lengths.

Table 5.2 – Comparison of the Taylor bubble length values for the stagnant water situation. For the laser diode photocell, the result for the four possible cases – i) LDR1 and Δt_N; ii) LDR1 and Δt_B; iii) LDR2 and Δt_N and iv) LDR2 and Δt_B – are presented.

Method	$\langle L_{tb} \rangle$ [mm]	$\langle L_{tb} \rangle$ [mm] case i)	$\langle L_{tb} \rangle$ [mm] case ii)	$\langle L_{tb} \rangle$ [mm] case iii)	$\langle L_{tb} \rangle$ [mm] case iv)
Laser diode photocell	-	96.97 ± 1.04	96.19 ± 1.00	95.78 ± 1.04	95.02 ± 1.01
High-speed camera	97.42	-	-	-	-

Source - Developed by the author.

As expected, for the LDP technique the different $\langle L_{tb} \rangle$ combinations result in similar values, close to the one obtained by the high-speed camera image analysis method.

From the presented results, we can conclude that the Laser Diode Photocell technique can be used as reliable measurement technique for Taylor bubbles rising in stagnant

liquid, even for high values of inverse viscosity number N_f.

5.5.1.2 Taylor bubbles rising in co-current single-phase flow

The Taylor bubble terminal velocity for the single-phase co-current flow condition ($j_l = 21.64 \times 10^{-2}$ m/s and $Re = 5684$) are shown in Tab. 5.3. The results from the PIV, LDP were calculated from an ensemble average of 250 acquisitions and the high-speed camera from 40 acquisitions.

Table 5.3 – Validation of the Taylor bubble terminal velocity ($\langle U_{tb,N} \rangle$ and $\langle U_{tb,B} \rangle$) rising in single-phase co-current flow condition ($j_l = 21.64 \times 10^{-2}$ m/s and $Re_l = 5684$).

Method	$\langle U_{tb,N} \rangle$ [m/s]	$\langle U_{tb,B} \rangle$ [m/s]
Laser diode photocell	0.449 ± 0.005	0.447 ± 0.003
PIV	0.447	-
High-speed camera	0.439	0.423

Source - Developed by the author.

As can be observed, the $\langle U_{tb,N} \rangle$ and $\langle U_{tb,B} \rangle$ results obtained with different techniques are close to each other, with a maximum deviation of 5.67 %.

Table 5.4 presents the Taylor bubble length $\langle L_{tb} \rangle$ calculated from the LDP and the high-speed camera image analysis method. For the single-phase co-current flow condition, the results differ in about 25.0 %. Since the $\langle U_{tb,N} \rangle$ and $\langle U_{tb,B} \rangle$ are similar for the two methods, the difference on the $\langle L_{tb} \rangle$ values can be attributed to the bubble travel time $\Delta t_1 = t_{2,1} - t_{1,1}$ and $\Delta t_2 = t_{2,2} - t_{1,2}$ in the LDR signals, due to the stronger oscillations of the Taylor bubble tail (see Fig. 5.27), recalling that, in the HSC analysis, the length is calculated from a slice located at the central region of the pipe, while the LDP signal will be affected by the three-dimensional oscillations of the interface at the bubble tail.

Through the analysis of the high-speed camera and PIV images from the co-current single-phase and the stagnant liquid flow conditions, it can be seen that the bubble bottom oscillations is stronger in the first case, as can be seen in Fig. 5.27. Polonsky et al. (1999b) reports the same behavior in their work, where the Taylor bubble bottom oscillating strength increase with the co-current liquid flow velocity. In addition, the difference between the results shown in Tab. 5.4 is about 20.0 mm, which is similar to the bottom oscillation amplitudes observed in the high-speed footage.

From the results presented in the paragraphs above, the LDP technique is suitable for measuring the $\langle U_{tb} \rangle$ values in the co-current single-phase flow conditions. However, it should be used with caution when measuring the $\langle L_{tb} \rangle$; since for high inverse viscosity

Table 5.4 – Comparison of the Taylor bubble length values for the single-phase co-current flow condition ($j_l = 21.64 \times 10^{-2}$ m/s and $Re_l = 5684$). For the laser diode photocell, the result for the four possible cases – i) LDR1 and Δt_N; ii) LDR1 and Δt_B; iii) LDR2 and Δt_N and iv) LDR2 and Δt_B – are presented.

Method	$\langle L_{tb} \rangle$ [mm]	$\langle L_{tb} \rangle$ [mm] case i)	$\langle L_{tb} \rangle$ [mm] case ii)	$\langle L_{tb} \rangle$ [mm] case iii)	$\langle L_{tb} \rangle$ [mm] case iv)
Laser diode photocell	-	126.25 ± 2.18	124.06 ± 1.94	124.57 ± 1.96	122.42 ± 1.70
High-speed camera	101.255	-	-	-	-

Source - Developed by the author.

number N_f flows, the bottom tail oscillates strongly. For these cases, it is recommended the use of the HSC image processing technique for the measurement of $\langle L_{tb} \rangle$.

5.5.1.3 Taylor bubbles rising in co-current bubbly flows

The terminal Taylor bubble velocity, for the cases with the presence of dispersed bubbles in the liquid stream is shown in Tab. 5.5. The values obtained from LDP and high-speed camera $\langle U_{tb,N} \rangle$ are in good agreement. For both cases presented in Tab. 5.5, the LDP technique returns approximately the same value for $\langle U_{tb,N} \rangle$ and $\langle U_{tb,B} \rangle$, which is not observed in results from the high-speed camera. As mentioned earlier, the dispersed bubbles introduce fluctuations in the analog LDR1 and LDR2 signals(see Figs. 5.7b) and c)). Due to these fluctuations, the LDP technique is not capable to accurately acquire the velocity based on the bubble tail passage. Additionally, for the $\overline{\langle \alpha_g \rangle} = 4.9\%$ case, dispersed bubbles accumulate on the tail region, causing the LDRs signals to mislead the Taylor bubble bottom passage.

In the $\overline{\langle \alpha_g \rangle} = 0.7\%$ case, the dispersed bubbles in the tail region does not affect significantly the bubble bottom passage detection, since the high-speed camera results from this case is not as different from the single-phase co-current flow condition. In these experiments, as the Taylor bubble rises, some dispersed bubbles enter the liquid film. As these bubbles exit the liquid film, they shear the gas-liquid interface in the bottom region, causing the bubble bottom to oscillate. Since the oscillations are even stronger as those found in the single-phase co-current flow condition, the LDP technique cannot measure adequately the $\langle U_{tb,B} \rangle$ values.

In addition, the $\langle U_{tb,N} \rangle$ obtained with PIV does not agree with the values obtained from the high-speed camera and the LDP technique, for these cases. This is because, in

the presence of dispersed bubbles, the Taylor bubble nose oscillates not remaining in the center of the duct. The Taylor bubble deforms due to induced turbulence from dispersed bubbles and also due to collisions with them. Hence, the Taylor bubble does not retain a constant shape, rising in a "zig-zag" motion. Since the nose tip velocity is defined as the average liquid axial velocity in the duct centreline, this means that in some PIV frames the instantaneous nose position is not aligned at the pipe center. Thus, it is expected that the $U_{tb,N}$ values from the PIV method results in smaller values than those acquired by the LDP technique and from the high-speed camera images.

Table 5.5 – Validation of the Taylor bubble terminal velocity ($\langle U_{tb,N} \rangle$ and $\langle U_{tb,B} \rangle$) rising in co-current bubbly flow condition ($j_l = 21.64 \times 10^{-2}$ m/s and $Re_l = 5684$).

Method	j_g [m/s]	α_g [-]	$\langle U_{tb,N} \rangle$ [m/s]	$\langle U_{tb,B} \rangle$ [m/s]
Laser diode photocell	$2.38 \cdot 10^{-3}$	0.7 %	0.476 ± 0.005	0.477 ± 0.003
PIV			0.454	-
High-speed camera			0.478	0.459
Laser diode photocell	$19.83 \cdot 10^{-3}$	4.9 %	0.489 ± 0.005	0.489 ± 0.004
PIV			0.438	-
High-speed camera			0.489	0.473

Source - Developed by the author.

Table 5.6 show the Taylor bubble $\langle L_{tb} \rangle$ acquired by the LDP technique and those calculated from the high-speed camera image analysis method. As expected, the results from the results do not agree very well, with the LDP technique overestimating the Taylor bubble length. Again, since the LDP technique cannot correctly detect the bubble bottom passage, it cannot also accurately acquire the Taylor bubble travel time through the two LDRs.

The results presented in Tabs. 5.5 and 5.6 indicate that the LDP technique can only accurately calculate the Taylor bubble nose velocity $\langle U_{tb,N} \rangle$ values.

Figure 5.28 presents a comparison of the Taylor bubble nose velocities for co-current flow measured with the LDP technique and high-speed camera image analysis, for different dispersed gas volume fraction and different liquid superficial velocities. The parameter α_g in the abscissas represents the volume fraction of dispersed bubbles, not the total volume fraction. A clear trend is observed where, initially, the Taylor bubbles rising velocity is increased by the presence of dispersed bubbles and for higher α_g, this velocity decreases, maintaining, however, values higher than the case without dispersed bubbles. These trends and their relation with the flow structure around Taylor bubbles, including dispersed bubbles in the flow stream is under investigation. However, these results clearly

Table 5.6 – Comparison of the Taylor bubble length values for the bubbly co-current flow condition ($j_l = 21.64 \times 10^{-2}$ m/s and $Re_l = 5684$). For the laser diode photocell, the result for the four possible cases – i) LDR1 and Δt_N; ii) LDR1 and Δt_B; iii) LDR2 and Δt_N and iv) LDR2 and Δt_B – are presented.

Method	j_g [m/s]	α_g [-]	$\langle L_{tb} \rangle$ [mm]	$\langle L_{tb} \rangle$ [mm] case i)	$\langle L_{tb} \rangle$ [mm] case ii)	$\langle L_{tb} \rangle$ [mm] case iii)	$\langle L_{tb} \rangle$ [mm] case iv)
Laser diode photocell	$2.38 \cdot 10^{-3}$	0.7 %	-	130.73 ± 2.08	131.30 ± 2.07	131.19 ± 1.66	131.76 ± 1.65
High-speed camera			103.18	-	-	-	-
Laser diode photocell	$19.83 \cdot 10^{-3}$	4.9 %	-	136.47 ± 2.16	136.25 ± 2.04	135.99 ± 2.01	122.42 ± 1.88
High-speed camera			107.76	-	-	-	-

Source - Developed by the author.

indicate that the presence of dispersed bubbles in liquid slugs, will affect the whole flow structure around Taylor bubbles and this effect should be taken into account in the study of real slug flows.

5.5.2 Effect of the flow stream condition on the PIV dynamic masking procedure

In order to study the effect of the flow stream condition in the Taylor bubble gas-liquid interface obtained during the PIV dynamic masking procedure, the results obtained from this method are compared with image analysis method from the high-speed cameras. By using the two methods, the bubble nose shapes and the deviation of the nose tip radial position could be compared. The bubble nose tip radial position distribution is an important parameter, especially for the cases with dispersed bubbles, since bubble-induced turbulence causes strong fluctuations of the bubble nose tip position around the duct centreline position. Additionally, the Taylor bubble nose rising velocity distribution from the nearest position from the bubble tip was compared with the results presented in the previous section. The PIV spatial calibration and further verifications for single phase flow were performed in Chapter 3, which experimental setup shares the same PIV/LIF system, test section, and bubbly flow stream generator, used in this investigation for the "quasi-real" slug flow. For all the experiments done in this study, the time difference between the two consecutive frames for velocity measurement was defined following the guidelines discussed in Raffel et al. (2007). The interrogation size was maintained constant at 32 x 32 pixels throughout the experiments and these were overlapped by 50 %, between first and second frames. The velocity fields were computed by the Fast Fourier Transform (FFT) cross-correlation of the TSI Insight 4G software, which also removed spurious

Figure 5.28 – Influence of the dispersed gas volume fraction on the Taylor bubble nose tip velocity for co-current liquid flow and the comparison of the LDP and high-speed camera measurements. For the high-speed camera acquisitions, the error bars represents the ensemble standard deviation.

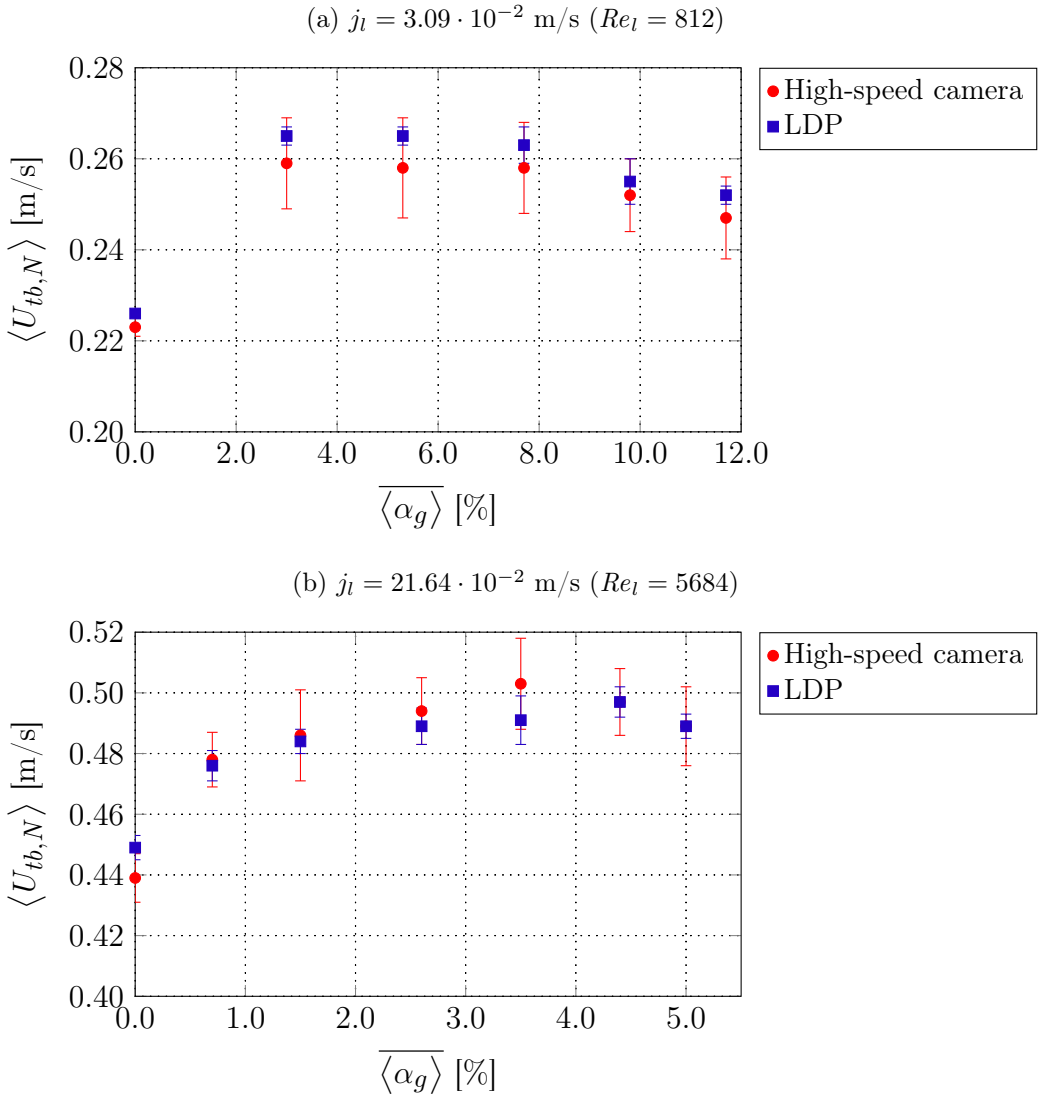

Source - Developed by the author.

velocity vectors through a signal-to-noise ratio (SNR) analysis. The SNR was set to 2.0, in order to remove those spurious vectors.

Figure 5.29 shows the nose tip radial axial position distribution (PDF) for different cases, obtained from the PIV (through the dynamic masking procedure) and high-speed camera image analysis.

These results support the visual observation that the presence of the dispersed bubbles induces a lateral motion on the Taylor bubble nose position. The PDFs showed that the bubble-induced turbulence also promotes a lateral motion on the bubble nose tip

position since the PDFs without dispersed bubbles are much narrower. These distributions also support the PIV dynamic masking procedure results are reliable since the distribution from both methods are close to each other. It is important to state, that the PIV spatial resolution is based on the interrogation window size (32x32 pixels in this study). Hence, the PIV results of Fig. 5.29 presents a smaller number of bins.

Figure 5.29 – Nose tip position distribution acquired by from the high-speed camera footage and the PIV frames in different flow stream conditions: a) j_l = 0.0 m/s and j_g = 0.0 m/s; b) j_l = 21.64 $\times 10^{-2}$ m/s and j_g = 0.0 m/s; c) j_l = 21.64 $\times 10^{-2}$ m/s, j_g = 2.38 $\times 10^{-3}$ m/s and $\overline{\langle \alpha_g \rangle}$ = 0.7 %; d) j_l = 21.64 $\times 10^{-2}$ m/s, j_g = 19.83 $\times 10^{-3}$ m/s and $\overline{\langle \alpha_g \rangle}$ = 4.9 %. The tip position was extracted from the high-speed camera images through an image analysis method (CERQUEIRA et al., 2018b). For the PIV, the nose tip position in each frame was acquired during the dynamic masking procedure.

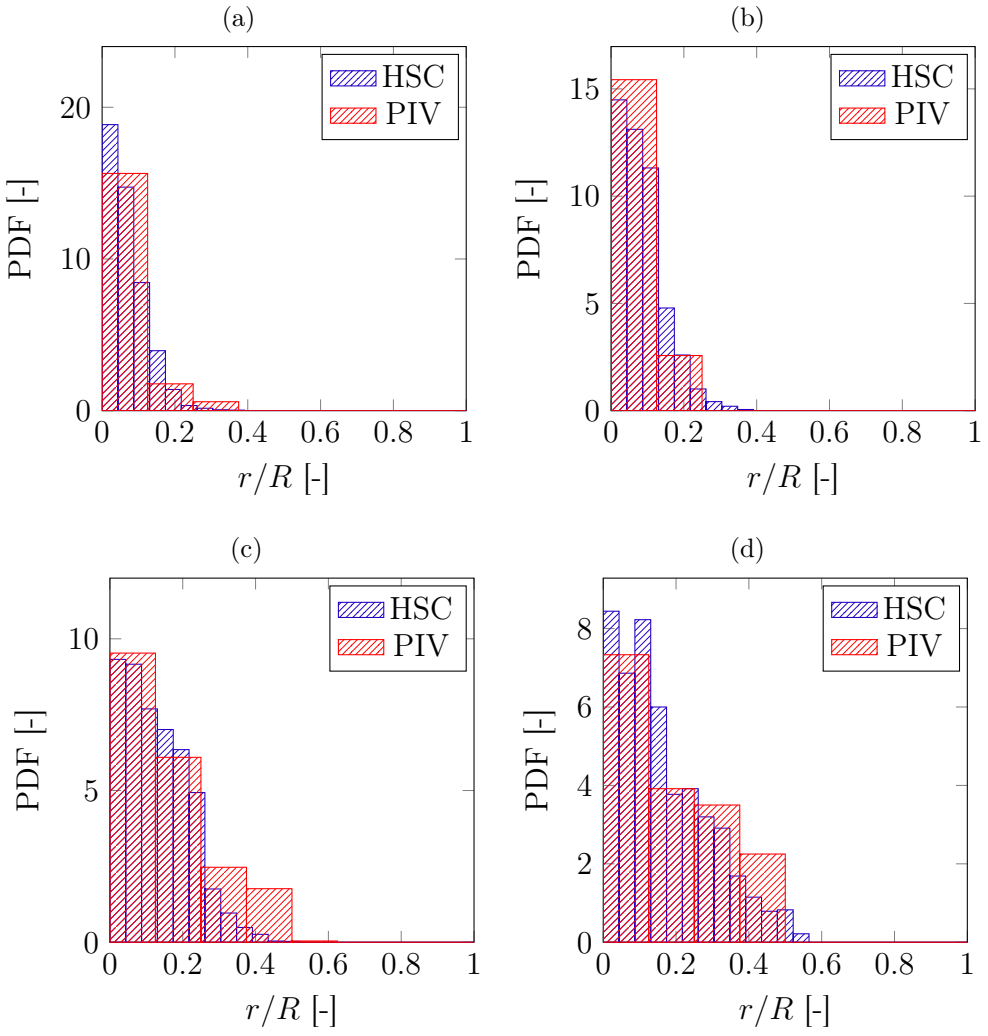

Source - Developed by the author.

Since the dynamic masking procedure is capable of finding the Taylor bubble nose

tip position from the PIV frames, it is possible to extract the axial velocity from the PIV interrogation in this location. As seen in Fig. 5.29, due to bubble-induced turbulence, in the presence of dispersed bubbles, the Taylor bubble nose position does not lie at the duct centerline. Thus, the axial velocity in the duct centerline results in smaller values than the Taylor bubble nose velocity, as seen in Tab. 5.5. However, since it was possible to find the approximate bubble nose position from the dynamic masking procedure, the high-speed camera, and LDP $\langle U_{tb,N} \rangle$ values could be compared from ensemble values from the nose tip interrogation windows. Figure 5.30 shows the PDF distribution of the axial velocity from these interrogation windows, including the average values and the values obtained by high-speed camera image analysis. The results of Fig. 5.30 are closer than those show in Tab. 5.5 for the duct centerline PIV values, since it is more likely that the dynamic masking procedure extracts the liquid velocity near the nose tip position.

Figure 5.30 – PIV nose velocity distribution near the Taylor bubble nose tip for the two "quasi-real" slug flow conditions: a) $j_l = 21.64 \times 10^{-2}$ m/s, $j_g = 2.38 \times 10^{-3}$ m/s and $\overline{\langle \alpha_g \rangle} = 0.7$ %; b) $j_l = 21.64 \times 10^{-2}$ m/s, $j_g = 19.83 \times 10^{-3}$ m/s and $\overline{\langle \alpha_g \rangle} = 4.9$ %. The PIV nose velocity was defined as the axial liquid velocity value in the interrogation window situated on top of captured nose tip position (see Fig. 5.20). The red line is located on the high-speed camera ensemble average Taylor bubble nose velocity, shown in Tab. 5.5. The dotted black line indicates the PIV ensemble average of the PDF distribution.

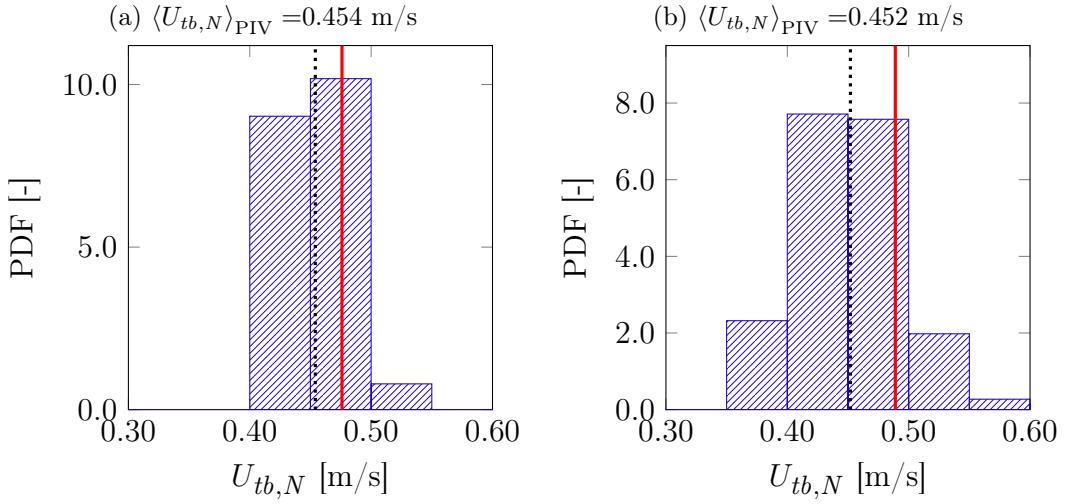

Source - Developed by the author.

An additional verification of the Taylor bubble nose shape was done by comparing the PIV masking results with the ones from the high-speed camera image analysis method. The comparison was based on the ensemble average results, shown in Fig. 5.31. In order to compare the bubble nose shape, Fig. 5.31 shows the probability occurrence of the

Taylor bubble nose position from both methods. The probability occurrence was computed through the following procedure,

1. Two matrices are created, $\mathrm{Mat_{PIV}}$ and $\mathrm{Mat_{HSC}}$, the first representing the PIV and the second the high-speed camera results. The matrix shape is based on the PIV vector resolution, so the high-speed camera pixel resolution is downscaled to the PIV interrogation window resolution (32x32 pixels). The matrices are initiated with zero values, and each matrix element represents a spatial region of the duct in the (x,y) image space;

2. For each flow condition, when a matrix element is inside the Taylor bubble region, its value is incremented by one. In the case of PIV, the matrix is incremented from the mask created to remove the Taylor bubble from the PIV velocity results. In both methods, the bubble nose coordinate reference frame is changed, so the bubble nose tip lies on the same axial position for all acquisitions.

3. After all the PIV frames or the high-speed frames are analyzed, the results are scaled by the maximum matrix element. Hence the $\mathrm{Mat_{PIV}}$ and $\mathrm{Mat_{HSC}}$ results in the Taylor bubble occurrence in each interrogation window, taking as reference the nose tip. This color field indicates the average shape of the bubble nose and the nose fluctuation.

Since the spatial resolution is the same in $\mathrm{Mat_{PIV}}$ and $\mathrm{Mat_{HSC}}$, it was possible to compute the difference from both methods, which is given on the third column of Fig. 5.31. From the obtained results, it can be seen that the high-speed camera does not capture the oscillations expected for the cases with the higher concentration of dispersed bubbles (Fig. 5.31 a) and c)). Furthermore, it seems that the nose shape obtained with HSC is more "rounded". This is because the HSC capture the projection of the bubble shadow while the PIV takes the bubble shape at the pipe mid-plane. Therefore, the shadow projection from the HSC image will not account the three-dimensional oscillations of the bubble nose. Thus, for the analysis of the nose shape and nose oscillations, the PIV with dynamic masking is more adequate. This observation does not affect the findings from the analysis of Fig. 5.29, since both methods capture the bubble nose tip distribution, but only the PIV images are capable of acquiring the whole nose shape fluctuation. The study of the tip oscillations is very important, once they modify the form drag of the Taylor bubbles (TUDOSE; KAWAJI, 1999).

Figure 5.31 – Taylor bubble nose shape acquired from the PIV dynamic masking procedure (Mat_{PIV}) and from the high-speed camera image (Mat_{HSC}) analysis method (CERQUEIRA et al., 2018b) for different flow stream configuration. The difference in the Taylor bubble nose outline ($\text{Mat}_{\text{PIV}} - \text{Mat}_{\text{HSC}}$) is given in the third column. The Mat_{PIV} were caculated from 400 PIV acquisitions and the Mat_{HSC} were sampled from 40 Taylor bubbles (each composed of 800 frames).

(a) $j_l = 0.0$ m/s and $j_g = 0.0$ m/s

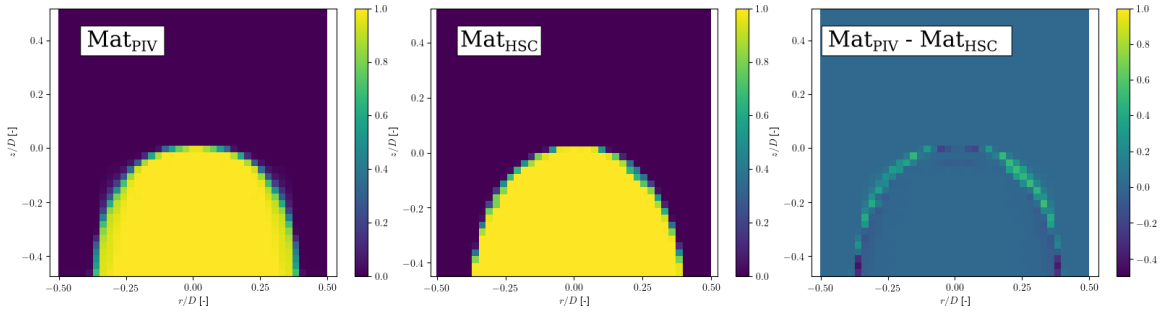

(b) $j_l = 21.64 \times 10^{-2}$ m/s and $j_g = 0.0$ m/s

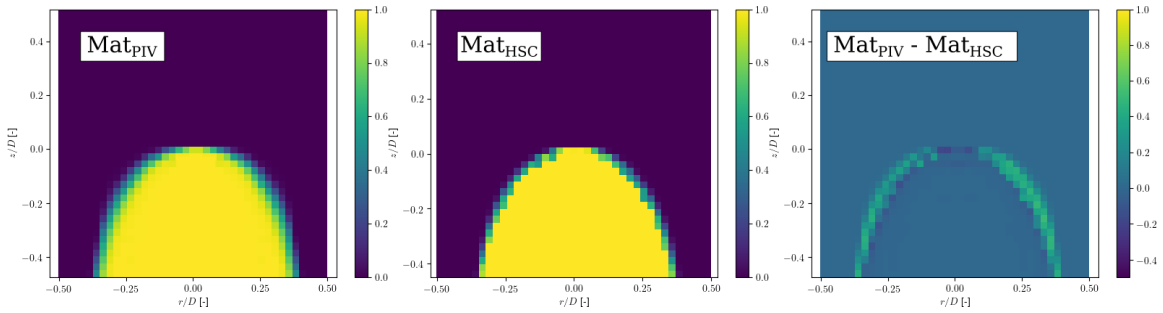

(c) $j_l = 21.64 \times 10^{-2}$ m/s, $j_g = 2.38 \times 10^{-3}$ m/s and $\overline{\langle \alpha_g \rangle} = 0.7$ %

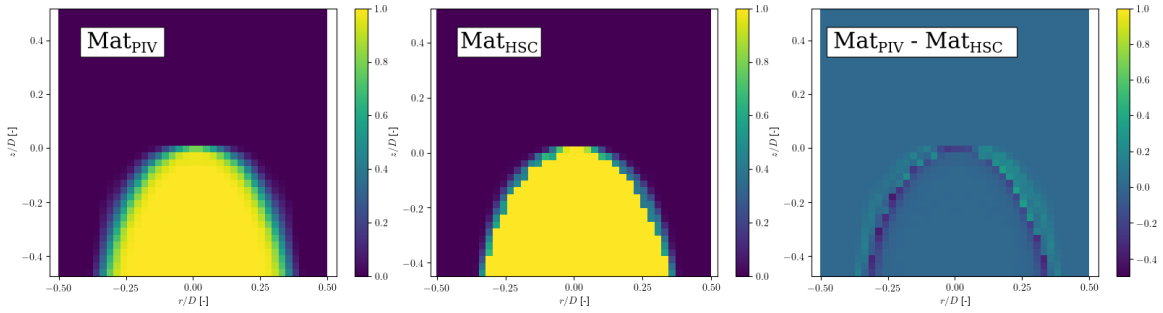

(d) $j_l = 21.64 \times 10^{-2}$ m/s, $j_g = 19.83 \times 10^{-3}$ m/s and $\overline{\langle \alpha_g \rangle} = 4.9$ %

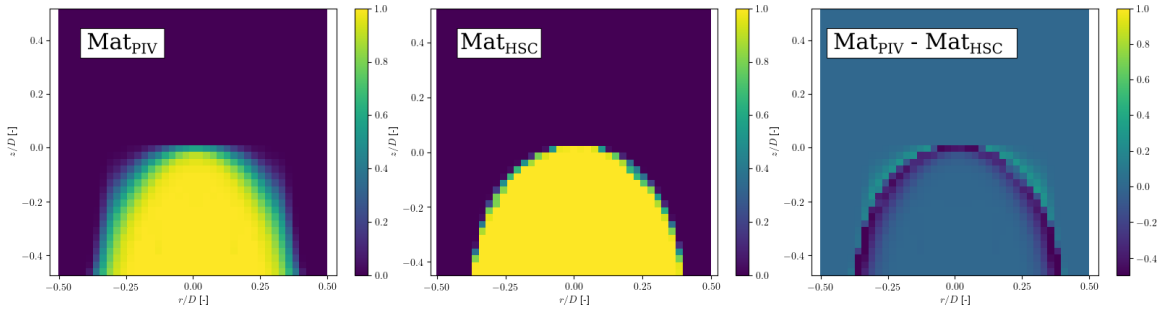

Source - Developed by the author.

5.5.3 Effect of the number of measurements on the ensemble averaged PIV velocity fields

In order to assess if the number of instantaneous acquisitions considered is adequate for the calculation of consistent averages, a study was performed for each flow situation, i.e, stagnant or flowing liquid, with or without dispersed bubbles, with the purpose of visualize the effect of increasing the number of instantaneous fields to the set taken into account for the ensemble average calculation. The number of instantaneous acquisitions (N_{PIV}) included in the set of the ensemble average was gradually increased until it is observed that the maximum deviation between the average calculated with the previous set and with the current one was below a certain tolerance. It is important to state, that a minimum wait time was respected between every Taylor bubble PIV acquisition, hence assuring that the PIV acquisition was not affected by the previous passage of a Taylor bubble. This time was in the range of 15 s to 35 s, depending on the liquid superficial velocity j_l of the flow stream condition. In addition, for some flow configurations, where the number of instantaneous fields N_{PIV} was high, the acquisitions were performed in different experiment sessions. In these cases, it was observed that this did not affect the results, ensuring the repeatability of experimental conditions.

Figures 5.32 and 5.33 present the ensemble average liquid velocity vector fields around the nose and tail region of Taylor bubbles for different N_{PIV}, for a case with high liquid superficial velocity (j_l = 21.64 $\times 10^{-2}$ m/s) and a relatively high fraction ($\overline{\langle \alpha_g \rangle}$ = 4.9 %) of dispersed bubbles. For theses cases, it is expected that a high number of acquisition be necessary to get consistent averaged fields. The thick red line indicates the gas-liquid interface position obtained from the PIV dynamic masking procedure (averaged over 500 acquisitions). This line is defined as the 0.5 iso-line value of the PIV Taylor bubble nose/tail probability occurrence matrix $\mathrm{Mat}_{\mathrm{PIV}}$ (see Fig. 5.29). In Fig. 5.33 it is interesting to note that the PIV dynamic masking procedure is capable of capturing the typical of the Taylor bubble bottom shape, despite of the strong fluctuation observed in instantaneous acquisitions.

In cases a) of Figs. 5.32 and 5.33, 100 acquisitions (N_{PIV}=100) were used to calculate the ensemble averages, while the second cases (b)) represent an averaging over N_{PIV}=500 acquisitions. As expected, a higher number of instantaneous acquisition is needed to get consistent averages at the tail region, due to the stronger fluctuations.

Figure 5.34 presents the axial liquid velocity profiles ($\langle w_l(r) \rangle$) along the pipe radius, at the nose and tail regions for different flow conditions, averaged over sets with different numbers of instantaneous fields. These profiles were taken at $z/D = 0.1$ above the nose tip an $z/D = -0.2$ below bubble tail. Again, as the fluctuations are less intense at the bubble

Figure 5.32 – Ensemble average liquid velocity vector fields around the Taylor bubble nose for the $j_l = 21.64 \times 10^{-2}$ m/s, $j_g = 19.83 \times 10^{-3}$ m/s and $\alpha_g = 4.9$ % flow stream configuration for two different number of instantaneous fields: a) N_{PIV}=100 and b) N_{PIV}=500.

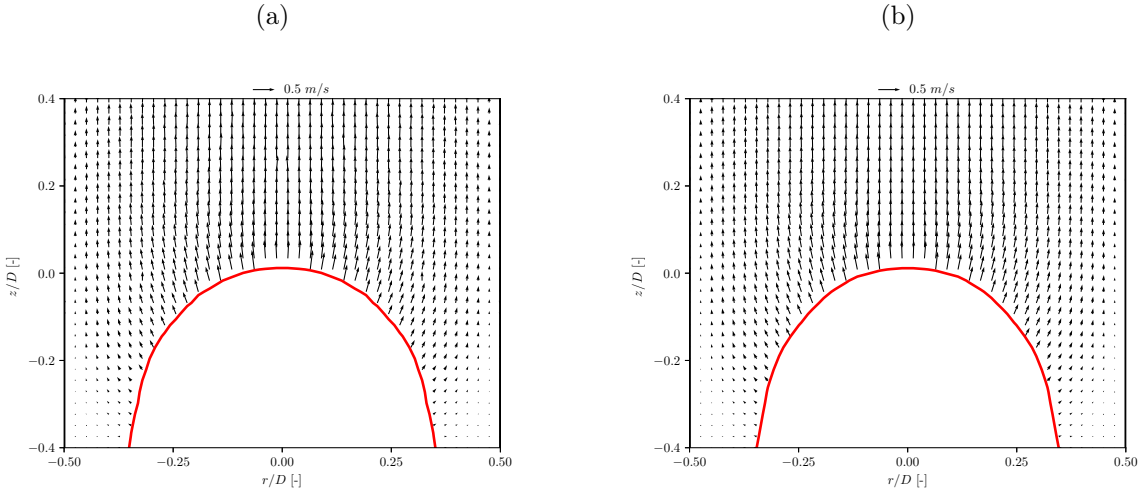

Source - Developed by the author.

nose, averages over a few instantaneous fields are enough to calculate a representative averaged field. On the other side, in the tail, as already observed, a higher number of acquisitions is needed to get consistent averages. In Figs. 5.32b), d) and f), consistent profiles were only acquired with twice the number of instantaneous fields as those required for the analysis of the nose region. In addition, as expected, in the cases with the presence of dispersed bubbles, an even higher number of acquisitions were needed to get consistent averages at the tail and nose region.

Figure 5.35 shows the turbulence kinetic energy (TKE) k profile at the $z/D = -0.2$ position from the bubble tail position for three different flow configurations, and for different values of N_{PIV}.

From the PIV instantaneous acquisitions, the turbulent kinetic energy k is defined as,

$$k = \frac{1}{2}\left[v_{l,rms}(r)^2 + w_{l,rms}(r)^2\right] \tag{5.8}$$

The analysis is performed in the tail position, since a higher number of instantaneous acquisitions were required due to the strong fluctuations in this region. From those profiles, it is clear that N_{PIV} above 300 (or higher, for the cases with higher concentrations of dispersed bubbles) is required to calculate turbulence parameters in the tail region of Taylor bubbles.

Figure 5.33 – Ensemble average liquid velocity vector fields around the Taylor bubble tail for the $j_l = 21.64 \times 10^{-2}$ m/s, $j_g = 19.83 \times 10^{-3}$ m/s and $\overline{\langle \alpha_g \rangle} = 4.9$ % flow stream configuration for two different number of instantaneous fields: a) N_{PIV}=100 and b) N_{PIV}=500.

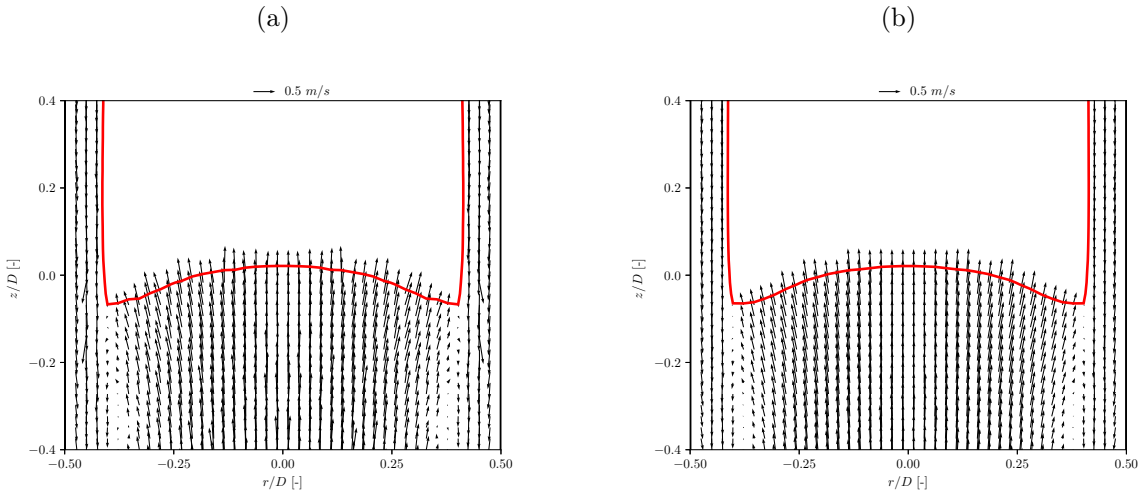

Source - Developed by the author.

5.5.4 Velocity fields around Taylor bubbles in co-current flow in the presence of dispersed bubbles

This section presents some results for the velocity fields around Taylor bubbles with the presence of small dispersed bubbles in the liquid stream. These results are presented in order to show the potential of the experimental techniques described in this Chapter. However, further analysis and discussion of the flow structure are presented in the next Chapter.

The results are presented for different values of the liquid superficial velocity and different values of the superficial velocity of dispersed bubbles. To facilitate the results visualization and interpretation, the reference frame is defined as moving with the bubble (Moving Frame of Reference, MFR), as depicted in Fig. 5.36, where the resulting streamlines for the fixed and moving frame of reference are shown.

It is important to point out again that the superficial velocity of the gas phase corresponds only to the dispersed bubbles, which is calculated from the gas flow rate measured at the gas flowmeter, and the Taylor bubbles air injected independently in the bubbly flow generated at the test section.

Figure 5.37 presents typical axial $\langle w_l(r) \rangle$ and radial $\langle v_l(r) \rangle$ liquid velocity profiles at the nose and tail region for cases with and without the presence of dispersed bubbles in the liquid stream.

Figure 5.34 – Effect of the number of instantaneous fields considered in the calculation of the ensemble averaged fields, at nose (left) and wake (right) regions, for three different flow stream configurations: a) and b) $j_l = 0.0$ m/s and $j_g = 0.0$ m/s; c) and d) $j_l = 21.64 \times 10^{-2}$ m/s and $j_g = 0.0$ m/s; e) and f) $j_l = 21.64 \times 10^{-2}$ m/s, $j_g = 19.83 \times 10^{-3}$ m/s and $\overline{\langle \alpha_g \rangle} = 4.9$ %.

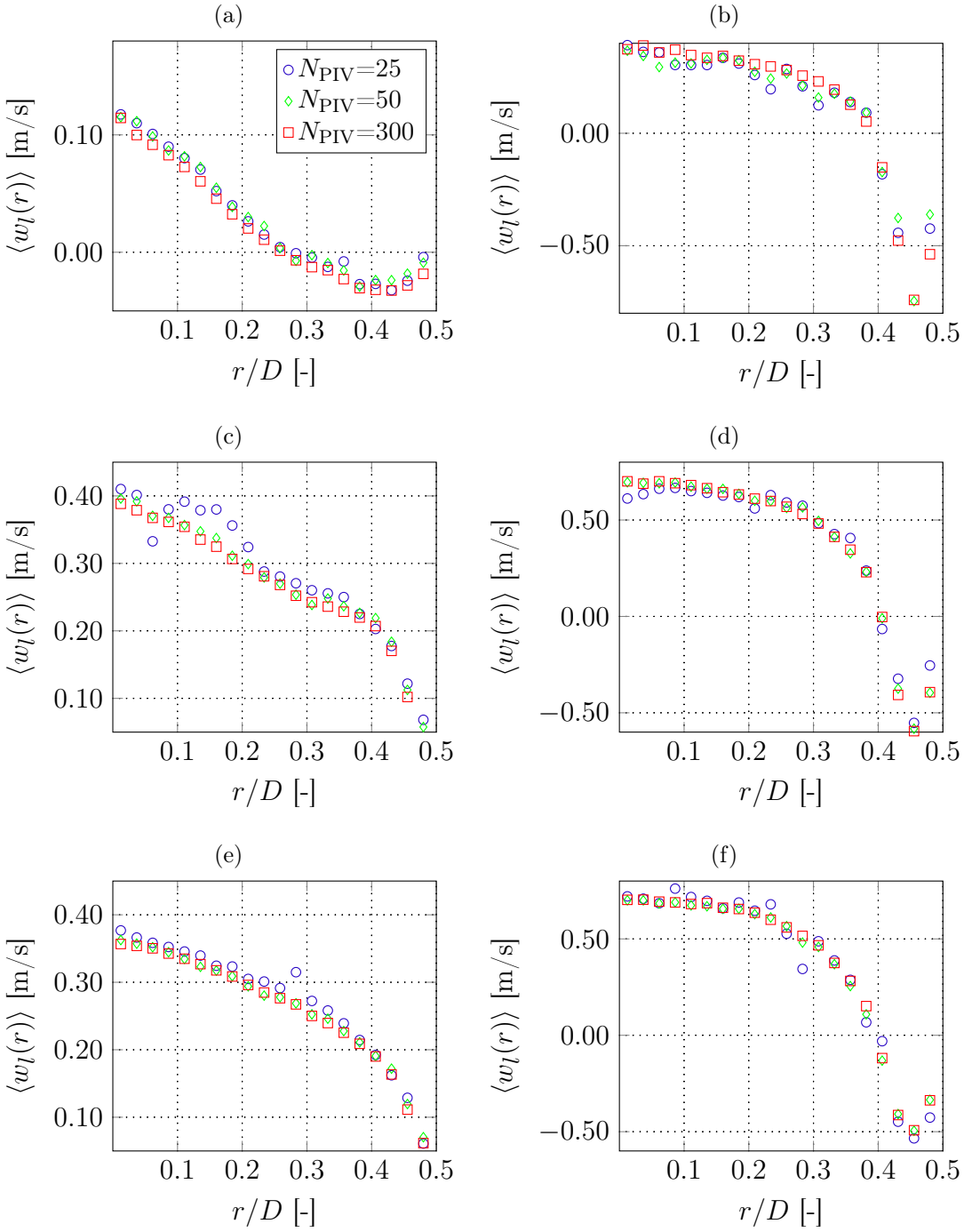

Source - Developed by the author.

Figure 5.35 – Effect of N_{PIV} on the turbulent kinetic energy calculation in the tail region position $z/D = -0.2$ in three different flow stream configurations: a) j_l = 0.0 m/s and j_g = 0.0 m/s; b) j_l = 21.64 $\times 10^{-2}$ m/s and j_g = 0.0 m/s; c) j_l = 21.64 $\times 10^{-2}$ m/s, j_g = 19.83 $\times 10^{-3}$ m/s and $\overline{\langle \alpha_g \rangle}$ = 4.9 %.

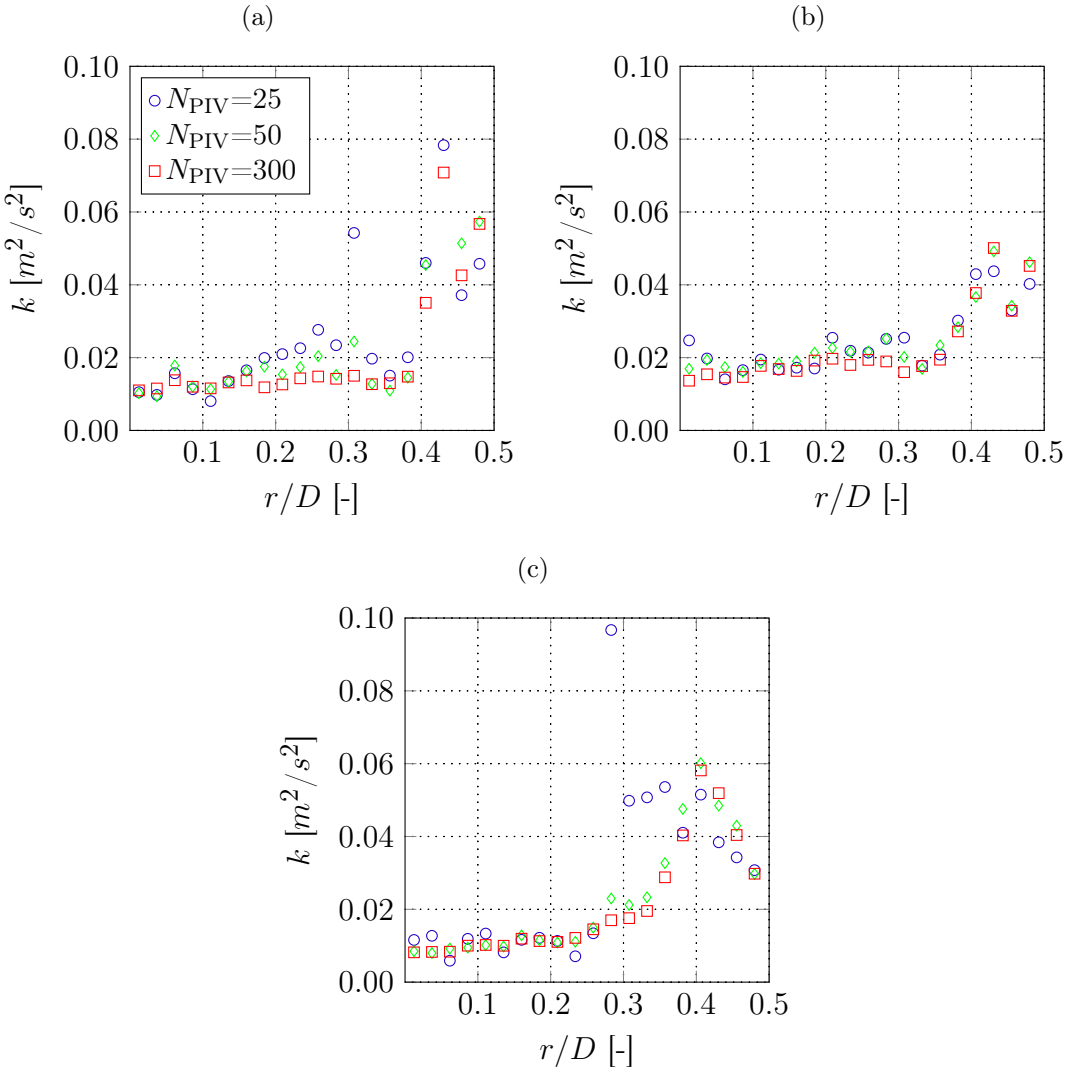

Source - Developed by the author.

Figure 5.38 shows the streamlines and the turbulent kinect energy k field at the tail region of Taylor bubbles for the cases with and without gas dispersed bubbles in the liquid stream. Clearly, the presence of dispersed bubbles in the liquid stream significantly affects the flow structure around Taylor bubbles. One of the most evident aspects is the increase of the recirculation length at the tail region of Taylor bubbles, which is also associated to the higher rising velocity attained by Taylor bubbles, when dispersed bubbles are present in the liquid stream. In addition, a higher turbulent kinetic energy intensity is observed in the case with dispersed bubbles.

In the next chapter, a detailed analysis of the flow structure around Taylor bubbles

Figure 5.36 – Streamlines of the ensemble averaged flow at the (a) nose and (b) rear of the Taylor bubble. The left streamlines are plotted with a fixed frame of reference (FFR) and those on the right with a moving frame o reference (MFR). The change of reference frame used the $\langle U_{tb,N} \rangle$ values of the high-speed camera method, given in Sec. 5.5.1.

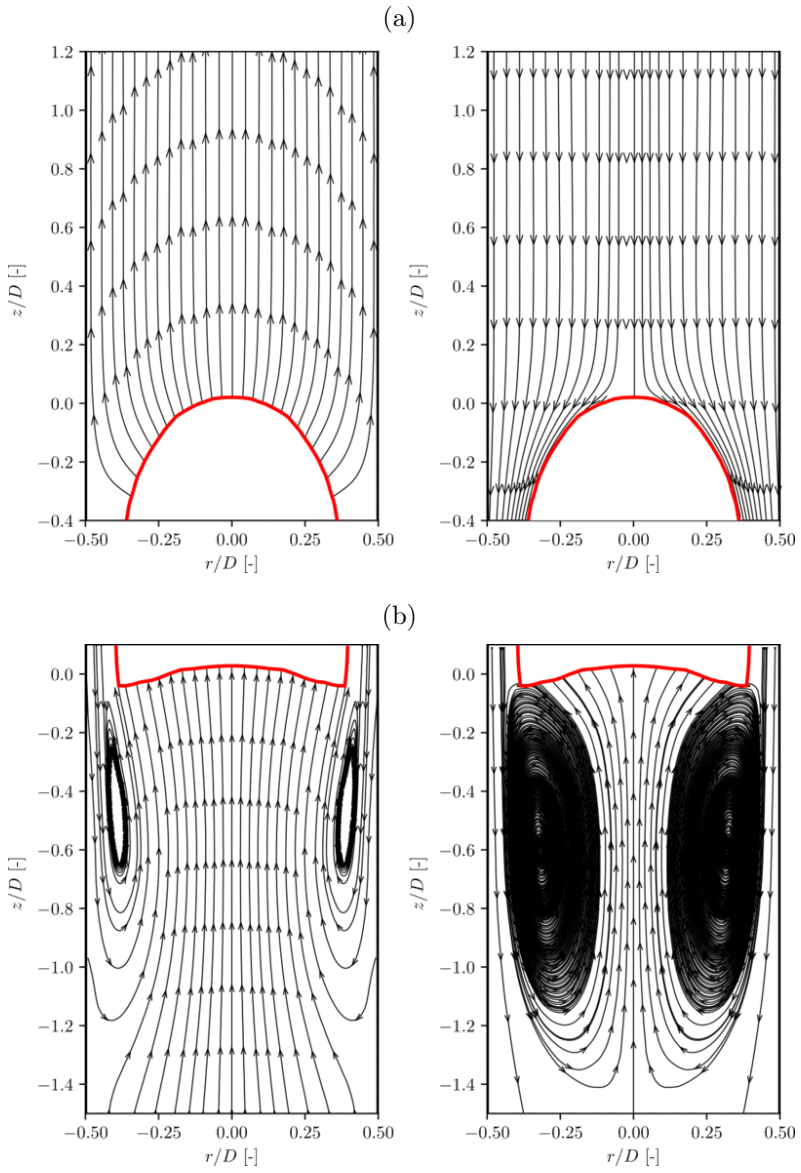

Source - Developed by the author.

in the presence of dispersed bubbles will be presented.

Figure 5.37 – Velocity profiles at the nose (a) and wake (b) regions with and without the presence of dispersed bubbles in the liquid stream for the same liquid superficial velocity $j_l = 21.64 \times 10^{-2}$ m/s. The plots on a) were taken at the $z/D = 0.06$ above the Taylor bubble nose. The plots on b) were taken at $z/D = 0.4$ below the Taylor bubble tail position.

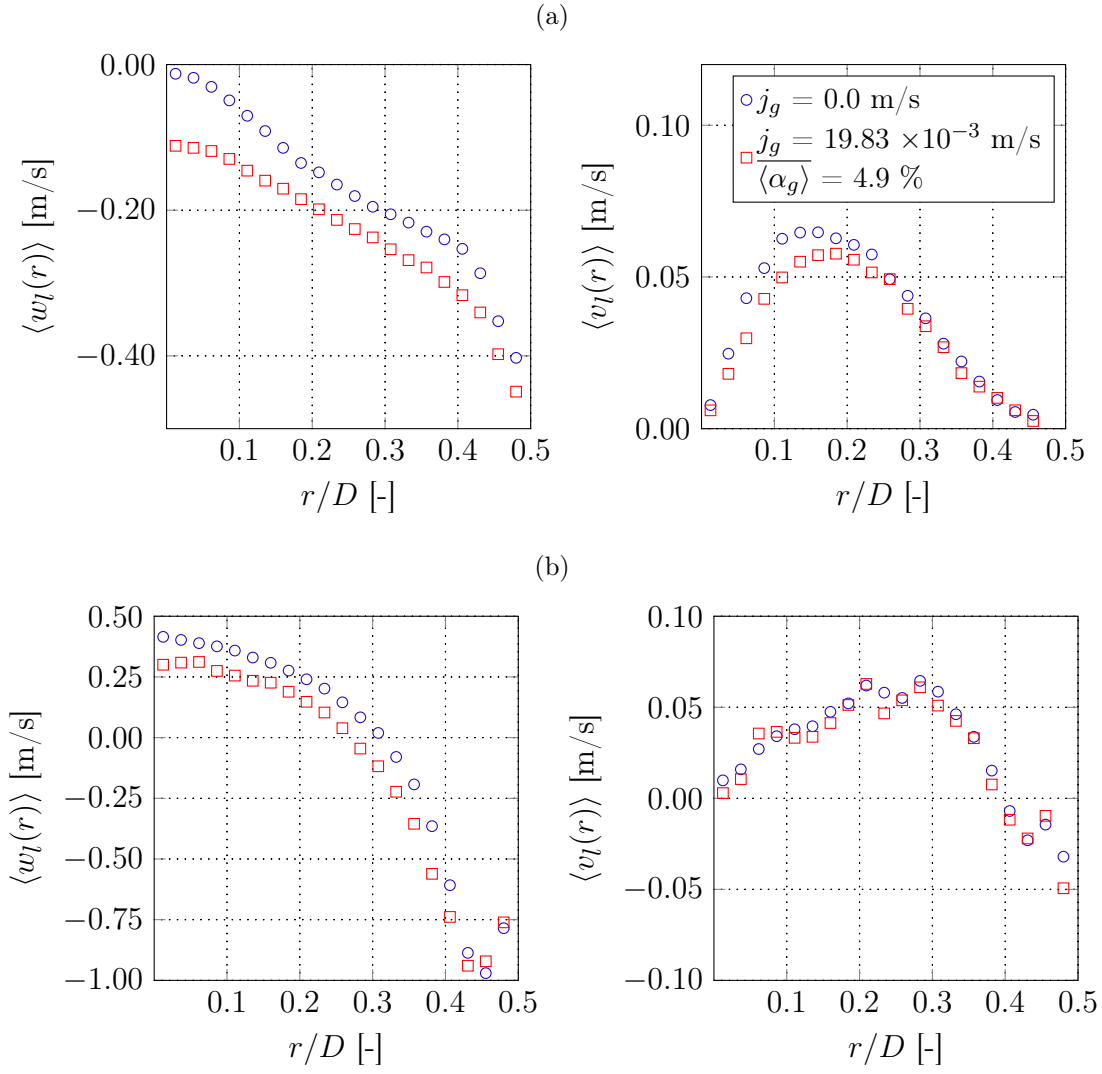

Source - Developed by the author.

Figure 5.38 – Streamlines of Taylor bubbles (left) and turbulent kinetic energy k field(right) at the tail region, for different concentration of dispersed bubbles, for $j_l = 21.64 \times 10^{-2}$ m/s and: a) $j_g = 0.0$ m/s and b) $j_g = 19.83 \times 10^{-3}$ m/s and $\overline{\langle \alpha_g \rangle} = 4.9$ %.

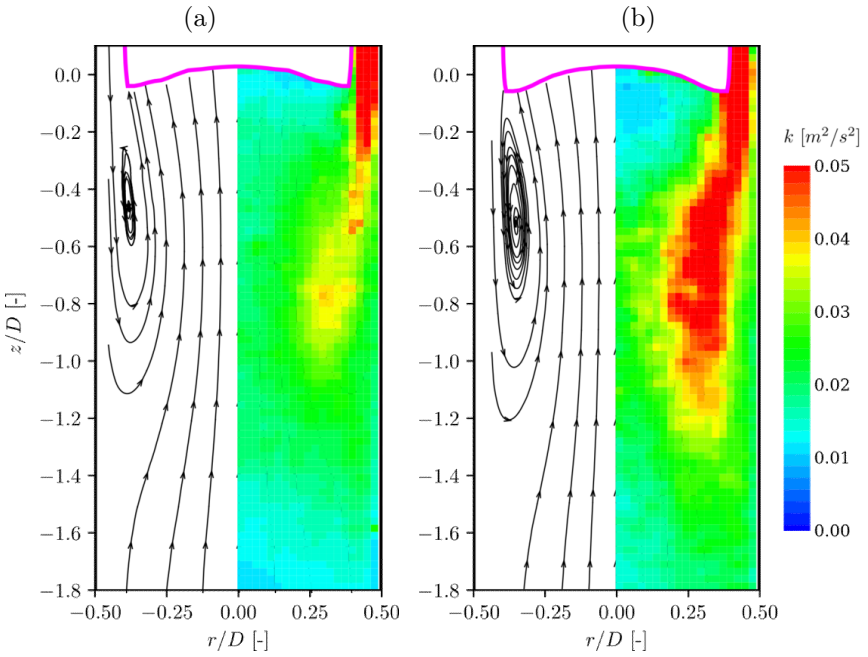

Source - Developed by the author.

5.6 CONCLUSIONS

In this chapter, an experimental apparatus and instrumentation for the experimental investigation of the flow around a single Taylor bubble in the presence of dispersed bubbles were developed and validated. Although this does not represent the real slug flow situation, the flow condition generated in this experiment represents a much more realistic situation than the simple Taylor flow usually considered in the previous studies of the flow structure around Taylor bubbles. The experimental set-up allowed the acquisition of consistent PIV average velocity fields due to its controlled operational conditions, such as i) specification of the dispersed gas superficial velocity; ii) the controlled Taylor bubbles length and mainly iii) control of the Taylor bubble passage period at the PIV test section and iv) and the PIV triggering synchronization.

The Laser Diode Photocell technique (LPD), was analyzed and validated as a measurement technique for the Taylor bubble length and rising velocity (nose and bottom). In addition, this technique was used for the synchronization of PIV image acquisition and the Taylor bubbles passage at the test section. Although this technique had been already used in the literature, slight modifications had to be introduced to deal with the presence of the dispersed bubbles. In order to asses the LDP ensemble averaged results, its values were compared with the ones acquired from an image analysis methods based on high-speed camera footage with minimum uncertainty errors. From this comparison, in the cases with the presence of dispersed bubbles, the LDP technique fails to detect the bubble bottom passage instant correctly. The failure in detecting the bubble bottom is associated with the oscillating tail movement from the high N_f and also the presence of dispersed bubbles in this region, which intensifies those oscillations and mislead the LDR signals due to its high dispersed bubble concentration in this area. However, in these situations, the LDP technique results in reliable Taylor bubble nose velocities. In addition, the LDP technique was used to synchronize the PIV acquisitions with Taylor bubbles around a predefined position.

The consideration of high inverse viscosity number (N_f) and, additionally, the presence of small dispersed bubbles, turn the flow very chaotic, in particular, in the tail region. Thus, leading to the need for the acquisition of a large number of PIV instantaneous fields to get consistent ensemble averaged results.

Due to the strong fluctuations, the PIV triggering synchronization is not enough to ensure that the Taylor bubble nose or tail remains in the same position for all the acquisitions. In addition, the strong interface fluctuations impede the use of fixed masking and, due to the three-dimensional nature of these oscillations, the shadowgraphy cannot

be used. Hence, in order to circumvent these issues, a PIV dynamic masking procedure was developed, aiming first to detect the Taylor bubbles position in the PIV images and, later, to remove the region occupied by them in the PIV analysis. The ensemble averaged gas-liquid interface from the PIV dynamic masking procedures were compared against the results from the high-speed camera image analysis acquisitions. This comparison showed that the dynamic masking procedure precisely reconstructs the Taylor bubble shapes, demonstrating that this procedure can be used to study the flow around Taylor bubbles. However, the fact that PIV takes the image at the pipe central plane (different from the HSC, that captures the shadow projection), resulted in better predictions of the bubble shape. Furthermore, the treatment proposed here, allows the calculation of the nose fluctuation intensity, at least in qualitative terms, which influences the Taylor bubble rising velocity, due to the form drag modification (TUDOSE; KAWAJI, 1999).

The PIV results show that the presence of dispersed bubbles strongly affects the flow field around Taylor bubbles. First, the PIV dynamic masking showed that the fluctuations of the Taylor bubble nose tip radial position are significantly affected by the induced dispersed bubble turbulence. As dispersed bubbles are injected to the flow stream, the Taylor bubble rising moving is altered, its nose position fluctuates around the duct centerline, contrary to the cases without dispersed bubbles, where the radial position dispersion of the nose tip is weak, indicating that the bubble nose shape does not fluctuate significantly during its rising motion. From the PIV liquid velocity profiles behind the tail, the results showed that due to strong fluctuations caused by the dispersed bubbles, a higher number of instantaneous fields is required to gather consistent ensemble averaged results.

The experimental apparatus and image processing techniques described in this work can produce reliable ensemble average results, which can be used to analyze the effect of the dispersed bubbles on the flow structure around Taylor bubbles, including turbulence fields and interface fluctuations. Therefore, the methodology described here may help in providing new physical insights about heat and mass transfer process in liquid slug regions. Additionally, the techniques described in this work can be further extended to analyze real gas-liquid vertical and horizontal flows.

Chapter 6

Experimental Study of the Flow Structure around Taylor Bubbles in the Presence of Dispersed Bubbles

This part has been published as:
CERQUEIRA, Rafael F.L. and PALADINO, E. E., Experimental study of the flow structure around Taylor bubbles in the presence of dispersed bubbles. International Journal of Multiphase Flow, v. 133, p. 103450, 2020.

ABSTRACT

This chapter presents an experimental study focusing on the interactions between the dispersed and Taylor bubbles in a slug flow pattern. In order to better investigate these interactions, a manufactured slug flow was studied, where a single Taylor bubble are injected in a bubbly flow background stream, under controlled and repeatable conditions, controlling the bubbly flow superficial gas and liquid velocity, and also the Taylor bubble length. In this way ensemble-averaged results can be obtained over several Taylor bubbles. The flow was analyzed through laser diode photocell, high-speed camera imaging and PIV techniques. Results revealed that the terminal Taylor bubble velocity is affected by the gas volume fraction of the bubbly background flow. Ensemble average velocity profiles are presented for Taylor bubble nose and tail. Since the experimental apparatus used in the present work allowed a large number of instantaneous PIV acquisitions, the turbulent

statistics around the Taylor bubble can be also calculated. These experimental results could be used for the implementation and validation of multidimensional CFD models for flows with different interface length scales.

6.1 INTRODUCTION

This chapter presents the results obtained from the experimental apparatus and instrumentation described in the previous chapter. The flow structure around Taylor bubbles (large scale interface), including the presence of dispersed bubbles (short scale interfaces) and the interactions among them is analyzed in details. First, a short motivation and a review of recent papers approaching the flow structure around Taylor bubbles will be presented.

Slug flow is a common pattern in gas-liquid two-phase flow in pipes, which occurs in a relatively wide range of superficial velocities of both phases. It is encountered in several industrial processes as in the chemical process industry, energy transformation and oil production. Besides, due to this intermittent characteristic, several flow assurance related problems arise in oil production systems, including slug induced corrosion (CO_2 and H_2S) (NEŠIĆ, 2007; YAN; CHE, 2011) and control and structural problems associated to pressure fluctuations, mainly in situations of severe slugging. Its modeling is complex, mainly because of its intermittent characteristic and the fact that interfaces of different scales are present in the fluid domain, which does not allow to classify it into "dispersed" or "separated" pattern, as is common in most modeling approaches (FABRE; LINÉ, 1992).

The slug flow consists of long bullet shaped bubbles, called Taylor bubbles, followed by liquid slug, typically containing dispersed small bubbles. In order to simplify the models and make them generally applicable, several authors used the concept of "slug unit" (WALLIS, 1969), which is defined as a region composed by a Taylor bubble and the subsequent liquid slug, and the whole flow is considered as a sequence of slug units. As the Taylor bubble rises, the liquid is displaced and flows through a thin annular film formed between the gas-liquid interface and the pipe walls. This film exits from the bubble rear, expanding and creating a recirculation pattern in this region. The intensity and length of those patterns are of great importance since it can be associated with global flow parameters, such as heat and mass transfer coefficients in the liquid slug region (HAYASHI et al., 2014; SCAMMELL; KIM, 2015; SILVA et al., 2019). Therefore, local flow information is fundamental for the development of closure correlations. This fact has motivated the numerical and experimental investigation of the local flow structure around Taylor bubbles (CAMPOS; DE CARVALHO, 1988; CAMPOS; CARVALHO, 1988; VAN

HOUT et al., 2002c; BUGG; SAAD, 2002; SOUSA et al., 2005; NOGUEIRA et al., 2006b; ARAÚJO et al., 2012, 2013; SHABAN; TAVOULARIS, 2018).

The literature on modeling and experimentation in slug flows is very vast, and thus, it is beyond the scope of this work to present detailed review. In terms of slug flow modeling, mechanistic 1D models (TAITEL; DUKLER, 1976; TAITEL; BARNEA, 1990) were used to compute real flow situations as, for instance, flow in oil production wells. However, in most cases, models for the determination of engineering parameters like pressure drop and gas hold-up (usually referred to the "slug unit"), depends on closure parameters as Taylor bubble velocity, film thickness and velocity distribution around Taylor bubble, which are needed for the closure of mechanistic models.

Aiming the development of closure model for slug flow, some authors (BUGG; SAAD, 2002; TAHA; CUI, 2006b; ARAÚJO et al., 2012; SHABAN; TAVOULARIS, 2018) have attempted detailed multidimensional simulations to investigate in details the flow structure around Taylor bubbles. Despite the success of modeling Taylor slug flows, those multidimensional models cannot be used in slug flows where small dispersed bubbles are present (TAITEL; BARNEA, 1990). In these flow situations, typically find in oil/gas production and transport lines, the presence of large (Taylor bubbles) and small (dispersed bubbles) interfacial scales in the same domain represents a challenge form the modeling point of view. In an attempt to model a more realistic situation, Yan and Che (2011) presented a model for gas-liquid flows with different interface scales, considering a dispersed (bubbly) phase flowing together with Taylor bubbles. Still, no model validation was presented, probably, because of the lack of consistent experimental results for this flow situation. Thus, the data generation for the development and validation of such models is another important motivation for this research.

In the past, several researchers developed detailed experimental studies of the flow around individual Taylor bubbles rising in a stagnant or flowing liquid, using PIV or PST (Pulsed Shadow Technique) techniques (CAMPOS; CARVALHO, 1988; POLONSKY et al., 1999a; BUGG; SAAD, 2002; VAN HOUT et al., 2002c; NOGUEIRA et al., 2003, 2006b; SHEMER et al., 2007; LIU et al., 2013; SANTOS; COELHO PINHEIRO, 2014). However, the formation of the slug flow in vertical pipelines usually arises from bubbly flow pattern, when gas superficial velocity is increased and Taylor bubbles are formed by the coalescence of the small dispersed bubbles, but a significant fraction of these small bubbles still remains as a dispersed phase flowing in the liquid slug and around Taylor bubbles. This is substantially different from the flow of Taylor bubbles in a liquid, without small dispersed bubbles, which is also called Taylor flow. In real applications, Taylor flow is usually encountered in mini and microchannels or in cases of very low superficial liquid

velocities, which promotes the coalescence of small bubbles. Despite this fact, most papers presenting fundamental studies of the flow structure around Taylor bubbles, specifically those aiming to measure the velocity fields around them, consider Taylor flow, i.e., without the presence of small dispersed bubbles. A summary of the main experimental research papers showing measurements of the velocity fields around Taylor bubbles is presented in Tab. 6.1. This summary excludes other papers addressing the measurement of global parameters of slug flows as bubble or slug length, bubble velocities, pressure drop, etc.

Table 6.1 – Summary of the main experimental studies of the flow around Taylor bubbles.

Author	Technique	Fluids and conditions	D_{duct}	N_f	Results
Campos and Carvalho (1988)	Photography analysis	Air bubbles in stagnant water and water-glycerol solutions	19 - 52 mm	8199 - 37120	Photographic study of the wake of Taylor bubbles
Polonsky et al. (1999a)	PIV	Air bubbles in stagnant, upward and downward water flow	25 mm	12380	Investigates the effect of the liquid velocity field on the Taylor bubbles motion
Bugg and Saad (2002)	PIV and CFD	Air bubbles in stagnant olive oil	19 mm	90	CFD model validation for axial and radial velocity components, through PIV measurements
Van Hout et al. (2002c)	PIV	Air bubbles in stagnant water	25 mm	12380	Axial and radial velocity profiles at the nose, film and wake
Nogueira et al. (2003)	PIV and PST	Air bubbles in stagnant aqueous solution	32 mm	200	Axial and radial velocity profiles at the nose, film and wake
Nogueira et al. (2006b)	PIV and PST	Air bubbles in stagnant water and water-glycerol solutions	32 mm	15-17929	Axial and radial velocity profiles at wake
Shemer et al. (2007)	PIV	Air bubbles in upward water flow	25 mm	12380	Axial and radial velocity profiles at the nose, film and wake
Liu et al. (2013)	PIV	Nitrogen vapor bubbles in stagnant liquid nitrogen	3 - 16 mm	2551-31489	Flow structure at the wake region in liquid nitrogen under various inclinations
Santos and Coelho Pinheiro (2014)	PIV and PST	Air bubbles in stagnant water	32 mm	14076-16316	Studied the effects of gas expansion in the flow structure

Source - Developed by the author.

Recently, to investigate the influence of the presence of the small dispersed bubbles on the flow structure around Taylor bubbles, the present authors developed in Cerqueira et al. (2019b) (Chapter 5) a novel experimental apparatus and a set of measurement techniques for the study of "quasi-real" slug flows. Due to challenging complexity of charactering such flows, Chapter 5 focus on the implementation of these novel experimental techniques. The techniques developed in this work were used to generate and analyze a "quasi-real" slug flow pattern, where the flow structure around single Taylor bubbles flowing into a co-current air-water bubbly flow stream, was studied. The experiment is based on a "three field flow" concept, i.e., liquid, continuous gas (Taylor bubbles) and dispersed gas, where the flow rates of liquid and dispersed gas were controlled and also the Taylor bubbles sizes.

This experimental apparatus allowed the study of the flow around Taylor bubbles in the presence of small dispersed bubbles under controlled conditions which cannot be assured in a "real" slug flow, i.e., generated by simply mixing the phases at appropriate superficial velocities.

The Taylor bubbles were analyzed through a Laser diode photocell (LDP), PIV and digital imaging processing techniques. The LDP technique measured Taylor bubbles length

and velocity, and its signal was used to synchronize the PIV system. A dynamic masking procedure was developed to remove the Taylor bubbles from the PIV images. This masking technique was combined with a technique for the discrimination of the dispersed bubbles, reported in Chapter 5, allowing for the measurement of the liquid phase velocity. The combination of those experimental and instrumentation techniques allowed the acquisition of consistent ensemble averaged velocity fields around Taylor bubbles with the presence of small dispersed bubbles.

This work aims to advance in the investigation of the flow around Taylor bubbles by considering the presence of small dispersed bubbles in the liquid stream. Although this scenario does not characterize the real slug flow pattern, it is represented in a more realistic way than the Taylor flow. However, this investigation intends to be a fundamental study with focus on the interaction of Taylor and dispersed bubbles, and not for directly measure real slug flow parameters.

Following these motivations, this paper presents a study of the flow structure around Taylor bubbles, in the presence of dispersed bubbles, aiming to,

- Understand the influence of the presence of a dispersed phase on the flow structure around Taylor bubbles, and
- Generate data for the implementation and validation of multidimensional CFD models for flows comprehending different interface lengths scales, which includes slug flow.

The experimental apparatus and flow measurement techniques used to obtain the following results were developed and validated in the previous chapter and published in Cerqueira et al. (2019b). This apparatus allowed the study the flow structure around Taylor bubbles with controlled length, into a liquid stream containing small dispersed bubbles, which superficial velocities (of liquid and dispersed bubbles) were also controlled. In the next section, results obtained from this investigation will be presented. These constitute the main experimental results of this thesis.

6.2 RESULTS AND DISCUSSION

This section presents the results obtained from the experimental study described in the previous sections. First, the experimental matrix is presented, which shows the flow configuration of each experiment conducted in this work. Then, an analysis of the effect of the dispersed gas phase on the Taylor bubble terminal velocity will be presented through the results of the Laser Diode Photocell (LDP) and High-Speed Camera (HSC) techniques.

Then, in order to gain a better insight into those results, the flow structure around the Taylor bubbles will be explored through the detailed information of analysis of the HSC footages and the ensemble averaged PIV results for the velocity and turbulence fields of the liquid phase.

The analyses presented are based on the averaged values of the variables, where the notation $\langle \bullet \rangle$ represents ensemble average results and $\overline{\bullet}$ represents a spatially averaged value over the duct cross-section. Further details on the averaging procedure can be found in Chapter 3 and 5.

Table 6.2 shows the experimental conditions of the experiments conducted in this work, where the liquid j_l and gas j_g superficial velocities were calculated based on the gas and liquid flow rate measurements. The experiments were conducted with two superficial liquid velocities, with experimental points lying in the laminar ($Re_l = 812$) and turbulent ($Re_l = 5684$) regimes based on the liquid Reynolds number $Re_l = \rho_l \overline{\langle v_l \rangle} D/\nu_l$. The air-water system configuration and the pipe geometry used in the present work, resulted in the following dimensional Morton $Mo = g\mu_l^4/\rho_l\sigma^3$ and Eötvös $Eo = \rho_l g D^2/\sigma = {N_f}^{4/3} Mo^{1/3}$, $Eo = 94$ and $\log(Mo) = -10.6$. According to (PINTO et al., 1998), in this set of dimensional numbers and liquid flow rates, the back of the Taylor bubble should present an open and turbulent wake in the two studied set of j_l experiments. The parameter β corresponds to the gas to total superficial velocities relationship, $\beta = j_g/(j_g + j_l)$. It is important to state that the Taylor bubble was not taken into account in the calculation of the gas j_g superficial velocities and the gas volume fraction $\overline{\langle \alpha_g \rangle}$. Additionally, the valve timing and chamber pressure were adjusted to produce Taylor bubbles with an approximate constant size of $\langle L_{tb} \rangle \approx 100.0$ mm.

The gas volume fraction $\overline{\langle \alpha_g \rangle} = j_g/\overline{\langle w_g \rangle}$, where $\overline{\langle w_g \rangle}$ is calculated from PTV method for dispersed bubbles, and the mean equivalent spherical bubble diameter $\overline{\langle d_b \rangle}$ (CLIFT et al., 2005b) are calculated using the bubble tracking method described in Chapter 3.

In all the experiments in Tab. 6.2 rising velocity of Taylor bubbles were measured through the LDP technique and footage obtained by the high-speed camera. As commented in (CERQUEIRA et al., 2019b), the number of instantaneous acquisitions can get up to 500 instantaneous fields in order to result in consistent average velocity fields. This means it was necessary to inject up to 500 Taylor bubbles to extract reliable information of the flow structure. Since each bubble was injected at an interval of approximately 30 seconds, the total experiment time could last around 5 hours for acquiring the velocity fields in the nose and tail region of the Taylor bubbles. Due to the different flow structures around the nose and tail, mainly the order of the velocity magnitudes, it was necessary to acquire the

PIV images around the tail or nose in different sessions. Therefore, since the acquisitions through the PIV technique required a greater effort than the high-speed camera filming and LDP analysis, not all the points of Tab. 6.2 were analyzed through the PIV technique.

Table 6.2 – Test Matrix of the experiments performed in this work.

Experiment No.	j_l $[m/s]$	j_g $[m/s]$	β $[-]$	$\overline{\langle \alpha_g \rangle}$ $[-]$	$\overline{\langle d_b \rangle}$ $[mm]$	PIV
1	$3.09 \cdot 10^{-2}$	0.0	–	–	–	**Yes**
2		$5.89 \cdot 10^{-3}$	0.160	0.036	1.92	**Yes**
3		$9.66 \cdot 10^{-3}$	0.238	0.053	1.99	No
4		$13.55 \cdot 10^{-3}$	0.305	0.077	2.01	**Yes**
5		$15.34 \cdot 10^{-3}$	0.332	0.098	2.08	No
6		$19.83 \cdot 10^{-3}$	0.391	0.117	2.25	**Yes**
7	$21.64 \cdot 10^{-2}$	0.0	–	–	–	**Yes**
8		$2.38 \cdot 10^{-3}$	0.013	0.007	1.70	**Yes**
9		$5.89 \cdot 10^{-3}$	0.026	0.016	1.82	No
10		$9.66 \cdot 10^{-3}$	0.043	0.026	1.90	No
11		$13.55 \cdot 10^{-3}$	0.059	0.038	1.95	**Yes**
12		$15.34 \cdot 10^{-3}$	0.066	0.043	1.98	No
13		$19.83 \cdot 10^{-3}$	0.084	0.051	2.09	**Yes**

Source - Developed by the author.

As commented by several authors (SERIZAWA; KATAOKA, 1990; LIU; BANKOFF, 1993; FUJIWARA et al., 2004; HOSOKAWA; TOMIYAMA, 2013; KIM et al., 2016), the size of the dispersed bubbles can influence the Bubble Induced Turbulence (BIT) and therefore affect the interaction between the Taylor and the small bubbles. Ideally, the size distribution of the small dispersed bubbles should be controlled, but the experimental apparatus used in this work could not suffice such requirement. However, by looking at the bubble size distributions (BSD) from Fig. 6.2, calculated by the bubble shape estimator described in Chapter 4, the results show that the porous filter used to generate the bubbly stream produced bubbles with a similar bubble size distribution. According to Fig. 6.2 the single outlier is the one from Exp. 8, the experimental condition with the lowest void fraction from all the experimental data set. Therefore, it is assumed that the bubble size distribution of the dispersed bubble stream does not add a spurious contribution to the analysis of the flow structure around the Taylor bubbles.

Additionally, as aforementioned, the size of the Taylor bubbles was controlled trough precise valve timing and pressure regulation on the control volume reservoir. Figure 6.1 shows instantaneous snapshots, acquired through the high-speed camera, for each of the flow conditions listed in Tab. 6.2. From Fig. 6.1 one can notice the differences in the amount

of the dispersed bubbles present in the flow in each experimental point and observe that despite the coalescence and breakup mechanisms, common on this flow regime (KOCKX et al., 2005), the Taylor bubble length remains constant. Also, Fig. 6.1 provides a visual reference of the bubbble size distribution, previously showed by the plots in Fig. 6.2. As more representative visual example, Videos 5 and 6 of the supplementary material given in Appendix B show high-speed camera videos from the Taylor bubbles rising in different experimental conditions listed in Tab. 6.2.

Figure 6.1 – Instantaneous photographs of the flow pattern produced by the experimental apparatus used in this work for the different experimental conditions listed in Tab. 6.2.

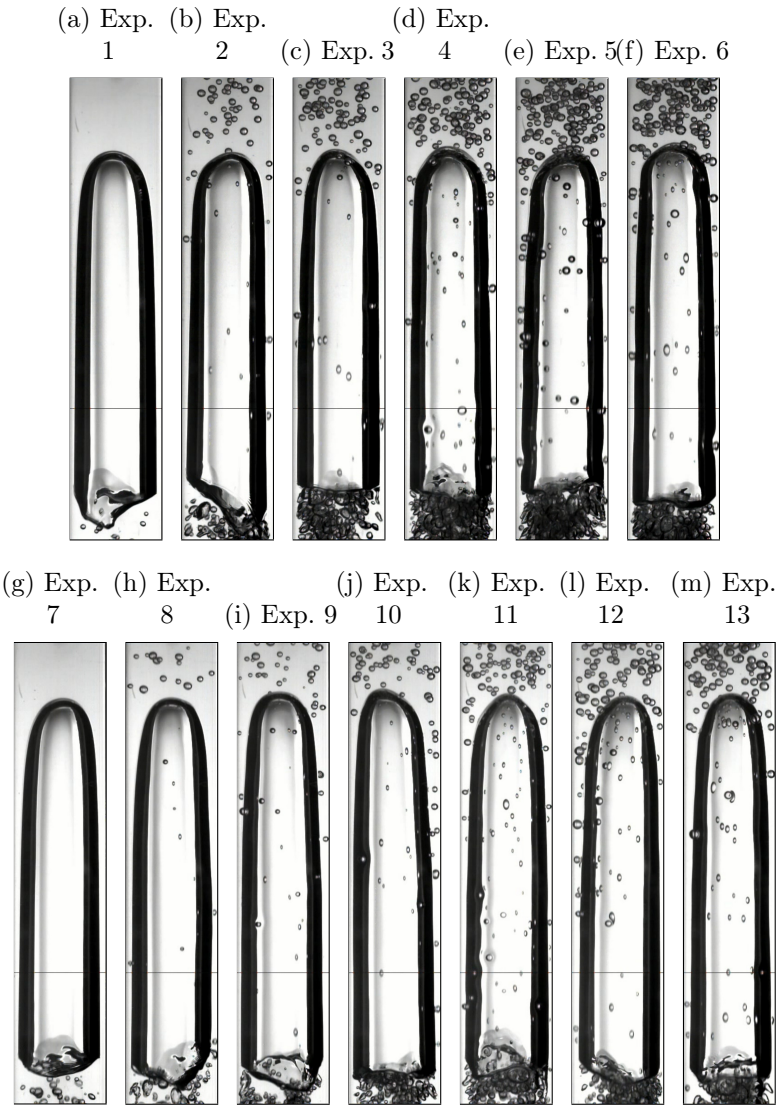

Source - Developed by the author.

Figure 6.2 – Bubble size distribution (BSD) of the secondary bubbly flow from the experimental points shown in Tab. 6.2, with a superficial gas velocity of: a) $j_l = 3.09 \cdot 10^{-2}$ m/s and b) $j_l = 21.64 \cdot 10^{-2}$ m/s.

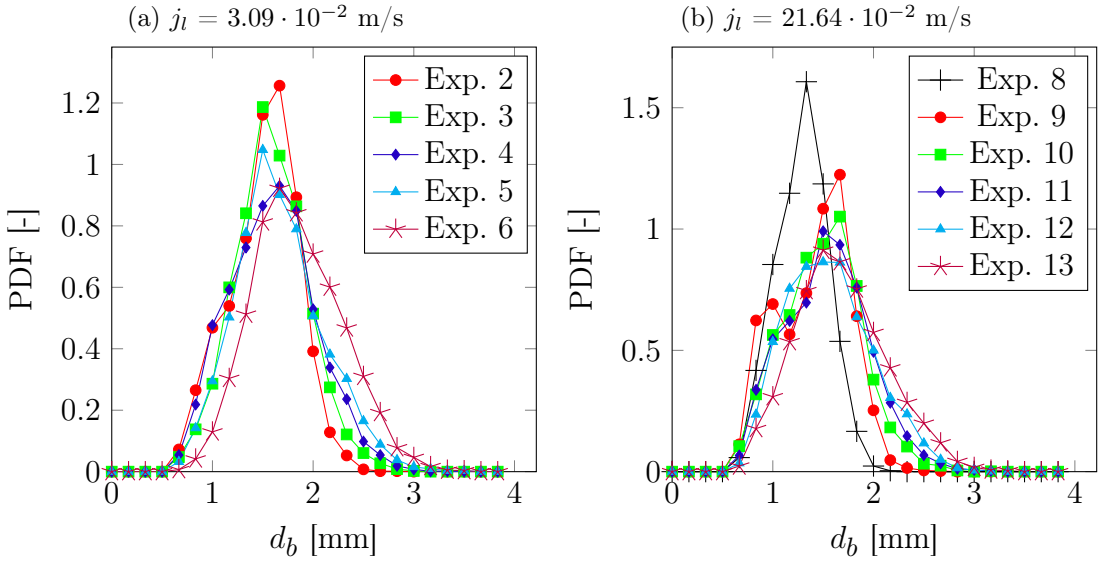

Source - Developed by the author.

6.2.1 Effect of the dispersed bubbles on the Taylor bubble rising velocity

Figure 6.3 presents the ensemble averaged Taylor bubble rising velocities $\langle U_{tb} \rangle$ measured through the high-speed camera image analysis and the LDP technique, and its associated uncertainty, for different dispersed gas volume fraction and different liquid superficial velocities. Each point in Fig. 6.3 is the average of at least 50 samples for the high-speed camera and 100 for the LDP technique. Those results were first shown in Chapter 5, but are shown here again to discuss its results further. However, in the present work, more detailed analysis are proposed, correlating them with PIV and HSC results, in order to give some insights about the rising velocity behaviour and how is influenced by the presence of dispersed bubbles.

From the results shown in Fig. 6.3 it is clear that the dispersed bubbles affect the rising movement of the Taylor bubble, since its terminal velocity $\langle U_{tb} \rangle$ is higher when comparing to a flow situation with absence of small bubbles ($\overline{\langle \alpha_g \rangle} = 0.0$). According to Fig. 6.3, the Taylor bubbles rising velocity is increased by the presence of dispersed bubbles until a maximum point is reached, from where the rising velocity $\langle U_{tb} \rangle$ starts to decrease. It is important to state that due to the experimental setup limitations, smaller void fraction values (of dispersed bubbles) for the cases with $j_l = 3.09 \cdot 10^{-2}$ m/s could not be produced.

In order to better understand the effect of the dispersed bubbles on the terminal

velocity, the flow structure around the Taylor bubbles is studied through the PIV technique and the digital image analysis from high-speed camera videos. The next sections are then dedicated to the analysis and discussion of these results.

Figure 6.3 – Effect of the dispersed bubbles on the Taylor bubble rising velocity and its associated uncertainty, for different dispersed gas volume fraction and different liquid superficial velocities: a) $j_l = 3.09 \cdot 10^{-2}$ m/s and b) $j_l = 21.64 \cdot 10^{-2}$ m/s. The filled points are carefully analyzed through the PIV technique.

(a) $j_l = 3.09 \cdot 10^{-2}$ m/s

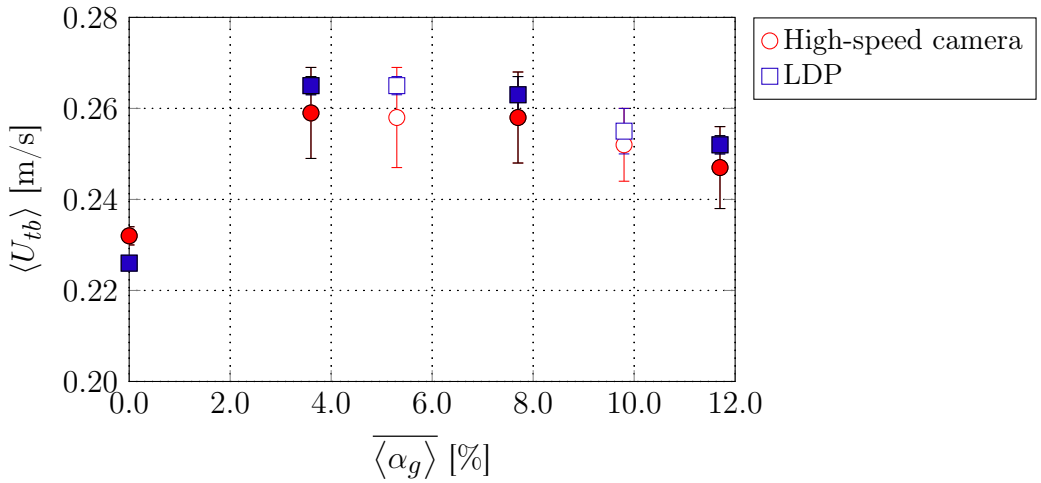

(b) $j_l = 21.64 \cdot 10^{-2}$ m/s

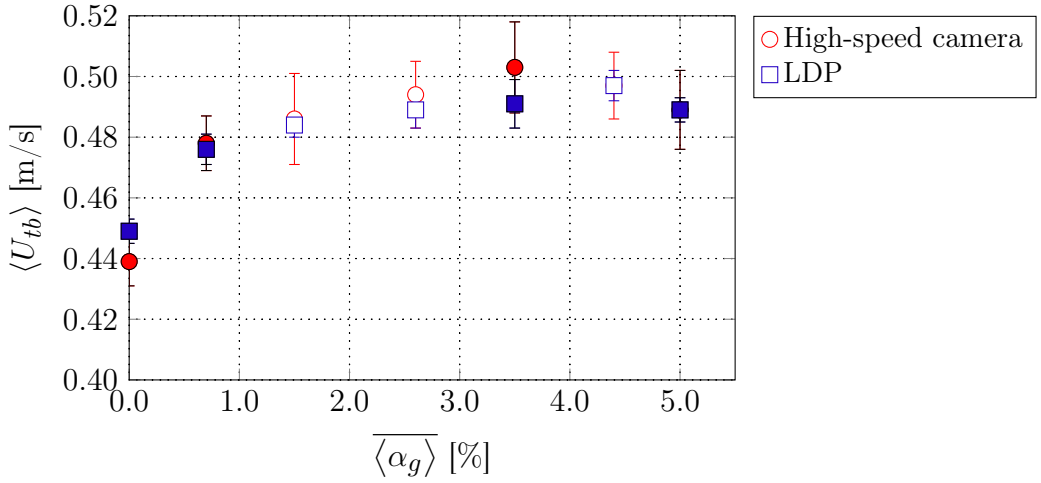

Source - Developed by the author.

6.2.2 Effect of the dispersed bubbles on the rising movement and shape profile of the Taylor bubbles

As shown the Section 6.2.1, the terminal velocity of the Taylor bubbles is increased by the presence of the dispersed bubbles on the flow, at least for low concentration of dispersed bubbles in the liquid stream. The main mechanism observed to explain this behaviour is the effect of vortex shedding of dispersed bubbles in the liquid stream above Taylor bubbles nose, inducing fluctuations that tend to accelerate the Taylor bubbles.

An analogous phenomenon has already been observed experimentally (PINTO; CAMPOS, 1996; CAMPOS; DE CARVALHO, 1988) and numerically (ARAÚJO et al., 2013; SHABAN; TAVOULARIS, 2018) in the Taylor bubble coalescence process. In a train of two Taylor bubbles, when a certain minimum distance separates the two bubbles, the trailing bubble gets affected by flow disturbances of the leading bubble and coalesces into a single Taylor bubble. Prior to coalescing, the trailing Taylor bubble, affected by the upcoming liquid flow, rises with a lateral movement and an oscillating nose shape. Those perturbations, mainly caused by the turbulent flow generated by the leading bubble and the low pressure field in the wake region due to the liquid recirculation, accelerates the trailing Taylor bubble, increasing its instantaneous rising velocity. In order to better understand this behavior, Tudose and Kawaji (1999) measured the total drag force of symmetric and deformed plastic Taylor bubble models, positioning the model bubbles in the center of a vertical pipe and with eccentric deviations. According to the authors' findings, the total drag force on the bubble is reduced by the lateral displacement of the bubble position from the tube center axis and the nose shape deformation.

In the present work, the same mechanism is observed when analyzing the motion of the Taylor bubbles by the high-speed camera images. It is possible to observe the mechanism in different Taylor bubbles rising throughout Videos 5 and 6 of the supplementary material given in Appendix B. As a specific example, Video 7 of the supplementary material given in Appendix B, shows the rising motion of two Taylor bubbles in the same experimental condition. In this clip, due to the induced fluctuations from the dispersed bubbles, the rising motion of the two Taylor bubbles is different, with the first bubble rising faster and exhibiting a strong nose deformation.

From the high-speed camera footage and a digital imaging analysis, it was possible to extract the nose shape profile and thus its tip position, defined as the highest point of the nose profile. In Fig. 6.4 the oscillations of bubbles tip can be observed and are larger, when dispersed bubbles are present in the liquid stream. As an example of the method used in this work and described in Cerqueira et al. (2018b), Fig. 6.4 shows the Taylor

bubble nose shape profile and its tip position along different instants of its rising motion.

Figure 6.4 – Snapshots of a rising Taylor bubble flowing under experimental condition 2 of Tab. 6.2. The Taylor bubble nose profile is given by the green line and its instantaneous tip position is shown by the red point. In this figure, the reference frame is attached to Taylor bubble nose.

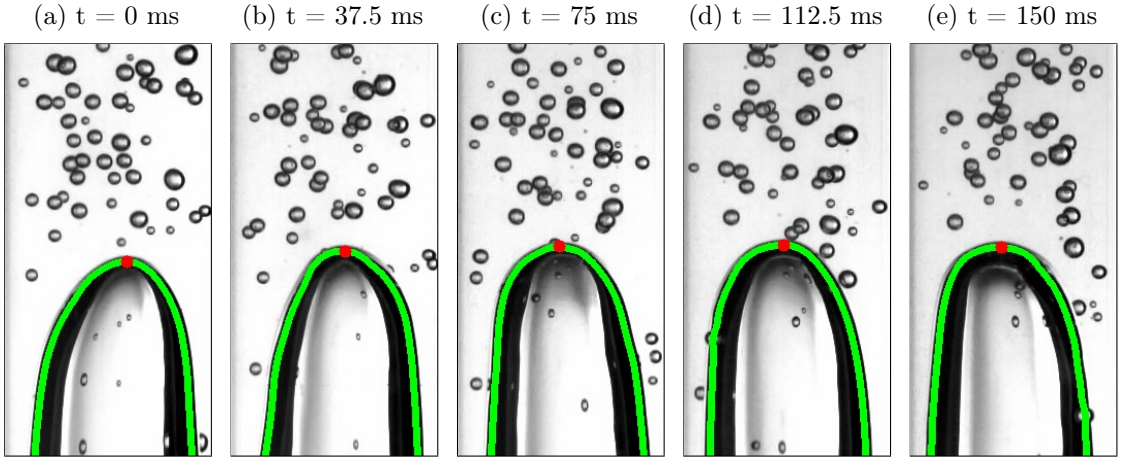

Source - Developed by the author.

Recalling the findings of Tudose and Kawaji (1999), an analysis was also conducted to observe the effect of the dispersed bubbles on the nose shape distortion. As a starting point, this relation was first analyzed by the lateral displacement of the Taylor bubble nose tip position. Figures 6.5 and 6.6 show the probability density function (PDF) of the nose lateral displacement of the Taylor bubble tip, from the central position, obtained from the high-speed camera images of the flow conditions listed in Tab. 6.2. From these distributions, it is clear that the the dispersed bubble modifies the rising motion of the Taylor bubble, with the nose tip traveling further away from the duct centerline, near $|r/R| = 0.3$ for Exp. 2 ($\overline{\langle \alpha_g \rangle} = 3.6$ %) and $|r/R| = 0.25$ for Exp. 8 ($\overline{\langle \alpha_g \rangle} = 0.7$ %). Thus, for both j_l, a small amount of dispersed bubbles is enough to add fluctuations that promote a lateral motion of the nose tip of Taylor bubbles. The impact is higher in the $j_l = 3.08 \cdot 10^{-2}$ m/s set of experiments, since when comparing the PDFs of Exp. 1 (absent of dispersed bubbles) and 2 ($\overline{\langle \alpha_g \rangle} = 3.6\%$), where the Re_l indicates background liquid laminar flow regime and the bubble induced turbulence (BIT) can have a significant impact of the flow structure. As commented by Kim et al. (2016), in bubbly flows with a laminar background liquid flow, even a small number of bubbles $\overline{\langle \alpha_g \rangle} = \mathrm{O}(0.01)$ %, can strongly promote turbulent fluctuations in liquid stream.

Although the dispersed bubbles significantly alters the nose tip motion on Exp. 2, the PDF from Exps. 2 – 6 present similar profiles. This visual observation can be seen

on the plots of Fig. 6.9, where the standard deviation $\sigma_{\text{PDF}}^{\text{nose}}$ from the data fitted PDF equivalent Gaussian functions are presented for the experiments performed in this work. As shown in those plots, Exps. 2 – 6 have almost the same $\sigma_{\text{PDF}}^{\text{nose}}$, indicating that bubble induced fluctuations cannot further increase the lateral motion of the Taylor bubbles. However, this is not the case for the $j_l = 21.64 \cdot 10^{-2}$ m/s results, where the trend of Fig. 6.9b) shows that the nose tip eccentric motion gets higher by increasing the number of dispersed bubbles.

Besides the nose tip position, it was possible to analyze the two-dimensional shape of the Taylor bubbles produced by the nose shape profile from the digital imaging analysis of the high-speed camera images. The green line of Fig. 6.4 shows an example of such profile. Considering the nose shape oscillations found in experiments where the dispersed bubbles were present, the results of Figs. 6.7 and 6.8 show the two-dimensional probability matrices of the Taylor bubble nose shape profile for different experimental points. The procedure describing the steps in producing those matrices is detailed in Cerqueira et al. (2018c), and its values represent the probability of a Taylor bubble nose outline occurrence taken from all the high-speed camera images. Thus, values closer to 1.0 indicates that a Taylor bubble is likely to be in that region, while values closer to 0.0 represents the opposite. According to the results, one can observe that as dispersed bubbles are added to the background flow, the nose shape deforms more and more, since the contours shifts from a sharp definition of the interface location to a spread region of the interface location.

Despite Figs. 6.7 and 6.8 show signs of the oscillating motion of the Taylor bubbles, they do not present a significant modification on the average nose shape, here defined as the iso-line with Prob. = 0.5, due to the dispersed bubbles. For $j_l = 3.08 \cdot 10^{-2}$ m/s the dispersion (or "diffusiveness") of the nose profiles seems similar, following the trends of the nose tip distribution of Figs. 6.5 and 6.9. To quantify this sort of observation, the area between the two dotted lined in Figs. 6.7 and 6.8 is calculated by the variable $I_{\text{def.}}^{\text{nose}}$. Its value is plotted together with $\sigma_{\text{PDF}}^{\text{nose}}$ in Fig. 6.9, aiming to understand the link between the nose tip lateral movement and the nose shape deformation. According to Fig. 6.9 there is a strong correlation between the nose lateral movement and the total deformation of profile, as seen by the $I_{\text{def.}}^{\text{nose}}$ and $\sigma_{\text{PDF}}^{\text{nose}}$ points plotted against the bubbly stream void fraction. In Fig. 6.8, the region delimited by the iso-lines of Prob.=0.1 and 0.9 gets ticker as $\overline{\langle \alpha_g \rangle}$ increases , indicating that the oscillations of the Taylor bubble nose increases as more dispersed bubbles are added to the background stream. As observed with the $j_l = 3.08 \cdot 10^{-2}$ m/s cases, there is a strong correlation between $I_{\text{def.}}^{\text{nose}}$ and $\sigma_{\text{PDF}}^{\text{nose}}$, i.e., the lateral movement of the nose tip and the Taylor bubble deformation.

The results showed in Figs. 6.5 – 6.9 demonstrates that, even for a laminar back-

ground liquid flow, a small amount of the dispersed bubbles disturbs the flow ahead of the Taylor bubble, leading to oscillations on its nose shape and inducing a lateral motion on its rising path. However, despite that BIT intensity increases with the void gas fraction, as shown by the results of Hosokawa and Tomiyama (2013), Kim et al. (2016), and Cerqueira et al. (2018c), those perturbations do not seem to intensify or damp the nose shape oscillations as more dispersed bubbles are added to the bubbly stream. Instead, for $j_l = 3.08 \cdot 10^{-2}$ m/s, the results show that oscillations seem to have reached a limiting value. For the$j_l = 21.64 \cdot 10^{-2}$ m/s flow condition, the nose shape oscillation increases linearly with the gas volume fraction, indicating that the BIT intensity is still affecting the Taylor bubble rising movement. It is also interesting to note that the numerical values of $I_{\text{def.}}^{\text{nose}}$ and $\sigma_{\text{PDF}}^{\text{nose}}$ of Fig. 6.9b) are lower than those of Fig. 6.9a), suggesting the existence of a oscillation limit of the Taylor bubbles.

The analysis presented in the current sub-section is important to give a first glance on the relation between the BIT intensity and the rising motion of Taylor bubbles when dispersed bubbles are present. The observations made here agree, partially, with the conclusions found in Tudose and Kawaji (1999) that there is a relation between the nose shape deformation and the terminal rising velocity. Nevertheless, it is important to remember, that unlike the experiments performed in Tudose and Kawaji (1999), the deformation and lateral movement of the Taylor bubbles are not imposed, but a direct result from the bubbly flow ahead of the Taylor bubble. Thus, it can be concluded that the lateral movement of the Taylor bubbles by the BIT intensity is not the single mechanism acting on the modification of the terminal velocity. Hence, a detailed analysis of the PIV ensemble averaged fields is going to be presented in the next sections to further explore the results of Fig. 6.3.

6.2.3 Ensemble average flow images

Figures 6.10 and 6.11 presents the ensemble average images flow images from the high-speed camera videos. These images were obtained inspired by ideas presented in Amaral et al. (2013) and Pipa et al. (2014), which aims in finding an image that represents and characterizes the flow condition. Since the Taylor bubble nose and tail position were tracked from the high-speed camera videos, it was possible to align all the Taylor bubbles into a single reference position from its tail and nose. From those aligned images, it was then possible to create an average of the gas phase distribution around the Taylor bubbles through a simple average of pixel intensity of each frame. A similar procedure was used in Amaral et al. (2013) to represent the shape of Taylor bubbles in horizontal two-phase

Figure 6.5 – Probability density function (PDF) of the nose tip position, showing its lateral displacement from the duct center line, of the experimental points 7–3 of Tab. 6.2 with a superficial liquid velocity of $j_l = 3.08 \cdot 10^{-2}$ m/s. The solid lines on the graphs represent the data fitted equivalent Gaussian function.

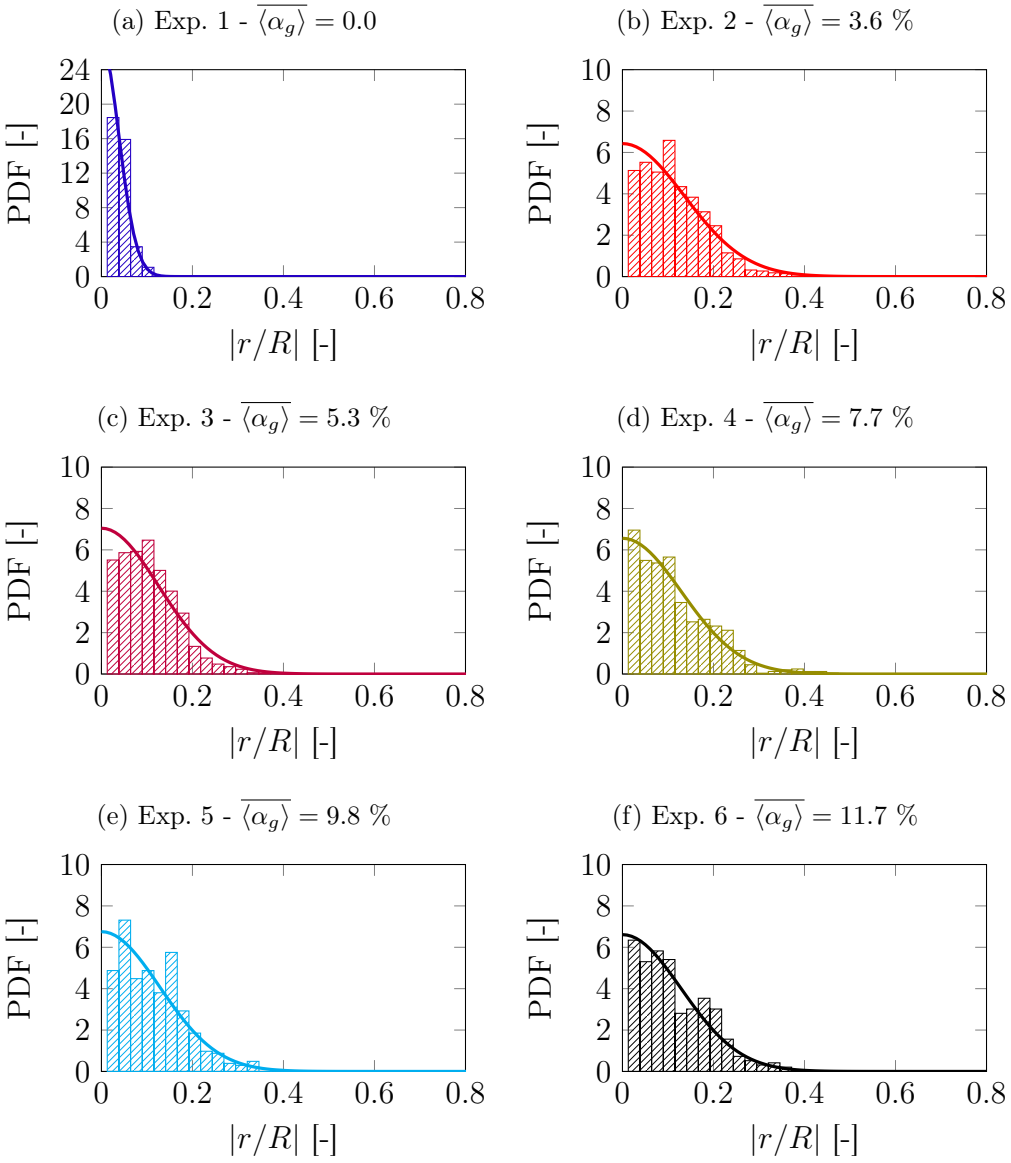

Source - Developed by the author.

slug flow. The images shown in Figs. 6.10 and 6.11, together with Videos 8–11 of the supplementary material given in Appendix B, despite its qualitative nature, are important on the analysis of the PIV results for liquid phase velocity, presented in next section.

In Figs. 6.10 and 6.11, outside the Taylor bubble, as the pixel intensity decreases, i.e. the image gets "darker", the local void fraction is higher and "brighter" region represent lower volume fractions of dispersed bubbles. Thus, from those figures, one can visualize the gas volume fraction of each experiment and also its distribution around the Taylor bubbles.

Figure 6.6 – Probability density function (PDF) of the nose tip position, showing its lateral displacement from the duct center line, of the experimental points 7–3 of Tab. 6.2 with a superficial liquid velocity of $j_l = 21.64 \cdot 10^{-2}$ m/s. The solid lines on the graphs represent the data fitted equivalent Gaussian function.

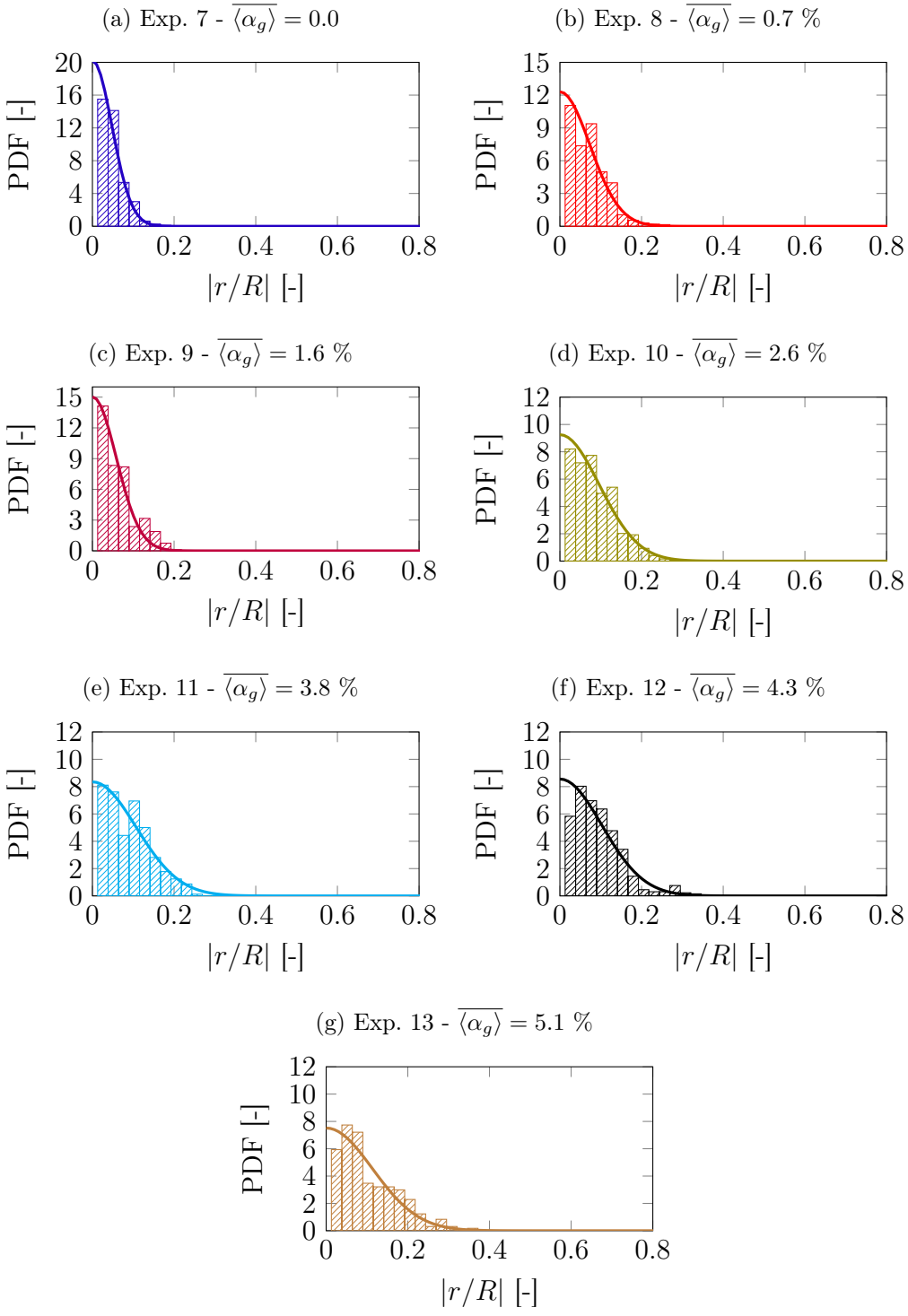

Source - Developed by the author.

Figure 6.7 – Taylor bubble nose shape probability occurrence matrix from the high-speed camera images for $j_l = 3.08 \cdot 10^{-2}$ m/s. The continuous line represents the iso-line with probability (Prob.) equals to 0.5, while the dotted lines represent the iso-lines of 0.10 and 0.90.

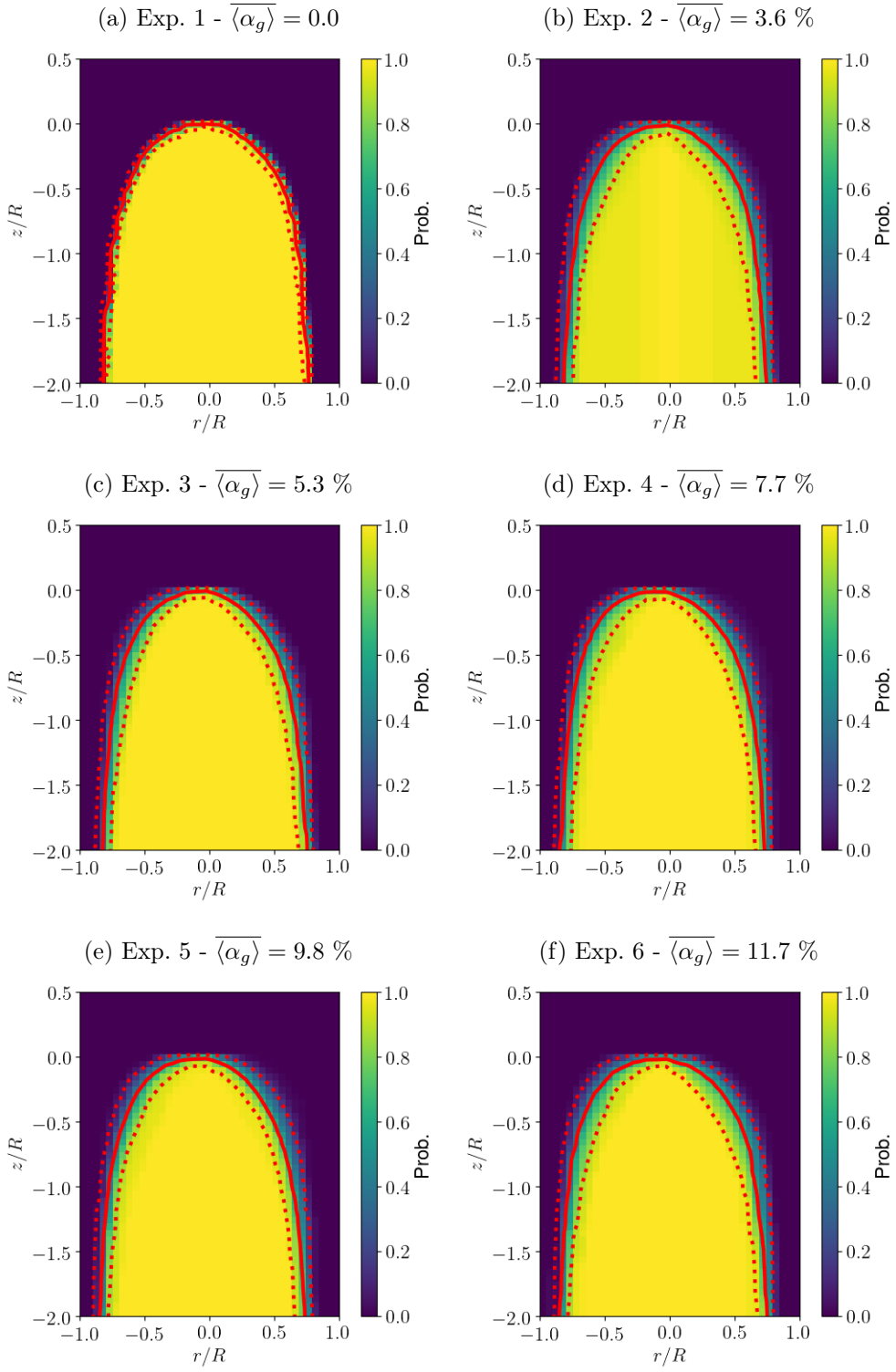

Source - Developed by the author.

Figure 6.8 – Taylor bubble nose shape probability occurrence matrix from the high-speed camera images for $j_l = 21.64 \cdot 10^{-2}$ m/s. The continuous line represents the iso-line with probability (Prob.) equals to 0.5, while the dotted lines represent the iso-lines of 0.10 and 0.90.

(a) Exp. 7 - $\overline{\langle \alpha_g \rangle} = 0.0$

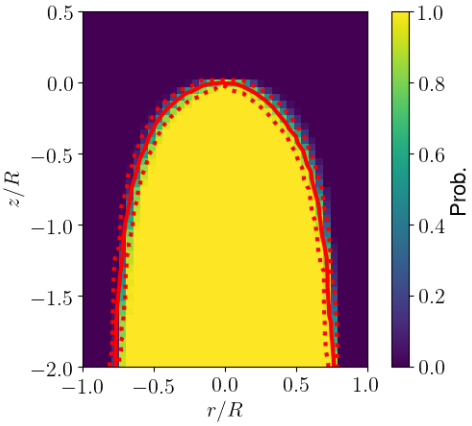

(b) Exp. 8 - $\overline{\langle \alpha_g \rangle} = 0.7$ %

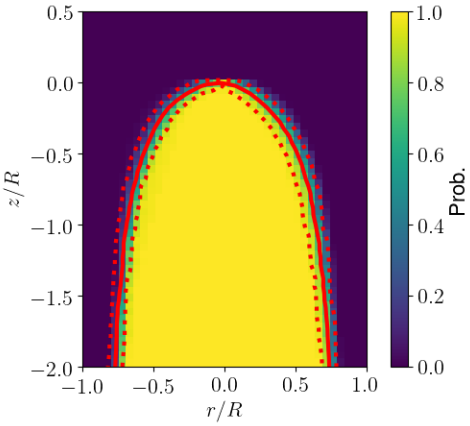

(c) Exp. 10 - $\overline{\langle \alpha_g \rangle} = 2.6$ %

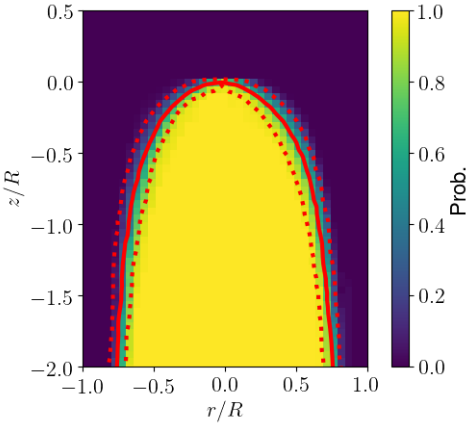

(d) Exp. 11 - $\overline{\langle \alpha_g \rangle} = 3.8$ %

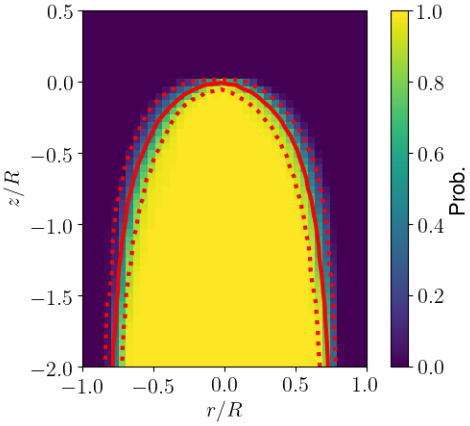

(e) Exp. 12 - $\overline{\langle \alpha_g \rangle} = 4.3$ %

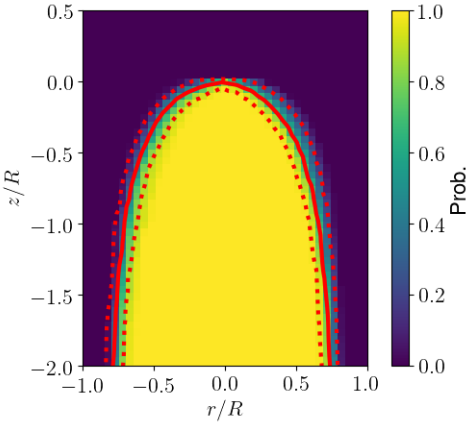

(f) Exp. 13 - $\overline{\langle \alpha_g \rangle} = 5.1$ %

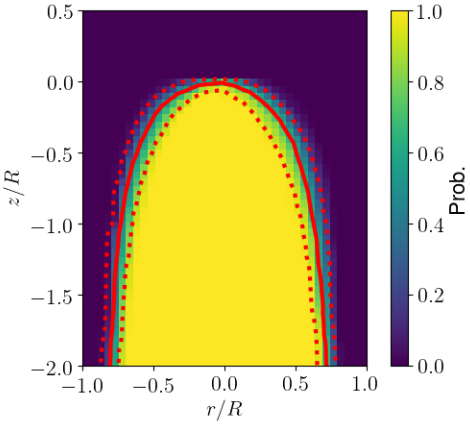

Source - Developed by the author.

Figure 6.9 – The $\sigma_{\text{PDF}}^{\text{nose}}$ and $I_{\text{def.}}^{\text{nose}}$ from each experimental point, given in Tab. 6.2, plotted against the void fraction value of the background bubbly flow.

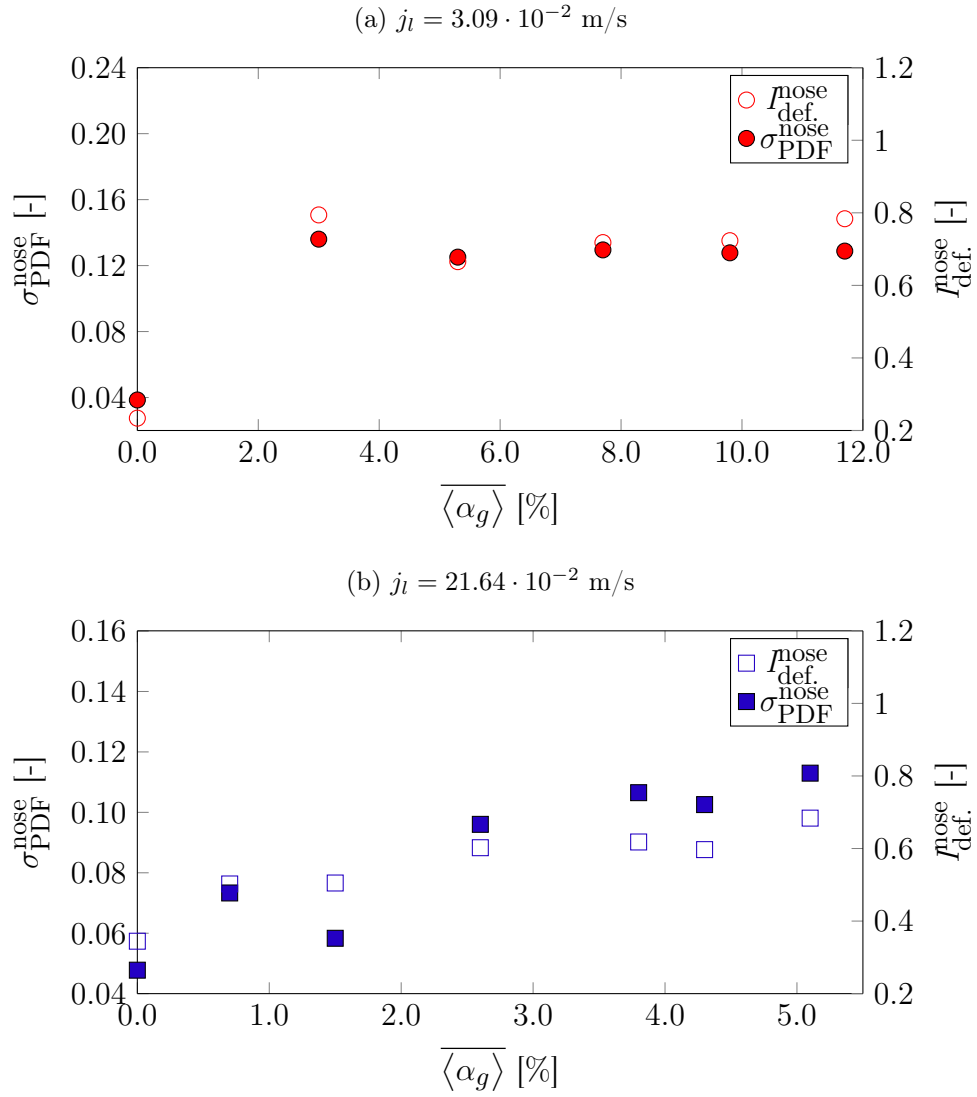

Source - Developed by the author.

According to the images, the upward liquid velocity induced by the Taylor bubbles at nose region is sufficient to push away the dispersed bubbles from the nose region, since the intensity distribution around this region is brighter than the region far away from the Taylor bubble nose position.

As shown in Figs. 6.10 and 6.11, small dispersed bubbles concentrate in the wake region of the Taylor bubbles, due to the recirculating motion generated by the film expansion. As more dispersed bubbles are injected to the background stream, Fig. 6.10b) gradually evolves to a larger and darker region. Despite no dispersed bubbles are being injected on the liquid stream in Exps. 1 and 7, a sligtly darker region is observed in the average images of these experiments, resulting from the presence of some dispersed

bubbles (as can be observed in Videos 10 and 11 of the supplementary material given in Appendix B). These dispersed bubbles occur due to the natural oscillation of the Taylor bubble bottom, which eventually breaks the large scale gas-liquid interface into small dispersed bubbles, promoting some gas entrainment from Taylor bubbles break-up. However, the presence of dispersed bubbles at wake region of Taylor bubbles is negligible in these experiments (Exps. 1 and 7) and it was considered that this did not affected the average liquid velocity fields.

Details about the Taylor bubble bottom and nose oscillations, seen in the footages of Videos 8 and 9 of the supplementary material given in Appendix B can also be inferred from the average high-speed camera images. The nose shape oscillation due to the dispersed bubbles, discussed in the previous section, is observed by the "blurred" Taylor bubble nose in averaged images of Figs. 6.10b) – 6.10f) and Figs. 6.11a) – 6.11g. The same blurriness can be found in the bottom of the Taylor bubble, showing the characteristic wake oscillation, for Taylor bubbles rising in low Morton numbers situations. However, according to images of Fig. 6.10 (i.e., mainly observed for lower values of j_l), the tail seems to be more "defined" in averaged images, indicating that the tail oscillation decreases as the more dispersed bubble are added to the background stream. This trend can be clearly observed in Videos 10 and 11 of the supplementary material given in Appendix B. The explanation for this behaviour is that the effect of buoyancy force on dispersed bubbles, concentrated at wake region of Taylor bubbles, prevents this oscillation, which also strongly affects the whole flow structure at wake region, as will be discussed in next section through PIV results of liquid phase.

6.2.4 Effect of the dispersed bubbles on the flow structure around the Taylor bubbles

As discussed in previous sections, the rising velocity of Taylor bubbles is affected by the presence of dispersed bubbles in the liquid stream. In this section, the ensemble averages of liquid phase velocities and turbulence fields obtained by PIV measurements, combined with phase discrimination techniques discussed and detailed in Chapters 3 to 5, are presented and discussed to better comprehend how the small bubbles modify the flow structure around the Taylor bubbles.

6.2.4.1 Mean liquid velocity results

Figures 6.12 and 6.13 present the PIV ensemble average fields showing the flow structure around the Taylor bubble nose, for the experiments where PIV measurements were applied (as annotated in Tab. 6.2). These figures present the velocity vector plots, and

Figure 6.10 – Ensemble average flow images from the high-speed camera videos for the $j_l = 3.09 \cdot 10^{-2}$ m/s experimental points. The footage used to create those average images can be seen in Videos 8 – 11 of the supplementary material given in Appendix B.

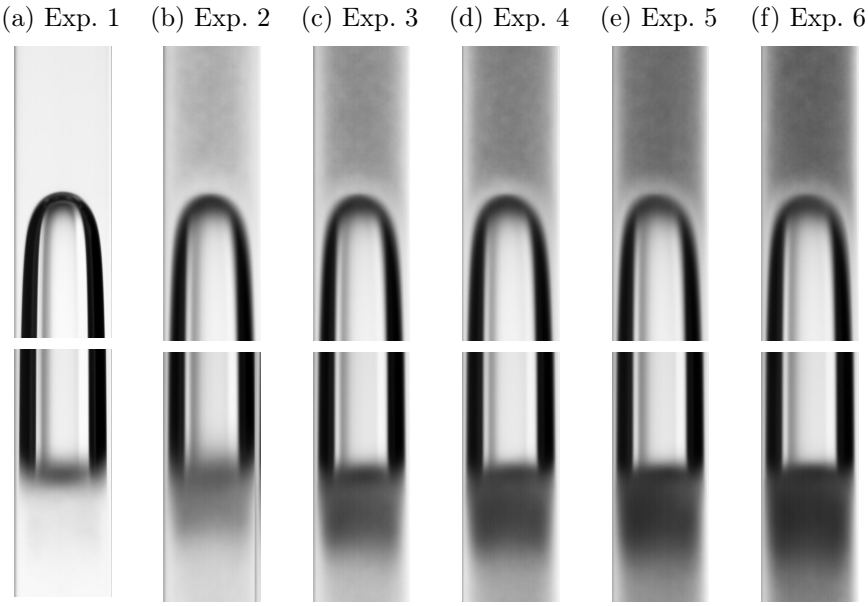

Source - Developed by the author.

contour plots of the radial $\langle v_l(r,z)\rangle$ and axial $\langle w_l(r,z)\rangle$ velocities of liquid phase. In Figs. 6.12 and 6.13 , the continuous line represents the iso-line with probability of encountering a region occupied by Taylor bubbles (Prob.) equal to 0.5, which was considered as the "average interface position", while the dotted lines represent the iso-lines of 0.10 and 0.90 of this probability. The following representation is used when presenting the flow structure around the Taylor bubbles throughout this section. According to the velocity fields show in Figs. 6.12 and 6.13, the influence of the dispersed bubbles on the flow structure around the Taylor bubbles is very clear for the cases with $j_l = 3.09 \cdot 10^{-2}$ m/s, while for the higher superficial liquid velocity cases, $j_l = 21.64 \cdot 10^{-2}$ m/s, this influence is not as pronounced. From the results given in Fig. 6.12, one can observe that the dispersed bubbles modify the flow structure ahead ($z/R > 0$) and below the tip of the Taylor bubble nose ($z/R < 0$). However, the velocity fields shown in Fig. 6.13, for $j_l = 21.64 \cdot 10^{-2}$ m/s, it is only possible to visualize small modifications on the axial $\langle w_l(r,z)\rangle$ velocity field near the Taylor bubble nose. For both superficial liquid velocities considered in the experiments, there is only a small impact of the bubbly stream void fraction $\overline{\langle \alpha_g \rangle}$ on the radial $\langle v_l(r,z)\rangle$ liquid velocities around the Taylor bubbles.

In order to better understand the flow structure around the Taylor bubbles, it is

Figure 6.11 – Ensemble average flow images from the high-speed camera videos for the $j_l = 21.64 \cdot 10^{-2}$ m/s experiments. The footage used to create those average images can be seen in Videos 8 – 11 of the supplementary material given in Appendix B.

(a) Exp. 7 (b) Exp. 8 (c) Exp. 9 (d) Exp. 10 (e) Exp. 11 (f) Exp. 12 (g) Exp. 13

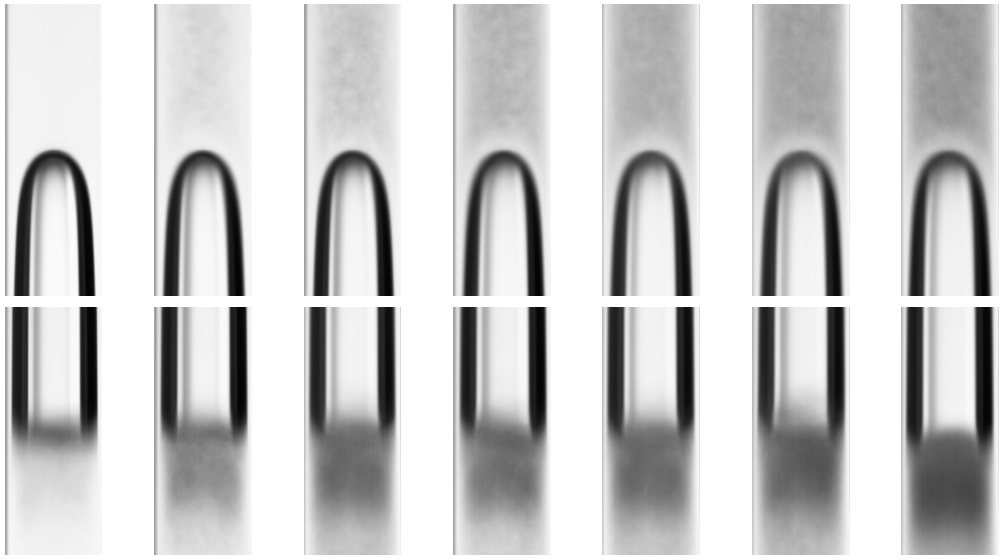

Source - Developed by the author.

important first, to understand the effect of the dispersed bubbles in the flow far away from the bubble nose. Figures 6.14 and 6.15 shows the axial ensemble average velocity $\langle w_l(r,z)\rangle$ and turbulent kinetic energy $k(r,z)$ profiles ahead from the Taylor bubble nose (z/R=2.50) the cases addressed in Fig. 6.12 and 6.13, respectively. The bubble induced turbulence is clearly observed in the turbulent kinetic energy profiles, as reported in (CERQUEIRA et al., 2018c) and Chapter 3. For the experiments with the lowest liquid superficial velocity, $j_l = 3.09 \cdot 10^{-2}$ m/s, the axial profiles show an increase of the liquid velocity in the core region and a deceleration near the pipe wall. Regarding the $j_l = 21.64 \cdot 10^{-2}$ m/s experimental set, the axial profiles changes from a flat to a more convex profile as $\overline{\langle \alpha_g \rangle}$ is increased.

Back to the analysis of flow structure around Taylor bubbles, it is interesting to explore the average ensemble liquid velocities profiles in different sections in order to infer the effect of the dispersed bubbles on the local flow structure. As the Taylor bubble rises, a certain amount of liquid is displaced, affecting the flow ahead of it. The flow modification due to this liquid displacement can be visualised from the ensemble average velocity vectors and, especially, in the axial ensemble average velocity $\langle w_l(r,z)\rangle$ plots of Fig. 6.12, where this modification is more pronounced. For the $j_l = 3.09 \cdot 10^{-2}$ m/s, the

Figure 6.12 – PIV ensemble average fields from the $j_l = 3.09 \cdot 10^{-2}$ m/s experiments around the Taylor bubble nose. First row: Ensemble-average velocity vector plots; Second row: Contour plot of the ensemble average radial liquid velocity $\langle v_l(r,z)\rangle$; Third row: Contour plot of the ensemble average axial liquid velocity $\langle w_l(r,z)\rangle$; The velocity vectors on the first row spaced by 4 interrogation windows in each direction for better visualization.

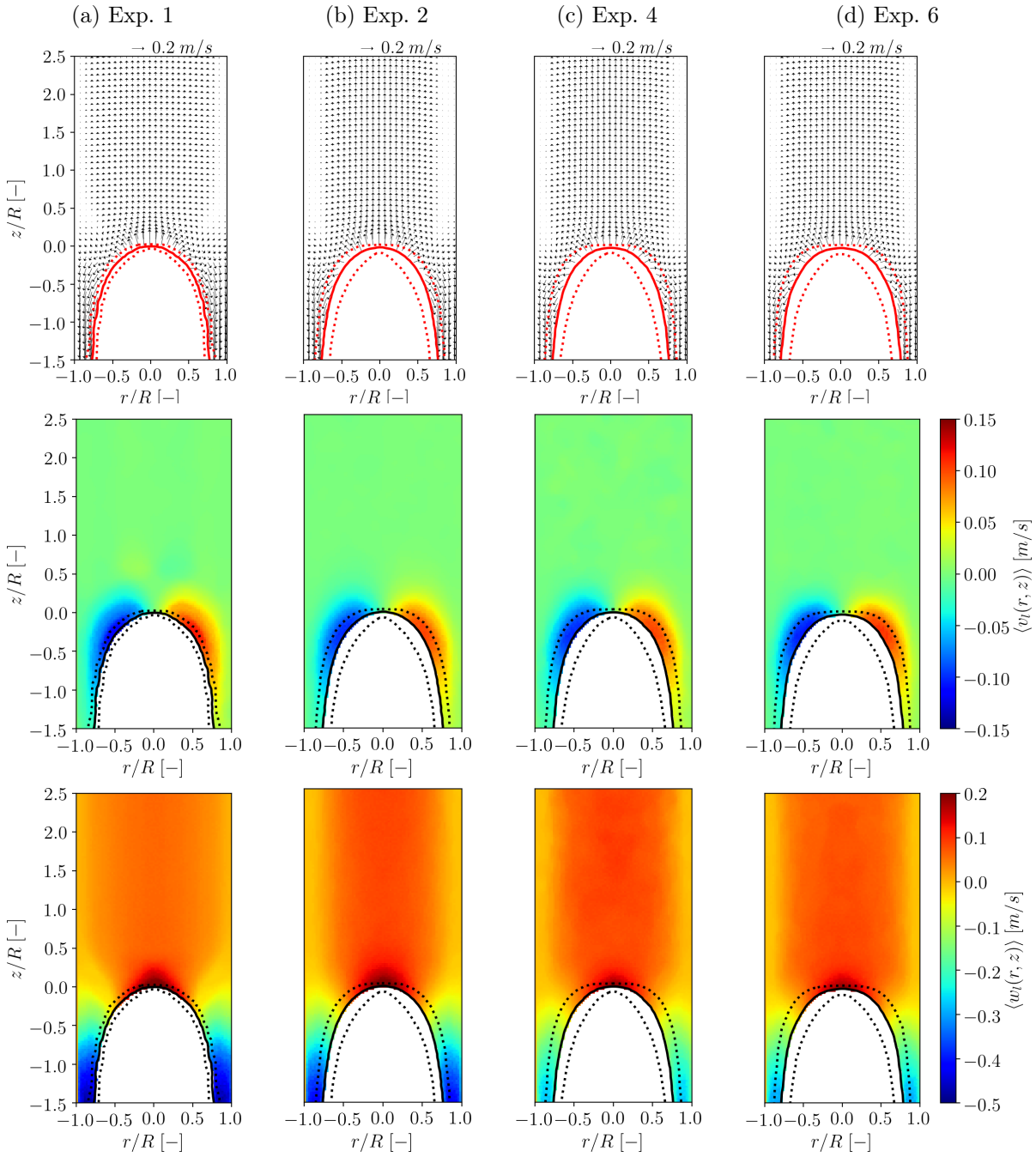

Source - Developed by the author.

Figure 6.13 – PIV ensemble average fields from the $j_l = 21.64 \cdot 10^{-2}$ m/s experiments around the Taylor bubble nose. First row: Ensemble-average velocity vector plots; Second row: Contour plot of the ensemble average radial liquid velocity $\langle v_l(r,z)\rangle$; Third row: Contour plot of the ensemble average axial liquid velocity $\langle w_l(r,z)\rangle$; The velocity vectors on the first row spaced by 4 interrogation windows in each direction for better visualization.

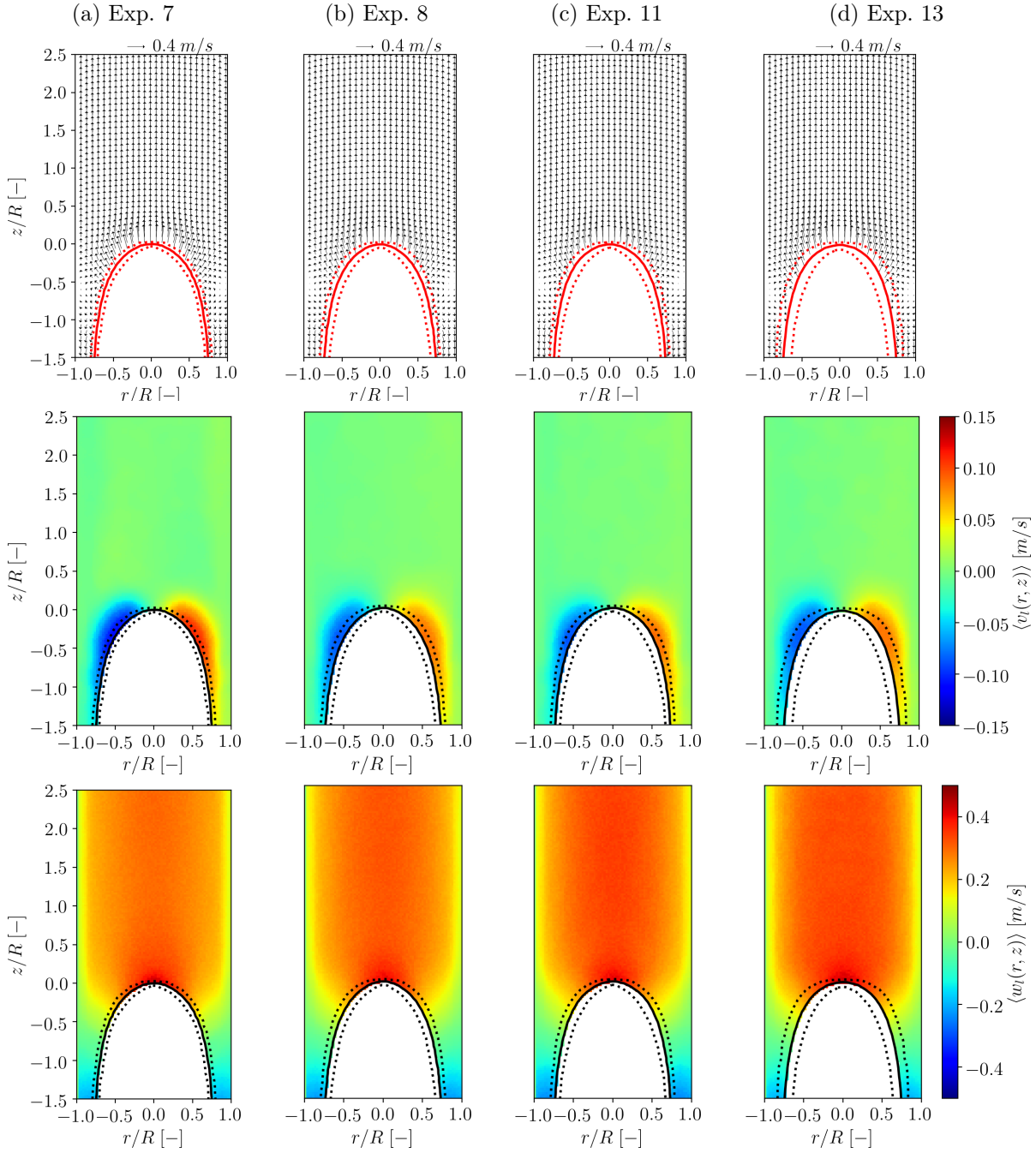

Source - Developed by the author.

Figure 6.14 – Axial ensemble average velocity $\langle w_l(r,z)\rangle$ and turbulent kinetic energy $k(r,z)$ profiles away from the Taylor bubble nose (z/R=2.50) for the background laminar flow regime ($j_l = 3.08 \cdot 10^{-2}$) experimental points. The solid line in the axial ensemble average velocity $\langle w_l(r,z)\rangle$ plot represents the theoretical parabolic laminar parabolic profile for $j_l = 3.08 \cdot 10^{-2}$ m/s.

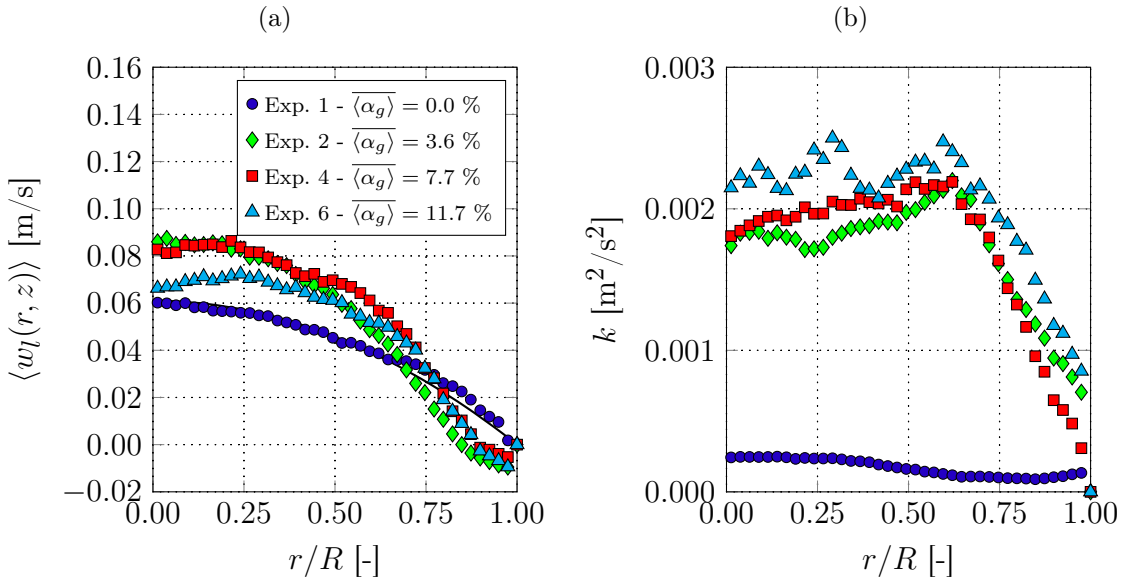

Source - Developed by the author.

results show that as dispersed bubbles are added to the background flow, i.e., as the void fractions $\overline{\langle\alpha_g\rangle}$ is increased, the extent of the region affected by Taylor bubble induced flow is reduced, while the same behavior cannot be as clearly visualized in Fig. 6.13 for the $j_l = 21.64 \cdot 10^{-2}$ m/s experiments.

In order to visualize the extent of the region effected by Taylor bubble ahead of its nose, Fig. 6.16 plots the residual variable $\Gamma(z)$ (NOGUEIRA et al., 2003), defined as the sum of r.m.s. of the deviation between the axial velocity profile in a position z and away from the Taylor bubble nose, where the flow is not affected by the Taylor bubble (considered at 2.5 radial distances from the nose tip, $z/R = 2.50$). By comparing the series of two j_l experiments without dispersed bubbles, one can observe that the cases with higher j_l require a longer distance from the Taylor bubble to approach its "far-field" values. The same trend was observed in the work of Nogueira et al. (2006a), where the presence of the Taylor bubble is felt at a longer distance from its tip.

However, as dispersed bubbles are added to the flow, the results of Fig. 6.16 show a reduction on the Taylor bubble region of influence on the flow ahead, since the $\Gamma(z)$ curves decays faster as $\overline{\langle\alpha_g\rangle}$ is increased, This can be observed for both values j_l, but is more pronounced for lower j_l. In the absence of dispersed bubbles, the extent of the

Figure 6.15 – Axial ensemble average velocity $\langle w_l(r,z)\rangle$ and turbulent kinetic energy $k(r,z)$ profiles away from the Taylor bubble nose (z/R=2.50) for the background turbulent flow regime ($j_l = 21.64 \cdot 10^{-2}$ m/s) experimental points. The dashed lines in the $k(r,z)$ profiles represents experimental results from Eggels et al. (1994).

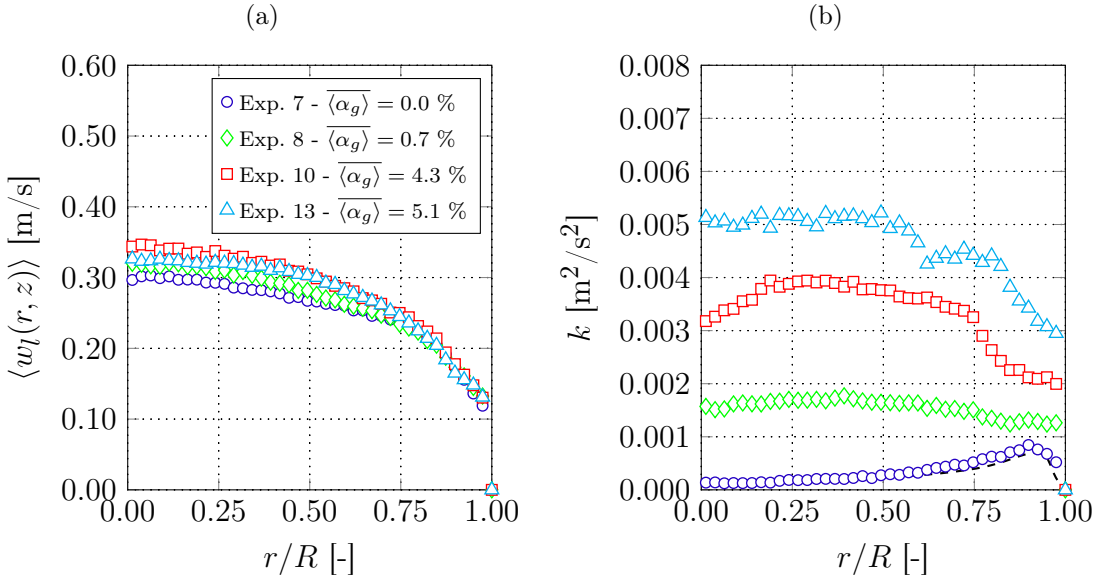

Source - Developed by the author.

Taylor bubble region of influence is limited by the inertial and viscous forces of the flow. However, in the bubbly flow regime, the dispersed bubbles incorporates an additional resistance mechanism, thus reducing the Taylor bubble influence on the flow ahead of it. This mechanism is probably related to the buoyancy introduced by the dispersed bubbles and also to the lateral liquid flow induced by them. Thus, as more dispersed bubbles are present in the flow, greater is the dampening of this induced liquid motion, and shorter is the region of influence of the Taylor bubble ahead of it. Since part of this dissipative mechanism is dependent on the dispersed bubbles and therefore by its size and distribution, the small deviation of the plot of Exp. 4 in Fig. 6.16a) can be attributed to its BSD and the complex interaction mechanism between the different sized bubbles.

In order to analyze in detail the modifications of the flow structure due to the dispersed bubbles around the Taylor bubble nose, the ensemble average velocity profiles $\langle v_l(r,z)\rangle$ and $\langle w_l(r,z)\rangle$ in different sections ahead of the Taylor bubble nose are presented in Figs. 6.17 to 6.20 for all the cases analyzed with PIV (as shown in Tab. 6.2). According to the results given in Figs. 6.17 to 6.20, the magnitude of the radial velocities $\langle v_l(r,z)\rangle$ is higher for the smaller liquid superficial velocities j_l. This behavior is expected, since as j_l increases, the Taylor bubble nose shape gets slimmer due to a higher flow rate coming

Figure 6.16 – Residual variable $\Gamma(z)$ (NOGUEIRA et al., 2003), defined as the sum of r.m.s. of the deviation between the axial velocity profile in a position z and away at the Taylor bubble nose $z/R = 2.50$.

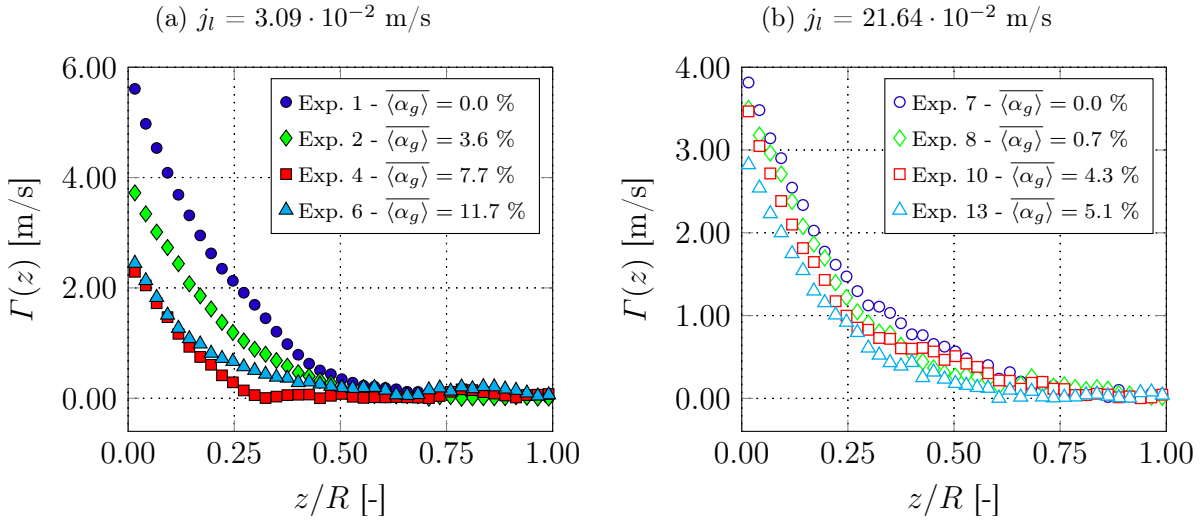

Source - Developed by the author.

downwards, when considering a reference frame attached to bubble nose (NOGUEIRA et al., 2006a). Thus, with a thicker annular liquid film, a reduction on the radial liquid $\langle v_l(r,z)\rangle$ profiles magnitude is observed.

From distances away than $z/R = 0.20$ away from the Taylor bubble nose tip, the $\langle v_l(r,z)\rangle$ plots shown in Fig. 6.19 and 6.20 have values closer to zero, indicating that in these positions, the Taylor bubble is not affecting the flow ahead of it. This is related to the reduction of the induced upward liquid discussed above, as the induced liquid flow is dampened by the presence of dispersed bubbles.

From distances away than $z/R = 0.20$, the $\langle v_l(r,z)\rangle$ plots shown in Fig. 6.19 and 6.20 have values closer to zero, indicating that in these positions, the Taylor bubble is not affecting the flow ahead of it.

It is expected that the liquid centerline axial velocity at $z/R = 0.00$ position be close to the terminal rising velocity given in Fig. 6.3. However, for the cases where the dispersed bubbles are present, as the void fraction is increased, the centerline velocity does not follow the same trend visualized in Fig. 6.3, but present values lower than the expected U_{tb}. As already mentioned in Chapter 5, due to oscillating rising motion and the deformations on the nose shape profile due to the presence of dispersed bubbles, the Taylor bubble nose is not always positioned at the duct centerline. In the axial velocity profiles where $j_l = 3.09 \cdot 10^{-2}$ m/s, since the point where the maximum velocity is distributed around the duct centerline in each PIV frame, when analyzing the ensemble average of

the instantaneous PIV acquisitions, a "flatter" axial velocity profile is expected. This is observed in the plots of Fig. 6.17, where the axial velocity profile shifts from a sharp velocity profile in Exp. 1 to a smoother one as the void fraction of dispersed bubbles is increased. For the cases with a higher liquid superficial velocity, $j_l = 21.64 \cdot 10^{-2}$ m/s, except the plot for the case with higher $\overline{\langle \alpha_g \rangle}$ (Exp. 13), there is not a significant change in the axial velocity profiles close to the Taylor bubble nose. According to the results of Fig. 6.20, which shows the axial velocity profiles in the distance $z/R = 1.00$ ahead of the Taylor bubble position, the axial velocity profiles in both superficial liquid velocities are similar to those far away from the Taylor bubble nose, following the results given in Fig. 6.16.

Figure 6.21 present the liquid velocity profiles at the film region formed between Taylor bubbles an pipe wall, at 1.5 radial distances from the Taylor bubble nose tip. As seen in the plots of Fig. 6.12, the flow structure between the Taylor bubble interface and the pipe wall ($z/R < 0.0$) is modified due to the presence of the dispersed bubbles. However, due to the higher liquid flow rate in the cases shown in Fig. 6.13, there is not a visible difference in this region as the $\overline{\langle \alpha_g \rangle}$ is increased. As can also be observed in the contour plots of $\langle w_l(r,z) \rangle$ for the $j_l = 3.09 \cdot 10^{-2}$ m/s experiments, the intensity of the axial liquid velocity in this region is reduced by the presence of dispersed bubbles. Additionally, the same profile for the $j_l = 21.64 \cdot 10^{-2}$ m/s experiments is given in Fig. 6.21.

According to the results shown in Fig. 6.21, as dispersed bubbles are added to the flow, except for Exp. 13, the case with higher $\overline{\langle \alpha_g \rangle}$, the liquid film velocity increases, following the opposite trend to the observed in the cases with $j_l = 3.09 \cdot 10^{-2}$ m/s. It is believed that for these cases where the liquid flow rate is higher, except for the Exp. 13 flow condition, that the mechanism relative to the dispersed bubbles described in the paragraph above do not play a major role in the annular liquid film.

The reduction of the axial velocity in the liquid film, seen in Fig. 6.21 for $j_l = 3.09 \cdot 10^{-2}$, can be due to competing mechanisms associated with the presence of the dispersed bubbles. When the dispersed bubbles are dragged through the liquid film, they deform the Taylor bubble interface, increasing the local thickness of the film, decreasing the velocity of the falling liquid film. The entrainment and subsequent deformation of the Taylor bubble interface can be observed in Videos 8 – 11 of the supplemental material given in Appendix B. On the other side, the liquid volume fraction of the liquid film decreases as more dispersed bubbles entrain into this film, increasing the downward velocity of the liquid phase. Additionally, the buoyancy forces acting on the dispersed bubbles, which is transferred through interfacial drag to the liquid phase, attenuates the descending

Figure 6.17 – Radial $\langle v_l(r,z)\rangle$ and axial $\langle w_l(r,z)\rangle$ liquid velocity profiles at different distances ahead of the Taylor bubble nose from the ensemble average PIV results at $\mathbf{z/R = 0.01}$ from the tip position.

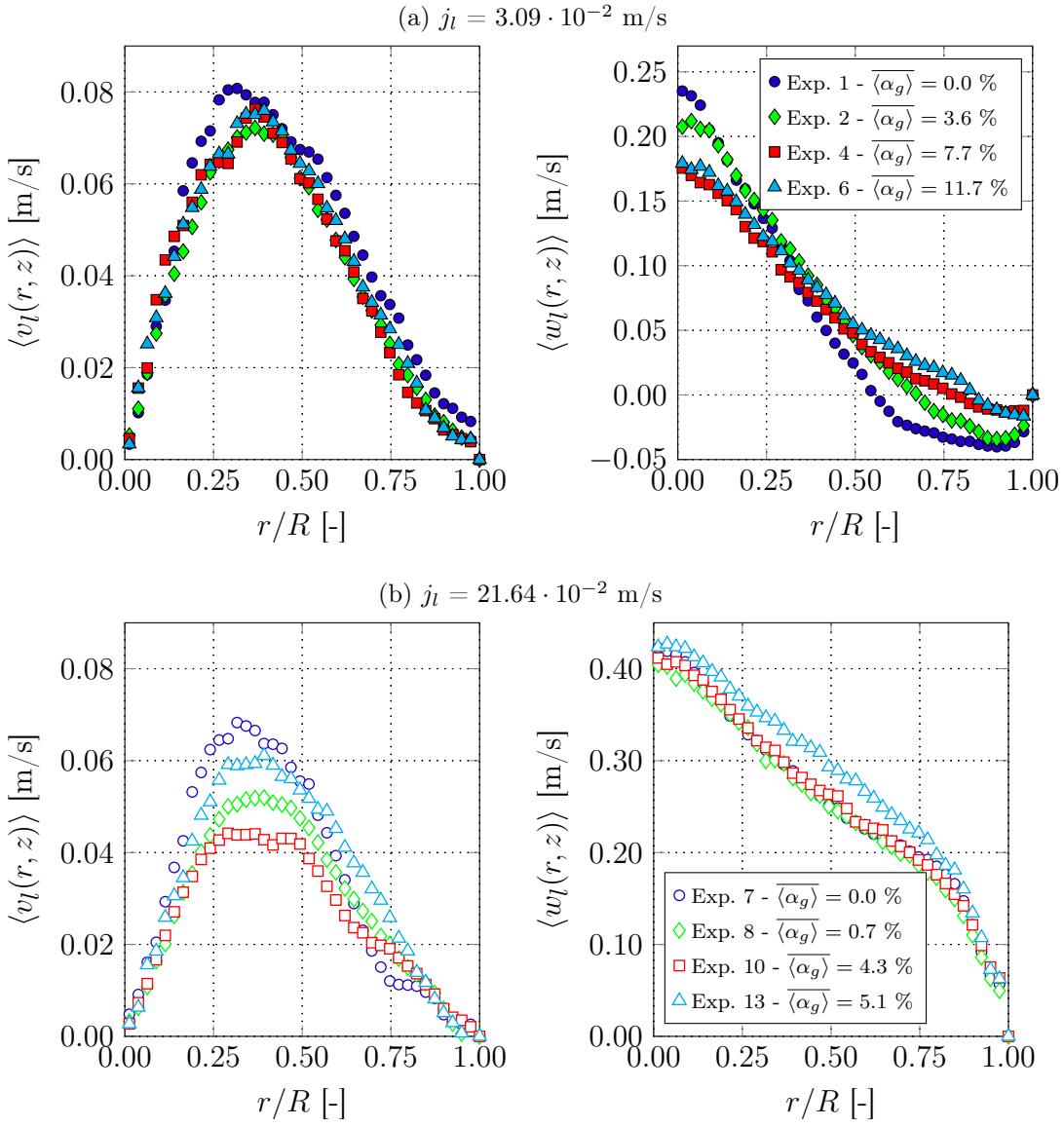

Source - Developed by the author.

momentum of the falling liquid film. These competing effects act in different intensities depending on rising velocity of Taylor bubbles, liquid inertia (which increases with j_l) and quantity of dispersed gas, explaining the different trends observed in velocity profiles of the liquid film.

From the profiles shown in Fig. 6.21, it is not possible to affirm if the flow is fully developed until $z/R = -1.5$, specially for the cases with higher superficial liquid velocity, which presents an accentuate negative slope with z/R. Hence, Fig 6.22 shows the maximum downward liquid velocity in the film region from $0.0 < z/R < -1.5$, which can

Figure 6.18 – Radial $\langle v_l(r,z)\rangle$ and axial $\langle w_l(r,z)\rangle$ liquid velocity profiles at different distances ahead of the Taylor bubble nose from the ensemble average PIV results at $\mathbf{z/R = 0.20}$ from the tip position.

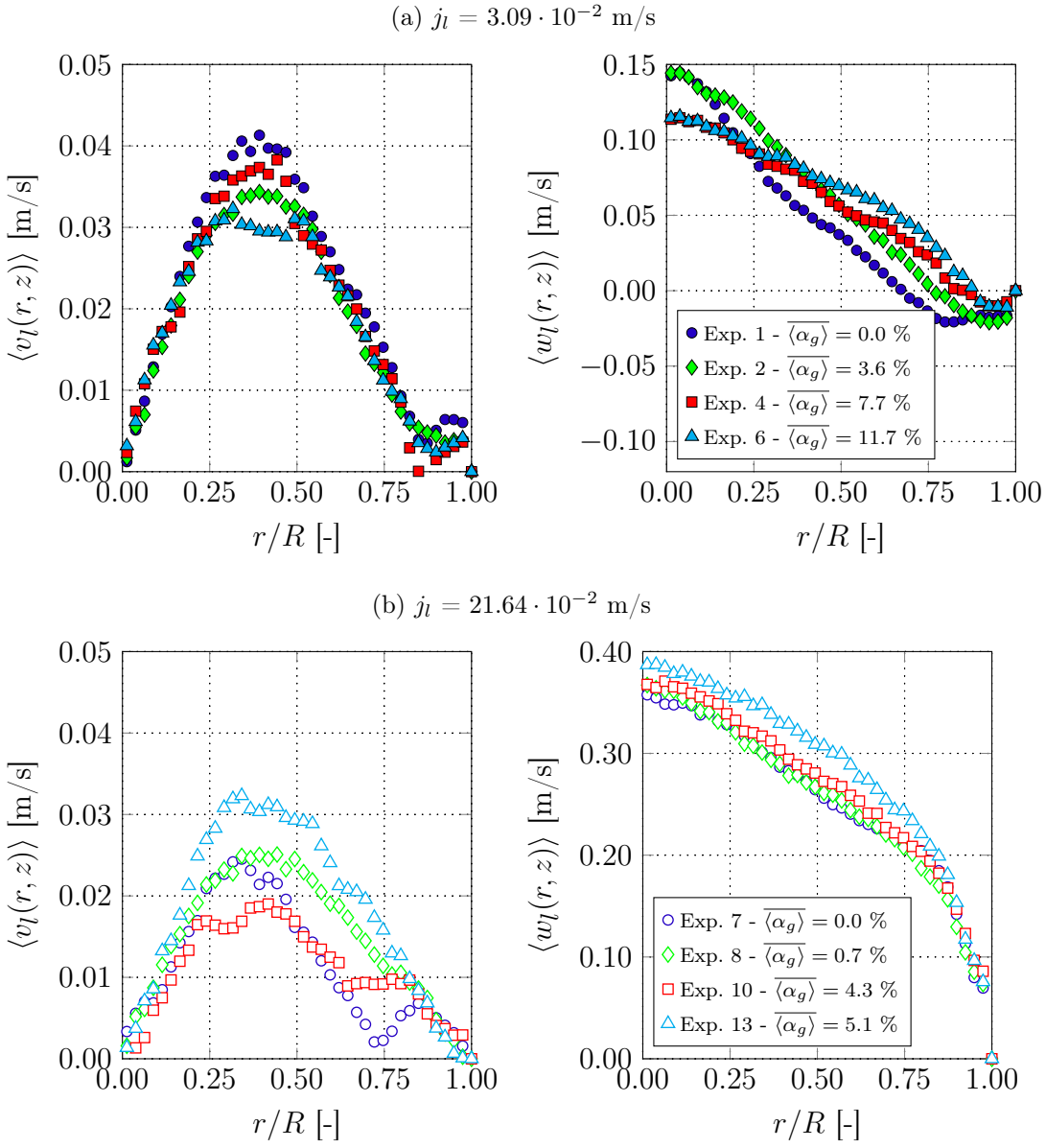

Source - Developed by the author.

be used to visualize the flow development. According to the results shown in Fig. 6.22a), the curves from Exp. 4 and 6 indicate that the fully developed flow is achieved in a shorter distance from the Taylor bubble nose. The evolution of the maximum downward velocities at liquid film for the cases with higher j_l given in Fig. 6.22b) shows that the liquid flow reversal is occurring around a position $-0.50 < z/R < -0.40$ from the bubble nose tip. This can be deduced by the values close to zero in the maximum downward velocity (i.e., zero values means that velocity is zero or positive) and by closely analyzing the liquid

Figure 6.19 – Radial $\langle v_l(r,z)\rangle$ and axial $\langle w_l(r,z)\rangle$ liquid velocity profiles at different distances ahead of the Taylor bubble nose from the ensemble average PIV results at $\mathbf{z/R = 0.50}$ from the tip position.

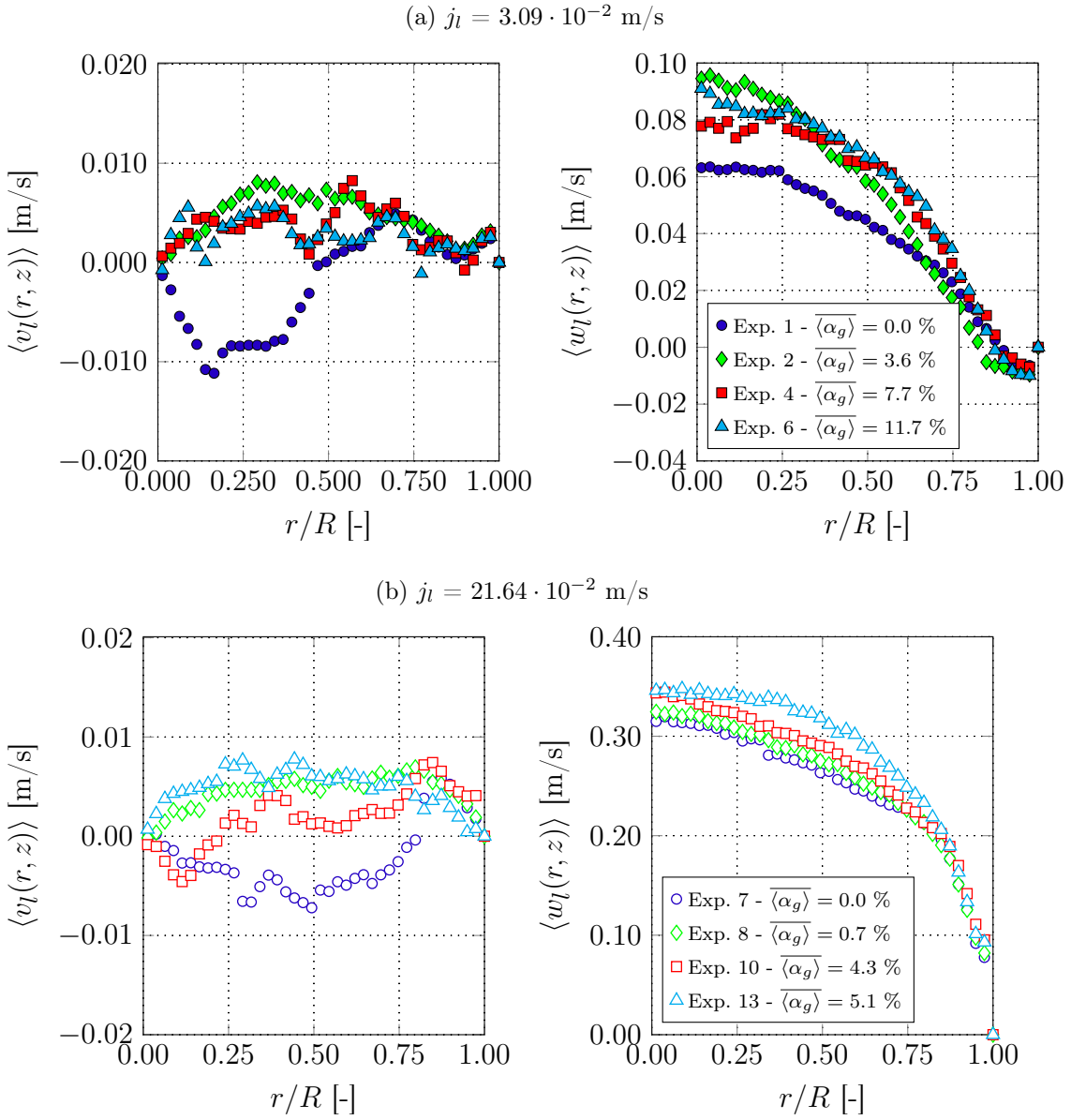

Source - Developed by the author.

velocity vector plots of Fig. 6.13. That is not the case for the plots given in Fig. 6.22a), where a flow reversal region is not observed within the Taylor bubble nose. According to the velocity vector plots of Fig. 6.12, the liquid flow reversal occurs in a distance between $0.40 < z/R < 0.50$ away from the Taylor bubble nose.

Here it is important to state that the aim of this work is to analyze the flow around the Taylor bubbles and effort was dedicated to acquiring PIV images as far from the bubble nose and tail position as possible. Thus, when defining the region of interest of the

Figure 6.20 – Radial $\langle v_l(r,z)\rangle$ and axial $\langle w_l(r,z)\rangle$ liquid velocity profiles at different distances ahead of the Taylor bubble nose from the ensemble average PIV results at $\mathbf{z/R = 1.00}$ from the tip position.

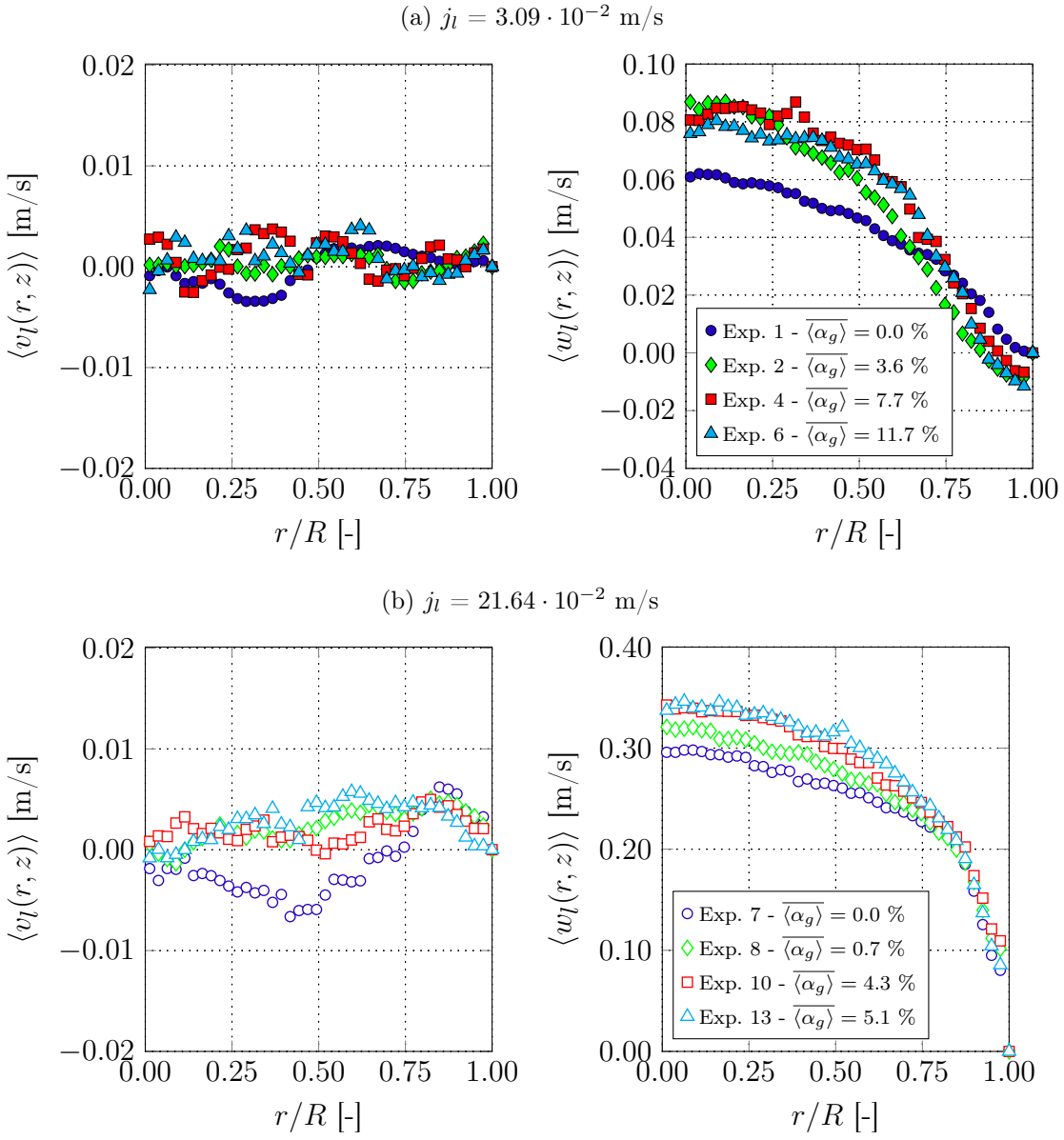

Source - Developed by the author.

PIV acquisitions, the liquid film region was not captured further, and the PIV settings were configured to get higher correlations around the Taylor bubble. As already reported in literature (NOGUEIRA et al., 2003; VAN HOUT et al., 2002c), in order to acquire consistent values in the liquid film region, the PIV camera must be positioned closer to the pipe wall in order to increase the number of interrogation windows. For this reason, the results regarding the liquid film region in the present work must be analyzed with care. However, the authors believe that the trends observed with the current experimental setup

are valid and could be validated in a future work focusing on the effect of the dispersed bubbles on this particular region with an increased spatial resolution.

Figure 6.21 – Ensemble average PIV results of the axial liquid velocity in the liquid film region (at $z/R = -1.5$).

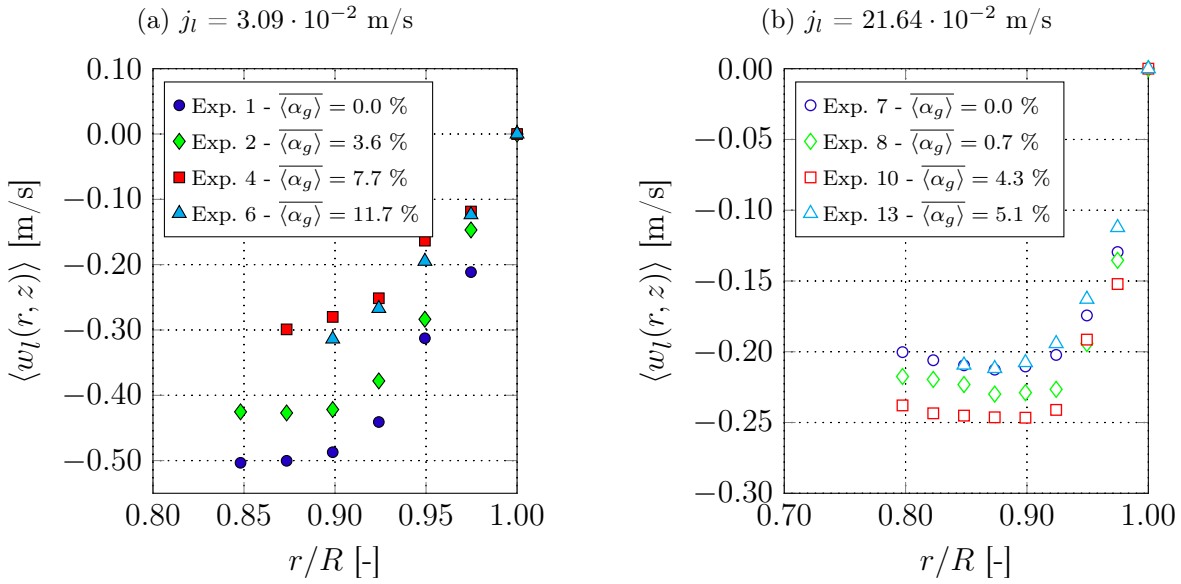

Source - Developed by the author.

Figures 6.23 – 6.26 show the flow structure of the liquid phase below the Taylor bubbles tails. The PIV ensemble average results for the liquid phase velocities are shown in different flow configurations. As seen by those results, the presence of dispersed bubbles around the Taylor bubbles modifies the flow structure around and far away from its tail position. By comparing the mean liquid vector velocity and contour plots of the different j_l flow conditions it is clear that the effect of the dispersed bubbles is stronger in the case with the lower superficial liquid velocities, as also observed at nose region.

From the vector velocity plots and contours of Figs. 6.23 and 6.24, the main features of the flow modification arising from the addition of dispersed bubbles are: i) a decrease and posterior increase (for highest values of $\overline{\langle\alpha_g\rangle}$) of penetration length of the expansion at the exit of the liquid film; ii) modification of the recirculation structure behind the Taylor bubble, increasing the recirculation length; iii) decrease of the recirculation intensity, i.e., the values of the axial and radial liquid velocity components, at the wake region. As in previous results, the influence of dispersed bubbles ir more evident for lower j_l. For the $j_l = 21.64 \cdot 10^{-2}$ m/s the only evident modification observed is the increase of the axial wake length in Exps. 10 and 13 (Fig. 6.26).

To better understand and analyse the flow structure at the wake region, and the influence of the dispersed bubbles in the stream, radial $\langle v_l(r,z)\rangle$ and axial $\langle w_l(r,z)\rangle$ liquid

Figure 6.22 – Maximum downward axial velocity in the liquid film region from the ensemble averaged PIV results.

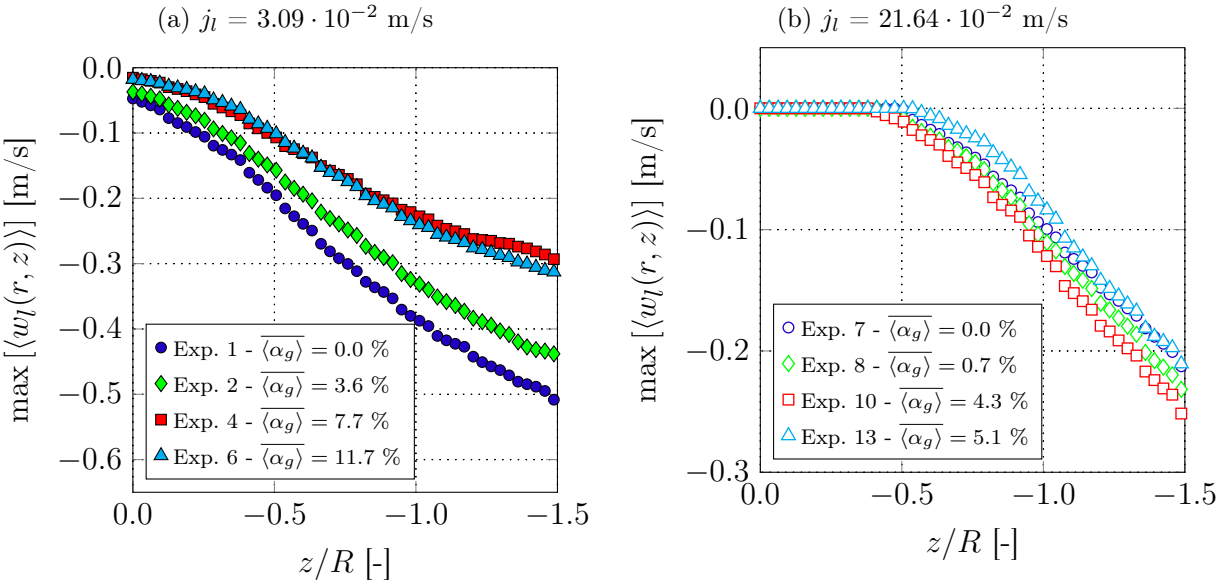

Source - Developed by the author.

velocity profiles were extracted in the different experiments and are presented in Figs. 6.27 to 6.31.

For the axial velocity profiles $\langle w_l(r,z)\rangle$, a flat distribution is observed near the core region, with velocity values close to the terminal velocity of the Taylor bubbles. Moving from the core region and approaching the wall region, there is an abrupt decrease in the axial velocity followed by a change in direction in the liquid velocity, representing the liquid jet exiting the annular film region.

Regarding the annular liquid jet, for the two j_l sets of experiments, the relation between the $\overline{\langle\alpha_g\rangle}$ and the maximum liquid velocity observed at the film entrance (Fig. 6.21) still holds at a distance $z/R = -0.20$ below the Taylor bubble bottom.

According to Fig. 6.27a), the axial $\langle w_l(r,z)\rangle$ profiles for $j_l = 3.09 \cdot 10^{-2}$ m/s only differ in the near-wall region next to liquid annular jet. From the curves of Fig. 6.27, differences due to the dispersed bubbles are seen in the flow core region and also in the $\langle v_l(r,z)\rangle$ profiles.

Farther away, in a section distant $z/R = -0.50$ (Fig. 6.28) from the Taylor bubble bottom, differences are observed throughout the entire cross-sectional area of the pipe for the two liquid superficial velocities. In this position, the axial velocity does not have such a flat profile as in the previous section, and the observed downward liquid jet becomes wider.

Figure 6.23 – PIV ensemble average fields fro the $j_l = 3.09 \cdot 10^{-2}$ m/s experiments around the Taylor bubble tail. First row: Ensemble-average velocity vector plots; Second row: Ensemble-average velocity vector plots streamlines; The velocity vectors on the first row spaced by 4 interrogation windows in each direction for better visualization.

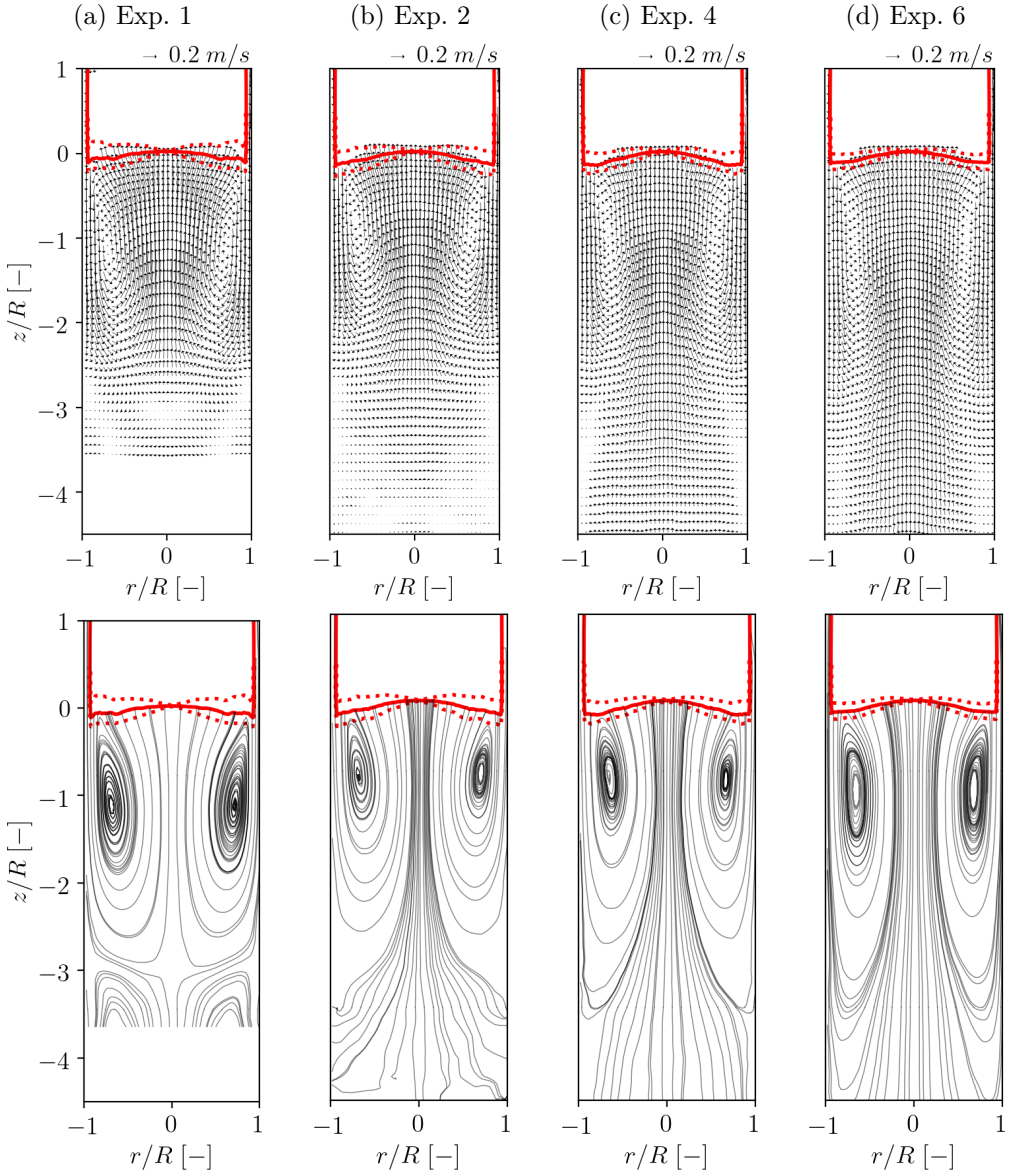

Source - Developed by the author.

Although the axial and radial liquid velocity profiles develop into higher values, different trends are observed on the two j_l sets of experiments. For the case with $j_l = 3.09 \cdot 10^{-2}$ m/s, as the void fraction is increased, the intensity of the liquid recirculation decreases, since the axial and radial velocity profiles present lower values as more dispersed bubbles are added to the background flow. The opposite trend is observed with the $j_l = 21.64 \cdot 10^{-2}$ m/s experiments, where the $\langle v_l(r,z) \rangle$ and $\langle w_l(r,z) \rangle$ present higher values as

Figure 6.24 – PIV ensemble average fields from the $j_l = 3.09 \cdot 10^{-2}$ m/s experiments around the Taylor bubble tail. First row: Contour plot of the ensemble average radial liquid velocity $\langle v_l(r,z)\rangle$; Second row: Contour plot of the ensemble average axial liquid velocity $\langle w_l(r,z)\rangle$;

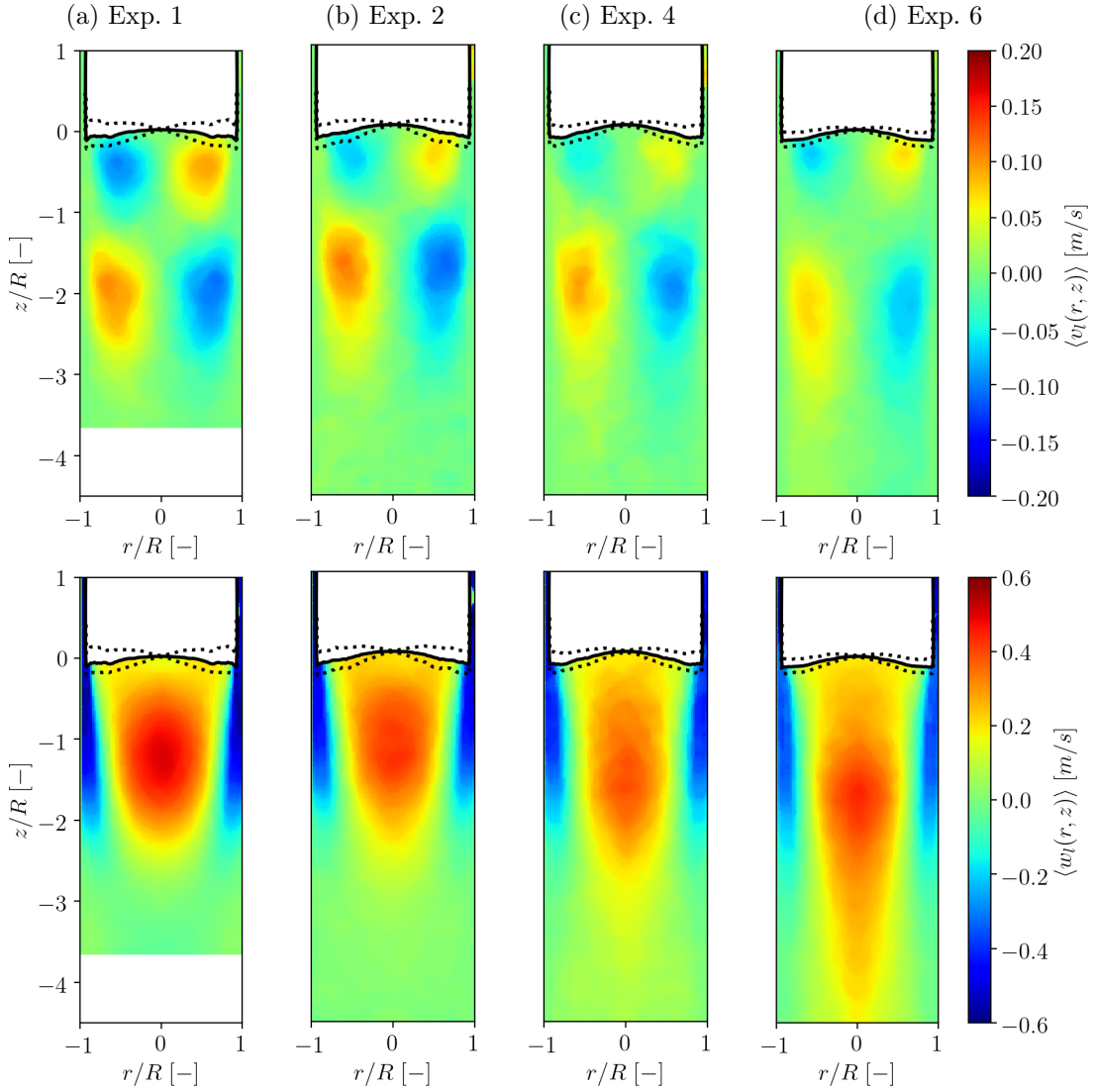

Source - Developed by the author.

$\overline{\langle \alpha_g \rangle}$ is increased.

At $z/R = -1.00$, according to the axial velocity profiles for both j_l series, the results of Fig. 6.29 shows that liquid jet located at the near-wall region keeps getting wider. According to the results for the $j_l = 3.09 \cdot 10^{-2}$ m/s experiments, the axial velocity profiles shown that the liquid recirculation on the wake region is still losing intensity as more bubbles are added to the background flow. For the $j_l = 21.64 \cdot 10^{-2}$ m/s experiments, the $\langle w_l(r,z)\rangle$ plots are collapsing into a single curve on the core region, while some differences are observed in the near-wall region within the downward liquid jet.

Figure 6.25 – PIV ensemble average fields fro the $j_l = 21.64 \cdot 10^{-2}$ m/s experiments around the Taylor bubble tail. First row: Ensemble-average velocity vector plots; Second row: Ensemble-average velocity vector plots streamlines; The velocity vectors on the first row spaced by 4 interrogation windows in each direction for better visualization.

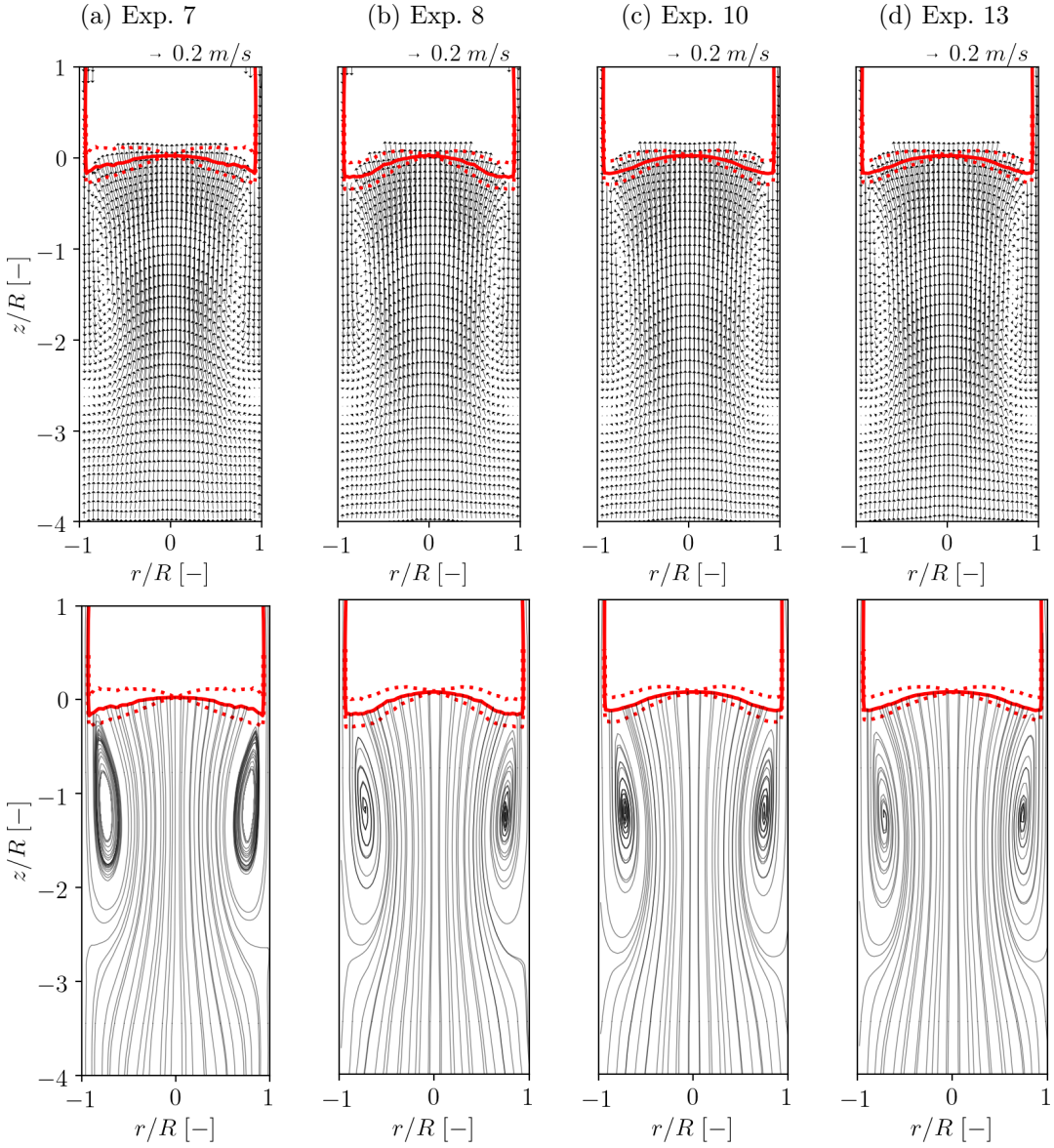

Source - Developed by the author.

Velocity profiles at $z/R = -2.00$, presented in Fig. 6.30 shows that in the core region ($0.0 < r/R < 0.75$), an inflection of the trend presented earlier is observed in the $j_l = 3.09 \cdot 10^{-2}$ m/s experiments. In this position, the axial velocity of Exp. 1 present lower values on the core region than the plots from the experiments with dispersed bubbles, which was not the case in the figures previously shown. Additionally, in both j_l series, the $\langle v_l(r,z) \rangle$ and $\langle w_l(r,z) \rangle$ liquid velocity profiles show that the liquid recirculation found in

Figure 6.26 – PIV ensemble average fields from the $j_l = 21.64 \cdot 10^{-2}$ m/s experiments around the Taylor bubble tail. First row: Contour plot of the ensemble average radial liquid velocity $\langle v_l(r,z)\rangle$; Second row: Contour plot of the ensemble average axial liquid velocity $\langle w_l(r,z)\rangle$;

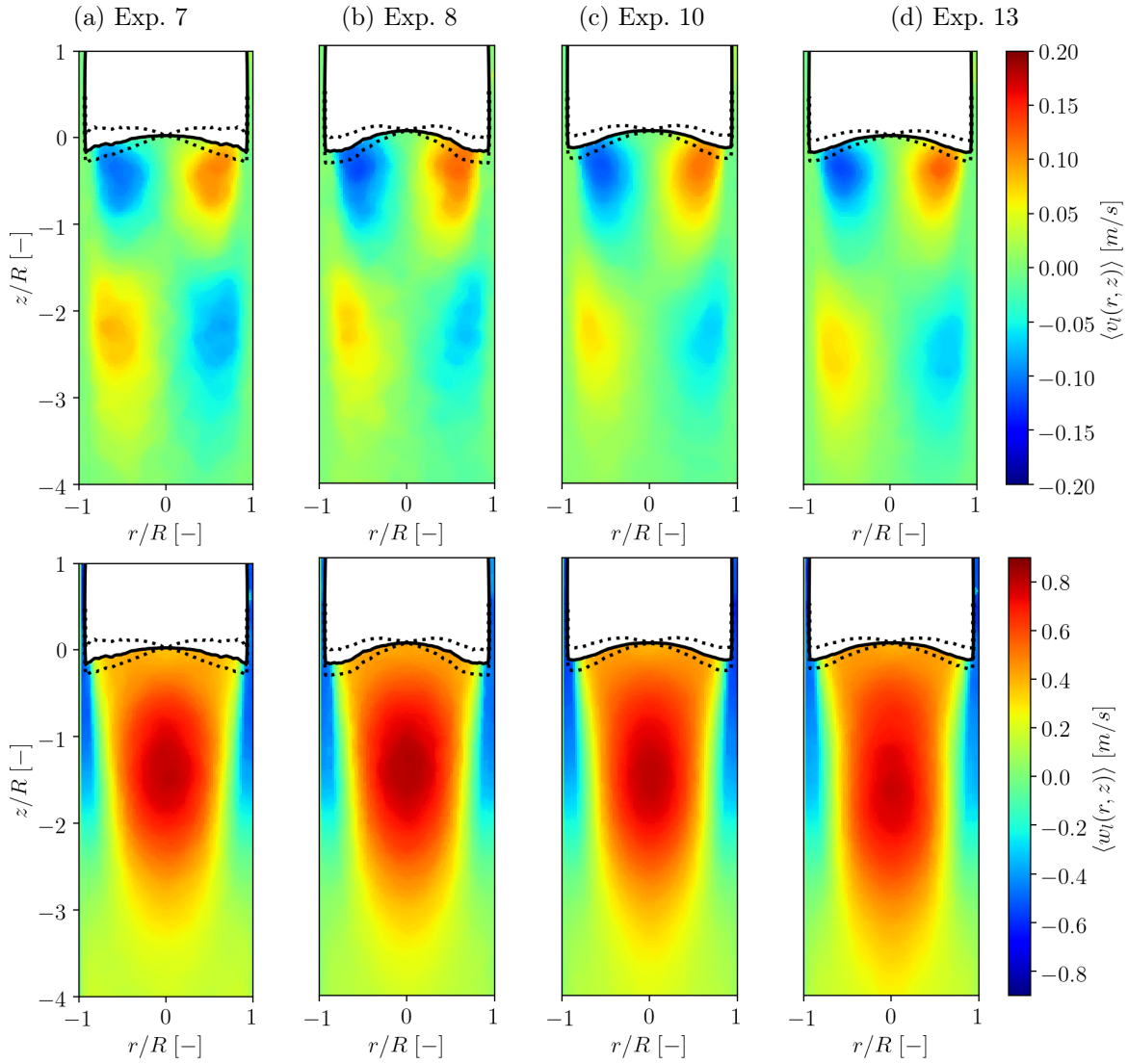

Source - Developed by the author.

the wake region gets stronger with $\overline{\langle \alpha_g \rangle}$.

The profiles shown in Fig. 6.31, farther away from the bottom position at $z/R = -3.00$, show that as more dispersed bubbles are present in the flow, higher are the values of the axial $\langle w_l(r,z)\rangle$ and radial $\langle v_l(r,z)\rangle$ velocity liquid profiles. This increase with $\overline{\langle \alpha_g \rangle}$ suggests that the influence of the Taylor bubble on the flow field in the wake region is stronger when dispersed bubbles are present and extends farther away, than the case without dispersed bubbles.

Figures 6.32 and 6.33 illustrate the wake length of Taylor bubbles, i.e., the length

Figure 6.27 – Ensemble averaged instantaneous PIV radial $\langle v_l(r,z)\rangle$ and axial $\langle w_l(r,z)\rangle$ liquid velocity profiles at a section $\mathbf{z/R = -0.20}$ below the Taylor bubble bottom position.

(a) $j_l = 3.09 \cdot 10^{-2}$ m/s

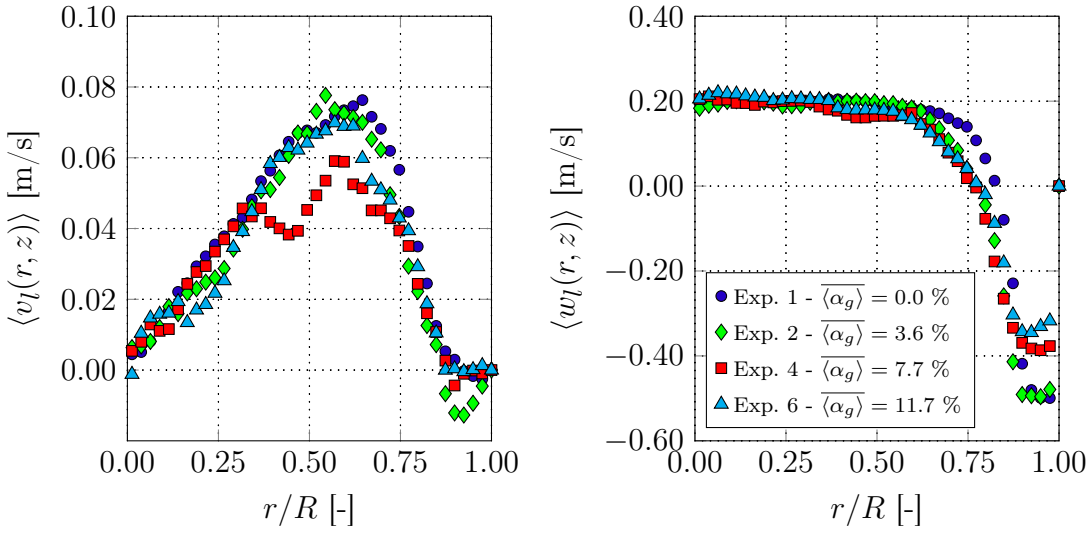

(b) $j_l = 21.64 \cdot 10^{-2}$ m/s

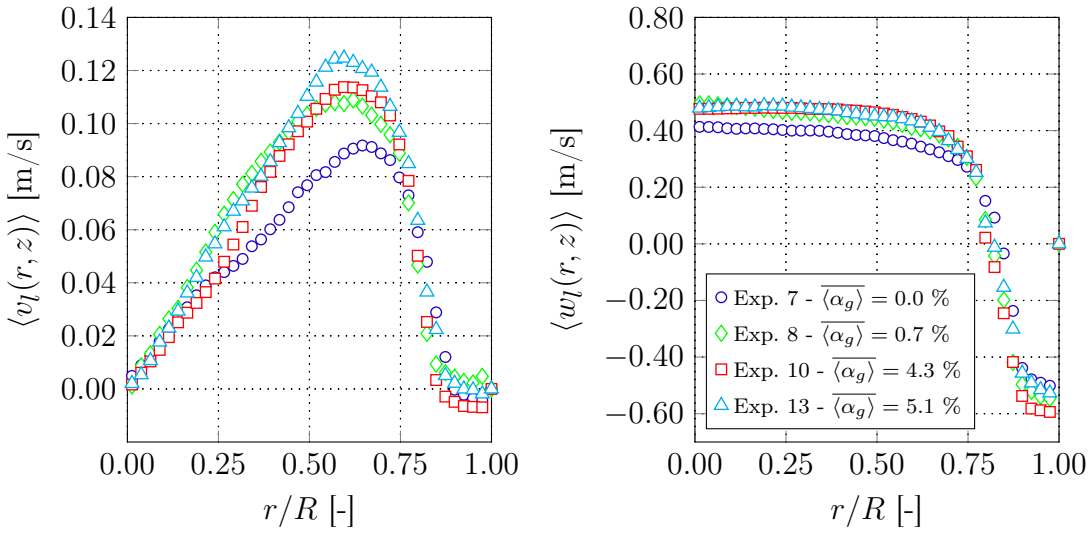

Source - Developed by the author.

of the region affected by the passage of Taylor bubbles, and how this length in influenced by the dispersed bubbles. This influence is observed through the centerline ($r/R = 0.0$) axial velocities and the residual variable $\Gamma(z)$ as a function of the distance from the bubble bottom. These curves show, as already observed in previous results, that the wake length trends to become longer as dispersed bubbles are present in the flow. The $\Gamma(z)$ and $\langle w_l(r,z)\rangle|_{r=0.0}$ curves shown in Fig. 6.32 for the cases with $j_l = 3.09 \cdot 10^{-2}$ m/s, with and without dispersed bubbles, present differences on the magnitude of the values and

Figure 6.28 – Ensemble averaged instantaneous PIV radial $\langle v_l(r,z)\rangle$ and axial $\langle w_l(r,z)\rangle$ liquid velocity profiles at a section $\mathbf{z/R = -0.50}$ below the Taylor bubble bottom position.

(a) $j_l = 3.09 \cdot 10^{-2}$ m/s

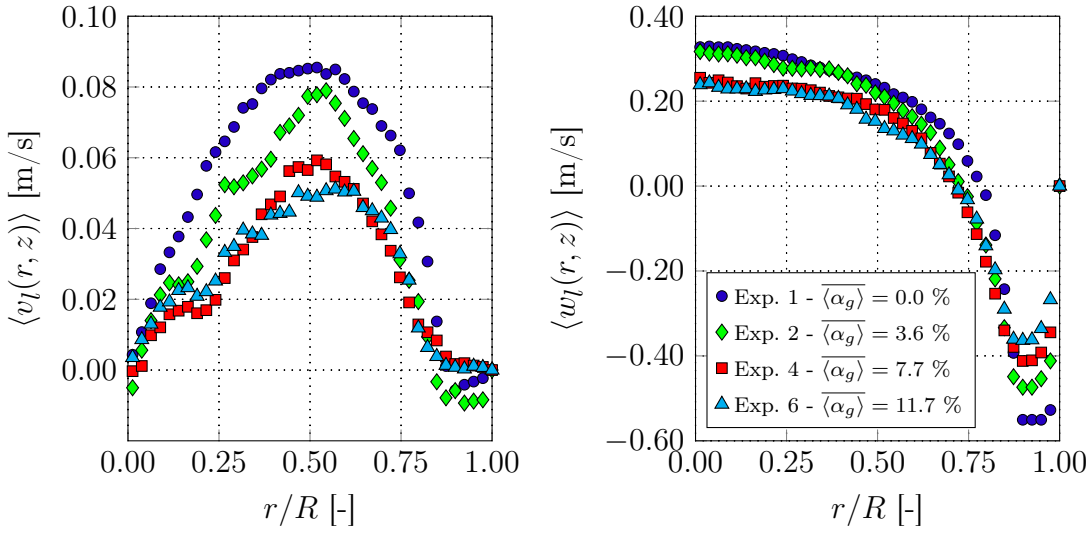

(b) $j_l = 21.64 \cdot 10^{-2}$ m/s

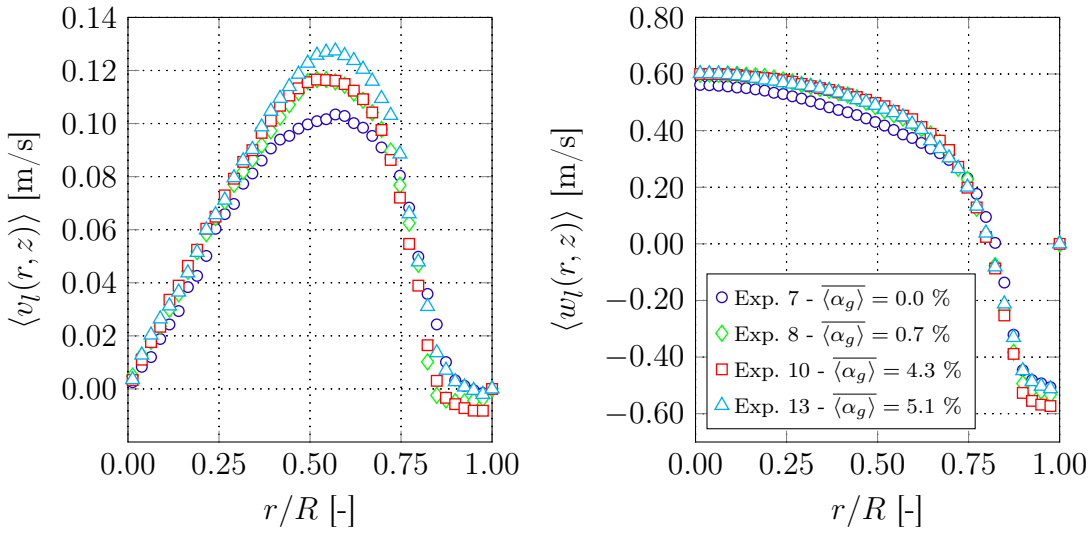

Source - Developed by the author.

also on its shape.

In the case of $j_l = 3.09 \cdot 10^{-2}$ m/s (Fig. 6.32) without dispersed bubbles the $\Gamma(z)$ curve presents an inflection point near $z/R \approx -2.80$, which is near the position where the centerline axial velocity becomes negative, as seen in Fig. 6.32b). The negative centerline velocities and this inflection on the $\Gamma(z)$ curve are not observed in the cases with dispersed bubble. As already observed by Van Hout et al. (2002c), for Taylor bubbles rising in a stagnant water column, without the presence of dispersed bubbles, the change of sign in

Figure 6.29 – Ensemble averaged instantaneous PIV radial $\langle v_l(r,z)\rangle$ and axial $\langle w_l(r,z)\rangle$ liquid velocity profiles at a section $\mathbf{z/R = -1.00}$ below the Taylor bubble bottom position.

(a) $j_l = 3.09 \cdot 10^{-2}$ m/s

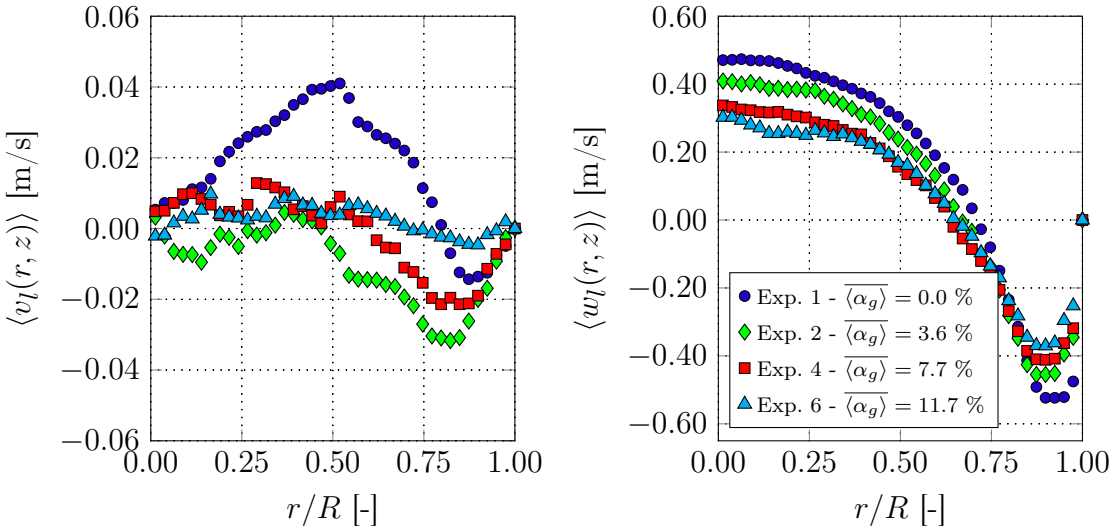

(b) $j_l = 21.64 \cdot 10^{-2}$ m/s

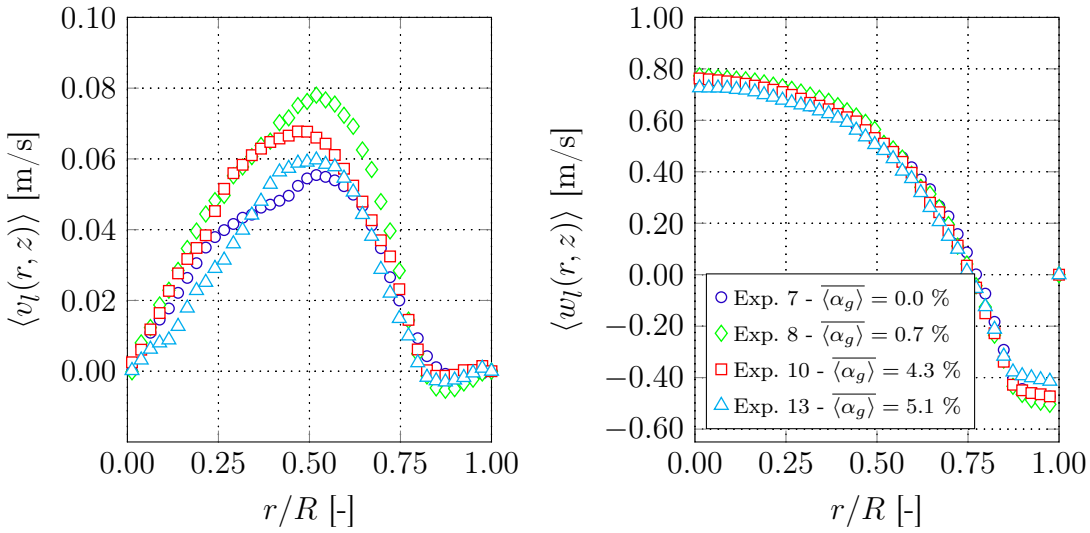

Source - Developed by the author.

the centerline axial velocity profiles indicates the presence of secondary vortex rings with opposite sense of rotation, which is visible in the streamline plots for Exp. 1 in Fig. 6.23. The absence of this secondary vortex in the remainder cases of Fig. 6.32 is perhaps due to the dissipation of this large scale flow structure caused by the dispersed bubbles or by the latter inducing fluctuations on the flow which hinders the liquid shear-induced turbulence.

According to the $\Gamma(z)$ curves of Fig. 6.33, the same behavior is observed for the experiments with higher j_l ($j_l = 21.64 \cdot 10^{-2}$ m/s). However, for this set of experiments,

Figure 6.30 – Ensemble averaged instantaneous PIV radial $\langle v_l(r,z)\rangle$ and axial $\langle w_l(r,z)\rangle$ liquid velocity profiles at a section $\mathbf{z/R = -2.00}$ below the Taylor bubble bottom position.

(a) $j_l = 3.09 \cdot 10^{-2}$ m/s

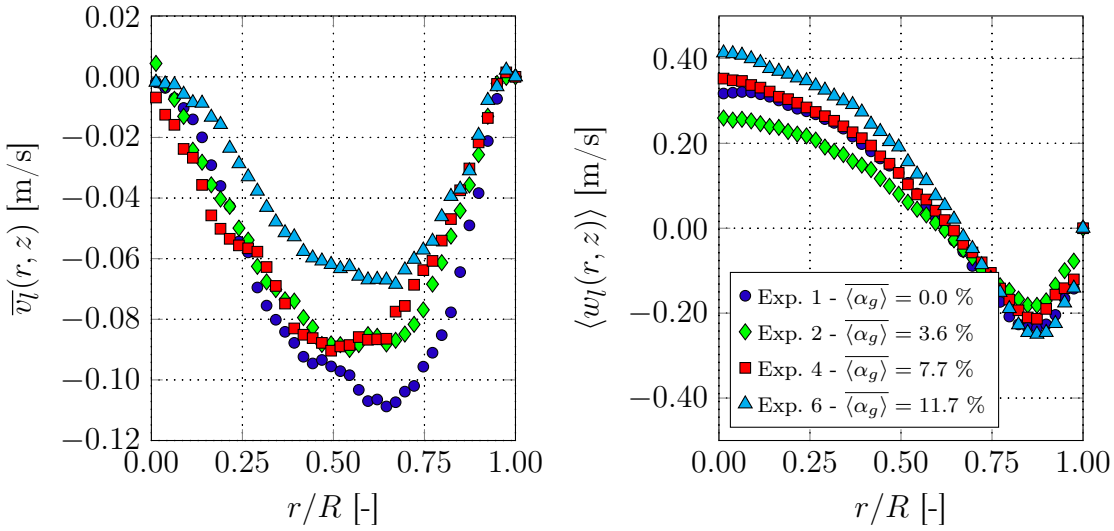

(b) $j_l = 21.64 \cdot 10^{-2}$ m/s

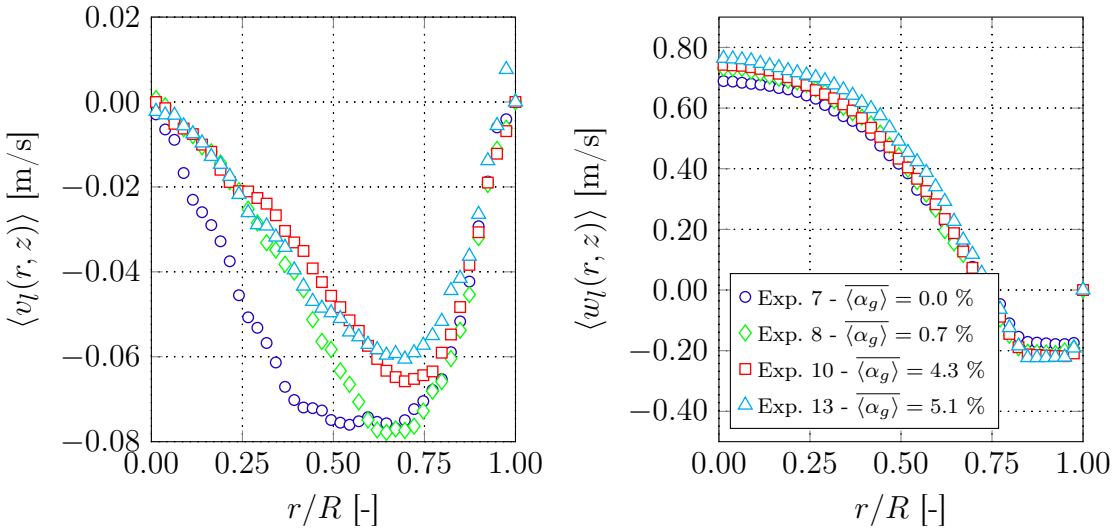

Source - Developed by the author.

due to its liquid inertia dominance, the effect of $\overline{\langle\alpha_g\rangle}$ is not as strong as the $j_l = 3.09 \cdot 10^{-2}$ m/s experiments.

According to the centerline profiles, for both values of j_l, there is a relation between the position of its maximum and the quantity of dispersed bubbles in the flow. As $\overline{\langle\alpha_g\rangle}$ increases, the maximum centerline position moves further downstream, away from the Taylor bubble bottom position. This shift towards downstream is due to induced upward liquid flow from the dispersed bubbles at the wake region. During the rising motion of

Figure 6.31 – Ensemble averaged instantaneous PIV radial $\langle v_l(r,z)\rangle$ and axial $\langle w_l(r,z)\rangle$ liquid velocity profiles at a section $\mathbf{z/R = -3.00}$ below the Taylor bubble bottom position.

(a) $j_l = 3.09 \cdot 10^{-2}$ m/s

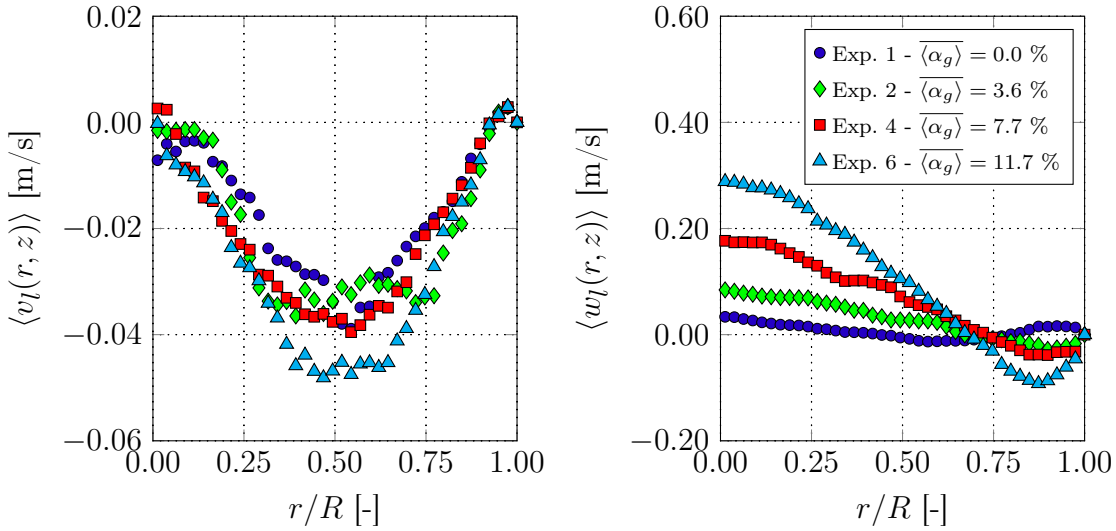

(b) $j_l = 21.64 \cdot 10^{-2}$ m/s

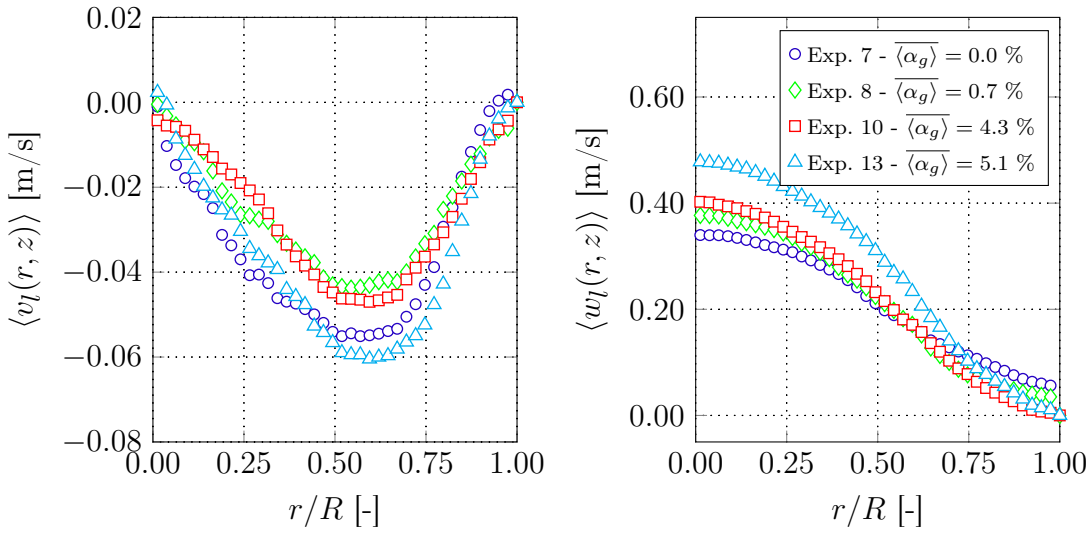

Source - Developed by the author.

the Taylor bubbles, as observed in Videos 10 and 11 of the supplementary material given in Appendix B, it is possible to visualize a region where the dispersed bubbles present a recirculating motion behind the Taylor bubble. Since more bubbles are present behind the Taylor bubble, higher is the induced upward liquid flow due to its presence, which in turn increases the recirculating motion length and shifts the maximum liquid velocity position away from the Taylor bubble bottom.

Figure 6.32 – Flow field behavior at the wake of the Taylor bubbles for $j_l = 3.09 \cdot 10^{-2}$ m/s: a) Residual variable $\Gamma(z)$ (NOGUEIRA et al., 2003), and b) Centerline pipe($r = 0.0$) axial velocity in different positions z from the bottom position.

(a)

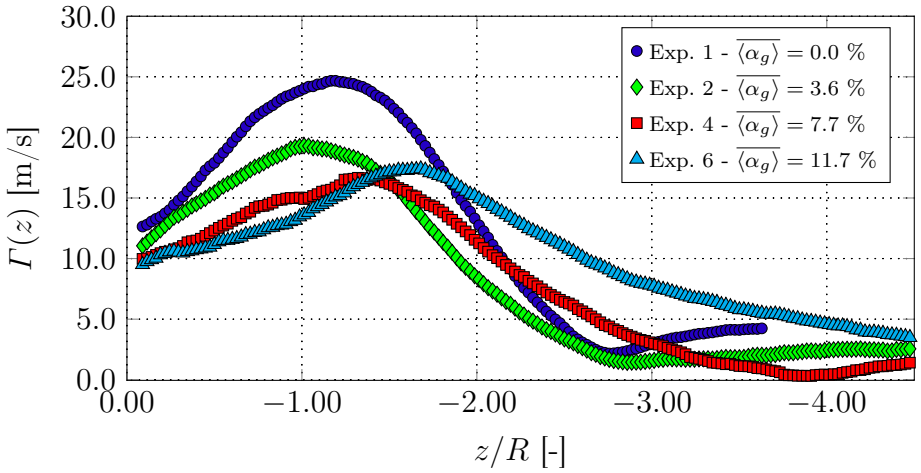

(b)

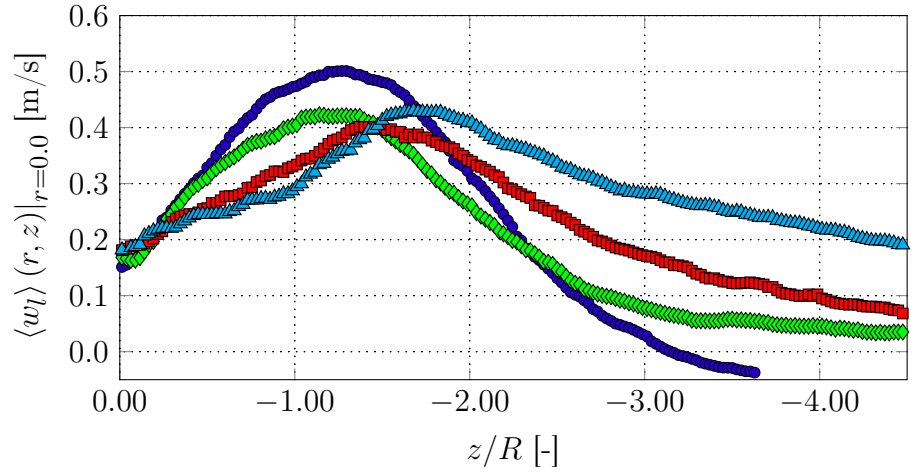

Source - Developed by the author.

6.2.4.2 Turbulent statistics of the liquid phase

According to the presented results, the flow structure around the Taylor bubbles is substantially modified by the presence of the dispersed bubbles. In addition, it was shown that the influence of the small dispersed gas phase is less pronounced as j_l is increased. Those conclusions were all based on the ensemble average liquid velocity profiles. Considering the high number of PIV acquisitions in each experiment, around the Taylor bubble nose and bottom, it was possible to compute the turbulent liquid statistics of the flow, such as the r.m.s. values of the radial $v'_{l,rms}(r,z)$ and axial $w'_{l,rms}(r,z)$ velocity component fluctuations. Additionally, the turbulent kinetic energy $k(r,z) = 1/2\left[(v'_{l,rms})^2 + (w'_{l,rms})^2\right]$

Figure 6.33 – Flow field behavior at the wake of the Taylor bubbles for $j_l = 21.64 \cdot 10^{-2}$ m/s: a) Residual variable $\Gamma(z)$ (NOGUEIRA et al., 2003), and b) Centerline pipe($r = 0.0$) axial velocity in different positions z from the bottom position.

(a)

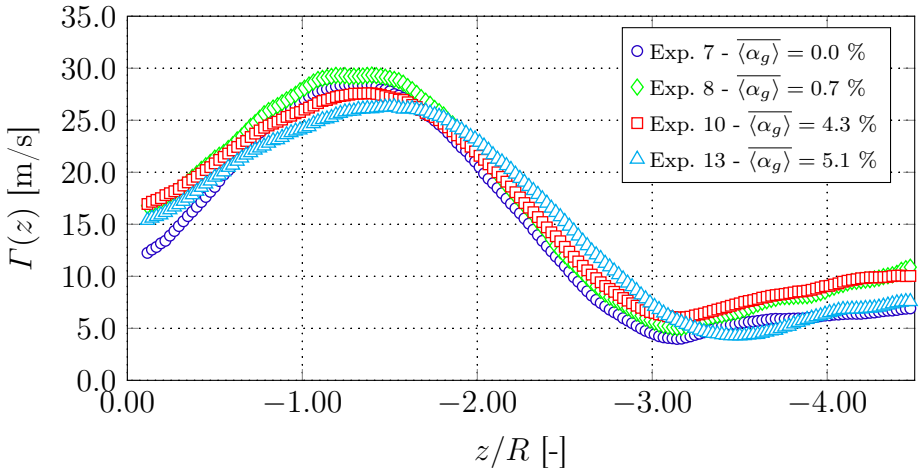

(b)

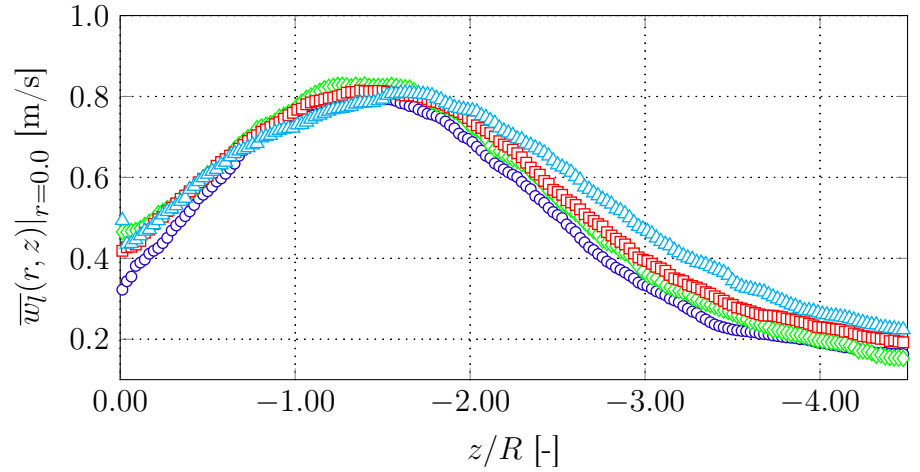

Source - Developed by the author.

and the Reynolds stress $\langle v'w'(r,z)\rangle$ were calculated. The turbulence field around Taylor bubbles is strongly related to mass transfer rates in liquid slug regions which is associated with the slug induced corrosion problems. Therefore, the analysis of turbulence fields and how they are influenced by dispersed bubbles is valuable regarding this application. The results of those turbulent liquid flow statistics, together with an analysis of the local liquid phase turbulence modification due to the presence of the dispersed bubbles, are given in the next paragraphs.

Figures 6.34 and 6.35 present the contour plots of the r.m.s. values of the radial $v'_{l,rms}(r,z)$ and axial $w'_{l,rms}(r,z)$ velocity component fluctuations around the Taylor bub-

ble nose. As observed,independently of the liquid superficial velocity, the influence of the Taylor bubble on turbulent fields is constrained to a distance $z/D < 0.5$ above their nose tip. The strong differences in turbulent fields away from Taylor bubbles noses are due to the bubble induced turbulence, as already observed in Figs 6.14 and 6.15. However it possible to visualize regions of local maxima close the Taylor bubble nose, between $0.2 < |r/R| < 0.9$, which are due to the nose shape deformation and the Taylor bubble eccentric rising motion, with is induced by the presence of dispersed bubbles.

On the other hand, the contour plots of the axial $w'_{l,rms}(r,z)$ velocity component fluctuations show the influence of the Taylor bubbles up to an approximate distance $z/D < 0.5$ above the nose tip. Analyzing the $w'_{l,rms}(r,z)$ values distribution closer to the nose, it is possible to observe a region with a local maxima, which can also be associated with the Taylor bubble nose oscillation.

The same findings from the $v'_{l,rms}(r,z)$ and $w'_{l,rms}(r,z)$ fields around the Taylor bubble nose are again observed in the turbulent kinetic energy $k(r,z)$ distributions. However, from the $k(r,z)$ distributions, the effect of the dispersed bubbles on the turbulent intensity is better visualized. By comparing the contour plots of Exp. 7 (Re_l=5684 and $\overline{\langle \alpha_g \rangle}$=0.0) from Fig. 6.35 with the results of the experiments with dispersed bubbles of Fig. 6.34 which has a laminar Re_l=812 , one can observe that the BIT produced by the dispersed bubbles case in the $j_l = 3.09 \cdot 10^{-2}$ m/s is comparable or higher from those observed in a shear induced turbulent flow of Exp. 7, following the trends observed by Kim et al. (2016), for bubbly flows.

Close to the bubble nose, when comparing to single-phase flow cases, there is an increase in the $k(r,z)$ field, which is, as already discussed, due to the Taylor bubble nose oscillations due to the dispersed bubbles.

Figures 6.36 and 6.37 present the turbulent statistics for the liquid phase at the wake region of Taylor bubbles, for the $j_l = 3.09 \cdot 10^{-2}$ m/s experiments. Fluctuations (r.m.s.) of radial and axial velocity components (Fig. 6.36) and turbulent kinetic energy and Reynolds stress distributions (Fig. 6.37) are presented. Streamlines are also represented allowing to get a better visualization of the flow field and how the average and turbulent variables are associated and influenced by the presence of dispersed bubbles. The analogous results for $j_l = 21.64 \cdot 10^{-2}$ m/s are presented in in Figs. 6.38 and 6.39.

From the results presented in Figs. 6.36 from 6.39 it is evident that the addition of dispersed bubbles in the flow modifies the turbulent structure behind the Taylor bubble. Comparing the effect of the $\overline{\langle \alpha_g \rangle}$ on the turbulent and on the average liquid velocity fields, it is clear that the dispersed bubbles have a stronger influence on the turbulence structure of the flow.

Figure 6.34 – PIV ensemble average fields from the $j_l = 3.09{\cdot}10^{-2}$ m/s experiments around the Taylor bubble nose. First row: Contour plot of the r.m.s. values of the radial velocity component fluctuations $v'_{l,rms}(r,z)$; Second row: Contour plot of the r.m.s. values of the axial velocity component fluctuations $w'_{l,rms}(r,z)$; Third row: Contour plot of the turbulent kinetic energy k.

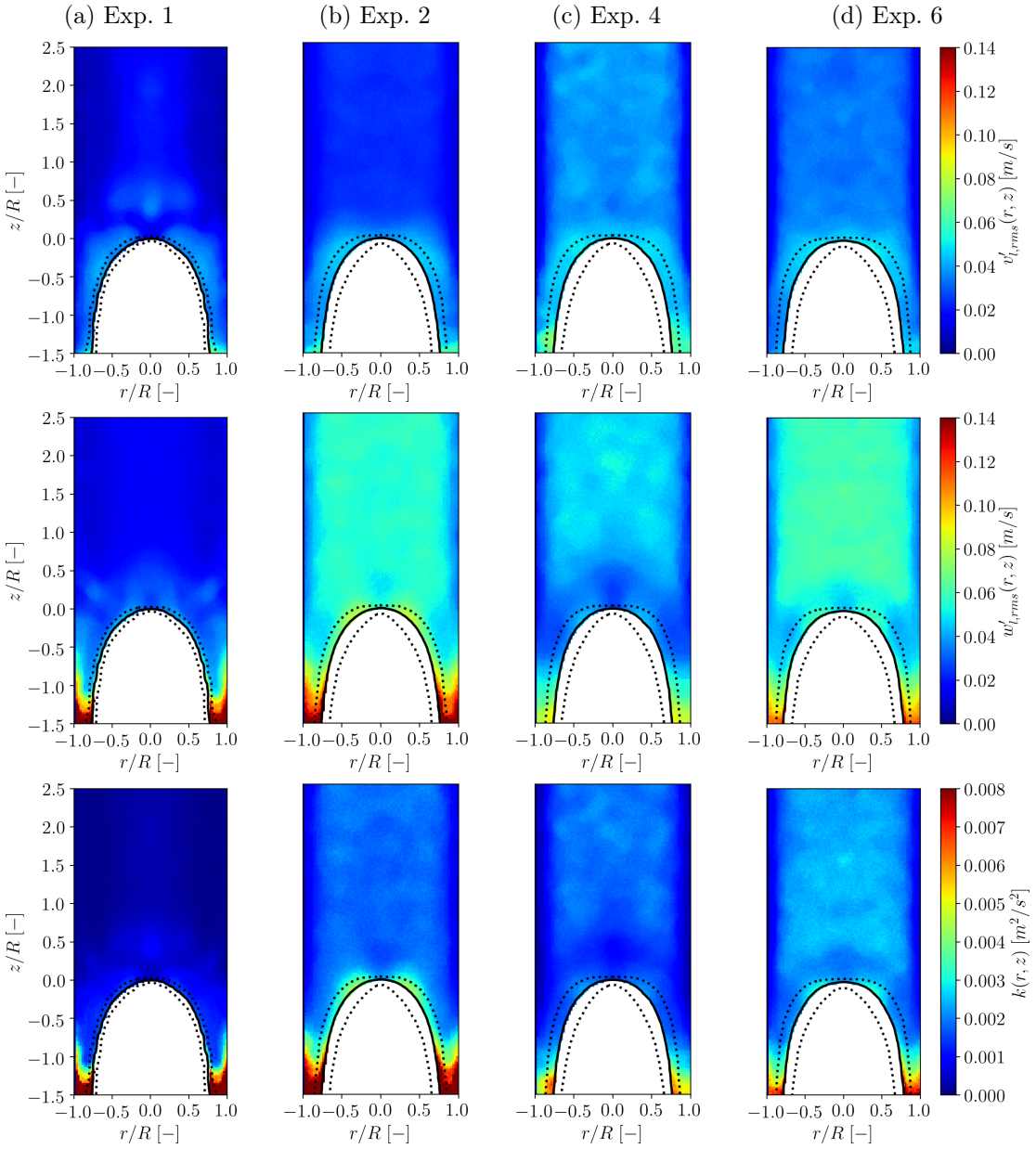

Source - Developed by the author.

In the turbulence fields for lower liquid superficial velocity, $j_l = 3.09 \cdot 10^{-2}$ m/s, shown in Figs. 6.36 and 6.37, it can be observed that the addition of a small quantity of dispersed bubbles (Exp. 2) substantially increases the turbulence intensity at wake region of the Taylor bubbles. The Reynold stress (second row of Fig. 6.37) is more intense for the case without dispersed bubbles, due to higher intensity of the wake vortex. However,

Figure 6.35 – PIV ensemble average fields from the $j_l = 21.64 \cdot 10^{-2}$ m/s experiments around the Taylor bubble nose. First row: Contour plot of the r.m.s. values of the radial velocity component fluctuations $v'_{l,rms}(r,z)$; Second row: Contour plot of the r.m.s. values of the axial velocity component fluctuations $w'_{l,rms}(r,z)$; Third row: Contour plot of the turbulent kinetic energy $k(r,z)$.

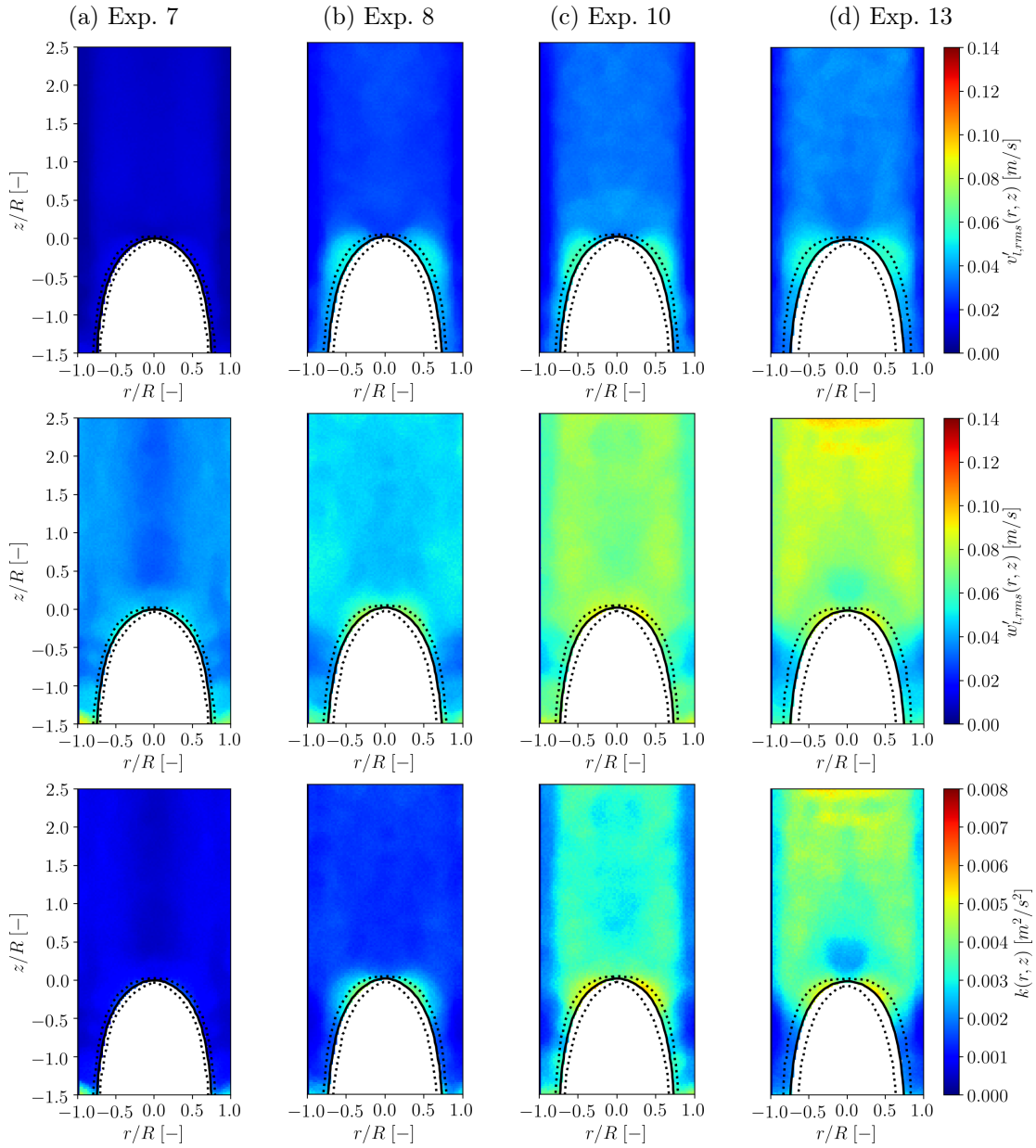

Source - Developed by the author.

a further increase of dispersed bubbles seems to decrease the turbulence intensity, due to the higher void fraction at wake region. This interesting finding can be observed on the tail motion of the Taylor bubble bottom in Video 10 of the supplementary material given in Appendix B, where the bubble bottom oscillates strongly from Exp. 2 to Exp. 1, while for the remainder cases, the tail oscillation is suppressed with an increase of $\overline{\langle \alpha_g \rangle}$.

Additionally, the void fraction increase at wake region suppresses the vertical motion of dispersed bubbles, resulting from the film ejection and buoyancy effect. As can be seen in Video 10 of the supplementary material given in Appendix B, the mean free path of dispersed bubbles decreases as $\overline{\langle \alpha_g \rangle}$ is increased. Besides, through the visualisation of this video, it is clear that this peak of $w'_{l,rms}(r,z)$ close to the wall is due to the dispersed bubbles that are "ejected" from the annular liquid film. By analysing the trajectories of the dispersed bubbles flowing through and exiting the annular film, it is possible to observe that as $\overline{\langle \alpha_g \rangle}$ is increased, longer is its travelled path until its absorption by the liquid recirculation.

Figures 6.38 and 6.39 present the turbulence structure for the $j_l = 21.64 \cdot 10^{-2}$ m/s set of experiments. Due to higher liquid velocity in those experiments, the movement of the dispersed bubbles does not have the same impact on the modification of the turbulent structure, as shown in the $j_l = 3.09 \cdot 10^{-2}$ m/s results.

From the contour plots, when comparing the cases with and without the presence of dispersed bubbles, one can observe a decrease on the $v'_{l,rms}(r,z)$ intensity near the Taylor bubble bottom and small modifications on the local structure away from the bottom position. However, the $w'_{l,rms}(r,z)$ and turbulent kinetic energy, results shown that the turbulent intensity increases with $\overline{\langle \alpha_g \rangle}$. As more bubbles are added to the flow, an increase in the turbulence intensity at the center of liquid recirculation is observed. In general, the increase of $\overline{\langle \alpha_g \rangle}$ results in an increase of turbulence at the wake region, for Exp. 8 and 10. Nevertheless, for the same reasons discussed for the case of $j_l = 3.09 \cdot 10^{-2}$ m/s, a further increase of j_g (Exp. 13) results in a decrease of turbulence intensity at this region. From the turbulent results of the set of j_l experiments, it is possible to observe that the decrease of the turbulent intensity in the wake region shifts to lower $\overline{\langle \alpha_g \rangle}$ as j_l increases. From the turbulent results of the set of j_l experiments, it is possible to observe that the decrease of the turbulent intensity in the wake region shifts to lower $\overline{\langle \alpha_g \rangle}$ as j_l increases.

The relation between $\overline{\langle \alpha_g \rangle}$ and turbulence intensity at wake region of Taylor bubbles, observed for both values of liquid superficial velocity, can be directly related with the behavior of terminal rising velocity of Taylor bubbles, shown in Fig. 6.3. It is clearly seen that the values of $\overline{\langle \alpha_g \rangle}$ for which U_{tb} decrease coincides with those where the turbulence intensity is decreased by the concentration of bubbles at the wake region.

Figure 6.36 – PIV ensemble average fields from the $j_l = 3.09 \cdot 10^{-2}$ m/s experiments around the Taylor bubble bottom. First row: Contour plot of the r.m.s. values of the radial velocity component fluctuations $v'_{l,rms}(r,z)$; Second row: Contour plot of the r.m.s. values of the axial velocity component fluctuations $w'_{l,rms}(r,z)$;

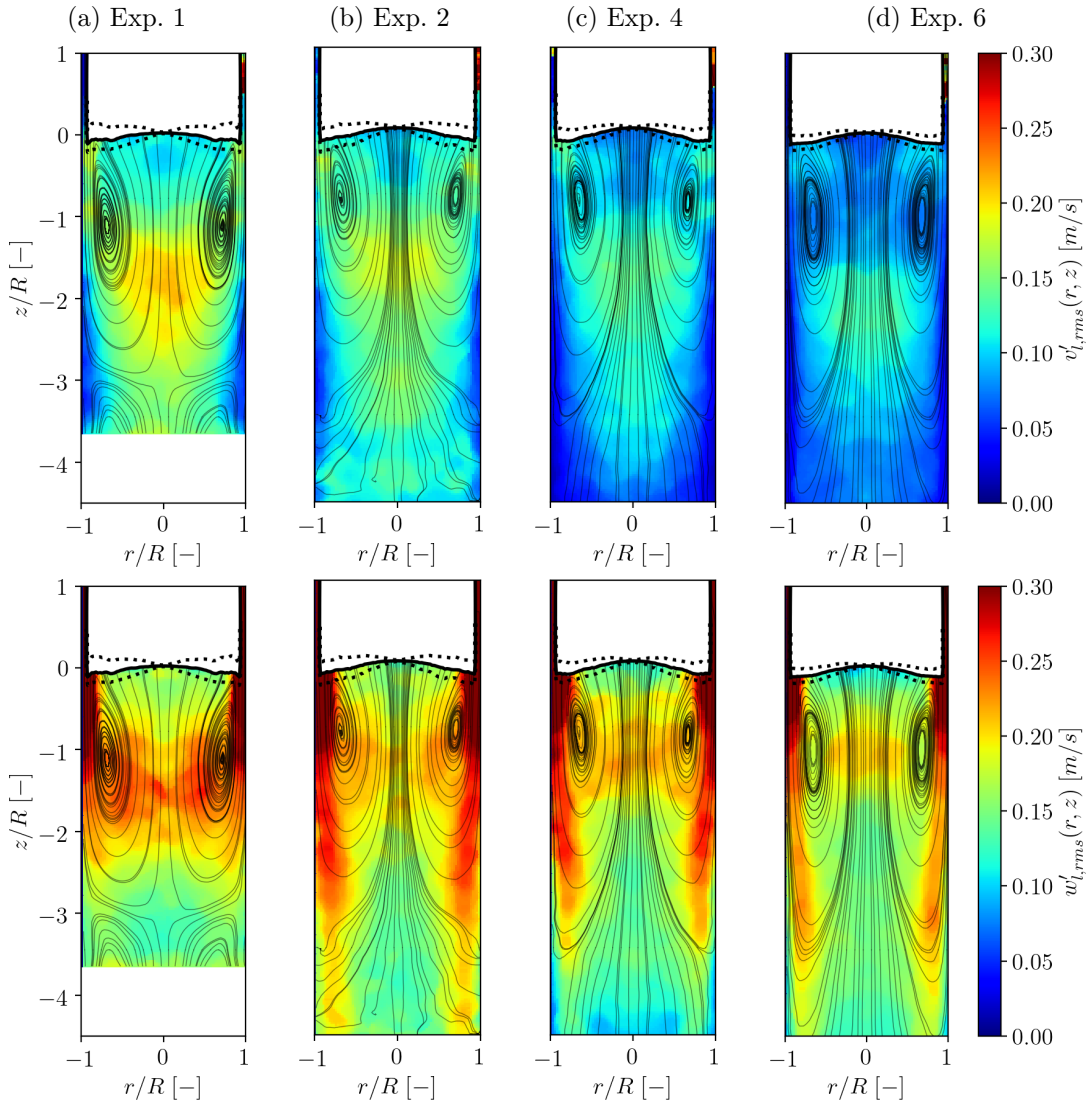

Source - Developed by the author.

Figure 6.37 – PIV ensemble average fields from the $j_l = 3.09 \cdot 10^{-2}$ m/s experiments around the Taylor bubble bottom. First row: Contour plot of the turbulent kinetic energy $k(r, z)$; Second row: Contour plot of the liquid Reynolds stresses $\langle v_l' w_l'(r, z) \rangle$.

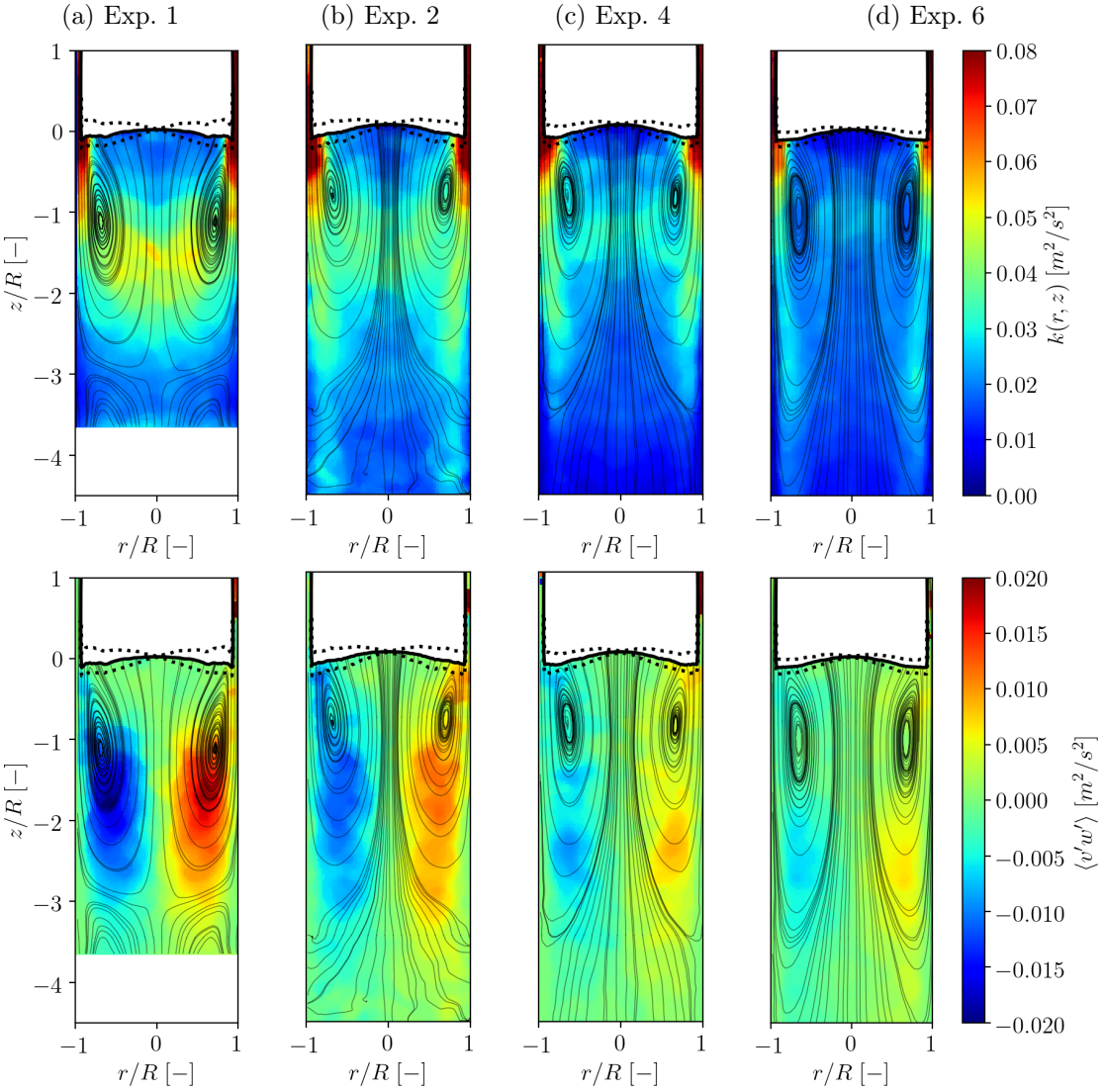

Source - Developed by the author.

Figure 6.38 – PIV ensemble average fields from the $j_l = 21.64 \cdot 10^{-2}$ m/s experiments around the Taylor bubble bottom. First row: Contour plot of the r.m.s. values of the radial velocity component fluctuations $v'_{l,rms}(r,z)$; Second row: Contour plot of the r.m.s. values of the axial velocity component fluctuations $w'_{l,rms}(r,z)$;

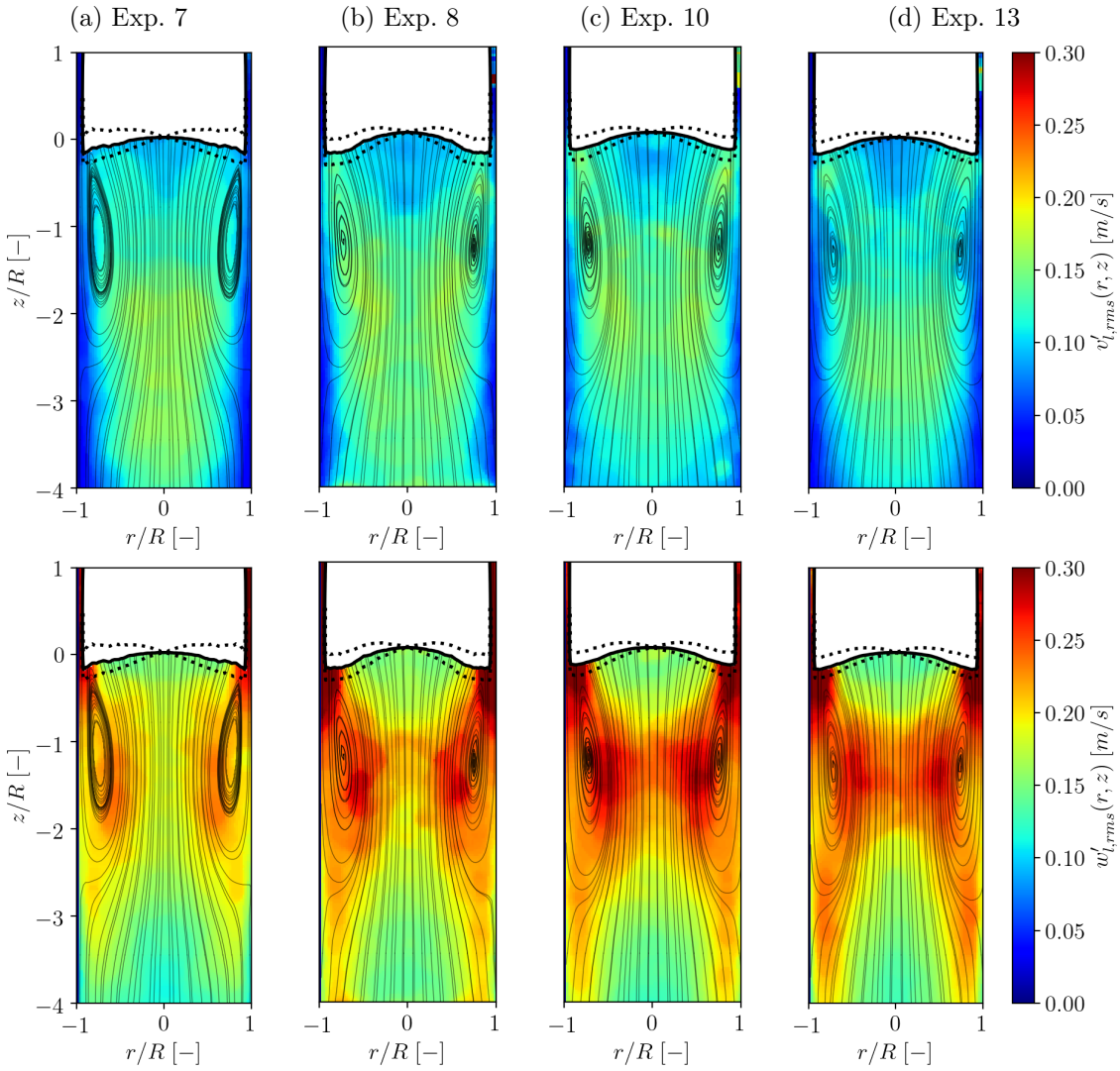

Source - Developed by the author.

Figure 6.39 – PIV ensemble average fields from the $j_l = 21.64 \cdot 10^{-2}$ m/s experiments around the Taylor bubble bottom. First row: Contour plot of the turbulent kinetic energy $k(r, z)$; Second row: Contour plot of the liquid Reynolds stresses $\langle v_l' w_l'(r, z) \rangle$.

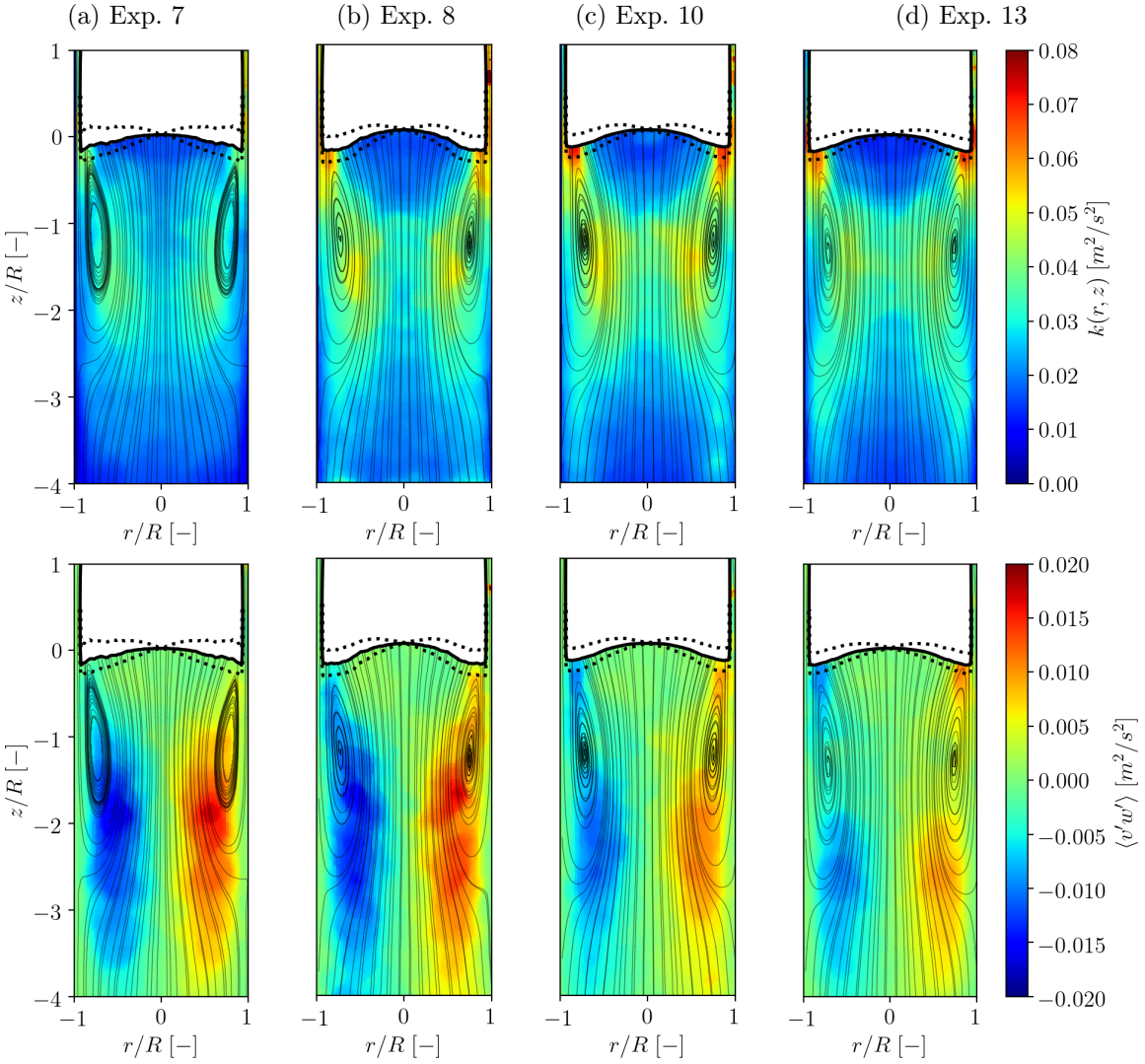

Source - Developed by the author.

6.3 CONCLUSIONS

In order to better comprehend the interactions between the small dispersed and Taylor bubbles in real slug flow, the experimental apparatus and measurement techniques developed and described in Chapters 3 and 5, were used to investigate those interactions in a "manufactured" slug flow.

To investigate the effect of the dispersed bubbles on the flow structure around a single Taylor bubble, the flow was characterized through the Laser Diode Photocell (LDP), high-speed camera imaging, and PIV techniques. The results of the LPD and high-speed camera imaging technique were capable of measuring the effect of the amount of dispersed bubbles on the background flow, i.e., void fraction $\overline{\langle \alpha_g \rangle}$, on the Taylor bubble terminal rising velocity. Thus, from the results of two different liquid superficial velocities j_l, the experiments revealed that the terminal velocity increases with $\overline{\langle \alpha_g \rangle}$, but not in a linear fashion.

As observed in previous works (PINTO; CAMPOS, 1996; CAMPOS; DE CARVALHO, 1988; TUDOSE; KAWAJI, 1999; ARAÚJO et al., 2013; SHABAN; TAVOULARIS, 2018), the rising velocity is strongly correlated with the eccentric motion of the deforming nose of the Taylor bubbles. Based on those findings, and the relation between the $\overline{\langle \alpha_g \rangle}$ and the Taylor bubble rising velocity, image analysis from high-speed camera footage was used to perform a qualitative and qualitative analysis on the effect dispersed bubbles on the rising movement and the nose shape profile of the Taylor bubbles. It was observed that, for the same j_l, when dispersed bubbles are present, the nose shape oscillation and deformation is enhanced. However, the deformation and oscillation of the Taylor bubble nose do not completely explain the behaviour of U_{tb}.

Some of the experimental conditions were also characterized by the PIV technique, measurements the liquid velocity fields around Taylor bubbles, for different j_l and j_g. These results provide additional insights about the interaction of dispersed and Taylor bubbles and also provide interesting data for CFD model validation.

The PIV results in the nose and wake region of the Taylor bubbles showed that the effect of the dispersed bubbles on flow structure of liquid phase was stronger on the lower j_l, due to lower liquid flow inertia. In both j_l series of experiments, it was observed a reduction on the extent of the region affected by induced flow ahead of the Taylor bubbles as $\overline{\langle \alpha_g \rangle}$ was increased. From the PIV results analysis, this reduction is due to the additional dissipative mechanism from the dispersed bubbles.

The flow structure at the wake region of Taylor bubbles is strongly modified by the presence of the dispersed bubbles and, as expected, its influence is stronger on the

lower liquid superficial velocity j_l set of experiments. From the presented results, in both j_l flow conditions, it was observed that the wake length, located behind the Taylor bubble, increased with the gas volume fraction $\overline{\langle \alpha_g \rangle}$ of the background bubbly flow. This modification suggests that the length of the region of influence of the Taylor bubble on the flow field behind depends on the amount of dispersed bubbles on the flow.

From the measurement techniques developed, it was also possible to analyze the turbulent structure of the flow. The analysis of the turbulent structure around the Taylor bubble nose revealed peaks of turbulent intensity near the nose centerline, which are a direct effect of the nose oscillation and deformation observed in the high-speed camera footages. According to the turbulent flow statistics at the wake region of the Taylor bubbles the turbulent intensity is first enhanced with the addition of dispersed bubbles in the flow, for lower $\overline{\langle \alpha_g \rangle}$ and then suppressed with cases for higher values of $\overline{\langle \alpha_g \rangle}$. This is due to the effect of the intense Bubble Induced Turbulence (BIT) which results from the strong relative motion of dispersed bubbles. These small bubbles are ejected from the liquid film around Taylor bubbles and then rise due to buoyancy. However, at a larger concentration of dispersed bubbles, this motion is reduced and so is the turbulence at the wake region. This phenomenon can be observed in Videos 10 and 11 of the supplementary material given in Appendix B.

Results hereby presented, besides a detailed analysis motion and the flow structure of the Taylor bubbles, provide experimental data that can be used for the implementation and validation of multidimensional CFD models for flows with different interface length scales.

Chapter 7

Numerical Implementation of a Two-Phase Gas-Liquid Model with different Interface Length Scales

Parts of the present chapter are in preparation to the International Journal of Multiphase Flows as:
DE CERQUEIRA R. F.L., EVRARD D., DENNER F. and VAN WACHEM, B.G.M, PALADINO E. E. Multiscale modeling and validation of slug flow with small dispersed bubbles.

ABSTRACT

This chapter presents the development and implementation of a multiscale three-dimensional CFD model for the simulation of two-phase gas-liquid flows with different interface length scales, with focus on slug pattern with experimental validation. The model is based on the coupling of the Volume-of-Fluid (VOF) method, used to model large-scale interface dynamics, and the Discrete Bubble Model (DBM) for modeling the small-scale bubbles. A validation study is conducted independently for the VOF method and DBM, by comparing the numerical results with experimental data found in the literature, showing a good agreement. The coupled VOF-DBM model is used to study a liquid-gas two-phase flow with different interface length scales, where large Taylor bubbles and small dispersed bubbles are present. The results show that the presence of the small dispersed bubbles

alters the flow structure around the Taylor bubble, increase the terminal velocity of the Taylor bubble and affects the flow structure in the wake region, which is directly related to heat and mass transfer rates in slug flow.

7.1 INTRODUCTION

Gas-liquid two-phase flows present different complex phase morphologies in industrial flows and nature. These phase arrangements are, in various situations, characterized by the presence of a large range of interface scales. In pipe flows, these phase arrangements are characterized by well-established flow patterns. Slug flows are examples of two-phase flow patterns with diverse interface length scales, where large Taylor bubbles, the characteristic interface length scale of which is of the order of duct diameter, flow together with small dispersed bubbles.

Computational Fluid Dynamics (CFD) is an important tool for multiphase flow analysis, since it allows a detailed investigation of the physical mechanisms that define these complex structures. The modeling of flows with different interface length scales is challenging as most models are developed for flows with large or small scale interfaces. Typically, models for flows with large interfaces are based on the capturing or tracking of the interface position and motion, using methods such as Volume-of-Fluid (VOF) methods (HIRT; NICHOLS, 1981; SCARDOVELLI; ZALESKI, 1999), front tracking (UNVERDI; TRYGGVASON, 1992), level-set methods (OSHER; SETHIAN, 1988) or two-fluid methods (e.g.,Lakehal et al. (2002)). These approaches generally assume that the gas-liquid interface is well resolved and the computational mesh size is much smaller than the interface length scale. Thus, its application for cases where interface length scales are much smaller than the domain scale or mesh size is not feasible with the computational power available today, at least for industrial applications. Hence, flows involving bubbles or droplets with size similar to or smaller than the mesh spacing, i.e. dispersed phases, are usually modeled through some averaging process in an Eulerian frame (WALLIS, 1969; ISHII; HIBIKI, 2011) or through Lagrangian particle tracking.

From the point of view of numerical modeling and associated computational cost, the different interface length scales can be characterized based on the ratio of the physical interface length scale and the computational mesh spacing. Thus, an interface is said to have a large scale when the model is able to capture its shape and position with a sufficiently resolved mesh, such as a Taylor bubble rising in a vertical duct. When this is not the case, the interface is said to have a small scale, for instance, in a bubbly flow pattern. However, in several realistic two-phase flows the gas and liquid phases are spatially

distributed with different interface length scales in the same domain. This is the case of the slug flow pattern which is the focus of this study, but other examples such as annular flow in ducts, where liquid phase morphology comprises a continuous film (large interface) and droplets, or atomizing sprays (EVRARD et al., 2019), can be encountered.

In recent years, attempts at modeling two-phase flows with different interface length scales by coupling numerical models suitable for modeling large-scale and small scale interfaces, using an Eulerian-Eulerian framework (i.e., all phases resolved in an Eulerian frame), have been made. Through the use of this approach, Cerne et al. (2001), (YAN; CHE, 2010) and Wardle and Weller (2013) coupled the Two-Fluid-Model (TFM) with the Volume-of-Fluid (VOF) method, while (ŠTRUBELJ; TISELJ, 2011) developed a unified framework coupling the Level-Set method (LS) with the TFM. An alternative is the modification of the original TFM through an additional interfacial compressive force, which enables the standard model to distinguish the different interfacial scales, such as the GENTOP model proposed by Hänsch et al. (2012). However, these approaches require the use of several user-defined parameters and empirical closure models to distinguish the different interfacial lengths. This dependency on empirical models and constants makes the generalization of such models difficult, because a different set of closure parameters may be necessary for each application to model the flow accurately.

An alternative solution, when interfaces of different scales are present in the fluid domain, is the coupling of a large-scale interface model with a Lagrangian tracking for the dispersed phase, which is treated as particles. This approach has been extensively applied for the study of the primary breakup in liquid sprays. Interface tracking or capturing methods are used to model well resolved interface structures, such as the liquid jet issuing from a nozzle, and Lagrangian particle tracking is used to model small underresolved flow structures, i.e. the atomized droplets. To this end, small droplets are identified and transferred from the fully resolved representation to a Lagrangian particle tracking framework when their resolution on the Eulerian mesh is not satifactory anymore, and vice versa (HERRMANN, 2010; EVRARD et al., 2019).

For the case of flows with bubbles, the combination of interface capturing and Lagrangian tracking of dispersed particles have been mostly used for the study of bubbles flowing in solid-liquid slurries (LI et al., 1999; LIU; LUO, 2018; PENG et al., 2020), tracking the solid particles in a Lagrangian frame of reference. The Lagrangian tracking of dispersed particles allows for the inclusion of more detailed physics of the particle motion and a poly-disperse particulate phase can be easily incorporated into the model in an inexpensive way (when compared with the solution in an Eulerian frame, where a set of transport equations must be solved for each size group). Recently, Hua (2015) proposed a

numerical model for the simulation of multiple scale interfaces based on the coupling of the VOF and the Lagrangian particle tracking methods. The model was used to simulate a large bubble flowing in a 2D channel in the presence of suspended micro-bubbles. It was implemented in a commercial package considering "hard sphere" collisions among the dispersed bubbles (i.e., collisions are considered to be instantaneous and binary) and no interaction is considered between the small dispersed bubbles and the large resolved interfaces.

In this chapter, a three-dimensional CFD model for gas-liquid two-phase flow with different interface length scales is proposed, based on the coupling of the VOF method and the Discrete Bubble Model (DBM) (DARMANA et al., 2005). The model incorporates a consistent physical approach for interactions among dispersed bubbles and bubble-wall collisions, considering a soft-sphere model. For the interaction between dispersed bubbles and large, resolved interfaces, it is proposed a new model that accounts for the numerical challenges presented by the implicit gas-liquid interface representation in the VOF method, which is validated with an experiment proposed by (SATO et al., 2011). The VOF model is validated with experimental results from (NOGUEIRA et al., 2006b) and (NOGUEIRA et al., 2006a) for the laminar flow around Taylor bubbles and the DBM model is validated with experiments for bubbly flow in viscous fluids from (KASHINSKY; TIMKIN, 1999). The proposed model is subsequently applied to study the flow structure around Taylor bubbles rising in a bubbly flow stream, and then analyze the interactions among these bubbles with different interface length scales.

This chapter is organized into five sections. Section 7.2 describes the two models used in the multiscale framework, detailing the coupling strategy used in coupling the VOF and the DBM frameworks. Section 7.3 details the computational details regarding the simulations performed in the present work. Section 7.4 first presents a numerical validation of the VOF and DBM frameworks and, secondly, uses the proposed multiscale model to perform a computational study of a two-phase flow with different interface length scales. Finally, Section 7.5 summarizes the main conclusions of this chapter.

7.2 NUMERICAL FRAMEWORK

The multiscale model proposed is based on the coupling of the Volume-OF-Fluid (VOF) method for the capturing of the large scale interfaces and the Discrete Bubble Method (DBM) for the Lagrangian tracking of dispersed bubbles. In this section, the numerical methods are discussed, presenting the governing equations of the two methods and the adopted coupling strategy. A fully-coupled pressure-based algorithm with a second-

order finite-volume discretization (DENNER et al., 2020) is used as the basis for the proposed multiscale model.

7.2.1 Large Scale Interface modeling

The Volume-of-Fluid (VOF) method (HIRT; NICHOLS, 1981) is used to model the large-scale interface, which are adequately resolved by the computational mesh. The VOF method uses a colour function γ to distinguish the different phases in the computational domain. The value of the colour function γ is defined in each cell as,

$$\gamma\left(x,t\right)=\begin{cases}1 & \text{liquid}\\ \\ 0 & \text{gas (large scale interface)}\end{cases} \tag{7.1}$$

Through this definition, a cell for which $0<\gamma<1$ contains an interface. The colour function γ is advected by the transport equation as,

$$\frac{\partial\gamma}{\partial t}+\nabla\cdot\left(\boldsymbol{u}\,\gamma\right)+\nabla\cdot\left[\gamma\left(1-\gamma\right)\boldsymbol{u}_{c}\right]=0 \tag{7.2}$$

The third term on the left-hand side of Eq. (7.2) is used to compress the gas-liquid interface where the term $\gamma\left(1-\gamma\right)$ ensures that the interfacial compressive term only acts at the interfacial region. The compressive velocity, $\boldsymbol{u}_{c}$, is proportional to the unit normal vector $\boldsymbol{n}$,

$$\boldsymbol{u}_{c}=C_{\gamma}\left|\boldsymbol{u}_{f}\right|\boldsymbol{n} \tag{7.3}$$

where $\boldsymbol{u}_{f}$ is the velocity in the control volume's face and C_{γ} is a constant that controls the strength of the artificial compressive force, which was defined as $C_{\gamma}=1.0$ from numerical tests. Details regarding this approach can be found in Rusche (2002). The colour function γ in Eq. (7.2) is advected through Van Leer's TVD (Total Variation Diminished) scheme (VAN LEER, 1974), while the transient term is discretized using a Crank-Nicholson scheme. The combination of these high order schemes in space and time with the use of the compressive velocity resulted in an adequate advection of the interface, without numerical diffusion.

The continuity and momentum equations for the liquid phase, considering the inclusion of the interfacial tension and DBM coupling forces, are given by,

$$\frac{\partial(\alpha_{l}\rho)}{\partial t}+\boldsymbol{\nabla}\cdot\left(\alpha_{l}\rho\boldsymbol{u}\right)=0 \tag{7.4}$$

$$\frac{\partial(\alpha_{l}\rho\boldsymbol{u})}{\partial t}+\boldsymbol{\nabla}\cdot\left(\alpha_{l}\rho\boldsymbol{u}\boldsymbol{u}\right)=-\alpha_{l}\boldsymbol{\nabla}P+\boldsymbol{\nabla}\cdot\left(\alpha_{l}\boldsymbol{T}\right)+\rho\alpha_{l}\boldsymbol{g}+\boldsymbol{f}_{\sigma}+\boldsymbol{f}_{DBM} \tag{7.5}$$

where p is the pressure, $\boldsymbol{g}$ is the gravitational acceleration and $f_{\sigma,i}$ is the volumetric source term due to surface tension. In Eqs. (7.4) and (7.5) α_l represents the liquid volume fraction, which takes into account the volume occupied by dispersed bubbles in the liquid phase. The momentum coupling occurs through f_{DBM}, which represents the momentum transfer from the dispersed phase to the continuous mixture. However, as will be discussed later, the dispersed bubbles are not allowed in the region occupied by a continuous gas phase. Therefore, this momentum exchange is only given between liquid and dispersed phase. The stress tensor $\boldsymbol{T}$ for an incompressible Newtonian fluid is defined as,

$$\boldsymbol{T} = \mu \left[\Big((\nabla \boldsymbol{u}) + (\nabla \boldsymbol{u})^T \Big) - \frac{2}{3} \boldsymbol{I} (\nabla \cdot \boldsymbol{u}) \right] \tag{7.6}$$

The density ρ and viscosity μ are calculated through the colour function γ value as,

$$\rho = \rho_l (1 - \gamma) + \rho_g \gamma \tag{7.7}$$

$$\mu = \mu_l (1 - \gamma) + \mu_g \gamma \tag{7.8}$$

where the subscript g denotes the gas phase and l the liquid phase.

In Eq. (7.5), the surface tension force $\boldsymbol{f}_\sigma$ is modeled through the CSF method (BRACKBILL et al., 1992) and is defined as,

$$\boldsymbol{f}_\sigma = \sigma \kappa \, \nabla \gamma \tag{7.9}$$

where σ is the surface tension coefficient and κ represents the interface curvature, defined as,

$$\kappa = \nabla \cdot \boldsymbol{n} \tag{7.10}$$

and the $\boldsymbol{n}$ is the interface vector normal is calculated as,

$$\boldsymbol{n} = \frac{\nabla \gamma}{|\nabla \gamma|} \tag{7.11}$$

Additionally, in Eqs. (7.9) – (7.11), Laplacian smoothing is used to mollify the colour function fields, reducing the occurrence of unrealistic velocity fields, also known as parasitic currents, around the sharp gas-liquid interface.

The term $\boldsymbol{f}_{DBM}$ in Eq. (7.5) is a volumetric force generated by the presence of dispersed bubble in a cell volume and its definition is described in the following paragraphs.

7.2.2 Small Scale Interface modeling

In the DBM, the motion of each individual bubble is governed by Newton's second law, which reads as

$$m_{b,i} \frac{d \boldsymbol{u}_{b,i}}{dt} = \boldsymbol{f}^b_{b,i} + \boldsymbol{f}^h_{b,i} + \sum_{j=1} \boldsymbol{f}^c_{b,ij} \tag{7.12}$$

where i is the bubble number, $\boldsymbol{u}_{b,i}$ is the instantaneous velocity of the bubble. In Eq. (7.12), the right hand side of the equation represents the external forces acting on the dispersed bubble. Those can be divided into the contributions due to buoyancy ($\boldsymbol{f}^b_{b,i}$), to the interaction with the fluid ($\boldsymbol{f}^h_{b,i}$) and to collisions with the surrounding j-th particles ($\boldsymbol{f}^c_{b,ij}$).

The combined gravity and buoyancy force term is defined as:

$$\boldsymbol{f}^b_{b,i} = V_{b,i}\,\boldsymbol{g}\,(\rho_b - \rho_l) \tag{7.13}$$

where $V_{b,i}$ ($= \pi {d_{b,i}}^3/6$) is the volume of the dispersed bubble with a diameter $d_{b,i}$.

7.2.2.1 Hydrodynamic forces

In the present work, the net hydrodynamic forces from the continuous fluid-bubble interaction considers the forces due to drag, virtual mass, transverse lift, pressure gradient and wall lubrication force, given as

$$\begin{aligned}\boldsymbol{f}^h_{b,i} =& \frac{3}{4} V_{b,i}\,\rho_l C_{D,i}\left(\boldsymbol{u} - \boldsymbol{u}_{b,i}\right)\left|\boldsymbol{u} - \boldsymbol{u}_{b,i}\right| \\ &+ V_{b,i}\,\rho_l C_{VM,i}\left(\frac{D\boldsymbol{u}}{Dt} - \frac{d\boldsymbol{u}_{b,i}}{dt}\right) \\ &+ V_{b,i}\,\rho_l C_{L,i}\left[\left(\boldsymbol{u} - \boldsymbol{u}_{b,i}\right) \times \left(\nabla \times \boldsymbol{u}\right)\right] \\ &+ V_{b,i}\,\rho_l \frac{D\boldsymbol{u}}{Dt} \\ &+ \boldsymbol{f}^{wl}_{b,i}\end{aligned} \tag{7.14}$$

where $\boldsymbol{u}$ ($= [u, v, w]$) is the undisturbed continuous fluid velocity at the dispersed bubble position. The force $\boldsymbol{f}^{wl}_{b,i}$ represents the wall lubrication force, which arises from the liquid film drainage when a bubble is moving towards a wall.

The coefficients C_D, C_{VM} and C_L correspond to drag, virtual mass and lift force coefficients, respectively. The drag force coefficient C_D is calculated by the correlation of Tomiyama et al. (1998) for contaminated systems,

$$C_D = \max\left[\frac{24}{Re_b}\left(1.0 + 0.15{Re_b}^{0.687}\right), \frac{8}{3}\frac{Eo}{Eo+4}\right] \tag{7.15}$$

where Re_b is the Reynolds number of the dispersed bubble,

$$Re_B = \frac{\rho_l \left|\boldsymbol{u}_{B,i} - \boldsymbol{u}\right| d_{b,i}}{\mu_L} \tag{7.16}$$

and Eo is its Eötvös number,

$$Eo = \frac{\left(\rho_l - \rho_g\right)\,|\boldsymbol{g}|\,{d_{b,i}}^2}{\sigma} \tag{7.17}$$

A constant virtual mass coefficient $C_{VM} = 0.5$ is considered (AUTON, 1984). The correlation of Tomiyama et al. (2002) is used to calculate the transverse lift C_L,

$$C_L = \begin{cases} \min\left[0.288\tanh(0.121Re_b), f(Eo_\perp)\right], & Eo_\perp \leq 4 \\ f(Eo_\perp), & Eo_\perp > 4 \end{cases} \tag{7.18}$$

and

$$f(Eo_\perp) = 0.00105Eo_\perp^3 - 0.0204Eo_\perp^2 + 0.474 \tag{7.19}$$

where $Eo_\perp$ is the Eötvös number is based on the assumption that the dispersed bubble is an oblate spheroid with its major axis equals to $d_{\perp b,i}$. Here, $d_{\perp b,i}$ was calculated through the Wellek et al. (1966) correlation, with

$$d_{\perp b,i} = d_{b,i}\sqrt[3]{1.0 + 0.163Eo^{0.757}} \tag{7.20}$$

The wall lubrication force $\boldsymbol{f}_{b,i}^{wl}$, is modeled as

$$\boldsymbol{f}_{b,i}^{wl} = \frac{V_{b,i}\rho_l}{d_{b,i}} C_{wl} \left|\boldsymbol{u}_{B,i} - \boldsymbol{u}\right|^2 \boldsymbol{n}_w \tag{7.21}$$

where $\boldsymbol{n}_w$ represents the unit normal vector pointing away from the duct wall and C_{wl} is the wall lubrication coefficient given by the Tomiyama (1998) correlation.

7.2.2.2 Bubble collision model

The soft-sphere model of Peña-Monferrer et al. (2018) is used in the present work to approximate bubble collisions. In this model, the stiffness of the bubbles is determined as a function of surface area increase due to bubble deformation. From the assumption that the bubble conserves its volume during a collision, it is possible to admit that the surface energy (ΔW_σ) increase due to deformation can be calculated as:

$$\Delta W_\sigma = \sigma\left(S_t - S_{t-\Delta t}\right) \tag{7.22}$$

where σ is the surface tension coefficient, and S_t and $S_{t-\Delta t}$ are the surface area during and before the collision takes place. Under the assumption that the bubble has a spherical shape and it deforms into an oblate spheroid during collision, Eq. (7.22) can be rewritten as,

$$\Delta W_\sigma = \sigma\left(S_{oblate} - S_{sphere}\right) \tag{7.23}$$

where S_{sphere} is the surface area of a sphere and S_{oblate} is the surface area of an oblate spheroid. Assuming that a deformed bubble behaves like a Hookean spring when the

bubble deformation is small and ellipsoidal (SATO et al., 2011), the following relation can be deduced,

$$\Delta W_\sigma = \frac{1}{2} K_i \delta ij^2 \tag{7.24}$$

where δij is the normal overlap between two bubbles i and j. Thus, from Eqs. (7.23) and (7.24), the bubble stiffness K_i of can be calculated as,

$$K_i = \frac{2\sigma \left(S_{oblate} - S_{sphere} \right)}{{\delta_{ij}}^2} \tag{7.25}$$

As shown in Fig. 7.1, assuming that once a bubble collides its shape deforms to an oblate spheroid with its minor axis along the collision direction, the minor and major axes of the deformed oblate spheroid are defined as

$$a_i = r_i - \delta_{ij} \tag{7.26}$$

and

$$b_i = \sqrt{{r_i}^3 / a_i} \tag{7.27}$$

respectively, where Eq. (7.26) arises from the bubble-bubble overlap and Eq. (7.27) from the sphere to oblate spheroid volume conservation. Therefore, from this simplified mass-spring model, bubble-bubble collisions can be approximated by an equivalent spring system, with the bubble collisional force $\boldsymbol{f}^c_{b,ij}$ resulting in

$$\boldsymbol{f}^c_{b,ij} = \frac{K_i K_j}{K_i + K_j} \delta_{ij} \boldsymbol{n}_{ij} \tag{7.28}$$

where $\boldsymbol{n}_{ij}$ is the unit vector between the two colliding bubbles. In the case of a bubble-wall collision, as shown on the right of Fig. 7.1, the bubble collisional force results in,

$$\boldsymbol{f}^c_{b,iw} = K_i \delta_{iw} \boldsymbol{n}_{iw} \tag{7.29}$$

where δ_{iw} is the overlap between the bubble and the wall, and $\boldsymbol{n}_{ij}$ is the unit vector towards the wall.

7.2.2.3 Eulerian-Lagrangian framework interpolation

In the equations presented in the previous section, the bubble motion in the Lagrangian formulation involves tracking the properties of individual dispersed bubbles and the fluid properties at the centroids of the bubbles. Therefore, it is necessary to interpolate values that are stored at the cell centres of the fluid Eulerian mesh to the fluid particles and vice versa. In the proposed multiscale model, this is achieved by the use of an equidistant Cartesian particle mesh that completely overlaps the fluid Eulerian mesh employed for

Figure 7.1 – Illustration of (left) a bubble-bubble collision and (right) a bubble-wall collision, including the main quantities related to the soft-sphere model.

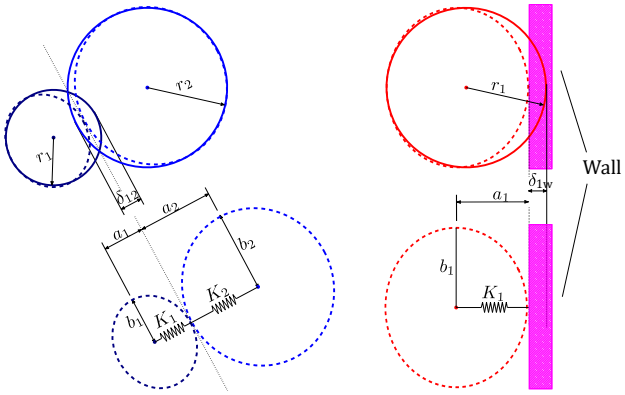

Source - Developed by the author.

the flow calculation of the continuous phases and the large scale interfaces. This "background" particle mesh, schematically illustrated in Fig. 7.2, acts as a framework for the calculation of the position and velocities of the Lagrangian bubbles, and also facilitates the interpolation of interfacial forces from and to the fluid Eulerian mesh. Additionally, since the Lagrangian bubbles always belong to a single particle mesh cell, they can easily be located when bubble-bubble interactions need to be computed.

Figure 7.2 – Schematic representation of the equidistant Cartesian particle mesh (red) and the fluid Eulerian mesh employed for the flow calculations (blue).

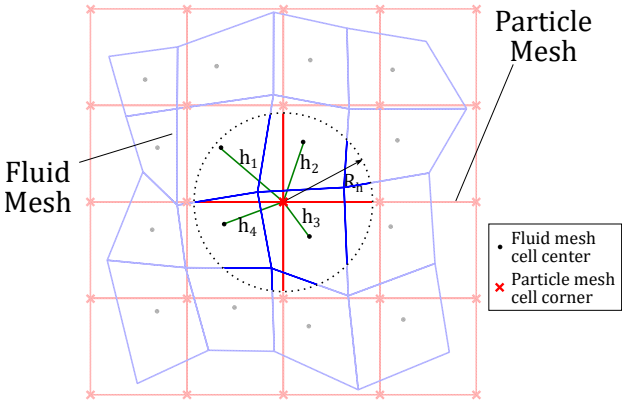

Source - Adapted from Wachem et al. (2002).

In the following paragraphs, the Eulerian-Lagrangian framework interpolation is summarized following the description found in MultiFlow's manual and theory guide (WACHEM et al., 2002).

Interpolation from the fluid mesh to the particle mesh

By using an auxiliary particle mesh, as depicted in Fig. 7.2, the cell-centered variables from the Eulerian mesh are interpolated to the corners of the particle mesh by an inverse distance weighting, using the Eulerian mesh cells neighboring the corners of the particle mesh cell. For a given variable ϕ the value in the particle cell corner (PCC) is given by,

$$\phi_{\mathrm{PCC}} = \sum_{j=1}^{NB} W_j \phi_j \tag{7.30}$$

where the weighting coefficients W_i are calculated by

$$W_j = \frac{h_j^{-2}}{\sum_{k=1}^{NB} h_k^{-2}} \tag{7.31}$$

In Eqs. (7.30) and (7.31), NB represents the interpolations points of the fluid mesh that lies within a distance R_h from the particle cell corner position and h_j is the distance from the point to the interpolation location,

$$h_j = \sqrt{\left(x_{PCC} - x_j\right)^2 + \left(y_{PCC} - y_j\right)^2 + \left(z_{PCC} - z_j\right)^2} \tag{7.32}$$

where $\boldsymbol{x}_{PCC}$ is the particle cell corner position and $\boldsymbol{x}_j$ are the coordinates of the j-th interpolation location.

This interpolation procedure is used to interpolate the liquid phase velocity $\boldsymbol{u}$ to the particle mesh, which later is used to calculate the interfacial forces on Lagrangian bubbles.

Interpolation from the particle mesh to the fluid mesh

The variables interpolated from the particle mesh to the fluid mesh, such as the volume fraction of dispersed bubbles and the DBM-liquid phase momentum coupling term $\boldsymbol{f}_{DBM}$ present in Eq. (7.5), are computed as described in the next paragraphs.

During run-time, all fluid mesh cells occupying a part of the volume of a particle mesh cell, and their relative contributions to the volume are determined. Thus, per particle mesh cell, the following relation must hold,

$$\sum_{n=1}^{\text{fluid cells}} V_{r,n} = 1, \tag{7.33}$$

where $V_{r,n}$ is the relative volume of the particle mesh cell occupied by underlying fluid mesh cell n. When the relative volume is multiplied with the volume of a particle mesh

cell, the actual volume is obtained. A similar statement can be made for any fluid cell; as it is completely covered with particle mesh cells,

$$\sum_{1=1}^{\text{particle mesh cells}} V_{r,i}(l)V_{PC}(l) = V_i, \tag{7.34}$$

where $V_{r,i}(l)$ represents the relative volume of fluid mesh cell i occupying particle mesh cell l and V_{PC} represents the particle mesh cell volume. As the particle mesh is Cartesian and equidistant, V_{PC} is a constant throughout the domain. A schematic illustration of the particle mesh to the fluid mesh interpolation is given in Fig. 7.3

Figure 7.3 – The particle mesh properties are interpolated to the underlying fluid cells using the relative volumes (filled). In this example, the highlighted particle mesh cells are contributing to the interpolation process for a given fluid mesh cell, where thee contribution weight of each different particle mesh cell is proportional to the filled area.

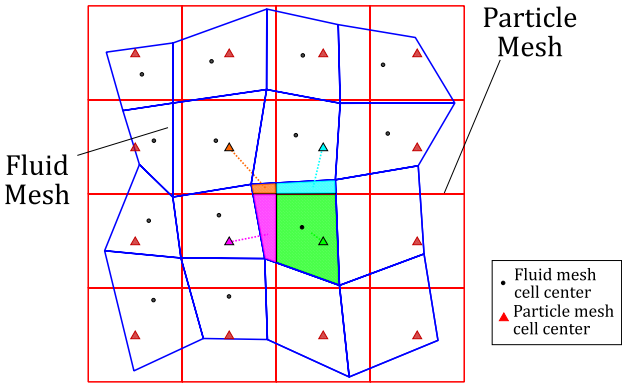

Source - Adapted from Wachem et al. (2002).

There are two types of interpolation, (1) the interpolation of scalar, here defined as a generic variable ϕ, and (2) interpolation of a force or a flux, represented by the generic variable Φ.

Considering the first case, the value of a variable in a fluid cell i determined from its particle mesh cell values becomes,

$$\phi_i = \frac{1}{V_i} \sum_{l=1}^{\text{particle mesh cells}} V_{r,i}(l)V_{PC}(l)\phi_{PC}(l) \tag{7.35}$$

where V_i is the volume of fluid mesh cell i and ϕ_{PC} is the particle mesh cell value. Hence, it should be noted that the units of ϕ_{PC} in the Lagrangian framework are the same as in of ϕ in the Eulerian framework. This is the case of the liquid phase volume fraction α_l.

Now, considering the second case, a flux or a force, denoted as Φ_{PC} in the Lagrangian frame, and as Φ in the Eulerian framework, should now be expressed on a per

volume basis. This is done through by a particle cell volume averaging procedure as,

$$\begin{aligned}\Phi_i &= \frac{1}{V_i} \sum_{l=1}^{\text{particle mesh cells}} V_{r,i}(l) V_{PC}(l) \frac{\Phi_{PC}(l)}{V_{PC}(l)} \\ &= \frac{1}{V_i} \sum_{1=1}^{\text{particle mesh cells}} V_{r,i}(l) \Phi_{PC}(l)\end{aligned} \tag{7.36}$$

This is the case of the bubble hydrodynamic forces $\boldsymbol{f}_{b,i}^{h}$ which are interpolated to the Eulerian framework as $\boldsymbol{f}_{DBM}$, the source term in the liquid momentum equations (Eq. (7.5)).

Interpolation from the particle mesh cell to the particle element

Once a variable is interpolated from the fluid cell to the particle cell, the next step is to interpolate this information to the individual bubbles, the positions of which are known on the particle mesh. To this end, a trilinear interpolation is employed to calculate the values at a given point in the space. In trilinear interpolation, the properties of the eight corners of an interpolation box are weighted onto the bubble location $\boldsymbol{x}_b$ to obtain the interpolated value. For a generic variable ϕ, the interpolated value is given by,

$$\phi_{b,i} = \sum_{l=1}^{8} W_l \Phi_{PC,N}, \qquad W_l = \frac{1/d_l^2}{\sum_{l=1}^{8} 1/d_l^2} \tag{7.37}$$

where $\Phi_{PC,N}$ are the nodal values in the particle mesh, previously interpolated from the Eulerian grid, and d_l^2 are the respective distances between nodes and bubbles centers.

A schematic representation of the interpolation from the particle cell to the particle element is presented in Fig. 7.4.

This interpolation is used, for instance, to calculate the liquid phase velocity values $\boldsymbol{u}$ from the particle mesh to the particle element, since this information is necessary to model the hydrodynamic forces as seen in Eq. 7.14.

Interpolation from the particle element to the particle mesh cell

When a variable is interpolated from a single bubble to the particle mesh, it should be taken into consideration that a bubble does not necessarily lie solely within one particle mesh cell. This situation is represented in Fig. 7.5, where a bubble is lying in multiple particle mesh cells. When a variable is interpolated from an individual bubble to the particle mesh, it is weighted by the volume of the bubble lying within each particle mesh cell. Hence,

$$\phi_{\mathrm{PC}}(j) = \sum_{i=1}^{\text{N particles}} \frac{\mathrm{V_{P,i}}(j)}{V_{b,i}} \phi_{\mathrm{B},i}, \tag{7.38}$$

Figure 7.4 – A two-dimensional Cartesian particle cell with corners $(x_{i+[0,1]}, y_{i+[0,1]})$ and a particle located at (x_b, y_b).

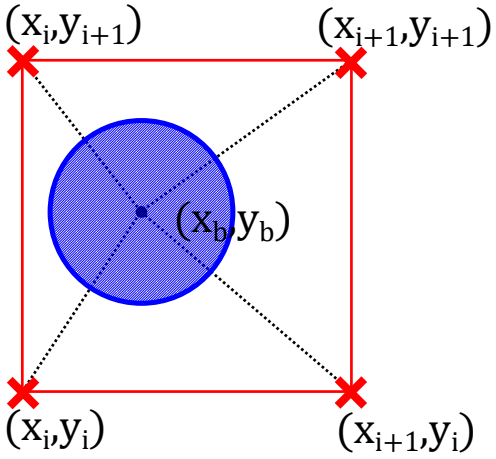

Source - Adapted from Wachem et al. (2002).

where $\phi_{\mathrm{PC}}(j)$ represents the value of ϕ in the particle mesh cell j center, $\mathrm{V_{P,i}}(j)$ represents the volume of a bubble i lying in a particle mesh j, $V_{b,i}$ is the volume of the bubble i, and $\phi_{\mathrm{B},i}$ represents the value of ϕ at bubble i.

Figure 7.5 – Schematic representation of a bubble lying on multiple particle cells and the weighted volume contribution in each particle mesh cell center.

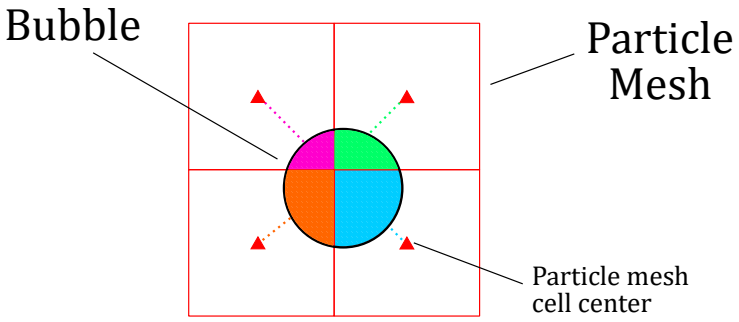

Source - Adapted from Wachem et al. (2002).

For the liquid-phase volume fraction α_l calculation, first the value is calculated on the each particle mesh cell. This is done by looping over all the bubbles lying in the particle mesh cell and summing up the volume of the bubbles partition lying within the cell boundaries, as depicted by the filled area in Fig. 7.5. Then, the α_l is interpolated to the fluid mesh and its value can be used when solving Eqs. 7.4 and 7.5.

7.2.3 VOF-DBM Coupling Strategy

In order to use the VOF method used to model large scale interfaces in conjunction with the DBM for the small dispersed bubbles, additional steps are necessary to couple

the two methods, as described in the following.

7.2.3.1 Accounting for the large scale interface in the Eulerian-Lagrangian interpolation

As detailed in Section 7.2.3, the DBM employed in the present work uses an auxiliary background mesh to perform interpolations between the Eulerian and the Lagrangian frameworks. However, when interpolating between the two frameworks, the operations presented so far do not account for the presence of a large-scale interface, which is resolved on the Eulerian fluid mesh. When interpolating the from the fluid to the particle mesh, the liquid-phase values are filtered by the colour function, modifying Eq. (7.30) as,

$$\phi_{\mathrm{PCC}} = \sum_{j=1}^{NB} (1 - \gamma_i)\, w_j \phi_j \tag{7.39}$$

which ensures that the interpolated values represent the liquid phase fields. This modification is important to correct the undisturbed liquid-phase velocity seen by the bubbles (Eq. (7.14)) in mesh cells close to the large-scale interface. Additionally, when interpolating field operators, such as $\mathrm{D}\boldsymbol{u}/\mathrm{D}t$ and $\nabla \times \boldsymbol{u}$, these are first evaluated on the Eulerian fluid mesh and then interpolated to the particle mesh.

When interpolating from the particle mesh to the Eulerian fluid mesh in cells that contain a large scale interface ($0 < \gamma < 1$), care must be taken when calculating the liquid phase volume fraction α_l and the DBM-liquid phase coupling term $\boldsymbol{f}_{DBM}$, which may result in conservation inconsistencies when advecting the colour function. In order to avoid this issue, no interpolation is performed in particle mesh cells in which $(1 - \gamma_{\mathrm{PCC}}) < \gamma_{par}$ and, therefore the liquid phase volume fraction remains $\alpha_l = 1.0$ and $\boldsymbol{f}_{DBM} = 0.0$. In the present work, $\gamma_{par} = 0.05$ following preliminary tests, which also showed that this parameter does not have a significant effect on the final result, because the compression term of the VOF advection equation, Eq. (7.2), ensures in a sharp large scale interface.

7.2.3.2 Collisions between dispersed bubbles and a large scale interface

When a small dispersed bubble encounters a large scale interface scale, it can coalesce or a collision may occur, depending on the Weber number based on the relative velocity between the dispersed bubbles and the large interface. For the case under study in this work, according to experimental observations with high speed camera, which results were presented in Chapter 6, only a small number of the dispersed bubbles coalesce with the large Taylor bubble, although collisions are frequent. Therefore, it is necessary to model the collision process between the small dispersed bubbles and the large scale interfaces. The collision model implemented in this work is based on the one presented in Sato et al.

(2011) for the bouncing of a bubble on a free surface and the modification of the collision model proposed by Hua (2015), which considers a restitution coefficient in the direction of the large scale interface normal, maintaining constant the tangential component of the relative velocity constant. The model used in the present work is based on the normal vector of the large scale interface in the vicinity of the dispersed bubbles as well as the local information of the colour function, as schematically illustrated in Fig. 7.6.

Figure 7.6 – Schematic representation of the collision model used in the present work. Left pane: A small dispersed bubble approaches a large scale interface at time instant t, deforming it a following moment in $t + \Delta t$; Middle pane: The equivalent mass-spring model representing the large scale and small bubble deformation; Right pane: Colour function γ distribution of the fluid mesh and the large interface normal vector $\boldsymbol{n}$ which are interpolated to bubble position.

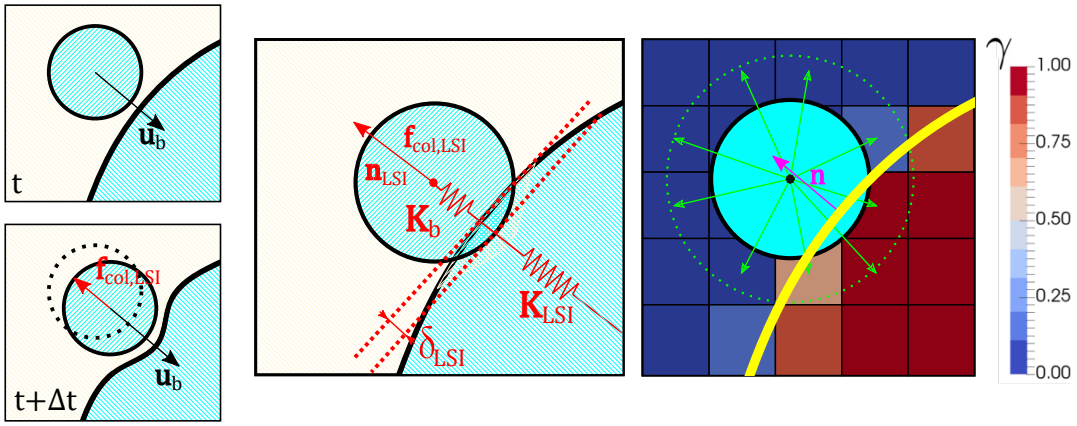

Source - Developed by the author.

According to Sato et al. (2011), as the bubble bounces on a free surface, both the bubble and large scale interface deform. Thus, contrary to the bubble-wall collision described in Section 7.2.2.2, the large scale interface is not rigid, and the collision model should account for its deformation. Furthermore, when colliding with the duct wall, the unit normal vector pointing to the wall is readily available since the wall is a domain boundary, which is not the case in the collision with a large scale interface, where the interface position is implicitly captured by the colour function distribution (Fig. 7.6). Therefore, in the present work, a suitable model is developed to account for the collisions between the large-scale interface and the small dispersed bubbles in the coupled VOF-DBM framework.

For the collision modeling, it is first necessary to make the information of the large scale interface position readily available to the DBM method. This is accomplished by interpolating the γ colour function field, and the large scale interface normal vector $\boldsymbol{n}$ to

the particle mesh and ,subsequently, to the position of the dispersed bubbles, as described in Section 7.2.2.3. According to Sato et al. (2011) and following the bubble collision model discussed in Section 7.2.2.2, the collision can be approximated by a mass-spring system. In this case, as illustrated in the middle pane of Fig. 7.6, the mass-spring system is composed by two springs representing the bubble (K_b) and the large-scale interface deformation (K_{LSI}). Thus, the bubble collisional force $\boldsymbol{f}_{col,LSI}$ can be calculated as,

$$\boldsymbol{f}_{col,LSI} = \frac{K_b K_{LSI}}{K_b + K_{LSI}} \delta_{LSI} \boldsymbol{n}_{LSI} \tag{7.40}$$

where δ_{LSI} represents the thin-liquid film between the small bubble and the large-scale interface and $\boldsymbol{n}_{LSI}$ is the unit vector normal to the large scale interface. In Eq. (7.40), following Sato et al. (2011), the large scale stiffness is approximated as $K_{LSI} = 2.0 \times 1.819\sigma$. Following the collision model presented in the previous section, K_b is calculated by Eq. (7.25), with the overlap between the dispersed bubble and the large-scale interface, which is defined as δ_{LSI}. Despite this assumption, due to the use of an algebraic VOF method, where the interface is not geometrically reconstructed, the δ_{LSI} overlap value, the exact large scale interface position and its normal vector $\boldsymbol{n}_{LSI}$ are not readily available.

For the $\boldsymbol{n}_{LSI}$ vector, fluid mesh interpolated values are used to approximate the large scale interface normal direction $\boldsymbol{n}$, as illustrated in the diagram on the right pane of Fig. 7.6, which shows the colour function distribution and the a approximate normal vector $\boldsymbol{n}$ near a large-scale interface. Since the precise explicit interface position is not given by the employed algebraic VOF method, the overlap δ_{LSI} is approximate through an empirical relation, which describes the overlap between the large scale interface and the bubble by the interpolated colour function γ at a given bubble position. The proposed relation is defined as sigmoid-type function as,

$$\delta_{\mathrm{LSI}} = r_b \left[1.0 + e^{-C_{\mathrm{LSI}}(\gamma - 0.5)} \right]^{-1}, \tag{7.41}$$

where C_{LSI} is a parameter used to define the model sensitivity regarding the approximate interface position. As observed in Eq. (7.41), besides depending on the local colour function γ, the overlap is also a function of the bubble size, where the maximum overlap between the bubble and the large scale interface is $\delta_{LSI} = r_b$ in Eq. (7.41). In order to illustrate the relation proposed by Eq. (7.41), Fig. 7.7 presents schematically the the force magnitude $\left|\boldsymbol{f}_{col,LSI}\right|$ (Eq. (7.40)) for three C_{LSI} values. As observed in Fig. 7.7, the relation is centered around $\gamma = 0.5$ and the slope of the curve increases with increasing C_{LSI} and, therefore, the bubble bounces off the large scale interface. From high speed camera videos of experiments from the previous chapter, it is observed that the small bubbles bounce

smoothly during the collisions. Hence, the value of C_{LSI} is defined as 20, which results in a smooth transition.

Figure 7.7 – Schematic illustration of the force magnitude $\left|\boldsymbol{f}_{col,LSI}\right|$ (Eq. (7.40)) for three different C_{LSI} values.

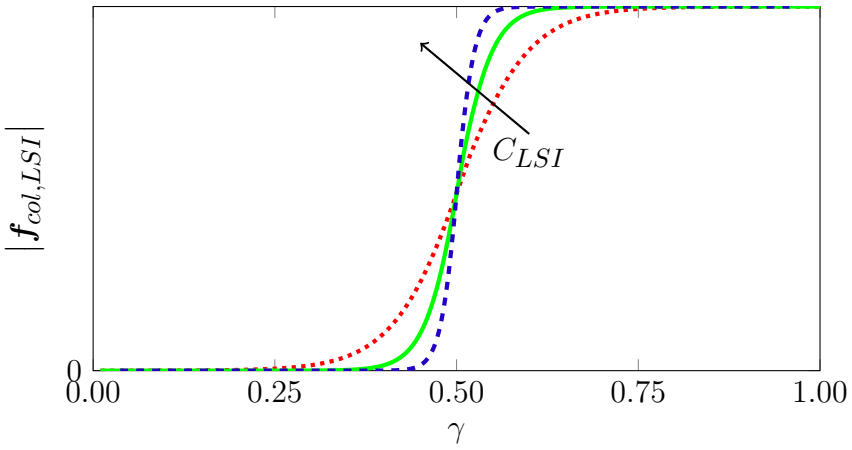

Source - Developed by the author.

In summary, when a dispersed bubble approaches the large scale interface, the normal vector of the large scale interface is interpolated to the bubble position, thus defining the collision direction $\boldsymbol{n}_{\mathrm{LSI}}$. Additionally, the colour function γ from the Eulerian fluid mesh is interpolated to the bubble position, which is then used to calculate the overlap δ_{LSI} trough Eq. (7.41). When δ_{LSI} and $\boldsymbol{n}_{\mathrm{LSI}}$ are known at the position of the bubble, the collision force $\boldsymbol{f}_{col,LSI}$ is computed from Eq. (7.40) and added to collisional force term of Eq. (7.12). In spite of the assumptions in the formulation of this model, in particular for the γ_{par}-threshold, the model captures more of the underlying physics of the phenomenon than previous models. In Hua (2015), for instance, a constant restitution coefficient was used to compute the restitution force of the bubble-interface collision.

7.2.4 Computational implementation considerations

The equations governing the gas-liquid flow resolved on Eulerian fluid mesh, see Section 7.2.1, are discretised using a second-order finite-volume method with a collocated variable arrangement and solved in a single linear system of coupled equations (DENNER; WACHEM, 2014; DENNER et al., 2020). For the small dispersed bubbles, the instantaneous position and velocity vectors are obtained from the integration of the equation of motion in the Lagrangian frame of reference, through a Verlet scheme, where each bubble trajectory is solved sequentially, and collisions are computed at the end of a time-step.

Regarding the time marching procedure, since it is necessary to resolve the motion of the small dispersed bubbles and large scale gas-liquid interfaces, two different time scales are considered. For the large scale interface, as commented by Gopala and van Wachem (2008), in order to maintain a sharp interface while advecting the flow, the fluid time step must be limited to a small Courant Number ($Co = u\Delta t_f/\Delta x$) in the order of $Co = 0.05$, where Δt_f is the fluid time step and Δx = the local mesh spacing. However, since such requirement results in high computational costs, the sub-cycling strategy adopted in Gopala and van Wachem (2008) used here. By using this approach, for a given Courant number, $Co = 0.25$ in the present work, the global mass, from which results in the pressure field, and momentum conservation equations are solved initially, and later the VOF equation is fractionally updated n times, where n represents the number of subcycles pre-defined in the code, which is set as $n = 5$ in the simulations presented here. For the dispersed bubble trajectory, due to the small time scales, a similar sub-cycling approach is adopted when integrating the equations of motion in the DBM. In order that the dispersed bubbles notice the changes in the local flow velocity, a sufficient small DBM time step Δt_b is required. Additionally, to correctly simulate bubble collisions, small time steps Δt_b are required to avoid inaccurate or unstable bubble collisions. Thus, the time step must be smaller than its critical value $\Delta t_{b,crit}$, which is expressed as the natural frequency of equivalent spring-mass system (TSUJI et al., 1993),

$$\Delta t_{b,crit} = 2\pi\sqrt{\frac{m_b}{K}} \tag{7.42}$$

Therefore, at the beginning of each DBM loop, the critical time step $\Delta t_{b,crit}$ was calculated and the the DBM time step defined as $\Delta t_b = 0.1\Delta t_{b,crit}$ in order to correctly compute the bubbles trajectory. As commented earlier, since the fluid time step is usually larger than the DBM time step ($\Delta t_f > \Delta t_b$), a sub-cycling approach to simulate the small dispersed bubbles motion to reduce the total computational cost associated in using small time steps. Thus, after solving the continuous gas and liquid flow velocities in the Eulerian frame, the bubble trajectories were computed in n_{DBM} subcycles,

$$n_{\mathrm{DBM}} = \min\left[100, \mathrm{ceil}\left(\frac{\Delta t_f}{0.1\Delta t_{b,crit}}\right)\right] \tag{7.43}$$

where a minimum of 100 DBM subcycles was pre-defined to prevent any sort of numerical instabilities. By using this sub-cycling approach, the DBM-liquid phase momentum coupling term $\boldsymbol{f}_{DBM}$ present in Eq. (7.5) was time-averaged over the total n_{DBM} time steps.

7.3 MODEL IMPLEMENTATION FOR THE FLOW OF TAYLOR BUBBLES IN THE PRESENCE OF DISPERSED BUBBLES

The numerical model proposed in the previous sections is applied to the study the flow structure around Taylor bubbles rising in a bubbly flow stream. This is called "quasi-real" slug flow as it represents a more realistic model for the slug flow, than previous studies which considered isolated Taylor bubbles (BUGG; SAAD, 2002; TAHA; CUI, 2006b; KANG et al., 2010; ARAÚJO et al., 2012; SHABAN; TAVOULARIS, 2018; FREDERIX et al., 2020).

The computational domain is a circular tube with an internal diameter of D=26.2mm and length of $L = 20D$, as illustrated in Fig. 7.8. In order to reduce the total computational cost of the simulations and increase the mesh resolution around the Taylor bubble, the simulations are performed in a frame of reference attached to the Taylor bubble, i.e., in a Moving Frame of Reference (MFR). Using a MFR, the Taylor bubble remains in a fixed position throughout the simulation. A no-slip boundary condition is applied at the duct wall, which moves with the opposite of the rise velocity of the Taylor bubble. Liquid is injected at the top of the domain with the opposite of the rise velocity of the Taylor bubble and the bottom of the duct is an outlet boundary.

When dispersed bubbles are present, such as in the case of the VOF-DBM multiscale framework adopted in this work, a periodic boundary condition in the axial direction is applied. In this case, dispersed bubbles that exit through the bottom boundary re-entered the domain through the top boundary. This approach allows to carefully control the volume fraction of the dispersed bubbles $\overline{\langle \alpha_g \rangle}$, defining it as the ratio of the volume of the dispersed phase and the volume of the flow domain. During the initialization of the simulation, bubbles are added in random positions throughout the domain until a predefined value of $\overline{\langle \alpha_g \rangle}$ is reached. Hence it is not necessary to control the radial distribution of the dispersed bubbles from the injection procedure at the domain inlet, as done by Peña-Monferrer et al. (2018). Using periodic boundary conditions in the DBM, the radial distribution of the dispersed bubbles is obtained naturally when the flow is fully developed. In order to maintain the Taylor bubble in a fixed position, the strategy used in Rusche (2002) is used in the simulations, where the centre of mass of the Taylor bubble is computed at each time-step and a "PID-like" controller is applied to control this position based on a pre-defined target value. It is important to state that the frame acceleration induced by the MFR control loop is added as a supplementary body force in the governing equations of the continuous gas and liquid phases, solved in the Eulerian frame of reference, as well as the DBM.

Figure 7.8 – Computational domain, mesh and boundary conditions used in the present work: a) cross-section of the mesh and b) initial and boundary conditions, domain dimensions and mesh refinement regions.

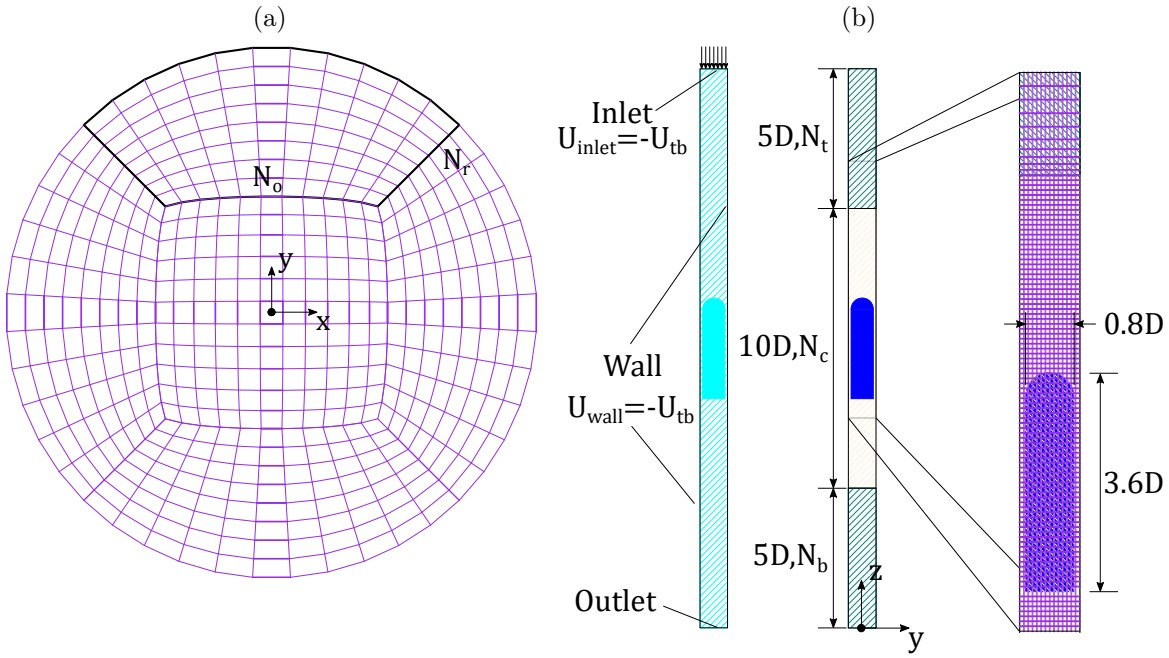

Source - Developed by the author.

Since the simulations were performed using the MFR approach and the Taylor bubble was fixed in space, it was possible to refine the mesh around the Taylor bubble in the Z-direction while keeping a lower resolution near the domain inlet and outlet. A full hexahedral multiblock mesh, with "O-topology" in the cross section, was used to have a better control of mesh quality and refinement. Three mesh resolutions were evaluated in the present work, which parameters are shown in Fig. 7.8 and their values listed in in Tab. 7.1. In configurations 2 and 3 of Tab. 7.1, since more cells were used in the radial direction, it was possible to refine the mesh near the duct wall. Moreover, the mesh spacing in the transition regions shown in Fig. 7.8 was defined to guarantee a smooth transition between the different mesh resolutions in the Z-direction.

Table 7.1 – Properties of the different meshes used in the present work. The different mesh parameters are illustrated in Fig. 7.8.

Mesh	N_o	N_r	N_t	N_c	N_b	N_{total}
Mesh 1	15	13	16	180	16	181,412 cells
Mesh 2	17	18	24	270	24	436,800 cells
Mesh 3	20	23	32	360	32	855,943 cells

Source - Developed by the author.

The Taylor bubble is initialized as a hemisphere connected with a cylinder of the same radius, with an initial radius of $0.8D$ and an initial length of $3.6D$. Therefore, the control volumes that lied inside this region were defined as $\gamma = 1.0$ during iniatilisation. The computational geometry and the Taylor bubble initial position were set to ensure that, in all simulations developed in this work, the incoming flow was fully developed in front of the Taylor bubble nose and that the result behind the bubble was not affected by the outlet boundary condition position. Additionally, care was taken to ensure that the bubbly flow reached a fully developed condition away from the Taylor bubble nose in the cases of VOF-DBM simulations.

7.4 RESULTS AND DISCUSSION

In this section, the proposed coupled VOF-DBM framework is validated and applied for the study of quasi-slug flows, considering the flow around Taylor bubbles in the presence of dispersed bubbles. First, an independent validation of the bubble-interface collision, VOF and DBM models is conducted, which are validated through the comparison with experimental results available in the literature. The model for the collision between dispersed bubbles and large interfaces is validated through a simplified experiment conducted by Sato et al. (2011), which studies the collision and rebound of a small bubble and an horizontal gas-liquid interface. The DBM model is validated with experiments for bubbly flow in vertical pipes and the VOF implementation is validated with experimental results for the flow around Taylor bubbles rising in liquid stream, without dispersed bubbles. Subsequently, the dispersed bubbles are incorporated in the model for the Taylor bubble flow and their influence on the flow structure is analyzed.

7.4.1 Model validation

7.4.1.1 Bubble - Interface collision model

In order to verify the large-scale interface model, a test case similar to the bouncing bubble experiment from Sato et al. (2011) is considered. In this experiment, a small nitrogen bubble of 1.20 mm is injected in a rectangular water tank, while a high-speed camera tracked the bubble motion. This test case compares the instantaneous vertical bubble position and velocity obtained from the simulations and the experiments from Sato et al. (2011). Figure 7.9 shows the test-case setup, where the tank is filled up to a height of 15 cm, to ensure that the dispersed bubble can assume its terminal velocity.

In the experiment, the bubble rises to the free surface and collides with the gas-liquid interface, whereby the bubble bounces from the interface numerous times. According

Figure 7.9 – Schematic representation of the numerical domain and initialization of the test case used to verify the bubble-interface collision model.

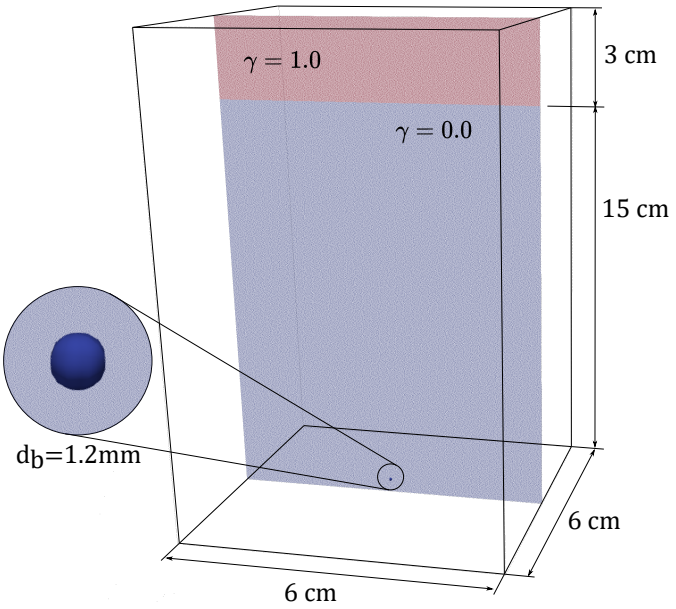

Source - Developed by the author.

to the data from Sato et al. (2011), for a nitrogen bubble of $d_b = 1.2$ mm, the bouncing occurs three times until the moment of coalescence. The comparison of the bubble vertical position versus time, after bubble bouncing, from the numerical simulations and the experimental results is shown in Fig. 7.10.

In the experimental footage, the dispersed bubble and the free surface deform during the collision and a significant contact time is observed. For the present test case, due to the simplifications associated with the DBM method, this contact time is not significant. Therefore, to compare the test case results with the experiments of Sato et al. (2011), the instantaneous results are divided into three "bouncing" moments. According to the results, the bubble bouncing motion is damped by the large scale interface, following the experimental observation, presenting a good agreement with the experimental results. The main outcome from this comparison is that the bubble velocity and the maximum vertical displacements after the bouncing of the bubble from the gas-liquid interface are adequately calculated with the proposed model, and support the value $C_{\mathrm{LSI}} = 20$ (see Eq. 7.41) adopted in this simulation.

7.4.1.2 Laminar Taylor bubble flow

In order to validate the VOF method, the results of fully-resolved simulations of a Taylor bubble in a laminar flow, using the three mesh configurations detailed in Tab. 7.1,

Figure 7.10 – Results of the test case run used to verify in the large-small interface collision model. Instantaneous values of the dispersed bubble position (top) and velocity (bottom) after bouncing with the free-surface in three different moments. Experimental results from Sato et al. (2011).

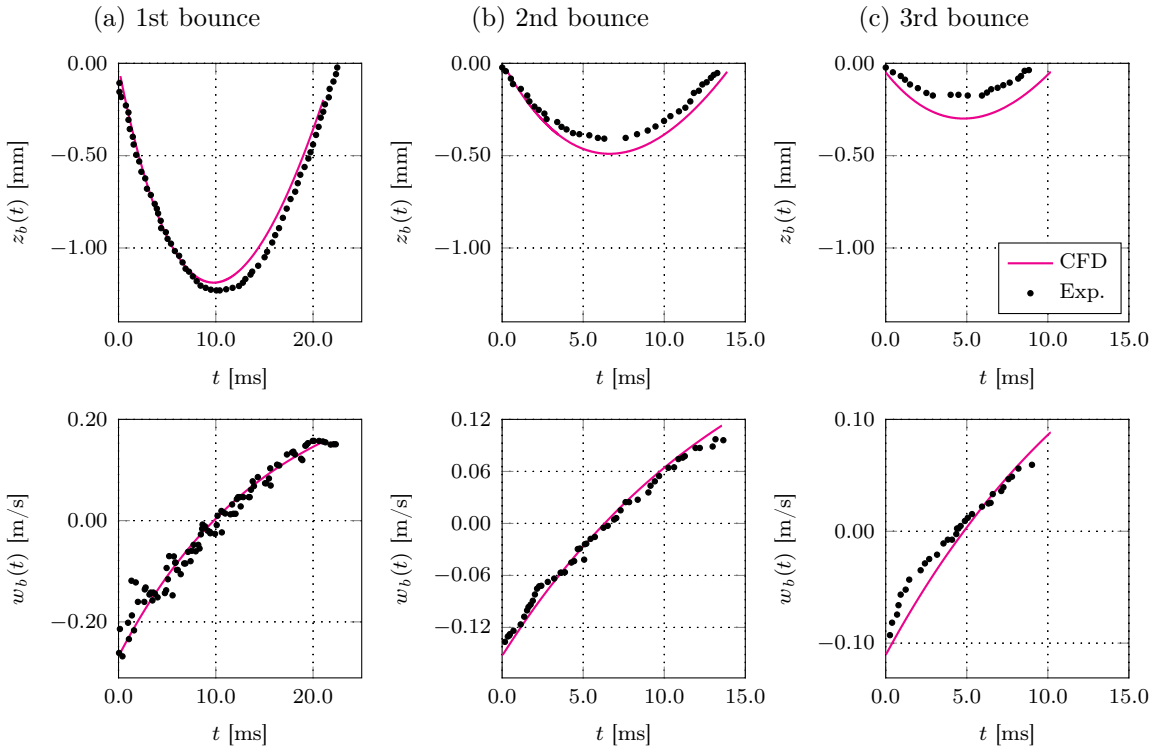

Source - Developed by the author.

are compared against experimental data from the literature.

The first validation is conducted against the results of Nogueira et al. (2006b) and Nogueira et al. (2006a), who studied the flow structure around air Taylor bubbles rising in a stagnant column of aqueous-glycerol solutions. Different glycerol concentrations were used in the experiments to modify the Morton number, $Mo = g\mu_L^4/\rho_L\sigma^3$ and the inverse viscosity numbers, $N_f = \sqrt{\rho_L^2 g D^3/\mu_L^2}$. In the experiments, the instantaneous velocity fields in the nose and the wake regions of the Taylor bubble were obtained using PIV measurements. These measurements for the case with $Mo = 4.31 \times 10^{-2}$ and $\mathrm{N}_f = 110$ are used to compare the velocity fields around the nose and in the wake of the Taylor bubble predicted by the employed numerical framework. Test cases, with relatively low values of N_f and high values of Mo were chosen as a first approach for the model validation in this chapter, once the resulting flow is laminar and more stable at wake region. These flow conditions facilitate the simulation convergence and less refined grids are required. In the next chapter, the model is applied for the study of "quasi-real" slug flows in air-water systems, for which N_f and Mo are, respectively, of the order of 10^4 and 10^{-12}, and

compared with the experimental results presented in Chapter 6.

To ensure that the simulation results are comparable to the experimental measurements, the recording of the transient average of Taylor bubble terminal velocity U_{tb} and the averaging procedure for the liquid velocity fields are initiated after at least 5.0 flow-through times (FFTs) from the beginning of the simulation, with FFT defined as

$$\mathrm{FTT} = \frac{L_{tb}}{U_{tb}} \tag{7.44}$$

where L_{tb} is the Taylor bubble length. The simulation results are extracted at the middle y-z plane of the computational domain, see Fig. 7.8, which is the PIV plane used by Nogueira et al. (2006b) and Nogueira et al. (2006a).

Figure 7.11 presents the comparison of radial and axial velocity profiles in the Taylor bubble tail region from experimental measurements and numerical results for the three different mesh configurations listed in Tab. 7.1. In Fig. 7.12 the comparison is presented for the bubble nose region. It should be noted that the results shown in Figs. 7.11 and 7.12 are given in the fixed frame of reference, following the results presented by Nogueira et al. (2006b) and Nogueira et al. (2006a). In order to change the frame of reference of the CFD results, from a moving to a fixed frame of reference, the terminal Taylor bubble velocity U_{tb} was added to the z-direction (w component) velocity values. According to the experimental correlation proposed by Viana et al. (2003), a Taylor bubble rising in a stagnant column of liquid in the given operating conditions should result in a expected terminal velocity of $U_{tb} = 0.155$ m/s, which is very close to the value of $U_{tb} = 0.158$ m/s obtained for the "Mesh 3". As can be observed, all the mesh resolutions listed in Tab. 7.1 are able to capture the velocity profiles in the region behind the Taylor bubble as well as in front of the Taylor bubble well, with some larger deviations for the coarser one (Mesh 1). Although the liquid velocity profiles result in acceptable results using either of the three mesh resolutions, "Mesh 3" produces the best agreement with the experimental results and, therefore, is used in the rest of the simulations.

In addition to the comparison of the velocity profiles, the terminal velocities of Taylor bubbles rising in stagnant columns under different flow conditions is compared with classic correlations from the literature. For this purpose, simulations are performed with "Mesh 3" (Tab. 7.1) for different Morton (Mo) and Eötvös (Eo) numbers, (which can be related as, $\mathrm{Eo} = \rho_L g D^2/\sigma = \mathrm{N}_f{}^{4/3}\mathrm{Mo}^{1/3}$) and compared against the correlations of White and Beardmore (1962) and Viana et al. (2003) based on the corresponding Froude number $Fr = U_{tb}/\sqrt{gD}$. As observed in Figure 7.13, the terminal velocities predicted by the simulation is in very good agreement with both experimental correlations, in both log(Mo)=-2 and log(Mo)=-6 configurations.

Figure 7.11 – Comparison of numerical and experimental results (NOGUEIRA et al., 2006b) of the axial $w(y,z)$ (left pane) and radial $v(y,z)$) (right pane) liquid velocity profile in different positions from the Taylor bubble bottom. The z/D position starts at the bottom position.

(a) z/D=-0.05

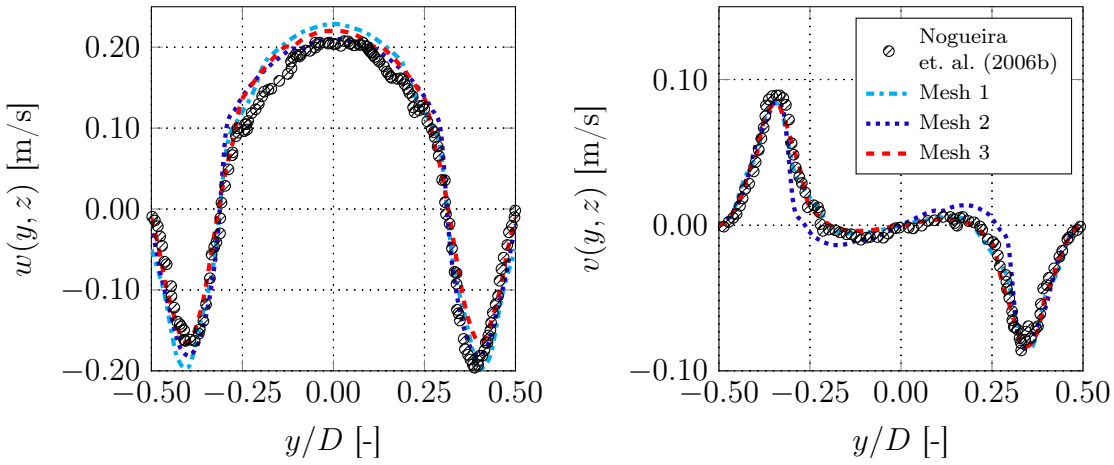

(b) z/D=-0.35

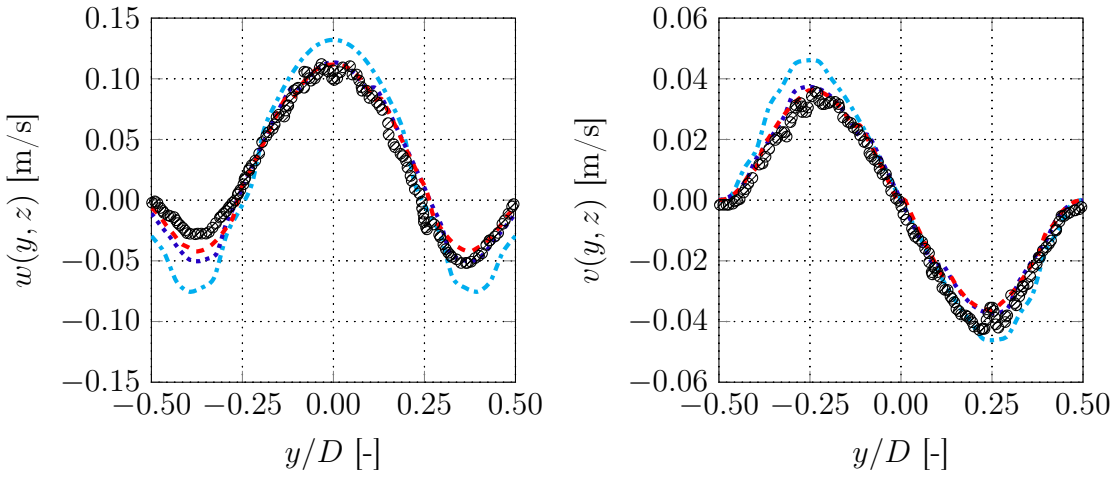

Source - Developed by the author.

To better understand the flow configuration under the considered operating conditions and present a qualitative validation, Fig. 7.14 presents the bubble shape obtained from the iso-contour based on $\gamma = 0.5$ as well as the flow field around the Taylor bubble. The results in Fig. 7.14 show the expected Taylor bubble shape and flow configuration previously reported in the literature (TAHA; CUI, 2006a; KANG et al., 2010; ARAÚJO et al., 2012; MORGADO et al., 2016). For a fixed Mo number and increasing Eo number, the tail of the Taylor bubble from a concave to a convex shape, and the length of the wake flow recirculation pattern increases. This pattern is clearly observed in the results of the simulations in Fig. 7.14.

Figure 7.12 – Comparison of numerical and experimental results (NOGUEIRA et al., 2006a) of the axial $w(y, z)$ liquid velocity profile in different positions near the Taylor bubble nose. The z/D position starts at the bubble nose position.

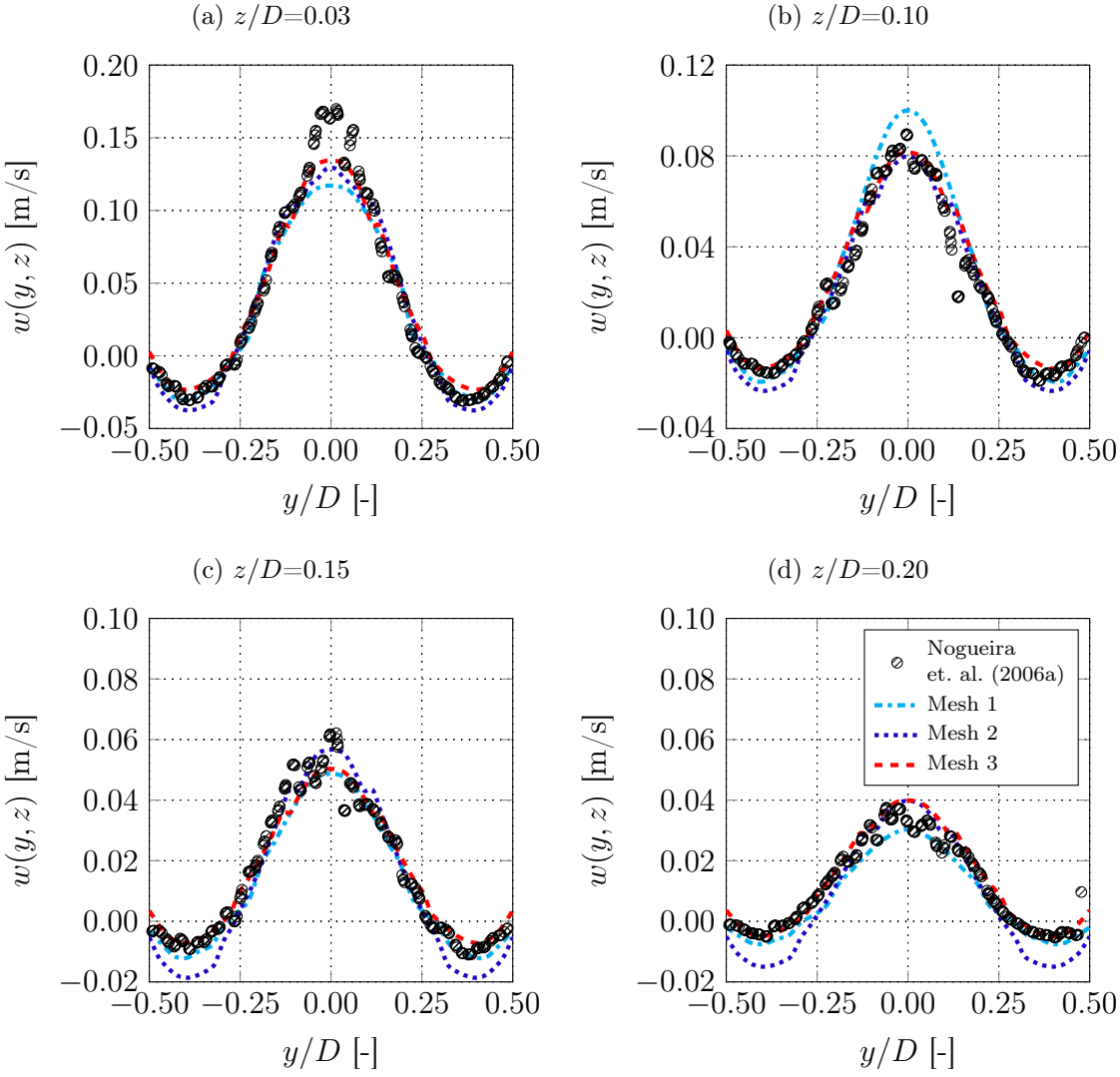

Source - Developed by the author.

In addition, in Figs. 7.14 g) and h) the shape of the Taylor bubble and the ensuing flow are not axisymmetric. The instantaneous fields and shapes observed in these two cases are in accordance with the experimental observations described by Campos and Carvalho (1988), where the recirculation pattern in the wak of the Taylor bubble exhibits different regimes. According to Campos and Carvalho (1988), based on the N_f values of the cases presented in Figs. 7.14 g) and h), the Taylor bubble is in the *transitional wake regime*. In this flow regime, which ranges from $500 < N_f < 1500$, the flow is still in the laminar regime, but the wake experiences periodic oscillations and vortex shedding is observed behind the Taylor bubble. In these cases, the terminal velocity of the Taylor bubble also

Figure 7.13 – Taylor bubble terminal velocities from the CFD simulations simulated with the "Mesh 3" mesh configuration listed in Tab. 7.1 in different operating conditions against experimental U_{tb} correlations found in the literature from White and Beardmore (1962) and Viana et al. (2003).

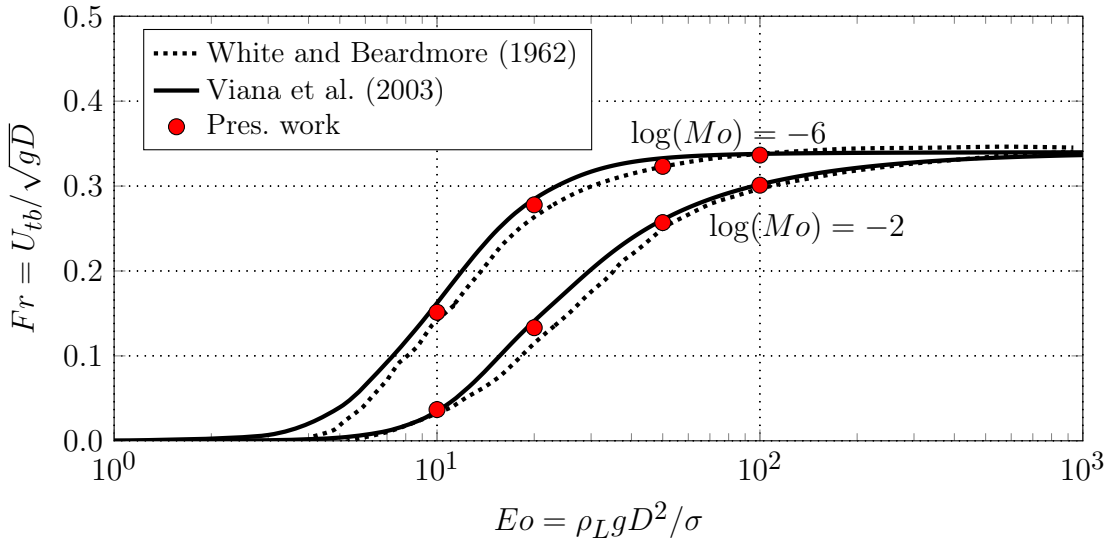

Source - Developed by the author.

exhibits fluctuations and the time-average value is taken.

From the results presented in this section, it can be concluded that the VOF method used in the present work together with "Mesh 3", see Tab. 7.1, can simulate a Taylor bubble rising in a stagnant column of liquid accurately under different operating conditions.

7.4.1.3 Laminar bubbly flow

The DBM, used to model the small scale interfaces, is validated by comparing the numerical results against experimental data from Kashinsky and Timkin (1999). In their work, Kashinsky and Timkin (1999) conducted an experimental characterization of a vertical upward bubbly flow at laminar Re numbers by Laser Doppler Anemometetry (LDA) and an electrodiffusional method. The experimental data consists of the liquid and gas velocity profiles, together with the distribution of the void fraction in a given section of the duct.

In Kashinsky and Timkin (1999) the experimental setup consisted of a vertical pipe with an internal diameter of $D = 14.8$ mm and a total length of $L = 6.5$ m. Since the measurement section was located far away from the gas/liquid inlet, the experimental data is assumed to be fully developed. In order to reduce the computational costs associated with simulating the entire test section described in Kashinsky and Timkin (1999), a mesh

Figure 7.14 – Estimated Taylor bubble shape from the $\gamma = 0.5$ iso-contour and the flow structured around the Taylor bubble in different operating conditions.

(a) log(Mo)=-2, Eo=10, N_f=17.8

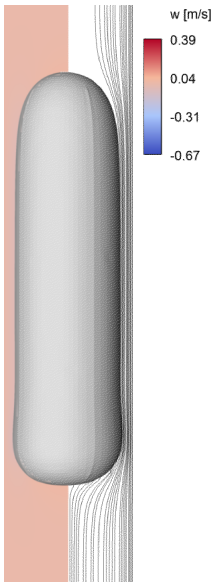

(b) log(Mo)=-2, Eo=30, N_f=29.6

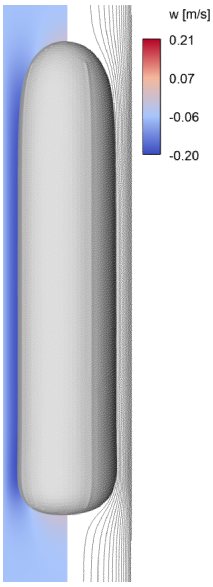

(c) log(Mo)=-2, Eo=50, N_f=59.4

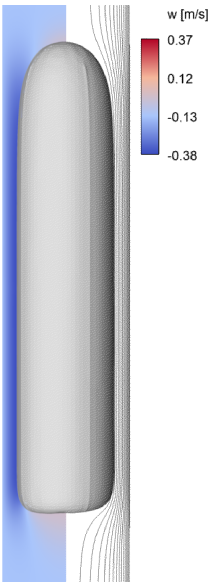

(d) log(Mo)=-2, Eo=100, N_f=100

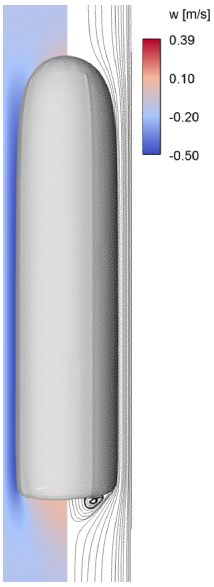

(e) log(Mo)=-6, Eo=10, N_f=178

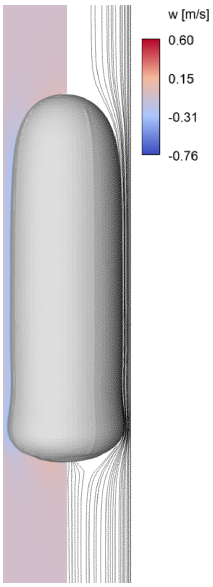

(f) log(Mo)=-6, Eo=30, N_f=296

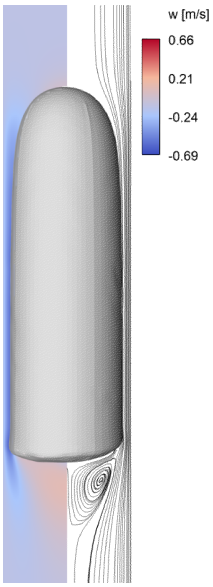

(g) log(Mo)=-6, Eo=50, N_f=594

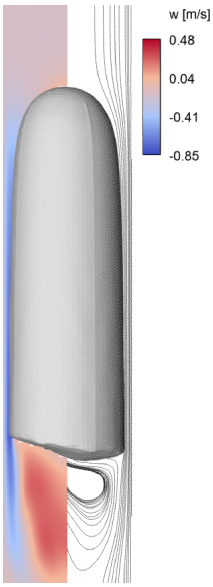

(h) log(Mo)=-6, Eo=100, N_f=1000

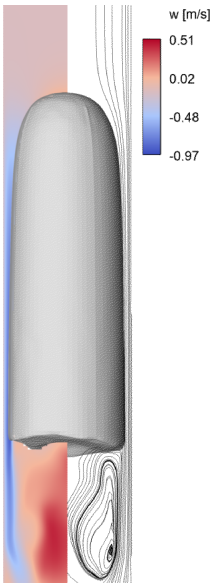

Source - Developed by the author.

arrangement, similar to the one presented in Fig. 7.8, is used in the presented simulations, combined with periodic boundary conditions for the liquid phase and the dispersed bubbles in the axial direction. By using this approach, the total mesh height is reduced to a total height of $L = 10.0D$. Different mesh configurations are considered and compared against the experiments, with the parameters for N_o, N_r and N_c following from Tab. 7.1. As described previously, the proposed CFD-DBM implementation uses an auxiliary particle mesh, which overlaps the Eulerian fluid mesh. Preliminary studies varying the particle mesh size V_{PC} and the interpolating distance h_j, see Fig. 7.2, suggest that a value of 1.5 times the largest bubble diameter is sufficient for an accurate interpolation of the relevant quantities between the fluid and particle mesh. Due to the transient nature of bubbly flows, the experimental data of Kashinsky and Timkin (1999) consists of time-averaged results. Thus, the same averaging procedure is adopted with the simulation results. The time-averaging procedures starts after reaching a statistical steady state, at approximately 4.0 FTTs, where Eq. (7.44) uses the characteristic flow velocity of approximately 0.15 m/s and the total domain height of $L = 148.0$ mm.

In order to better illustrate the transient nature of the simulated bubbly flows, Video 12 of the supplementary material given in Appendix B presents a video from one of the simulations used in the numerical validation presented here. This video shows the time evolution of the instantaneous liquid velocity field and the movement of the dispersed bubbles in a transversal section of the domain. Together with the liquid velocity field, a transient plot presents the instantaneous liquid velocity in a probe point located at the domain centre, showing a transient-like "signal" reflecting the flow fluctuations from the dispersed bubbles.

For the validation of the CFD-DBM model, an experimental run was chosen from the work of Kashinsky and Timkin (1999) to compare the numerical results. The validation of the CFD-DBM model is conducted against the experimental measurements of Kashinsky and Timkin (1999) for a superficial liquid velocity $j_l = Q_l/A_{duct}$ of 0.103 m/s and a global gas volume fraction of $\overline{\langle \alpha_g \rangle} = 2.0\%$, while the dispersed bubbles have an approximately constant diameter of $d_b = 1.1$ mm. In addition, to ensure a laminar flow of the liquid phase, the experiments were conducted using an aqueous glycerol solution with a viscosity of $\mu_l = 3.92 \times 10^{-3}$ Pa $\cdot$ s and a density of $\rho_l = 1120$ kg/m^3, resulting in a Reynolds number of $Re = 435.5$. Since periodic boundary conditions are applied for the simulations, an additional source term is added to the momentum equations (Eq. (7.5)) to drive the flow. In order to obtain the same liquid velocity as measured in the experiments, the driving force term was adjusted at each time-step.

Figure 7.15 shows the time-averaged velocity of the liquid and of the dispersed

bubbles, as well as the time-averaged gas void fraction, predicted by the simulations, alongside the experimental measurements of Kashinsky and Timkin (1999), for the three considered mesh configurations. The profiles of the liquid velocity of the simulations are averaged over 5 FFTs along the axis of symmetry of the cylindrical duct, at a distance of $z = 5.0D$ from the bottom boundary. For the dispersed bubble velocity and the gas void fraction, the information from the Lagrangian particles position, shape and instantaneous position are used to average the values into a line located at the same position. The simulation results in Fig. 7.15 show a good agreement with the experimental measurements of all three considered quantities. The results of the average gas void fraction demonstrate that the proposed model is able to reproduce the peak in volume fraction near the wall reported by Kashinsky and Timkin (1999) with all three considered meshes, with only minor differences between the profiles.

From the results presented so far, it can be concluded that the proposed VOF-DBM method is able to represent laminar bubbly flows in vertical pipes accurately.

The validation presented in this and the previous section brings reliability for the VOF and DBM model that will be used, in the next section to simulate the flow around Taylor bubbles in the presence of dispersed bubbles.

7.4.2 Simulation of manufactured slug flow

The proposed multiscale model is applied to simulate a manufactured slug flow where a Taylor bubble (large scale interface) is injected in a bubbly flow of dispersed bubbles (small scale interfaces). By injecting both bubble types independently, it is possible to control the gas void fraction of the bubbly flow and, therefore, study the effect of the dispersed bubbles around the Taylor bubbles for different void fractions. This flow situation represents a more realistic slug flow than cases with isolated Taylor bubbles, as studied in (BUGG; SAAD, 2002; TAHA; CUI, 2006a; KANG et al., 2010; ARAÚJO et al., 2012; SHABAN; TAVOULARIS, 2018; FREDERIX et al., 2020), among other references.

In order to better understand the effect of dispersed bubbles on the flow structure around Taylor bubbles, a Taylor bubble is injected into a stagnant bubble column, i.e the superficial velocity is $j_l = 0.0$ m/s. The liquid phase is a aqueous-glycerol solution, with a water weight percentage of 75%, resulting in the following set of non-dimensional numbers: $\log(\mathrm{Mo}) = -5.1$, $\mathrm{Eo} = 120$ and $\mathrm{N}_f = 712$. As in the work of Kashinsky et al. (1993) and Kashinsky and Timkin (1999), the liquid properties were chosen to maintain the pipe Re_l number within the laminar regime to avoid the need of more sophisticated Bubble Induced Turbulence (BIT) models necessary when simulating low Morton flows

Figure 7.15 – Experimental results from Kashinsky and Timkin (1999) and the numerical results from the present work from simulations with the different mesh configurations listed in Tab. 7.1. From top to bottom: a) liquid velocity profile $\langle w(y,z)\rangle$; b) dispersed bubble velocity profile $\langle w_g(y,z)\rangle$ and c) gas volume fraction profile $\langle \alpha_g(y,z)\rangle$. Those results present time-averaged profiles taken in a line located located $z = 5.0D$ away from the bottom B.C.

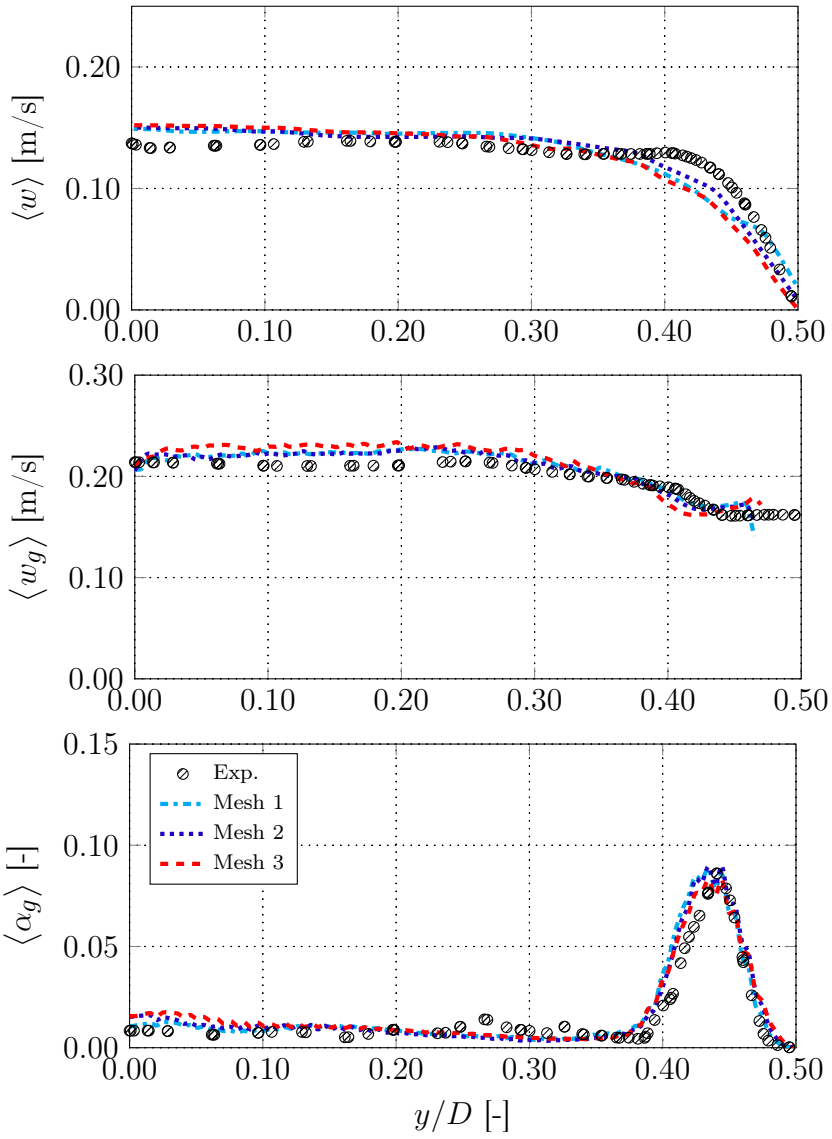

Source - Developed by the author.

(log(Mo) < -10.0), e.g., air-water flows, or even models for the turbulence closure in the liquid phase. The resulting laminar flow allows to study the effect of dispersed bubbles on the flow around Taylor bubbles without interference by other phenomena, such as turbulence. In the next chapter, this "manufactured" slug flow will be studied in air-water systems and turbulence closure models for the liquid phase and BIT, will be incorporated. The transient simulations are performed with "Mesh 3" (Tab. 7.1) and the computational

domain setup shown in Section 7.3 considering five flow configurations, with gas volume fractions of the dispersed bubbles of $\langle \alpha_g \rangle \in \{0.0\%, 2.0\%, 3.5\%, 5.0\%, 7.0\%\}$. The small dispersed bubbles are injected in the domain according to the size distribution obtained for the experiments in aqueous-glycerol solution, from Exp. 7 of Chapter 4, which resulted in a narrow and nearly symmetric bubble size distribution.

For the simulation of the "quasi-slug" flow regime, first, a Taylor bubble is simulated for a sufficient period until a statistical steady state is reached. Then, dispersed bubbles are injected randomly in the computational domain of this simulation, following the reference bubble size distribution, until a pre-defined $\overline{\langle \alpha_g \rangle}$ is reached, taking care not to inject dispersed bubbles inside the Taylor bubble. The simulations are then re-run until a statistical steady state is reached again. An additional overview of the simulated "quasi-real" slug flow can be encountered in Video 13 of the supplementary material given in Appendix B, which presents the transient VOF-DBM simulations in the different background bubbly configurations, while Video 14 of the supplementary material given in Appendix B present a close-up view around the Taylor bubbles.

Figure 7.16 – Example of the manufactured "quasi-real" slug flow regime simulated cases, illustrating the different background bubbly flow void fractions.

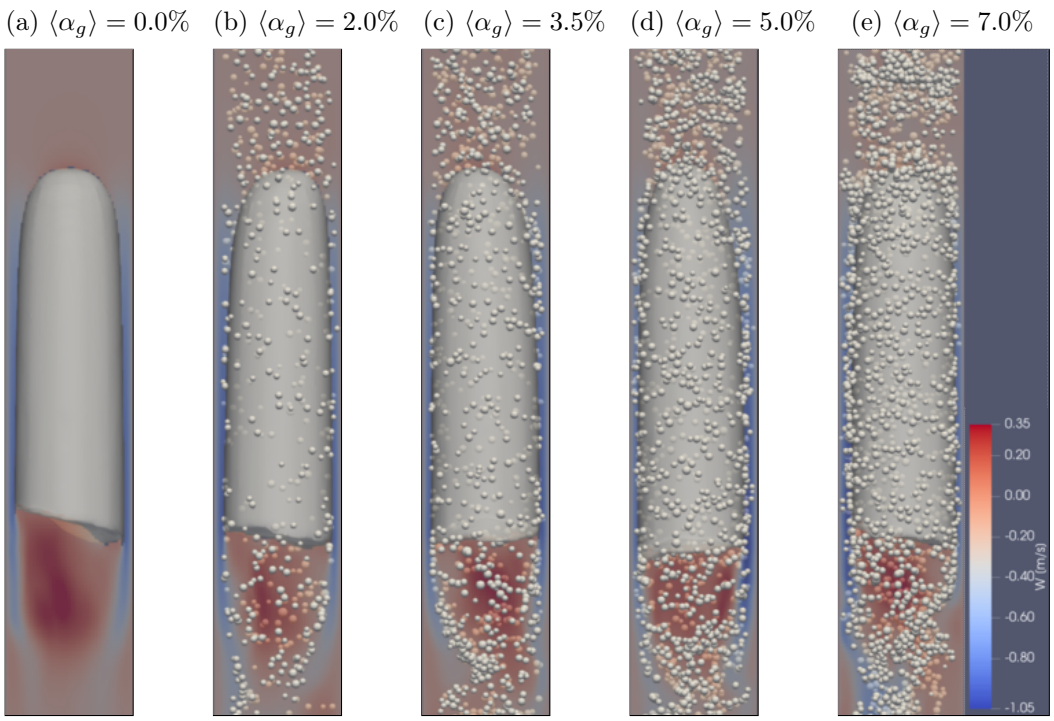

Source - Developed by the author.

As mentioned before, some of the simulated flow conditions yield a Taylor bubble in the transitional wake regime, where the flow is laminar, but the flow in the wake of

the Taylor bubble is unsteady due to vortex shedding, resulting in an unstable motion of the bubble tail. Video 15 of the supplementary material given in Appendix B of the supplementary material shows the motion of the tail of the Taylor bubble and the instantaneous axial and radial velocities of the liquid, illustrating the unsteady behaviour of the flow in the wake region of the Taylor bubble. In addition, when dispersed bubbles are present, the liquid motion in the wake region becomes more unstable. Therefore, the simulation results are averaged over time. In order to produce consistent and statically converged time-averaged results, the instantaneous fields and values are averaged for a period of, at least, 10.0 FTTs, after reaching a statistically developed flow.

7.4.2.1 Effect of the small dispersed bubbles on the rise velocity of the Taylor bubble

As observed experimentally in Chapter 6, the presence of small dispersed bubbles introduce oscillations in the flow ahead of the Taylor bubble, affecting its terminal rise velocity. According to the experimental results, these modifications also influence the flow in the wake region of the Taylor bubble. Figure 7.17 shows the instantaneous $U_{tb}(t)$ rise velocity of the Taylor bubble and its time-averaged value $\langle U_{tb} \rangle$ for the considered flow configurations. For the case of a stagnant liquid column ($\langle \alpha_g \rangle = 0.0\%$), the correlation of Viana et al. (2003) is also plotted in the transient plot of Fig. 7.17, showing a maximum deviation of 2.2% for the time simulated.

The influence of the dispersed bubbles on the rise velocities of the Taylor bubble is evident in the results shown in Fig. 7.17. From the transient $U_{tb}(t)$ plots, increasing the volume fraction of the dispersed bubbles leads to larger fluctuation of the rise velocity of the Taylor bubble and, based on the $\overline{\langle \alpha_g \rangle}$ vs. $\langle U_{tb} \rangle$ plot, a larger terminal velocity of the Taylor bubble. A similar trend was observed in the experimental results of Chapter 6, although a higher N_f fluid system was studied. A small number of dispersed bubbles is enough to perturb the rising motion of the Taylor bubbles, promoting a large increase of the rise velocity at relatively low volume fraction of the dispersed phase, $\overline{\langle \alpha_g \rangle}$, and then becoming a near asymptotic increase of $\langle U_{tb} \rangle$ vs. $\overline{\langle \alpha_g \rangle}$.

According to the experimental findings in Chapter 6, there is a strong correlation between the rise velocity of the Taylor bubble and the deformation and lateral oscillation of the nose of the Taylor bubble. The deformation of the frontal region of the Taylor bubble, which is a direct result of the fluctuations induced by the dispersed bubbles ahead of the Taylor bubble, modifies the total drag force experienced by the Taylor bubble.

From the results of Chapter 6 and the experimental work of Tudose and Kawaji (1999), which measured the total drag force of symmetric and deformed plastic Taylor

Figure 7.17 – Effect of the dispersed bubbles on the rise velocity of the Taylor bubble for different dispersed gas volume fractions, showing its transient (left pane) and time-averaged terminal (right pane) rise velocity.

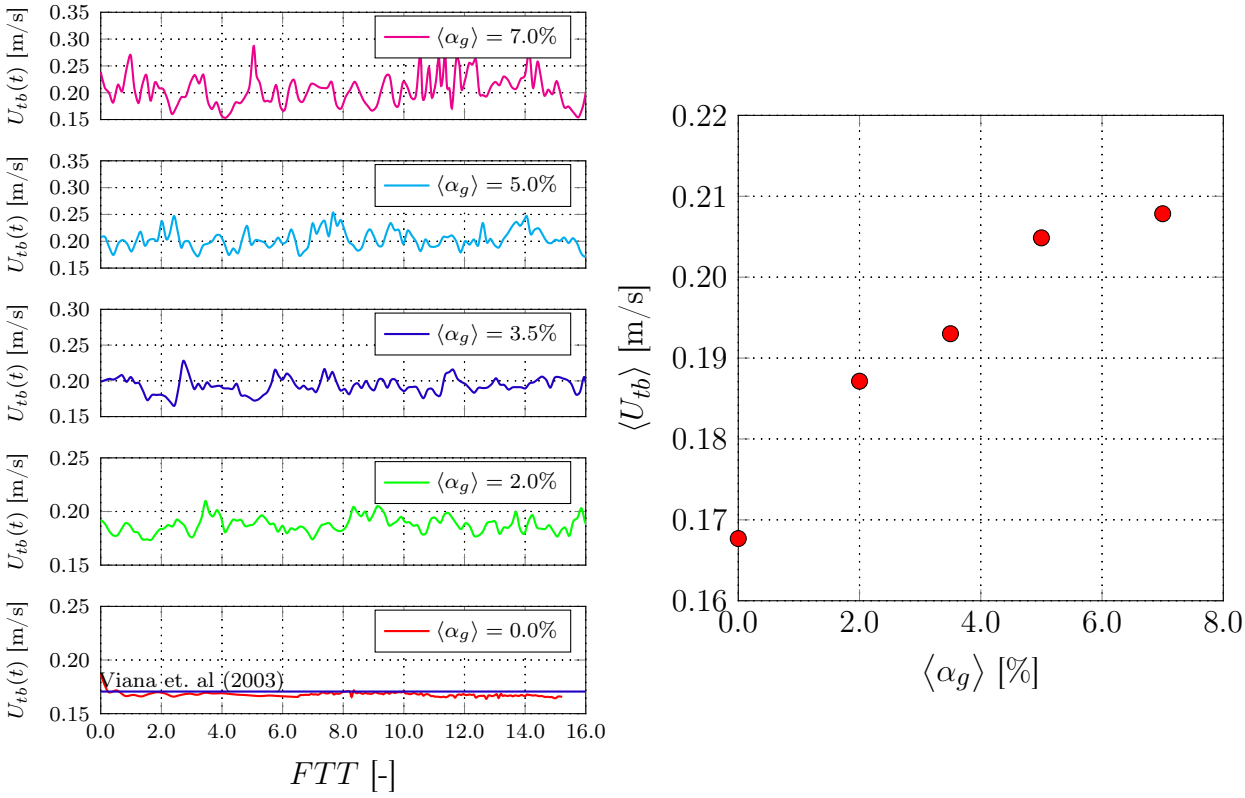

Source - Developed by the author.

bubble models, the nose deformation results in an eccentric motion of the Taylor bubble, which in turns reduces the total drag force, accelerating the Taylor bubble rise. This effect is clearly observed in the results of the simulations. Figure 7.18 presents the radial position of the Taylor bubble nose $y_{nose}/D(t)$, taken from the middle y-z plane of the computational domain, during the simulation of the different tested cases. Additionally, Fig. 7.18 also present the Probability Density Function (PDF) of this displacement.

A clear correlation can be observed between the oscilation of the nose tip of the Taylor bubble (Fig. 7.18) and the transient rise velocity $U_{tb}(t)$ (Fig. 7.17). As observed, without the presence of dispersed bubbles, the nose tip of the Taylor bubble remains fixed on the duct centerline, with minimal deviations from the linear rise. However, in the "quasi-slug" flow, the Taylor bubble exhibits a stronger lateral motion, which can be a combination of two factors. The first factor is the flow perturbation caused by the rise of the small dispersed bubbles in front of the Taylor bubble, which may deform the nose of the Taylor bubble, inducing a lateral movement. The second factor is dispersed bubbles entering the liquid film formed between the Taylor bubble and the duct wall. Since the

Figure 7.18 – Lateral movement of the Taylor bubble nose tip over time (left) and Probability density function (right) of the nose tip position from different background bubbly flow void fractions.

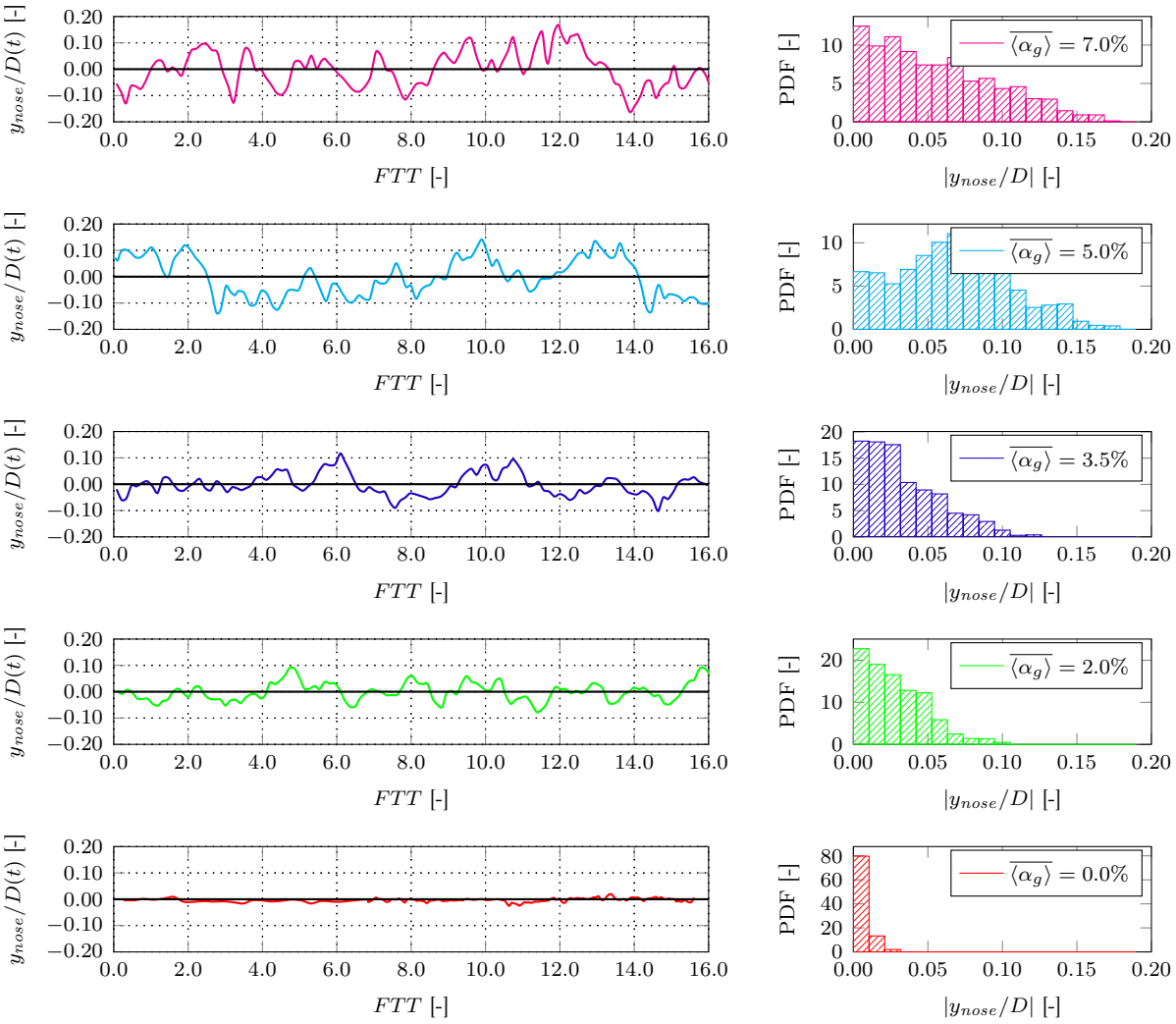

Source - Developed by the author.

dispersed bubbles do not enter uniformly into the liquid film, the small dispersed bubbles deform the Taylor bubble unevenly, perturbing the liquid film and, thus, enhancing the lateral movement.

As a visual reference, in Video 15 of the supplementary material given in Appendix B it is possible to observe the transient lateral motion and interface deformation of the Taylor bubble in detail. Interestingly, the PDF of the case with $\overline{\langle\alpha_g\rangle} = 5.0\%$ exhibits a different distribution of the nose tip position compared to the other cases, revealing strong oscillations of the nose tip. This difference may explain the small change in the terminal velocities between the cases with $\overline{\langle\alpha_g\rangle} = 5.0\%$ and $\overline{\langle\alpha_g\rangle} = 7.0\%$.

The next section is dedicated to the detailed analysis of the time-averaged flow fields around the Taylor bubbles, aiming to further comprehend the effect of the small dispersed bubbles on the flow structure.

7.4.2.2 Effect of the dispersed bubbles on the flow structure around the Taylor bubbles

Figures 7.19 and 7.20 present the time-averaged liquid velocity fields around the Taylor bubble nose and tail for the different background bubbly flow conditions analyzed in this work. The time-averaged distribution of the gas volume fraction of the dispersed bubbles, $\langle \alpha_g \rangle$, around the Taylor bubble nose and tail in the considered flow conditions are presented in Fig. 7.21. The data generation for the plots shown in Fig. 7.21 uses the same methodology used to create the dispersed bubbles average profiles shown in Fig. 7.15, where, instead of performing a line average, the averaging procedure is done on a two-dimensional plane.

In the region near the nose tip of the Taylor bubble, the radial liquid velocity $\langle v \rangle$ reduces for an increasing void fraction $\overline{\langle \alpha_g \rangle}$ of dispersed bubbles. This reduction is associated with the eccentric motion and deformation of the Taylor bubble nose, as well as the flow induced by the dispersed bubbles. Once there is no net liquid flow, the dispersed bubbles induce a downward near-wall film flow even ahead of the Taylor bubble, as observed in the streamlines shown in Fig. 7.19. This downward moving liquid enters directly into the Taylor bubble film, reducing the lateral displacement of the liquid at the passage of the Taylor bubble. In addition, the change in the nose shape alters the flow downstream of the Taylor bubble nose, creating a transient asymmetric liquid film which is not constant and, on average, wider than in the case with $\overline{\langle \alpha_g \rangle} = 0.0$. This difference in the liquid film thickness leads to a reduction of the time-averaged axial downward velocity close to the Taylor bubble nose region.

In the axial direction, a significant change of the magnitude of the $\langle w \rangle$ velocity component is not observed in Fig. 7.19. As a result of the eccentric nose motion, the narrow velocity distribution observed in the case with $\overline{\langle \alpha_g \rangle} = 0.0\%$ progresses from a concentrated peak to a wide velocity distribution, because more bubbles are present in the flow. Since the peak velocity is located close to the Taylor bubble tip, as its position oscillates laterally, the location of the peak follows the movement and, when averaged over time, this peak "spreads" across the duct radius. A similar modification of the flow structure is observed in the experimental results of Chapter 6 as a result of the deformation of the Taylor bubble nose and oscillation of its tip. A better visualization of the flow structure described above can be encountered in the animation of Video 15 of the supplementary material given

Figure 7.19 – Time averaged velocity fields around the Taylor bubble nose for different simulated background bubbly flow conditions. First row: Velocity vector plots; Second row: Velocity vector plots streamlines; Third row: Contour plot of the ensemble average radial liquid velocity $\overline{v}$; Fourth row: Contour plot of the ensemble average axial liquid velocity $\overline{w}$.

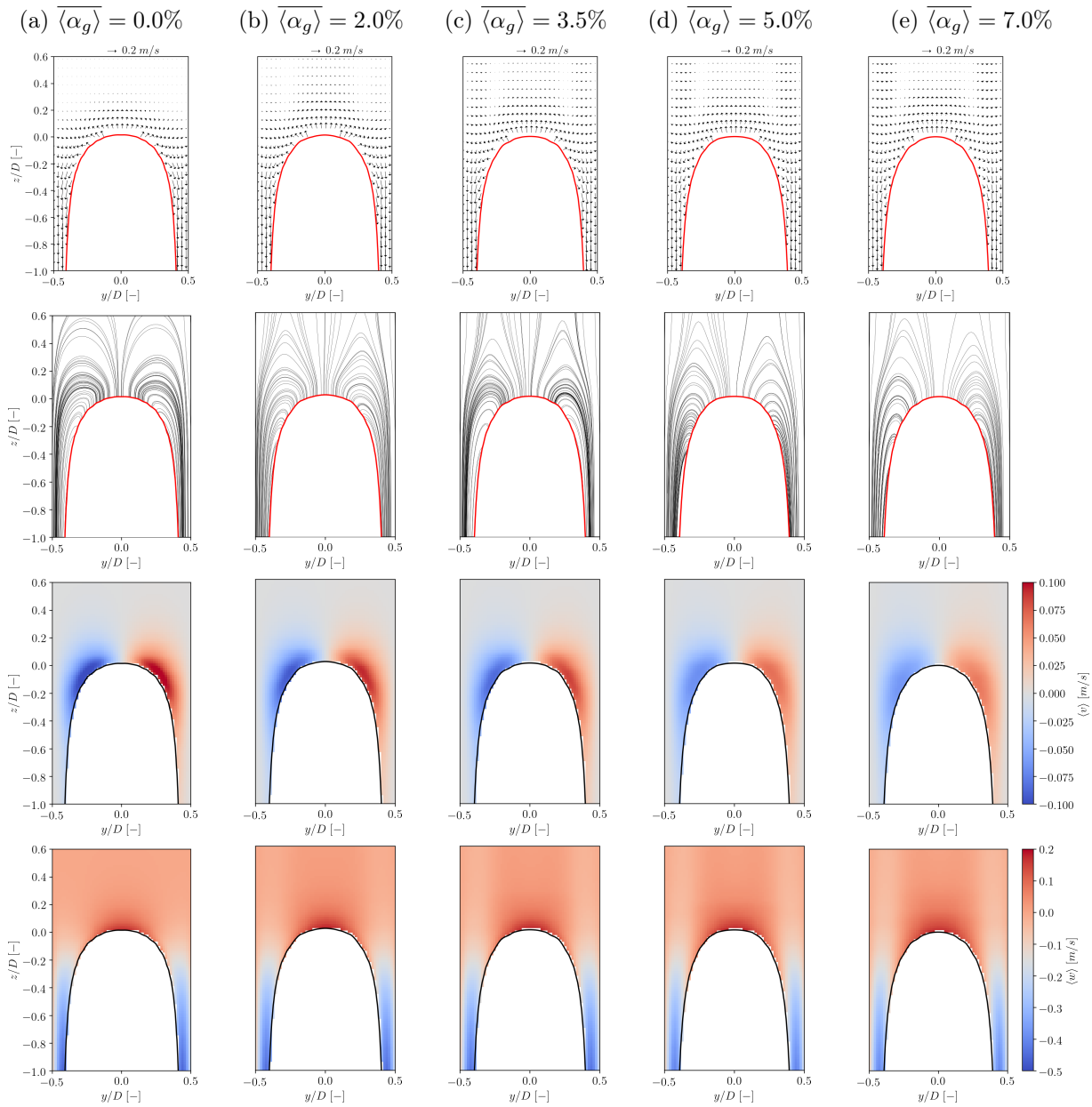

Source - Developed by the author.

in Appendix B which shows the instantaneous axial and radial liquid velocity contours around the Taylor bubble for different dispersed bubbles volume fractions.

The time-averaged velocity fields of Fig. 7.20 show that the effect of the dispersed bubbles on the flow structure is stronger around the Taylor bubble tail than its nose. For the case of the stagnant column and more viscous fluid, which is different from those cases

Figure 7.20 – Time averaged fields around the Taylor bubble tail from the different simulated background bubbly flow conditions. First row: Velocity vector plots; Second row: Velocity vector plots streamlines; Third row: Contour plot of the ensemble average radial liquid velocity $\langle v \rangle$; Fourth row: Contour plot of the ensemble average axial liquid velocity $\langle w \rangle$.

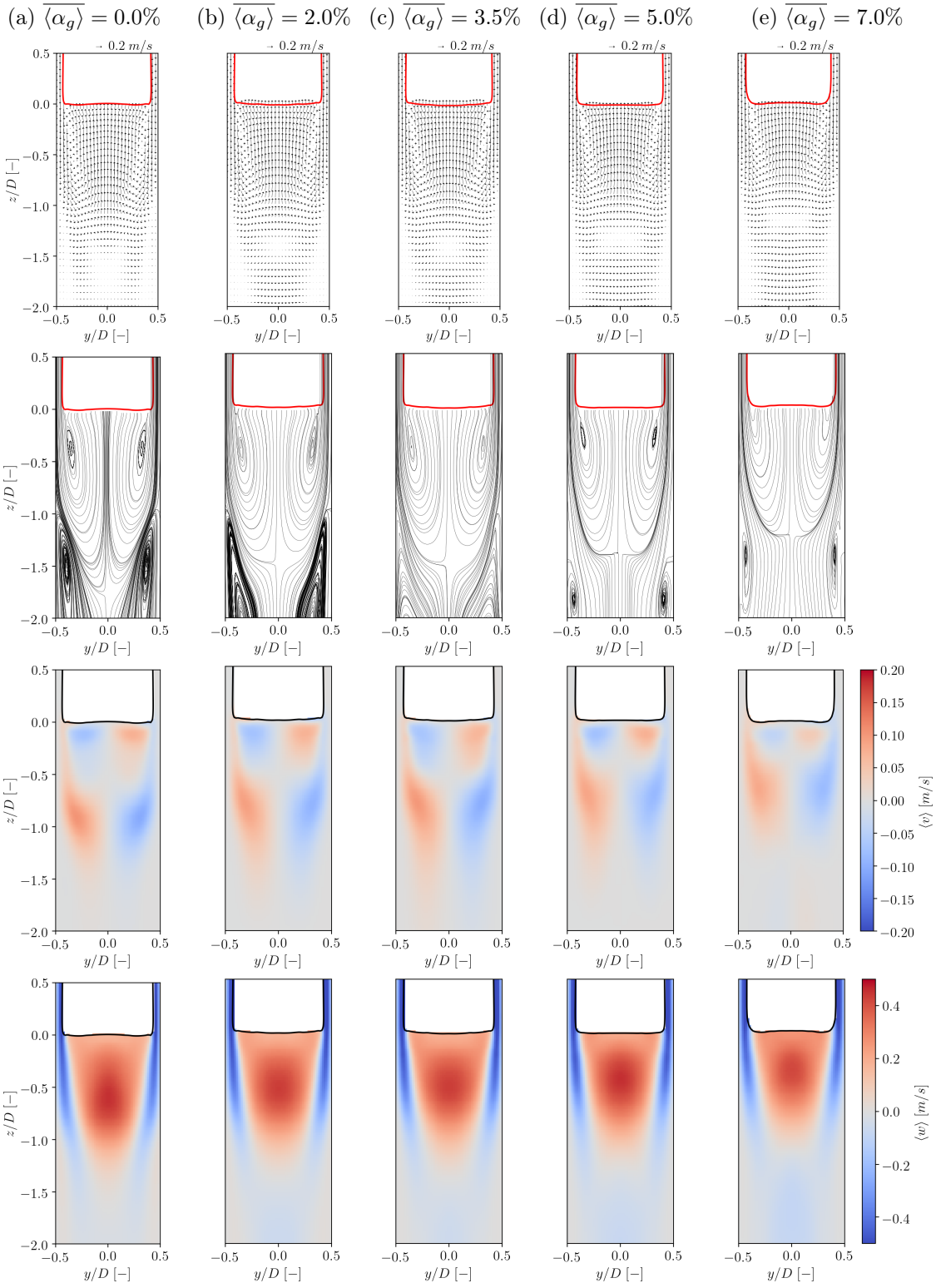

Source - Developed by the author.

studied in Chapter 6, the volume of the main recirculation is decreased as $\overline{\langle \alpha_g \rangle}$ increases. In addition, a secondary recirculation, which appears further away from the Taylor bubble tail, also tends to be weaker for higher values of $\overline{\langle \alpha_g \rangle}$. This behavior is due to the upward liquid motion induced by the dispersed bubbles in the central region of the duct, which is opposed to the downward motion in this region induced by the secondary vortex.

The contours of the time-averaged volume fraction of the dispersed bubbles, $\langle \alpha_g \rangle$, are shown in Fig. 7.21 for different $\overline{\langle \alpha_g \rangle}$. The distribution of $\langle \alpha_g \rangle$ in the central plane is consistent with the flow structure observed from the streamlines. The double vortex structure induces a higher concentration of dispersed bubbles in the central region of the duct, below the Taylor bubble tail.

Figures 7.22 and 7.23 present the contour plots of the root mean square (rms) values of the fluctuation of the radial $v'_{l,rms}$ and axial $w'_{l,rms}$ velocity components around the Taylor bubble nose and tail. These fluctuations are induced by the dispersed bubbles, as the background flow is laminar. Hence, as more dispersed bubbles are present in the flow, larger fluctuations are generated ahead of the Taylor bubble which induces oscillation of the nose of the Taylor bubble, leading to an oscillatory motion of the Taylor bubble. On account of these oscillations, the velocity fluctuations shown in Fig. 7.22 exhibit higher values near the Taylor bubble nose, which increases with the bubbly flow gas volume fraction $\overline{\langle \alpha_g \rangle}$.

Figure 7.23 presents the velocity fluctuations around and below the Taylor bubble tail, showing that the intensity of the fluctuations increases with $\overline{\langle \alpha_g \rangle}$ in the bulk of the wake recirculation and close to the Taylor bubble tail. The first modifications of the local structure of $v'_{l,rms}$ can be attributed to the fluctuations induced by the dispersed bubbles, which by visual inspection of Fig. 7.21, indicates the presence of a large number of bubbles in the bottom half of the liquid recirculating wake ($-1.5 < z/D < -0.5$). According to Videos 14 and 15 of the supplementary material given in Appendix B, in the regions where the intensity of $v'_{l,rms}$ is higher, it is possible to observe a recirculating motion by the dispersed bubbles. The increase of $v'_{l,rms}$ close to the Taylor bubble is due to the oscillations of the tail interface, which, as shown in Videos 14 and 15 of the supplementary material given in Appendix B, increases with the concentration of dispersed bubbles present in the flow.

From the analysis of the distribution of the volume fraction of the dispersed bubbles, given in Fig. 7.21, and the fluctuation of the liquid velocity along the axial direction, $w'_{l,rms}$, it becomes clear that the modification of the flow and the velocity fluctuations is not only caused by the recirculating motion of the dispersed bubbles on the Taylor bubble wake, but also by the modification of thickness of the liquid film between the Taylor bubble

Figure 7.21 – Time-averaged dispersed bubble gas volume fraction $\langle \alpha_g \rangle$ distribution around the Taylor bubble nose and tail in the different simulated conditions.

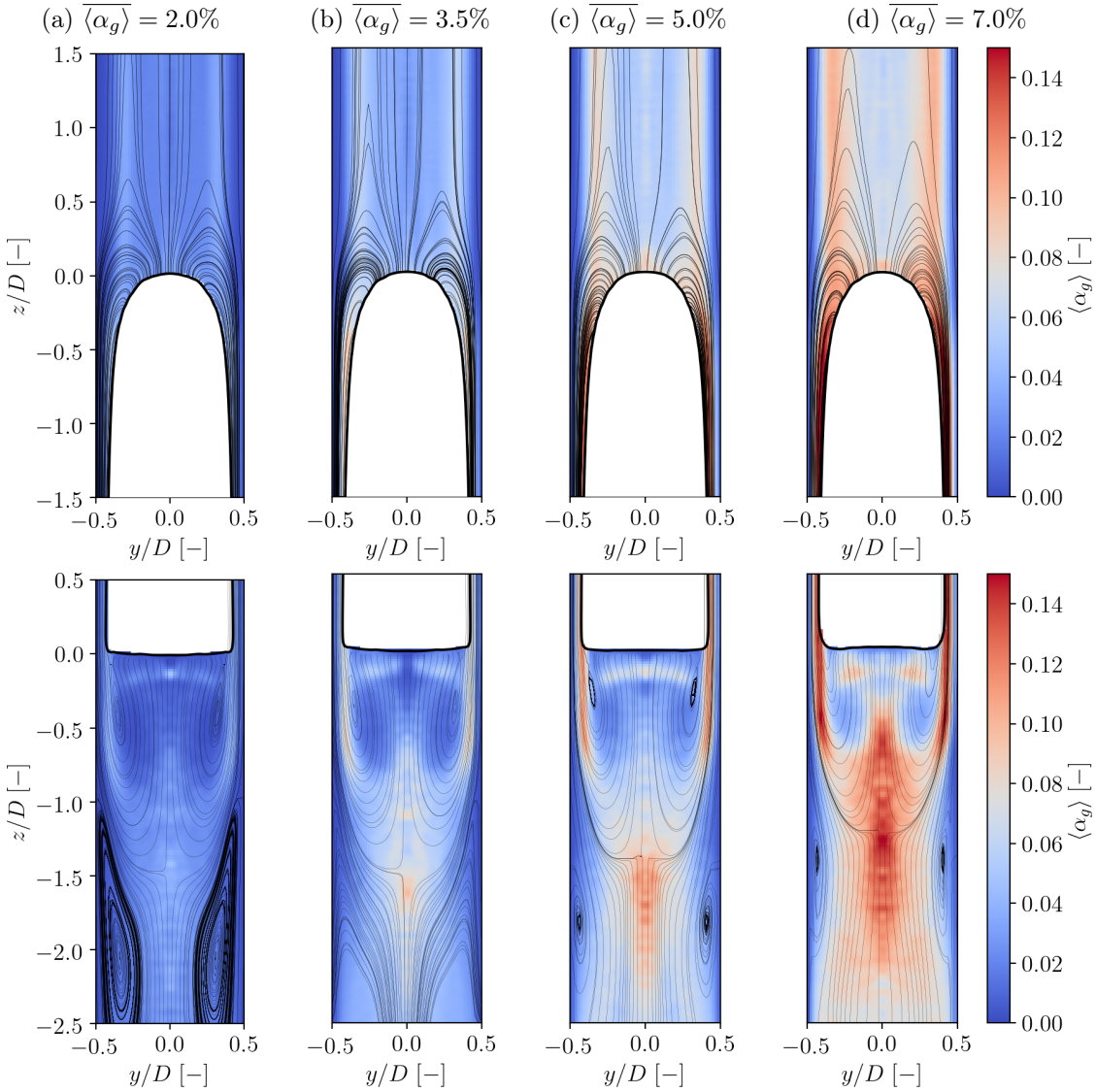

Source - Developed by the author.

and the duct wall, which creates an oscillatory and asymmetrical jet exiting towards the recirculation bulk.

Figure 7.22 – Velocity fluctuations around the Taylor bubble nose from the different simulated background bubbly flow conditions. Contour plot of the r.m.s. values of the radial (first row) and axial (second row) velocity component fluctuations.

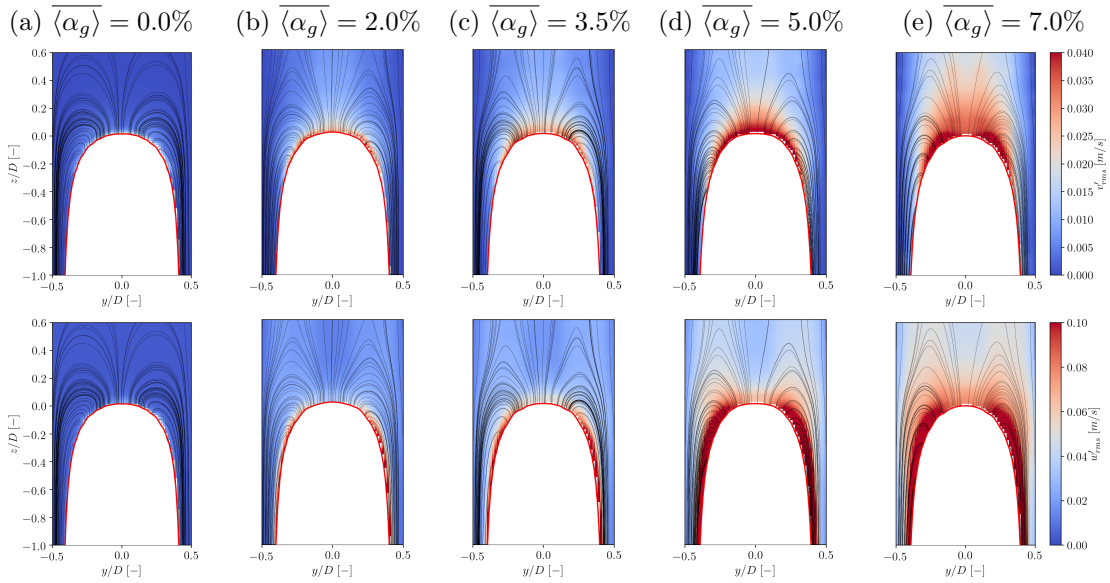

Source - Developed by the author.

Figure 7.23 – Velocity fluctuations around the Taylor bubble tail from the different simulated background bubbly flow conditions. Contour plot of the r.m.s. values of the radial (first row) and axial (second row) velocity component fluctuations.

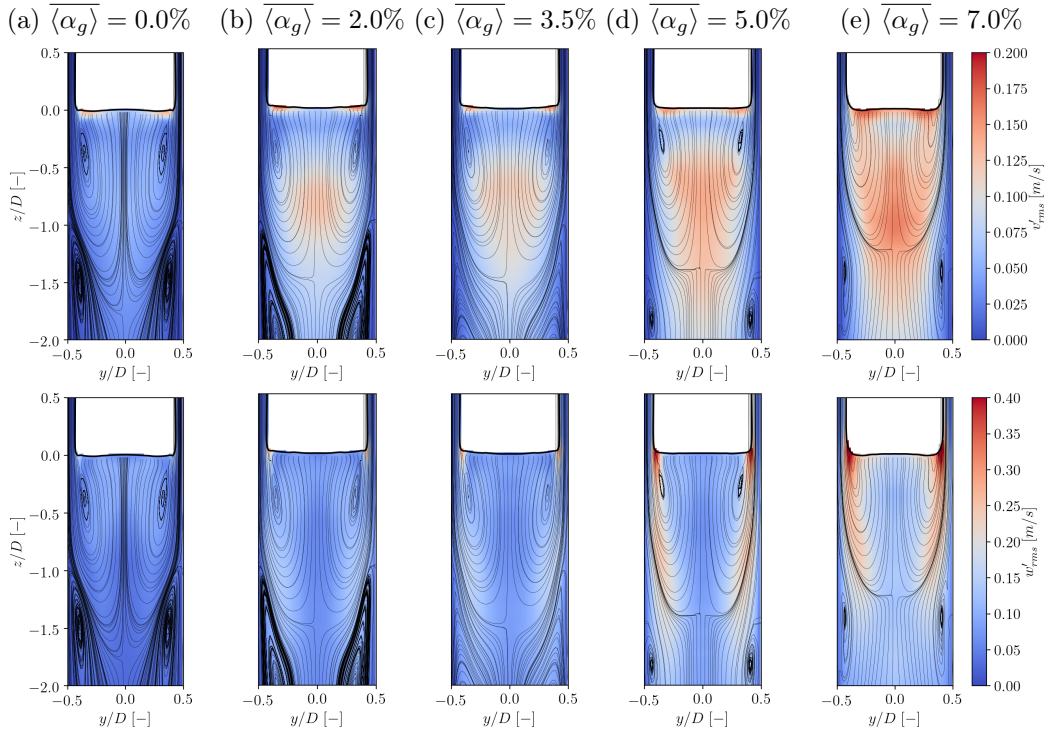

Source - Developed by the author.

7.5 CONCLUSIONS

This chapter presented the development of a two-phase gas-liquid multiscale three-dimensional CFD model capable of simulating gas-liquid flows with different interface length scales. The multiscale CFD model is based on the coupling of a model based on the VOF method to model the large-scale interface flow, and the Discrete Bubble Method (DBM), a Lagrangian-based model, to simulate the motion of dispersed bubbles (small-scale interfaces).

The multiscale model was implemented in the multiphase Finite Volume Method (FVM) based CFD in-house code MultiFlow (WACHEM et al., 2002). Modifications were added to the MultiFlow code to account for the consistent modeling of the inter-phase coupling between the liquid and the multiscale gas phase. Collision models were incorporated to account for the collision among dispersed bubbles based on a soft-sphere model and collisions between the dispersed bubbles and large interfaces are modeled based on the interpolation of the interface normal vector and colour function of the VOF method to the DBM framework.

The VOF and DBM model were independently validated from experimental data found in the literature, presenting a good agreement between the numerical and experimental results. Then, the proposed multiscale model was used to conduct a numerical study of the "quasi-real" slug flow regime, where Taylor bubbles (large scale interface) are injected in a bubbly (small scale interface) column.

The numerical study of the flow around Taylor bubbles showed that the presence of small dispersed bubbles significantly affects the Taylor bubble terminal velocity. According to the different simulated cases within the "quasi-real" slug flow regime, as more dispersed bubbles are present in the flow, higher is the terminal Taylor bubble terminal velocity and the eccentric fluctuations as it rises through the bubble column.

It was also observed that as the number of dispersed bubbles present in the flow increases, the transient Taylor bubble deformation due to the induced perturbations from the dispersed bubbles is higher. Those, in turn, alters the Taylor bubble interface, deforming the once uniform downward liquid film to a non-uniform liquid film inducing a stronger oscillation in the expanding jet at the wake region. Thus, the flow structure in the back of the Taylor bubble, which is deeply affected by liquid jet exiting the liquid film, is also modified. Those modifications lead to the reduction of the wake liquid recirculation volume and the increase of the turbulent intensity in the region.

The CFD model developed and implemented in the present chapter may be used as a baseline for further advanced models. Those could include modeling the liquid shear-

induced turbulent, and more sophisticated models for the bubble induced turbulence, which may be dominant in two-phase flows with low Morton number, typically found in engineering applications and processes, such as air-water two-phase flows.

Chapter 8

Numerical modeling of quasi-real slug flows in air-water systems

ABSTRACT

This chapter presents the modifications of the multiscale VOF-DBM coupled model to allow its use in low liquid viscosity systems, more precisely, air-water flow systems. Therefore, liquid and bubble-induced turbulence models are introduced to the baseline CFD model presented earlier. Due to these modifications, a validation study is conducted independently for the VOF method and DBM, by comparing the numerical results with air-water experimental data from the previous chapters, presenting good agreement. In addition, the results from the modified VOF-DBM model are compared against experimental manufactured air-water slug flows results, presenting a certain level of agreement. The multiscale VOF-DBM model is used to perform a numerical study on air-water manufactured air-water slug flows in different background bubbly flow configurations. According to the results, the gas volume fraction of the dispersed bubbles alters the flow structure around the Taylor bubble, increasing the Taylor bubble terminal velocity and the turbulent intensity on the wake region.

8.1 INTRODUCTION

In the previous Chapter, a two-phase gas-liquid multiscale three dimensional CFD model was developed to simulate flows with different interface length scales. The VOF

model, used to model the large scale interface scales, and the DBM method, used in the modeling the small scale interface scales, were independent validated through results found in the literature, presenting good agreement. Additionally, the effect of the dispersed bubble volume fraction in the "quasi-real" slug flow regime was studied through the coupled VOF-DBM multiscale model. The numerical model results allowed further insights on the modification of the flow structure around Taylor bubbles, due to the presence of dispersed bubbles, which are difficult to be observed experimentally.

In this Chapter, the models described in Chapter 7 are modified to allow its use on flow with low viscosity liquid phase, more precisely, air-water flow systems. In these configurations, the low liquid viscosity results in higher inverse viscosity N_f and lower Morton Mo numbers. Hence, additional models are required to consider the turbulence in the liquid phase which is enhanced Bubble-Induced Turbulence (BIT).

As in Chapter, 7, the VOF and DBM, now modified for the application to air-water systems, are compared with experimental data from Chapters 3 to 6. The"quasi-real" slug flow numerical results are further investigated to reveal important insights from the modification due to the small dispersed bubbles around Taylor bubble.

8.2 MODEL MODIFICATIONS FOR AIR-WATER SYSTEMS

The numerical model used here is based on the one presented in Chapter 7, with modifications due to the resulting lower Morton Mo and Reynolds Re numbers from the air-water system studied here. Those modifications include the use of SIT and BIT model in the liquid phase to account for the turbulence due to the dispersed bubbles. Therefore, the liquid phase stress tensor $\boldsymbol{T}$ from Eq. 7.5 is modified to incorporate the turbulence closure models. In Eq. (7.5), when defining the momentum stress tensor, the laminar liquid viscosity is replaced by an effective liquid viscosity $\mu_{l,eff}$ (ZHANG et al., 2006), which take into account the turbulent viscosity induced by shear within the liquid phase and the bubble induced turbulence (BIT). The BIT is in fact, also shear induced due to the relative velocity between phase, and from the vortex shedding of bubbles. However, (SATO et al., 1981) propose to model the effective viscosity as a linear superposition of model representing each phenomena. Then, the effective viscosity of the liquid phase is defined as,

$$\mu_{l,eff} = \mu_{l,L} + \mu_{l,SIT} + \mu_{l,BIT} \tag{8.1}$$

composed by the contributions of the molecular viscosity $\mu_{l,L}$, the shear-induced turbulent viscosity $\mu_{l,SIT}$ and the bubble-induced turbulent viscosity $\mu_{l,BIT}$.

The shear-induced turbulent viscosity $\mu_{l,SIT}$ is calculated using the sub-grid scale (SGS) model of Vreman (2004), which does not require a wall-damping function. The same model was used by Darmana et al. (2009), where the authors employ the same sub-grid scale model on the simulation of a homogeneous pseudo-2D bubble column operated at relatively high gas hold-ups (up to 8.0%) through the use of DBM. In the SGS model of Vreman (2004), the turbulent viscosity $\mu_{l,SIT}$ is defined as,

$$\mu_{l,SIT} = 2.5\rho_l C_{SIT}^2 \sqrt{\frac{B_\beta}{A_{ij}A_{ij}}} \tag{8.2}$$

where C_{SIT} is a model constant, which is set to its typical value of 0.1 (DARMANA et al., 2009), $A_{ij} = \partial u_j/\partial x_i$, $B_\beta = \beta_{11}\beta_{22} - \beta_{12}^2 + \beta_{11}\beta_{33} - \beta_{13}^2 + \beta_{22}\beta_{33} - \beta_{23}^2$ and $\beta_{ij} = \Delta_i^2 \alpha_{mi}\alpha_{mj}$. Δ_i is the filter width which is based on the cell volume value as $\Delta_i = V_i^{1/3}$.

For the bubble-induced turbulence, the algebraic model proposed by Sato et al. (1981) was adopted to model the Bubble Induced Turbulence in the liquid phase. In this model, the bubble-induced turbulent viscosity is calculated as,

$$\mu_{l,BIT} = \rho_l C_{\mu,BIT} d_B^* \left|\boldsymbol{u}_b^* - \boldsymbol{u}_l\right| \tag{8.3}$$

where d_B^* and $\boldsymbol{u}_b^*$ are average local bubble diameter and velocity on the fluid mesh, which are interpolated from the Lagrangian bubbles to the background particle mesh and then t the fluid mesh. $C_{\mu,BIT}$ is a model constant for which the typical value is define as 0.6 (SATO et al., 1981). In the next section, a parametric study is conducted to evaluate a more suitable $C_{\mu,BIT}$ constant the better fit the experimental results obtained in this thesis.

Due to the different expected flow and bubble dynamics for the air-water system, the bubble force modeling used on Chapter 7 was modified accordingly. Experimental visualizations of the flow, such as high-speed camera and also the PIV/LIF raw images were used to support the implementation of the numerical model. From those experimental observations, the lift force from Eq. (7.12) was removed from the DBM modeling since the bubbles did not show lateral migration, in these experimental conditions. In this chapter, only the cases with lower liquid superficial velocity ($j_l = 3.09 \cdot 10^{-2}$ m/s) from the set studied in Chapter 6 were considered for comparison. For this j_l, even for the lowest j_g considered, a downward liquid flow region is observed near the wall for the bubbly flow condition (i.e., without Taylor bubbles) and, therefore, the bubbles are mainly concentrated in the core region. Standard lift model are no adequate to represent this flow situation with inflection in velocity profiles. As an example, Fig. 8.1 show the raw PIV/LIF

images from the two bubbly flow conditions used for the validation of the bubble flow model, where no evidence of a lateral migration is observed, with the bubbles presenting a uniform distribution on the bulk region. After the removal of the lift force contribution, the remainder forces and closure models are kept the same as the presented in Section 7.2.2.

Figure 8.1 – Images from the PIV/LIF acquisitions in two different gas superficial velocities with $j_l = 3.09 \cdot 10^{-2}$ m/s.

(a) $j_g = 5.89 \cdot 10^{-3}$ m/s
$\overline{\langle \alpha_g \rangle} = 2.9\%$

(b) $j_g = 15.34 \cdot 10^{-3}$ m/s
$\overline{\langle \alpha_g \rangle} = 8.4\%$

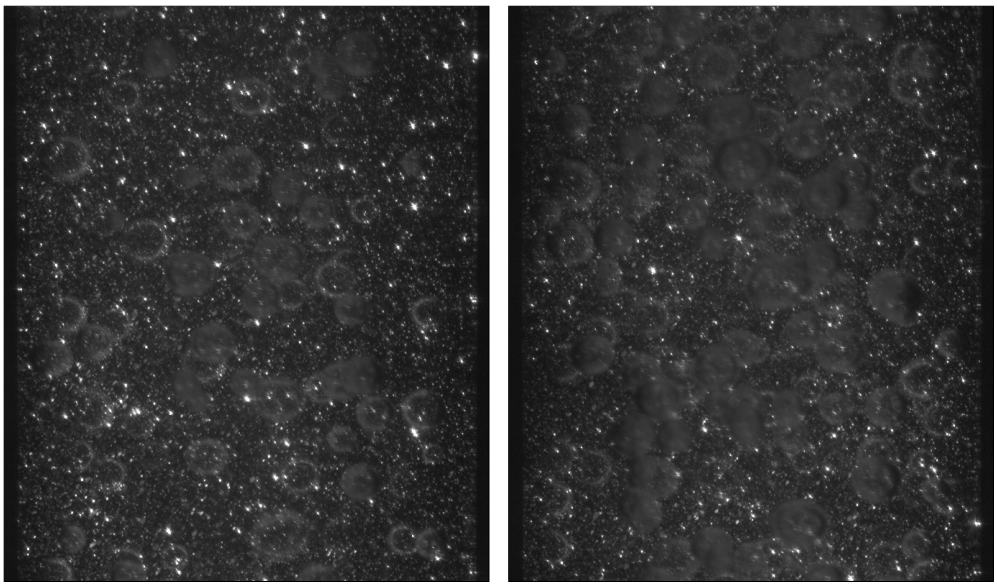

Source - Developed by the author.

Regarding the Taylor bubble flow modelling, according to Pinto et al. (1998), even for the stagnant column situation ($j_l = 0.0$ m/s), for a 26.2 mm internal diameter pipe in a air-water system configuration ($N_f = 13275$), the flow behind a Taylor bubble lies within the turbulent wake regime. Therefore, even for a situation where there is no net liquid flow, a turbulence model is needed for modeling the flow around the Taylor bubble. Shaban and Tavoularis (2018) used the Spalart-Allmaras Improved Delayed Detached Eddy Simulation (ID-DES) (SHUR et al., 2008), available in OpenFOAM (JASAK et al., 2007) to simulate the flow around an air Taylor bubble rising in a stagnant water column. The simulations lied on the turbulent wake flow regime from Pinto et al. (1998) and the results were compared against the experimental data from Van Hout et al. (2002c). According to the numerical/experimental comparison study, then average liquid profiles presented good agreement. At the same time, the turbulent statistics presented similar profiles only far from the Taylor bubble bottom position $z/D < -1.0$.

Recently, Frederix et al. (2020) simulated a turbulent air-water co-current Taylor bubble flow ($Re = 8250$) using the LES with the Vreman (VREMAN, 2004) sub-grid scale (SGS) model. In order to assess the accuracy of the simulation results, the authors compared the numerical liquid velocity profiles in the wake of the Taylor bubble from the experiments of Shemer et al. (2007). As, Shaban and Tavoularis (2018), good agreement was found between the experimental and numerical average liquid profiles, while the turbulent statistics resulted in different values, despite the qualitative agreement.

In the present work, motivated by the availability of the Vreman (VREMAN, 2004) sub-grid scale model on the MultiFlow (WACHEM et al., 2002) solver and the good results obtained by Frederix et al. (2020), the Vreman (2004) sub-grid scale model is used throughout the simulations conducted in this chapter.

8.2.1 VOF and DBM validation in air-water system configurations

In Chapter 7, the VOF and the DBM method were validated against experimental results from the literature. Despite the good agreement with the numerical results, those experiments represented low N_f and Re number flows, where the effects of turbulence and further flow disturbances are negligible. Therefore, the flow is more stable and, its interaction with interfaces is, in general, more easily resolved in the VOF context. Usually VOF modeling of flow with high N_f and Re numbers is more challenging from the numerical point of view. In the present chapter the DBM and VOF results are compared against experimental results for the air-water system configurations, taken from the methods and techniques described in Chapters 3 to 6.

8.2.1.1 VOF model validation for the flow around Taylor bubbles in air-water systems

For the VOF validation, two sets of PIV air-water experiments were conducted to characterize the flow around the Taylor bubble in order to generate experimental data to be compared against the numerical results. In the first experimental point, the needle valve located in the liquid inlet of the experimental bench (see Fig. 5.2) was closed and the Taylor bubbles were injected in a stagnant water column ($j_l = 0.0$ m/s). For the second PIV experiment, the Taylor bubbles were injected in co-current water flow, with a superficial velocity of $j_l = 3.09 \cdot 10^{-2}$ m/s. The results of this last experiment were first shown in Chapter 6 and represent the Exp. 1 of Tab. 6.2.

As in the cases presented earlier, the numerical results presented here and also the DBM validation are averaged over time to allow the comparison with the ensemble averaged PIV results. Video 16 of the supplemental material given in Appendix B shows

a transient animation of the CFD simulations, presenting the estimated Taylor bubble shape ($\gamma = 0.5$ iso-contour) and the axial (z-direction) liquid velocity distribution around the bubble. In addition, the liquid velocity profiles shown in this section are presented in a fixed frame of reference. With respect to the terminal Taylor bubble velocity, the CFD simulations resulted in a $U_{tb} = 0.174$ m/s for the stagnant column situation ($j_l = 0.0$ m/s), and $U_{tb} = 0.226$ m/s for the co-current flow configuration ($j_l = 3.09 \cdot 10^{-2}$ m/s), resulting in a maximum deviation of 1.5% from its experimental values, $U_{tb} = 0.174$ m/s and $U_{tb} = 0.232$ m/s. As previously discussed, the U_{tb} values are averaged over a time period due to the unsteady motion of the Taylor bubbles in the low N_f regime. In addition, due the high N_f and Re numbers and the need for increased resolution in the near-wall region, finer meshes than those used in Chapter 7 were required for the study presented here. Following Fig. 7.8, the mesh consisted on the following configuration: $N_o = 30$; $N_r = 30$; $N_t = 450$; $N_c = 40$ and $N_b = 40$. This mesh configuration resulted in a total number of $N_{total} = 2,285,809$ cells, with an increased mesh resolution close to the duct wall.

Figure 8.2 present the comparison between the numerical and experimental centerline pipe axial liquid velocity profile below the Taylor bubble position for the two j_l experiments. A very good agreement is observed between the numerical and the experimental profiles, with the CFD simulations predicting the maximum centerline axial velocity position close to the one observed experimentally.

Figures 8.3 and 8.4 present the liquid velocity profiles in different sections below the Taylor bubble bottom position. In both cases, in the stagnant column and co-current situations, a good agreement is observed between the numerical and experimental liquid velocity profiles, in the same level as observed in Shaban and Tavoularis (2018) and Frederix et al. (2020). The liquid velocity profiles around the nose are shown in Figs 8.5 and 8.6, which also present a good agreement between the numerical and experimental profiles.

Concerning the comparison of the numerical and experimental turbulent fields, Fig. 8.7 present the turbulent statistics behind the Taylor bubble bottom from the PIV experiments and CFD simulations, showing the contour plots of r.m.s. values of the radial and axial liquid velocity components and the liquid Reynolds stresses. As observed in Fig. 8.7, and also reported in Shaban and Tavoularis (2018) and Frederix et al. (2020), the results do not show an exact agreement on the magnitude of the turbulent field statistics, but rather a qualitative agreement. Therefore, contrary to the comparison based on averaged profiles shown earlier, the analysis of the turbulent fields is based on the qualitative analysis of the contour plots. According to the results, the Vreman SGS

Figure 8.2 – Comparison between the numerical and experimental centerline pipe axial liquid velocity profile below the Taylor bubble bottom position.

(a) $j_l = 0.0$ m/s

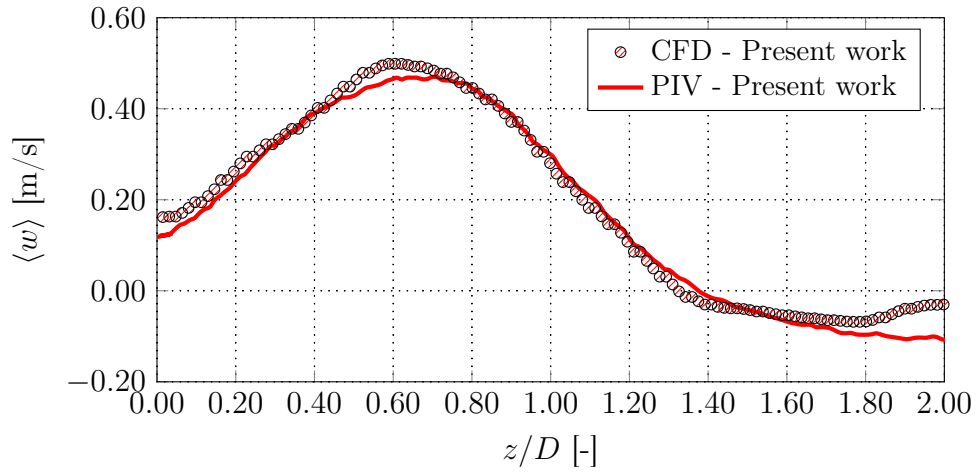

(b) $j_l = 3.09 \cdot 10^{-2}$ m/s

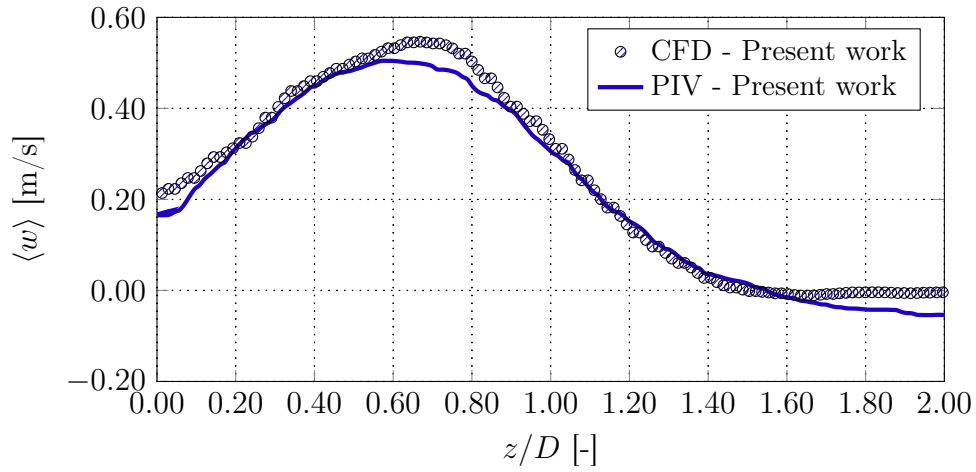

Source - Developed by the author.

model employed in the present simulations was able to predict the turbulence intensity enhancement close to the duct wall out of the sudden expansion (formed by the jet exiting the Taylor bubble liquid film) and the lower level of turbulent intensity close to the Taylor bottom ($0.0 < z/D < -0.5$). The main difference on the PIV and CFD results of Fig. 8.7 is the shape (averaged) of the Taylor bubble bottom, which in the PIV results present a concave shape, while the CFD results present a convex bottom. These differences on bottom shape may come from the combination of experimental and numerical errors. On the experimental side, optical distortions due to light scattering when acquiring the PIV images may occur, distorting the shape near the wall, while on the numerical side, the SGS model may be "over-damping" the Taylor bottom oscillation.

Figure 8.3 – Comparison between the numerical and experimental liquid velocity profiles of the axial (left) and radial (right) components in different sections below the Taylor bubble bottom position for $j_l = 0.0$ m/s.

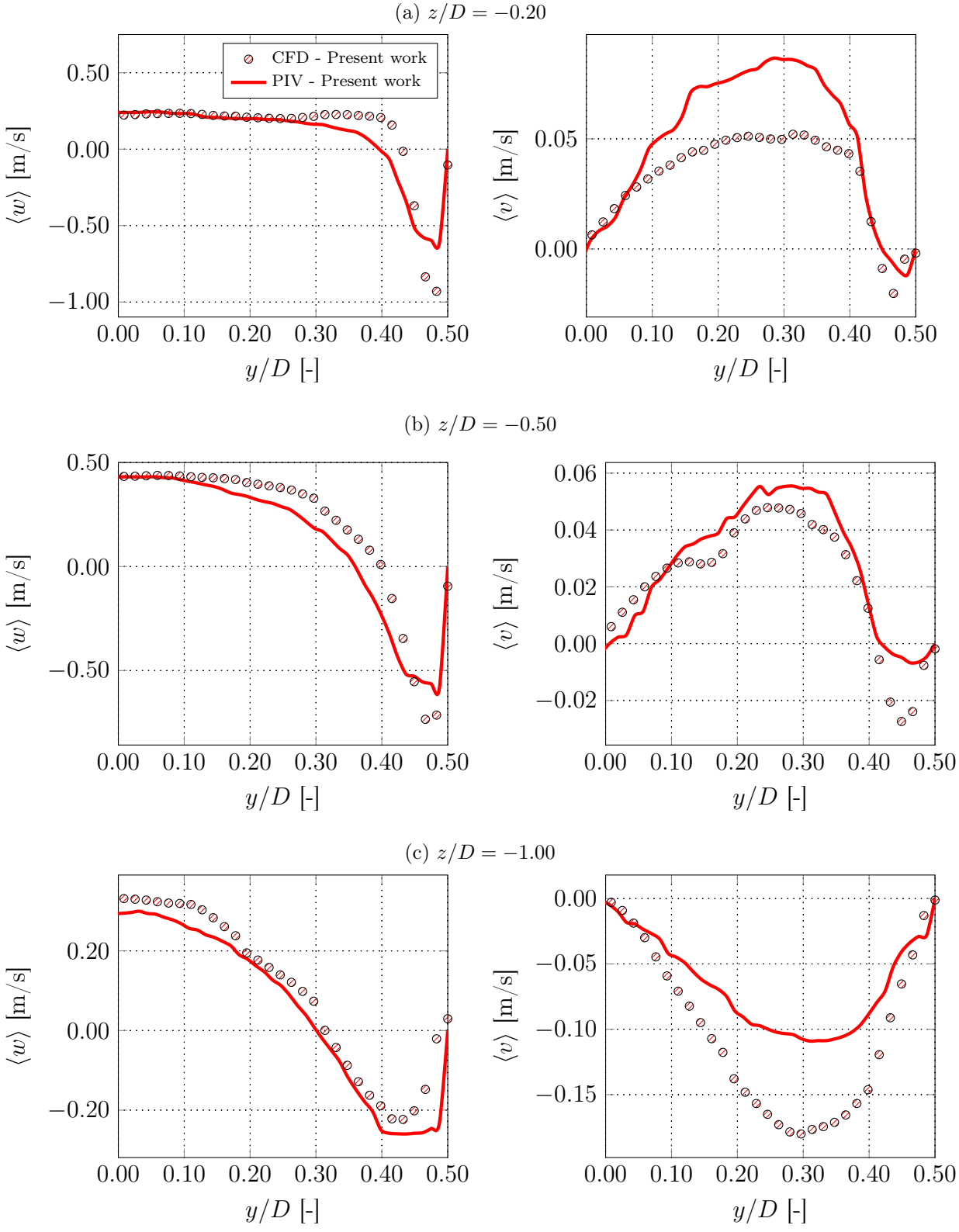

Source - Developed by the author.

Figure 8.4 – Comparison between the numerical and experimental liquid velocity profiles of the axial (left) and radial (right) components in different sections below the Taylor bubble bottom position for $j_l = 3.09 \cdot 10^{-2}$ m/s.

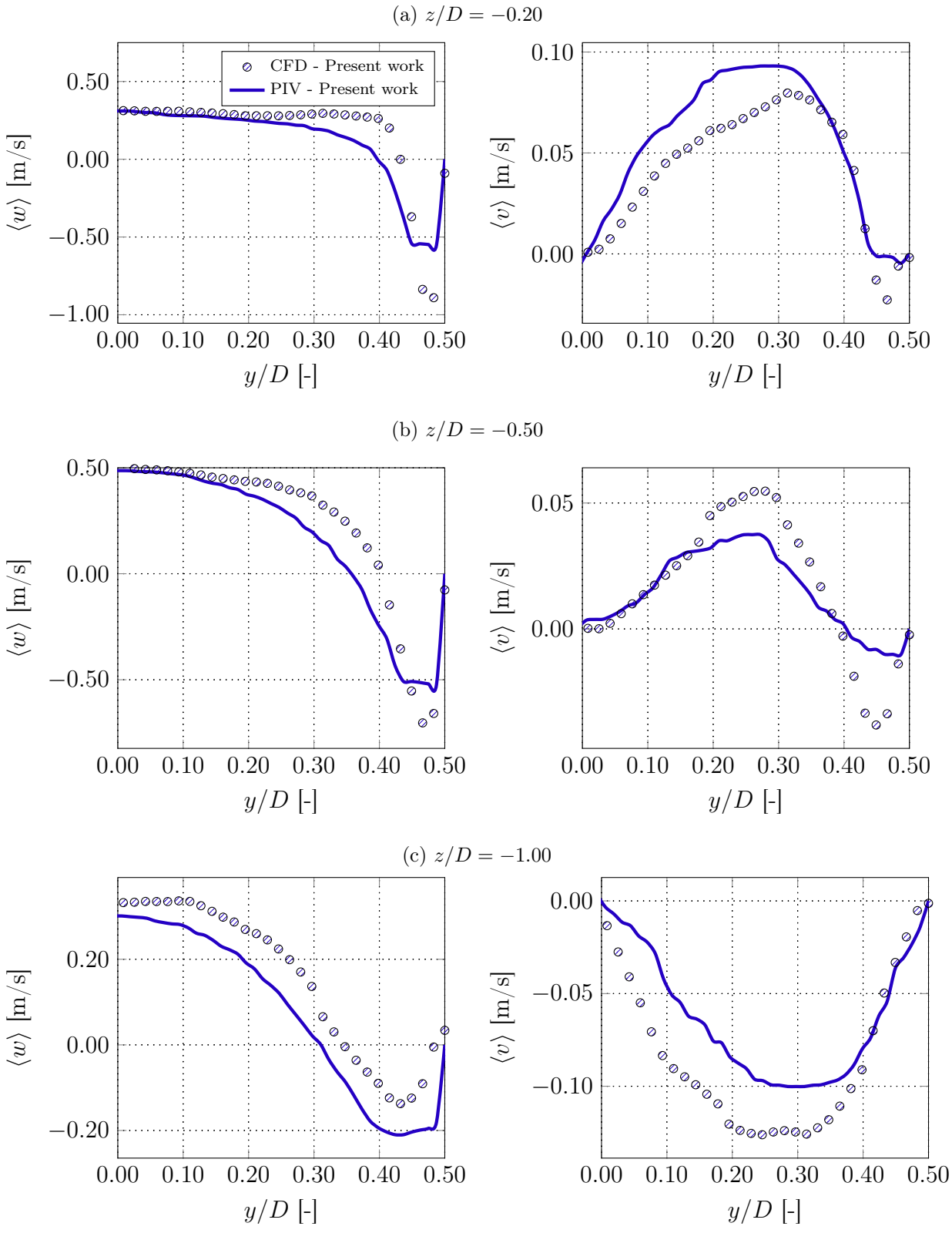

Source - Developed by the author.

Figure 8.5 – Comparison between the numerical and experimental liquid velocity profiles of the axial (left) and radial (right) components in different sections around the Taylor bubble nose tip position for $j_l = 0.0$ m/s.

(a) $z/D = 0.10$

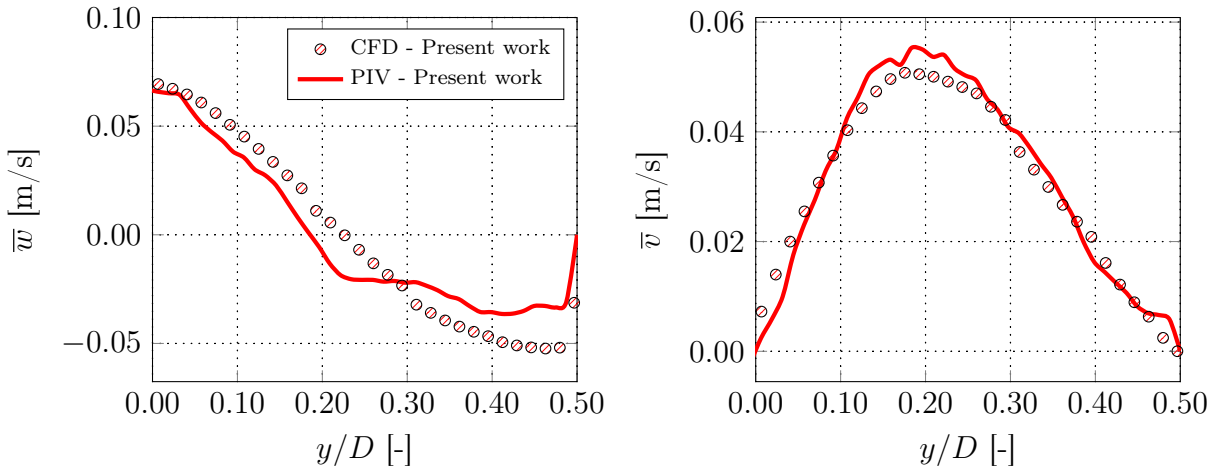

(b) $z/D = 0.05$

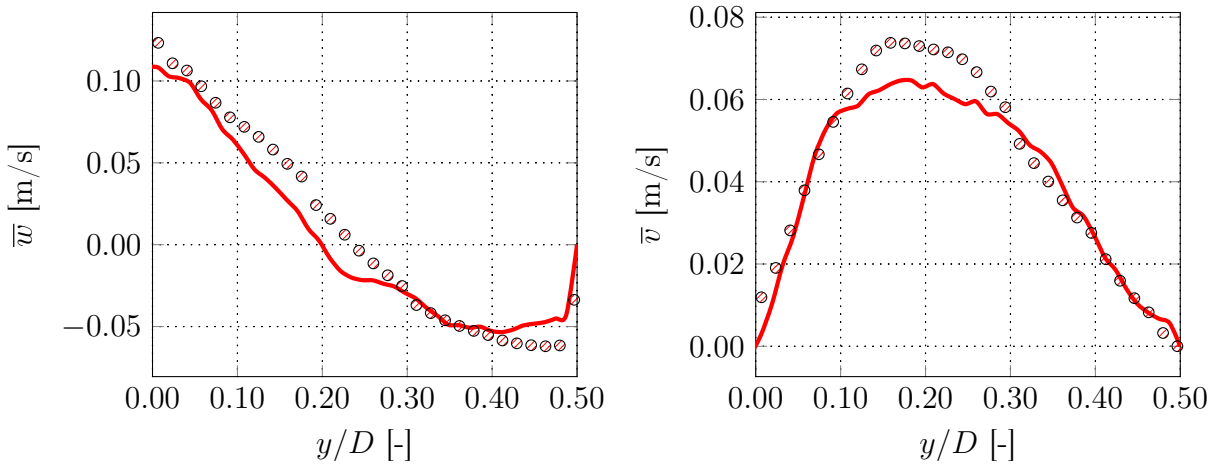

(c) $z/D = -0.10$

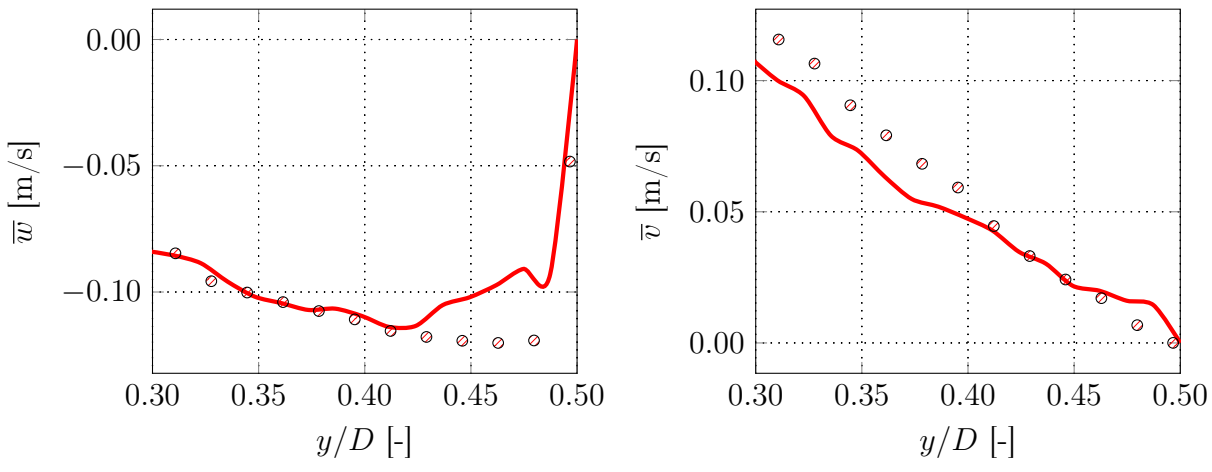

Source - Developed by the author.

Figure 8.6 – Comparison between the numerical and experimental liquid velocity profiles of the axial (left) and radial (right) components in different sections around the Taylor bubble nose tip position for $j_l = 3.09 \cdot 10^{-2}$ m/s.

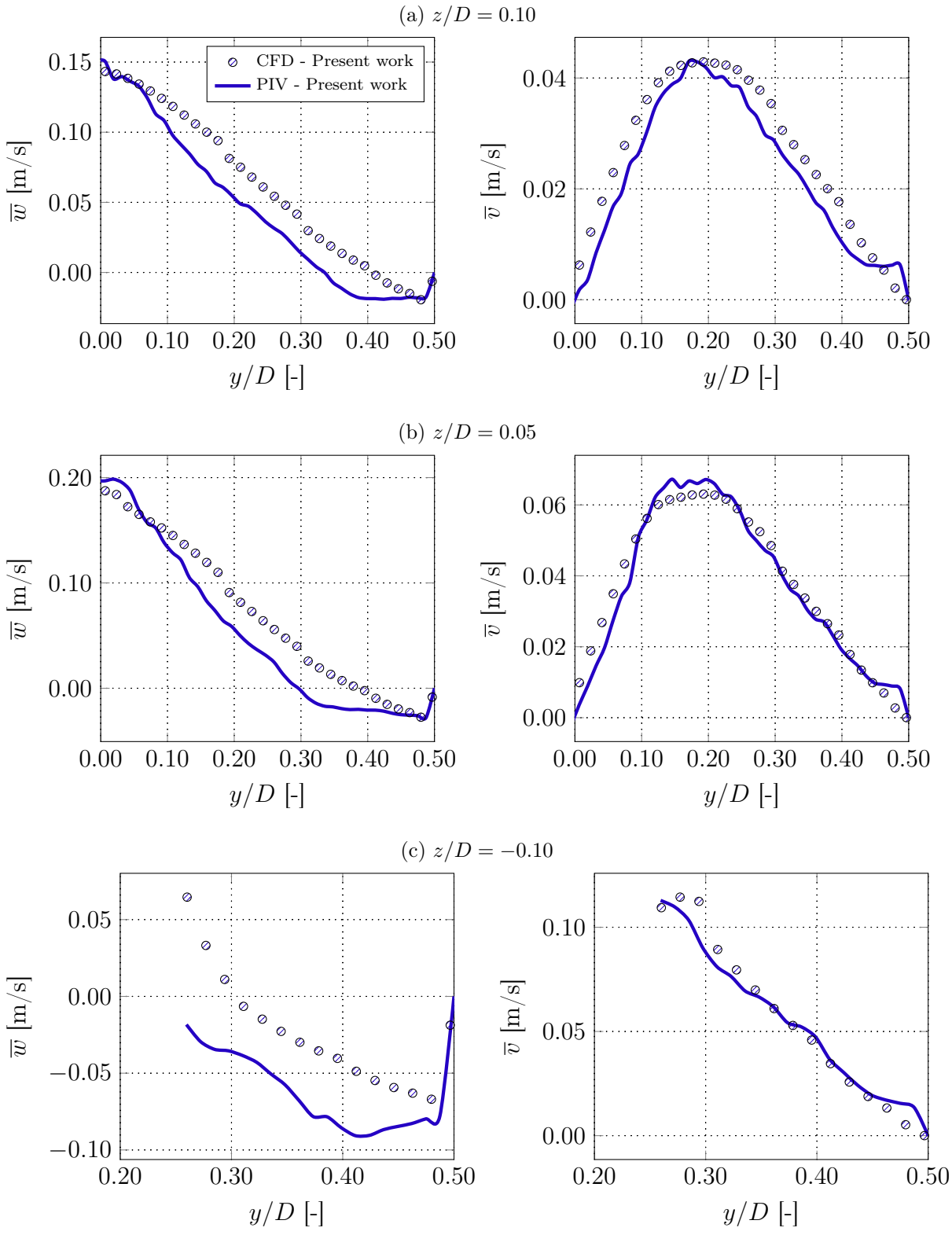

Source - Developed by the author.

In general, from the experimental validation study presented in this section, it is possible to conclude that the VOF method and the SGS turbulence model adopted in the present simulations produce results which represent adequately the flow structure around Taylor bubbles, for the conditions of the experiments developed in this work.

8.2.1.2 DBM Validation

In the previous chapter, the Discrete Bubble Model (DBM) was validated through the comparison of the numerical results against data from the work of Kashinsky and Timkin (1999), for bubbly flows with moderate Monumbers ($\log(Mo) \approx -8.5$) and low liquid Reynolds numbers ($Re_l = 435.5$). According to the validation study presented earlier, the DBM results present good agreement with the experimental results for those flow conditions. However, in those cases the turbulence (internal shear) induced in the liquid phase was negligible and the Bubble Induced Turbulence (BIT) did not play a major role.

In the present chapter, the experiments developed in this work in air-water system and 26.2 mm internal diameter pipe resulted in higher Reynolds ($Re_l = 812$) and lower Morton ($\log(Mo) \approx -10.58$) numbers. Therefore, the DBM model first presented in Chapter 7 was modified accordingly and compared against the experimental bubbly flow PIV data from Chapter 3.

The experimental validation of the Discrete Bubble Model is conducted by comparing the ensemble average numerical and experimental results of the liquid phase from the PIV results shown in Chapter 3. Two experimental points were chosen from Tab. 3.1, representing the air-water bubbly flow experiment with $j_l = 3.09 \cdot 10^{-2}$ m/s and two experiments with $j_g = 5.89 \cdot 10^{-2}$ m/s (Exp. 8 with $\langle \alpha_g \rangle = 2.9$ %) and $j_g = 15.34 \cdot 10^{-2}$ m/s (Exp. 10 with $\langle \alpha_g \rangle = 8.4$ %) m/s. Following the DBM validation conducted in the previous chapter, periodic boundary conditions and a reduced domain of $L = 10.0D$ are employed in the simulations, using the same mesh resolution parameters described in Section 8.2.1.1. In order to better reproduce the experimental results, when initializing the simulation, the dispersed bubbles are added to the domain following the bubble size distribution acquired from the analysis of the corresponding high-speed camera images, as shown in Chapter 4.

Figure 8.8 shows the experimental and numerical results from the two studied flow conditions, presenting the time-averaged axial velocity and the r.m.s fluctuations of the axial and radial liquid velocity components. As in the previous chapter, the CFD results from the Fig. 8.8 were averaged over a period of 5.0 FTTs in a line located in the

middle section of the numerical domain. As observed, for the numerical results, due to the uncertainty regarding the $C_{\mu,BIT}$ BIT model constant from Sato et al. (1981), four liquid velocity profiles, each with a different $C_{\mu,BIT}$ value.

According to Fig. 8.8, the $C_{\mu,BIT}$ value influences the axial velocity distribution and turbulent statistics in the two studied bubbly flow configurations. From the given results, the typical 0.60 value of $C_{\mu,BIT}$ presents small deviations from the experimental axial liquid velocity distribution. However, this configuration is still capable of predicting the axial liquid velocity distribution, with a flatter distribution on the core region and the downward moving liquid film near the pipe wall. Additionally, the parametric study on the $C_{\mu,BIT}$ revealed that a smaller value, or simply neglecting the term, provides better results. Despite of providing better results on the $\overline{\langle \alpha_g \rangle} = 2.9\%$ bubbly flow experiments ((Fig. 8.8a)), the simulations performed with $C_{\mu,BIT} = 0.0$ on the $\overline{\langle \alpha_g \rangle} = 8.4\%$ configuration presented numerical instabilities which did not lead to a converged solution. The hypothesis here is that the additional diffusion introduced by the BIT model, trend to stabilize the simulations. Regarding the turbulent statistics, in the case with lower gas volume fraction (Fig. 8.8a) $\overline{\langle \alpha_g \rangle} = 2.9\%$) a good agreement is, in general, observed on the radial and axial r.m.s fluctuations between the experimental and numerical profiles, where the different values of $C_{\mu,BIT}$ considered, lead to better or worse agreement for the different component fluctuations.

For the second case of higher gas volume fraction, $\overline{\langle \alpha_g \rangle} = 8.4\%$ (Fig. 8.8b)), the numerical simulations over-predict the turbulent intensity on both radial and axial components. On this second case, with a higher gas volume fraction, despite over-predicting the axial centerline velocity, the axial liquid distribution resulted in better results with the $C_{\mu,BIT} = 0.60$ value.

In general, the results of Fig. 8.8 show a good agreement between the numerical and experimental results. Particularly, when keeping in mind the associated uncertainties related to the use of PIV technique on experimental characterization of bubbly flows, where even with the image processing methods described in Chapter 3, still suffer from "noise" due to the light scattered by the interface of the dispersed bubbles. In addition, according to the parametric $C_{\mu,BIT}$ study, the typical 0.60 value of $C_{\mu,BIT}$ presented better results, when considering the different values of $\overline{\langle \alpha_g \rangle}$ and component fluctuations, and will be used in further simulations.

Figure 8.7 – Comparison of the experimental(left) and numerical (right) turbulent fields around the Taylor bubble bottom for: a)$j_l = 0.0$ m/s and b) $j_l = 3.09 \cdot 10^{-2}$ m/s. First row: Contour plot of the r.m.s. values of the radial velocity component fluctuations $v'_{l,rms}(r,z)$; Second row: Contour plot of the r.m.s. values of the axial velocity component fluctuations $w'_{l,rms}(r,z)$; Third row: Contour plot of the liquid Reynolds stresses $\overline{v'w'}$.

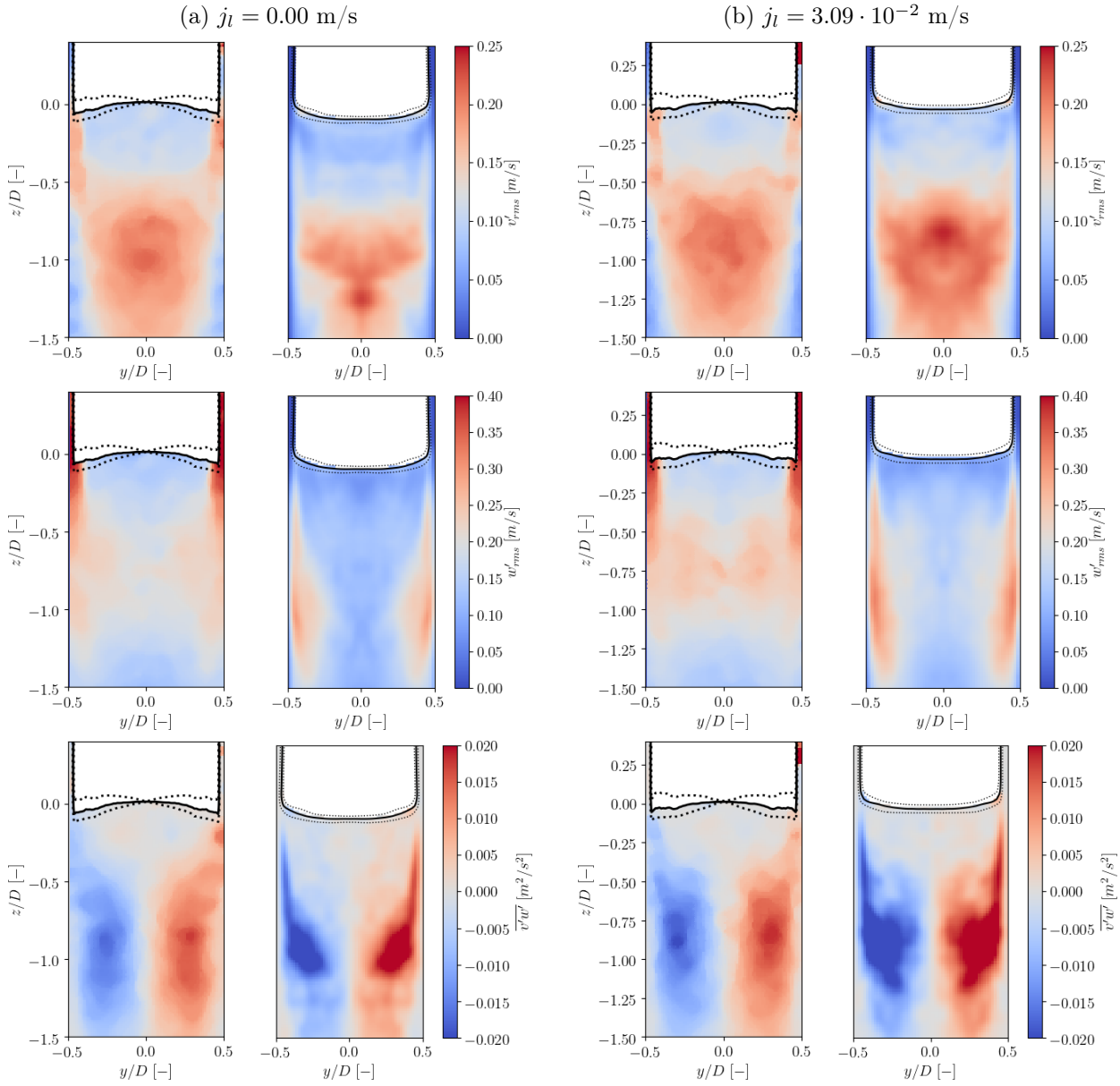

Source - Developed by the author.

Figure 8.8 – Comparison of the numerical and experimental (PIV) liquid velocity profiles presenting the radial profile of the time-averaged axial velocity (top), r.m.s fluctuations of the radial velocity components (middle) and its axial component (bottom). The numerical results also present the effect of the $C_{\mu,BIT}$ on the average axial liquid velocity and turbulent statistics. The superficial liquid velocity is set to $j_l = 3.09 \cdot 10^{-2}$ m/s.

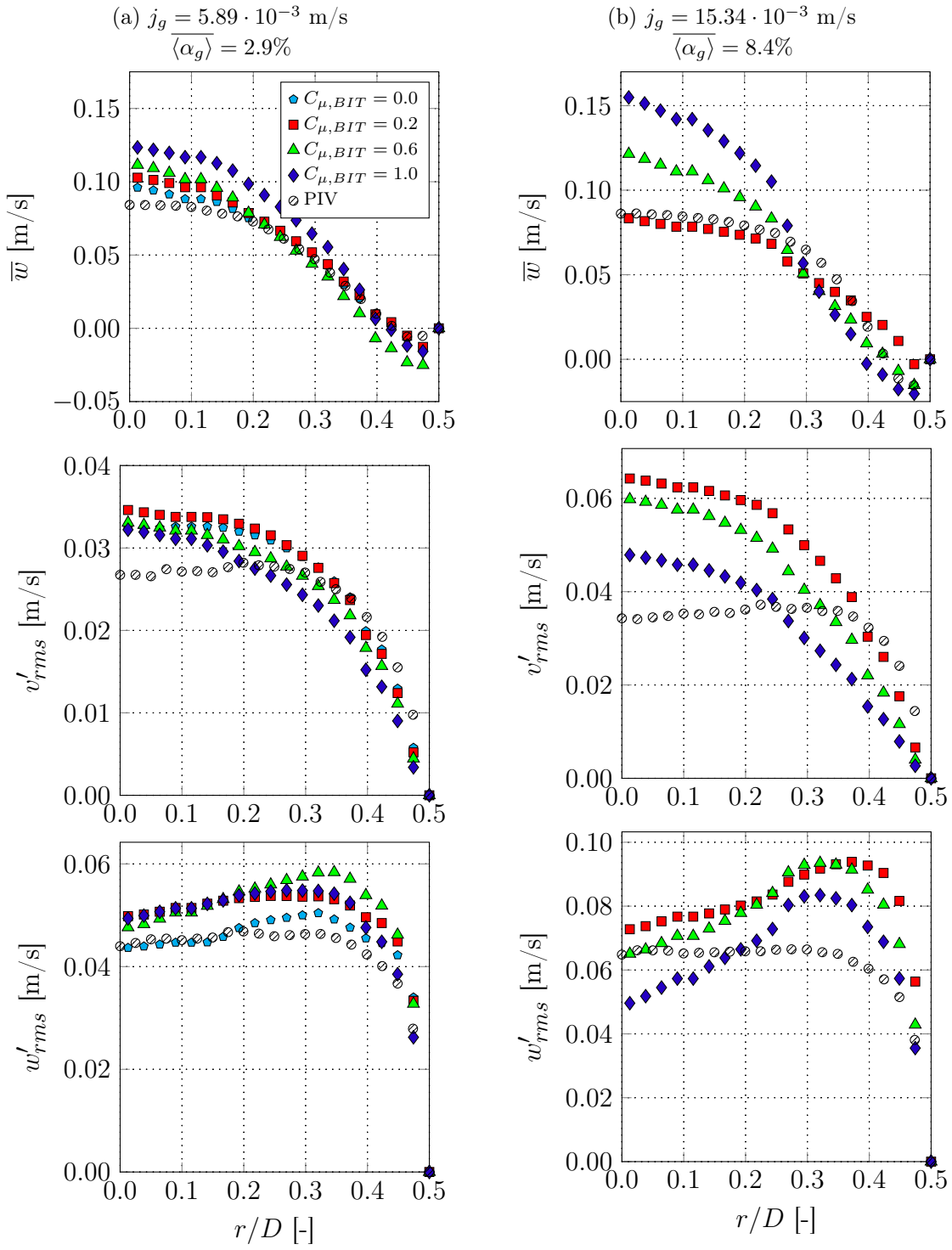

Source - Developed by the author.

8.3 AIR-WATER "QUASI-REAL" FLOW

In order to study the effect of the volume fraction of dispersed bubbles $\overline{\langle \alpha_g \rangle}$ on the flow structure around the Taylor bubbles, air-water manufactured slug flow simulations were conducted in this section. Aiming to use some of the results from Chapter 6 for comparison with numerical results, the same test section geometry was used for the air-water simulations. Due to the difficulties in simulating high Re_l flows, only the background laminar liquid flow configuration from the previous chapters, $j_l = 3.09 \cdot 10^{-2}$ m/s, were considered. Additionally, aiming to gain a better insight on the modifications due to the dispersed bubbles, cases with lower void fractions were simulated here, since the experimental setup described in the previous Chapters could not operate on these configurations. The numerical setup, the VOF-DBM simulation initialization and the averaging procedure follows the description presented in Section 7.4.2.

A total of five flow conditions were simulated, each with a different background bubbly configuration: a) $\overline{\langle \alpha_g \rangle} = 0.00$ %; b) $\overline{\langle \alpha_g \rangle} = 0.95$ %; c) $\overline{\langle \alpha_g \rangle} = 1.75$ %; d) $\overline{\langle \alpha_g \rangle} = 2.45$ % and e) $\overline{\langle \alpha_g \rangle} = 3.60$ %. The bubbly flow configuration for condition e), represents the Exp. 2 flow condition from the experimental study presented in Chapter 6, and its results will be used to assess the simulation results. In order to provide a qualitative picture of the different simulated cases, Video 17 of the supplementary material given in Appendix B presents the transient VOF-DBM animations of the different background bubbly conditions, while Video 18 presents a close-up view around the Taylor bubbles.

8.3.1 Experimental verification of the CFD results

The VOF and DBM model were previously independently validated by comparing the results from the numerical simulations against the experimental results from the air-water experiments conducted in the present work. In this section, the numerical results obtained for the flow of Taylor bubbles in a bubbly flow stream are compared with those obtained in the experimental investigation conducted in this work, presented in Chapter 6. First, the effect of dispersed bubbles on rising velocity of Taylor bubbles is analyzed and model results are compared with experimental ones. In addition, the results for nose oscillations are also compared once, as already discussed, these are closely related to the increase of rising velocity of Taylor bubbles when flowing together with dispersed bubbles. Then, a comparison is presented for the flow structure in the wake of Taylor bubbles, for the cases with and without dispersed bubbles.

8.3.1.1 Effect of the dispersed bubbles on the Taylor bubble rising velocity

Figure 8.9 presents the Taylor bubble rising velocity from air-water manufactured slug flow simulations, for different volume fraction of dispersed bubbles, $\overline{\langle \alpha_g \rangle}$. As done in the previous Chapter, due to the induced fluctuations from the dispersed bubbles, the rise velocity of Taylor bubbles present a fluctuating behavior. Therefore, velocities shown in Fig. 8.9 presents the time-averaged values of $\langle U_{tb} \rangle$. In order to compare the numerical and experimental results, the terminal velocities obtained from the high-speed camera images, given in Chapter 6 are also plotted in Fig. 8.9.

According to Fig. 8.9, the results from the numerical simulations follows the trend observed experimentally in Chapter 6 and numerically in Chapter 7, where $\langle U_{tb} \rangle$ increases with the void fraction from the background bubbly flow. As observed in Fig. 8.9, the predicted $\langle U_{tb} \rangle$ from the CFD simulations presents a good agreement with the experimental values in the $\overline{\langle \alpha_g \rangle} = 3.6\%$ background bubbly flow condition, with approximately 4.5 % deviation from the experimental result.

Figure 8.9 – Effect of the dispersed bubbles on the Taylor bubble rising velocity from the experimental results of Chapter 6 and the multiscale CFD models. The error bars on the experimental results represent the associated uncertainty. The superficial liquid velocity is set to $j_l = 3.09 \cdot 10^{-2}$ m/s.

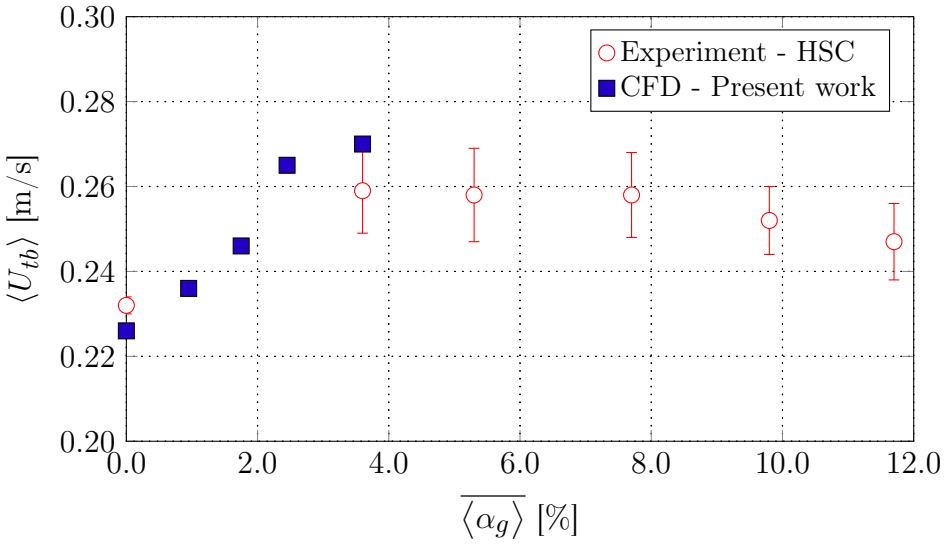

Source - Developed by the author.

As discussed in previous chapters, there is a direct correlation between the terminal rising velocity of the Taylor bubble and the deformation and radial oscillations of the Taylor bubble nose interface. As more bubbles are present in the flow, higher is the flow perturbation ahead of the nose position, leading to stronger oscillations of the Taylor

bubble. This mechanism was observed in numerical results from Chapter 7 in the case of air-glycerol "quasi-real" slug flow stagnant column simulations and experimentally in Chapter 6 in an air-water system. From the cases simulated in the present Chapter, Fig. 8.10 show the PDFs from the nose tip displacement, where it is clear that the multiscale model correctly reproduces the mechanisms observed in experiments in Chapter 6. The results show that as the volume fraction of dispersed bubbles $\overline{\langle \alpha_g \rangle}\%$ increases, stronger is the lateral movement of the Taylor bubbles. Additionally, the PDF obtained for the case of $\overline{\langle \alpha_g \rangle} = 3.6\%$ is compared with the experimental PDF obtained in Chapter 6, presenting good agreement.

8.3.1.2 Results comparison of the flow structure around Taylor bubbles in the presence of dispersed bubbles

Figure 8.11 shows the contour plots of the averaged liquid velocity and turbulent kinetic energy fields at the wake region of Taylor bubble. The experimental and numerical results are qualitatively compared for the cases without dispersed bubbles ($\overline{\langle \alpha_g \rangle} = 0.0$) and for $\overline{\langle \alpha_g \rangle} = 3.6$ %, which represents, respectively the flow conditions of Exp. 1 and 2 in Chapter 6.

According to the results presented in Fig. 8.11, the CFD model does not capture the modification of the flow structure in the wake region adequately, due to the presence of dispersed bubbles. The observed differences may arise from the experimental uncertainties from the PIV techniques, but more probably from the limitations of the models used in the CFD simulations. Differently from the case of the nose region, where the CFD model was able to capture the trends of flow modifications due to the dispersed bubbles, the flow in the wake region presents additional complexities. In this region, turbulence modeling and closure models for the interfacial transfer between the liquid and dispersed bubbles could have a higher impact on the results.

The results comparison presented in this section demonstrate that the multi-scale VOF-DBM model is capable to predict, to a certain extent, the flow modifications around the Taylor bubbles due to dispersed bubbles in air-water systems. The oscillations and deformation of the Taylor bubble nose, induced by the momentum transferred from dispersed bubbles to liquid phase ahead of Taylor bubbles, and its effect on U_{tb}, are adequately predicted by the CFD model, following the experimental results of Chapter 6. These findings, in particular the PDFs shown Fig. 8.10e), supports the low Mo modifications from the baseline VOF-DBM model presented in Chapter 7, since the nose lateral movement is a direct effect from the SIT and BIT from the flow ahead of the Taylor bubble. On

Figure 8.10 – Probability density function (PDF) of the nose tip position from different backgroundbubbly flow gas volume fractions.

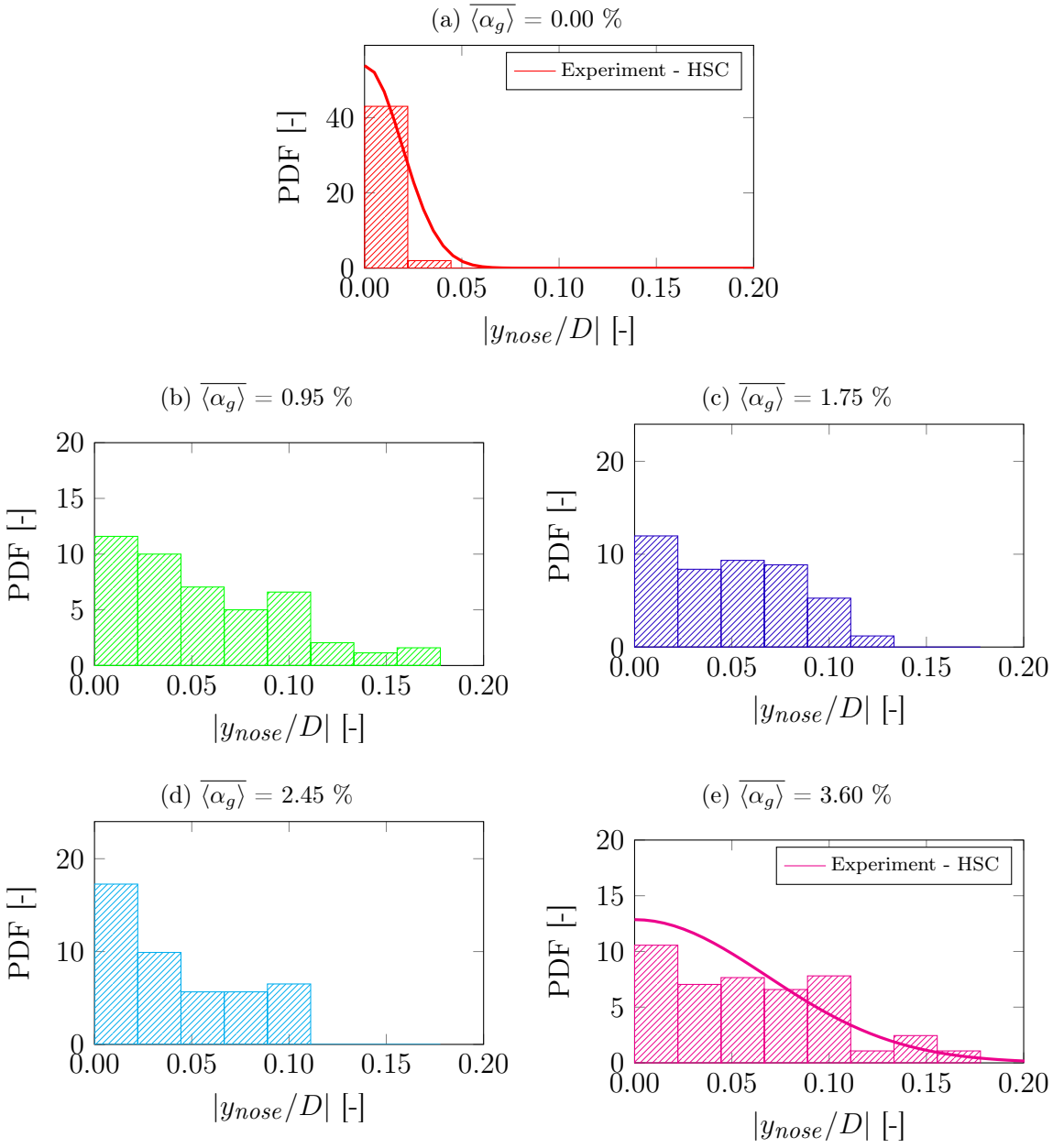

Source - Developed by the author.

the other side, the flow structure modifications by the dispersed bubbles, at the wake region of Taylor are not adequately predicted by the CFD model. In this regard, further closure models for turbulence interactions and other closure models for phenomena that become significant at low Mo and high N_f numbers, such as the Basset forces(MUNIZ; SOMMERFELD, 2020) must be implemented an its effect on the flow, analyzed.

Figure 8.11 – Modifications on the flow structure behind the Taylor bubbles due to the dispersed bubbles from the experimental results (left) and predicted by the CFD model (right). The contour plots show the ensemble average radial (top) and axial (middle) liquid velocity and the turbulent kinetic energy (bottom) distribution.

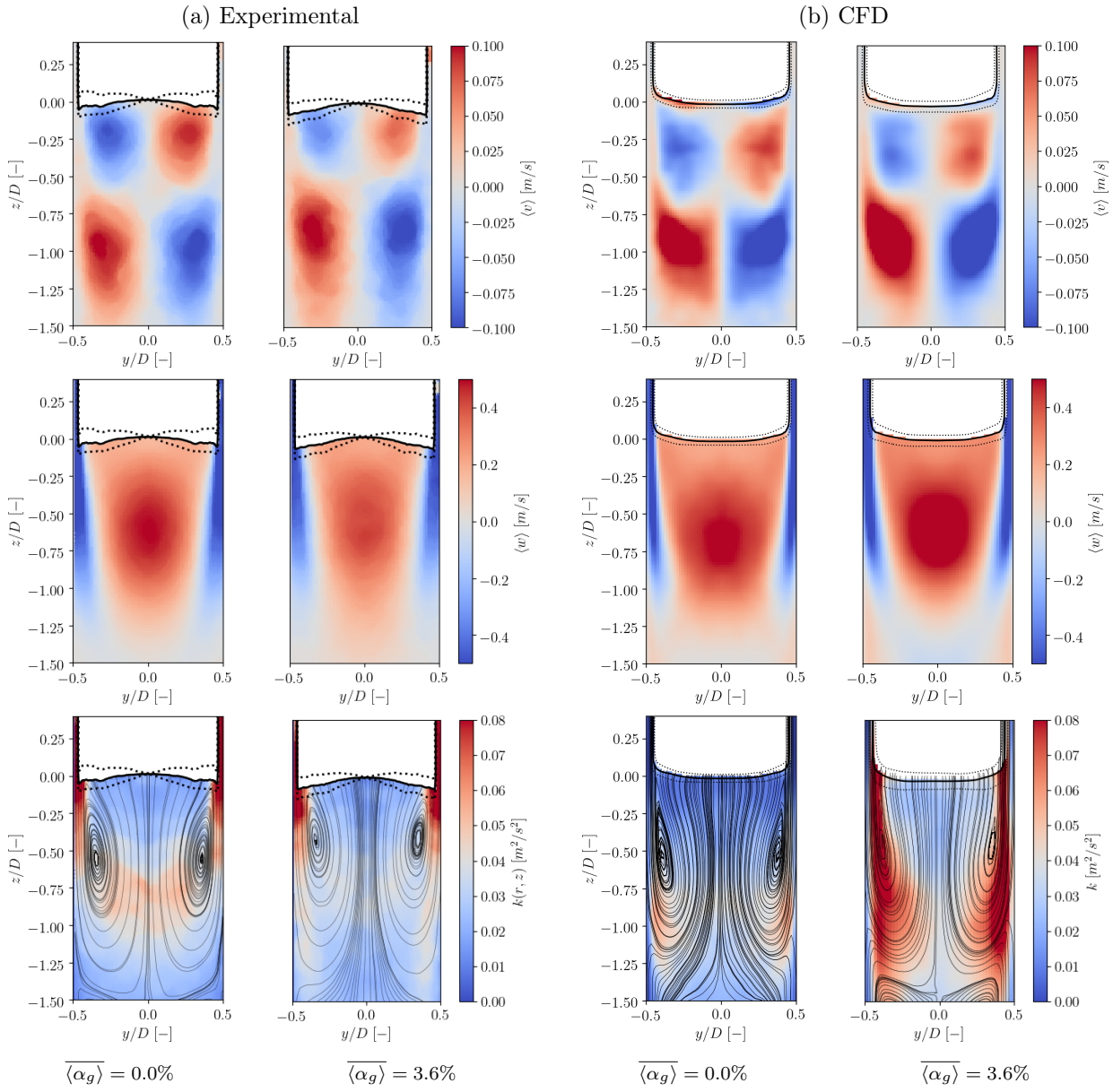

Source - Developed by the author.

8.3.2 Effect of the dispersed bubbles on the flow structure around the Taylor bubbles in an air-water system

In this section, the implemented CFD model Is used to conduct a study of the flow structure around Taylor bubbles in the presence of dispersed bubbles. The results are presented for averaged velocities and turbulence statistics, following the same numerical

averaging procedure presented in the previous Chapter.

Figures 8.12 and 8.13 show the time-averaged liquid velocity fields around the Taylor bubbles nose and bottom in different background bubbly configurations.

According to the results of Fig. 8.12, around the Taylor bubble nose, the modifications introduced by the dispersed bubbles follow the same trends observed in the results of Chapter 7, where the radial component of the liquid velocity reduces as $\overline{\langle \alpha_g \rangle}$ increases and the axial component, $\overline{w}$ distribution is modified due to the lateral motion of the Taylor Bubble noses. This behavior is due to the induced downward velocity in the near wall regions and the higher peak velocity in the central region, when dispersed bubbles are present in the background flow. This background flow structure also promotes a thicker film at the nos region and a more pointed nose shape.

Figure 8.12 – Time averaged velocity fields around the Taylor bubble nose for different simulated background bubbly flow conditions. First row: Velocity vector plots; Second row: Contour plot of the ensemble average radial liquid velocity $\overline{v}$; Third row: Contour plot of the ensemble average axial liquid velocity $\overline{w}$.

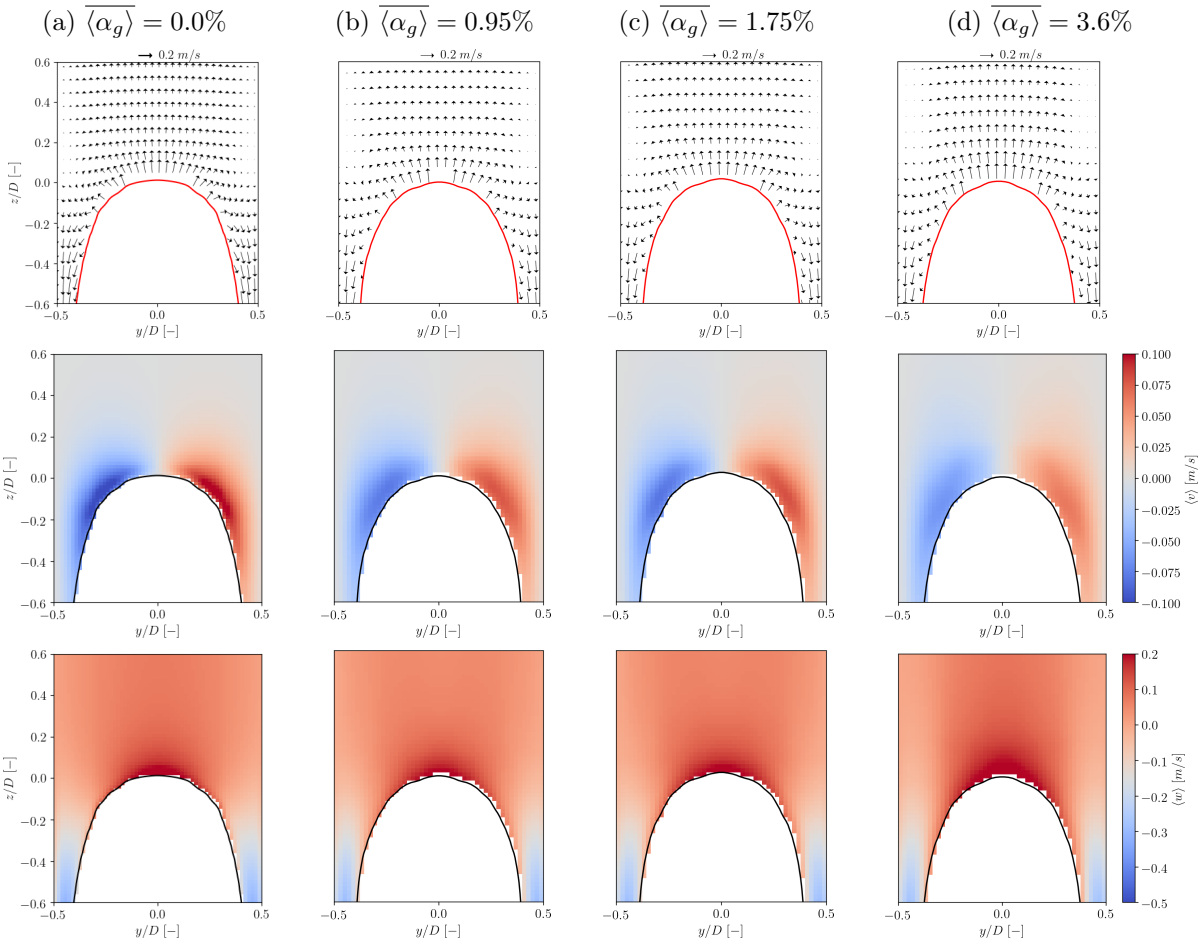

Source - Developed by the author.

The results obtained from the CFD model for the flow structure in the wake region, and its modification introduced BY the dispersed bubbles are presented below. However, once these results do not follow the experimental observation, they are presented only for a qualitative overview but no further analysis can be performed on these results.

Video 19 of the supplementary material given in Appendix B present the instantaneous axial and radial liquid velocity contours around the Taylor bubble for different $\overline{\langle \alpha_g \rangle}$ simulated cases.

Figure 8.14 shows the turbulent fields around and below the Taylor bubble tail. The results from the velocity component fluctuations show that the turbulent intensity follows the trend observed on the average liquid velocity. According to the contour plots from Fig. 8.14 the turbulent intensity increases in the first manufactured slug flow case, Fig. 8.14b), and then further decreases with $\overline{\langle \alpha_g \rangle}$. The observed decrease of the turbulent intensity with the dispersed bubbles void fraction $\overline{\langle \alpha_g \rangle}$ agrees with the experimental observed behavior from the $j_l = 3.09 \cdot 10^{-2}$ m/s from Chapter 6.

Figure 8.13 – Time averaged fields around the Taylor bubble tail from different simulated background bubbly flow conditions. First row: Velocity vector plots; Second row: Velocity vector plots streamlines; Third row: Contour plot of the ensemble average radial liquid velocity $\overline{v}$; Fourth row: Contour plot of the ensemble average axial liquid velocity $\overline{w}$.

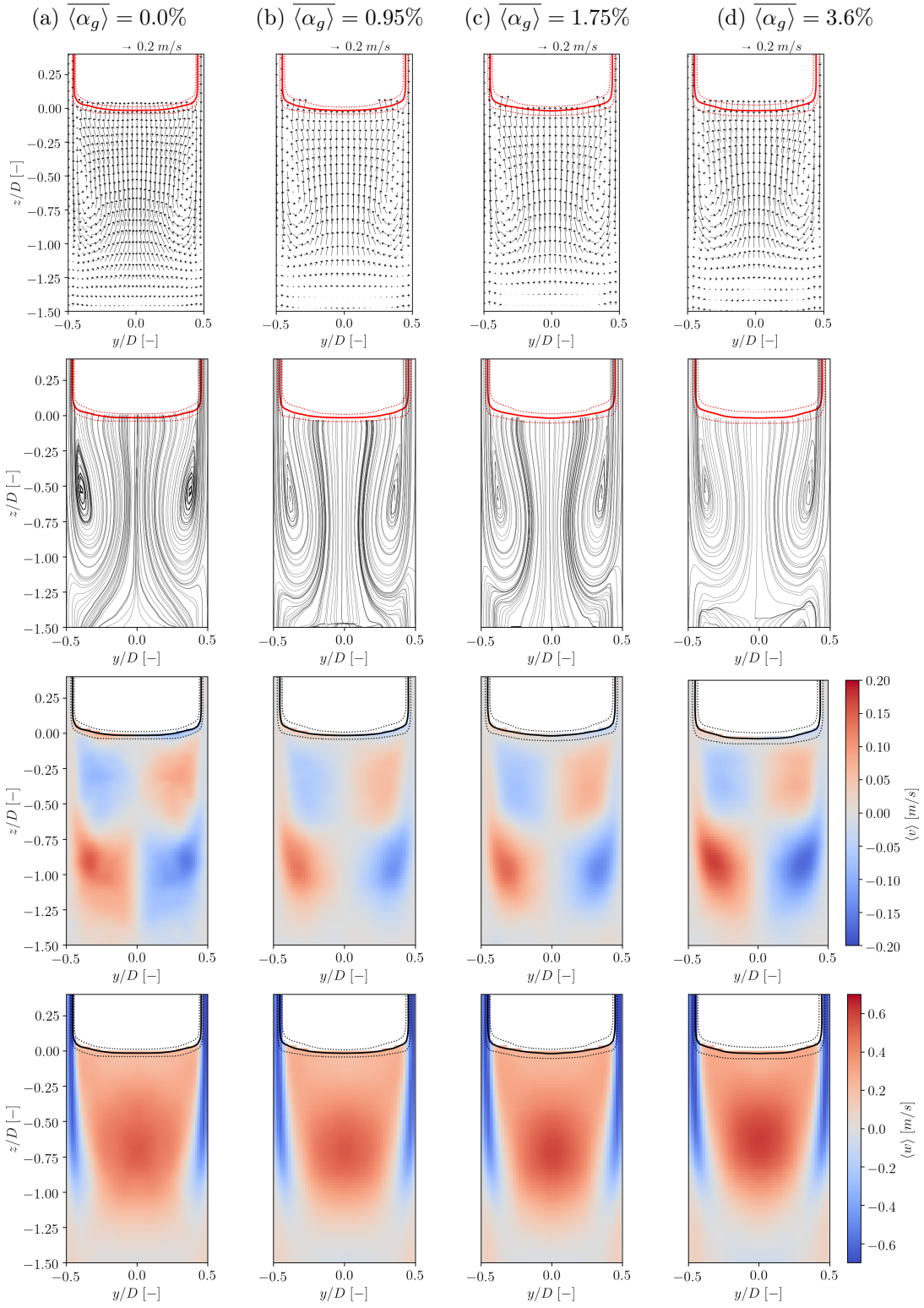

Source - Developed by the author.

Figure 8.14 – Turbulent fields around the Taylor bubble tail from the different simulated background bubbly flow conditions. First row: Contour plot of the r.m.s. values of the radial velocity component fluctuations v'_{rms}; Second row: Contour plot of the r.m.s. values of the axial velocity component fluctuations w'_{rms}; Third row: Contour plot of the turbulent kinetic energy k.

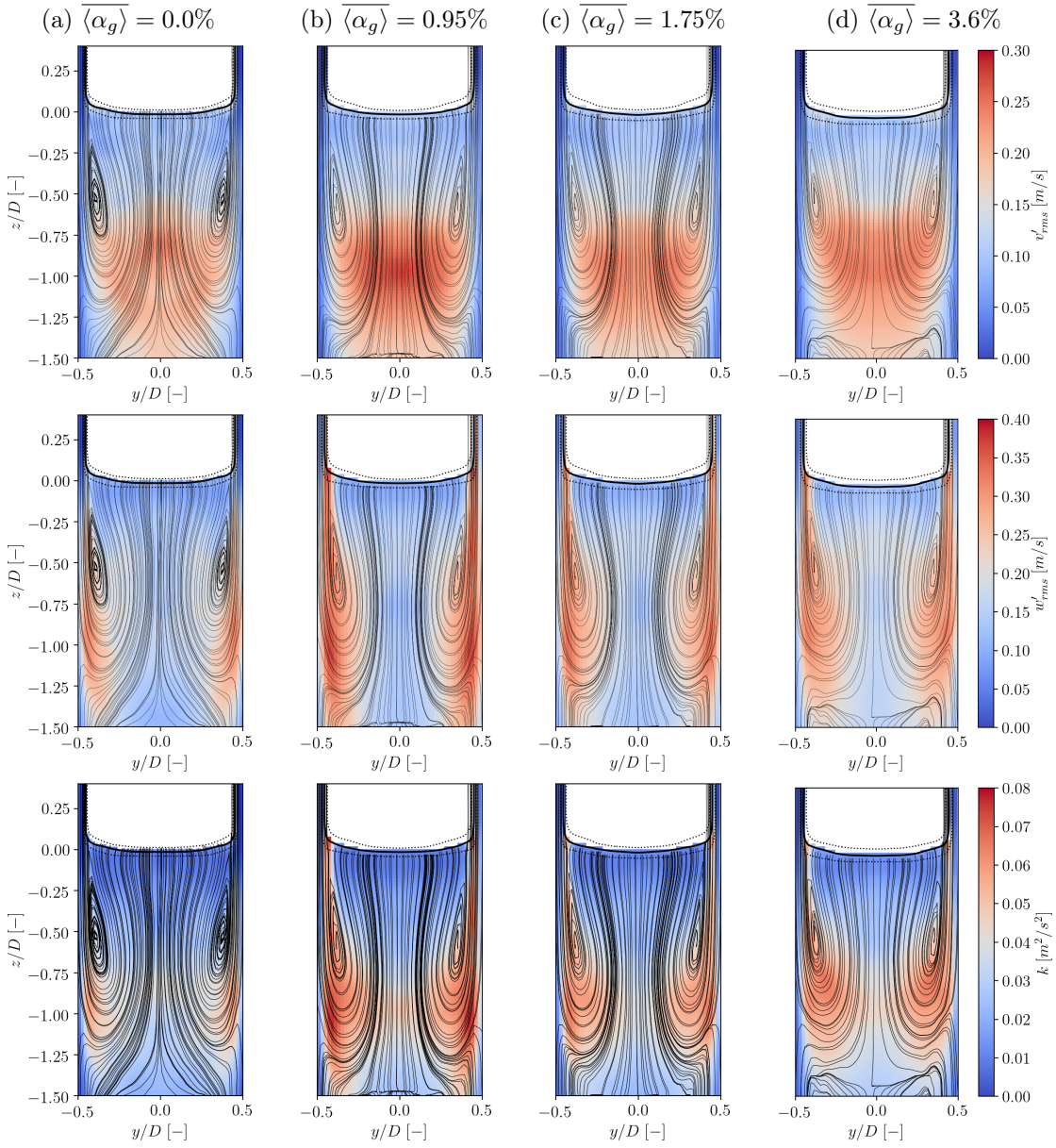

Source - Developed by the author.

8.4 CONCLUSIONS

This chapter presented the modifications of the coupled VOF-DBM multiscale model described in Chapter 7, where the baseline model was extended to allow its use on low liquid viscosity system, such as air-water flow configurations, common in engineering applications. Therefore, liquid and bubble-induced turbulence models were added to the previously implemented CFD model. Additionally, further modifications were introduced in the DBM model from the experimental observations presented throughout Chapters 3 to 6.

In order to verify the modified CFD model, the DBM and VOF methods were independently validated from air-water experimental data from the previous chapters, presenting good agreement. Additional verification analysis was conducted by comparing the numerical and experimental results of a manufactured air-water slug flow condition, previously presented in Chapter 6. According to the VOF-DBM verification, the CFD model presented agreement into a certain extent, capturing the increase of the terminal Taylor bubble velocity, the oscillation and deformation of the Taylor bubble nose interface. However, at the wake region of Taylor, the numerical model was not able to adequately predicted flow structure modifications by the dispersed bubble.

The CFD multiscale model was used to conduct a numerical study of the effect of the dispersed bubbles on the flow structure around the Taylor bubbles in an air-water system. This study considered background bubbly flows with lower void fractions than those presented in Chapter 6 and could not be studied in the experimental setup used in this thesis. The numerical results from this study complemented the experimental observations from the previous chapter and allowed a better comprehension of the modification on the flow structure by the dispersed bubbles.

Chapter 9

Summary and final remarks

Following the thesis organization, this chapter presents a general summary of the main contributions of this work and recommendations for future work. Conclusions about specific studies developed, were presented in each chapter.

9.1 CONCLUSIONS

Due to the complexity of the different flow morphologies found in real two-phase flows, great effort is devoted for better understanding two-phase liquid-gas flows, with different phase morphologies and interfacial length scales in the same flow domain. These may come from experimental investigations, which aims the detailed measurement through different methods and techniques, and also, through detailed multi-dimensional numerical studies. Following those two approaches, this thesis presented an experimental and numerical study of two-phase flows with different interface length scales, aiming at the characterization and further understanding of the complex interactions among fluid phases with different interfacial length scales. Therefore, this thesis focused on the study of the manufactured "quasi-real" slug flow regime, which is similar to the vertical slug flow regime and is composed by independent injection of Taylor bubbles in a bubbly stream. Then, from this approach, it was possible to study a flow similar to the real slug flow, where gas-liquid interfaces of different length scales co-exist, but with controlled conditions. These included control of the gas and liquid superficial velocities, the Taylor bubbles length and the dispersed bubble gas volume fraction.

The experimental characterization of two-phase flows is a challenging task since the

presence of the gas-liquid interfaces interferes the flow measurement an additional effort is required to circumvent these issues. In particular, when applying the Particle Image Velocimetry (PIV), the primary experimental technique used in the present thesis, the gas-liquid interfaces disperse the light from the laser source, deteriorating the measured liquid velocity fields. Aiming at the acquisition of consistent characterization of bubbly flows, Chapter 3 present a novel method the phase discrimination in PIV images, which allows the use of the technique even in dense bubbly flows. Moreover, Chapter 3 presents a novel Particle Tracking Velocimetry (PTV) technique that allows the experimental characterization of the gas phase by tracking the individual motion of the small dispersed gas in high-speed camera images. As opposed to other PTV technique implementations found in the literature until this moment, the technique described in Chapter 3 can be applied in dense bubbly flows situation.

Despite the success of PTV technique presented in Chapter 3 in the characterization of dense bubbly flows, the developed method cannot correctly capture the bubble shape in those gas volume fraction situations. To overcome this limitation, Chapter 4 presents a Convolution Neural Network (CNN) based method for the bubble identification and shape reconstruction of bubbles in bubbly flows using high-speed camera images. The method robustness allows for the consistent estimation of the Bubble Size Distributions (BSD) even in the dense bubbly flows.

After overcoming the experimental limitations from the presence of the small interface length scales in Chapters 3 and 4 , Chapter 5 presents the developed experimental apparatus for manufacturing of a three-field phase flow, i.e., manufactured "quasi-real" slug flow regime, where a liquid, small and large scale gas phases co-existed. As with the small dispersed bubbles, the acquisition of the PIV images around the Taylor bubble is not straight forward, since the gas-liquid interface disperses the light from the light source. In addition, the air-water two-phase flow studied in this thesis results in higher inverse viscosity numbers N_f, which results in a strongly fluctuating flow. Therefore, as an advance from the current experimental studies found in the literature, a dynamic masking procedure was developed to identify the Taylor bubbles in the raw PIV images and remove the spurious vectors from the liquid velocity fields. In addition, a triggering system based on the signal of a Light Diode Technique (LDP) analogue signal was developed to allow the acquisition of consistent PIV liquid velocity fields around the Taylor bubble. The PTV technique described in Chapter 3 was further extended to identify, track and reconstruct the shape of Taylor bubbles in high-speed camera images. The experimental apparatus and measurement techniques were extensively validated and verified, ensuring that the experimental setup was able to produce a manufactured air-water slug flows and the flow

around the Taylor bubble could be characterized by the different experimental techniques.

In Chapter 6 the techniques developed from Chapters 3 to 5 are used to conduct an experimental study of the flow structure around Taylor bubbles in the presence of dispersed bubbles, through the experimental characterization of manufactured air-water slug flows in different operating conditions. The results show that the rising velocity is strongly correlated with the eccentric motion of the deforming nose of the Taylor bubble. It was observed that, for the same liquid superficial velocity j_l, when dispersed bubbles are present, the nose shape oscillation and deformation is enhanced. According to the PIV results and the visual analysis of the high-speed camera videos, the flow structure behind the Taylor bubble is strongly modified by the presence of the dispersed bubbles.

Through the deeper understanding acquired from the experimental observations and results from Chapter 6, a multiscale three-dimensional CFD model is developed in Chapter 7 for the simulation of liquid-gas two-phase flow with different interface length scales. The numerical model is based on the coupling of the VOF method and the Discrete Bubble Model (DBM), incorporating a consistent physical approach for interactions among dispersed bubbles and bubble-wall collisions, considering a soft-sphere model, and the interaction between dispersed bubbles and large scale interfaces. Besides the implementation of the multiscale VOF-DBM model, the two methods are independently verified through the comparison of the numerical results against experimental data found in the literature. The proposed multiscale model was used to conduct a numerical study on a simplified "quasi-real" slug flow regime, where the Taylor bubbles were injected in a bubbly viscous stagnant liquid column. Despite the simplifications, the numerical results followed the experimental observations from Chapter 6. According to the CFD results, the presence of small dispersed bubbles significantly affects the Taylor bubble terminal velocity, increasing its terminal velocity as more dispersed bubbles are added to the background bubbly flow. Moreover, it was shown that the flow structure in the back of the Taylor bubble is deeply affected by liquid jet exiting the liquid film.

The multiscale model developed in Chapter 7 is then modified in Chapter 8 to allow its application for the case of air-water flow systems, where liquid phase viscosity is one order of magnitude lower, resulting in much higher inverse viscosity N_f and lower Morton Mo numbers. Hence, additional models are incorporated into the baseline multiscale VOF-DBM model developed in Chapter 7, which address the liquid and bubble induced turbulence (BIT). The DBM and VOF methods were independently validated from air-water experimental data from Chapters 3 to 5, presenting good agreement. The modified CFD multiscale model was used to conduct a numerical study of the effect of the dispersed bubbles on the flow structure around the Taylor bubbles in an air-water system in lower

void fraction configurations. The results from these simulations revealed the need of further improvement of the turbulence and interfacial closure model to represent this complex flows, mainly in the wake region of Taylor bubbles where the small dispersed bubbles interact with flow recirculation, resulting in a very challenging flow in terms of modeling.

The experimental study on two-phase flows with different interface length scales presented in this thesis resulted in not only detailed experimental results, but also in the development of novel experimental methods and techniques, which can be applied to different two-phase flow morphologies. Thus, from the methodology point of view, the methods described in this thesis should be seen as a contribution of this thesis. The experimental results, in particular those considering different interfacial length scales, are important for a better comprehension of the complex interactions between different flow morphologies present in real slug air-water flows. In addition, the detailed experimental results are an important contribution, since this data can be used as verification and validation data in novel multidimensional CFD models. The multiscale VOF-DBM model developed is the main numerical contribution from this thesis, since until the present moment, most of the numerical advances considered large bubbles flowing in solid-liquid slurries, or did not incorporated the detailed physics present in the bubble dynamics of bubbly flow. In addition, the novel VOF-DBM model was verified against experimental results from this thesis, showing that the developed multiscale model was able to predict part of the features and modifications observed in the experimental study on manufactured slug flows.

9.2 RECOMMENDATIONS FOR FUTURE WORKS

Based on the advances presented in this thesis, suggestion and recommendations for futures works are presented here.

The experimental techniques described throughout Chapters 3 and 4 could be employed to detailed experimental characterization of bubbly flows, aiming a better comprehension of the bubble-induced turbulence in different pipe diameters and geometries. The CNN-based approach presented in Chapter 4 could also be extended for the identification of dispersed bubbles or phase discrimination in PIV raw images, allowing for detailed characterization of bubbly flows. In particular, the use of an accurate phase discrimination method, based on deep-learning methods, could allow the reconstruction of the void fraction distribution on the PIV plane, which is currently not feasible with the method described in Chapter 3. Regarding the PTV method, mortification on the optical arrangement used in this thesis could achieve a thin depth of field, and simple adjustments in

the CNN-based method described in Chapter 4 would allow the discrimination of focused and defocused bubbles. Those suggestions would lead to extensive experimental data that could be easily compared to CFD results.

Regarding the experimental apparatus and techniques described in Chapter 5, those could be used for the detailed characterization of real air-water slug flows and also for the experimental study on the train of Taylor bubbles in controlled conditions. Those experimental results, together with the numerical multiscale models described in Chapters 7 and 8 could be employed to a better comprehension of complex interactions between the different interface length scales in air-water slug flows. Moreover, further experimental investigations, such as the study ogf bubbly flows in sudden expansion or accelerated flows, could be investigated through the experimental methods and techniques described in this thesis. In special, those experimental investigations could be employed on the development of new numerical models, such as BIT or closure models required for the DBM or models based on the Eulerian-Eulerian approach.

Bibliography

ACUÑA, C. A.; FINCH, J. A. Tracking velocity of multiple bubbles in a swarm. **International Journal of Mineral Processing**, Elsevier B.V., v. 94, n. 3-4, p. 147–158, 2010.

AKHMETBEKOV, Yerbol K.; ALEKSEENKO, Sergey V.; DULIN, Vladimir M.; MARKOVICH, Dmitriy M.; PERVUNIN, Konstantin S. Planar fluorescence for round bubble imaging and its application for the study of an axisymmetric two-phase jet. **Experiments in Fluids**, v. 48, n. 4, p. 615–629, 2010.

AMARAL, Carlos EF do; ALVES, Rafael F; SILVA, Marco J da; ARRUDA, Lúcia VR; DORINI, Leyza; MORALES, Rigoberto EM; PIPA, Daniel R. Image processing techniques for high-speed videometry in horizontal two-phase slug flows. **Flow Measurement and Instrumentation**, Elsevier, v. 33, p. 257–264, 2013.

ARAÚJO, J. D.P.; MIRANDA, J. M.; PINTO, A. M.F.R.; CAMPOS, J. B.L.M. Wide-ranging survey on the laminar flow of individual Taylor bubbles rising through stagnant Newtonian liquids. **International Journal of Multiphase Flow**, v. 43, p. 131–148, 2012.

ARAÚJO, JDP; MIRANDA, JM; CAMPOS, JBLM. Flow of two consecutive Taylor bubbles through a vertical column of stagnant liquid—A CFD study about the influence of the leading bubble on the hydrodynamics of the trailing one. **Chemical Engineering Science**, Elsevier, v. 97, p. 16–33, 2013.

AUTON, Timothy Robert. **Dynamics of bubbles, drops, and particles in motion in liquids.** 1984. PhD thesis – University of Cambridge.

BARNEA, D.; LUNINSKI, Y.; TAITEL, Y. Flow pattern in horizontal and vertical two phase flow in small diameter pipes. **The Canadian Journal of Chemical Engineering**, Wiley Subscription Services, Inc., A Wiley Company, v. 61, n. 5, p. 617–620, 1983.

BESAGNI, Giorgio; INZOLI, Fabio. Comprehensive experimental investigation of counter-current bubble column hydrodynamics: Holdup, flow regime transition, bubble size distributions and local flow properties. **Chemical Engineering Science**, Elsevier, v. 146, p. 259–290, 2016.

BRACKBILL, JU; KOTHE, Douglas B; ZEMACH, C1. A continuum method for modeling surface tension. **Journal of computational physics**, Elsevier, v. 100, n. 2, p. 335–354, 1992.

BRADSKI, G. The OpenCV Library. **Dr. Dobb's Journal of Software Tools**, 2000a.

BRADSKI, Gary. The OpenCV Library. **Dr. Dobb's Journal: Software Tools for the Professional Programmer**, Miller Freeman Inc., v. 25, n. 11, p. 120–123, 2000b.

BRÖDER, D; SOMMERFELD, M. Planar shadow image velocimetry for the analysis of the hydrodynamics in bubbly flows. **Measurement Science and Technology**, v. 18, n. 8, p. 2513–2528, 2007.

BRÖDER, D.; SOMMERFELD, M. An advanced LIF-PLV system for analysing the hydrodynamics in a laboratory bubble column at higher void fractions. **Experiments in Fluids**, v. 33, p. 826–837, 2002.

BUGG, J. D.; SAAD, G. A. The velocity field around a Taylor bubble rising in a stagnant viscous fluid: Numerical and experimental results. **International Journal of Multiphase Flow**, v. 28, n. 5, p. 791–803, 2002.

CAMPOS, J. B. L. M.; CARVALHO, J. R. F. Guedes De. An experimental study of the wake of gas slugs rising in liquids. **Journal of Fluid Mechanics**, Cambridge University Press, v. 196, n. -1, p. 27, 1988.

CAMPOS, JBLM; DE CARVALHO, JRF Guedes. An experimental study of the wake of gas slugs rising in liquids. **Journal of Fluid Mechanics**, Cambridge University Press, v. 196, p. 27–37, 1988.

CERNE, Gregor; PETELIN, Stojan; TISELJ, Iztok. Coupling of the Interface Tracking and the Two-Fluid Models for the Simulation of Incompressible Two-Phase Flow. **Journal of Computational Physics**, v. 171, n. 2, p. 776–804, 2001.

CERQUEIRA, R.F.L. **Metodos de Captura da Interface em Escoamentos Multifasicos**. [S.l.], 2016. Monografia de Estudo Dirigido, Programa de Pos-Graduacao em Engenharia, Universidade Federal de Santa Catarina, Florianopolis-SC, Brasil.

CERQUEIRA, R.F.L.; PALADINO, E.E.; YNUMARU, B.K.; MALISKA, C.R. Image processing techniques for the measurement of two-phase bubbly pipe flows using particle image and tracking velocimetry (PIV/PTV). **Chemical Engineering Science**, Pergamon, v. 189, p. 1–23, 2018a.

CERQUEIRA, Rafael FL de; PALADINO, Emilio E; BRITO, Ronei M; MALISKA, Clovis R; MENEGHINI, Cristiano. Experimental apparatus and flow instrumentation for the investigation of a quasi-real slug flows in vertical ducts. **Experimental Thermal and Fluid Science**, Elsevier, v. 102, p. 421–451, 2019a.

CERQUEIRA, Rafael FL de; PALADINO, Emilio E; BRITO, Ronei M; MALISKA, Clovis R; MENEGHINI, Cristiano. Experimental apparatus and flow instrumentation for the investigation of a quasi-real slug flows in vertical ducts. **Experimental Thermal and Fluid Science**, Elsevier, v. 102, p. 421–451, 2019b.

CERQUEIRA, RFL; PALADINO, EE; MALISKA, CR. A computational study of the interfacial heat or mass transfer in spherical and deformed fluid particles flowing at moderate Re numbers. **Chemical Engineering Science**, Elsevier, v. 138, p. 741–759, 2015.

CERQUEIRA, RFL; PALADINO, EE; YNUMARU, BK; MALISKA, CR. Development of a Particle Tracking Velocity Measurement Technique for the Study of Gas-liquid Flows With Different Interfacial Length Scales in Vertical Pipes. In: PROCEEDINGS of the 17th Brazilian Congress of Thermal Sciences and Engineering. [S.l.]: ABCM, 2018b.

CERQUEIRA, RFL; PALADINO, EE; YNUMARU, BK; MALISKA, CR. Image processing techniques for the measurement of two-phase bubbly pipe flows using particle image and tracking velocimetry (PIV/PTV). **Chemical Engineering Science**, Elsevier, 2018c.

CHOLLET, François et al. **Keras**. [S.l.: s.n.], 2015. `https://keras.io`.

CLIFT, Roland; GRACE, John R; WEBER, Martin E. **Bubbles, drops, and particles**. [S.l.]: Courier Corporation, 2005a.

CLIFT, Roland; GRACE, John R; WEBER, Martin E. **Bubbles, drops, and particles**. [S.l.]: Courier Corporation, 2005b.

DA SILVA ., M. J.; THIELE, S.; ABDULKAREEM, L.; AZZOPARDI, B. J.; HAMPEL, U. High-resolution gas-oil two-phase flow visualization with a capacitance wire-mesh sensor. **Flow Measurement and Instrumentation**, Elsevier Ltd, v. 21, n. 3, p. 191–197, 2010.

DANTEC DYNAMICS. **Measurement Principles of PIV**. [S.l.: s.n.], 2020 (accessed June 3, 2020). Available from: `https://www.dantecdynamics.com/solutions-applications/solutions/fluid-mechanics/particle-image-velocimetry-piv/measurement-principles-of-piv/`.

DARMANA, D.; DEEN, N. G.; KUIPERS, J. A.M. Detailed modeling of hydrodynamics, mass transfer and chemical reactions in a bubble column using a discrete bubble model. **Chemical Engineering Science**, v. 60, n. 12, p. 3383–3404, 2005.

DARMANA, D.; DEEN, N. G.; KUIPERS, J. A.M.; HARTEVELD, W. K.; MUDDE, R. F. Numerical study of homogeneous bubbly flow: Influence of the inlet conditions to the hydrodynamic behavior. **International Journal of Multiphase Flow**, Elsevier Ltd, v. 35, n. 12, p. 1077–1099, 2009.

DAVIES, RM; TAYLOR, Geoffrey Ingram. The mechanics of large bubbles rising through extended liquids and through liquids in tubes. In: [s.l.]: The Royal Society London, 1950. v. 200. P. 375–390.

DELNOIJ, E; KUIPERS, J a M; SWAAIJ, W P M van; WESTERWEEL, J. Measurement of gas-iquid two-phase flow in bubble columns using ensemble correlation {PIV}. **Chemical Engineering Science**, v. 55, n. 17, p. 3385–3395, 2000.

DENNER, Fabian. **Balanced-force two-phase flow modelling on unstructured and adaptive meshes**. 2013. PhD thesis.

DENNER, Fabian; EVRARD, Fabien; WACHEM, Berend GM van. Conservative finite-volume framework and pressure-based algorithm for flows of incompressible, ideal-gas and real-gas fluids at all speeds. **Journal of Computational Physics**, Elsevier, p. 109348, 2020.

DENNER, Fabian; WACHEM, Berend G. M. van. Fully-Coupled Balanced-Force VOF Framework for Arbitrary Meshes with Least-Squares Curvature Evaluation from Volume Fractions. **Numerical Heat Transfer, Part B: Fundamentals**, v. 65, n. 3, p. 218–255, 2014.

DHILLON, Anamika; VERMA, Gyanendra K. Convolutional neural network: a review of models, methodologies and applications to object detection. **Progress in Artificial Intelligence**, Springer Berlin Heidelberg, n. 0123456789, 2019.

DUMITRESCU, Dumitru Theodor. Strömung an einer Luftblase im senkrechten Rohr. **ZAMM-Journal of Applied Mathematics and Mechanics/Zeitschrift für Angewandte Mathematik und Mechanik**, Wiley Online Library, v. 23, n. 3, p. 139–149, 1943.

EGGELS, JGM; UNGER, F; WEISS, MH; WESTERWEEL, J; ADRIAN, RJ; FRIEDRICH, R; NIEUWSTADT, FTM. Fully developed turbulent pipe flow: a comparison between direct numerical simulation and experiment. **Journal of Fluid Mechanics**, Cambridge University Press, v. 268, p. 175–210, 1994.

EVRARD, Fabien; DENNER, Fabian; WACHEM, Berend van. A multi-scale approach to simulate atomisation processes. **International Journal of Multiphase Flow**, Elsevier, v. 119, p. 194–216, 2019.

FABRE, J; LINÉ, A. Modeling of two-phase slug flow. **Annual review of fluid mechanics**, Annual Reviews 4139 El Camino Way, PO Box 10139, Palo Alto, CA 94303-0139, USA, v. 24, n. 1, p. 21–46, 1992.

FAGHRI, Amir; ZHANG, Yuwen. **Transport phenomena in multiphase systems**. [S.l.]: Academic Press, 2006.

FERZIGER, Joel H; PERIĆ, Milovan. **Computational methods for fluid dynamics**. [S.l.]: Springer Berlin, 1996. v. 3.

FRANCOIS, Marianne M; CUMMINS, Sharen J; DENDY, Edward D; KOTHE, Douglas B; SICILIAN, James M; WILLIAMS, Matthew W. A balanced-force algorithm for continuous and sharp interfacial surface tension models within a volume tracking framework. **Journal of Computational Physics**, v. 213, n. 1, p. 141–173, 2006.

FREDERIX, EMA; KOMEN, EMJ; TISELJ, I; MIKUŽ, B. LES of Turbulent Co-current Taylor Bubble Flow. **Flow, Turbulence and Combustion**, Springer, p. 1–25, 2020.

FU, Yucheng; LIU, Yang. Development of a robust image processing technique for bubbly flow measurement in a narrow rectangular channel. **International Journal of Multiphase Flow**, Elsevier Ltd, v. 84, p. 217–228, 2016a.

FU, Yucheng; LIU, Yang. Experimental study of bubbly flow using image processing techniques. **Nuclear Engineering and Design**, Elsevier B.V., v. 310, p. 570–579, 2016b.

FUJIWARA, Akiko; MINATO, Daijyu; HISHIDA, Koichi. Effect of bubble diameter on modification of turbulence in an upward pipe flow. **International Journal of Heat and Fluid Flow**, v. 25, n. 3, p. 481–488, 2004.

GARNIER, C; LANCE, M; MARIÉ, J.L. Measurement of local flow characteristics in buoyancy-driven bubbly flow at high void fraction. **Experimental Thermal and Fluid Science**, v. 26, n. 6, p. 811–815, 2002.

GASKELL, P. H.; LAU, A. K. C. Curvature-compensated convective transport: SMART, A new boundedness- preserving transport algorithm. **International Journal for Numerical Methods in Fluids**, v. 8, n. 6, p. 617–641, 1988.

GLITZ, Karime Louise Zenedin et al. **Modelagem numérica de parâmetros da interface e sua aplicação na simulação do efeito Jamin**. 2012. PhD thesis. Tese de Doutorado, Programa de Pós-Graduação em Engenharia, Univerisade Federal de Santa Catarina, Florianopolis-SC, Brasil.

GOPALA, Vinay R.; VAN WACHEM, B. G M. Volume of fluid methods for immiscible-fluid and free-surface flows. **Chemical Engineering Journal**, v. 141, n. 1-3, p. 204–221, 2008.

HAAS, Tim; SCHUBERT, Christian; EICKHOFF, Moritz; PFEIFER, Herbert. BubCNN : Bubble detection using Faster RCNN and shape regression network. **Chemical Engineering Science**, Elsevier Ltd, v. 216, p. 115467, 2020.

HAELSSIG, Jan B; TREMBLAY, Andre Y; THIBAULT, Jules; ETEMAD, Seyed Gh. Direct numerical simulation of interphase heat and mass transfer in multicomponent vapour–liquid flows. **International Journal of Heat and Mass Transfer**, Elsevier, v. 53, n. 19, p. 3947–3960, 2010.

HÄNSCH, Susann; LUCAS, Dirk; KREPPER, Eckhard; HÖHNE, Thomas. A multi-field two-fluid concept for transitions between different scales of interfacial structures. **International Journal of Multiphase Flow**, Elsevier, v. 47, p. 171–182, 2012.

HAYASHI, Kosuke; HOSODA, Shogo; TRYGGVASON, Gretar; TOMIYAMA, Akio. Effects of shape oscillation on mass transfer from a Taylor bubble. **International journal of multiphase flow**, Elsevier, v. 58, p. 236–245, 2014.

HERRMANN, Marcus. A parallel Eulerian interface tracking/Lagrangian point particle multi-scale coupling procedure. **Journal of computational physics**, Elsevier, v. 229, n. 3, p. 745–759, 2010.

HIBIKI, T.; HOGSETT, S.; ISHII, M. Local measurement of interfacial area, interfacial velocity and liquid turbulence in two-phase flow. **Nuclear Engineering and Design**, v. 184, n. 2-3, p. 287–304, 1998.

HIRT, Cyril W; NICHOLS, Billy D. Volume of fluid (VOF) method for the dynamics of free boundaries. **Journal of computational physics**, Elsevier, v. 39, n. 1, p. 201–225, 1981.

HONKANEN, Markus; SAARENRINNE, Pentti; STOOR, Tuomas; NIINIMÄKI, Jouko. Recognition of highly overlapping ellipse-like bubble images. **Meas. Sci. Technol. Meas. Sci. Technol**, v. 16, n. 16, p. 1760–1770, 2005.

HOSOKAWA, Shigeo; TOMIYAMA, Akio. Bubble-induced pseudo turbulence in laminar pipe flows. **International Journal of Heat and Fluid Flow**, v. 40, p. 97–105, 2013.

HUA, Jinsong. CFD simulations of the effects of small dispersed bubbles on the rising of a single large bubble in 2D vertical channels. **Chemical Engineering Science**, Elsevier, v. 123, p. 99–115, 2015.

IOFFE, Sergey; SZEGEDY, Christian. Batch normalization: Accelerating deep network training by reducing internal covariate shift. **arXiv preprint arXiv:1502.03167**, 2015.

ISHII, Mamoru; HIBIKI, Takashi. **Thermo-fluid dynamics of two-phase flow**. [S.l.]: Springer, 2011.

ISO, IEC; OIML, BIPM. Guide to the Expression of Uncertainty in Measurement. **Geneva, Switzerland**, 1995.

JAIN, Deepak; KUIPERS, J. A.M.; DEEN, Niels G. Numerical study of coalescence and breakup in a bubble column using a hybrid volume of fluid and discrete bubble model approach. **Chemical Engineering Science**, Elsevier, v. 119, p. 134–146, 2014.

JASAK, Hrvoje; JEMCOV, Aleksandar; TUKOVIC, Zeljko, et al. OpenFOAM: A C++ library for complex physics simulations. In: IUC DUBROVNIK, CROATIA. INTERNATIONAL workshop on coupled methods in numerical dynamics. [S.l.: s.n.], 2007. P. 1–20.

JIA, Yangqing; SHELHAMER, Evan; DONAHUE, Jeff; KARAYEV, Sergey; LONG, Jonathan; GIRSHICK, Ross; GUADARRAMA, Sergio; DARRELL, Trevor. Caffe: Convolutional Architecture for Fast Feature Embedding. **arXiv preprint arXiv:1408.5093**, 2014.

JING, L.; KWOK, C. Y.; LEUNG, Y. F.; SOBRAL, Y. D. Extended CFD-DEM for free-surface flow with multi-size granules. **International Journal for Numerical and Analytical Methods in Geomechanics**, 2016.

KANG, Chang-Wei; QUAN, Shaoping; LOU, Jing. Numerical study of a Taylor bubble rising in stagnant liquids. **Physical Review E**, APS, v. 81, n. 6, p. 066308, 2010.

KARN, Ashish; ELLIS, Christopher; ARNDT, Roger; HONG, Jiarong. An integrative image measurement technique for dense bubbly flows with a wide size distribution. **Chemical Engineering Science**, v. 122, p. 240–249, 2015.

KASHINSKY, O. N.; TIMKIN, L. S. Slip velocity measurements in an upward bubbly flow by combined LDA and electrodiffusional techniques. **Experiments in Fluids**, v. 26, n. 4, p. 305–314, 1999.

KASHINSKY, O.N.; TIMKIN, L.S.; CARTELLIER, a. Experimental study of "laminar" bubbly flows in a vertical pipe. **Experiments in Fluids**, v. 15-15, n. 4-5, p. 308–314, 1993.

KEANE, Richard D; ADRIAN, Ronald J. Theory of cross-correlation analysis of PIV images. **Applied scientific research**, Springer, v. 49, n. 3, p. 191–215, 1992.

KIM, Minki; LEE, Jun Ho; PARK, Hyungmin. Study of bubble-induced turbulence in upward laminar bubbly pipe flows measured with a two-phase particle image velocimetry. **Experiments in Fluids**, Springer Berlin Heidelberg, v. 57, n. 4, p. 55, 2016.

KIM, S.; FU, X. Y.; WANG, X.; ISHII, M. Development of the miniaturized four-sensor conductivity probe and the signal processing scheme. **International Journal of Heat and Mass Transfer**, v. 43, n. 22, p. 4101–4118, 2000.

KINGMA, Diederik P; BA, Jimmy. Adam: A method for stochastic optimization. **arXiv preprint arXiv:1412.6980**, 2014.

KOCKX, J. P.; NIEUWSTADT, F. T.M.; OLIEMANS, R. V.A.; DELFOS, R. Gas entrainment by a liquid film falling around a stationary Taylor bubble in a vertical tube. **International Journal of Multiphase Flow**, v. 31, n. 1, p. 1–24, 2005.

KREPPER, Eckhard; LUCAS, Dirk; FRANK, Thomas; PRASSER, Horst-Michael; ZWART, Phil J. The inhomogeneous {MUSIG} model for the simulation of polydispersed flows. **Nuclear Engineering and Design**, v. 238, n. 7, p. 1690–1702, 2008.

KULKARNI, Amol A.; JOSHI, Jyeshtharaj B.; KUMAR, V. Ravi; KULKARNI, Bhaskar D. Application of multiresolution analysis for simultaneous measurement of gas and liquid velocities and fractional gas hold-up in bubble column using LDA. **Chemical Engineering Science**, v. 56, n. 17, p. 5037–5048, 2001.

LAKEHAL, D; MEIER, M; FULGOSI, M. Interface tracking towards the direct simulation of heat and mass transfer in multiphase flows. **International Journal of Heat and Fluid Flow**, Elsevier, v. 23, n. 3, p. 242–257, 2002.

LAU, Y.M.; DEEN, N.G.; KUIPERS, J.A.M. Development of an image measurement technique for size distribution in dense bubbly flows. **Chemical Engineering Science**, v. 94, p. 20–29, 2013.

LEONARD, B.P. The ULTIMATE conservative difference scheme applied to unsteady one-dimensional advection. **Computer Methods in Applied Mechanics and Engineering**, North-Holland, v. 88, n. 1, p. 17–74, 1991.

LEONARD, Brian Phillip. Simple high-accuracy resolution program for convective modelling of discontinuities. **International journal for numerical methods in fluids**, Wiley Online Library, v. 8, n. 10, p. 1291–1318, 1988.

LI, Feng-chen; HISHIDA, Koichi. **Particle Image Velocimetry Techniques and its Applications in Multiphase Systems**. [S.l.]: Elsevier, 2009. v. 37, p. 87–147.

LI, Yong; ZHANG, Jianping; FAN, Liang-Shih. Numerical simulation of gas–liquid–solid fluidization systems using a combined CFD-VOF-DPM method: bubble wake behavior. **Chemical Engineering Science**, Elsevier, v. 54, n. 21, p. 5101–5107, 1999.

LINDKEN, Ralph; MERZKIRCH, W. A novel PIV technique for measurements in multiphase flows and its application to two-phase bubbly flows. **Experiments in Fluids**, v. 33, n. 6, p. 814–825, 2002.

LIOVIC, Petar; LAKEHAL, Djamel. Multi-physics treatment in the vicinity of arbitrarily deformable gas–liquid interfaces. **Journal of Computational Physics**, Elsevier, v. 222, n. 2, p. 504–535, 2007.

LIU, Yi-Peng; WANG, Ping-Yang; WANG, Jing; DU, Zhao-Hui. Investigation of Taylor bubble wake structure in liquid nitrogen by PIV Technique. **Cryogenics**, Elsevier, v. 55, p. 20–29, 2013.

LIU, Qi; LUO, Zheng-Hong. CFD-VOF-DPM simulations of bubble rising and coalescence in low hold-up particle-liquid suspension systems. **Powder technology**, Elsevier, v. 339, p. 459–469, 2018.

LIU, T J; BANKOFF, S G. Structure of air-water bubbly flow in a vertical pipe - I. Liquid mean velocity and turbulence measurements. **International Journal of Heat and Mass Transfer**, v. 36, n. 4, p. 1049–1060, 1993.

LOBANOV, Pavel; PAKHOMOV, Maksim; TEREKHOV, Viktor. Experimental and numerical study of the flow and heat transfer in a bubbly turbulent flow in a pipe with sudden expansion. **Energies**, v. 12, n. 14, 2019.

MALISKA, Clovis Raimundo. **Transferência de calor e mecânica dos fluidos computacional .** [S.l.]: Grupo Gen-LTC, 2017.

MALLOUPPAS, George; WACHEM, Berend van. Large Eddy Simulations of turbulent particle-laden channel flow. **International Journal of Multiphase Flow**, 2013.

MARTÍN ABADI et al. **TensorFlow: Large-Scale Machine Learning on Heterogeneous Systems**. [S.l.: s.n.], 2015. Software available from tensorflow.org. Available from: `https://www.tensorflow.org/`.

MAYOR, T. S.; FERREIRA, V.; PINTO, A. M.F.R.; CAMPOS, J. B.L.M. Hydrodynamics of gas-liquid slug flow along vertical pipes in turbulent regime-An experimental study. **International Journal of Heat and Fluid Flow**, v. 29, n. 4, p. 1039–1053, 2008.

MAYOR, T. S.; PINTO, A. M F R; CAMPOS, J. B L M. An image analysis technique for the study of gas-liquid slug flow along vertical pipes - associated uncertainty. **Flow Measurement and Instrumentation**, v. 18, n. 3-4, p. 139–147, 2007.

MORGADO, A. O.; MIRANDA, J. M.; ARAÚJO, J. D.P.; CAMPOS, J. B.L.M. Review on vertical gas–liquid slug flow. **International Journal of Multiphase Flow**, Elsevier Ltd, v. 85, p. 348–368, 2016.

MOUKALLED, Fadl; MANGANI, L; DARWISH, Marwan, et al. **The finite volume method in computational fluid dynamics**. [S.l.]: Springer, 2016. v. 113.

MUNIZ, Marcelo; SOMMERFELD, Martin. On the force competition in bubble columns: A numerical study. **International Journal of Multiphase Flow**, Elsevier Ltd, p. 103256, 2020.

NAKORYAKOV, V. E.; KASHINSKY, O. N.; BURDUKOV, A. P.; ODNORAL, V. P. Local characteristics of upward gas-liquid flows. **International Journal of Multiphase Flow**, v. 7, n. 1, p. 63–81, 1981.

NEŠIĆ, Srdjan. Key issues related to modelling of internal corrosion of oil and gas pipelines–A review. **Corrosion science**, Elsevier, v. 49, n. 12, p. 4308–4338, 2007.

NICKLIN, D J. Two-phase bubble flow. **Chemical Engineering Science**, Pergamon Press Ltd, v. 17, p. 693–702, 1962.

NOGUEIRA, S.; RIETHMULER, M.L.; CAMPOS, J.B.L.M.; PINTO, A.M.F.R. Flow in the nose region and annular film around a Taylor bubble rising through vertical columns

of stagnant and flowing Newtonian liquids. **Chemical Engineering Science**, v. 61, n. 2, p. 845–857, 2006a.

NOGUEIRA, S.; RIETHMULLER, M. L.; CAMPOS, J. B.L.M.; PINTO, A. M.F.R. Flow patterns in the wake of a Taylor bubble rising through vertical columns of stagnant and flowing Newtonian liquids: An experimental study. **Chemical Engineering Science**, v. 61, n. 22, p. 7199–7212, 2006b.

NOGUEIRA, S.; SOUSA, R. G.; PINTO, A. M.F.R.; RIETHMULLER, M. L.; CAMPOS, J. B.L.M. Simultaneous PIV and pulsed shadow technique in slug flow: A solution for optical problems. **Experiments in Fluids**, Springer-Verlag, v. 35, n. 6, p. 598–609, 2003.

NOH, William F; WOODWARD, Paul. SLIC (simple line interface calculation). In: SPRINGER. PROCEEDINGS of the Fifth International Conference on Numerical Methods in Fluid Dynamics June 28–July 2, 1976 Twente University, Enschede. [S.l.: s.n.], 1976. P. 330–340.

OLSSON, Elin; KREISS, Gunilla. A conservative level set method for two phase flow. **Journal of Computational Physics**, Elsevier, v. 210, n. 1, p. 225–246, 2005.

OSHER, Stanley; SETHIAN, James A. Fronts propagating with curvature-dependent speed: algorithms based on Hamilton-Jacobi formulations. **Journal of computational physics**, Elsevier, v. 79, n. 1, p. 12–49, 1988.

OTSU, Nobuyuki. A threshold selection method from gray-level histograms. **IEEE Transactions on Systems, Man, and Cybernetics**, v. 9, n. 1, p. 62–66, 1979.

PANDELAERS, Lieven; VERHAEGHE, Frederik; WOLLANTS, Patrick; BLANPAIN, Bart. An implicit conservative scheme for coupled heat and mass transfer problems with multiple moving interfaces. **International Journal of Heat and Mass Transfer**, Elsevier, v. 54, n. 5, p. 1039–1045, 2011.

PANG, Mingjun; WEI, Jinjia. Experimental investigation on the turbulence channel flow laden with small bubbles by PIV. **Chemical Engineering Science**, Elsevier, v. 94, p. 302–315, 2013.

PASZKE, Adam et al. Automatic differentiation in PyTorch, 2017.

PEÑA-MONFERRER, C.; MONRÓS-ANDREU, G.; CHIVA, S.; MARTÍNEZ-CUENCA, R.; MUÑOZ-COBO, J. L. A CFD-DEM solver to model bubbly flow. Part I: Model development and assessment in upward vertical pipes. **Chemical Engineering Science**, 2018.

PENG, Zhengbiao; GE, Linhan; MORENO-ATANASIO, Roberto; EVANS, Geoffrey; MOGHTADERI, Behdad; DOROODCHI, Elham. VOF-DEM Study of Solid Distribution Characteristics in Slurry Taylor Flow-Based Multiphase Microreactors. **Chemical Engineering Journal**, Elsevier B.V., p. 124738, 2020.

PINTO, A. M.F.R.; COELHO PINHEIRO, M. N.; CAMPOS, J. B.L.M. Coalescence of two gas slugs rising in a co-current flowing liquid in vertical tubes. **Chemical Engineering Science**, v. 53, n. 16, p. 2973–2983, 1998.

PINTO, AMFR; CAMPOS, JBLM. Coalescence of two gas slugs rising in a vertical column of liquid. **Chemical Engineering Science**, Elsevier, v. 51, n. 1, p. 45–54, 1996.

PIPA, Daniel R; SILVA, Marco J da; MORALES, Rigoberto EM; ZIBETTI, Marcelo VW. Typical bubble shape estimation in two-phase flow using inverse problem techniques. **Flow Measurement and Instrumentation**, Elsevier, v. 40, p. 64–73, 2014.

POLETAEV, Igor; TOKAREV, Mikhail P; PERVUNIN, Konstantin S. Bubble Recognition Using Neural Networks: Application to the Analysis of a Two-Phase Bubbly Jet. **International Journal of Multiphase Flow**, Elsevier Ltd, p. 103194, 2020.

POLONSKY, S; SHEMER, L; BARNEA, D. The relation between the Taylor bubble motion and the velocity field ahead of it. **International Journal of Multiphase Flow**, v. 25, n. 6-7, p. 957–975, 1999a.

POLONSKY, S.; BARNEA, D.; SHEMER, L. Averaged and time-dependent characteristics of the motion of an elongated bubble in a vertical pipe. **International Journal of Multiphase Flow**, v. 25, n. 5, p. 795–812, 1999b.

POZZETTI, Gabriele; PETERS, Bernhard. A multiscale DEM-VOF method for the simulation of three-phase flows. **International Journal of Multiphase Flow**, 2018.

RAFFEL, M; WILLERT, C.E; SCARANO, F; KAHLER, C; WERELEY, S.T; KOMPENHANS, J. **Particle Image Velocimetry**. [S.l.: s.n.], 2018.

RAFFEL, Markus; WILLERT, C E; WERELEY, S T; KOMPENHANS, Jürgen. **Particle Image Velocimetry**. [S.l.: s.n.], 2007. P. 51–60.

RASBAND, Wayne S et al. **ImageJ**. [S.l.]: Bethesda, MD, 1997.

REN, Shaoqing; HE, Kaiming; GIRSHICK, Ross; SUN, Jian. Faster r-cnn: Towards real-time object detection with region proposal networks. In: ADVANCES in neural information processing systems. [S.l.: s.n.], 2015. P. 91–99.

RIDER, William J.; KOTHE, Douglas B. Reconstructing Volume Tracking. **Journal of Computational Physics**, v. 141, n. 2, p. 112–152, 1998.

ROSA, Eugênio S. **Escoamento Multifásico Isotérmico: Modelos de Multifluidos e de Mistura**. [S.l.]: Bookman, 2012.

RUDMAN, Murray. Volume-Tracking Methods for Interfacial Flow Calculations. **International Journal for Numerical Methods in Fluids**, v. 24, n. 7, p. 671–691, 1997.

RUSCHE, Henrik. **Computational fluid dynamics of dispersed two-phase flows at high phase fractions**. 2002. PhD thesis – Imperial College London.

SANTOS, L. M T; COELHO PINHEIRO, M. N. Flow around individual Taylor bubbles rising in a vertical column with water: Effect of gas expansion. **International Journal of Multiphase Flow**, Elsevier Ltd, v. 63, p. 39–51, 2014.

SANTOS, L. M.T.; SENA ESTEVES, M. T.M.; COELHO PINHEIRO, M. N. Effect of gas expansion on the velocity of individual Taylor bubbles rising in vertical columns with water: Experimental studies at atmospheric pressure and under vacuum. **Chemical Engineering Science**, v. 63, n. 18, p. 4464–4474, 2008.

SATHE, Mayur J.; THAKER, Iqbal H.; STRAND, Tyson E.; JOSHI, Jyeshtharaj B. Advanced PIV/LIF and shadowgraphy system to visualize flow structure in two-phase bubbly flows. **Chemical Engineering Science**, v. 65, n. 8, p. 2431–2442, 2010.

SATO, A; SHIROTA, M; SANADA, T; WATANABE, M. Modeling of bouncing of a single clean bubble on a free surface. **Physics of Fluids**, American Institute of Physics, v. 23, n. 1, p. 013307, 2011.

SATO, Y; SADATOMI, M; SEKOGUCHI, K. Momentum and heat transfer in two-phase bubble flow—I. Theory. **International Journal of Multiphase Flow**, Elsevier, v. 7, n. 2, p. 167–177, 1981.

SCAMMELL, Alex; KIM, Jungho. Heat transfer and flow characteristics of rising Taylor bubbles. **International Journal of Heat and Mass Transfer**, Elsevier, v. 89, p. 379–389, 2015.

SCARDOVELLI, Ruben; ZALESKI, Stéphane. Direct numerical simulation of free-surface and interfacial flow. **Annual Review of Fluid Mechanics**, Annual Reviews 4139 El Camino Way, PO Box 10139, Palo Alto, CA 94303-0139, USA, v. 31, n. 1, p. 567–603, 1999.

SERIZAWA, Akimi; KATAOKA, Isao. Turbulence suppression in bubbly two-phase flow. **Nuclear Engineering and Design**, v. 122, n. 1-3, p. 1–16, 1990.

SERIZAWA, Akimi; KATAOKA, Isao; MICHIYOSHI, Itaru. Turbulence Structure of Air-Water Bubbly Flow - I . Measuring Techniques. **International Journal of Multiphase Flow**, v. 2, n. 3, p. 221–233, 1975a.

SERIZAWA, Akimi; KATAOKA, Isao; MICHIYOSHI, Itaru. Turbulence structure of air-water bubbly flow-II. local properties. **International Journal of Multiphase Flow**, v. 2, n. 3, p. 235–246, 1975b.

SETHIAN, JA; SMEREKA, Peter. Level set methods for fluid interfaces. **Annual Review of Fluid Mechanics**, Annual Reviews 4139 El Camino Way, PO Box 10139, Palo Alto, CA 94303-0139, USA, v. 35, n. 1, p. 341–372, 2003.

SHABAN, H.; TAVOULARIS, S. Detached eddy simulations of rising Taylor bubbles. **International Journal of Multiphase Flow**, Elsevier Ltd, v. 0, p. 1–12, 2018.

SHEMER, L.; GULITSKI, A.; BARNEA, D. On the turbulent structure in the wake of Taylor bubbles rising in vertical pipes. **Physics of Fluids**, v. 19, n. 3, 2007.

SHEN, Liping; SONG, Xiangqun; IGUCHI, Manabu; YAMAMOTO, Fujio. A method for recognizing particles in overlapped particle images. **Pattern Recognition Letters**, v. 21, n. 1, p. 21–30, 2000.

SHONIBARE, Olabanji Y.; WARDLE, Kent E. Numerical investigation of vertical plunging jet using a hybrid multifluid-VOF multiphase CFD solver. **International Journal of Chemical Engineering**, Hindawi, v. 2015, p. 1–14, 2015.

SHUR, Mikhail L; SPALART, Philippe R; STRELETS, Mikhail Kh; TRAVIN, Andrey K. A hybrid RANS-LES approach with delayed-DES and wall-modelled LES capabilities. **International Journal of Heat and Fluid Flow**, Elsevier, v. 29, n. 6, p. 1638–1649, 2008.

SILVA, MCF; CAMPOS, JBLM; ARAÚJO, JDP. Mass transfer from a soluble Taylor bubble to the surrounding flowing liquid in a vertical macro tubeA numerical approach. **Chemical Engineering Research and Design**, Elsevier, v. 144, p. 47–62, 2019.

SIMONNET, M.; GENTRIC, C.; OLMOS, E.; MIDOUX, N. Experimental determination of the drag coefficient in a swarm of bubbles. **Chemical Engineering Science**, 2007.

SOUSA, R. G.; PINTO, A. M F R; CAMPOS, J. B L M. Effect of gas expansion on the velocity of a Taylor bubble: PIV measurements. **International Journal of Multiphase Flow**, v. 32, n. 10-11, p. 1182–1190, 2006a.

SOUSA, R. G.; RIETHMULLER, M. L.; PINTO, A. M.F.R.; CAMPOS, J. B.L.M. Flow around individual Taylor bubbles rising in stagnant polyacrylamide (PAA) solutions. **Journal of Non-Newtonian Fluid Mechanics**, v. 135, n. 1, p. 16–31, 2006b.

SOUSA, R.G.; RIETHMULLER, M.L.; PINTO, A.M.F.R.; CAMPOS, J.B.L.M. Flow around individual Taylor bubbles rising in stagnant CMC solutions: PIV measurements. **Chemical Engineering Science**, v. 60, n. 7, p. 1859–1873, 2005.

SRIVASTAVA, Nitish; HINTON, Geoffrey; KRIZHEVSKY, Alex; SUTSKEVER, Ilya; SALAKHUTDINOV, Ruslan. Dropout: a simple way to prevent neural networks from overfitting. **The journal of machine learning research**, JMLR. org, v. 15, n. 1, p. 1929–1958, 2014.

ŠTRUBELJ, L.; TISELJ, I. Two-fluid model with interface sharpening. **International Journal for Numerical Methods in Engineering**, v. 85, n. 5, p. 575–590, 2011.

SUBRAMANIAM, Shankar. Lagrangian-Eulerian methods for multiphase flows. **Progress in Energy and Combustion Science**, v. 39, n. 2-3, p. 215–245, 2013.

SUN, Rui; XIAO, Heng. Diffusion-based coarse graining in hybrid continuum-discrete solvers: Applications in CFD-DEM. **International Journal of Multiphase Flow**, v. 72, p. 233–247, 2015.

SUN, Xiaodong; PARANJAPE, Sidharth; KIM, Seungjin; OZAR, Basar; ISHII, Mamoru. Liquid velocity in upward and downward air-water flows. **Annals of Nuclear Energy**, v. 31, n. 4, p. 357–373, 2004.

TAHA, Taha; CUI, Z.F. CFD modelling of slug flow in vertical tubes. **Chemical Engineering Science**, v. 61, n. 2, p. 676–687, 2006a.

TAHA, Taha; CUI, ZF. CFD modelling of slug flow in vertical tubes. **Chemical Engineering Science**, Elsevier, v. 61, n. 2, p. 676–687, 2006b.

TAITEL, Y; BARNEA, D; DUKLER, AE. Modelling Flow Pattern Transitions for Steady Upward Gas-Liquid Flow in Vertical Tubes. **AIChE Journal**, v. 26, n. 3, p. 345–354, 1980.

TAITEL, Yehuda; BARNEA, Dvora. Two-phase slug flow. In: ADVANCES in heat transfer. [S.l.]: Elsevier, 1990. v. 20. P. 83–132.

TAITEL, Yemada; DUKLER, Abe E. A model for predicting flow regime transitions in horizontal and near horizontal gas-liquid flow. **AIChE journal**, Wiley Online Library, v. 22, n. 1, p. 47–55, 1976.

TOMIYAMA, Akio. Struggle with computational bubble dynamics. **Multiphase Science and Technology**, v. 10, n. 4, p. 369–405, 1998.

TOMIYAMA, Akio; KATAOKA, Isao; ZUN, Iztok; SAKAGUCHI, Tadashi. Drag coefficients of single bubbles under normal and micro gravity conditions. **JSME International Journal Series B Fluids and Thermal Engineering**, The Japan Society of Mechanical Engineers, v. 41, n. 2, p. 472–479, 1998.

TOMIYAMA, Akio; TAMAI, Hidesada; ZUN, Iztok; HOSOKAWA, Shigeo. Transverse migration of single bubbles in simple shear flows. **Chemical Engineering Science**, Elsevier, v. 57, n. 11, p. 1849–1858, 2002.

TSUJI, Yutaka; KAWAGUCHI, Toshihiro; TANAKA, Toshitsugu. Discrete particle simulation of two-dimensional fluidized bed. **Powder technology**, Elsevier, v. 77, n. 1, p. 79–87, 1993.

TUDOSE, E. T.; KAWAJI, M. Experimental investigation of Taylor bubble acceleration mechanism in slug flow. **Chemical Engineering Science**, v. 54, n. 23, p. 5761–5775, 1999.

UBBINK, Onno. **Numerical prediction of two fluid systems with sharp interfaces**. 1997. PhD thesis – Imperial College London.

UNVERDI, Salih Ozen; TRYGGVASON, Grétar. A front-tracking method for viscous, incompressible, multi-fluid flows. **Journal of Computational Physics**, Academic Press Professional, Inc., v. 100, n. 1, p. 25–37, 1992.

VAN HOUT, R.; BARNEA, D.; SHEMER, L. Translational velocities of elongated bubbles in continuous slug flow. **International Journal of Multiphase Flow**, v. 28, n. 8, p. 1333–1350, 2002a.

VAN HOUT, R.; BARNEA, D.; SHEMER, L. Translational velocities of elongated bubbles in continuous slug flow. **International Journal of Multiphase Flow**, v. 28, n. 8, p. 1333–1350, 2002b.

VAN HOUT, R.; GULITSKI, A.; BARNEA, D.; SHEMER, L. Experimental investigation of the velocity field induced by a Taylor bubble rising in stagnant water. **International Journal of Multiphase Flow**, v. 28, n. 4, p. 579–596, 2002c.

VAN LEER, Bram. Towards the ultimate conservative difference scheme. II. Monotonicity and conservation combined in a second-order scheme. **Journal of computational physics**, Academic Press, v. 14, n. 4, p. 361–370, 1974.

VERSTEEG, Henk Kaarle; MALALASEKERA, Weeratunge. **An introduction to computational fluid dynamics: the finite volume method**. [S.l.]: Pearson Education, 2007.

VIANA, Flavia; PARDO, Raimundo; YÁNEZ, Rodolfo; TRALLERO, José L.; JOSEPH, Daniel D. Universal correlation for the rise velocity of long gas bubbles in round pipes. **Journal of Fluid Mechanics**, v. 494, n. 494, s0022112003006165, 2003.

VREMAN, AW. An eddy-viscosity subgrid-scale model for turbulent shear flow: Algebraic theory and applications. **Physics of fluids**, American Institute of Physics, v. 16, n. 10, p. 3670–3681, 2004.

WACHEM, Berend G. M. van; DENNER, Fabian; EVRARD, Fabien. **MultiFlow: A Fully Coupled Multiphase Flow solver**. 2002.

WALLIS, Graham B. **One-dimensional two-phase flow**. [S.l.]: McGraw-Hill New York, 1969. v. 1.

WANG, S.K.; LEE, S.J.; JONES, O.C.; LAHEY, R.T. 3-D turbulence structure and phase distribution measurements in bubbly two-phase flows. **International Journal of Multiphase Flow**, v. 13, n. 3, p. 327–343, 1987.

WARDLE, Kent E; WELLER, Henry G. Hybrid multiphase CFD solver for coupled dispersed/segregated flows in liquid-liquid extraction. **International Journal of Chemical Engineering**, Hindawi, v. 2013, 2013.

WELLEK, RM; AGRAWAL, AK; SKELLAND, AHP. Shape of liquid drops moving in liquid media. **AIChE Journal**, Wiley Online Library, v. 12, n. 5, p. 854–862, 1966.

WHITE, E.T.; BEARDMORE, R.H. The velocity of rise of single cylindrical air bubbles through liquids contained in vertical tubes. **Chemical Engineering Science**, v. 17, n. 5, p. 351–361, 1962.

XUE, Ting; QU, Liqun; CAO, Zhaofeng; ZHANG, Tao. Three-dimensional feature parameters measurement of bubbles in gas-liquid two-phase flow based on virtual stereo vision. **Flow Measurement and Instrumentation**, Elsevier Ltd, v. 27, p. 29–36, 2012.

YAN, Kai; CHE, Defu. A coupled model for simulation of the gas–liquid two-phase flow with complex flow patterns. **International Journal of Multiphase Flow**, Elsevier, v. 36, n. 4, p. 333–348, 2010.

YAN, Kai; CHE, Defu. Hydrodynamic and mass transfer characteristics of slug flow in a vertical pipe with and without dispersed small bubbles. **International Journal of Multiphase Flow**, Elsevier, v. 37, n. 4, p. 299–325, 2011.

YEOH, Guan Heng; TU, Jiyuan. **Computational techniques for multiphase flows**. [S.l.]: Elsevier, 2009.

YOUNGS, David L. Time-dependent multi-material flow with large fluid distortion. **Numerical methods for fluid dynamics**, Academic Press New York, v. 24, p. 273–285, 1982.

ZENIT, Roberto; KOCH, Donald L; SANGANI, Ashok S. Measurements of the average properties of a suspension of bubbles rising in a vertical channel. **Journal of Fluid Mechanics**, Cambridge University Press, v. 429, p. 307–342, 2001.

ZHANG, D.; DEEN, N. G.; KUIPERS, J. A.M. Numerical simulation of the dynamic flow behavior in a bubble column: A study of closures for turbulence and interface forces. **Chemical Engineering Science**, v. 61, n. 23, p. 7593–7608, 2006.

ZHANG, Wen Hui; JIANG, Xiaoya; LIU, Yin Mingzi. A method for recognizing overlapping elliptical bubbles in bubble image. **Pattern Recognition Letters**, Elsevier B.V., v. 33, n. 12, p. 1543–1548, 2012.

ZHOU, Xinquan; DOUP, Benjamin; SUN, Xiaodong. Measurements of liquid-phase turbulence in gas-liquid two-phase flows using particle image velocimetry. **Measurement Science and Technology**, v. 24, n. 12, p. 125303, 2013.

ZIEGENHEIN, T; GARCON, M; LUCAS, D. Particle tracking using micro bubbles in bubbly fl ows. **Chemical Engineering Science**, Elsevier, v. 153, p. 155–164, 2016.

ZIEGENHEIN, T.; LUCAS, D. On sampling bias in multiphase flows: Particle image velocimetry in bubbly flows. **Flow Measurement and Instrumentation**, v. 48, p. 36–41, 2016.

APPENDIX A

Laser diode photocell technique uncertainty analysis

The laser diode photocell results were calculated through the ensemble average, and the evaluation of the uncertainty in measurement followed the guidelines shown in (ISO; OIML, 1995). This section shows how the expanded uncertainty of the Taylor bubble rising velocity (nose and bottom) and its length was determined.

The laser diode photocell detailed on Section 5.3, detects the Taylor bubble passage period by post-processing an analog signal, capturing the instants depicted on Fig. 5.5. By using these time instants, it is possible to compute the bubble rising velocity and its length. In the following paragraphs, to avoid repetition, the ensemble and expanded uncertainty analysis for $U_{tb,B}$ is omitted since it follows the same guidelines of $U_{tb,N}$. For the same reason, the Taylor bubble length procedure will be presented using only $U_{tb,B}$.

For each single experiment, the Taylor bubble nose rising velocity $U_{tb,N}$ is defined as,

$$U_{tb,N} = \frac{L_D}{t_{2,1} - t_{1,1}} = \frac{L_D}{\Delta t_N} \tag{A.1}$$

The ensemble average of this value can be defined as,

$$\left\langle U_{tb,N} \right\rangle = \frac{L_D}{\langle \Delta t_N \rangle} \tag{A.2}$$

where $\langle \Delta t_N \rangle$ is defined for all the $N_{samples}$ experiments in a specific flow condition.

$$\langle \Delta t_N \rangle = \frac{\sum_{i=1}^{N_{samples}} \Delta t_{Ni}}{\sum_{i=1}^{N_{samples}}} \tag{A.3}$$

The expanded uncertainty associated with $U_{tb,N}$ results in (ISO; OIML, 1995),

$$u_{unc}\left(U_{tb,N}\right) = \sqrt{\left(\frac{\partial U_{tb,N}}{\partial L_D}\right)^2 \cdot u_{unc}^2\left(L_D\right) + \left(\frac{\partial U_{tb,N}}{\partial \Delta t_N}\right)^2 \cdot u_{unc}^2\left(\Delta t_N\right)} \tag{A.4}$$

where,

$$u_{unc}\left(L_D\right) = \frac{L_{D,resol.}}{2\sqrt{3}} \tag{A.5}$$

and

$$u_{unc}\left(\Delta t_N\right) = \frac{\max(\Delta t_N) - \min(\Delta t_N)}{\sqrt{3}} + \frac{\sigma(\Delta t_N)}{N_{samples}} \tag{A.6}$$

Thus, the expanded uncertainty is defined as,

$$u_{unc}\left(U_{tb,N}\right) = \sqrt{\left(\frac{1}{\Delta t_N}\right)^2 \cdot u_{unc}^2\left(L_D\right) + \left(-\frac{L_D}{{\Delta t_N}^2}\right)^2 \cdot u_{unc}^2\left(\Delta t_N\right)} \tag{A.7}$$

The Taylor bubble length L_{tb} for a single experiment can be define as,

$$L_{tb} = U_{tb,N} \cdot \Delta t_n = \frac{L_D}{\Delta t_N} \cdot \Delta t_s \tag{A.8}$$

where Δt_n is the period between the instants $t_{s,1}$ and $t_{s,2}$ of the LDR1 ($s = 1$) and LDR2 ($s = 2$) analog signals. Hence, the ensemble average value is defined as,

$$\langle L_{tb} \rangle = \frac{L_D}{\langle \Delta t_N \rangle} \cdot \langle \Delta t_s \rangle \tag{A.9}$$

where the ensemble average time difference $\langle \Delta t_s \rangle$ is calculated analogously as Δt_N.

The, the associated expanded uncertainty for L_{tb} is defined as,

$$u_{unc}\left(L_{tb}\right) = \sqrt{\left(\frac{\partial L_{tb}}{\partial L_D}\right)^2 \cdot u_{unc}^2\left(L_D\right) + \left(\frac{\partial L_{tb}}{\partial \Delta t_s}\right)^2 \cdot u_{unc}^2\left(\Delta t_s\right) + \left(\frac{\partial L_{tb}}{\partial \Delta t_N}\right)^2 \cdot u_{unc}^2\left(\Delta t_N\right)} \tag{A.10}$$

with $u_{unc}\left(\Delta t_N\right)$ using the same expression presented on Eq. A.7.

The final expression for $u_{unc}\left(L_{tb}\right)$ can be expanded to,

$$u_{unc}\left(L_{tb}\right) = \sqrt{\left(\frac{\Delta t_s}{\Delta t_N}\right)^2 \cdot u_{unc}^2\left(L_D\right) + \left(\frac{L_D}{\Delta t_N}\right)^2 \cdot u_{unc}^2\left(\Delta t_s\right) + \left(-\frac{L_D \Delta t_s}{\Delta t_N^2}\right)^2 \cdot u_{unc}^2\left(\Delta t_N\right)} \tag{A.11}$$

APPENDIX B

Supplementary materials

The supplementary materials, including high-speed camera and CFD animation videos, used in this work are listed above. The videos are avaliable for visualizaton **here** and the supplementary materials can be downloaded **here**.

Video 1 - `SM_1_PTV.mp4`

This video present high-speed camera footage, in different bubbly flow configurations, where the bubbles are identified from the method described in Section 3.4.1 and also from the internal contour described in Section 3.4.2.

Video 2 - `SM_2_bub_shape.mp4`

This video presents a high-speed camera footage of each bubbly flow experiment conducted in Chapter 4, highlighting the CNN-based technique described in Chapter 4, where the dispersed bubbles are identified, and its shape reconstructed.

Video 3 - `SM_3_bub_vel.mp4`

This video present dispersed bubbles identified by the CNN-based technique described in Chapter 4, highlighting the instantaneous rising velocities and the reconstructed bubble shape.

Video 4 - `SM_4_tb_and_ptv.mp4`

This video presents the rising motion of Taylor bubbles in a manufactured air-water slug flow with j_l=$21.64 \cdot 10^{-2}$ m/s in different gas superficial velocities j_g. The Taylor bubbles are identified and tracked by the method described in Section 5.3.3, while the PTV technique described in Chapter 3 is used for the experimental characterization of the small dispersed gas bubbles. As a side note, those are earlier results from this thesis, where the method described in Chapter 4 was still on an early development stage. Nevertheless, the CNN-based method is currently coupled with the Taylor bubble tracking computational routines.

Videos 5 and 6 - `SM_5_manufc_ql_1.mp4` and `SM_6_manufc_ql_7.mp4`

These videos presents the high-speed camera footage of the manufactured slug flow condition with superficial liquid velocities of $j_l = 3.09 \cdot 10^{-2}$ m/s (**Video 5**) and $j_l = 21.64 \cdot 10^{-2}$ (**Video 6**). In both footages, it is possible to observe a Taylor bubble rising in different superficial gas velocities, i.e., flowing in bubbly flows with different gas volume fractions. On these videos, it is possible to visualize the Taylor bubble interface deformation and the modifications on the terminal rising velocity by the presence of the dispersed bubbles.

Video 7 - `SM_7_tb_ris_modif.mp4`

This clip presents the rising motion of two Taylor bubbles in the same experimental condition (same liquid j_l and gas j_g superficial velocities), highlighting how the induced fluctuations of the dispersed bubbles modify the instantaneous rising velocity. In this video, the first Taylor bubble rises faster and exhibits a stronger nose deformation.

Videos 8 and 9 - `SM_8_nose_ql_1.mp4` and `SM_9_nose_ql_7.mp4`

These two videos present the rising motion of different Taylor bubbles from different manufactured slug flow conditions in a superficial liquid velocity of $j_l = 3.09 \cdot 10^{-2}$ m/s (**Video 8**) and $j_l = 21.64 \cdot 10^{-2}$ m/s (**Video 9**). In these clips, the reference frame, through the techniques described in Chapter 5, is positioned in the Taylor bubble nose tip position. Therefore, it is easy to visualize the interaction between the small dispersed bubbles and the Taylor bubble, in particular, the nose deformation and lateral tip movement oscillation. Additionally, the reconstructed nose shape is shown by a green line in those footages, while a red dot presents the nose tip position.

Videos 10 and 11 - `SM_10_bottom_ql_1.mp4` and `SM_11_bottom_ql_7.mp4`

As in Videos 5 and 6, these two clips present the rising motion of different Taylor bubbles from different manufactured slug flow conditions in a superficial liquid velocity of $j_l = 3.09 \cdot 10^{-2}$ m/s (**Video 10**) and $j_l = 21.64 \cdot 10^{-2}$ m/s (**Video 11**). However, the reference frame is positioned on the Taylor bubble bottom. From those clips, one can visualize the formation of bubble recirculation region on the Taylor bubble wake and the motion of the dispersed bubbles that exits the liquid film. Also, the modification of the Taylor bubble oscillation pattern by the dispersed bubbles is visualized.

Video 12 - `SM_12_dbm_val.mp4`

This video presents an animation of a DBM simulation used in the validation study presented in Chapter 7. The clip shows the time evolution of the instantaneous liquid velocity field and the movement of the dispersed bubbles in a transversal section of the domain. Together, with the liquid velocity field, a transient plot presents the instantaneous liquid velocity in a probe point located at the domain centre, showing a transient-like "signal" reflecting the flow fluctuations from the dispersed bubbles.

Videos 13 and 14 - `SM_13_vof_dbm_all.mp4` and `SM_14_vof_dbm_zoom.mp4`

Video 13 presents an animation of the transient VOF-DBM air-glycerol stagnant column simulations in different background bubbly configurations, where the whole 20.D length numerical domain is shown. In this animation, it is possible to visualize the three-dimensional motion of the dispersed bubbles and the induced Taylor bubble deformation due to the latter. In order to better observe the modifications of the different interfacial length scale interaction, **Video 14** presents the latter video with a close-up view on the Taylor bubble.

Video 15 - `SM_15_vof_dbm_center.mp4`

This animation presents the results of the transient VOF-DBM air-glycerol stagnant column simulations in different background bubbly configurations, presenting the instantaneous axial and liquid velocity around the Taylor bubble. In addition, the video presents the interface deformation of the Taylor bubble and the movement of the small dispersed bubbles which are crossing the middle plane section from the contour plots. The black circles represent the dispersed bubbles with its corresponding cross-sectional diameter on the visualization plane.

Video 16 - SM_16_vof_aw.mp4

This clip presents animation of the VOF air-water simulations (absent of dispersed bubbles), showing the estimated Taylor bubble shape ($\gamma = = 0.5$ iso-contour) and the axial (z-direction) liquid distribution around the bubble for the stagnant column situation (left) and co-current flow with $j_l = 3.09 \cdot 10^{-2}$ m/s (right).

Videos 17 and 18 - SM_17_vlag_AW.mp4 and SM_18_vlag_zoom_AW.mp4

Video 17 presents an animation of the transient VOF-DBM air-water co-current simulations in different background bubbly configurations, where the whole 20.D length numerical domain is shown. In this animation, it is possible to visualize the three-dimensional motion of the dispersed bubbles and the induced Taylor bubble deformation due to the latter. In order to better observe the modifications of the different interfacial length scale interaction, **Video 18** presents the latter video with a close-up view on the Taylor bubble.

Video 19 - SM_19_vof_dbm_center_AW.mp4

This animation presents the results of the transient VOF-DBM air-water co-current simulations in different background bubbly configurations, presenting the instantaneous axial and liquid velocity around the Taylor bubble. In addition, the video presents the interface deformation of the Taylor bubble and the movement of the small dispersed bubbles which are crossing the middle plane section from the contour plots. The black circles represent the dispersed bubbles with its corresponding cross-sectional diameter on the visualization plane.